Characterisation and Application of an Ebola Virus Glycoprotein Pseudotyped Influenza Virus (E-S-FLU)



Huiyuan Julie Xiao

Exeter College

&

Human Immunology Unit

Weatherall Institute of Molecular Medicine

University of Oxford

A thesis submitted for the degree of Doctor of Philosophy

Hilary 2019

Word count (main text only): approximately 48,000 words

ABSTRACT

Characterisation and Application of an Ebola Virus Glycoprotein Pseudotyped Influenza Virus (E-S-FLU)

Huiyuan Julie Xiao D.Phil.

Exeter College Hilary 2019

Ebola virus (EBOV) is a single-stranded RNA virus from the Filoviridae family. It is a biosafety level 4 pathogen, and infection causes fatal haemorrhagic fever in humans, yet no approved vaccines or therapeutics are available.

We describe a new EBOV surrogate, E-S-FLU, a single-cycle Influenza virus pseudotyped (coated) with the EBOV glycoprotein (GP). E-S-FLU does not contain any genetic information from EBOV, and encodes enhanced green fluorescence protein as a reporter that replaces the Influenza virus hemagglutinin. It can thus be handled in biosafety level 1 containment for laboratory analysis. We show that E-S-FLU mimics wild-type EBOV during the process of cell entry. Infection of cells by E-S-FLU was dependent on the Niemann-Pick type C1 protein, the well-characterised receptor for EBOV entry at the late endosomal/lysosomal membrane. In addition, known small molecule entry inhibitors that blocked wild-type EBOV infection *in vitro* blocked E-S-FLU with similar potency.

We employed E-S-FLU to screen a library of 1,280 pharmacologically active compounds for inhibition of virus entry. We identified 215 inhibitory compounds with very dispersed targets. The majority of the inhibitors shared a cationic amphiphilic feature, and this had the strongest correlation with specific inhibition of E-S-FLU infection, regardless of the pharmacological group of the drugs.

The two-pore channels 1 and 2 (TPC1/2), and acid sphingomyelinase (ASM), both localised in the lysosomal membrane, have been proposed as candidate drug targets. To test this, we knocked out the corresponding genes from HeLa cells using the CRISPR/Cas 9 technique. We showed that EBOV-GP dependent infection by E-S-FLU was not affected in TPC1/2 or ASM deficient HeLa cells, and concluded that these proteins are not required for EBOV infection.

Our results suggest that the most effective cationic amphiphilic drugs act by concentrating in the lysosome, and by binding and destabilising the GP, and intercalating in the lysosomal membrane, may interfere directly with the fusion function of the EBOV-GP.

DECLARATION

I, declare that the majority of the work described in this thesis represents my own work, except where stated below. Contributions made by others have been acknowledged within the text and in the individual figure legends. It has never been submitted for any other degree.

A substantial part of my D.Phil. work has been published (Xiao et al., *Journal of Virology*, **92**, e00941-17) and I played a major role in writing the manuscript (along with my supervisor Professor Alain Townsend). I have used some of the text and figures from the paper without modification in this thesis, with a citation to the paper.

Chapter 3 Development and characterisation of E-S-FLU

- GP-HA hybrid protein was designed and developed by Alain Townsend.
- Holly Sadler and Alain Townsend in the lab have designed and engineered a fusion-defective HA protein: H7CFv3, a mutated version of an H7 haemagglutinin protein sourced from H7N9 Influenza (A/HK/125/2017).
- Experiments in section 3.5: Dual pseudotyped S-FLU H7CFv3/E-S-FLU, was done together by the author and a medical student Declan Pang as part of his undergraduate project.

Chapter 4 Drug screening and mechanisms of inhibition of EBOV infection

- Experiments described in section 4.3.4 were done by our collaborators Nick Platt and Frauke Fuchs (Department of Pharmacology, University of Oxford).
- Lysosomal permeability staining experiment (section 4.3.5) was conducted by our collaborator Gokhan Yilmaz (Department of Pharmacology, University of Oxford).

Chapter 5 Niemann-Pick Type C 1/2 Proteins, Acid Sphingomyelinase and EBOV Infection

- The design and verification of the guide sgRNAs used to knock out *NPC2* and *SMPD1* gene from HeLa cells were carried out by Dr Philip Hublitz from the Genome Editing Service at the Weatherall Institute of Molecular Medicine.
- The sphingosine HPLC experiment was conducted together with Mylene Huebecker (Platt lab, Department of Pharmacology, University of Oxford).

- Our collaborator Doris Höglinger (Heidelberg University) measured sphingosine trafficking in live cells by using a photo-crosslinkable and clickable trifunctional sphingosine (pacSph).

- Single nucleotide polymorphisms in NPC1 was identified by Mary Carrington (National Institutes of Health) by genotyping NPC1 genes from a small cohort of African patients who died or survived EBOV infection after the 2014-2015 outbreak.

Chapter 6 Calcium and EBOV Infection

- The design and verification of the guide sgRNAs used to knock out *TPCN1* and *TPCN2* gene from HeLa cells were carried out by Dr Philip Hublitz from the Genome Editing Service at the Weatherall Institute of Molecular Medicine.

- Functional assay of *TPCN1*KO and *TPCN2*KO HeLa cells was conducted by our collaborator Anthony Morgan (Galione group, Department of Pharmacology, University of Oxford).

Chapter 7 Drugs that bind EBOV-GP

- The crystallography and thermal shift assay experiments were done by Dr Jingshan Ren and Dr Yuguang Zhao (Stuart group, STRUBI, University of Oxford).

- Our collaborator Peter Halfmann (University of Wisconsin-Madison) conducted experiment to select toremifene-resistant mutant EBOV viruses in the presence of GP-binding drugs, and measured the growth rate in the presence of toremifene and arbidol.

ACKNOWLEDGEMENTS

I would like to take this opportunity to thank everyone who has provided tremendous help during my D.Phil. study, and without which I would not have been able to complete this thesis.

First of all, I would like to express my appreciation to my supervisor Professor Alain Townsend. At the time when I was applying for my D.Phil., my Master supervisor Christoph Tang, who I also must give thanks to, said to me, Alain is the best supervisor in Oxford. If he takes you, you must go. Now after four years and a half, I can say with full certainty that I have really received the best supervision and support. Alain always shows great interest in the topics we are working on, sometimes he enthusiastically reads papers and sends references to us in the middle of the night (no complaints really!). He understands the ups and downs we may encounter in the lab as he is still doing experiments every day. He always replies to our emails promptly, which is one privilege of being his student, and we can always nudge him in his office “with an open door”. When I had to extend my study, he very generously supported me with a stipend from the Townsend-Jeantet Fund. Not to mention his free lessons on British slang and poetry, from which I’m afraid I have picked up only a little, such as “Ship-shaped and Bristol fashion”, which I hope can be used to describe this thesis.

Many thanks for everyone in the Townsend lab, for Pramila Rijal (now Dr Rijal!), Lisa Schmanski, Holly Sadler, Francesca Donnellan, Jack Tan, also our previous group member Dr Tim Powell, Samara Rosendo Machado and my student Declan Pang. A special thank note you Wenwen Xu, who told me all the tips when I came for an interview and assured to me how fantastic this lab was (and still is) when I visited. Everyone has been very friendly and helpful, and the group has a very collaborative and pleasant atmosphere. We are all familiar with each other’s work and ready to help and brainstorm for ideas in lab meetings, lunch and uncountable coffee breaks. I am very grateful for everyone’s help during my thesis writing, for loads of useful advice, and for patiently proofreading the chapters for me.

We have built up an excellent collaboration with the Department of Pharmacology at Oxford University. I would like to thank my collaborators Frances Platt, Nick Platt and everyone who contributed to the Ebola and drug project: Gokhan Yilmaz, Mylene Huebecker, Frauke Fuchs and Paul Fineran. I also would like to thank Anthony Morgan, Margarida Ruas da Silva and Antony Galione from the Galione lab for the work related to TPC, calcium blocking drugs and EBOV. They have provided a lot of support and expertise in understanding pharmacological molecules, the mechanism of action of Niemann Pick type C1 protein, and calcium channels. Thanks for the Galione group for providing the Tpcn1/2KO murine cell-

lines and Wim Annaert from Vlaams Instituut voor Biotechnologie for providing the NPC1 KO HeLa cell lines.

I want to express my appreciation to our collaborator Peter Halfmann. Although we have never met, Peter has done much exciting work in selecting toremifene-resistant mutants. Many thanks to Edward Wright, who has provided me with the EBOV-GP pseudotyped lentivirus right after he moved to Sussex University, and transported the reagents in person.

Thanks to Doris Höglinger from Heidelberg University, who has generated the most beautiful images in this thesis. Moreover, she was still replying to my emails when she was waiting for her labour. I sincerely wish all goes well with her new-born baby and the family.

I would like to thank many of my friends and colleagues at the Weatherall Institute of Molecular Medicine, who made it a wonderful place to study and work. Thanks to Philip Hublitz for the amazing support on the CRISPR projects, and his advice and help when I got stuck with PCRs. Thanks to our incredible team in the WIMM FACS facility. Especially for Craig Waugh, Kevin Clark, also to Sally-Ann Clark and Paul Sopp. They are very lovely and supportive, thanks for their patience in doing numerous long sorts for me. I also would like to thank Alastair Waugh, Matthew Husband, Keith Bourne and Elizabeth Stephens from the Human Immunology Unit for their excellent support.

I am grateful to Jan Rehwinkel and Persephone Borrow for their solid advice and guidance during my Transfer and Confirmation of status examinations.

I would also like to thank my friends and other fellow students at the WIMM and from Exeter college and apologise for not being able to meet up more often for dinners.

Last but not least, I would like to express my sincere appreciation to my beloved family, who are always very supportive of my education.

TABLE OF CONTENTS

TABLE OF CONTENTS i

LIST OF ABBREVIATIONS viii

LIST OF FIGURES xii

LIST OF TABLES xviii

LIST OF APPENDICES xix

Chapter 1 General Introduction 1

1.1 Ebola virus 1

1.1.1 Virus taxonomy and nomenclature 1

1.1.2 Outbreak history 2

1.1.3 Pathogenesis, tropism and transmission 4

1.1.4 Virus biology 6

1.2 The mechanism of cell entry by Ebola virus 11

1.2.1 Attachment 12

1.2.2 Macropinocytosis 14

1.2.3 Endocytosis and cathepsin B/L processing 15

1.2.4 Receptor binding 17

1.2.5 Fusion 19

1.2.6 Calcium ions and calcium channel in EBOV entry 22

1.3 Ebola virus surrogates 22

1.4 Vaccine candidates for Ebola virus disease 27

1.5 Therapeutics for Ebola virus disease 29

1.6 Aim of this study 33

Chapter 2 Materials and Methods 35

2.1 Materials and reagents 35

2.1.1 Buffers and media 35

2.1.2 Drugs and small molecules 36

2.1.3 Cells and culture conditions 36

2.1.4 Primers and sgRNAs (guide RNA for CRISPR/Cas 9 knockout) 38

2.1.5 Pseudotyped viruses 41

2.1.6 Antibodies and plasma samples 42

2.2 Pseudotyped influenza virus (S-FLU) production 43

2.2.1 Seed S-FLU virus 43

2.2.2 E-S-FLU virus production 44

2.2.3 GP-HA hybrid protein pseudotyping S-FLU 45

2.2.4 Dual pseudotyped S-FLU: H7CFv3/E-S-FLU 46

2.3 Pseudotyped virus infection and titration 47

2.3.1 S-FLU virus titration on MDCK-SIAT1 cells 47

2.3.2 S-FLU virus infection in HeLa and MEF cells 48

2.3.3 S-FLU infection in B cell-line 48

2.3.4 GP-lentivirus infection and titration 49

2.4 Monitoring E-S-FLU and H5-S-FLU virus growth 49

2.4.1 S-FLU virus growth curve 49

2.4.2 Imaging S-FLU replication by IncuCyte® 50

2.5 Antibody micro-neutralisation (MN assay) 50

2.6 Drug inhibition assay 51

2.6.1 Individual drug titration 51

2.6.2 WGA staining as an estimate of drug toxicity 52

2.6.3 CLARIOstar® plate reader settings 52

2.6.4 LOPAC®1280 library screen 53

2.7 E-S-FLU virus sandwich ELISA assay 54

2.8 Fluorescence microscope pictures 55

2.9 FACS sorting 55

2.10 LogP and pKa^{base} calculation 55

2.11 NPC1 phenotype assays 56

2.11.1 LysoTracker® staining 56

2.11.2 Filipin staining 56

2.11.3 Amplex® Red staining 57

2.11.4 Sphingomyelin OlyA staining 57

2.12 Lysosomal membrane permeability staining 58

2.13 Synergy drug inhibition assay 59

2.13.1 Synergy drug inhibition experiment 59

2.13.2 Synergy calculation and Bliss additivity 60

2.14 CRISPR/Cas 9 genetic knockout 63

2.14.1 Choosing target exon and designing sgRNAs 64

2.14.2 Verification of sgRNAs by surveyor assay 64

2.14.3 HeLa cell sgRNA transfection and single cell cloning 66

2.15 Genomic DNA isolation 67

2.16 Genomic DNA PCR 68

2.17 RNA isolation 70

2.18 Reverse transcriptase PCR (RT-PCR) 70

2.19 DNA gel band isolation and sequencing 71

2.20 Sphingosine high-performance liquid chromatography (HPLC)… 72

2.21 Visualisation of sphingosine trafficking in HeLa cells 74

2.22 NPC1 mutagenesis and cloning 75

2.23 Ca^{2+} signal imaging 78

2.24 Thermolysin treatment of E-S-FLU 79

2.25 EBOV-GP mutagenesis 80

2.26 Immunofluorescence assay (IFA) 81

2.27 Drug selected EBOV escape mutant 82

2.27.1 Growth kinetics of wild-type and toremifene resistant viruses… 83

Chapter 3 Development and characterisation of E-S-FLU 85

3.1 Introduction 85

3.2 E-S-FLU production and titration 89

3.3 E-S-FLU characterisation 96

3.3.1 E-S-FLU infection requires NPC1 96

3.3.2 E-S-FLU neutralisation by anti-EBOV-GP antibodies 97

3.3.3 E-S-FLU neutralisation with NIBSC immunoglobulin samples..... 101

3.3.4 E-S-FLU inhibition by various EBOV inhibitors 103

3.4 GP-HA hybrid pseudotyping 108

3.5 Dual pseudotyped S-FLU: H7CFv3/E-S-FLU 112

3.5.1 Rationale of the H7CFv3/E-S-FLU design 112

3.5.2 H7CFv3/E-S-FLU production and titration..... 115

3.5.3 H7CFv3/E-S-FLU infection is NPC1 dependent..... 117

3.5.4 Antibody neutralisation of H7CFv3/E-S-FLU..... 119

3.5.5 Drug inhibition of H7CFv3/E-S-FLU 121

3.5.6 H7CFv3/E-S-FLU infection of B lymphocytes 124

3.6 Discussion and future work 125

Chapter 4 Drug screening and mechanisms of inhibition of EBOV infection 135

4.1 Introduction 141

4.2 LOPAC®1280 library screen 141

4.2.1 E-S-FLU vs. H5-S-FLU drug screening results 142

4.2.2 Comparison with the screen by Johansen *et al.* 145

4.3 Dissecting drug inhibition mechanisms 147

4.3.1 Reduced infection vs. reduced viral gene expression ... 148

4.3.2 Long-QT drugs 153

4.3.3 Cationic amphiphilic drugs (CADs) 156

4.3.4 NPC1 phenotype inducers 160

4.3.5 CADs that induced lysosomal membrane permeability . 172

4.4 Drug combinations and synergy 177

4.5 Discussion and future work 182

4.5.1 E-S-FLU is a useful tool for drug screens 183

4.5.2 Long-QT: a side effect to watch out for in treating EBOV 185

4.5.3 CADs vs. EBOV: what is the target? 187

4.5.4 Synergistic drug combinations for treating EBOV 195

Chapter 5 Niemann-Pick Type C 1/2 Proteins, Acid Sphingomyelinase and EBOV Infection 205

5.1 Introduction 205

5.2 EBOV infection in NPC2 deficient cells 209

5.2.1 *NPC2* knockout design 209

5.2.2 Genetic confirmation of *NPC2*KO HeLa cells 213

5.2.3 Functional assays of *NPC2*KO HeLa cells 215
5.2.4 EBOV-GP pseudotyped virus infection in NPC2 deficient cells 220
5.3 EBOV infection in ASM deficient cells 223
5.3.1 *SMPD1*KO design 223
5.3.2 Genetic confirmation of *SMPD1*KO cells 226
5.3.3 Functional assays of *SMPD1*KO cells 229
5.3.4 EBOV-GP pseudotyped virus infection in ASM deficient cells 231
5.4 NPC1 polymorphism and EBOV infection 233
5.5 Discussion and future work 240
5.5.1 NPC2 and EBOV-GP dependent infection 241
5.5.2 ASM and EBOV-GP dependent infection 242
5.5.3 EBOV and NPC1 polymorphism 246
Chapter 6 Calcium and EBOV Infection 249
6.1 Introduction 249
6.2 Drugs that affect Ca^{2+} flux and EBOV inhibition 251
6.3 EBOV infection of embryonic fibroblasts from *Tpcn1/2* knockout mice 260
6.4 EBOV infection in *TPCN1/2* knockout HeLa cells 264
6.4.1 *TPCN1* and *TPCN2* knockout design 264
6.4.2 Genetic confirmation of *TPCN1*KO and *TPCN2*KO cells 269
6.4.3 Functional assays of TPCN1KO and TPCN2KO HeLa cells 276

6.4.4 EBOV-GP pseudotyped virus infection in TPC1/2 deficient cells 278

6.5 Overexpression of pore-mutants of TPC2 and E-S-FLU infection 280

6.6 Discussion and future work 285

6.6.1 TPC1/2 and EBOV-GP dependent infection 287

6.6.2 Calcium channel blockers and EBOV-GP dependent infection 289

Chapter 7 Drugs that bind EBOV-GP 295

7.1 Introduction 295

7.2 EBOV-GP binding drugs 302

7.3 Drug inhibition of thermolysin treated E-S-FLU 306

7.4 Site-directed mutagenesis of the drug binding pocket 310

7.5 Drug-resistant EBOV mutants 322

7.6 Discussion and future work 325

7.6.1 Drugs that bind EBOV-GP 325

7.6.2 Site-directed mutagenesis of the drug binding site 329

7.6.3 Toremifene-resistant EBOV-GP mutations 330

7.6.4 Summary 332

Chapter 8 Final Summary 335

Bibliography 345

LIST OF ABBREVIATIONS

BDBV	Bundibugyo virus
BOMV	Bombali virus
BSA	Bovine serum albumin
BSL	Biosafety level
CAD	Cationic amphiphilic drug
CDC	Centers for Disease Control and Prevention
CFR	Case fatality rate
ChAd	Chimpanzee adenovirus
CID_{50}	Cell infective dose at 50%
CIP	Calf intestinal alkaline phosphatase
CTD	Cytoplasmic domain
DAPI	4',6-diamidino-2-phenylindol
DMEM	Dulbecco's modified eagle's medium
DNA	Deoxyribonucleic acid
DRC	Democratic Republic of the Congo
EBOV	Ebola virus
EBV	Epstein-Barr virus
EC50	Half maximal effective concentration
eGFP	enhanced green fluorescence protein
ELISA	Enzyme-linked immunosorbent assay
EVD	Ebola virus disease
FACS	Fluorescence activated cell sorting
FCS	Fetal calf serum

FITC	Fluorescein isothiocyanate
FL	Fusion loop
GC	Glycan cap
GP	Glycoprotein
HA	Haemagglutinin
HR	Heptad repeats
hERG	Human ether-a-go-go
HPAI	Highly pathogenic avian Influenza
HRP	Horseradish peroxidase
IC50	Half maximal inhibitory concentration
IFA	Immunofluorescence assay
IFL	Internal fusion loop
LB	Luria broth
LGAL-3	Lysosomal galactin-3
MAb	Monoclonal antibody
MDCK	Madin-Darby canine kidney
MEURI	Monitored emergency use of unregistered and investigational interventions statement
MFI	Median fluorescence intensity
MLD	Mucin-like domain
MN	Micro-neutralisation
MPER	Membrane-proximal external region
MVA	Modified vaccine Ankara
MW	Molecular weight
NA	Neuraminidase

NAADP	Nicotinic acid adenine dinucleotide phosphate
NCBI	National Center for Biotechnology Information
NEB	New England Biolabs
NIBSC	National Institute for Biological Standards and Control
NP	Nucleoprotein
NPC	Niemann-Pick type C
PBS	Phosphate-buffered saline
PCR	Polymerase chain reaction
PKR	protein kinase R
RBR	Receptor binding region
RESTV	Reston virus
RNA	Ribonucleic acid
RPM	Revolutions per minute
RPMI	Roswell Park Memorial Institute
RT-PCR	Reverse transcription polymerase chain reaction
S-FLU	Signal minus Influenza
sGP	Soluble glycoprotein
SIAT	Sialytransferase
ssGP	Small soluble glycoprotein
SUDV	Sudan virus
TAFV	Taï Forest virus
$TCID_{50}$	Tissue culture infectious dose at 50%
TIM	T-cell immunoglobulin and mucin domain
TM	transmembrane
TMD	Transmembrane domain

TPC	two-pore channel
TPCK	Tosyl phenylalanyl chloromethyl ketone
VGM	Virus growth medium
VP	Viral protein
VSV	Vesicular stomatitis virus
WHO	World Health Organization

LIST OF FIGURES

Figure 1. 1 Model of Ebola virus entry, cellular tropism and pathogenesis 5

Figure 1. 2 Ebola virus structure..... 7

Figure 1. 3 EBOV GP structure 9

Figure 1. 4 Transcriptional editing for GP gene expression 11

Figure 1. 5 Schematic diagram of the pathway of EBOV cell entry..... 12

Figure 1. 6 Proposed mechanisms of EBOV attachment to cell..... 14

Figure 1. 7 Mechanism of EBOV-GP proteolysis by cathepsin B and L..... 16

Figure 1. 8 EBOV GP fusion..... 21

Figure 1. 9 Production of EBOV-GP pseudotyped virus and virus-like particles 25

Figure 2. 1 Schematic diagram demonstrating drug synergy assay 61

Figure 2. 2 Double sgRNAs CRISPR/Cas 9 strategy 63

Figure 2. 3 Surveyor assay verifying sgRNAs in 293T cells..... 65

Figure 2. 4 gDNA PCR conditions 69

Figure 2. 5 RT-PCR conditions..... 71

Figure 2. 6 Photo-cross-linkable and clickable sphingosine (pacSph) 74

Figure 2. 7 NPC1 mutagenesis PCR condition 77

Figure 2. 8 EBOV-GP mutagenesis PCR condition..... 81

Figure 3. 1 S-FLU design and infection mechanism 87

Figure 3. 2 Stable expression of EBOV-GP on the surface of transduced MDCK-SIAT1 cells 91

Figure 3. 3 Pseudotyping of S-FLU virus with EBOV-GP..... 92

Figure 3. 4 Real-time S-FLU spreading in E-SIAT and H5-SIAT cells 94

Figure 3. 5 E-S-FLU virus requires NPC1 receptor expression for infection of HeLa cells 97
Figure 3. 6 Antibody neutralisation of pseudotyped E-S-FLU virus, H5-S-FLU virus, and EBOV-GP-pseudotyped lentivirus 98
Figure 3. 7 Fluorescence microscopy pictures of antibody neutralisation assays 99
Figure 3. 8 Sequence alignment of NPC1 protein domain C region..... 100
Figure 3. 9 E-S-FLU and wild-type EBOV neutralising NIBSC plasma samples 103
Figure 3. 10 Tetrandrine inhibition assay with the E-S-FLU and H5-S-FLU pseudotyped viruses 104
Figure 3. 11 Fluorescence microscopy pictures of tetrandrine inhibition assay 105
Figure 3. 12 Design of GP-HA hybrid protein 109
Figure 3. 13 Stable expression of EBOV-GP and GP-HA hybrid protein on the surface of transduced MDCK-SIAT1 cell-line 110
Figure 3. 14 No infective pseudotyped S-FLU produced from EH-SIAT cells .. 111
Figure 3. 15 Detection of pseudotyped S-FLU particle by virus ELISA 112
Figure 3. 16 Design and production of H7CFv3/E-SIAT cell 115
Figure 3. 17 Virus titration of H7CFv3/E-S-FLU and E-S-FLU 117
Figure 3. 18 H7CFv3/E-S-FLU requires NPC1 receptor expression for infection of HeLa cells..... 118
Figure 3. 19 Antibody micro-neutralisation assay of H7CFv3/E-S-FLU 120
Figure 3. 20 Drug inhibition assay with the E-S-FLU and H7CFv3/E-S-FLU pseudotyped viruses 123
Figure 3. 21 H7CFv3/E-S-FLU infection in B lymphocytes..... 124

Figure 4. 1 LOPAC®1280 library drug composition ……141

Figure 4. 2 Drugs from the LOPAC®1280 library that inhibited the E-S-FLU virus 144

Figure 4. 3 Fluorescence microscope pictures of “reduced” vs. “dimmer” inhibitors 151

Figure 4. 4 FACS analysis pattern of drug that causes the “reduced” vs. “dimmer” inhibition 152

Figure 4. 5 hERG binders in the E-S-FLU drug inhibition assay 155

Figure 4. 6 LogP, pKa^{base} plot for 65 most potent E-S-FLU inhibitors 160

Figure 4. 7 NPC disease pathogenesis model 161

Figure 4. 8 Drugs that bind NPC1 directly 163

Figure 4. 9 Lysotracker staining of drug treated cells 167

Figure 4. 10 Filipin fluorescence staining microscopy 168

Figure 4. 11 Amplex® Red cholesterol assay 169

Figure 4. 12 Sphingomyelin OlyA staining 170

Figure 4. 13 LGAL-3 punctate staining in drug treated MDCK-SIAT1 cells 176

Figure 4. 14 Assay for synergy by drug combinations 178

Figure 4. 15 Synergy drug screen results 180

Figure 4. 16 Summary of two synergy drug screens 181

Figure 4. 17 EBOV entry in the lysosome 188

Figure 4. 18 Drug inhibition mechanism 1: NPC1 binding drugs 190

Figure 4. 19 Drug inhibition mechanism 2: additional host target 192

Figure 4. 20 Drug inhibition mechanism 3: target membrane fusion 194

Figure 4. 21 EBOV cell entry mechanism and potential drug modes of action 196

Figure 5. 1 Structure of bovine NPC2 protein …… 210

Figure 5. 2 Schematic diagram of *NPC2* exon 3 knockout by CRISPR/Cas 9 . 211

Figure 5. 3 NPC2 specific sgRNAs tested in surveyor assays 212

Figure 5. 4 *NPC2*KO HeLa genomic DNA PCR verification 214

Figure 5. 5 RT-PCR characterising *NPC2*KO HeLa clones..... 215

Figure 5. 6 Sphingosine level in *NPC1*KO and *NPC2*KO cells..... 217

Figure 5. 7 Pulse-chase photo-crosslinkable sphingosine in HeLa cells..... 218

Figure 5. 8 Sphingosine localisation and trafficking in *NPC1/2*KO HeLa cells . 219

Figure 5. 9 E-S-FLU infection in *NPC2*KO HeLa cells..... 221

Figure 5. 10 GP-lentivirus infection of *NPC1*KO and *NPC2*KO HeLa cells 222

Figure 5. 11 Sphingolipid metabolism and sphingomyelinase pathway 223

Figure 5. 12 Schematic diagram of *SMPD1* gene exon 2 knockout design by CRISPR/Cas 9 224

Figure 5. 13 *SMPD1* specific sgRNAs tested in surveyor assays 225

Figure 5. 14 *SMPD1*KO HeLa genomic DNA PCR verification 227

Figure 5. 15 Genetic modification of *SMPD1* with exon 2 flipped and reinserted 228

Figure 5. 16 RT-PCR characterisation of *SMPD1*KO HeLa clones..... 229

Figure 5. 17 Sphingosine level in *SMPD1*KO cells..... 230

Figure 5. 18 EBOV-GP pseudotyped virus infection in *SMPD1*KO HeLa cells 232

Figure 5. 19 NPC1 polymorphism and domain structure..... 235

Figure 5. 20 E-S-FLU infection in HeLa cells expressing NPC1 variants..... 237

Figure 5. 21 Sphingosine transport in NPC1 variant expressing HeLa cells 239

Figure 5. 22 Fan's model of drugs inhibiting EBOV via ASM 245

Figure 6. 1 LogP/pKa^{base} diagram for calcium-related drugs …… 258

Figure 6. 2 E-S-FLU infection of *Tpcn1/2*KO mice embryonic fibroblast (MEF) 261

Figure 6. 3 GP-lentivirus infection of *Tpcn1/2*KO MEF cells 263

Figure 6. 4 Human *TPCN1* gene and the corresponding peptide sequence.... 266

Figure 6. 5 Human *TPCN2* gene and corresponding peptide sequence..... 267

Figure 6. 6 *TPCN1* and *TPCN2* specific sgRNAs tested in surveyor assays... 268

Figure 6. 7 *TPCN1*KO HeLa genomic DNA PCR verification..... 270

Figure 6. 8 *TPCN2*KO HeLa genomic DNA PCR verification..... 271

Figure 6. 9 RT-PCR characterising *TPCN1*KO HeLa clones 274

Figure 6. 10 RT-PCR characterising *TPCN1*KO HeLa clones 275

Figure 6. 11 Effect of *TPC* knockout on Ca^{2+} signals 277

Figure 6. 12 E-S-FLU infection in *TPCN1*KO HeLa cells 278

Figure 6. 13 E-S-FLU infection in *TPCN2*KO HeLa cells 279

Figure 6. 14 HeLa transduced to express pore-mutants of TPC2 283

Figure 6. 15 E-S-FLU infection of HeLa overexpressing pore-mutants of TPC2 284

Figure 7. 1 EBOV-GP structure and the drug binding pocket 297

Figure 7. 2 Drugs that bind EBOV-GP..... 299

Figure 7. 3 Drugs tested in GP crystal soaking assay..... 303

Figure 7. 4 Imipramine-bound EBOV-GP structure 304

Figure 7. 5 Compound 118 and 118a virus inhibition assay..... 306

Figure 7. 6 Antibody neutralisation assay of thermolysin treated E-S-FLU 308

Figure 7. 7 Drug inhibition assay of thermolysin treated E-S-FLU 310

Figure 7. 8 Mutations introduced to EBOV-GP drug-binding site..... 312

Figure 7. 9 Sequence alignment of GP from ebolavirus and marburgvirus..... 313

Figure 7. 10 Workflow for producing mutated GP pseudotyped E-S-FLU..... 315

Figure 7. 11 Expression of mutated EBOV-GP on the surface of transduced MDCK-SIAT1 cells 316
Figure 7. 12 FACS sorting of cells with high level expression of GP..... 317
Figure 7. 13 Epitopes check for mutated EBOV-GP expressed at the cell surface 318
Figure 7. 14 Virus titration and ELISA for $E_{mutation}$-S-FLUs 319
Figure 7. 15 Fluorescence microscopic images of $E_{mutation}$-S-FLU infection..... 320
Figure 7. 16 Toremifene-selected mutant EBOV growth..... 323
Figure 7. 17 Toremifene inhibition assays with different species E-S-FLU 325
Figure 7. 18 Inhibitor-binding sites and mechanisms among class I viral fusion proteins..... 328
Figure 7. 19 Mutated residues mapped to the NPC1 bound EBOV-GP structure 332
Figure 8. 1 Proposed mechanisms of CADs inhibiting EBOV entry …… 343

LIST OF TABLES

Table 1. 1 Current taxonomy of Ebolavirus genus 1

Table 1. 2 Chronology and location of human Ebola virus disease outbreaks..... 3

Table 1. 3 Experimental EBOV therapeutics tested in clinical trials 30

Table 1. 4 Animal tests of EBOV entry inhibitors..... 32

Table 2. 1 List and recipe of media and buffers 35

Table 2. 2 List of cells used in this study 36

Table 2. 3 List of primers used in this study 38

Table 2. 4 List of sgRNAs used in this study for CRISPR/Cas 9 knockout 39

Table 2. 5 List of pseudotyped viruses used in this study 41

Table 2. 6 List of antibodies and plasma samples..... 42

Table 2. 7 Mutations introduced to H7 in H7CFv3..... 46

Table 3. 1 E-S-FLU and H5-S-FLU growth titre 95

Table 3. 2 Description of NIBSC samples 102

Table 3. 3 IC_{50} values of 13 drugs that inhibited E-S-Flu virus infection selected from the literature 107

Table 3. 4 Mutations introduced to H7 in H7CFv3..... 114

Table 4. 1 Comparison of drugs common to both the LOPAC®1280 library and the collection of Johansen et al. 146

Table 4. 2 24 drugs that inhibited both E-S-FLU and H5-S-FLU 149

Table 4. 3 Physicochemical properties of 65 most potent E-S-FLU inhibitors.. 157

Table 4. 4 A panel of 20 compounds tested for drug-induced NPC phenotype 165

Table 4. 5 Summary of biochemical phenotypes for drug treated cells..... 171

Table 4. 6 CADs that induced lysosomal membrane permeability tested in E-S-FLU drug inhibition assay 173
Table 4. 7 Drugs and conditions used in LGAL-3 assay 174
Table 4. 8 Potential synergistic drug combinations 179
Table 5. 1 Summary of sphingosine profile and susceptibility to E-S-FLU infection for cells studied in this chapter 240
Table 6. 1 44 calcium related drugs screened in this study 252
Table 6. 2 18 two-pore channels inhibiting drugs 255
Table 7. 1 Monoclonal antibodies used in this chapter 307
Table 7. 2 Mutations introduced to EBOV-GP 311
Table 7. 3 Summary of $E_{mutation}$-S-FLU production 321

LIST OF APPENDICES

Appendix Table 4. X1 228 small molecules that has inhibited E-S-FLU in this study 198

(BLANK PAGE)

Chapter 1 General Introduction

1.1 Ebola virus

1.1.1 Virus taxonomy and nomenclature

Ebola virus (EBOV) is a filamentous, lipid-enveloped RNA virus that belongs to the *Filoviridae* family, of the order *Mononegavirales*. It was first recognised and characterised as the aetiological agent of Ebola virus disease (EVD) epidemic that occurred in the Democratic Republic of the Congo (DRC, formerly Zaire) in 1976 (Emond *et al.* 1977; Burke, Declerq and Ghysebrechts 1978). Ebola was also responsible for a major outbreak in West Africa in 2014. Including Ebola virus (*Zaire ebolavirus species*), there are five confirmed and one proposed *ebolavirus* species from the *Ebolavirus* genus within the *Filoviridae* family, based on the most recently published virus nomenclature and classification (Kuhn *et al.* 2019) (summarised in Table 1.1). The differences between *ebolavirus* species in genetic and protein sequences range from 32 to 41%.

Table 1. 1 Current taxonomy of Ebolavirus genus

Genus name	Species name	Virus name	Virus name abbreviation
Ebolavirus	*Zaire ebolavirus*	Ebola virus	EBOV
	Sudan ebolavirus	Sudan virus	SUDV
	Bundibugyo ebolavirus	Bundibugyo virus	BDBV
	Taï Forest ebolavirus	Taï Forest virus	TAFV
	Reston ebolavirus	Reston virus	RESTV
	Bombali ebolavirus	Bombali virus	BOMV

Adapted from Kuhn et al. 2019.
Bombali ebolavirus is a recently proposed species (Goldstein et al. 2018).

1.1.2 Outbreak history

Four viruses from the *Ebolavirus* genus have been identified as the aetiological agents of Ebola virus disease (EVD) in humans: Ebola virus (EBOV), Sudan virus (SUDV), Bundibugyo virus (BDBV) and Taï Forest virus (TAFV), and the average case fatality rate (CFR) of human infection is 50 to 90% (Martines *et al.* 2014) (Table 1.2). There are no approved vaccines or therapeutics for EVD, and with the high mortality rate and the ability to transmit directly from human to human, these four viruses are classified as biosafety level 4 pathogens (BSL-4). Reston virus (RESTV) has not caused symptomatic human infections so far, however antibodies were found in staff who handled the infected monkeys suggesting that asymptomatic infections may have happened (Centers for Disease Control and Prevention (CDC) 1990, 2006).

The 1976 outbreak occurred in the Équateur province in the DRC gave rise to the first recognition of EVD. Since then, multiple EVD outbreaks as well as sporadic human cases have been reported, summarised in Table 1.2. The majority of cases appeared in Africa, with the DRC affected by the greatest number of outbreaks. The 10th EVD outbreak in the DRC is still ongoing, with 1301 confirmed cases and 819 deaths reported by the World Health Organization (WHO) from 1 August 2018 to 23 April 2019. The largest human EVD epidemic caused by EBOV in West Africa in 2014 resulted in nearly 30,000 human infections and more than 11,000 deaths.

Table 1. 2 Chronology and location of human Ebola virus disease outbreaks

Year	Country	Virus	Number of cases	Fatal cases (CFR)
1976	Democratic Republic of the Congo (DRC) formerly Zaire	EBOV	318	280 (88%)
1976	Sudan (South Sudan)	SUDV	284	151 (53%)
1976	England	SUDV	1	0 (0%)
1977	DRC (formerly Zaire)	EBOV	1	1 (100%)
1979	Sudan (South Sudan)	SUDV	34	22 (65%)
1994	Gabon	EBOV	52	31 (60%)
1994	Republic of Côte d'Ivoire	TAFV	1	0 (0%)
1995	DRC (formerly Zaire)	EBOV	315	250 (79%)
1996	Gabon	EBOV	37	21 (57%)
1996	Gabon	EBOV	60	45 (74%)
1996	South Africa	EBOV	2	1 (50%)
1996	Russia	EBOV	1	1 (100%)
2000	Uganda	SUDV	425	224 (53%)
2001	Gabon	EBOV	65	53 (81%)
2001	Republic of Congo	EBOV	59	43 (73%)
2002	Republic of Congo	EBOV	143	128 (89%)
2003	Republic of Congo	EBOV	35	29 (83%)
2004	Sudan (South Sudan)	SUDV	17	7 (41%)
2004	Russia	EBOV	1	1 (100%)
2005	Republic of Congo	EBOV	12	10 (83%)
2007	DRC (formerly Zaire)	EBOV	264	187 (71%)
2007	Uganda	BDBV	149	42 (32%)
2008	DRC (formerly Zaire)	EBOV	32	15 (47%)
2011	Uganda	SUDV	1	1 (100%)
2012	Uganda	SUDV	11	4 (36.4%)
2012	DRC (formerly Zaire)	BDBV	36	13 (36.1%)
2012	Uganda	SUDV	6	3 (50%)
2014	Guinea, Liberia, Sierra Leone	EBOV	28,610	11,308 (39%)
2014	United States	EBOV	4	1 (25%)
2014	Spain	EBOV	1	0 (0%)
2014	Senegal	EBOV	1	0 (0%)
2014	Nigeria	EBOV	20	8 (40%)
2014	Mali	EBOV	8	6 (75%)
2014	Italy	EBOV	1	0 (0%)
2014	DRC (formerly Zaire)	EBOV	69	49 (71%)
2017	DRC (formerly Zaire)	EBOV	8	4 (50%)
2018	DRC (formerly Zaire)	EBOV	54	33 (61%)
Present	DRC (formerly Zaire)	EBOV	1301	819 (63%)

CFR: Case fatality rate. Table modified from Martines et al. 2014 based on the information reported by Centers for Disease Control and Prevention (CDC).

1.1.3 Pathogenesis, tropism and transmission

EBOV can transmit from human to human via direct contact with the blood, body fluids or secretions from infected people. However, the stuttering chains of EVD outbreaks suggest that the virus is able to transmit zoonotically among its natural reservoirs. EBOV is known to spread and cause disease in non-human primates, especially in wild gorilla and chimpanzee populations (Formenty *et al.* 1999; Rouquet *et al.* 2005; Bermejo *et al.* 2006; Pigott *et al.* 2014). In addition, fruit bats have been nominated as the prime suspect of the asymptomatic reservoir for EBOV transmission (Leroy *et al.* 2005; Olival and Hayman 2014).

EBOV has a broad cell tropism shown both *in vitro* and *in vivo*. In infected humans and non-human primates, viral replication leads to cell necrosis and a pro-inflammatory response in multiple tissues. At the early stage of disease progression, monocyte, macrophages and dendritic cells become infected, and are responsible for propagating EBOV and initiating the inflammatory response by secreting cytokines and chemokines. Systemic dissemination of EBOV then occurs via the vascular and lymphatic systems (Gibb *et al.* 2001; Bray and Geisbert 2005; Connolly *et al.* 2008; Schnittler and Feldmann 2009; Zaki and Goldsmith 1999). Invasion of multiple organs and tissues follows, including liver, spleen, kidney, bone marrow and vascular endothelium. Extensive necrosis in these organs have been observed in autopsy and biopsy of EBOV infected people and in animal models (Figure 1.1) (Martines *et al.* 2014; Baseler *et al.* 2017).

The incubation period of EBOV infection in human ranges from 2 to 21 days. Initially, flu-like symptoms such as fever, chills, fatigue and myalgia occur. This

can subsequently develop into more systemic clinical presentations including nausea, vomiting, diarrhoea, chest pain, oedema, confusion and coma (Zaki and Goldsmith 1999; WHO 2014). In more severe and fatal cases, haemorrhagic symptoms appear at the peak of illness, followed by hypotensive shock and multi-organ failure (Fields Virology, 6th Edition).

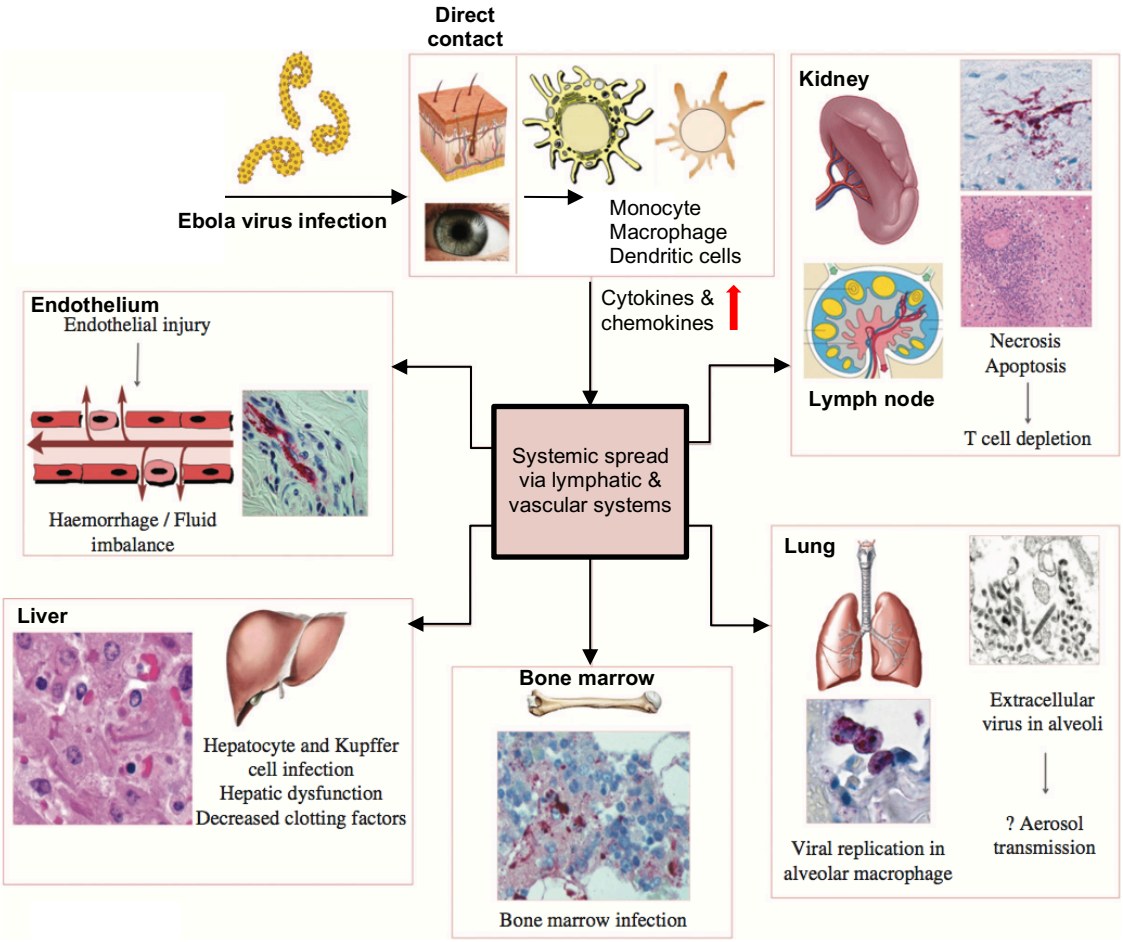


Figure 1. 1 Model of Ebola virus entry, cellular tropism and pathogenesis
Ebola virus (EBOV) enters the host via direct contact with mucous membrane or skin lesion. Monocytes, macrophages and dendritic cells in the bloodstream are first targeted, and infected cells then spread the virus to multiple tissues and organs via the vascular and lymphatic systems, causing systemic damage. Figure adapted from Martines *et al.* 2014.

1.1.4 Virus biology

EBOV and other Filoviruses share a characteristic filamentous morphology, observed under the electron microscope (Figure 1.2 A). The average length of EBOV is 1200 nm and the diameter is 80 nm. Roughly 50 nm of the diameter of the central space is taken by the ribonucleoprotein complex.

EBOV has a single-stranded negative-sense RNA genome, approximately 19 kilobases (kb) in length. There are seven genes encoded in EBOV, arranged in sequence: 3' leader → nucleoprotein (NP) gene → viral protein (VP) 35 gene → VP40 gene → glycoprotein (GP) gene → VP30 gene → VP24 gene → polymerase (L) gene → 5' trailer. 3' leader and 5' trailer are short non-coding extragenic sequences that are important for virus genome stability (Fields Virology, 6th Edition; Baseler *et al.* 2017).

Nucleoproteins (NP and VP30)

EBOV Nucleoprotein (NP) and VP30 interact strongly with the viral RNA forming the ribonucleoprotein complex. The oligomerised NP serves as an essential scaffold for the assembly of the nucleocapsid complex along with VP30, polymerase L and VP35 and the viral RNA (Dong *et al.* 2015; Sugita *et al.* 2018). VP30 binds directly to RNA via a zinc-finger motif, which is also important for the activation of transcription (Modrof, Becker and Muhlberger 2003; Hartlieb *et al.* 2007).

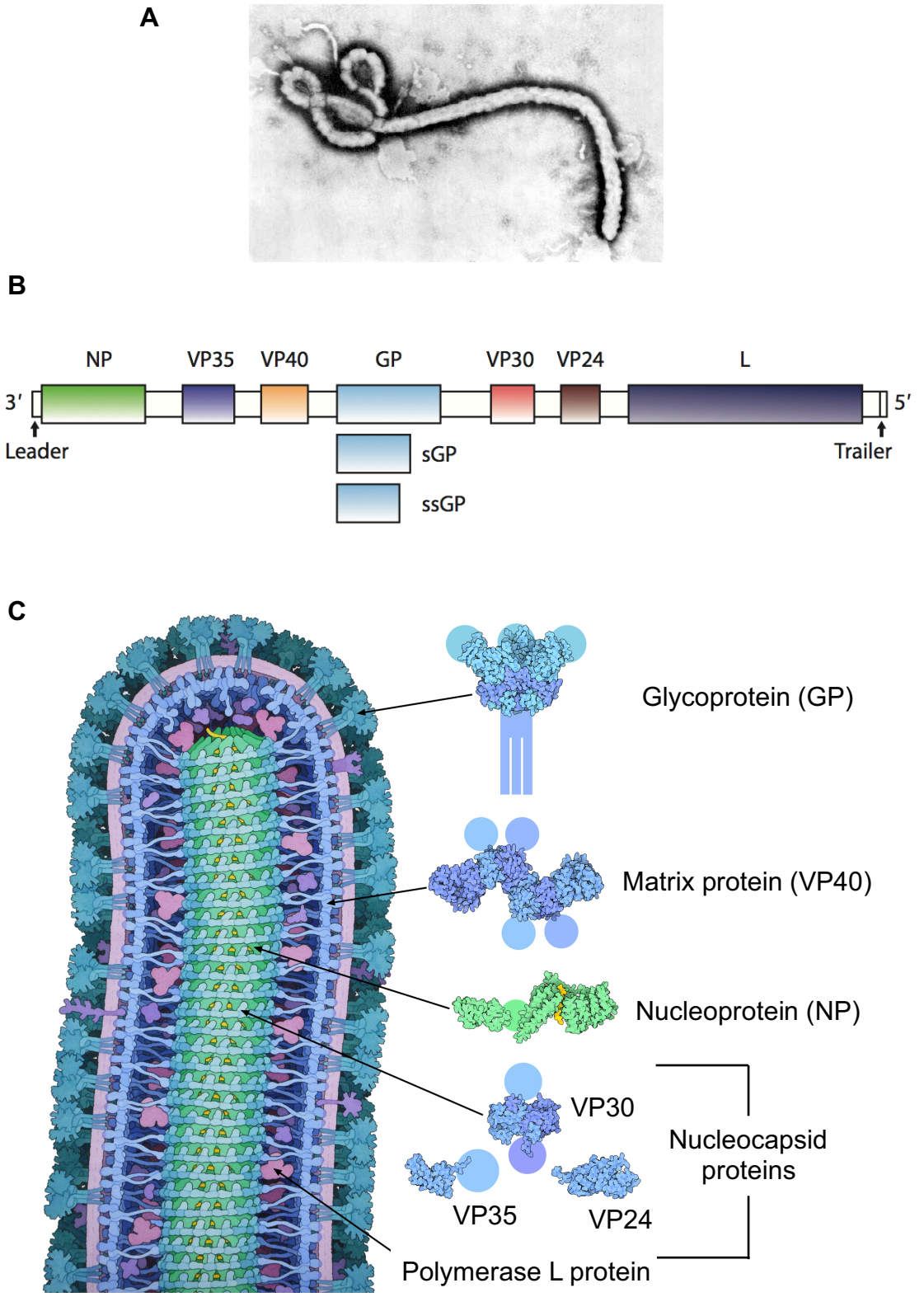


Figure 1. 2 Ebola virus structure

A: Electron microscopic image of an EBOV virion taken by Dr Frederick Murphy at the Centers for Disease Control and Prevention in 1976. **B**: EBOV genome organisation (adapted from Baseler *et al.* 2017). **C**: Cross-section through EBOV reconstructed based on published EBOV protein structures (Figure adapted from Goodsell 2014). Proteins are shown in blue, green and magenta, the RNA genome in yellow, and the membrane in light purple.

Polymerase complex proteins (L and VP35)

Polymerase L protein and VP35 are also part of the giant nucleocapsid complex. L protein is an RNA-dependent RNA polymerase, which is used by the virus for gene transcription and replication. VP35 acts as a cofactor for RNA synthesis, and its positively charged C-terminus has shown binding affinity to double-stranded RNA (Prins *et al.* 2010). VP35 is also a virulence factor that antagonises the innate immune response by inhibiting interferon production and interfering with the antiviral activity of host double-stranded RNA-dependent protein kinase R (Feng *et al.* 2006; Leung *et al.* 2009).

Matrix proteins (VP40 and VP24)

The matrix protein VP40 is associated with the virus membrane, and is critical for the process of virus budding by driving the formation of the filamentous shape, as well as incorporating the nucleocapsid (Gomis-Rüth *et al.* 2003; Bornholdt *et al.* 2013). VP24 protein interacts with NP in the nucleocapsid, and plays a role in genome packaging and nucleocapsid assembly (Banadyga *et al.* 2017). VP24 is also involved in virus evasion from innate immunity by antagonising type I interferon production (Basler 2015; Messaoudi, Amarasinghe and Basler 2015).

Glycoprotein (GP)

Glycoprotein (GP) is the best studied EBOV protein so far. It is the only transmembrane protein inserted in the lipid bilayer that coats the EBOV surface. For EBOV, GP is essential for the process of virus entry and pathogenesis of the virus. GP is also attractive to scientists as a promising vaccine candidate due to its antigenicity, and the critical role it plays in attachment, receptor binding, fusion

and entry. Newly expressed precursor GP0 polypeptide is cleaved by the furin protease into two fragments (GP1 and GP2 subunits), and they are held together as a heterodimer by a disulphide bond, and further trimerised to form the complete GP protein (Figure 1.3) (Lee *et al.* 2008).

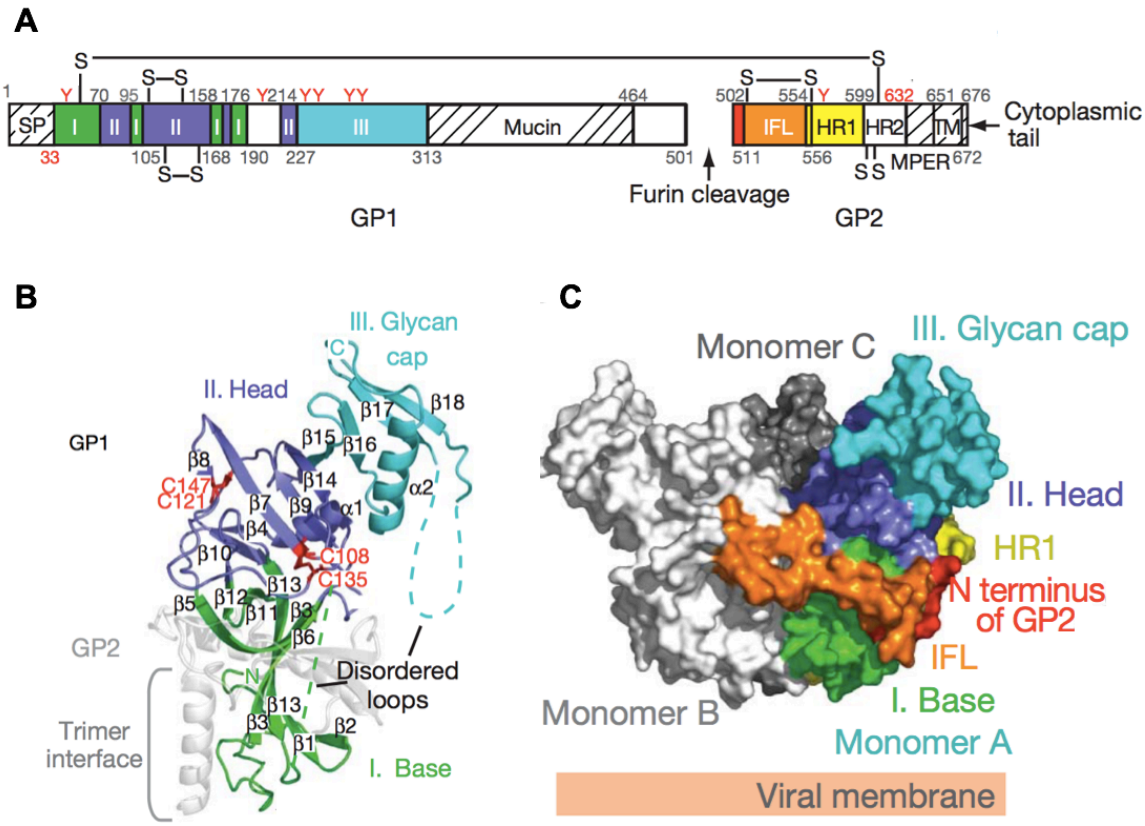


Figure 1. 3 EBOV-GP structure
The figure was adapted from Lee *et al.* 2008. (**A**) Schematic diagram for EBOV-GP. SP, signal peptide; S-S: disulphide bond; I, GP1 base; II, GP1 head; III, GP1 glycan cap; mucin, mucin-like domain (MLD); IFL: internal fusion loop; HR: heptad repeat; MPER: membrane-proximal external region; TM: transmembrane domain; red Y: predicted N-linked glycosylation sites. (**B**) The corresponding crystal structure for GP(1,2) monomer in cartoon representation. (**C**) The molecular surface of GP(1,2) trimer.

GP is a type I membrane protein, with most of its N-terminus protruding away from the viral membrane forming the ectodomain, and its C-terminus spans the membrane. GP1 is covered with N-linked and O-linked glycans, especially the mucin-like domain (MLD) that is rich in threonine and serine residues. After EBOV

is engulfed by the target cell, the highly glycosylated MLD and glycan cap domain are cleaved off by host proteases cathepsin B and L (Schornberg *et al.* 2006), exposing the receptor binding region (RBR) to interact with the host Niemann-Pick type C1 (NPC1) protein in the lysosome. Binding to NPC1 initiates fusion of the viral and lysosomal membranes through a major conformational change in GP2, followed by release of the viral nucleocapsid into the cytoplasm for replication (Skehel and Wiley 2000; Wang *et al.* 2016; White and Whittaker 2016).

The GP gene is also the only polycistronic EBOV gene that contains three reading frames. The primary transcription frame encodes for a soluble GP (sGP, 324 residues) and is largely expressed and secreted as homodimers during infection (Sanchez *et al.* 2002) (Figure 1.4). The role of sGP is not yet confirmed but is suggested to contribute to virus pathogenesis by acting as a decoy antigen (de La Vega *et al.* 2014). Transcriptional editing is required to switch from the sGP to the transmembrane GP reading frame, with an insertion of an extra non-templated adenosine near the middle of the GP gene (Sanchez *et al.* 2002). A more recently identified small soluble GP (ssGP, 298 residues) is also the product of transcriptional editing, requiring the insertion of two adenosines (Mehedi *et al.* 2011).

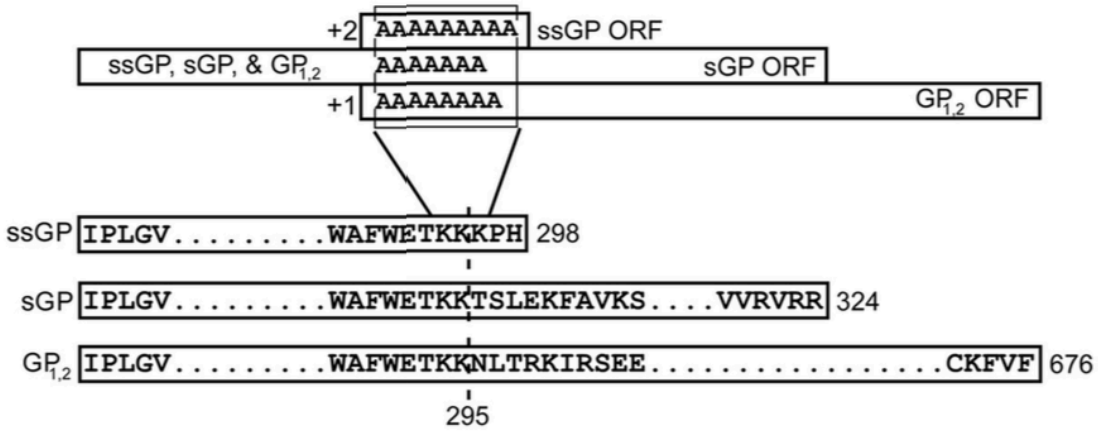


Figure 1. 4 Transcriptional editing for GP gene expression
Figure was taken from Mehedi *et al.* 2011. The open reading frame for the transmembrane form $GP_{1,2}$, soluble GP (sGP) and small soluble GP (ssGP). Transcription editing inserts one or two non-templated adenosine residues in the region of seven adenosine repeats and the resulting changes in protein sequence are shown in the diagram.

1.2 The mechanism of cell entry by Ebola virus

The scope of this thesis is mainly focused on the entry process in the EBOV life cycle. The broad cellular tropism of EBOV infection suggests that it uses a ubiquitous cell entry pathway. In this section, I will briefly introduce our current understanding of the EBOV entry mechanism, and state out how host factors are involved and interact with the virus in each step (Figure 1.5).

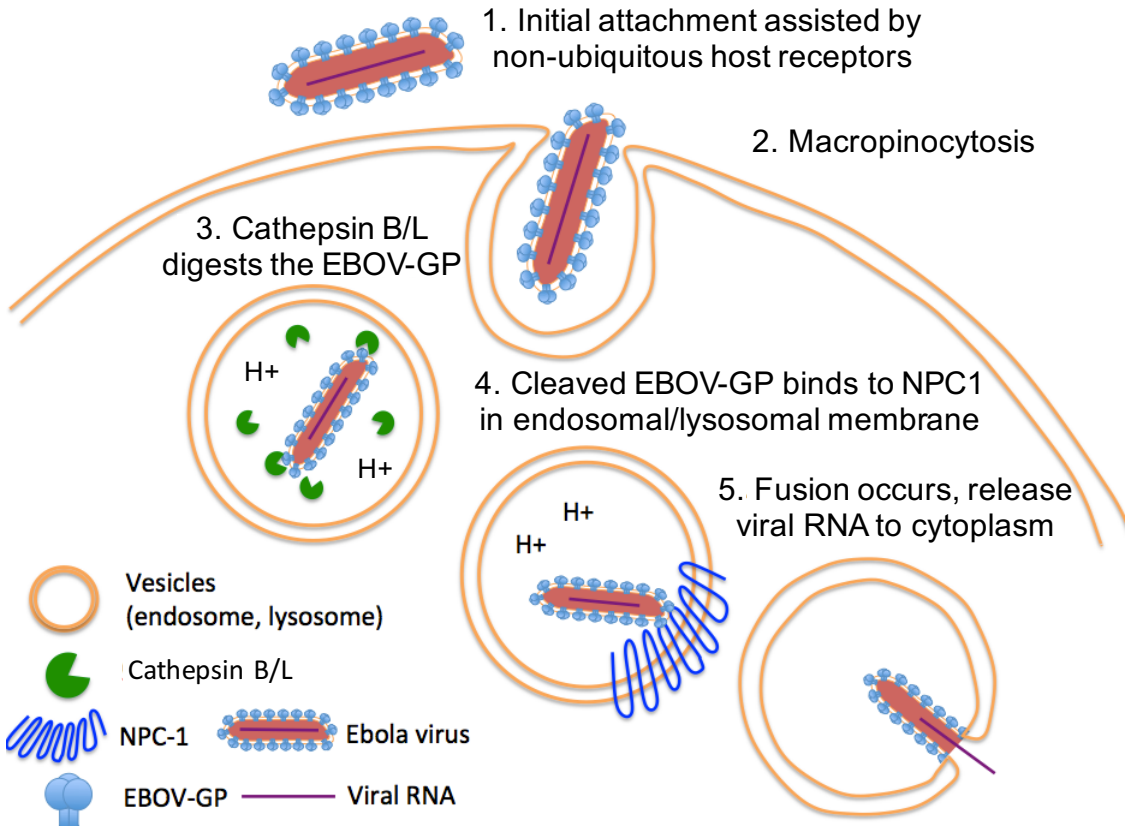


Figure 1. 5 Schematic diagram of the pathway of EBOV cell entry
Ebola virus (EBOV) initially attaches to the cell surface membrane with the assistance of non-ubiquitous host molecules such as DC-SIGN/DC-SIGNR, LSECtin, human macrophage galactose/N-acetylgalactosamine asialoglycoprotein receptor (hMGL), and TIM-1. EBOV is then engulfed into endosomal vesicles through macropinocytosis. In the acidic lumen of the endosome, EBOV-GP is cleaved by host proteases cathepsin B/L to expose the receptor binding region. Processed EBOV-GP is then able to bind to the NPC1 protein at the lysosomal membrane, which triggers membrane fusion, and release the viral genome to the cytoplasm for replication.

1.2.1 Attachment

The first barrier EBOV virions encounter during cell infection is the target cell plasma membrane. Several host factors have been shown to interact with EBOV and are involved in the initial attachment step. This is mostly shown by correlating the expression of a given host surface protein with the cell susceptibility to EBOV infection. Transduction of these factors switches naturally non-infectible cells (such as Jurkat cells) permissive to EBOV infection, which is then blocked by

specific antibodies. However, it is now more accepted that there is no ubiquitous factor that is absolutely required for EBOV attachment (Zapatero-Belinchón *et al.* 2019).

Potential mechanisms of EBOV cell attachment are summarised in Figure 1.6. C-type lectins such as DC-SIGN/DC-SIGNR and L-SIGN (dendritic cell and liver/lymph node-specific ICAM-3-grabbing non-integrin) interact with the high mannose N-linked glycans on EBOV-GP (Alvarez *et al.* 2002; Simmons *et al.* 2003a; Marzi *et al.* 2004; Ji *et al.* 2005). Other attachment factor candidates such as tyrosine kinase receptor Axl and folate receptor α (FRα), may interact with EBOV-GP at non-glycosylated sites (Simmons *et al.* 2003b; Sinn *et al.* 2003; Shimojima, Ikeda and Kawaoka 2007; Brindley *et al.* 2011). ASGP-R (hepatic asialoglycoprotein receptor) and hMGL (human macrophage galactose- and N-acetylgalactosamin-specific C-type lectin) have been shown to interact with the O-linked glycans on the mucin-like domain (Lin *et al.* 2003; Takada *et al.* 2004). This interaction may not be a necessary requirement for EBOV entry, as deletion of the mucin-like domain does not affect EBOV entry and infection (Jeffers, Sanders and Sanchez 2002). TIM-1 (T-cell immunoglobulin and mucin domain protein 1) has been proposed to attach the virus both via phosphatidylserine in the virus lipid membrane as well as directly interacting with EBOV-GP at the receptor binding region (Kondratowicz *et al.* 2011; Kuroda *et al.* 2015; Yuan *et al.* 2015).

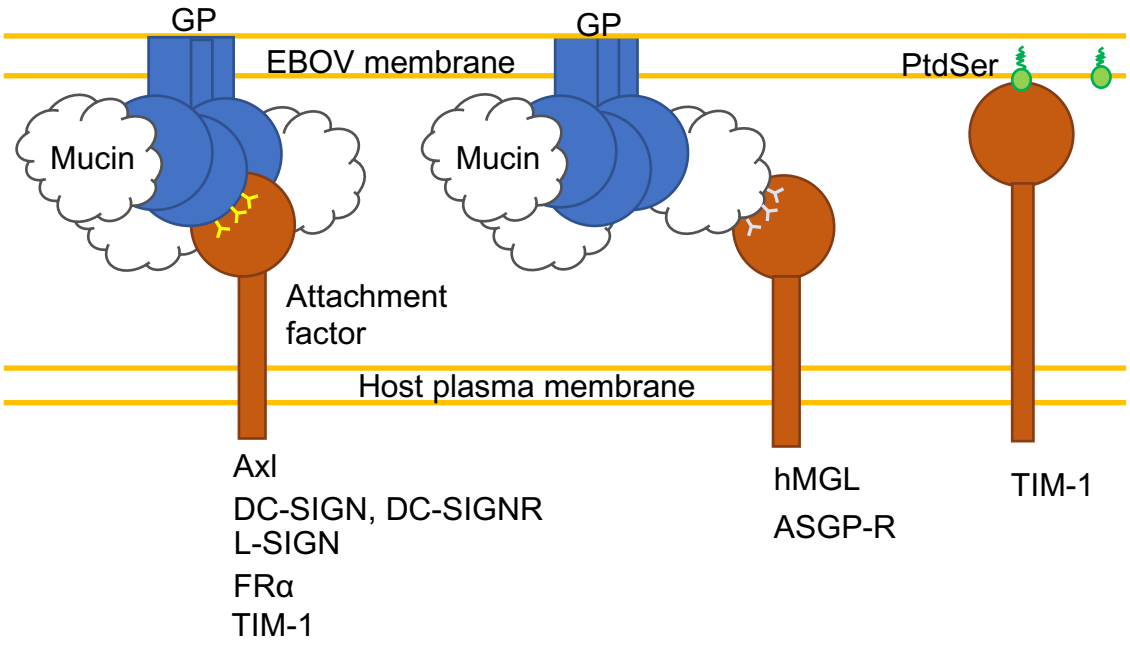


Figure 1. 6 Proposed mechanisms of EBOV attachment to cell
Multiple host membrane proteins have been shown to interact with EBOV at the attachment step. C-type lectins are proposed to bind either to the N-linked glycans on EBOV-GP (yellow Y shape), or to O-linked glycans (light grey Y shape) on the mucin-like domain (Mucin). TIM-1 has been shown to interact directly with both GP and phosphatidylserine (PtdSer) in the virus lipid envelope. Prospective host factors are listed below each model.

1.2.2 Macropinocytosis

Macropinocytosis is an endocytic process used by most cell types for taking up large quantities of extracellular fluid, and it is exploited by larger viruses such as EBOV, vaccinia virus and herpes virus for cell entry (Swanson and Watts 1995; Fields Virology, 6th edition). EBOV endocytosis through macropinocytosis has been observed by several groups with multiple experimental approaches. Confocal fluorescence imaging has shown the co-localisation of EBOV with macropinosome markers SNX5 (sorting nexin 5) in real-time analysis (Nanbo *et al.* 2010). Typical membrane ruffling triggered by EBOV was observed by transmission electron microscopy (Mulherkar *et al.* 2011). Moreover, regulatory

kinases and GTPases upstream and downstream of macropinocytosis are required for wild-type EBOV infection (Saeed *et al.* 2008, 2010; Quinn *et al.* 2009).

Taking all the evidence together, we can summarise the macropinocytosis mechanism as the following sequence: after the initial attachment step, EBOV-GP binding signals the activation of phosphoinositide-3 kinase (PI3K), possibly via tyrosine kinase receptor such as Axl. PI3K then phosphorylates its downstream target Akt and Rac1, which then regulates actin rearrangement and assembles sorting nexin SNX5 to the EBOV bound site. As the result, membrane ruffles surround and internalise the virus in a macropinosome, and EBOV enters the endolysosome trafficking pathway (Nanbo *et al.* 2010).

1.2.3 Endocytosis and cathepsin B/L processing

After being engulfed into the cell, EBOV is trafficked from the periphery of the cytoplasm towards the perinuclear region, following the maturation of early endosome to late endosome. The vesicle luminal pH gradually decreases as the endosome matures and it receives newly synthesised digestive enzymes from the trans-Golgi network (TGN) (Pryor and Luzio 2009; Huotari and Helenius 2011; Luzio *et al.* 2014). At the same time, EBOV-GP is processed by acid-dependent endosomal cysteine proteases cathepsin B and L. As described in section 1.1.4, EBOV-GP is a trimer of GP(1,2) heterodimers. GP1 is highly glycosylated, with its C-terminus spiking out as the head. GP2 contains the transmembrane domain and the fusion domain, which is more buried at the base with the GP1 N-terminus. Host cysteine proteases cathepsin B and L digest the 130 kDa GP1 into an 18 kDa core

GP_{CL} by cleaving off the mucin-like domain and the glycan cap to expose the receptor binding region (Figure 1.7).

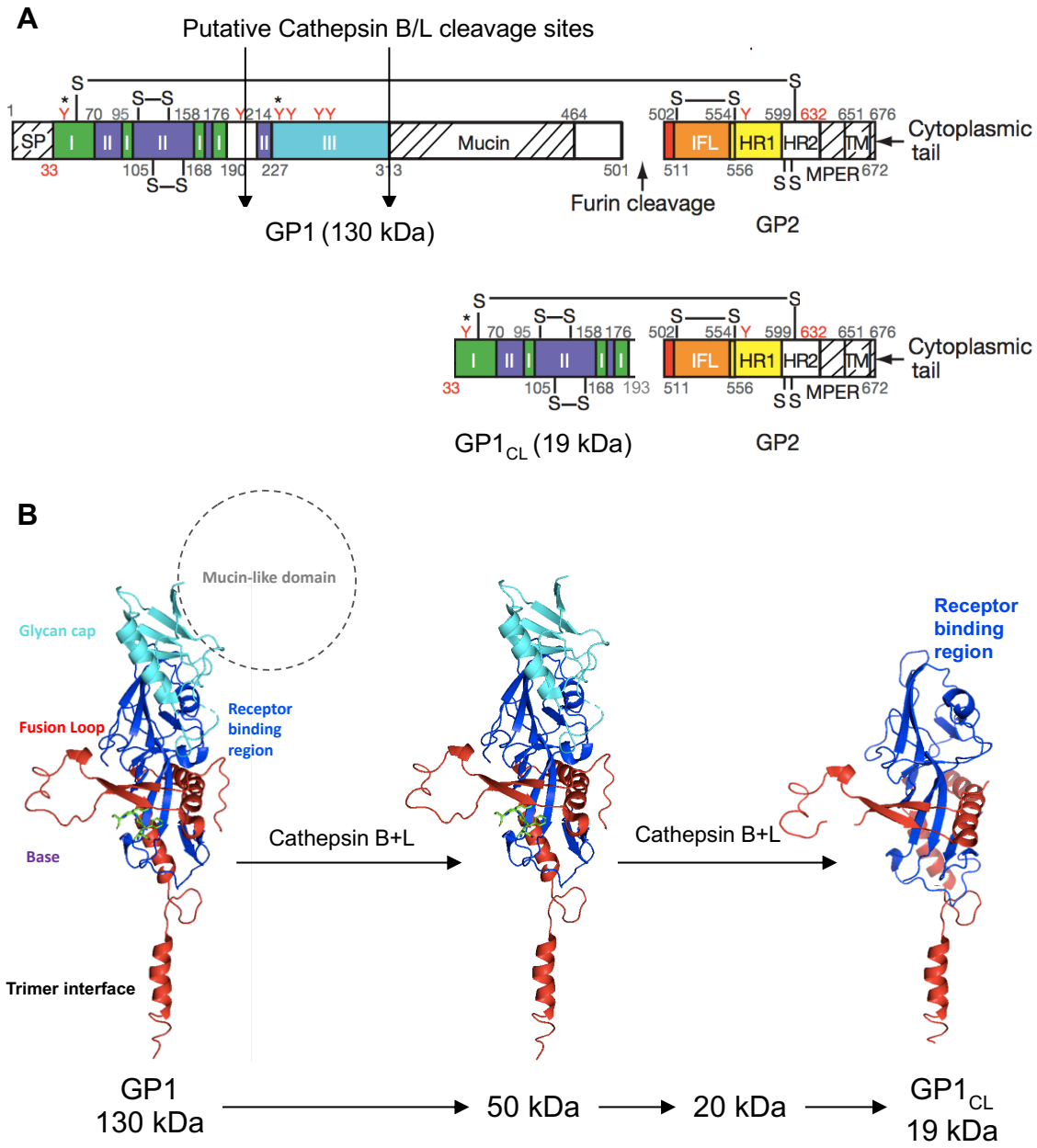


Figure 1. 7 Mechanism of EBOV-GP proteolysis by cathepsin B and L
A: Putative cathepsin B and L cleavage sites in GP1 subunit lead to removal of the highly glycosylated mucin-like domain (Mucin) and glycan cap (III) region (figure adapted from Lee *et al.* 2008). **B**: Proposed cathepsin digestion of GP1 is shown in relation to the published EBOV-GP structures. The model presented is adapted from Brecher *et al.* 2011. The full-length GP1 has a molecular weight of 130 kDa (blue + cyan) (PDB file 5JQ3, published by Zhao *et al.* 2016). The mucin-like domain structure is not yet determined (grey broken line circle). GP2 is coloured red. Removal of the mucin-like domain resulted in a 50 kDa intermediate, which is further cleaved into 20 kDa and then 18 kDa $GP1_{CL}$, exposing the receptor binding region (structure based on PDB file 5F1B, Wang *et al.* 2016).

Several groups have shown that cathepsin B is essential for EBOV-GP proteolysis (Chandran *et al.* 2005; Schornberg *et al.* 2006; Kaletsky, Simmons and Bates 2007; Brecher *et al.* 2011; Gnirß *et al.* 2012). Cathepsin L alone is neither necessary nor sufficient for priming GP, but is able to facilitate cathepsin B's function. In contrast, GP from Sudan virus (SUDV) and Bundibugyo virus (BUDV) in the same virus genus, are processed by endosomal proteases separate from cathepsin B and L (Misasi *et al.* 2012). A recent study showed fatal infection of cathepsin B and L deficient mice by mouse-adapted EBOV, which also suggested a more redundant use of proteases for EBOV entry (Marzi, Reinheckel and Feldmann 2012).

The proteolytic processing of EBOV-GP by cathepsin B/L can be mimicked by genetically engineered deletion of the mucin-like domain GPΔmucin and *in vitro* digestion of GP by a bacterial protease thermolysin (Jeffers, Sanders and Sanchez 2002; Schornberg *et al.* 2006; Wang *et al.* 2016). Pseudotyped vesicular stomatitis virus (a non-replicating model to study EBOV entry, described in section 1.3) coated with the cleaved GP ($GP1_{CL}$ and intact GP2 heterodimer) infected better than virus coated with the full-length GP, and its infection was no longer inhibited by cathepsin B or L specific inhibitors (Wong *et al*. 2010) Interestingly, the virus bearing $GP1_{CL}$-GP2 was still blocked by a more broad spectrum cysteine protease inhibitor E64, suggesting that additional trigger factors may require protease activities (Schornberg *et al.* 2006; Wong *et al.* 2010; Spence *et al.* 2016).

1.2.4 Receptor binding

The virus-containing late endosome eventually fuses with a lysosome. Carette *et al.* showed that cells with mutated subunits of the HOPS complex (homotypic

fusion and vacuole protein sorting), which tethers vesicles together to fuse, were no longer permissive to EBOV entry (Luzio, Bright and Pryor 2007; Carette *et al.* 2011). Live cell imaging tracked the membrane fusion event occurred after EBOV containing vesicles co-localised with the late-endosomal marker Rab7, lysosomal marker LAMP-1 and the EBOV-GP receptor NPC1 (Simmons *et al.* 2016; Spence *et al.* 2016).

EBOV requires the Niemann-Pick type C1 protein (NPC1), a ubiquitous multi-pass transmembrane protein found in late endosomal/ lysosomal membranes, to trigger the last stage of entry: penetration from the lysosome to cytoplasm (Carette *et al.* 2011; Côté *et al.* 2011; Miller *et al.* 2012; Herbert *et al.* 2015). The exact physiological function of NPC1 is not yet fully established, but it has been shown to be involved in endocytic transport and regulation of cholesterol and lipid levels in the late endosome/lysosome compartment (Liscum 2000; Ko *et al.* 2001; Babalola *et al.* 2007; Lloyd-Evans *et al.* 2008). Defective NPC1 leads to a neurovisceral lysosomal storage disease NPC (Vanier 2010).

NPC1 is the ubiquitous receptor for GP in the lysosome. Mutagenesis and structural studies have established the interaction between the NPC1 domain C (the second luminal domain) and the cathepsin cleaved core of EBOV-GP (GP_{CL}) (Miller *et al.* 2012; Gong *et al.* 2016; Wang *et al.* 2016). Deletion of NPC1 completely abolished EBOV cell entry *in vitro*, and protected mice from EBOV lethality (Herbert *et al.* 2015). NPC2 is a soluble protein involved in the same cholesterol transport pathway with NPC1. Although mutations in NPC1 and NPC2 cause similar clinical phenotypes, cells and mice without NPC2 expression were

still permissive to EBOV infection (Carette *et al.* 2011; Côté *et al.* 2011; Herbert *et al.* 2015).

1.2.5 Fusion

EBOV-GP belongs to the class I viral membrane fusion protein family, and the mechanism of virus fusion has been carefully reviewed by White *et al.* (2016). The binding of the cleaved GP1 to NPC1 domain C initiates the fusion process, but additional trigger(s) may also be required. Evidence to support this comes from the lack of significant conformational change shown in the NPC1 bound GP complex structure compared to the unbound GP (Lee *et al.* 2008; Wang *et al.* 2016), with the GP2 subunit including the fusion loop remaining partially buried under the receptor binding region of GP1. One hypothesis is that GP1 is further cleaved or the disulphide bond linking GP1 and GP2 is reduced by lysosomal thiol reductase, but this requires further investigation (Schornberg *et al.* 2006; Wong *et al.* 2010; White and Whittaker 2016).

The fusion loop (FL) consists of the first 50 to 60 hydrophobic-rich residues at the N-terminus of GP2 (Figure 1.8) (Ruiz-Arguello *et al.* 1998; Ito *et al.* 1999). It undergoes a conformational change and inserts itself into the target lysosomal membrane, forming the pre-hairpin conformation. This process was nicely summarised by Gregory *et al.* with an analogy of a hand and a fist. The fusion loop is in a relaxed, open hand posture at neutral pH but clenches into a fist, reorienting the hydrophobic residues to the front tip of the fist, promoting interactions with the target lipid membrane (Liang *et al.* 2011; Gregory *et al.* 2014). After that, the three C-heptad helices from the GP2 trimer fold back to form a six-helical bundle with

the three N-heptad helices (Weissenhorn *et al.* 1998; Malashkevich *et al.* 1999; Skehel and Wiley 2000). The formation of six-helical bundle is highly energetically favoured at pH 5 and pulls the lysosomal membrane and the virus lipid envelop close together, entering into a hemifusion state (Harrison *et al.* 2011). Finally, the fusion loop comes close to interact with the membrane-proximal external region (MPER) and the transmembrane domain (TM), which drives the formation of a fusion pore to release viral nucleocapsid to the host cytoplasm (Regula *et al.* 2013; Lee *et al.* 2017)

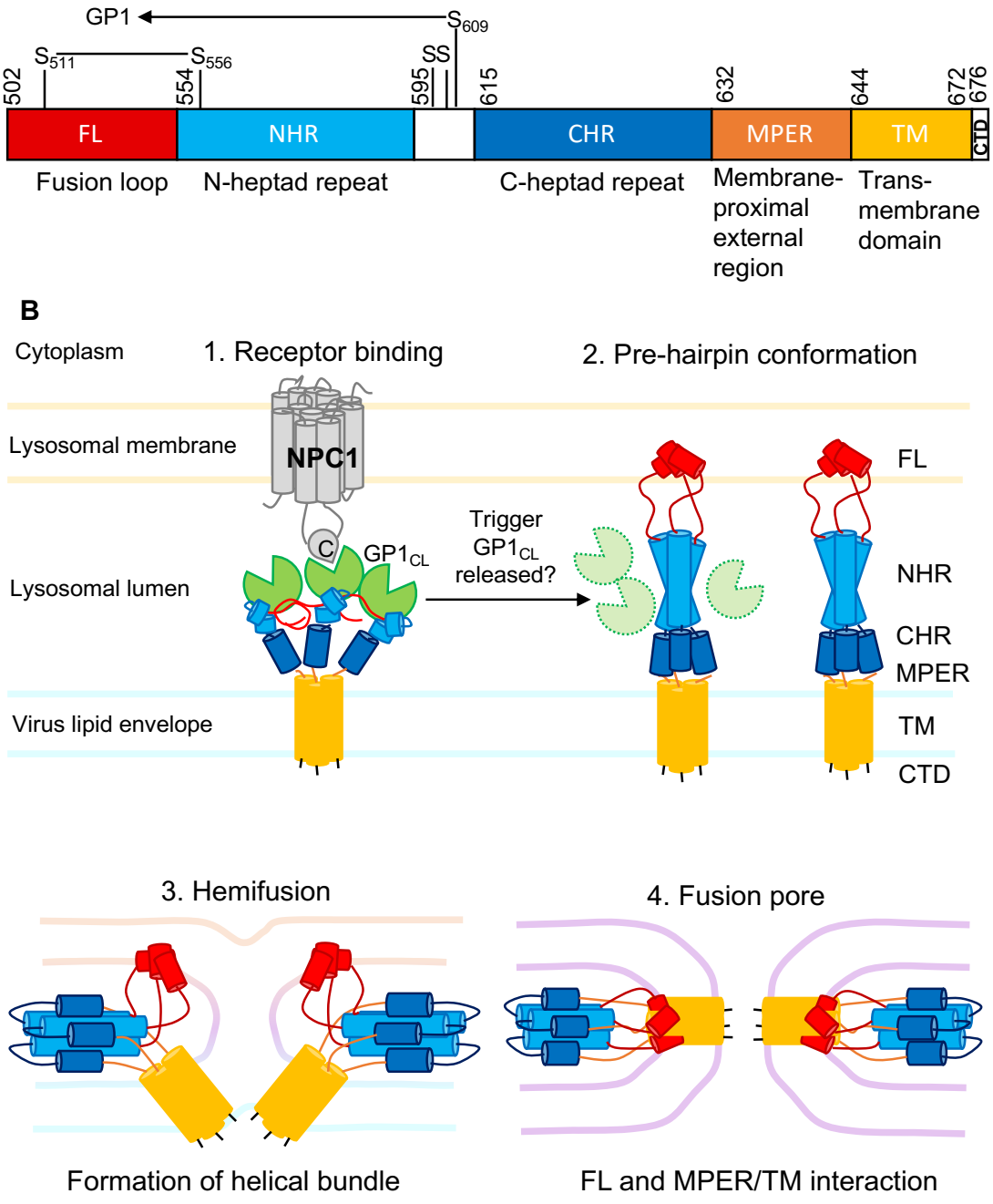


Figure 1. 8 EBOV-GP fusion

A: EBOV GP2 domain structure, figure adapted from Lee *et al.* 2017. **B**: Structural model of EBOV-GP mediated membrane fusion, figure adapted from Skehel and Wiley 2000; White and Whittaker 2016. Rod shape symbolises α helix structure. The colour coding matches with the corresponding domain colour displayed in **A**. 1. The process is initiated by the binding of cleaved GP1 ($GP1_{CL}$) to the C domain of the NPC1 protein in the lysosome. Additional trigger may be required to expose GP2 to undergo conformational changes. 2. GP2 inserts the hydrophobic fusion loop (FL) into the target membrane. 3. The N-heptad repeats (NHR) and C-heptad repeats (CHR) domains in the GP2 trimer form into a six-helical bundle pulling the two membranes together into a hemifusion intermediate stage. 4. Fusion loop (FL) interacts with the membrane-proximal external region/transmembrane domain (MPER/TM) to drive the formation of fusion pore.

1.2.6 Calcium ions and calcium channels in EBOV entry

A recent paper published by Sakurai *et al.* reported that a novel host factor, the two-pore channel 2 (TPC2) is involved in the EBOV entry process (Sakurai *et al.* 2015). TPC2 is a calcium-permeable cation channel found in the late-endosomal and lysosomal membrane (Patel and Kilpatrick 2018). It is regulated by nicotinic acid adenine dinucleotide phosphate (NAADP) to release Ca^{2+} from acidic calcium stores to the cytoplasm (Calcraft *et al.* 2009; Zong *et al.* 2009; Ruas *et al.* 2015). Sakurai *et al.* showed that EBOV infection was reduced in murine embryonic fibroblasts isolated from TPC2 deficient mice, and several calcium channel inhibitors blocked EBOV entry (Sakurai *et al.* 2015). Simmons *et al.* then demonstrated that GP-mediated fusion took place in endo/lysosomal vesicles containing both NPC1 and TPC2 (Simmons *et al.* 2016). However, the mechanism by which calcium channels affect EBOV entry remains unexplained. Early studies on a 16-residue fragment from the GP2 fusion loop hinted that Ca^{2+} concentration may alter the GP2 conformation during the fusion process (Ruiz-Arguello *et al.* 1998; Suárez *et al.* 2003). The involvement of TPC2 and calcium flux in EBOV entry will be further discussed in Chapter 6 (Calcium and EBOV Infection).

1.3 Ebola virus surrogates

EBOV is categorised as a biosafety level 4 (BSL-4) pathogen. The limited availability of BSL-4 containment facilities, as well as the potential health risks, and the demanding cost and time investment set up extra hurdles to EBOV research. EBOV surrogates that can be handled at a low containment level are therefore valuable as basic research models, diagnostic tools and potential vaccine candidates (Bentley *et al.* 2015).

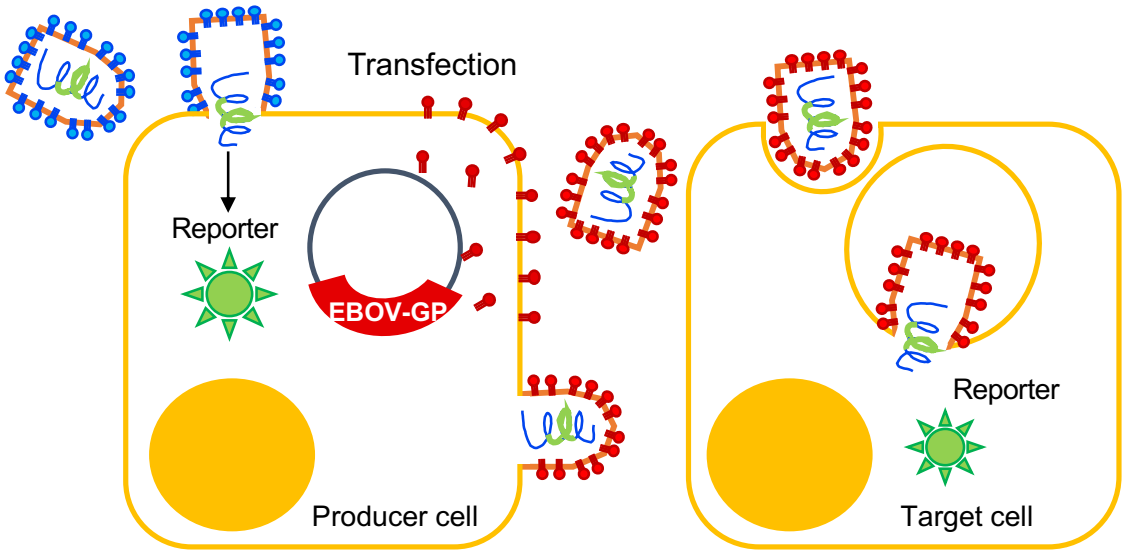
Virus pseudotyping refers to the method of incorporating heterologous viral envelope protein(s) into a single-cycle viral vector. The replication capacity of the viral vector is abrogated by deleting the gene encoding its own surface protein, or replacing it by a reporter, such as green fluorescence protein (GFP) or firefly luciferase. HEK293T cells or other production cell-lines are usually transiently transfected to express the supplemental coating protein for pseudotyping the viruses (Figure 1.9).

There are two main types of EBOV-GP pseudotyped viruses: the first is based on retroviral vectors such as murine leukaemia virus (MLV) (Wool-Lewis and Bates 1998) and human immunodeficiency virus (HIV) (Simmons *et al.* 2003b) (Figure 1.9 B); the other has a vesicular stomatitis virus (VSV) core with VSV glycoprotein gene deleted (Takada *et al.* 1997) (Figure 1.9 A). As reviewed in the previous sections, EBOV-GP is the only viral protein required for EBOV cell entry. Most of our current knowledge about the mechanism of EBOV entry, such as initial attachment, discovery of NPC1 as EBOV receptor, the proteolytic processing of EBOV-GP during entry were built on studies using pseudotyped viruses (Simmons *et al.* 2003b; Chandran *et al.* 2005; Schornberg *et al.* 2006; Carette *et al.* 2011; Spence *et al.* 2016). EBOV-GP is also the key target for neutralisation by antibodies (Lee *et al.* 2008; Saphire *et al.* 2018; Rijal *et al.* 2019). Many antibodies and potential therapeutic drug molecules have been screened with EBOV-GP pseudotyped viruses (Long *et al.* 2015; Furuyama *et al.* 2016; Saphire *et al.* 2018)

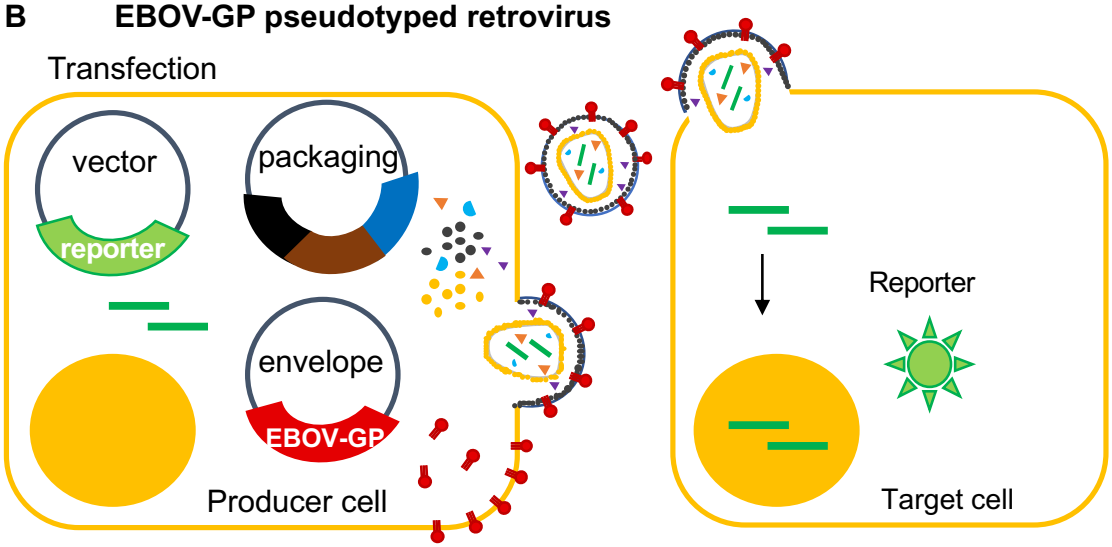
Another model for wild-type EBOV is EBOV virus-like particles (EBOV-VLPs) (Bavari *et al.* 2002; Warfield *et al.* 2003). VLPs are genome-free non-viral particles

produced by co-transfecting 293T cells to express EBOV-GP and the matrix VP40 protein alongside a reporter (Figure 1.9 C). EBOV-VLPs assemble into a similar shape and size to the authentic EBOV viewed by electron microscopy. They have been used to study EBOV macropinocytosis, which may depend on the filamentous shape of EBOV (Saeed *et al.* 2010). EBOV-VLPs and EBOV-GP pseudotyped lentivirus containing a firefly luciferase reporter have also been developed as a safe *in vivo* models to study EBOV infection and test potential therapeutics in protection experiments in mice (Li *et al.* 2016; Chen *et al.* 2018).

A EBOV-GP pseudotyped VSV



B EBOV-GP pseudotyped retrovirus



C EBOV virus-like particle (VLP) production

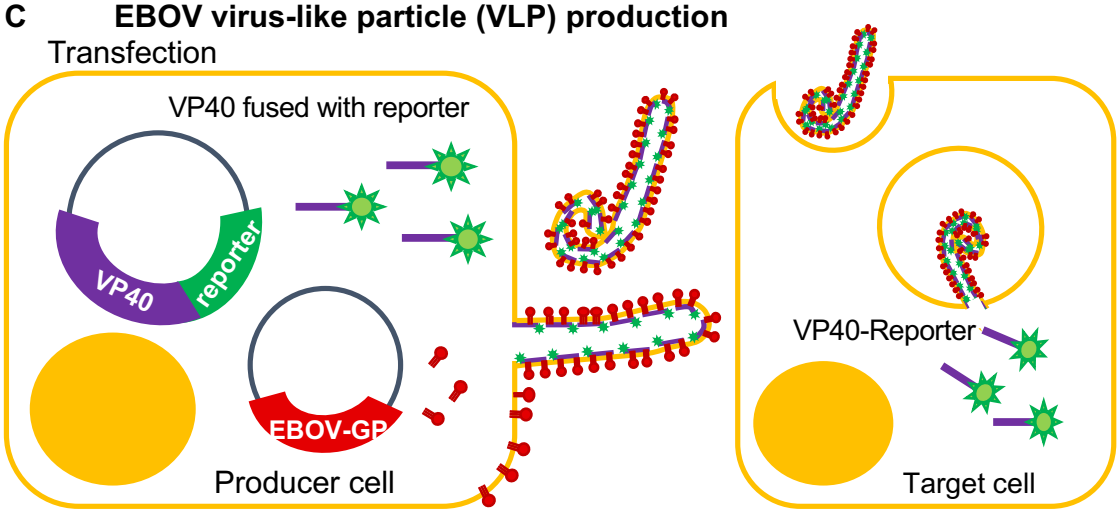


Figure 1. 9 Production of EBOV-GP pseudotyped virus and virus-like particles

Schematic diagram representing the production of different EBOV surrogates (adapted from Salata *et al.* 2019). **A**: Production of EBOV-GP pseudotyped vesicular stomatitis virus (VSV). The homologous envelop protein gene VSV-G is replaced by a reporter gene such as GFP (VSVΔG-GFP). The producer cell is transfected to express EBOV-GP to coat VSVΔG-GFP virions. **B**: EBOV-GP pseudotyped retrovirus is synthesised by co-transfecting the producer cell with three plasmids: the retroviral vector containing the reporter gene, the packaging vector (gag-pol) and the envelope vector encoding EBOV-GP. Pseudotyped retrovirus can transduce the target cell and express the reporter gene. **C**: EBOV virus-like particles (VLPs) are produced by co-transfecting the producer cell with plasmids containing EBOV-GP and VP40 fused with a reporter. VLPs bud into an EBOV-like filamentous shape and can then enters the target cell in an EBOV-GP dependent manner, releasing the reporter proteins. VLPs do not contain a viral genome.

Nonetheless, EBOV-GP surrogates are still different from the wild-type EBOV and vary in their biological properties and susceptibility to neutralising antibodies. Recently, the National Institute of Biological Standards and Control has compared 22 different EBOV-GP based *in vitro* assays with the wild-type EBOV for neutralisation by a small panel of antibodies and sera. The results showed variable but generally poor correlations between the pseudotypes and wild-type EBOV (Wilkinson *et al.* 2017). However, a recent comparison of *in vitro* neutralisation assays using several pseudotyped systems and wild-type EBOV revealed that a combination of assays with pseudotyped VSV predicted protection by antibodies *in vivo* better than wild-type EBOV neutralisation (Saphire *et al.* 2018). Saphire *et al.* also emphasised the deficiency of relying on a single screening assay. Therefore, designing and comparing additional EBOV-GP pseudotyped viruses is important to accurately determine the correlates of protection.

In this study, we describe the development of a new EBOV-GP pseudotyped virus based on a non-replicating Influenza virus S-FLU (Xiao *et al.* 2018). We deleted

the gene segment that encodes surface protein haemagglutinin (HA), and replaced it with an enhanced green fluorescent protein (eGFP) reporter (Powell *et al.* 2012). The E-S-FLU virus does not contain any genetic material from EBOV, and can infect cell-lines that do not express EBOV-GP or Influenza virus HA for only a single cycle. Therefore, it can be handled at biosafety level 1. We have shown that the E-S-FLU virus is easy to produce and that it resembles EBOV during the process of cell entry. We also compared the E-S-FLU virus with recombinant wild-type EBOV in drug screening assays, and the results were highly correlated.

Finally, E-S-FLU was used to screen for neutralisation by human monoclonal antibodies isolated from volunteers in an Ebola vaccine trial (Ewer *et al.* 2016) by my colleague Dr Pramila Rijal (Rijal *et al.* 2019). Eighty-two antibodies were isolated, of which thirty-two were shown to neutralise E-S-FLU. In collaboration with Erica Saphire (Scripps Research), neutralisation of E-S-FLU was shown to correlate with therapy for EBOV infection in a murine model (Saphire *et al.* 2018; Rijal *et al.* 2019). The E-S-FLU virus is therefore a useful novel surrogate for EBOV in studies *in vitro* and *in vivo*.

1.4 Vaccine candidates for Ebola virus disease

Since the discovery of EVD in 1976, multiple vaccine strategies have been investigated. The first EBOV vaccine was the heat- and formalin-inactivated EBOV vaccine, which showed protection in guinea pigs in 1980 (Lupton *et al.* 1980). Following from that, EBOV virus-like particles (VLPs), DNA vaccines and recombinant viral vector vaccines have shown good protection in animal models

(Warfield *et al.* 2003; Grant-Klein *et al.* 2012; Shedlock *et al.* 2013; Henao-Restrepo *et al.* 2017; Ledgerwood *et al.* 2017). Recent advances in EBOV vaccine development and promising vaccination strategies have been reviewed in detail (Ohimain 2016; Dhama *et al.* 2018). However, despite more than 40 years of research and effort, currently there are no licenced vaccines for EBOV prophylaxis, but we are not too far from that. During the 2014 outbreak in West Africa, the WHO approved fast-track regulation for testing vaccine candidates that had a good safety profile and promising efficacy *in vitro* and *in vivo* (WHO 2014). Here I would like to highlight the two most promising vaccine candidates.

The first vaccination platform combines a single dose of priming by a replication-defective chimpanzee adenovirus 3 vector encoding the glycoprotein (GP) of *Zaire ebolavirus* (ChAd3-EBOV), followed by a booster modified vaccinia Ankara (MVA) strain encoding the GP from EBOV (*Zaire),* Sudan virus and Marburg virus, and the nucleoprotein (NP) from Taï Forest virus. This vaccine protected non-human primates from lethal challenge with EBOV (Stanley *et al.* 2014), and showed a good safety profile and induced GP specific B-cell and T-cell immune responses in a phase I clinical trial (Ewer *et al.* 2016; Ledgerwood *et al.* 2017). A larger phase II efficacy trial is currently in progress.

The second one is the rVSV-ZEBOV vaccine, which is based on a recombinant, replication competent vesicular stomatitis virus vector expressing the EBOV-GP. The rVSV-EBOV vaccine protected against EBOV disease in several animal models including the non-human primates (Jones *et al.* 2005; Geisbert *et al.* 2008; Marzi *et al.* 2015). It was tested in a phase III ring vaccination efficacy trial in

humans in Guinea in 2015, and vaccination showed 100% efficacy, i.e. no EVD identified among the randomly assigned vaccinated contacts (Henao-Restrepo *et al.* 2017). In the 2018-2019 EBOV outbreak in DRC, over 80,000 people have already been vaccinated with the rVSV-EBOV vaccine to limit the further transmission of the virus (WHO 2019).

1.5 Therapeutics for Ebola virus disease

Presently, there are no approved therapeutics to treat EVD. EBOV infected patients receive supportive care to relieve the symptoms under the guidelines provided by the WHO, including rehydration and fluid replacement to manage electrolyte balance (WHO 2015). During the 2014-2015 EBOV outbreak, several potential treatment options were tested in small-sized clinical trials with less than 100 patients enrolled. Candidate therapeutics investigated in clinical trial phase I/II are: pooled convalescent plasma from recovered patients; an antibody cocktail ZMapp that includes 3 monoclonal antibodies targeting EBOV-GP; Favipiravir, an RNA polymerase inhibitor; and Tekmira TKM-100802, a siRNA that specifically cleaves EBOV RNA in cells (Table 1.3).

Table 1. 3 Experimental EBOV therapeutics tested in clinical trials

Therapeutics	Description	Clinical trial outcome	Reference
Convalescent blood product	Convalescent whole blood	8 patients treated, reduced mortality in treated patients (12.5% vs. 80%)	Mupapa *et al.* 1999
	Convalescent plasma (unknown level of neutralising antibodies)	No significant improvement in survival	van Griensven *et al.* 2016
	Convalescent whole blood	Significant improvement in survival compared to routine treatment; reduced viral load in 24hr	Sahr *et al.* 2017
ZMapp	EBOV-GP antibody cocktail	Improved survival rate but did not meet the prespecified statistical threshold for efficacy	Davey *et al.* 2016
Favipiravir	RNA-polymerase inhibitor	Inconclusive to efficacy, but may not be sufficient as a monotherapy	Sissoko *et al.* 2016
		Improved survival rate and reduced viral load	Bai *et al.* 2016
TKM-130803	siRNA targeting EBOV VP35 and L	No improvement shown to the severe patients compared to historic controls	Dunning *et al.* 2016
IFN β-1a	Interferon beta 1a	Treated patients had ~1.5 to 1.9-fold improved survival rate	Konde *et al.* 2017

Some of the results showed encouraging evidence for efficacy but required further investigation. On the one hand the sample size was generally too small to reach statistical significance (Davey *et al.* 2016), and on the other, some trials were unrandomised due to ethical considerations, which made it difficult to draw conclusions (Favipiravir, Sissoko *et al.* 2016). For the current outbreak in the Democratic Republic of Congo (DRC), WHO has revised its Monitored Emergency Use of Unregistered and Investigational Interventions (MEURI) statement for EVD (WHO 2018). New treatment trials have been launched in the DRC since November 2018, mainly with four EBOV therapeutic candidates: monoclonal

antibody 114 (Corti *et al.* 2016); antibody cocktails Remdesivir (Pascal *et al.* 2018) and ZMapp (Qiu *et al.* 2014; Davey *et al.* 2016); and an adenosine analogue GS-5734 (Warren *et al.* 2014; Siegel *et al.* 2016).

In order to identify additional candidates for EVD treatment, several research groups have screened libraries of approved drugs for inhibition of EBOV *in vitro* (Gehring *et al.* 2014; Kouznetsova *et al.* 2014; Johansen *et al.* 2015; Sun *et al.* 2017). The advantages of using repurposed drugs are apparent, as they have well understood safety and pharmacokinetics profiles in humans, and can be made available in large quantity in response to large-scale outbreaks.

Surprisingly, a wide variety of drugs inhibited EBOV entry *in vitro*. These ranged from ion channel blockers, estrogen receptor inhibitors, histamine receptor antagonists, anti-depressant reagents and cholinergic receptor inhibitors. A few of them protected mice under EBOV challenge, for instance, estrogen receptor modulators clomiphene and toremifene (Johansen *et al.* 2013). However, the dose of these drugs used to protect mice from EBOV was much higher than their equivalent dosage approved for use in humans, and some *in vivo* protection studies were not reproducible by other groups (Madrid *et al.* 2015) (Table 1.4).

Table 1. 4 Summary of animal tests of EBOV entry inhibitors

Drug	Current application	Animal	Dose in animal study (mg/kg/day)	Maximum daily dose in humans (mg/kg/day)	Survival rate	Reference
Amiodarone	Anti-arrhythmia	Mouse	180	8~12	10~40% (NS)	Madrid *et al.* 2015
		Guinea pig	160		0%	Dyall *et al.* 2018
Azithromycin	Antibiotic	Mouse	200	6~10	10~60% (NS)	Madrid *et al.* 2015
		Guinea pig	100		0%	Madrid *et al.* 2015
Bepridil	Angina pectoris treatment	Mouse	24	Withdrawn	100%	Johansen *et al.* 2015
Clomiphene	SERM; female fertility treatment	Mouse	30	1.25~2	90%	Johansen *et al.* 2013
		Mouse	120		0%	Madrid *et al.* 2015
Chloroquine	Anti-malarial drug	Mouse	180	2.5	70~80%	Madrid *et al.* 2015
		Guinea pig	100		0%	Madrid *et al.* 2015
		Guinea pig	68		0%	Dowall *et al.* 2015
Imipramine	Anti-depressant	Mouse	20	1.5	20% (NS)	Herbert *et al.* 2015
Sertraline	Anti-depressant	Mouse	20	2.5~4	70%	Johansen *et al.* 2015
Tilorone	Antiviral; interferon inducer	Mouse	25	Toxic in humans	90%	Ekins *et al.* 2018
Tetrandrine	Calcium channel blocker	Mouse	15	Not approved	80%	Sakurai *et al.* 2015
Toremifene	Breast cancer treatment	Mouse	30	0.75~1.2	50%	Johansen *et al.* 2013

SERM: selective estrogen receptor modulators.
NS: not significant
Maximum daily dose in humans: based on the British National Formulary (BNF)

Last but not least, the mechanism by which these repurposed drugs are inhibiting EBOV remains enigmatic. The fact that many drug screens were done on EBOV-GP pseudotyped viruses indicates that these drugs are EBOV entry inhibitors. Some studies have led to the discovery of host factors involved in the EBOV cell entry mechanism, such as NPC1 (Côté *et al.* 2011), and endo/lysosomal calcium channel: two-pore channel 1 and 2 (TPC1/2) (Sakurai *et al.* 2015). Lately, small molecules have been developed specifically targeting known host factors that are required for EBOV entry such as cathepsin B/L inhibitors (Linden *et al.* 2016; Penny *et al.* 2018). However, these remain at very early stage *in vitro* investigations.

1.6 Aim of this study

The first part of the thesis describes the development of a novel EBOV-GP pseudotyped Influenza virus, E-S-FLU, and the validation of its use as a BSL-1/2 surrogate for the study of EBOV (Chapter 3). As examples of applications, we screened a pharmacological molecule library LOPAC®1280 with our new pseudotyped virus E-S-FLU (Chapter 4), and E-S-FLU has been used in our laboratory to screen human monoclonal antibodies for neutralisation and to identify a new therapeutic cocktail (Rijal *et al.* 2019).

From the results of screening the LOPAC®1280 drug library, we wanted to understand the mechanism of inhibition of EBOV by drugs from different pharmacological groups. In collaboration with the Platt and Galione groups in the department of Pharmacology (University of Oxford), we began to assay the biochemical effect induced by a panel of EBOV inhibitors on the lysosome.

Moreover, we are interested in identifying the potential drug targets in the host and in EBOV. In Chapters 5 and 6, we have used the CRISPR/Cas 9 technique to knockout genes encoding proteins in the lysosomal membrane, including Niemann-Pick type C2 protein (NPC2), acid sphingomyelinase (ASM) (chapter 5), and two-pore channel 1 and 2 (TPC1/2) (Chapter 6), in order to study more definitively whether these molecules are playing an important role in EBOV entry. In Chapter 7, we report the work we did in collaboration with the Stuart group (Division of Structural Biology, University of Oxford) and the Halfmann group (University of Wisconsin) exploring the role of drugs that directly bind to EBOV-GP as a mechanism to inhibit EBOV entry *in vitro*.

Chapter 2 Materials and Methods

2.1 Materials and reagents

2.1.1 Buffers and media

Table 2. 1 List and recipe of media and buffers

Reagents	Volume	Content
10% formalin	500 ml	PBS + 50 ml 40% formaldehyde (Sigma; F8775)
50X TAE buffer	1000 ml	Distilled water + 242 g Tris base (MW: 121.1 g/mol) + 57.1 g glacial acetic acid + 100 ml 0.5 M EDTA
DMEM	500 ml	Dulbecco's Modified Eagle's Medium - high glucose (Sigma; D5796)
D10	500 ml	DMEM with 10% fetal calf serum, 2 mM glutamine (Sigma; G7513), 100 U/ml penicillin, and 100 µg/ml streptomycin (Sigma; P0781)
FACS fix buffer	500 ml	PBS + 5 ml FCS + 5 ml 40% formaldehyde (Sigma; F8775)
FACS wash buffer	500 ml	PBS + 5 ml FCS (1%)
FCS	500 ml	Fetal calf serum heat inactivated (Sigma; F9665)
HEPES buffer	100ml	1M HEPES buffer (Life Technologies; 15630056)
LB	500 ml	Distilled water + 7.75 g Luria Broth low salt (Sigma; L3022, L3397)
LB-Agar	500 ml	Distilled water + 7.75 g LB + 7.5 g Bacto-Agar (BD; MN663)
Lipofectamine 2000	1.5 ml	Lipofectamine 2000 transfection reagent (Life Technologies; 11668019)
Opti-MEM	100 ml	Opti-MEM I reduced serum medium (Life Technologies; 31985062)
PBS	500 ml	Distilled water + 5 phosphate-buffered saline tablets (Thermo Scientific Oxid; BR0014G)
R10	500 ml	RPMI-1640 (Sigma; R8758) with 10% fetal calf serum, 2 mM glutamine (Sigma; G7513), 100 U/ml penicillin, and 100 µg/ml streptomycin (Sigma; P0781)
Trypsin	100 ml	Trypsin-EDTA solution (Sigma; T3924)
Virus growth medium (VGM)	500 ml	DMEM with 0.1% bovine serum albumin (Sigma; A8327), 10 mM HEPES (Life technology; 15630056), 2 mM glutamine (Sigma; G7513), 100 U/ml penicillin, and 100 µg/ml streptomycin (Sigma; P0781)

2.1.2 Drugs and small molecules

All drug molecules, including the LOPAC®1280 library (LO4100-1EA) used in this study, were ordered from Sigma-Aldrich unless stated otherwise. AY9944 was ordered from Merck (Cat No. 190080); trans-Ned19 was kindly provided by our collaborator Antony Galione (Department of Pharmacology, University of Oxford); Favipiravir (T705) was ordered from Cambridge Biosciences (Cat No. 2778-5). Catalogue numbers for the rest of the individual drugs tested in the drug inhibition assays are listed in Appendix Table 4. X1 in Chapter 4. All drugs were dissolved and stored in 10 mM dimethyl sulfoxide (DMSO) at -20°C.

2.1.3 Cells and culture conditions

Table 2. 2 List of cells used in this study

Cells	Description	Reference
MDCK-SIAT1	Madin-Darby canine kidney epithelial cells; parental cells for all modified SIAT cells (ECACC source number: 05071502)	Matrosovich *et al.* 2003
E-SIAT	MDCK-SIAT1 cells lentiviral transduced to express full-length EBOV-GP (*Zaire* 2014 Makona, NCBI: KJ660346.2).	Xiao *et al.* 2018
EH-SIAT	MDCK-SIAT1 cells lentiviral transduced to express GP-HA hybrid protein (*Zaire* 2014 GP residue 1 to 648 joined with H1 from A/PR8/34 H1N1 residue 521 to 566)	Xiao *et al.* 2018
$E_{mutation}$-SIAT	MDCK-SIAT1 cells lentiviral transduced to express full length EBOV-GP (*Zaire* Makona 2014) with mutations stated	Xiao *et al.* 2018
H7CFv3/ E-SIAT	MDCK-SIAT1 cells lentiviral transduced to co-express *Zaire* EBOV-GP and fusion defective H7CFv3 haemagglutinin	
HeLa WT (1)	Parental HeLa cell for *TPCN*1KO, *TPCN2*KO, *NPC2*KO, *SMPD1*KO cells	ECACC: 93021013 (Sigma)
A17	Two-pore channel 1 (*TPCN1* gene) knockout HeLa cell-lines	
D139		
D149		
B14		

E18	Two-pore channel 2 (*TPCN2* gene) knockout HeLa cell-lines	
E64		
E182		
H12	Niemann-Pick type C2 (*NPC2* gene) knockout HeLa cell-lines	
H182		
I7	Acid sphingomyelinase (*SMPD1* gene) knockout HeLa cell-lines	
I16		
I93		
I147		
HeLa WT (2)	Human epithelioid cervix carcinoma cell-line; parental HeLa cell for ex2 and ex4 *NPC1*KO cells	Tharkeshwar *et al.* 2017
ex2 *NPC1*KO	Niemann-Pick type C1 (*NPC1* gene) knockout HeLa cell-lines	Tharkeshwar *et al.* 2017
ex4 *NPC1*KO	Niemann-Pick type C1 (*NPC1* gene) knockout HeLa cell-lines	Tharkeshwar *et al.* 2017
MEF	Murine embryonic fibroblast (primary cells), provided by Antony Galione (University of Oxford)	
AG-MEF WT	MEF cells from Antony Galione's group, parental wild-type MEF cells for *Tpcn1/2*KO AG-MEF	Ruas *et al.* 2014
AG-MEF *Tpcn1*KO	Two-pore channel 1 (*Tpcn1* gene) knockout AG-MEF cell ($Tpcn1^{tm1Dgen}$ mice)	Ruas *et al.* 2014
AG-MEF *Tpcn2*KO	Two-pore channel 2 (*Tpcn2* gene) knockout AG-MEF cell ($Tpcn2^{Gt(YHD437)Byg}$ mice)	Calcraft *et al.* 2009
AG-MEF DKO	*Tpcn1/2* double knockout AG-MEF cell	Ruas *et al.* 2015
CW-MEF WT	MEF cells from Christian Wahl-Schott's group, parental wild-type MEF cells for *Tpcn1*KO and *Tpcn2*KO CW-MEF	Arndt *et al.* 2014
CW-MEF *Tpcn1*KO	Two-pore channel 1 (*Tpcn1* gene) knockout CW-MEF cell ($Tpcn1^{Arndt\ et\ al.}$ mice)	Arndt *et al.* 2014
CW-MEF *Tpcn2*KO	Two-pore channel 2 (*Tpcn2* gene) knockout CW-MEF cell ($Tpcn1^{Grimm\ et\ al.}$ mice)	Grimm *et al.* 2014
293T	HEK293T cells	
B cell	Epstein-Barr virus (EBV) transformed B cell-line (provided by Tao Dong, University of Oxford)	

All cell types used in this study are adherent cells (MDCK-SIAT1, HeLa, murine embryonic fibroblasts (MEF) and HEK293T), except B cells, which are in suspension. All adherent cells were cultured in D10 medium for growth (DMEM with 10% fetal calf serum (FCS), 2 mM glutamine (Sigma; G7513), 100 U/ml penicillin, and 100 µg/ml streptomycin). B cells were cultured in R10 medium

(RPMI-1640 with 10% FCS, 2mM glutamine, 100 U/ml penicillin and 100 µg/ml streptomycin).

2.1.4 Primers and sgRNAs (guide RNA for CRISPR/Cas 9 knockout)

Table 2. 3 List of primers used in this study

Primer	Sequence	Purpose
JX001	CCCTTGGCTTCGTTAGAACGCGG	*NPC1* gene sequencing
JX002	AGACAACCTGCAGCTGCCTCTAC	
JX003	CTGTGACGAGTCTGTGGATGAGG	
JX004	GGGTCACAACCAATCCAGTTGAC	
JX005	CCACAAGAAAGGGGACTTCTTCTTTGTGTATGCCG	*NPC1* D502F mutagenesis
JX006	CGGCATACACAAAGAAGAAGTCCCCTTTCTTGTGG	
JX009	GCCATTTGTCTGCAGAATTGG	CRISPR plasmid sequencing
JX011	ATGATACAGAGAAGCTCCAGAGG	*NPC1* gene sequencing
JX012	GGTTAGACATTAAACGTCAAGAG	
JX013	CATGAGATTCCTGCCCATGTTCC	
JX014	CACATGGGCAGCTCCGTGTTC	
JX015	GTACCCTTTGGACCTAGTCTTGACATACAGATACTG	*NPC1* P434S mutagenesis
JX016	CAGTATCTGTATGTCAAGACTAGGTCCAAAGGGTAC	
JX017	GAGCAGATGGTCCCCAGATATGG	pHR-SIN plasmid sequencing
JX018	CGGTGGGAGGTCTATATAAGCAG	pCDNA3.1 plasmid sequencing
JX028	ATGGTCAAGGTGATGTGTCC	HeLa *TPCN1*KO gDNA PCR
JX029	ATGGAGGTGGCAGGAGAGTC	
JX030	GGCTCATGAAGACTGTGCAG	HeLa *TPCN2*KO gDNA PCR
JX031	CTTCTCTGTGCAAGGCTGAC	
JX032	TCACACTTCCTGCCAACATC	HeLa *TPCN1*KO gDNA PCR
JX033	GATGTTGGCAGGAAGTGTGA	
JX060	GTGACCGAGCAGGATGACAT	HeLa *TPCN2*KO gDNA PCR
JX061	TTGATCACGGGTATCCTGGA	
JX074	CTACCTCCAGGAAGGCGAGA	HeLa *TPCN1*KO RT-PCR
JX075	CATCTGGGAAATTGGCTGTG	
JX076	CCAGCACCGAGGTCTTGAC	
JX077	ACTTACCGCAGCATCCAAGT	HeLa *TPCN2*KO RT-PCR
JX078	TGCTATTCAGTACCGCTCCA	
JX079	AACAGGTAACCCTTCACAGAG	
JX081	CTTCCAGAACAGCCATTCCGTGC	*NPC1* gene sequencing
JX082	CCGAACAGGTAACCCTTCAC	HeLa *TPCN2*KO RT-PCR

JX083	CACCAACCAGCTGGCGAGCGTGGGCCTGA	EBOV-GP R64A mutagenesis
JX084	TCAGGCCCACGCTCGCCAGCTGGTTGGTG	
JX087	CCCCAACCTGCACGCCTGGACCACCCAGG	EBOV-GP Y517A mutagenesis
JX088	CCTGGGTGGTCCAGGCGTGCAGGTTGGGG	
JX089	GACCACCCAGGCCGAGGGCGCTG	EBOV-GP D522A mutagenesis
JX090	CAGCGCCCTCGGCCTGGGTGGTC	
JX091	CACCGAGGGCCTGGCGCACAACCAGGACG	EBOV-GP M548A mutagenesis
JX092	CGTCCTGGTTGTGCGCCAGGCCCTCGGTG	
JX093	GAGCTACTGTGATCCAGCCT	HeLa *NPC2*KO gDNA PCR
JX094	CCAGGCTAACCATCAGGTCA	
JX095	CCTTTCCCATTCCTGAGCCT	
JX096	AGGCTCAGGAATGGGAAAGG	
JX097	GGAAGTGAATGTGAGCCCAT	HeLa *NPC2*KO RT-PCR
JX098	CCCAGCAGAAGAGACTTTGG	
JX099	CACCATCACCCCATTGTGAC	HeLa *SMPD1*KO gDNA PCR
JX100	CCTGGGCAACATAGCAAGAT	
JX101	GCATCCTCTTCCTCACTGAC	
JX102	GTCAGTGAGGAAGAGGATGC	
JX103	CCAGGTTACATCGCATAGTG	HeLa *SMPD1*KO RT-PCR
JX104	GTGGAGTTGATCAAGAGCCA	
JX105	GCTGCGGAGCATGGGCCTGAACC	EBOV-GP V66M mutagenesis
JX106	TGGTTGGTGCTGCTCAGCTTGTC	
JX111	GAACTACGAAGAGGGCGAGTGGGCCGA	EBOV-GP A101E mutagenesis
JX112	ACCACCTTGGGTGGCACG	
JX115	GGTGGCCTTCATGATCCTGCCCC	EBOV-GP L184M mutagenesis
JX116	ACGCCCTCGGCAAAGGTG	
JX117	GGTGGCCTTCGCGATCCTGCCCCAGGC	EBOV-GP L184A mutagenesis
JX118	ACGCCCTCGGCAAAGGTG	
JX119	CTTCCTGATCGCGCCCCAGGCCAAGAAGGACTTCTTCAG	EBOV-GP L186A mutagenesis
JX120	GCCACCACGCCCTCGGCA	
JX121	CAACCTGCACGTCTGGACCACCCAGGAC	EBOV-GP Y517V mutagenesis
JX122	GGGTTGCACTTGGGCTGG	
JX123	CGAGGGCCTGGTGCACAACCAGG	EBOV-GP M548V mutagenesis
JX124	GTGTAGATGCCCTCGGCGG	
AT_7I5	ATGGGCGTGACCGGAATCCTGC	EBOV-GP sequencing
AT_7I6	GATGCAGATACGTGCACAAGGTGT	
AT_7I7	ACACCTTGTGCACGTATCTGCATC	
AT_7I8	CTGGAAAGTGAACCCCGAGATCG	
AT_7I9	CAGCACCGCCAGCGATACCCC	
AT_8A1	CTTCGGCCCTGCCGCCGAGGG	

Table 2. 4 List of sgRNAs used in this study for CRISPR/Cas 9 knockout

sgRNA name	sgRNA sequence
tpcn1_5' sgRNA#10	CACCGGTCCGTGGTTTACATTCATC
tpcn1_5' sgRNA#10	AAACGATGAATGTAAACCACGGACC
tpcn1_5' sgRNA#1	CACCGGTATGCGCAACACTAGGGAC
tpcn1_5' sgRNA#1	AAACGTCCCTAGTGTTGCGCATACC
tpcn1_5' sgRNA#6	CACCGGAGTAAGAGCACGTCAAGG
tpcn1_5' sgRNA#6	CACCCCTTGACGTGCTCTTACTCC
tpcn1_3' sgRNA#1	CACCGGTATTCCTACCGCAGTGT
tpcn1_3' sgRNA#1	AAACACACTGCGGTAGGAATACC
tpcn1_3' sgRNA#3	CACCGGAGCAAACCTACACTGCGGT
tpcn1_3' sgRNA#3	AAACACCGCAGTGTAGGTTTGCTCC
tpcn1_3' sgRNA#4	CACCGGTGCCATTCCATCCACGCAC
tpcn1_3' sgRNA#4	AAACGTGCGTGGATGGAATGGCACC
tpcn2_5' sgRNA#1	CACCGGTCCTTGATCACGGGTATCC
tpcn2_5' sgRNA#1	AAACGGATACCCGTGATCAAGGACC
tpcn2_5' sgRNA#2	CACCGGATGACTCCACCCGGCAGTG
tpcn2_5' sgRNA#2	AAACCACTGCCGGGTGGAGTCATCC
tpcn2_5' sgRNA#6	CACCGGTGATGCCGAGGCACTTACC
tpcn2_5' sgRNA#6	AAACGGTAAGTGCCTCGGCATCACC
tpcn2_3' sgRNA#5	CACCGGCCCACCCGGGACCTAGAAT
tpcn2_3' sgRNA#5	AAACATTCTAGGTCCCGGGTGGGCC
tpcn2_3' sgRNA#7	CACCGGCCCTGGAGGGGCGAGCCAAT
tpcn2_3' sgRNA#7	AAACATTGGCTCGCCCCTCCAGGGCC
tpcn2_3' sgRNA#10	CACCGGACCCAGTCAGTCGCCCC
tpcn2_3' sgRNA#10	AAACGGGGCGACTGACTGGGTCC
npc2_5' sgRNA#1	CACCGGTCAGTTGCCTTGTTAGATA
npc2_5' sgRNA#1	AAACTATCTAACAAGGCAACTGACC
npc2_5' sgRNA#2	CACCGGTAAACAACCTTATCTAACA
npc2_5' sgRNA#2	AAACTGTTAGATAAGGTTGTTTACC
npc2_5' sgRNA#3	CACCGGTTCTCCTAAGAAACTGTGA
npc2_5' sgRNA#3	AAACTCACAGTTTCTTAGGAGAACC
npc2_3' sgRNA#4	CACCGGCCATTATTGAGGACACGGG
npc2_3' sgRNA#4	AAACCCCGTGTCCTCAATAATGGCC
npc2_3' sgRNA#5	CACCGGAGATAGGTGCGGTGTT
npc2_3' sgRNA#5	AAACAACACCGCACCTATCTCC
npc2_3' sgRNA#6	CACCGGACTGGATTAGAGTTCTGA
npc2_3' sgRNA#6	AAACTCAGAACTCTAATCCAGTCC
smpd1_5' sgRNA#1	CACCGGTGAGTTACAGGGCAATATC
smpd1_5' sgRNA#1	AAACGATATTGCCCTGTAACTCACC
smpd1_5' sgRNA#2	CACCGGCCATTTCCAAACTGGGGCT
smpd1_5' sgRNA#2	AAACAGCCCCAGTTTGGAAATGGCC
smpd1_5' sgRNA#3	CACCGGAGATATTGCCCTGTAACTC
smpd1_5' sgRNA#3	AAACGAGTTACAGGGCAATATCTCC

smpd1_3' sgRNA#4	CACCGGTCTACTGTTTTGCCGCACC
smpd1_3' sgRNA#4	AAACGGTGCGGCAAAACAGTAGACC
smpd1_3' sgRNA#5	CACCGGAGCCAAATGAAGAGCACTA
smpd1_3' sgRNA#5	AAACTAGTGCTCTTCATTTGGCTCC
smpd1_3' sgRNA#6	CACCGGCAATCAGAGACAATGCCCC
smpd1_3' sgRNA#6	AAACGGGGCATTGTCTCTGATTGCC

2.1.5 Pseudotyped viruses

Table 2. 5 List of pseudotyped viruses used in this study

Pseudotyped virus	Coated protein	Reference No.
E-S-FLU (C15 *Zaire*)	Full-length EBOV-GP (*Zaire*, Makona C15 2014)	KJ660346.2
Mayinga E-S-FLU	Full-length EBOV-GP (*Zaire*, Mayinga 1976)	AF086833
Sudan E-S-FLU	Full-length SUDV-GP (*Sudan* Gulu 2000)	NC_006432.1
Bundibugyo E-S-Flu	Full-length BDBV-GP (*Bundibugyo* 2007)	NC_014373.1
Taï Forest E-S-FLU	Full-length TAFV-GP (*Taï Forest* 1994)	NC_014372.1
E(Δmucin)-S-FLU	Mucin-like domain deleted EBOV-GP (*Zaire*, Makona C15 2014, residue 313 to 463 deleted)	
$E_{mutation}$-S-FLU	Full-length EBOV-GP (*Zaire*, Makona C15 2014) with mutation introduced	
H7CFv3/E-S-FLU	Full-length EBOV-GP (*Zaire*, Makona C15 2014) and fusion defective H7 (H7N9 A/HK/125/2017)	GP: KJ660346.2; H7: GISAID: EPI977395 with eleven mutations
H5-S-FLU	Full-length H5 (H5N1 A/Vietnam/1203/2004)	GISAID: EF541403.1
H7-S-FLU	Full-length H7 (H7N9 A/HK/125/2017)	GISAID: EPI977395
GP-lentivirus	Full-length EBOV-GP (*Zaire*, Makona C15 2014)	KJ660346.2

2.1.6 Antibodies and plasma samples

Table 2. 6 List of antibodies and plasma samples

Primary antibody			
Antibody	**Target protein**	**Epitope**	**Reference**
KZ52	EBOV-GP	Base	Lee *et al.* 2008
100	EBOV-GP	Base	Corti *et al.* 2016; Misasi *et al.* 2016
66-6-3	EBOV-GP	Base	Rijal *et al.* 2019
66-4-C12	EBOV-GP	Base	Rijal *et al.* 2019
6D6	EBOV-GP	Fusion loop (FL)	Furuyama *et al.* 2016
P6 (VIC 82)	EBOV-GP	Glycan cap (GC)	Saphire *et al.* 2018; Rijal *et al.* 2019
125	EBOV-GP	Glycan cap (GC)	Rijal *et al.* 2019
66-4-A8	EBOV-GP	Mucin-like domain (MLD)	Rijal *et al.* 2019
114	EBOV-GP	Receptor binding region (RBR)	Corti *et al.* 2016; Misasi *et al.* 2016
C13C6	EBOV-GP	Receptor binding region (RBR)	Wilson *et al.* 2000; Murin *et al.* 2014
MR78	Marburg GP	Receptor binding region(RBR)	Hashiguchi *et al.* 2015
21D85A	H1 haemagglutinin	Head	Rijal; Not published
Z2B3	N1 neuraminidase		Rijal; Not published
AF9C	N1 neuraminidase		Rijal; Not published
4A-14	H7 haemagglutinin	Head	Huang *et al.* 2019
NIBSC samples			
Sample code	**Sample description**		**Reference**
9	Unimmunised bovine IgG (negative)		Wilkinson *et al.* 2017
36	NHBST healthy donor plasma (negative)		
28	NHSBT EBOV convalescent plasma		
43	Norwegian EBOV convalescent plasma		
79	American EBOV convalescent plasma		
31	Bovine IgG (immunised with VLP-*Zaire* EBOV-GP)		
88	Bovine IgG (immunised with *Zaire* and *Sudan* EBOV GP DNA)		
Secondary antibody			
Antibody		**Fluorescence label**	**Cat No.**
Goat anti-human IgG (H+L)		FITC	Life Technologies; H10301

Goat anti-Human IgG (H+L)	Alexa Fluor® 647	Life Technologies; A21445
Goat anti-Mouse IgG (H+L)	Alexa Fluor® 488	Life Technologies; A28175

2.2 Pseudotyped Influenza virus (S-FLU) production

2.2.1 Seed S-FLU virus

The pseudotyped S-FLU virus was generated on the basis of a non-replicating pseudotyped Influenza virus (S-FLU) that was previously described (Powell *et al.* 2012). We used a version that expresses enhanced green fluorescent protein (S-eGFP), which has its S-HA coding sequence replaced with an eGFP reporter gene. We isolated subclones of the original S-FLU virus that showed brighter fluorescence and found a single T60C mutation in the A/PR/8/34 HA signal sequence (NCBI reference sequence accession No. NC_002017.1) that abrogated an out-of-frame ATG, which had interfered with downstream eGFP expression. All subsequent versions of the S-FLU virus contain this enhancement, which gave a sufficiently bright fluorescence signal from infected cells to read on the CLARIOstar® fluorescence plate reader (setting see section 2.6.3).

Seed S-FLU viruses coated in H5, H7, or H1 HA were titrated by standard 50% tissue culture infective dose ($TCID_{50}$) assay on MDCK-SIAT1 cells by fluorescence detection. Wells containing clones of eGFP-expressing S-FLU virus 4 standard deviations above 16 control wells were detected with a plate reader (section 2.6.3), and the $TCID_{50}$/ml was calculated by the Reed-Muench method (Reed and Muench 1938). Seed viruses were doubly cloned by limiting dilution.

2.2.2 E-S-FLU virus production

E-S-FLU viruses were propagated and grown in Madin-Darby canine kidney epithelial (MDCK-SIAT1) cells (Matrosovich *et al.* 2003) transduced with lentivirus to express supplemental surface protein to coat the S-FLU virus (Powell *et al.* 2012; Xiao *et al.* 2018). cDNA encoding EBOV-GP from different EBOV species (Table 2.5) was human codon optimised and synthesised by GeneArt. Lentiviral vector pHR-SIN (Demaison *et al.* 2002) was engineered to incorporate the cDNA and was sequenced.

We transduced MDCK-SIAT1 cells to express EBOV-GP at the cell surface. EBOV-GP transduced cells were stained with EBOV-GP specific monoclonal antibody (MAb) KZ52 (Lee *et al.* 2008), which is specific to *Zaire* GP; or 66-4-C12, which is cross-reactive to bind GP from *Zaire*, *Bundibugyo* and *Sudan ebolavirus* species (Rijal *et al.* 2019), followed by a second layer of fluorescein isothiocyanate (FITC)-conjugated goat anti-human antibody (Life Technologies reference no. H10301). Stained cells were bulk-sorted with a fluorescence-activated cell sorter (FACS) to achieve maximal expression of EBOV-GP (E-SIAT cell-line). EBOV-GP was detected on 99% of the sorted cells and was stable and uniform up to at least the ninth passage after sorting.

Multiplicity of infection (MOI) of approximately 1 (~1 CID_{50}/cell) of seed S-FLU virus per cell was added to infect E-SIAT cells to produce E-S-FLU virus. Titration experiments revealed that seeding E-SIAT cells with MOI ~ 1 gave the highest titer of the E-S-FLU, whereas a lower MOI (~0.01 CID_{50}/cell) was adequate for seeding HA-SIAT cell-lines (Powell *et al.* 2012; Xiao *et al.* 2018). Seed S-FLU virus was

diluted in 10 ml viral growth medium (VGM) (Dulbecco's modified Eagle's medium (DMEM) with 0.1% bovine serum albumin, 10 mM HEPES, 2 mM glutamine, 100 U/ml penicillin, and 100 µg/ml streptomycin). Virus was removed after 2 hours of incubation and cells were washed with phosphate-buffered saline (PBS). 40 ml VGM was then added to the cells and incubated for 48 hours at 37°C in a 5% CO_2 without added trypsin. Replication of HA-pseudotyped viruses required the addition of trypsin as described previously (Powell *et al.* 2012). Culture supernatant was harvested and stored in aliquots at -80°C.

2.2.3 GP-HA hybrid protein pseudotyping S-FLU

We attempted to pseudotype the S-FLU Influenza virus with a hybrid GP-HA protein (EH) aiming to improve the yield of virus. GP-HA hybrid protein was designed by fusing the extracellular domain of EBOV-GP (*Zaire* Makona 2014, NCBI: KJ660346.2) with the transmembrane and cytoplasmic domain of Influenza HA from Influenza A/PR8/34 (NCBI: NC_002017.1). We identified the transmembrane domain of GP and HA based on their hydrophobicity plots. Both GP and HA protein sequences were analysed by the Kyte-Doolittle scale using the Enzyme X program. The C-terminal amino acid residues of GP were replaced by the HA C-terminus, and the joining point was adjusted by eye to form a continuous gradient of hydrophobicity. Based on this analysis, GP-HA was created as a hybrid of GP amino acid residue number 1 to 648 merged with H1 HA amino acid residue 521 to 566 (counting from the initiating methionine). MDCK-SIAT1 cells that were transduced to express GP-HA fusion protein were stained and sorted as described previously. This is the EH-SIAT cell-line.

2.2.4 Dual pseudotyped S-FLU: H7CFv3/E-S-FLU

Holly Sadler and Alain Townsend in our lab designed H7CFv3, a H7 haemagglutinin (H7N9 A/HK/125/2017; GISAID code: EPI977395) with eleven mutations (Table 2.7) introduced to abolish its fusion activity while maintaining the sialic acid binding affinity.

Table 2. 7 Mutations introduced to H7 in H7CFv3

Chain: Mutation	Description	Reference
HA1: R329Q	Inhibited cleavage of the precursor HA0 into HA1 and HA2	Orlich, Linder and Rott 1995; Chen *et al.* 1998; Stech *et al.* 2005; Katsura *et al.* 2012
HA1: S212C	Inter-chain disulphide bond to lock the HA head	Godley *et al.* 1992; Lee *et al.* 2015
HA1: S216C		
HA1: T30C	Inter-chain disulphide bond to lock the HA stem	
HA2: Q47C		
HA2: F63P	Prevent the complete conformational change of HA2 during fusion	Gruenke *et al.* 2002
HA2: F70P		
HA2: G1Q	Mutations in the fusion peptide, inhibited fusion	Cross *et al.* 2010
HA2: L2G		
HA2: I6G		
HA2: G8A		

Haemagglutinin numbering was based on the H3 numbering system reviewed in Burke and Smith 2014.

cDNA encoding H7CFv3 was human codon optimised and synthesised by GeneArt and cloned into lentiviral vector pHR-SIN (Demaison *et al.* 2002). We transduced E-SIAT cells to co-express EBOV-GP (*Zaire* Makona 2014, NCBI: KJ660346.2) and H7CFv3. Transduced cells were stained with mouse anti-GP antibody 6D6 (Furuyama *et al.* 2016) and human anti-H7 antibody 4A-14 (Huang *et al.* 2019), followed by Alexa Fluor® 647 conjugated goat anti-human IgG and

Alexa Fluor® 488 conjugated goat anti-mouse IgG for FACS analysis. Cells with high expression of both H7CFv3 and EBOV-GP were bulk sorted as H7CFv3/E-SIAT cell-line. 1 MOI of seed S-FLU was added to produce H7CFv3/E-S-FLU with the same method as described in section 2.2.2.

2.3 Pseudotyped virus infection and titration

2.3.1 S-FLU virus titration on MDCK-SIAT1 cells

100 µl of harvested culture supernatants containing the S-FLU viruses (e.g. E-S-FLU, H5-S-FLU) were titrated in 2-fold dilutions in VGM across a flat-bottom 96-well plate. MDCK-SIAT1 indicator cells were washed in PBS, and $3X10^4$ cells in 100 µl of VGM were added to each well and incubated for 18 to 24 hours (37°C, 5% CO_2). Medium was removed from the wells, and cells were fixed in 10% formalin (in PBS) for 30 min at 4°C. The virus titre was assessed by eGFP fluorescence analysed with a fluorescence plate reader (CLARIOstar®, section 2.6.3). The dilution of virus that gave 50% of the maximum plateau fluorescence signal (EC_{50}) was calculated by linear interpolation. The EC_{50} dilution obtained by best fit of the titration curve to the Poisson distribution was very similar (data not shown). The typical EC_{50} dilution for the E-S-FLU virus harvested after 48 hours were 1:8, compared to 1:500 for the H5-S-FLU or H7-S-FLU virus. From the EC_{50} dilution and the number of cells per well ($3X10^4$), the 50% cell infective dose (CID_{50}/ml) was calculated as $2X10^6$ in a typical E-S-FLU virus batch and $1.6X10^8$ in the H5-S-FLU virus batch.

2.3.2 S-FLU virus infection in HeLa and MEF cells

A total of $1X10^5$ HeLa or mice embryonic fibroblast (MEF) cells were seeded into a 24-well tissue culture plate in 500 µl of D10 medium (DMEM with 10% fetal calf serum, 2 mM glutamine, 100 U/ml penicillin, and 100 µg/ml streptomycin) the night before infection. After cells adhered to the wells, the medium was removed, and cells were washed once with PBS. 500 µl of undiluted E-S-FLU ($2X10^6$ CID_{50}/ml) were titrated in 2-fold dilutions in PBS, and H5-S-FLU ($1.6X10^8$ CID_{50}/ml) or H7-S-FLU ($1.92x10^8$ CID_{50}/ml) were titrated in VGM. Virus dilutions were pre-warmed to 37^{o}C and added to infect the cells overnight (18-24 hours, 37°C, 5% CO_2). After infection, cells were trypsinised and fixed with FACS fix buffer (PBS with 1% FCS and 0.4% formaldehyde. Percent infection was analysed by counting fluorescent cells in a flow cytometer. We observed an inhibitory effect when diluting E-S-FLU with VGM or DMEM when infecting HeLa and MEF cells, therefore we used PBS instead of VGM to dilute the virus.

2.3.3 S-FLU infection in B cell-line

An Epstein-Barr virus (EBV) transformed B cell-line was kindly provided by our collaborator Peng Yanchun (Tao Dong's lab, Weatherall Institute of Molecular Medicine, University of Oxford). $5X10^5$ cells were added to a well of round-bottomed 96-well plate. B cells were spun down at 1,400 rpm (revolutions per minute) for 5 min. Medium was removed and cells were resuspended with 100 µl of S-FLU virus titrated in 2-fold dilutions in VGM or R10 medium from undiluted harvested culture supernatant. After 18 to 24 hours infection (37°C, 5% CO_2), cells were spun down again at 1,400 rpm for 5 min and resuspended with FACS fix buffer. Percent infection was analysed by flow cytometry.

2.3.4 GP-lentivirus infection and titration

The EBOV-GP pseudotyped lentivirus (GP-lentivirus) was kindly provided by our collaborator Edward Wright (University of Sussex). GP-lentivirus used in this study was coated with the EBOV-GP from *Zaire* C15 (Makona 2014, NCBI: KJ660346.2). GP-lentivirus carries a firefly luciferase reporter gene. $3X10^4$ cells/well of HeLa or MEF cells were seeded in D10 in flat-bottomed 96-well plate the day before infection. Medium was removed and cells were washed once with PBS. 200 µl of GP-lentivirus was titrated from undiluted culture supernatant in 2-fold dilutions with VGM, and added to infect the cells for 48 to 72 hours. Infection was quantified by measuring luciferase reporter expression. Medium was removed from the wells, and cells went through one round of freeze-thaw cycle. 50 µl of Glo-lysis buffer (Promega; E2661) was added to lyse the cells for 15 min, and then 50 µl of Bright-Glo substrate (Promega; E2620) was added for a 10-min enzymatic reaction in dark at room temperature. 80 µl of the reaction mix was transferred to white opaque OptiPlates (PerkinElmer 6005290) for luminescence measurement with the GloMax-Multi detection system (Promega).

2.4 Monitoring E-S-FLU and H5-S-FLU virus growth

2.4.1 S-FLU virus growth curve

A 175 cm^2 flask of confluent E-SIAT and H5-SIAT cells were seeded with ~1 MOI of seed S-FLU virus in 10 ml VGM. After 2 hours of incubation with seed S-FLU virus, any remaining seed virus was removed by washing with PBS. 40 ml VGM was added to the cells, without trypsin for E-SIAT, and 0.75 µg/ml TPCK trypsin to H5-SIAT cells. Immediately 100 µl VGM was sampled as time point 0-hour post-seeding. Cells were then incubated in VGM for 72 hours at 37°C, 5% CO_2. Culture

supernatant was sampled every 3-hour period post-seeding and titrated on indicator MDCK-SIAT1 cells. The EC_{50} was calculated from the titration curve by linear interpolation. The CID_{50}/ml was calculated as described in section 2.3.1.

2.4.2 Imaging S-FLU replication by IncuCyte®

$3X10^4$ cells/well of MDCK-SIAT1, E-SIAT, or H5-SIAT cells were seeded in D10 in a flat-bottomed 96-well plate the day before infection. Medium was removed and cells were washed once with PBS. A total of 100 $TCID_{50}$ of seed S-FLU virus diluted in 200 µl VGM was added to infect cells and replicate. Live images of representative plaques were taken by IncuCyte® every 3 hours for 72 hours. E-SIAT cells supported the formation of small diffuse plaques, unlike the dense plaques formed on H5-SIAT cells.

2.5 Antibody micro-neutralisation (MN assay)

The micro-neutralisation (MN) assay was used to measure the inhibition titer of antibodies against virus entry *in vitro*. The assay was conducted as described by Powell *et al.* (Rowe *et al.* 1999; Powell *et al.* 2012) with minor modifications. S-FLU viruses were used at a concentration that gave close-to-maximum plateau fluorescence in infected MDCK-SIAT1 cells (~4 CID_{50}/cell). In a flat-bottomed 96-well plate, 50 µl volume of virus in VGM was pre-incubated with 50 µl of antibody at 2-fold dilutions for 2 hours. The beginning dilution of antibody or plasma sample (from NIBSC, Wilkinson *et al.* 2017) was stated in each experiment in the result section. A total of $3X10^4$ MDCK-SIAT1 cells in 100 µl of VGM was then seeded into each well for overnight infection (37°C, 5% CO_2). After infection, the medium was removed from the wells and the cells were fixed with 100 µl of 10% formalin

(in PBS) for 30 min at 4°C; the formalin was then replaced with 100 µl of PBS. The plates were analysed with a fluorescence plate reader (CLARIOstar®, section 2.6.3) and by fluorescence microscopy. The IC_{50} was calculated by linear interpolation.

Antibody MN assay with GP-lentivirus was conducted as follows: 50 µl of GP-lentivirus were pre-incubated with 50 µl of antibody at 2-fold dilutions for 2 hours, and $3X10^4$ MDCK-SIAT1 cells were added. Cells were incubated with virus for infection in VGM for 48 hours. Infection was quantified by measuring luciferase reporter expression. Medium was removed from the wells, and cells went through one round of freeze-thaw cycle. 50 µl of Glo-lysis buffer (Promega; E2661) was added to lyse the cells for 15 min, and then 50 µl of Bright-Glo substrate (Promega; E2620) was added for a 10-min enzymatic reaction in dark at room temperature. 80 µl of the reaction mix was transferred to white opaque OptiPlates-96 (PerkinElmer 6005290) for luminescence measurement with the GloMax-Multi detection system (Promega).

2.6 Drug inhibition assay

2.6.1 Individual drug titration

All small inhibitor molecules were stored in 10 mM DMSO at -20°C. Drugs were diluted in VGM to give a starting concentration of 100 µM (unless stated otherwise) and then titrated in 50 µl of VGM at 2-fold dilutions across a 96-well plate. A total of $3X10^4$ MDCK-SIAT1 cells were seeded in 50 µl of VGM and pre-incubated with the drug for 3 hours (37°C, 5% CO_2). A 100 µl volume of the E-S-FLU (4 CID_{50}/cell) or H5-S-FLU (4 CID_{50}/cell) virus diluted in VGM to give plateau expression of eGFP

in 3X10^4 MDCK-SIAT1 cells was then added for overnight infection. After infection, medium was removed and cells were fixed with 100 µl of 10% formalin (in PBS) for 30 min at 4°C. The formalin was then replaced with 100 µl of PBS, and the plates were analysed with a fluorescence plate reader (CLARIOstar®) as for the antibody MN assay. Infection and inhibition were quantified by measurement of the eGFP expression level, and the IC_{50} value was calculated by linear interpolation.

2.6.2 WGA staining as an estimate of drug toxicity

As the result of the toxic effect of many drug molecules on cells at high concentrations, dead cells were washed away before plate reading. This may give a falsely low eGFP fluorescence reading in the plate reader but can be detected by visual inspection in a fluorescence microscope. To estimate the number of cells remaining in each well, plates were stained with Alexa Fluor® 647 conjugated wheat germ agglutinin (WGA) (Life Technologies, W32466) after cells were fixed and washed once with PBS. WGA is a lectin that binds to sialic acid and *N*-acetylglucosaminyl residues at the cell surface. A 50 µl volume of 5 µg/ml WGA was added to each well and incubated for 15 min at room temperature in the dark. Plates were then washed twice with PBS before being read in 100 µl PBS.

2.6.3 CLARIOstar® plate reader settings

Fluorescence plate readout was performed in Costar 96-well cell culture plates (Costar no. 3799). We chose the Costar 96 microplate mode in the CLARIOstar® software. For measurement of eGFP levels, fluorescence excitation was at 483 nm (bandwidth of 8 nm) and emission was at 515 nm (bandwidth of 8 nm) with a

499 nm dichroic filter. Each well had 50 flashes at a 4-mm diameter and fluorescence readout from the top optic, giving the orbital averaging value. For measurement of Alexa Fluor® 647 (e.g. WGA staining in the drug inhibition assay, and 647 conjugated second layer in immunofluorescence assay), fluorescence excitation was at 630 nm (bandwidth of 30 nm) and emission was at 678 nm (bandwidth of 20 nm). Each well had 53 flashes at 4 mm and fluorescence readout from the top optic, giving the orbital averaging value. The focal length and gain were adjusted before each plate was read. Generally, the optimal focal length was 5.0 mm, the gain of the eGFP channel was adjusted to 3,000, and the gain for Alexa Fluor® 647 channel was adjusted to 2,500.

2.6.4 LOPAC®1280 library screen

LOPAC®1280 is a library of small molecules we ordered from Sigma (LO4100-1EA). Drugs were supplied as 10 mM solutions dissolved in DMSO, organised in 16 plates of 96-well plates (80 drugs per plate). In the first round of screening, we tested all the drugs at 5 μM and 100 μM in the drug inhibition assay against E-S-FLU and H5-S-FLU based on the method described in section 2.6.1. Infection was quantified by measuring eGFP fluorescence and toxicity was estimated by measuring WGA staining by CLARIOstar® fluorescence plate reader. This was further confirmed by observation under a fluorescence microscope. Drugs that inhibited E-S-FLU or H5-S-FLU were further titrated individually to calculate the IC_{50} value for inhibition.

Johansen *et al.* screened 2,635 compounds for antiviral activity against a genetically engineered Ebola virus that expresses eGFP (eGFP-EBOV) *in vitro*

(Johansen *et al.* 2015). In their supplementary Table S1, they listed all the experimental data for the small molecules they screened in their study. Of the 2,635 molecules they tested, 538 were also found in the Sigma LOPAC1280 library and were screened against the E-S-FLU virus in our study. We compared the inhibitory effects of these 538 compounds in both screenings (i.e., each molecule was either positive [inhibited infection] or negative [did not inhibit infection in the concentration range tested]) and performed a Fisher exact test to measure the significance of the association.

2.7 E-S-FLU virus sandwich ELISA assay

We used an enzyme-linked immunosorbent assay (ELISA) with virus to detect and quantify S-FLU in the harvested culture supernatant. On day 1, a 96-well NUNC plate was coated with 50 µl anti-N1 neuraminidase antibody AF9C 20 µg/ml (diluted in PBS + 0.1% BSA) at 4 ^{o}C overnight. On day 2, AF9C antibody was removed and the coated NUNC plate was blocked with 250 µl 5% milk solution (PBS) for 2 hours at room temperature or overnight at 4 ^{o}C. On day 3, milk solution was removed completely, and the plate was washed four times with 300 µl PBS. 200 µl of E-S-FLU titrated in 2-fold dilutions in VGM was added to the plates and incubated for 2 hours at room temperature or overnight at 4 ^{o}C. Unbound E-S-FLU virus was removed and plates were washed four times with PBS. Next, 50 µl of 2 µg/ml (PBS with 0.1% BSA) biotinylated anti-GP antibody C13C6 was added to the plates to detect any bound E-S-FLU virus and incubated for 2 hours at room temperature. Biotinylated C13C6 antibody was removed, and plates washed four times with PBS. 50 µl extravidin conjugated with horseradish peroxidase (HRP) (1:1600 diluted in PBS with 0.1% BSA) was added per well and plates incubated

at room temperature for 2 hours. Extravidin-HRP was removed and plate was washed thoroughly for four times with PBS. 50 µl HRP substrate (Bio-Rad, 1721064) was added per well, incubated for 5 min at room temperature, and quenched by 50 µl 1 M H_2SO_4. Plate was read with CLARIOstar® to measure absorbance at the wavelength of 450 nm.

2.8 Fluorescence microscope pictures

All fluorescence microscope pictures in this study (except confocal images) were taken using an AxioVert S100 (Zeiss) with X10 objective lens under bright-field channel, 488 nm wavelength channel (eGFP, FITC), 590 nm wavelength channel (mCherry) or 647 nm wavelength channel (Alexa Fluor® 647). Images were processed with Zen 2012 (Zeiss).

2.9 FACS sorting

Cell sorting was done by Craig Waugh and Kevin Clark (Weatherall Institute of Molecular Medicine, FACS facility) using a FACS Aria III cell sorter (BD Biosciences). Bulk sort cells were collected in D10 medium, spun down at 1,400 rpm for 5 min and resuspended in fresh D10 for further culturing. Single-cell sorting was collected in flat-bottomed 96-well tissue culture plates with 200 µl D10 for cloning.

2.10 LogP and pKa^{base} calculation

LogP (partition parameter) and pKa^{base} values (strongest basic pKa) mentioned in this study were either obtained from The Drugbank Database

(https://www.drugbank.ca), or estimated based on their chemical structures using the MarvinSketch and Chemicalize program (https://chemicalize.com).

2.11 NPC1 phenotype assays

Experiments described in section 2.11 were done by our collaborator Nick Platt and Frauke Fuchs (Department of Pharmacology, University of Oxford).

2.11.1 LysoTracker® staining

LysoTracker® staining was done based on the method described in (Lachmann *et al.* 2004). Murine macrophage J774 cells (ATCC TIB-67) or MDCK-SIAT1 cells were treated with drugs at a fixed concentration for 48 hours. Cells were trypsinised and washed with PBS and counted. 10^6 cells were resuspended in 50 µl PBS and mixed with 50 µl of 0.4 µM (diluted in PBS) LysoTracker® Green DND-26 (Invitrogen). Cells were stained for 10 min in dark at room temperature, then spun down and washed once with 100 µl PBS. Stained cells were resuspended in 250 µl PBS containing 0.5 µg/ml propidium iodide to distinguish dead cells, and immediately analysed by FACS.

2.11.2 Filipin staining

Murine macrophage J774 cells and MDCK-SIAT1 cells were seeded on coverslips and treated with drugs at a fixed concentration (as mentioned in the result Chapter 4) for 48 hours. A preliminary investigation was conducted to determine the maximal concentration of each drug that did not significantly impact upon cell viability after 48 hours of treatment. After drug treatment, cells were fixed with 4% paraformaldehyde (PFA) in PBS for 20 min on ice, then washed three times with

PBS. 1 ml of 1.5 mg/ml glycine (PBS) was added to incubate the coverslips for 10 min at room temperature to quench any remaining PFA, this was followed by washing three times with PBS. Cells were stained with 0.05 mg/ml filipin solution (PBS + 10% FCS + 0.2% Triton X100) for 2 hours at room temperature or overnight at 4 °C. After filipin staining, coverslips were washed three times with PBS and mounted. Microscopic pictures were taken using confocal microscope. Punctate staining was judged by visual inspection single blinded (i.e. scored without knowing the drug treatment). All drugs were tested in at least three independent experiments. +/- in the summary table (Table 4.5) was an indication that there was not an apparently consistent and reproducible effect of inducing punctate filipin staining.

2.11.3 Amplex® Red staining

Amplex® Red Cholesterol Assay Kit (Invitrogen, catalogue No. A12216) was used to quantify the cholesterol level in cells. J774 cells were treated with drugs at a fixed concentration for 48 hours, and assay was performed based on the manufacturer's manual.

2.11.4 Sphingomyelin OlyA staining

Ostreolysin A (OlyA) protein binds and stains cholesterol- and sphingomyelin-rich membranes as described in Skočaj *et al.* 2014. J774 cells and MDCK-SIAT1 cells were seeded on a microscope coverslip and cultured with drugs at a fixed concentration for 48 hours. After removing the medium with drugs, cells were rinsed with PBS and fixed with 3% paraformaldehyde for 30 min at room temperature on a rotary shaker. Cells were washed with PBS and then treated with

blocking and permeabilisation buffer (PBS + 1% Casein + 0.1% Triton X100) for 1 hour. Permeabilisation buffer was washed away with PBS, and cells were stained with eGFP conjugated OlyA and Hoechst nuclear dye for 30 to 45 min with gentle mixing at room temperature. Finally, cells were washed twice in PBS and mounted for confocal microscopy imaging. Punctate staining was judged by visual inspection single blinded (i.e. scored without knowing the drug treatment). All drugs were tested in at least three independent experiments. +/- in the summary table was an indication that there was not an apparently consistent and reproducible effect of inducing punctate OlyA-GFP staining.

2.12 Lysosomal membrane permeability staining

Lysosomal permeability staining experiment was conducted by our collaborator Gokhan Yilmaz (Department of Pharmacology, University of Oxford). The experiment was based on the lectin galactoside-binding soluble 3 (galectin/LGALS3) staining method described by Aits *et al.* 2015. The staining method was verified and optimised in MDCK-SIAT1 cells, using L- leucyl-L-leucine methyl ester (LLOMe, MP Biomedicals, catalogue No: 153142). LLOMe is a lysosomotropic agent that ruptures the lysosome which subsequently induces apoptosis (Uchimoto *et al.* 1999). 2 mM of LLOMe induced lysosomal membrane permeabilisation in MDCK-SIAT1 cells and resulted in >90% puncta positive cell staining after 1 to 6 hours treatment. Puncta colocalised with lysosomal-associated membrane protein LAMP1 staining.

To test the effect of drug treatment on lysosomal membrane permeability, MDCK-SIAT1 cells were grown on coverslips and treated with drugs at a fixed

concentration for 3 hours or 48 hours. After treatment, medium was removed, cells were washed once with PBS and fixed with 4% paraformaldehyde for 10 min at room temperature. After fixation, cells were washed three times with PBS, followed by blocking with 5% goat serum (PBS + 1% BSA + 0.3% Triton X100) for 20 min at room temperature. Primary antibody anti-mouse/human Mac3 (Galectin-3) (BioLegend; cat no: 126702) was diluted 1:1000 (PBS + 1% BSA + 0.3% Triton X 100) to stain cells overnight at 4 ^{o}C. Cells were washed for three times with PBS (0.25% BSA and 0.1% Triton X100), and incubated with secondary antibody Alexa Fluor® 488 conjugated anti-mouse antibody (diluted 1:1000 in PBS + 5% goat serum + 0.25% BSA and 0.1% Triton X100) for 1 hour at room temperature in the dark. Cells were washed with PBS and incubated with Hoechst nuclear stain (1:5000). The coverslips were washed twice in PBS before mounting.

For quantification, confocal microscopic pictures were taken of 5 random regions with more than 100 cells. Cells with more than 3 puncta were counted as positive. Experiment was repeated at least three times.

2.13 Synergy drug inhibition assay

2.13.1 Synergy drug inhibition experiment

A drug assay for synergy was used to test the inhibitory effect of drug pairs based on the method described in Williams *et al.* 2012, combined with the drug inhibition assay described in section 2.6.1. Prior to synergy experiments, individual drugs were titrated to inhibit E-S-FLU (section 2.6.1), and the concentration at which each drug inhibited 30% infection of virus was determined (referred as IC_{30}). To test the effect of drug A on drug B, 25 µl of drug A with concentration IC_{30} (diluted

in VGM) was mixed with 25 µl drug B titrated in 2-fold dilutions in VGM from 100 µM across the flat-bottomed 96-well plate. $3X10^4$ MDCK-SIAT1 cells in 50 µl VGM was added to incubate with the 50 µl drug mixture (drug A constant + drug B titration); or 50 µl titration of B only (25 µl drug B titration + 25 µl VGM); or drug A only (25 µl drug A at concentration IC_{30} + 25 µl VGM) for 3 hours (37°C, 5% CO_2) (Figure 2.1A). Each titration was tested in duplicate in the same experiment. 100 µl of the E-S-FLU (4 CID_{50}/cell) virus diluted in VGM to give plateau expression of eGFP in $3X10^4$ MDCK-SIAT1 cells was then added for overnight infection. After infection, medium was removed and cells were fixed with 100 µl of 10% formalin (in PBS) for 30 min at 4°C. The formalin was then replaced with 100 µl of PBS, and the plates were analysed with a fluorescence plate reader (CLARIOstar®). Inhibition% of a given well condition was calculated based on the reduction% of fluorescence compared to the fluorescence level in wells containing virus without drugs.

2.13.2 Synergy calculation and Bliss additivity

From the synergy inhibition assay experiment, we measured and plotted the inhibition% curve for (drug A constant IC_{30} + drug B titration) and for (drug B titration only) against drug B concentration (Figure 2.1 B). An average inhibition% for drug A constant was calculated from 8 repeat wells ($I_{[Aconstant]}$%). Based on drug B titration curve and $I_{[Aconstant]}$%, we calculated the Bliss additivity curve for drug B + A. The Bliss additivity equation calculates inhibition% by drug B + drug $A_{[constant]}$ = $I^{Bliss}_{[Bx+Aconstant]}$% = ($I_{[Bx]}$% + $I_{[Aconstant]}$%) - ($I_{[Bx]}$% * $I_{[Aconstant]}$%), assuming there was only an additive effect between the two drugs. We then calculated the sum of residuals between the experimental titration curve of drug B + drug $A_{constant}$ with the predicted Bliss Additivity curve for drug B + drug $A_{constant}$. 17 drugs were tested pairwise (289 pairs) and the complete experiment was repeated twice.

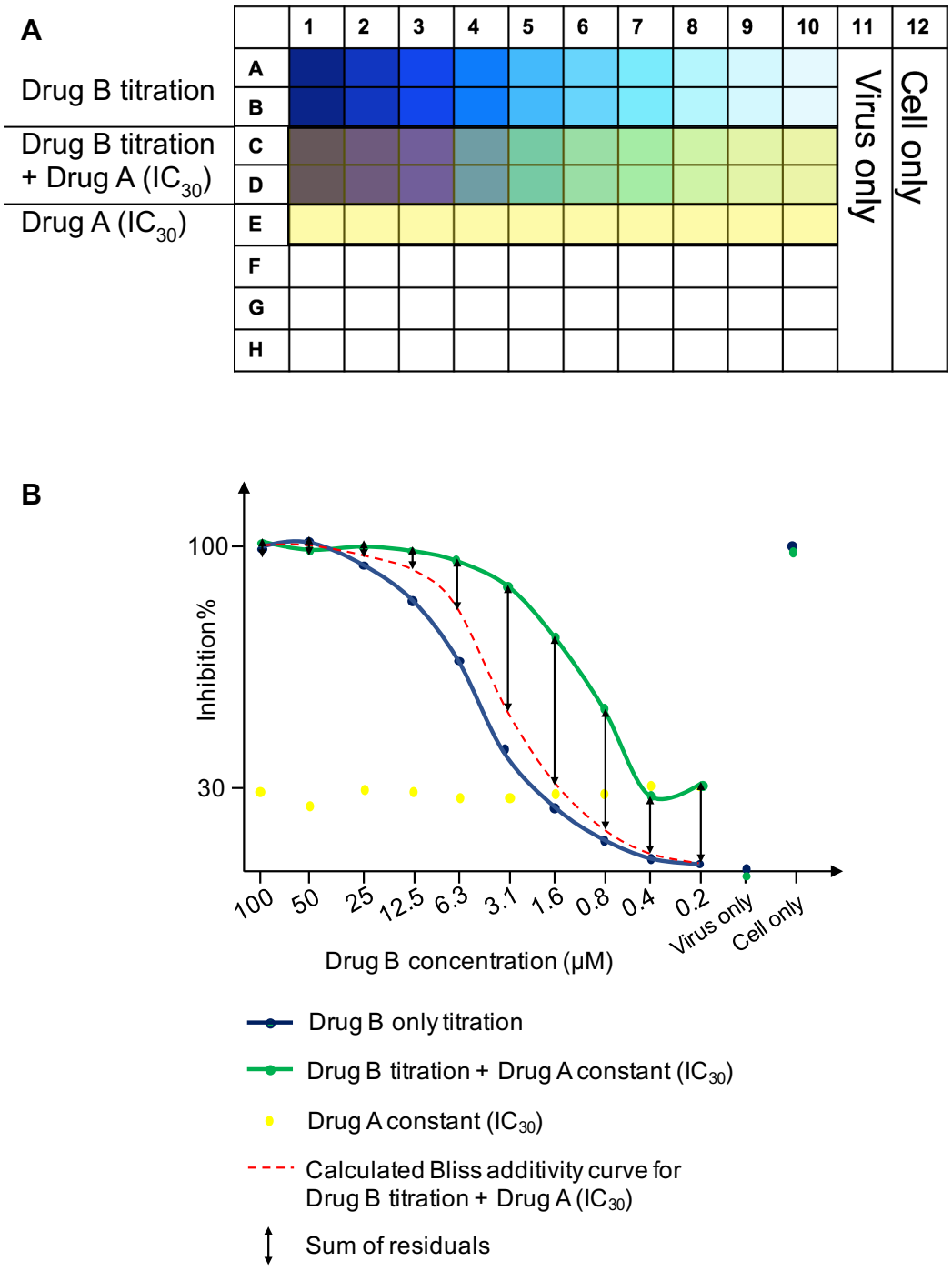


Figure 2. 1 Schematic diagram demonstrating drug synergy assay
A Plate design for drug synergy assay. Drug B was titrated either alone or with a constant concentration of drug A. The shades of blue indicate the concentration of drug B, the darker the higher the concentration. Drug A was held constant (light yellow). **B** An example result of drug B + A synergy assay set up in **A**. E-S-FLU infection expresses an eGFP reporter gene, and the Inhibition% was calculated based on the reduction of eGFP fluorescence from virus only control. The double headed arrows show how the sum of residuals was calculated between the

experimental inhibition curve of Drug B + A, and the calculated Bliss additivity curve for Drug B + A.

We selected potential synergising pairs if an effect beyond Bliss additivity was seen on both directions (i.e. drug A constant improved drug B titration inhibition and drug B constant improved drug A titration inhibition) in both experimental repeats. To select potential synergising drug pairs, we first removed the pairs that had a negative value of sum of residuals. For the remaining drugs, we multiplied the two sum of residuals from the repeats and selected drug pairs with values >1000 (an arbitrary threshold value) in both directions.

2.14 CRISPR/Cas 9 genetic knockout

The CRISPR/Cas 9 technique was used to specifically knockout four genes from HeLa cells: *TPCN1* (Two-Pore Channel 1), *TPCN2* (Two-Pore Channel 2), *NPC2* (Niemann-Pick disease Type C2) and *SMPD1* (Sphingomyelin Phosphodiesterase 1/ Acid Sphingomyelinase).

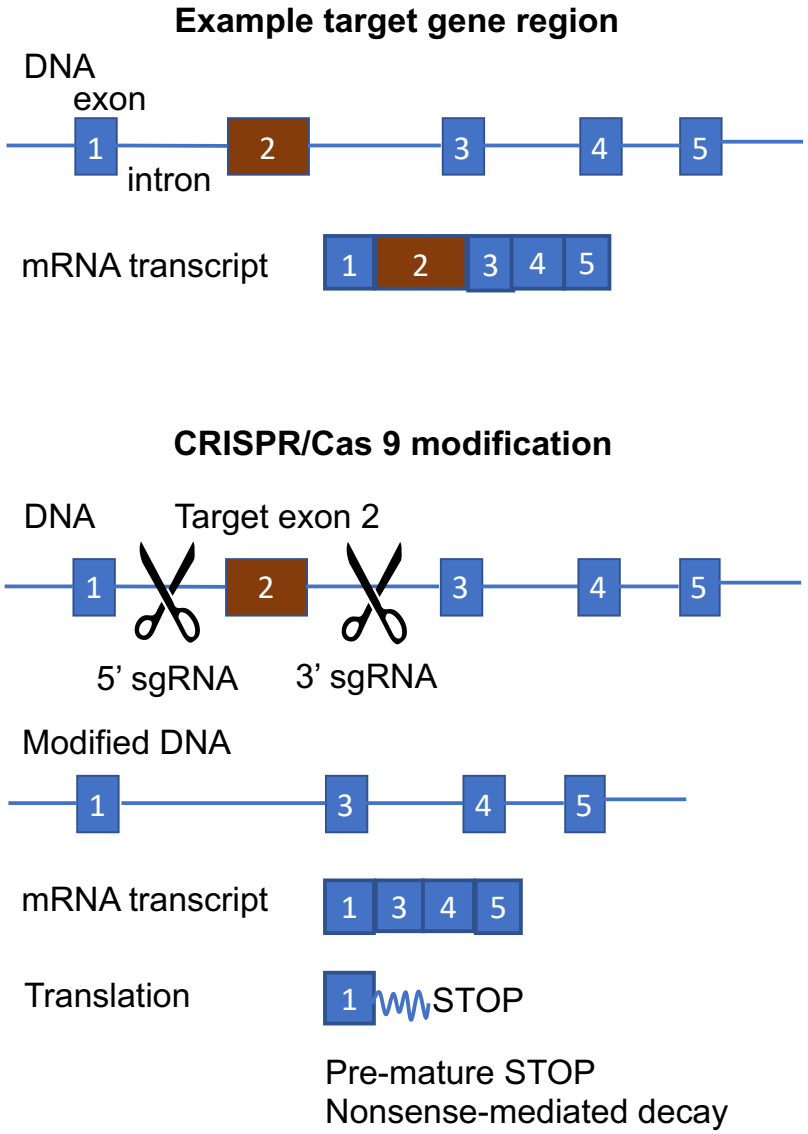


Figure 2. 2 Double sgRNAs CRISPR/Cas 9 strategy
Schematic diagram showing the CRISPR/Cas 9 strategy used in this study. Cas 9 enzyme was directed to cut at the upstream (5') and downstream (3') intron regions flanking the target exon, resulting in deletion of an exon. Deletions were designed to result in a frameshift in the modified mRNA transcript, thus introducing a pre-mature STOP codon and a non-functional peptide fragment. The altered mRNA may also undergo nonsense-mediated decay.

2.14.1 Choosing target exon and designing sgRNAs

The design of the CRISPR/Cas 9 knockout strategy was done in consultation with Dr Philip Hublitz from the Genome Engineering Service at the Weatherall Institute of Molecular Medicine. As HeLa cells are more than diploid at many chromosomal regions, we used the double sgRNAs strategy to delete the target exon (Figure 2.2) (Ran *et al.* 2013; Lonowski *et al.* 2017; Knott and Doudna 2018). The DNA sequence of 250 base pair (bp) upstream and downstream intronic region of the target exon were submitted to Massachusetts Institute of Technology (online: crispr.mit.edu) to design guide sgRNAs. We selected 6 sgRNAs from the list (3 from upstream 5', 3 from downstream 3') that ranked high in specificity and low in off-target recognition rates. The sgRNAs were cloned into CRISPR/Cas 9 encoding plasmid pX458 that contains an mRuby or eGFP fluorescence reporter gene.

2.14.2 Verification of sgRNAs by surveyor assay

Philip Hublitz verified all the sgRNAs in 293T cells. 293T cells were lipofectamine transfected three times with px458 plasmid containing the test sgRNA, Cas 9 enzyme and Ruby/eGFP fluorescence reporter gene. Genomic DNA was isolated from 293T cells 3 days after transfection. PCR amplified around 400-500 bp genomic region enclosing the sgRNA annealing with an unequal positioning, i.e. about 100-200 bp upstream and 200-300 bp downstream of the proposed cut site. Platinum HiFi Master Mix PCR kit (Life Technologies) was used, with conditions stated in the manufacturer's manual, with a modified annealing temperature to 62°C. The PCR product was checked on a 0.8% TAE agarose gel. If the tested sgRNA efficiently targeted cleavage of DNA, then mutations, insertions or

deletions would be introduced at the cut site and resulting in a heterogeneous mixture of the PCR product (Figure 2.3).

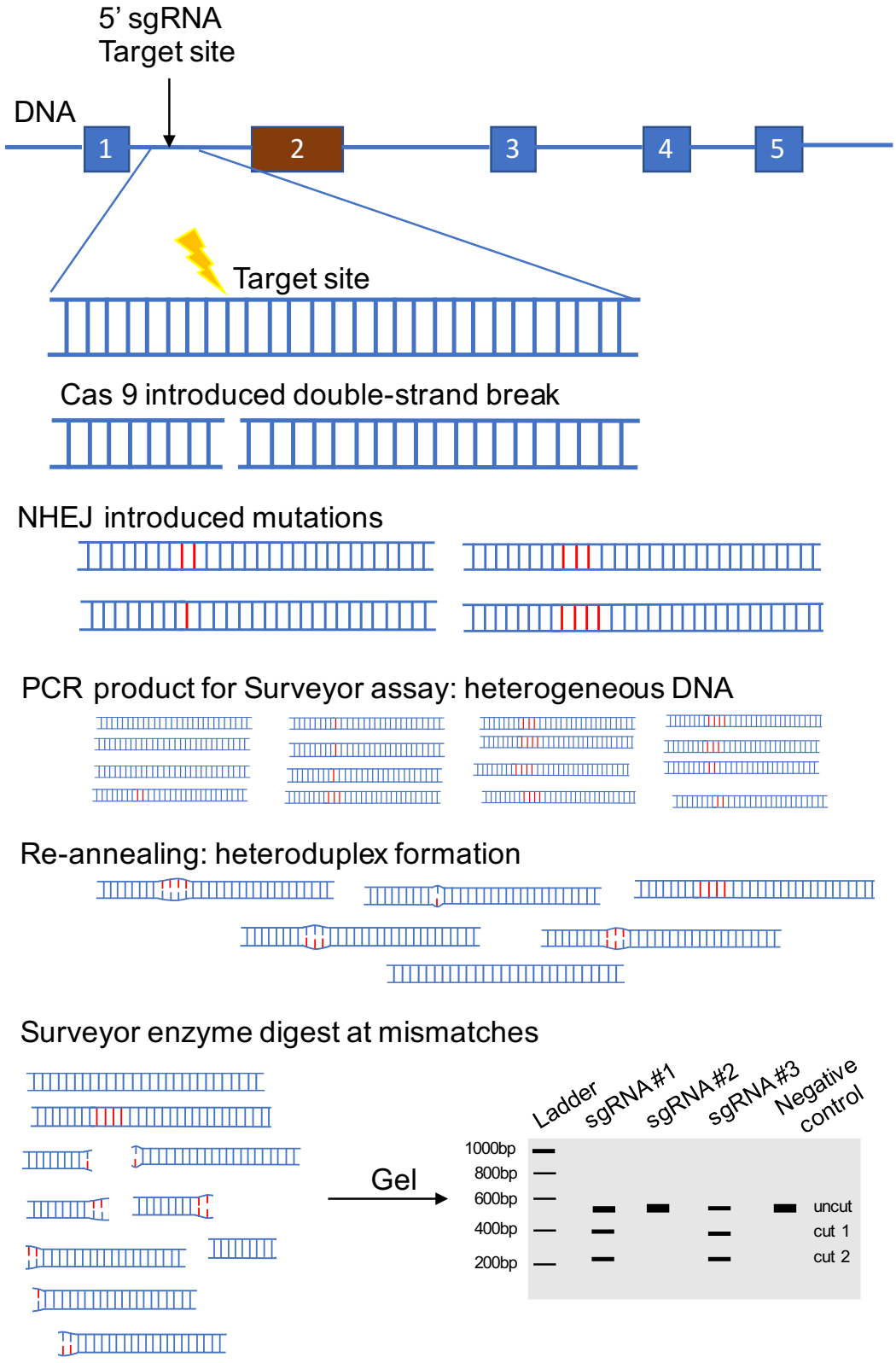


Figure 2. 3 Surveyor assay verifying sgRNAs in 293T cells

Schematic diagram showing the mechanism of the surveyor assay, adapted from (http://crispr.technology). Individual sgRNAs were verified for their efficiency of guiding Cas 9 to cut at the target site. Successful CRISPR digestion would lead to non-homologous end joining DNA repair, introducing mutations or indels at the cut site. PCR amplification of the region flanking the sgRNA targeted site with uneven upstream and downstream regions, results in a heterogenous mixture of DNA duplexes. Amplification products were subjected to re-annealing, which causes heteroduplex DNA formation. Surveyor enzyme cuts at mismatched regions in the heteroduplex DNAs, and the cut profile is resolved in a DNA agarose gel.

For re-annealing, the PCR product was heated up to 95 ^{o}C for 10 min, and gradually cooled down to 25 ^{o}C at a rate of 0.3 ^{o}C per second, forming heteroduplex DNA with mismatches. 10 µl re-annealed DNA mixture was mixed with 1.4 µl $MgCl_2$, 1 µl Enhancer and 1 µl surveyor nuclease; digested at 42 ^{o}C for 50 min and stopped by adding 1.5 µl STOP solution (Integrated DNA Technologies, catalogue number: 706021). Digested product was analysed on 2.5% TAE agarose gel (ethidium bromide), with loading buffer omitting any dye (10% glycerol + 50% w/v sucrose).

2.14.3 HeLa cell sgRNA transfection and single cell cloning

We selected a pair of 5’ sgRNA and 3’ sgRNA for each targeted gene based on the surveyor assay result. 5’ sgRNA and 3’ sgRNA were cloned into two separate px458 plasmids containing eGFP and mRuby reporter genes respectively. $1X10^5$ HeLa cells from an early passage were seeded in a 24-well plate in D10 medium the night before transfection. The next day, the medium was changed to 400 µl Opti-MEM I medium (Life Technologies, 31985062). 500 ng of each sgRNA (5’ and 3’) containing plasmid was incubated with 2 µl Lipofectamine 2000 (Life Technologies, 11668019) in 100 µl Opti-MEM I medium for 20 min at room temperature, and mixture added to transfect HeLa cells. Cells were transfected using the same conditions twice on successive days. The $mRuby^{+ve}$/$eGFP^{+ve}$

double fluorescence expressing cells were single-cell sorted by FACS three days after the second transfection. FACS sorting was conducted by Craig Waugh and Kevin Clark (Weatherall Institute of Molecular Medicine, FACS facility) using a FACS Aria III cell sorter (BD Biosciences). Single-cell clones were expanded in D10 medium.

2.15 Genomic DNA isolation

For isolating genomic DNA (gDNA) from single-cell clone culture, cells in a confluent 12-well plate well were washed with PBS and lifted using trypsin (Sigma; T3924). Cells were spun down for 5 min at 11,000 rpm, and the supernatant discarded. The cell pellet was resuspended with 500 µl of Lysis buffer (50 mM Tris HCl pH 8.0, 100 mM EDTA, 100 mM NaCl, 1% SDS) and 5 µl of 20 µg/ml proteinase K (Life Technologies, EO0491) and incubated overnight at 56 °C, 500 rpm.

The next day, cell lysate was cooled, and 600 µl of isopropanol was added. The precipitate was spun down at 15,000 rpm for 30 min at 2 °C. The supernatant was carefully removed and discarded, and 500 µl 70% ethanol was added to wash the pellet, spun at 15,000 rpm for 5 min at room temperature. Ethanol was removed and the pellet was air-dried for 15 min. To dissolve the gDNA pellet, 500 µl TE buffer (nuclease free water, 10 mM Tris·Cl, pH 8.0, 1 mM EDTA) was added and incubated for at least 4 hours or overnight at 55 °C at on a shaker at 1050 rpm. Dissolved gDNA concentration was determined by NanoDrop™ spectrophotometer, and gDNA was stored at 4 °C.

For isolating gDNA from confluent wells in 96-well plates, medium was removed and cells were washed once with PBS. The plate underwent one freeze-thaw cycle on dry ice. 50 µl of cell lysis buffer containing proteinase K (10 mM Tris HCl pH 7.5, 10 mM EDTA, 10 mM NaCl, 0.5% SDS, 50 µg proteinase K) was added to each well. The plate was parafilm-sealed with lid-on, and incubated in a sealed and humidified Tupperware box at 56 °C overnight. Next day, the plate was cooled down to room temperature for 30 min and all the liquid spun down to the bottom of the wells (1,400 rpm for 1 minute). 100 µl of ice cold NaCl/ethanol solution (150 µl of 5 M NaCl in 10 ml 100% ethanol) was added to each well without mixing, and incubated at room temperature for 30 min. Stringy precipitate became visible at the end of the incubation time. The plate was inverted carefully and slowly to remove ethanol, and tapped on tissue to soak off the remaining ethanol. 100 µl room temperature 70% ethanol was added to each well, pipetted to the corner of the wells and incubated for 5 min. Plate was again inverted carefully to remove ethanol and the remaining liquid was soaked off using tissue. The plate was then dried in a 56 °C oven for 10 to 15 min. 50 µl TE buffer was added to dissolve the gDNA pellet. The plate was sealed (STARLAB, E2796-9795) and incubated at 56 °C for 2 hours until the DNA completely dissolved.

2.16 Genomic DNA PCR

Genomic DNA (gDNA) PCR was conducted using a Phusion® High-Fidelity DNA Polymerase Kit (NEB, E0553L) or CloneAmp™ DNA Polymerase kit (Clonetech, 639298). The conditions are summarised in Figure 2.4. The PCR product was then loaded on 1% TAE agarose gel (ethidium bromide) with DNA Gel Loading Dye and 1 Kb Plus DNA Ladder (Life Technologies, 10787018).

Phusion PCR mix

Reagent	Volume	Final conc.
GC buffer (5X)	4 µl	1X
dNTP (10 mM)	0.4 µl	200 µM
Primer mix (forward + reverse, 10 µM each)	1 µl	0.5 µM each
DMSO	0.3 µl	1.5%
gDNA (~100 ng/µl)	1 µl	100 ng
Phusion Polymerase (2 units/µl)	0.2 µl	0.4 unit
Nuclease free water	13.1 µl	
Total volume	20 µl	

Phusion PCR thermal cycler program

Step 1	Initial denaturation	98 °C	1 minute
X35 cycle from step 2 – 4			
Step 2	Denaturation	98 °C	10 seconds
Step 3	Annealing	63 °C	1 minute
Step 4	Extension	72 °C	30 seconds per kb
Step 5	Final extension	72 °C	5 minutes
Step 6	Hold	4 °C	∞

CloneAmp PCR mix

Reagent	Volume	Final conc.
CloneAmp HiFi PCR Premix (2X)	5 µl	1X
Primer mix (forward + reverse, 5µM each)	0.5 µl	0.25 µM each
gDNA (~100 ng/µl)	0.5 µl	50 ng
Nuclease free water	4 µl	
Total volume	10 µl	

CloneAmp PCR thermal cycler program

Step 1	Initial denaturation	98 °C	1 minute
(X35 cycle from step 2 – 4)			
Step 2	Denaturation	98 °C	10 seconds
Step 3	Annealing	55 °C	15 seconds
Step 4	Extension	72 °C	5 seconds per kb
Step 5	Hold	4 °C	∞

Figure 2. 4 gDNA PCR conditions

A summary of the PCR mix and thermal cycler conditions used to amplify DNA from genomic DNA samples. Conditions were optimised based on the manufacturer's manuals from the Phusion® High-Fidelity DNA Polymerase Kit (NEB, E0553L) and the CloneAmp™ DNA Polymerase kit (Clonetech, 639298).

2.17 RNA isolation

RNeasy Plus Mini Kit (Qiagen, 74134) was used to isolate RNA from cultured cells. Medium was removed from a confluent well of a 6-well well plate (~1X10^6 HeLa cells). 600 µl RLT Plus buffer with 6 µl β-mercaptoethanol was added to lyse the cells. Lysate was spun through QIAshedder spin column (Qiagen, 79656) for 2 minutes at maximum speed in a micro-centrifuge at 4 ^oC, the eluent was collected, following the manufacturer's manual (Qiagen, 74134). RNA was stored in nuclease free water at -20 ^oC, and concentration was determined by NanoDrop™ spectrophotometer before each thaw and use.

2.18 Reverse transcriptase PCR (RT-PCR)

RT-PCR was conducted by using the SuperScript™ III One-Step RT-PCR System with the Platinum™ *Taq* High Fidelity DNA Polymerase kit (Life Technologies, 12574035). Conditions were optimised based on the manufacturer's manual (Figure 2.5). The PCR product was separated and analysed on a 1% TAE agarose gel.

SuperScript™ III One-Step RT-PCR

Reagent	Volume	Final conc.
Rx Mix buffer (2X)	10 µl	1X
Primer mix (forward + reverse, 4µM each)	1 µl	0.2 µM each
RNA (~100 ng/µl)	1 µl	100 ng
RT/Taq polymerase mix	0.4 µl	
RNase free water	7.6 µl	
Total volume	20 µl	

RT-PCR thermal cycler program

Step 1	Reverse transcription	50 °C	30 minutes
Step 2	Initial denaturation	944 °C	2 minutes
(X35 cycle from step 3 – 5)			
Step 3	Denaturation	94 °C	15 seconds
Step 4	Annealing	59 °C	30 seconds
Step 5	Extension	68 °C	1 minute per kb
Step 6	Final extension	68 °C	10 minutes
Step 6	Hold	4 °C	∞

Figure 2. 5 RT-PCR conditions
A summary of the reagent mixes and thermal cycler conditions used to reverse transcribe RNA and subsequently amplify cDNA by PCR. Conditions were optimised based on the manufacturer's manuals from the SuperScript™ III One-Step RT-PCR System with Platinum™ *Taq* High Fidelity DNA Polymerase kit (Life Technologies, 12574035).

2.19 DNA gel band isolation and sequencing

The DNA fragment was excised from the agarose gel with a clean and sharp scalpel. DNA was extracted from the gel band by using QIAquick® Gel Extraction Kit (Qiagen, 28706) following the manufacturer's manual. DNA was eluted with 20 µl nuclease free water and the eluent passed through the spin column twice to increase the yield of DNA. The concentration of extracted DNA was determined by NanoDrop™ spectrophotometer. DNA was sent to WIMM DNA Sequencing

Service for Sanger sequencing with the forward and reverse primers used to amplify the band in the PCR.

2.20 Sphingosine high-performance liquid chromatography (HPLC)

Sphingosine HPLC was used to quantify the amount of sphingosine in HeLa WT, *NPC1*KO (ex2, ex4 clones), *NPC2*KO (H12, H187 clone) and *SMPD1*KO (I7, I16, I93, I147). The method was a modification of the method described by He *et al.* 2005, and the experiment was done under the supervision of Mylene Huebecker (Department of Pharmacology, University of Oxford). Approximately $2X10^6$ HeLa cells were lifted using trypsin, spun down at 1,400 rpm for 5 min. Cells were washed once in PBS and spun down to a tight pellet, supernatant removed and cell pellet frozen and stored at -80 ^oC.

The frozen pellet was thawed on ice, and cells were resuspended in 250 µl PBS, mixing thoroughly to achieve a homogenate cell solution. 30 µl of the cell homogenate was used to quantify protein in a bicinchoninic acid (BCA) protein assay. 10 µl of sample (tested in triplicates) or bovine serum albumin (BSA) standards were mixed with 200 µl BCA solution (Sigma, B9643) with 4 µl copper sulphate (Sigma, C2284) and incubated at 37 ^oC for 30 min and quantified by measuring the absorbance at 562 nm using a CLARIOstar® plate reader.

To extract sphingosine from the cells, 100 µl of the cell homogenate was added to 500 µl of chloroform : methanol (1:2, v/v) and spiked with 3 µl of 0.1 mM C_{20} sphingosine standard (C_{20} SphStd) and sonicated for 10 min at room temperature. The control sample consisted of 100 µl PBS with 3 µl of 0.1 mM C_{18} added instead

of the cell homogenate. 500 µl of 1 M NaCl, 500 µl of chloroform, and 100 µl of 3 M NaOH was added to the sample, which was incubated for 15 min at room temperature, vortexing every 5 min. The sample mixture was then centrifuged at 3,000 rpm for 10 min and was separated out into 3 layers: aqueous, protein and organic solvent phase (with lipids dissolved in the organic phase).

A SPE NH2 column (Biotage, 470-0010-A) was conditioned with 2 X 1 ml chloroform, and the lower organic phase from the sample was loaded onto the column, with the flow-through discarded. Bound lipids (sphingosine) were eluted with three volumes of 300 µl acetone and collected in a fresh 15 ml tube. The eluent was then evaporated under nitrogen. The residue was redissolved in 50 µl pre-warmed ethanol with gentle vortexing. 50 µl of freshly prepared O-phthalaldehyde (OPA) labelling solution (1 mg OPA, 20 µl ethanol, 1 µl β-mercaptoethanol, 2 ml boric acid) was added to the lipid/ethanol solution, the sample was incubated at room temperature for 20 min in the dark, vortexing every 10 min. 100 µl of methanol : 5 mM Tris pH 7 (9:1, v/v) was added to the sample and centrifuged at 3,000 rpm for 2 min.

50 µl of the supernatant was injected to analyse by HPLC, using a Waters Alliance 2695 separations module, an in-line Waters 474 fluorescence detector separation and a 4.6 X 250 mm TSK gel-Amide 80 column (Anachem, Luton, UK). The retention times for C_{18} and C_{20} sphingosine were 4.08 and 5.80 minutes. The peak area ratio of C_{18} (sample) and C_{20} (300 pmol standard) was used to calculate the amount of sphingosine in the cell sample (pmol sphingosine per mg total protein). The experiment was repeated twice.

2.21 Visualisation of sphingosine trafficking in HeLa cells

Our collaborator Doris Höglinger (Heidelberg University) performed this experiment on several HeLa cell-lines generated in this study: WT HeLa, *NPC1*KO (ex2 clone), *NPC2*KO (H12 clone), *NPC1*KO (ex2 clone) with NPC1-mCherry transduced (WT, D520F, and P434S NPC1). The method has been previously described in Höglinger *et al.* 2017 (Figure 2.6).

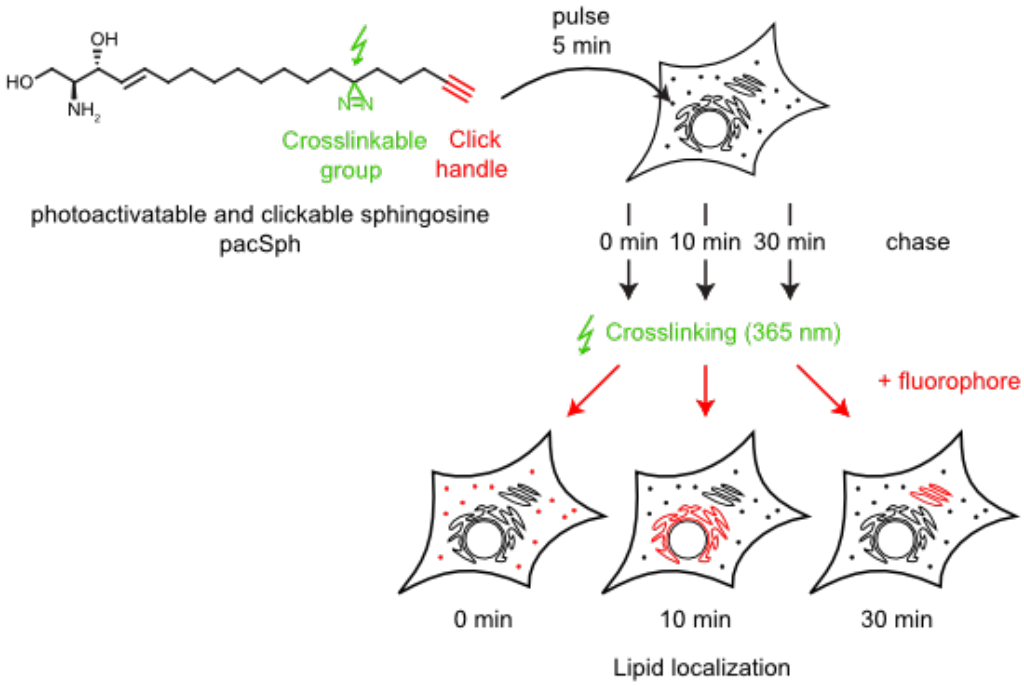


Figure 2. 6 Photo-cross-linkable and clickable sphingosine (pacSph)
Schematic diagram showing the mechanism of pacSph (Höglinger *et al.* 2017) used to visualise sphingosine localisation and trafficking. PacSph was loaded into live cells for 5 minutes and then chased for 0 min, 10 min or 30 min. Cells were UV-irradiated to activate the cross-linkable group, and imaged by confocal microscopy.

HeLa cells were seeded onto coverslips to 65 ~ 75 % confluency. Cells were then labelled with 1 µM photo-cross-linkable and clickable sphingosine (pacSph) in imaging buffer (20 mM HEPES, 115 mM NaCl, 1.2 mM $MgCl_2$, 1.2 mM glucose and 1.8 mM $CaCl_2$, pH 7.4/NaOH) for 5 min and chased for indicated times in imaging buffer at 37°C. Subsequently, cells were washed with PBS, then overlaid

with 0.5 ml of cold imaging buffer and UV-irradiated (using a Sylvania R 100 W lamp at λ~365 nm) on ice for 5 min. Cells were immediately fixed with pre-cooled methanol (MeOH) at −20 °C for 20 min. Non-cross-linked lipids were extracted by washing three times with 1 ml of $CHCl_3$/MeOH/AcOH (10:55:0.75) (v/v) and twice with PBS. Cells were then incubated with 50 µl of click mixture (1 µl 2 mM Alexa-488-azide, 125 µl 10 mM Cu(I)BF4 in acetonitrile and 0.5 ml PBS) for 1 hour at room temperature in the dark. Cells were then washed with PBS and incubated with 50 µl of primary antibody (rabbit α-LAMP1, Cell Signalling, 1:200 in PBS supplemented with 2% BSA and 0.3% Triton X-100) for 1 hour in the dark. Coverslips were briefly washed with PBS and incubated with secondary antibody (anti-rabbit conjugated to Alexa Fluor® 555, Cell Signalling, 1:800) for 30 min to 1 hour, washed briefly with PBS, and mounted in ProLong Gold Antifade mounting medium (Cell Signalling). Microscopic images were captured using a confocal laser-scanning microscope (Zeiss LSM800) with a 63X oil objective lens. Images were further processed using Fiji software and analysed using the FluoQ macro (PMID 23882997) for automatic extraction of intensity and co-localisation values. These values were then graphed using the ggplot package in R.

2.22 NPC1 mutagenesis and cloning

Lentiviral vector encoding cDNA for human NPC1 (NM_000271.4) with mCherry tag at the C-terminus was purchased from Source Bioscience (EX-I2083-Lv130-GS). NPC1-mCherry was cloned out from the Lv130 vector by restriction enzyme EcoRI and PmeI (blunt end) (digested at 37 ^{o}C, 1 hour), then inserted into pHR-SIN lentiviral vector pre-digested with EcoRI and blunt end enzyme SwaI and treated with calf intestinal alkaline phosphatase (CIP). NPC1-mCherry and pHR-

SIN vector were ligated using T4 ligase (NEB) at room temperature for 1 hour. 2 µl ligation mix was incubated with 15 µl high efficiency DH5α competent *E. coli* (NEB, C2987I) for transformation, following the manufacturer's manual, except expansion of transformed culture at 30 ^{o}C for 2 hours.

100 µl LB containing transformed bacteria were plated on low salt LB-agar plates containing 100 µg/ml ampicillin at 30 ^{o}C for 48 hours. Three single colonies were picked and expanded in 30 ml low salt LB with 100 µg/ml ampicillin 30 ^{o}C for 48 hours (on rotary shaker, 220 rpm). Plasmid was isolated from the bacterial culture using QIAprep Spin Miniprep Kit (Qiagen, 27106). Low salt LB medium (Sigma L3397, 0.5 g/L NaCl) combined with 30 ^{o}C growth temperature was required to avoid mutations occurring in the cloned NPC1 DNA.

For site-directed mutagenesis, a 1555 bp fragment encoding the N-terminus of NPC1 was cloned from Lv130 vector by restriction enzyme EcoRI (digested at 37 ^{o}C, 1 hour) and BsiWI (digested at 55 ^{o}C, 1 hour), and ligated into pCDNA3.1+ vector (EcoRI, BsiWI digested, CIP treated) using T4 ligase (NEB, ligation room temperature 1 hour). 2 µl ligation mix was incubated with 15 µl high efficiency DH5-alpha competent *E. coli* (NEB, C2987I) for transformation, following the manufacturer's manual. 100 µl LB containing transformed bacteria were plated on LB-agar plates containing 100 µg/ml ampicillin at 37 ^{o}C for 16 hours. Three single colonies were picked and expanded in 30 ml LB with 100 µg/ml ampicillin 37 ^{o}C for 16 hours (on rotary shaker, 220 rpm). Plasmid was isolated from the bacterial culture using QIAprep® Spin Miniprep Kit (Qiagen, 27106).

Phusion NPC1 mutagenesis PCR mix

Reagent	Volume	Final conc.
HF buffer (5X)	10 µl	1X
dNTP (10 mM)	1 µl	200 µM
Primer mix (forward + reverse, 10 µM each)	1 µl	0.2 µM each
Plasmid (1 ng/µl)	1 µl	1 ng
Phusion Polymerase (2 units/µl)	0.5 µl	1 unit
Nuclease free water	36.5 µl	
Total volume	50 µl	

Phusion mutagenesis PCR thermal cycler program

Step 1	Initial denaturation	98 °C	1 minute
X25 cycle from step 2 – 4			
Step 2	Denaturation	98 °C	10 seconds
Step 3	Annealing	65 °C	30 seconds
Step 4	Extension	72 °C	30 seconds per kb (3 min 30 s)
Step 5	Final extension	72 °C	10 minutes
Step 6	Hold	4 °C	∞

Figure 2. 7 NPC1 mutagenesis PCR condition
PCR mix ingredients and thermal cycler program using Phusion® High-Fidelity DNA Polymerase Kit (NEB, E0553L) for NPC1 mutagenesis.

Mutagenesis PCR was conducted by using the Phusion® High-Fidelity DNA Polymerase Kit (NEB, E0553L). Conditions are summarised in Figure 2.7. Mutagenesis PCR mix was DpnI treated for 1 hour at 37 °C. 5 µl DpnI treated PCR mix was used to transform competent DH5α *E. coli* (high efficiency) (NEB, C2987I), followed by expansion of bacterial colonies in ampicillin containing LB containing 100 µg/ml ampicillin at 37 °C for 16 hours. Plasmid was extracted using QIAprep Spin Miniprep Kit (Qiagen, 27106). Mutation was confirmed by Sanger sequencing. The 1555 bp fragment of NPC1 containing the correct mutations was then cloned back to pHR-SIN-NPC1-mCherry plasmid using EcoRI/BsiWI restriction enzymes.

Transformation of DH5α competent *E. coli* (High Efficiency) (NEB, C2987I) with plasmid was followed by expansion of colonies in low-salt LB at 30 ^{o}C for 48 hours. The complete sequence of NPC1 in pHR-SIN vector was verified by Sanger sequencing.

2.23 Ca^{2+} signal imaging

Our collaborator Antony Morgan (Department of Pharmacology, University of Oxford) has used the following method to indirectly characterise two-pore channel 1 and 2 (TPC1/2) function in WT, *TPCN1*KO (clone D149) and *TPCN2*KO (clone E64) HeLa cells. This method was developed based on the methods of Cancela, Churchill and Galione 1999; Yamasaki *et al.* 2004.

HeLa cells were seeded onto a 10-well Cellview Slide (Greiner) the day before transfection (50-80% confluency). The next day, cells were transiently transfected with the mouse cholecystokinin receptor-A (CCKR-A) tagged at its C-terminus with mTagBFP2 to verify expression (100ng MmCCKAR-mTagBFP2) using JetPEI transfection reagent (Polyplus) for 4-5 hours. CCKR-A was used because it is known to couple to nicotinic acid adenine dinucleotide phosphate (NAADP) in pancreatic acinar cells, and NAADP is known to act on the TPC1 and TPC2 Ca^{2+} channels. The following day (after 16 hours), cells were maintained at room temperature in a balanced salt solution (121 mM NaCl, 5.4 mM KCl, 0.8 mM $MgCl_2$, 6 mM $NaHCO_3$, 1.8 mM $CaCl_2$, 25 mM HEPES, 10 mM glucose, pH 7.4) for all steps. First, cells were loaded by incubating with a Ca^{2+} reporter (2 μM Calbryte-520/AM, 50 mins, room temperature). Following 15 min de-esterfication period, cells were imaged on a Nikon A1 confocal laser scanning microscope equipped

with standard blue and green channels (excitation 405 nm and 488 nm respectively); the blue channel was used to visualise mTagBFP2 and the green channel to monitor Ca^{2+} signals. An image was acquired every 3 s, and cells were stimulated with cholecystokinin (CCK-8 peptide, 0.1 - 0.3 nM).

HeLa cells do not respond to CCK unless CCKRs are expressed heterologously. Transfection efficiency was of the order of 40% and within a field of view. Only cells expressing MmCCKAR-mTagBFP2 were included for analysis. Each transfected cell was defined by a region of interest (ROI) and the Ca^{2+} signal versus time plotted for each single cell. Data were analysed using custom-written software (Magipix, Dr Ron Jacob, King's College London). A reduced Ca^{2+} signal implied impairment of NAADP-induced Ca^{2+} release from lysosomes through the TPCs.

2.24 Thermolysin treatment of E-S-FLU

Thermolysin protease (Sigma, P1512) was dissolved in HM buffer (20 mM HEPES, 130 mM NaCl and 20 mM MES and pH adjusted to 7.5). Thermolysin digestion was based on the method described by Hashiguchi *et al.* 2015 with some modifications. 2 ml undiluted E-S-FLU culture supernatant was incubated with 100 µl thermolysin (5 mg/ml in HM buffer) and 2 mM $CaCl_2$ at 37 ^{o}C for 2 hours. Control E-S-FLU was treated with 100 µl HM buffer and 2 mM $CaCl_2$. Treated E-S-FLU was filtered by Amicon® Ultra-15 Centrifugal Filter Units 100 kDa (Millipore, UFC910008), washed with 15 ml PBS and concentrated to 1 ml. The virus was then used in antibody micro-neutralisation assay or drug inhibition assays.

2.25 EBOV-GP mutagenesis

EBOV-GP (*Zaire* 2014, NCBI: KJ660346.2) cDNA was codon optimised and synthesised by GeneArt, cloned into pCDNA3.1+ vector and pHR-SIN lentiviral vector using EcoRI/NotI restriction digest (37 ^{o}C, 1 hour). Transformation, bacterial culture expansion and plasmid extraction was conducted as described in section 2.22 (NPC1 mutagenesis and cloning) with standard 37 ^{o}C *E. coli* growth condition. Mutagenesis was conducted by using NEB mutagenesis kit (E0522S), protocol summarised in Figure 2.8. Five µl of the mutagenesis mix after KLD reaction was used to transform 15 µl competent *E. coli* DH5α (high efficiency) (NEB, C2987I) following the manufacturer's manual. Transformed *E. coli* colonies were picked and expanded in LB (100 µg/ml ampicilin). Plasmids were isolated from the bacterial culture using QIAprep Spin Miniprep Kit (Qiagen, 27106).

GP mutagenesis (NEB mutagenesis kit)

Reagent	Volume	Final conc.
Q5 Hot Start High Fidelity Master Mix (2X)	5 µl	1X
Primer mix (forward + reverse, 5 µM each)	1 µl	0.5 µM each
Plasmid (5 ng/µl)	1 µl	5 ng
Nuclease free water	3 µl	
Total volume	10 µl	

NEB mutagenesis PCR thermal cycler program

Step 1	Initial denaturation	98 °C	30 seconds
X25 cycle from step 2 – 4			
Step 2	Denaturation	98 °C	10 seconds
Step 3	Annealing	68 °C	30 seconds
Step 4	Extension	72 °C	30 seconds per kb (4 minutes)
Step 5	Final extension	72 °C	10 minutes
Step 6	Hold	4 °C	∞

KLD reaction: incubated 1 hour at room temperature

Reagent	Volume	Final conc.
PCR product	1 µl	
KLD reaction buffer (2X)	5 µl	1X
KLD Enzyme Mix (10X)	1 µl	1X
Nuclease free water	3 µl	
Total volume	10 µl	

Figure 2. 8 EBOV-GP mutagenesis PCR condition
PCR mix ingredients and thermal cycler program using NEB mutagenesis kit (E0522S) for GP mutagenesis. PCR product was then treated with KLD enzyme for 1 hour at room temperature.

2.26 Immunofluorescence assay (IFA)

The day before staining, $3X10^4$ SIAT cells (E-SIAT or MDCK-SIAT1) were seeded in 50 µl D10 medium in a flat-bottomed 96-well tissue culture plate. Next day, medium was removed and cells were washed twice with PBS. Anti-GP or control antibody (50 µl of 10 µg/ml) diluted in PBS was added to cells, which were then

incubated at room temperature on a rotary shaker for 1 hour. After removing the first layer antibody, cells were washed three times with 300 µl PBS. Then 50 µl of Alexa Fluor® 647 conjugated goat anti-human antibody (diluted 1 in 400 in FACS wash buffer) was incubated with the cells in the dark for 1 hour at 4°C. Secondary antibody was removed and cells were washed three times with 300 µl PBS then fixed with FACS fix buffer and read using the CLARIOstar® fluorescence plate reader.

2.27 Drug selected EBOV escape mutant

EBOV escape mutant selection was conducted by Peter Halfmann (University of Wisconsin - Madison), using a biologically-contained EBOV (*Zaire ebolavirus*) EbolaΔVP30 virus expressing the green fluorescent protein (GFP) reporter gene, instead of the VP30 gene in the viral genome (Halfmann *et al.* 2008). EbolaΔVP30 viruses are approved for use under biosafety level-2 containment solely at the University of Wisconsin - Madison by the NIH and are exempt from the CDC Select Agent registration.

VeroVP30 cells (Vero cells transduced to stably express the VP30 gene from EBOV) were treated with toremifene (5 µM) for 4 hours prior to infection with EbolaΔVP30-GFP virus at an MOI of 0.1. After infection, cells were washed four times to remove any unbound virus and medium containing fresh toremifene (5 µM) was added back to the cells. Eight days after infection, cell culture supernatant was harvested and stored at -80°C for further analysis.

A 10-fold dilution series was made of the cell culture supernatant (10^{-1} to 10^{-4}). Dilutions or neat supernatant were used to infect a monolayer of VeroVP30 cells for 1 hour, at which time, cells were washed four times and then overlaid with 1.25% methylcellulose medium. Individual focus-forming units were isolated after eight days and expanded in medium containing 5 μM toremifene; a total of eight individual viral clones were isolated and expanded. Viral RNA was isolated using Qiagen's Viral RNA mini kit. The EBOV-GP open reading frame (ORF) mRNA was converted to cDNA first using a RT reaction (an oligo dT primer with SuperScript III (Invitrogen)) and the product was further amplified by PCR using primers that immediately flank the ends of the GP ORF (6000 forward and 8110 reverse) with Phusion DNA polymerase (NEB, E0553L). The gel purified PCR product was cloned and sequenced using the Zero Blunt PCR Cloning kit (Thermo Fisher Scientific). Three mutant clones were identified out of the eight viral clones tested. Each of the three mutant clones were passaged one more time with medium containing toremifene to determine if any additional mutants would arise. Five sub-clones for each of the three clones were isolated and the EBOV-GP was sequenced in a similar fashion.

2.27.1 Growth kinetics of wild-type and toremifene resistant viruses

VeroVP30 cells were seeded at a density of 200,000 cells per well in a TC-12 plate. The following day, cells were treated with 5 μM toremifene, 10 μM arbidol, or DMSO for 4 hours prior to infection with wild-type or toremifene-resistant EbolaΔVP30-GFP virus at an MOI of 0.001. After infection, cells were washed four times to remove any unbound virus and medium containing fresh toremifene,

arbidol or DMSO was added back to the cells. On days 3 and 6 after infection, cell culture supernatant was harvested and stored at -80^{o}C for further use.

To determine virus titres, a 10-fold dilution series was made of the cell culture supernatant (10^{-1} to 10^{-4}), and used to inoculate confluent VeroVP30 cells. After an incubation at 37^{o}C for 1 hour, unbound virus was washed off, and cells were overlaid with 1.25% methylcellulose medium for 7 days. Cells were then fixed with 10% neutral-buffered formalin and virus titres (focus-forming units) was determined by counting the number of infected cell foci identified using an immunohistochemistry assay performed with a virus-specific antibody.

Chapter 3 Development and characterisation of E-S-FLU

3.1 Introduction

This chapter describes the design, development and characterisation of a novel Ebola virus pseudotype: E-S-FLU, which contains a non-replicating Influenza A virus core from A/PR/8/1934, coated in the Ebola virus glycoprotein.

Ebola virus (EBOV) is a biosafety level 4 (BSL-4) agent, and this creates a significant hurdle for research as there are limited BSL-4 facilities available, and huge costs and time are required to conduct experiments at such a high containment level. This leads to the need for a model system that is safe to work with and mimics the behaviour of wild-type EBOV *in vitro*. Safe substitutes that can be handled at BSL-1/2 are handy tools for high-throughput screenings of inhibitory small molecules, monoclonal antibodies, diagnostic serology, as well as studying the biology of the virus.

EBOV is a lipid-enveloped RNA virus, as is Influenza. EBOV glycoprotein (EBOV-GP) is a trimeric membrane protein, and it is the only protein at the surface of EBOV. In this context, EBOV-GP and Influenza haemagglutinin (HA) are comparable trimeric class I viral membrane fusion proteins (Skehel and Wiley 2000; White and Whittaker 2016). EBOV-GP and Influenza HA play essential roles in the host cell attachment, cell entry and membrane fusion steps (reviewed in Chapter 1). Both undergo a major conformational change to form similar coiled coils (HA2 subunit in HA and GP2 subunit in GP), with extrusion of the receptor

binding head region during fusion (Weissenhorn *et al.* 1999). It therefore seemed reasonable to expect that EBOV-GP might be able to replace Influenza HA to provide these functions to an Influenza core particle.

We have developed our own surrogate for EBOV based on an Influenza core because our laboratory is familiar with this technology, and has been working for several years with an inactivated Influenza core particle coated in avian Influenza haemagglutinins, that would also require high level containment for the wild-type viruses. S-FLU is a non-replicating pseudotyped Influenza virus, in which the haemagglutinin (HA) signal sequence has been inactivated by mutation (hence the name "S-FLU" for signal-minus flu), and the coding sequence has been replaced by a reporter enhanced green fluorescent protein (eGFP) (Figure 3.1) (Martínez-Sobrido *et al.* 2010; Powell *et al.* 2012, 2019; Baz *et al.* 2015). S-FLU can propagate in MDCK-SIAT1 cells transduced to express Influenza HA (Powell *et al.* 2012).

Currently available viral surrogates for EBOV are pseudotyped with EBOV-GP, such as the retrovirus (Wool-Lewis and Bates 1998) and vesicular stomatitis virus (VSV) pseudotypes (Takada *et al.* 1997). Some EBOV viral-like particles (VLPs) also contain EBOV matrix protein (VP40) and nuclear protein (NP) (Bavari *et al.* 2002; Tscherne, Manicassamy and García-Sastre 2010; Li *et al.* 2016).

Different EBOV surrogates vary in their biology and susceptibility to antibodies and drugs in neutralisation assays in comparison to the wild-type EBOV. The National Institute of Biological Standards and Control (NIBSC) has compared 22 different

EBOV assays in quantifying serum antibodies, and the results showed generally poor correlations in comparison to neutralisation of the wild-type EBOV *in vitro* (Wilkinson *et al.* 2017). However, a recent comparison of neutralisation assays with GP-pseudotyped and recombinant VSV, eGFP-tagged recombinant EBOV and authentic wild-type EBOV, revealed that a combination of assays with pseudotyped VSV predicted protection by antibodies *in vivo* in mice better than wild-type EBOV neutralisation (Saphire *et al.* 2018). Therefore, designing and comparing new EBOV-GP pseudotyped viruses may contribute to improving the accuracy in determining correlation with protection.

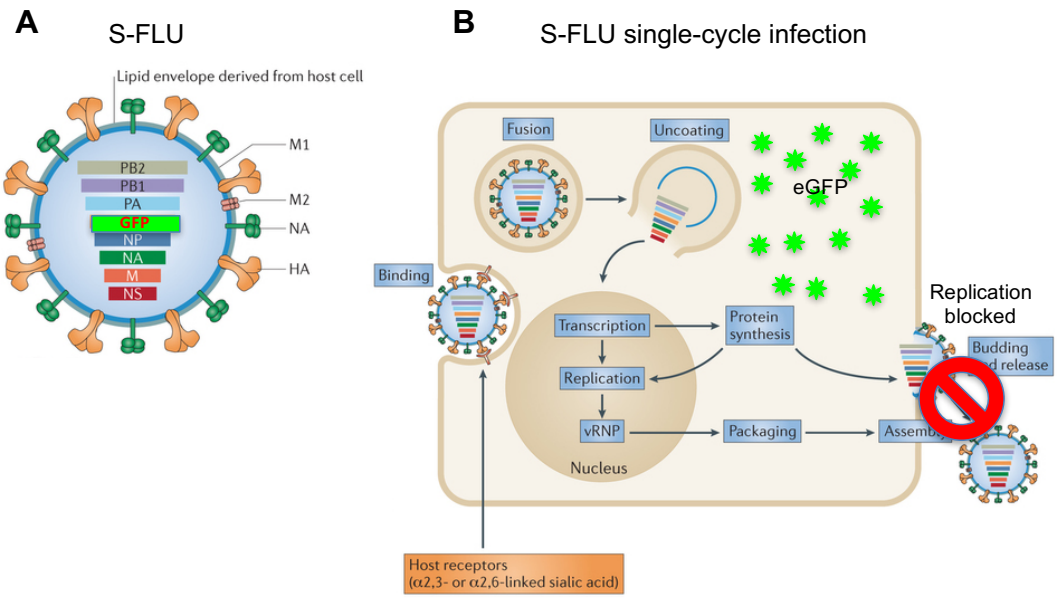


Figure 3. 1 S-FLU design and infection mechanism
Figure was adapted from Shi *et al.* 2014. **A**: S-FLU is a non-replicating Influenza virus with its haemagglutinin gene (HA) replaced by a reporter eGFP sequence. S-FLU can be pseudotyped with different HA proteins provided by the transduced packaging cells. **B**: After the first-round of infection, S-FLU enters the cell, releases its viral genome to the cytoplasm. eGFP is expressed and is fluorescently detectable as a reporter. Because there is no HA gene, replication is blocked as no HA protein is available for new virion assembly and budding.

In this chapter, H5-S-FLU is used as a control pseudotyped virus in parallel with E-S-FLU in various characterisation assays. H5-S-FLU is pseudotyped with H5

HA from a highly pathogenic avian Influenza virus (HPAI) A/Vietnam/1203/2004 (H5N1 clade 1) with the polybasic cleavage site converted to a trypsin site (Baz *et al.* 2015). H5-S-FLU and E-S-FLU contain the same viral genetic core from A/PR/8/1934 and only differ at the surface glycoprotein.

As might be expected, the Influenza particle coated in EBOV-GP did not replicate as efficiently as particles coated in Influenza HA. In the second part of this chapter, I describe two approaches designed to improve the titre of E-S-FLU produced in MDCK-SIAT1 cells. The first approach was pseudotyping S-FLU with a hybrid protein GP-HA that consists of the extracellular domain of EBOV-GP and the transmembrane and the cytoplasmic domains of Influenza HA (section 3.4). Previous Influenza research suggested that the transmembrane domain (TMD) and cytoplasmic domain (CTD) of HA play a role in the assembly and budding of Influenza viral particles (Jin *et al.* 1997; Melikyan *et al.* 1999; Zhang *et al.* 2000; Zhang, Pekosz and Lamb 2000; Nayak, Hui and Barman 2004; Chen *et al.* 2007; Welsch, Müller and Kräusslich 2007; Lakdawala, Fodor and Subbarao 2016). The TMD and CTD of HA may be required to interact with the Influenza virus matrix protein. Hence, we fused the extracellular domain of EBOV-GP to the TMD and CTD of HA, with the intention of improving the efficiency of assembly and the yield of E-S-FLU.

The second approach (in collaboration with D.Phil. student Holly Sadler from our lab) was to modify E-S-FLU production by including a non-functional haemagglutinin, H7CFv3, on the pseudotyped E-S-FLU surface to provide enhanced cell attachment. H7CFv3 is a mutated version of H7 haemagglutinin.

Multiple mutations were introduced to lock the H7 molecule in its pre-fusion state, and prevent fusion, while maintaining its receptor binding affinity. The aim was to use the fusion-defective haemagglutinin as a lectin to bind sialic acid and to enhance attachment of the pseudotyped virus to the target cell surface (section 3.5).

3.2 E-S-FLU production and titration

To incorporate EBOV-GP to the S-FLU viral surface, we used a lentiviral vector to transduce MDCK-SIAT1 cells to stably express full-length EBOV-GP protein from a cDNA encoding sequence from the *Zaire ebolavirus* isolated during the 2014 Ebola outbreak (NCBI: KJ660346.2, H. sapiens-wt/GIN/2014/Makona-Kissidougou-C15). The transduced cells were then bulk-sorted for high expression of EBOV-GP by fluorescence-activated cell sorting (FACS) using an anti-EBOV-GP specific monoclonal antibody KZ52 (Maruyama *et al.* 1999; Lee *et al.* 2008). We observed that the sorted MDCK-SIAT1 cells maintained a high expression of EBOV-GP up to at least the ninth passage, and this had no obvious toxicity or effect on cell morphology. We named the sorted cell population E-SIAT cells (Figure 3.2).

To produce EBOV-GP pseudotyped S-FLU (named E-S-FLU), a 50% infectious dose of cloned seed S-FLU virus was added to infect E-SIAT cells. Culture supernatant was harvested after 48 hours and titrated on indicator MDCK-SIAT1 cells. The EBOV-GP, like Influenza HA, requires cleavage into GP1 and GP2 for fusion to occur. The GP has a furin cleavage site, which can be cleaved by constitutively expressed furin, so replication *in vitro* does not require exogenously

added trypsin. All of our HAs from highly pathogenic Influenza viruses have had their furin cleavage sites converted to trypsin dependence – so these viruses do require added trypsin.

Infective E-S-FLU pseudovirions were produced, and the infected indicator cells expressed eGFP that was encoded in the E-S-FLU particle (Figure 3.3). This was detectable by fluorescence microscopy and a fluorescent plate reader CLARIOstar®. With the same method, we also successfully pseudotyped S-FLU with glycoproteins from 1976 Mayinga strain *Zaire ebolavirus* (EBOV) (NCBI: AF086833), *Sudan ebolavirus* (SUDV Gulu 2000, NCBI: NC_006432.1), *Bundibugyo ebolavirus* (BDBV 2007, NCBI: NC_014373.1) and *Taï Forest ebolavirus* (TAFV 1994, NC_014372.1) (Figure 3.3 C).

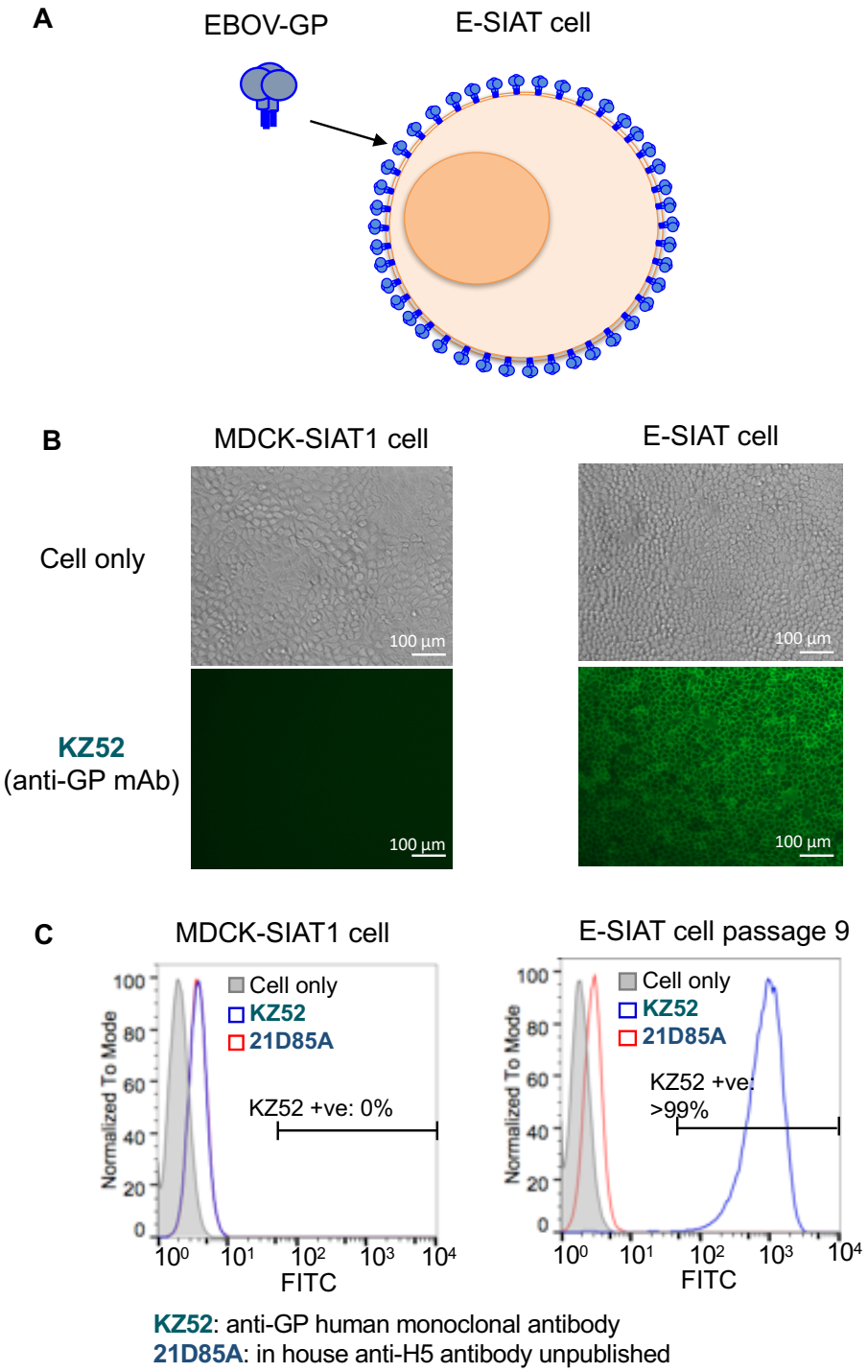


Figure 3. 2 Stable expression of EBOV-GP on the surface of transduced MDCK-SIAT1 cells

A: Schematic diagram shows MDCK-SIAT1 cells expressing full-length trimeric EBOV-GP (E-SIAT cells) at the cell surface. **B:** Immuno-fluorescence pictures of MDCK-SIAT1 and E-SIAT cells stained with KZ52 and an FITC-linked anti-human antibody. **C:** FACS plots of MDCK-SIAT1 cells and E-SIAT cells. Cells were stained with primary MAb KZ52 (anti-GP Mab, Lee *et al.* 2008) or 21D85A (anti-H5 MAb), followed by an FITC-linked anti-human secondary antibody. E-SIAT cells stably express GP at the cell surface up to at least the ninth passage, which can be detected with conformational MAb KZ52 specifically.

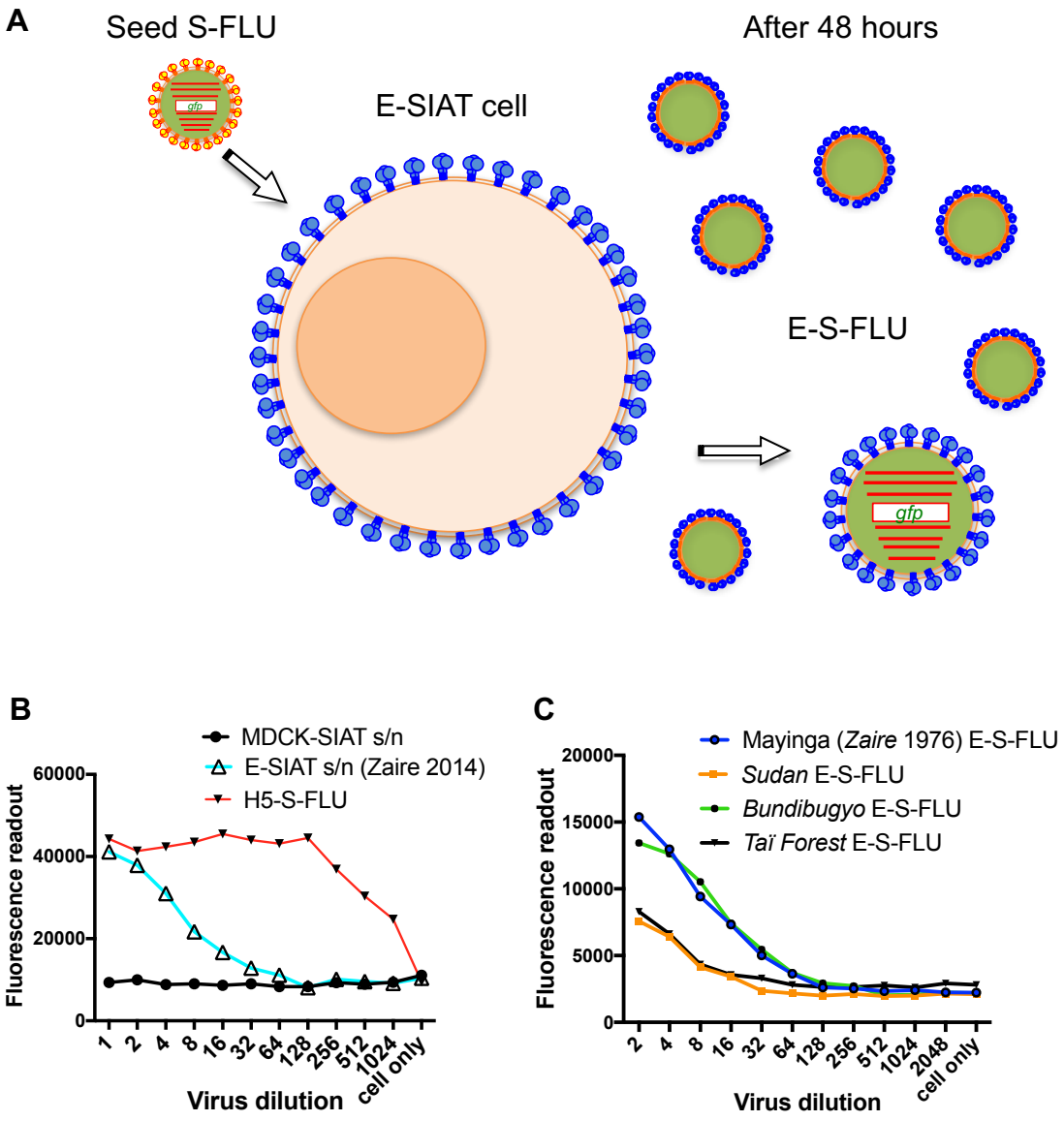


Figure 3. 3 Pseudotyping of S-FLU virus with EBOV-GP

A: Schematic diagram showing the production of E-S-FLU pseudotyped virus. E-SIAT cells were MDCK-SIAT1 cells transduced to express full length EBOV-GP from *Zaire ebolavirus* (EBOV, 2014 C15 strain). E-SIAT cells were seeded with 1 TCID50 of seed S-FLU virus per cell to generate EBOV-GP (cyan)- and H5 (red)-pseudotyped S-FLU viruses. Parental MDCK-SIAT1 cells were also included as a control. Culture supernatant (s/n) harvested after 48 hours was titrated in comparison to the H5-S-FLU virus in 2-fold dilutions on MDCK-SIAT1 indicator cells for 24 hours of infection, representative titration curves are shown in **(B)**. Infected cells expressing eGFP were detected and quantified with a CLARIOstar® fluorescence plate reader. With the same pseudotyping and titration method, we also produced and quantified E-S-FLU coated with GP from different *ebolavirus* species: *Zaire* (1976 Mayinga strain), *Sudan*, *Bundibugyo* and *Taï Forest* *ebolavirus*. Representative titration curves are shown in **(C)**.

Culture supernatant harvested containing E-S-FLU was titrated for infection of indicator MDCK-SIAT1 cells. Infection was quantified by measuring the eGFP level with a fluorescence plate reader CLARIOstar®. E-S-FLU pseudotyped with GP from *Bundibugyo ebolavirus*, and another *Zaire* strain (1976 Mayinga) showed similar viral titres, with fluorescence plateau at around 1 in 2 dilution, and a typical 50% effective concentration dilutions (EC_{50}) around 1 in 8 after 24 hours (Figure 3.3 C). *Sudan* and *Taï Forest* E-S-FLU contained around 4 to 8-fold lower titre than other E-S-FLUs. From the EC_{50} and the number of indicator cells in the well ($3X10^4$ cells/well) and the volume of virus used in the assay (50 µl), the 50% cell infective dose (CID_{50}) was calculated as ~2 X 10^6 cell infectious doses 50%/ml (CID_{50}, the amount of virus required to infect 50% of cells). The harvested culture supernatant from E-SIAT cells could be directly used in antibody neutralisation and drug inhibition assays without further purification steps. We further carried out characterisation experiments with the *Zaire* EBOV E-S-FLU (Makona/C15 2014 strain).

In the later sections of chapter, we compared E-S-FLU with H5-S-FLU in multiple characterisation assays. H5-S-FLU was pseudotyped with the same method but using the Influenza haemagglutinin H5 from Influenza virus H5N1/A/Vietnam/1203/2004 (Baz *et al.* 2015). H5-S-FLU differs from E-S-FLU only at the surface glycoprotein, and we used it in comparison to identify EBOV-GP specific effects. The viral titre of E-S-FLU was lower than the control H5-S-FLU (EC_{50} of 1 in 500, CID_{50} ~ $1.6X10^8$/ml) (Figure 3.3 B).

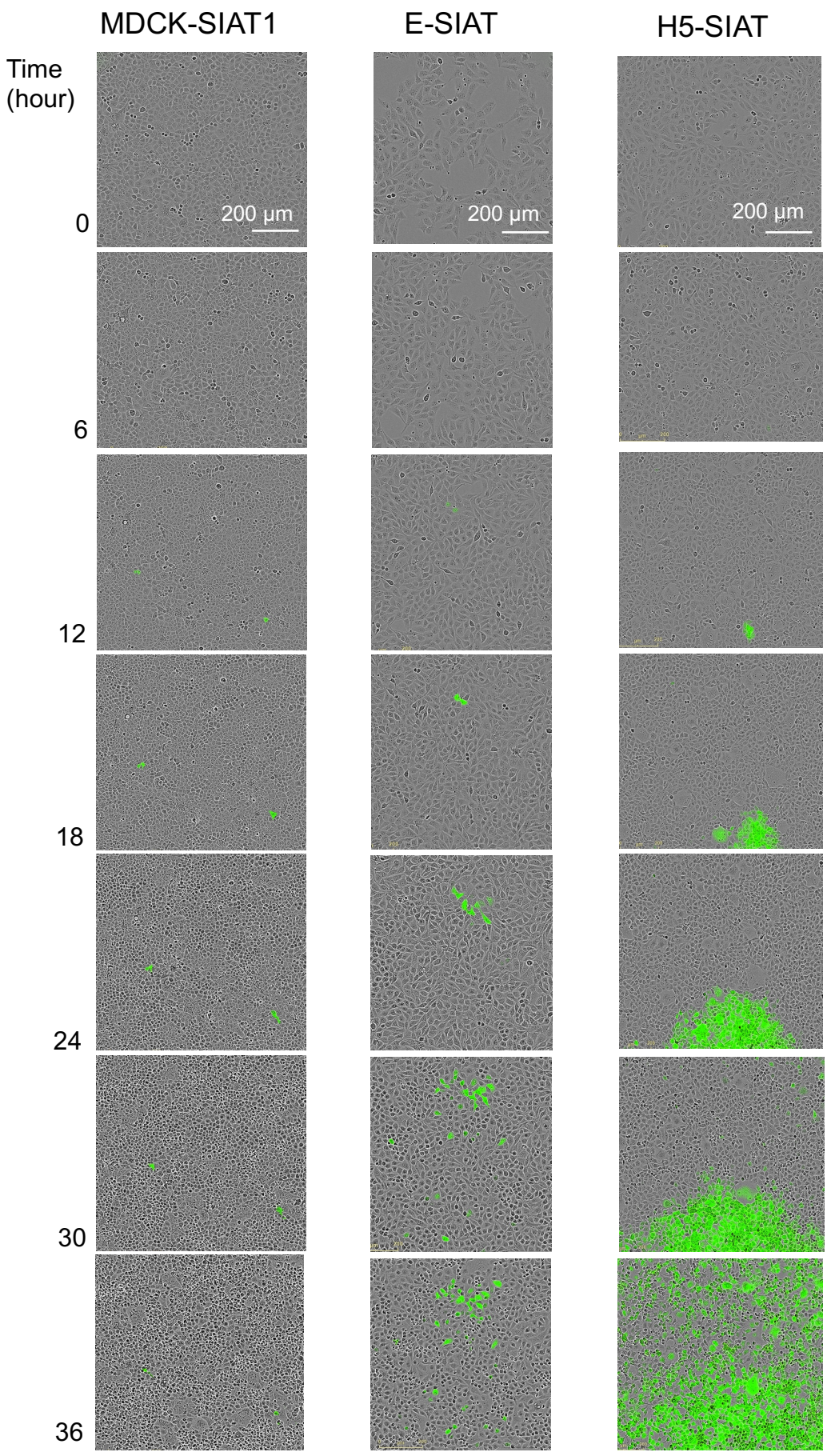

MDCK-SIAT1
E-SIAT
H5-SIAT
Time (hour)
0
6
12
18
24
30
36
200 μm
200 μm
200 μm

Figure 3. 4 Real-time S-FLU spreading in E-SIAT and H5-SIAT cells
A total of 100 $TCID_{50}$ of seed S-FLU virus was added to $3X10^4$ MDCK-SIAT1, E-SIAT, or H5-SIAT cells. E-SIAT and H5-SIAT cells are MDCK-SIAT1 cells transduced to express full-length EBOV-GP protein or Influenza H5 haemagglutinin at the cell surface respectively. Live images of representative plaques were taken by IncuCyte® every 3 hours. E-SIAT cells supported the formation of small diffuse plaques, unlike the dense plaques formed on H5-SIAT cells.

We first measured the growth rate of E-S-FLU and H5-S-FLU by titrating the culture supernatant every 6 hours after seeding for 72 hours (Table 3.1), and by imaging the replication and spreading of virus under a real-time fluorescence microscope IncuCyte® every 3 hours (Figure 3.4). We observed a much faster rate of replication for S-FLU in H5-SIAT cells compared to E-SIAT cells. A smaller and more diffuse fluorescent "plaque" was formed in E-SIAT compared to a more "meteor" shaped spread of plaque in H5-SIAT cells.

Table 3. 1 E-S-FLU and H5-S-FLU growth titre

Time point (hr)	E-S-FLU (CID_{50}/ml)	H5-S-FLU (CID_{50}/ml)
0	NA	NA
6	NA	NA
12	3.2×10^5	6.2×10^7
18	5.0×10^5	2.1×10^8
24	5.0×10^5	1.5×10^8
30	5.6×10^5	1.4×10^8
36	5.0×10^5	8.1×10^7
42	5.2×10^5	3.3×10^7
48	1.6×10^6	8.5×10^7
54	1.3×10^6	2.9×10^7
60	4.5×10^5	1.1×10^7
66	2.2×10^6	7.8×10^6
72	3.7×10^6	1.5×10^7

***Time point (hr)**: Time points when culture supernatant was harvested post-seeding, and CID_{50} titre on MDCK-SIAT1 cells.*
***CID_{50}/ml**: 50% cell infective dose. The CID_{50}/ml was calculated from the EC50 dilution (the dilution at which 50% of the cells were infected) and the number of cells per well ($3X10^4$).*
***NA**: no detectable virus.*

3.3 E-S-FLU characterisation

3.3.1 E-S-FLU infection requires NPC1

Niemann-Pick type C1 protein (NPC1) is a multi-transmembrane protein found in the lysosomal membrane of mammalian cells, mutations of which will cause a lipid storage disorder called Niemann-Pick type C disease. It is the well-established receptor required for EBOV entry (Carette *et al.* 2011; Côté *et al.* 2011; Miller *et al.* 2012). EBOV-GP, after cleavage by cathepsin B and L in acidic endosomes, binds to NPC1 protein in the lysosome and then triggers membrane fusion and release of the viral genome into the host cytoplasm. Influenza virus fuses at the early endosome stage and it does not require NPC1 for entry.

Our collaborator Wim Annaert kindly provided us with two *NPC1* knockout HeLa cell-lines generated by the CRISPR/Cas 9 technique and their parental wild-type HeLa cell (Tharkeshwar *et al.* 2017). We infected HeLa cells with E-S-FLU and the control H5-S-FLU (coated in H5 haemagglutinin), and quantified percentage infection by gating the eGFP positive population by FACS (Figure 3.5). We found that E-S-FLU infection was fully dependent on NPC1 protein expression, just as for wild-type EBOV. The control H5-S-FLU however, infected both wild-type and *NPC1*KO HeLa cells, as expected.

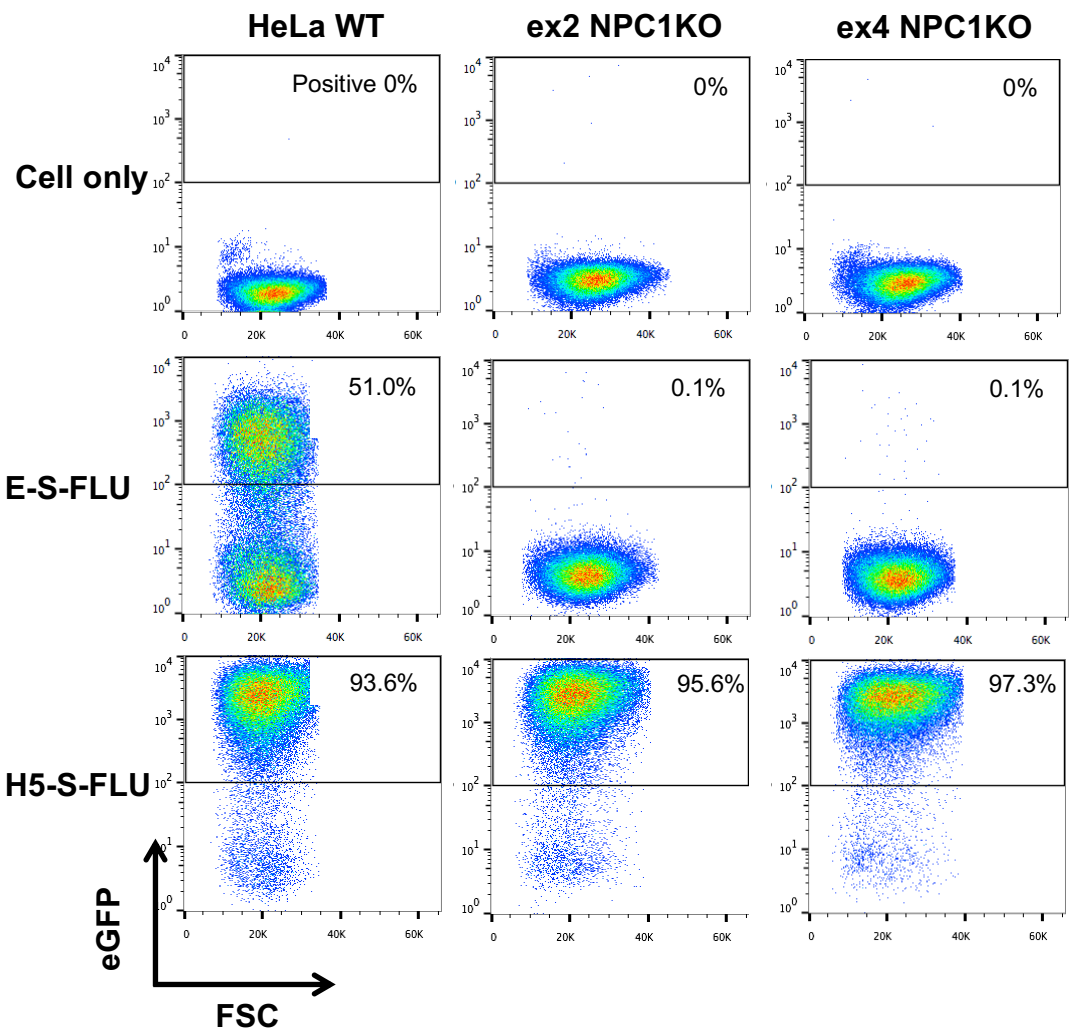


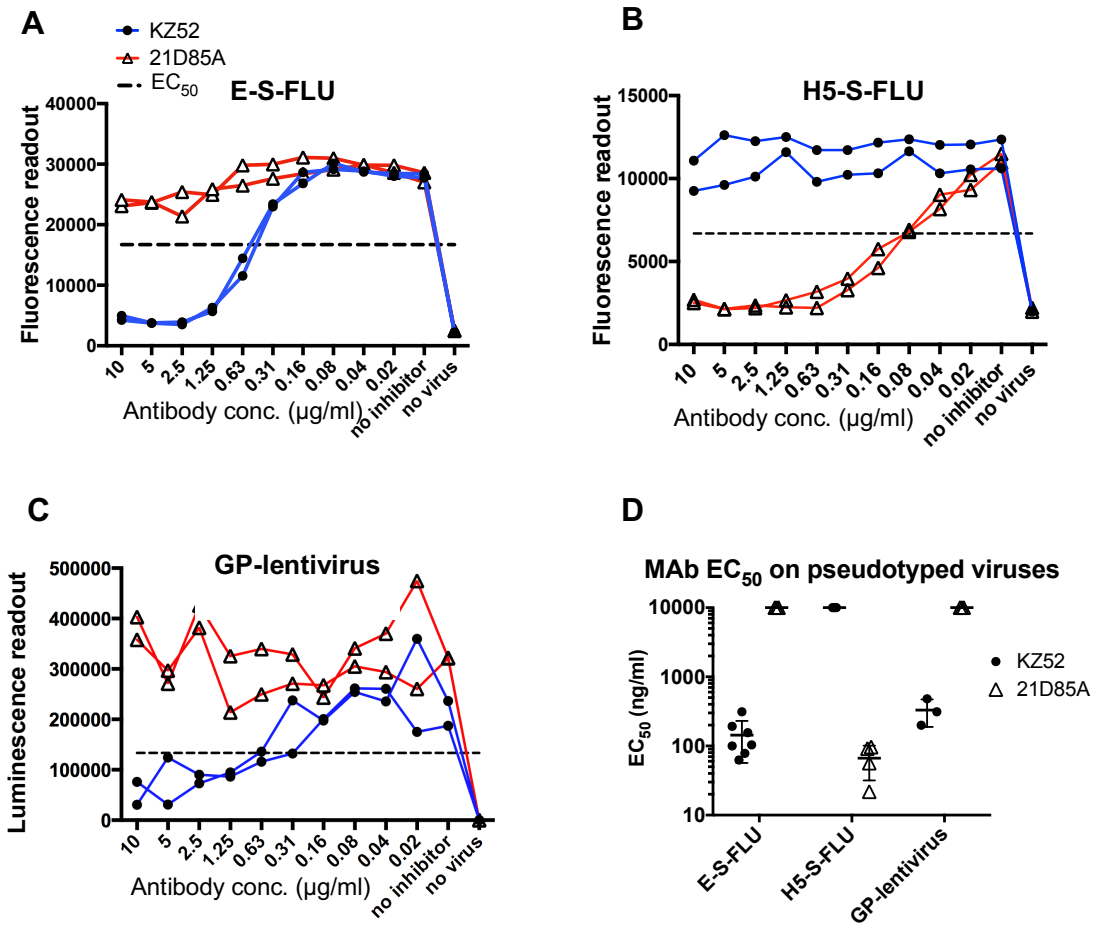
Figure 3. 5 E-S-FLU virus requires NPC1 receptor expression for infection of HeLa cells

Representative FACS plots of wild-type HeLa cells and two clones of *NPC1* knockout (KO) HeLa cells (ex2 *NPC1*KO and ex4 *NPC1*KO) infected with undiluted E-S-FLU and H5-S-FLU viruses. The S-FLU virus contains an eGFP reporter gene. The percentage of infected cells is the percentage of cells with an eGFP fluorescence of $>10^2$. WT, wild-type HeLa.

3.3.2 E-S-FLU neutralisation by anti-EBOV-GP antibodies

We tested defined neutralising antibodies to EBOV for inhibition E-S-FLU infection. E-S-FLU and the control pseudotyped H5-S-FLU virus were pre-incubated with human monoclonal antibody: KZ52 (anti-EBOV-GP, Lee *et al.* 2008) or 21D85A (an in house anti-H5 antibody) and then added to infect the indicator MDCK-SIAT1 cells. KZ52 binds specifically to EBOV-GP by recognising a conformational

epitope at the base of the protein (Maruyama *et al.* 1999; Lee *et al.* 2008). E-S-FLU infection was neutralised by KZ52 with 50% inhibition concentration (IC_{50}) at around 100 ng/ml, but it was not inhibited by anti-H5 antibody 21D85A. In contrast, control H5-S-FLU was neutralised by the 21D85A but not inhibited by KZ52 (Figure 3.6).

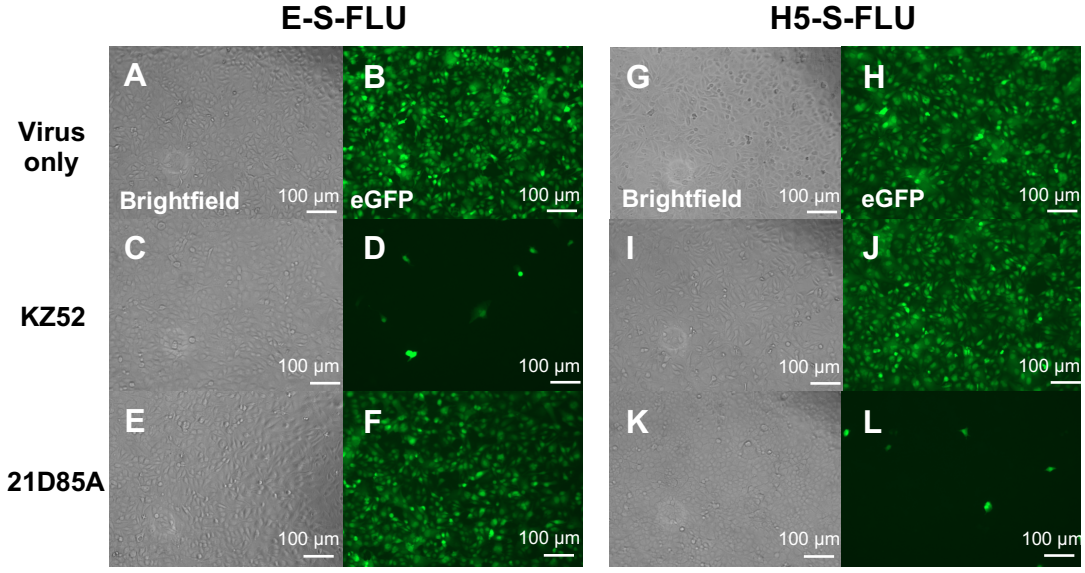


KZ52: anti-GP human monoclonal antibody Lee *et al.*, 2008. Structure PDB file 3CSY
21D85A: in house anti-H5 antibody unpublished

Figure 3. 6 Antibody neutralisation of pseudotyped E-S-FLU virus, H5-S-FLU virus, and EBOV-GP-pseudotyped lentivirus

Viruses were pre-incubated for 2 hours with antibody KZ52 (anti-GP) or 21D85A (anti-H5 antibody) before MDCK-SIAT1 indicator cells were added. Antibodies were titrated in 2-fold dilutions from 10 µg/ml. After 24 hours, infection was quantified by measuring eGFP expression (Influenza virus) or luminescence (lentivirus). Representative titration curves with technical duplicates are shown in panels **A** to **C**. A summary of the EC_{50}s of MAbs KZ52 and 21D85A for the three pseudotyped viruses is shown in panel **D**. Individual EC_{50}s from repeat experiments are shown with the geometric means and 95% confidence intervals. A value of 10,000 ng/ml was assigned to antibodies that did not neutralise.

Neutralisation was further confirmed under the fluorescent microscope, showing a clear reduction in the proportion of infected cells (Figure 3.7). We have also compared KZ52 in the micro-neutralisation assay with EBOV-GP pseudotyped lentivirus (GP-lentivirus), kindly provided by our collaborator Edward Wright (University of Sussex). All neutralisation assays were repeated at least three times. The average IC_{50} value of KZ52 neutralising E-S-FLU was similar to the IC_{50} to EBOV-GP pseudotyped lentivirus, and it was also similar to the published data on wild-type EBOV (IC_{50} 0.4 µg/ml against Ebola *Zaire* 1995 virus, Maruyama 1999). This shows that EBOV-GP is correctly folded in E-S-FLU particles, and infection of the indicator MDCK-SIAT1 cells was EBOV-GP dependent.



KZ52: anti-GP human monoclonal antibody Lee et al., 2008. Structure PDB file 3CSY
21D85A: in house anti-H5 antibody unpublished

Figure 3. 7 Fluorescence microscopy pictures of antibody neutralisation assays

Representative microscopy pictures (10X objective) of assays showing the specificity of E-S-FLU neutralisation by monoclonal antibodies (MAb). For "Virus only," the E-S-FLU and H5-S-FLU viruses were added directly to MDCK-SIAT1 cells. Infected cells express eGFP, shown as green cells. In the micro-neutralisation (MN) assay, virus was pre-incubated with 10 µg/ml MAb KZ52 (anti-GP) or 21D85A (anti-H5) antibody before the infection of MDCK-SIAT1 cells. Inhibition was visualised as a significantly reduced number of green fluorescent cells.

It is important to note that the MDCK-SIAT1 cell-line originates from dogs, but the NPC1 protein is highly conserved in vertebrates (Loftus *et al.* 2008; Miller *et al.* 2012). The NPC1 protein sequence from human (*Homo sapiens*) and (*Canis lupus familiaris*) share 88% sequence identity (https://www.ensembl.org). It has been shown previously that the NPC1 C domain contains the interacting loops that bind cleaved EBOV-GP (Krishnan *et al.* 2012; Miller *et al.* 2012; Wang *et al.* 2016). We further aligned the domain C region (amino acid 371 to 620, shown in Figure 3.8) from both species and showed 91% identity. Key residues in human NPC1 domain C that are in contact with EBOV-GP as previously identified in the crystal structure are highly conserved between human and dog (highlighted yellow in Figure 3.8).

```
Human                    371  VRVTTNPVDL  WSAPSSQARL  EKEYFDQHFG
Dog                           SRVTTNPVDL  WSAPGSQARL  EKEYFDAHFG
                               *********  ****.*****  **********

401  PFFRTEQLII  RAPLTDKHIY  QPYPSGADVP  FGPPLDIQIL  HQVLDLQIAI
     PFFRTEQLII  QAPHTSVHTY  QPYPSGSDVP  FGPPLDIGIL  HQVLDLQTAI
     **********  :** *. * *  ******:*** ******* **  ******* **

451  ENITASYDNE  TVTLQDICLA  PLSPYNTNCT  ILSVLNYFQN  SHSVLDHKKG
     ENITATYNNE  TVTLQDICVA  PLSPYNKNCT  IMSVLNYFQN  SHSMLDHKIG
     *****:*:**  ********:*  ******.***  *:********  ***:**** *

501  DDFFVYADYH  THFLYCVRAP  ASLNDTSLLH  DPCLGTFGGP  VFPWLVLGGY
     DDFYVYADYH  THLLYCVRAP  ASLNDTSLLH  DPCLGTFGGP  VFPWLVLGGY
     ***:******  **:*******  *********** **********  **********

551  DDQNYNNATA  LVITFPVNNY  YNDTEKLQRA  QAWEKEFINF  VKNYKNPNLT
     DDQNYNNATA  LVITFPVNNY  YNDTEKLQRA  QAWEKEFINF  VKNYENPNLT
     **********  **********  **********  **********  ****:*****

601  ISFTAERSIE  DELNRESDSD  620
     ISFTTERSIE  DELNRESNGD
     ****:*****  *******:.*
```

Figure 3. 8 Sequence alignment of NPC1 protein domain C region
NPC1 protein is the key receptor that EBOV-GP binds in the lysosomal membrane before fusion, and the domain C (amino acid 371 to 620) is known to directly interact with EBOV-GP. The figure shows the alignment of amino acid sequences of NPC1 protein domain C from human (*Homo sapiens)* and dog (*Canis lupus familiaris*) species. (*) denotes identical residues; (:) and (.) denote amino acids with similar functional groups. Yellow highlighted residues are sites that contact the receptor binding region of EBOV-GP in the crystal structure published by Wang *et al.* 2016.

3.3.3 E-S-FLU neutralisation with NIBSC immunoglobulin samples

We requested the panel of serum and plasma samples from NIBSC and tested them in our E-S-FLU system. We have tested sample code 9, 36, 28, 43, 79, 31 and 88, described as listed in Table 1 in Wilkinson *et al.* 2017. Sample 9 was the negative bovine immunoglobulin sample (IgG) and sample 36 was a negative plasma sample from a normal human blood donor. Sample 28, 43 and 79 were plasma prepared from convalescent patients. Sample 31 and 88 were bovine IgG after immunisation with recombinant *Zaire* GP or GP DNA from *Zaire* 95 and *Sudan* respectively (summarised in Table 3.2).

All samples were heat-inactivated before titrating in the micro-neutralisation assay, as described in section 3.3.2. All samples except sample 9 showed some level of inhibition against E-S-FLU infection. Sample 36, 28, 31 and sample 88 showed partial neutralisation (not reaching 100% inhibition at the highest concentration tested), while sample 43 and 79 inhibited E-S-FLU to more than 90%. IC_{50} values are the dilution of each sample from the original stock at which E-S-FLU infection was reduced by 50% (Table 3.2). The same set of samples were tested in 22 different assays, including neutralisation assays with wild-type EBOV, assay 11a and 12b (Wilkinson *et al.* 2017). We plotted the IC_{50} values of the 7 samples tested from E-S-FLU neutralisation (y-axis) against the neutralisation results reported against wild-type EBOV from assay 11a and 12b. The correlation coefficient (R^2) when compared with lab 11a was 0.48 (0.38 when negative samples removed) and 0.74 when compared with lab 12b (0.70 with negative samples removed) respectively (Figure 3.9).

Table 3. 2 Description of NIBSC samples

NIBSC sample code	Sample description	11a	12b	E-S-FLU
9	Unimmunised bovine IgG (negative)	<	<	<
36	NHBST healthy donor plasma (negative)	<	<	38
28	NHSBT EBOV convalescent plasma	45	30	52
43	Norwegian EBOV convalescent plasma	27	20	187
79	American EBOV convalescent plasma	181	160	314
31	Bovine IgG (immunised with VLP-*Zaire* GP)	91	20	35
88	Bovine IgG immunised with *Zaire* and *Sudan* GP DNA)	64	20	5

Table adapted from Wilkinson et al. 2017.
***11a and 12b**: two labs performed neutralisation assay with wild-type EBOV using the same set of NIBSC samples.*
***E-S-FLU**: neutralisation IC_{50} values on E-S-FLU pseudotyped virus.*
*(**<**): no detected neutralisation.*

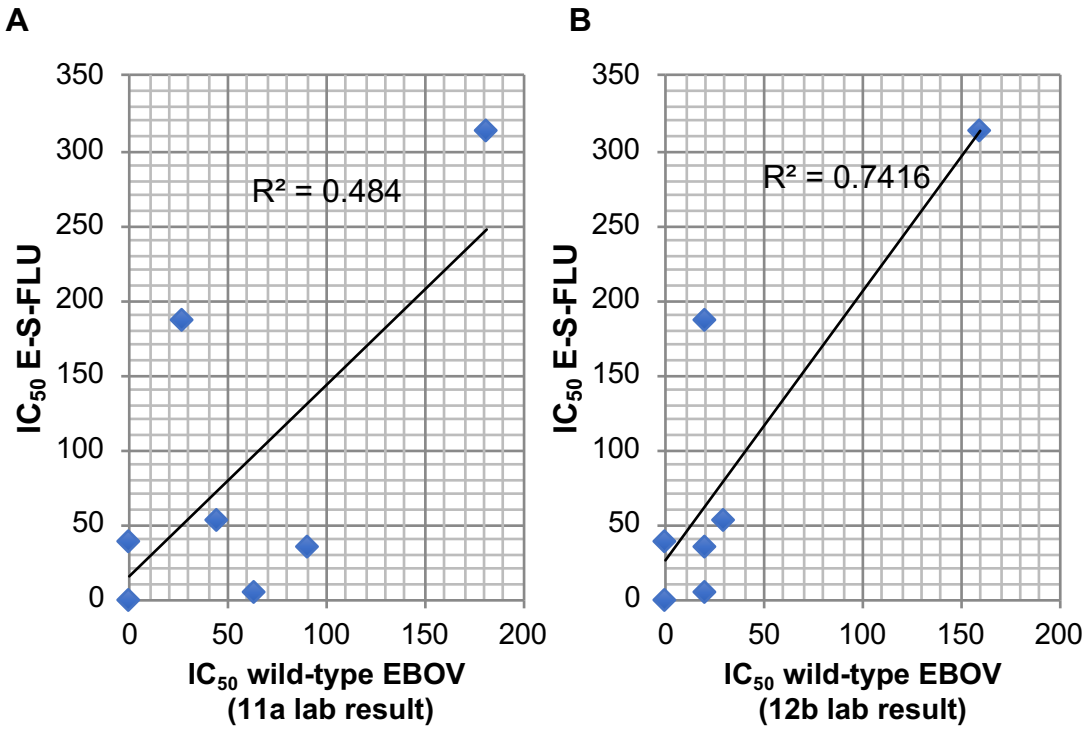


Figure 3. 9 E-S-FLU and wild-type EBOV neutralising NIBSC plasma samples
Scatter plot of titres from E-S-FLU neutralisation (y axis) against results from wild-type neutralisation assays from (**A**) laboratory 11a (x axis) correlation coefficient R^2= 0.48; (**B**) titre results from laboratory 12b (R^2 = 0.74).

3.3.4 E-S-FLU inhibition by various EBOV inhibitors

We have established a drug inhibition assay using E-S-FLU. The indicator MDCK-SIAT1 cells were pre-incubated with drugs at different concentrations and were then infected with E-S-FLU or H5-S-FLU at a saturating dose for 24 hours. H5-S-FLU is a control pseudotyped virus that matched for everything with E-S-FLU except the coating glycoprotein. Figure 3.10 shows an example of drug inhibition by tetrandrine. After 24 hours, cells were fixed with 10% formalin, and infection was quantified by measuring the level of eGFP fluorescence using a fluorescence plate reader CLARIOstar®. IC_{50} is the drug concentration at which eGFP fluorescence was reduced by 50%.

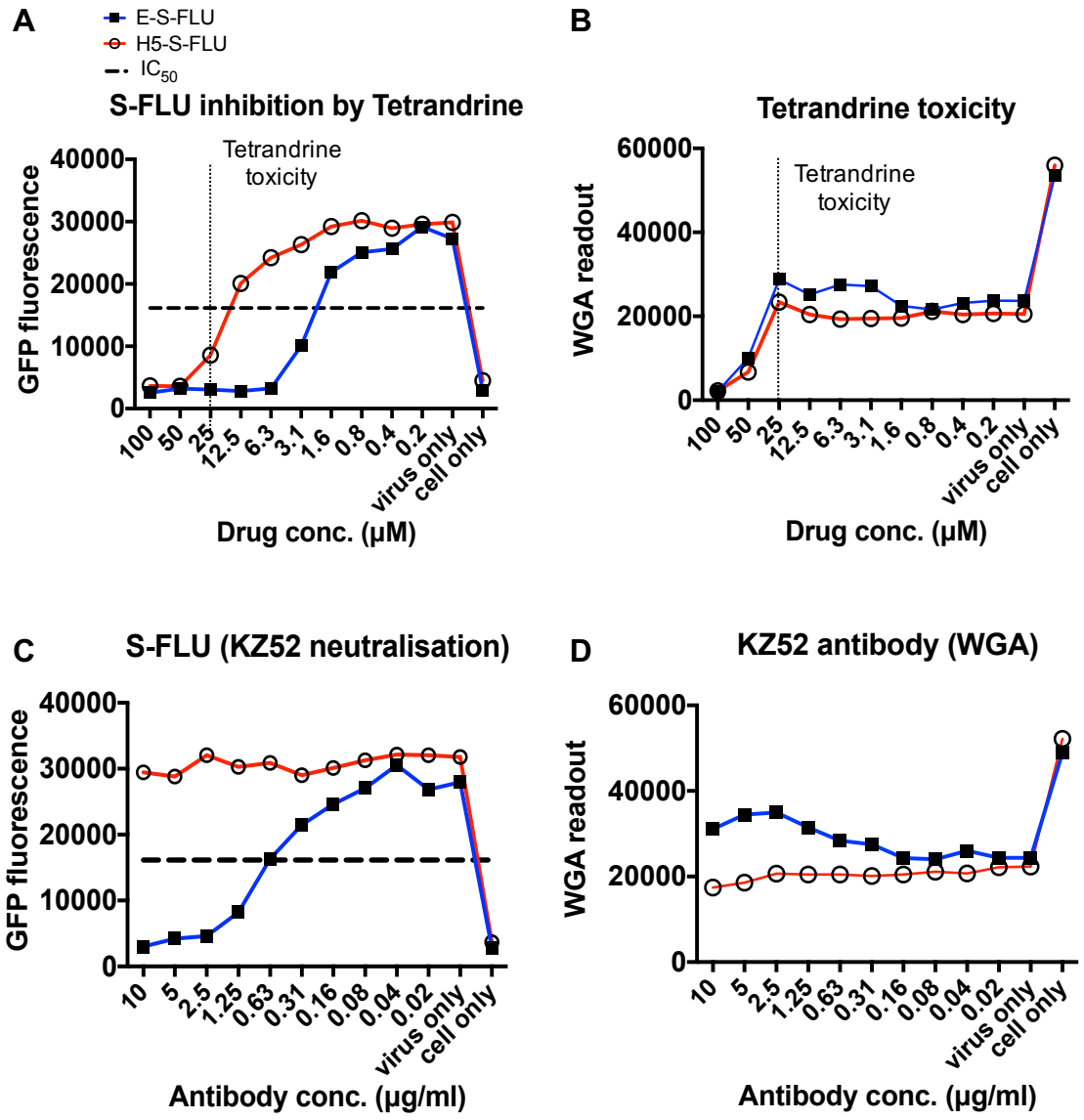


Figure 3. 10 Tetrandrine inhibition assay with the E-S-FLU and H5-S-FLU pseudotyped viruses

Tetrandrine was titrated from 100 to 0.2 µM in the drug inhibition assay against the E-S-FLU and H5-S-FLU viruses. Cells were pre-incubated with tetrandrine for 3 hours and infected with virus for 24 hours. **A**: Virus infection was quantified by measuring eGFP expression with a fluorescence plate reader. **B**: WGA was added to stain cell membrane sialic acid and N-acetylglucosaminyl residues as an estimation of the number of cells remaining in each well after fixation and washing. Toxicity reduces the WGA fluorescence as cells detach from the plastic. A drop in WGA staining in cells treated with >25 µM tetrandrine suggested that 25 µM was the toxicity limit of the drug. (**C and D**) Control inhibition of E-S-FLU and H5-S-FLU with an anti-EBOV-GP antibody KZ52, infection quantified by measuring eGFP expression, and the cells were stained with WGA. KZ52 was not toxic to the indicator MDCK-SIAT1 cells. Note that the S-FLU virus expresses neuraminidase, which partially reduces WGA binding between “cell only” and “virus only” in (**B** and **D**). Neutralisation of the S-FLU virus is associated with some increase in WGA binding as neuraminidase expression in infected cells is reduced.

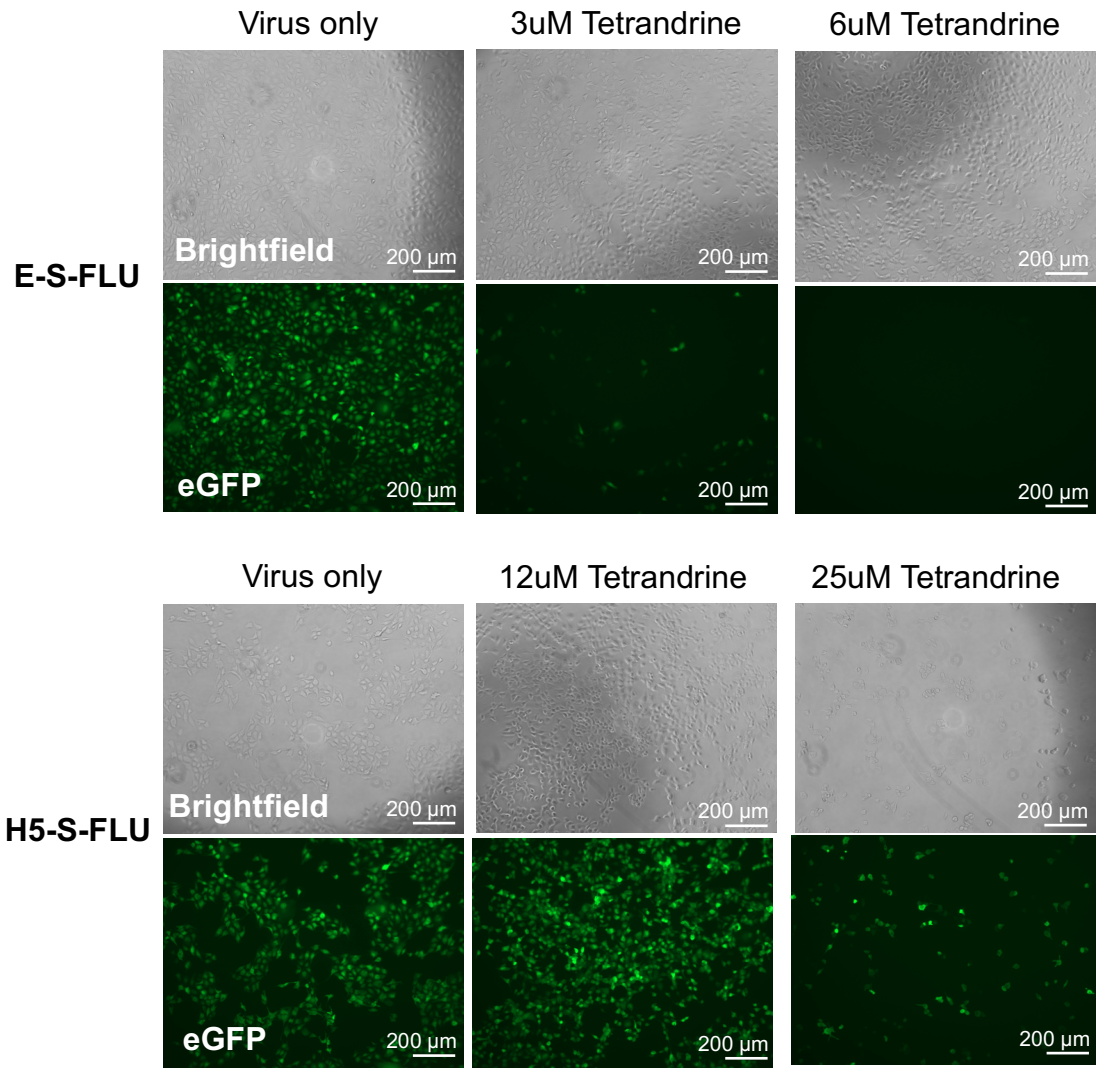


Figure 3. 11 Fluorescence microscopy pictures of tetrandrine inhibition assay

Indicator MDCK-SIAT1 cells were pre-treated with tetrandrine for 3 hours, and infected by E-S-FLU or H5-S-FLU for 24 hours. Fluorescent microscopy pictures were taken after infection and fixation in brightfield and eGFP channels. Note that the toxicity of tetrandrine at 25 µM resulted in a reduction in the number of cells in the brightfield channel. The remaining cells at 25 µM were still infected by H5-S-FLU.

Because most drugs are toxic to cells at high concentration, we estimated toxicity by staining the cells with fluorescently labelled wheat germ agglutinin, Alexa Fluor® 647 conjugated WGA, after infection, fixation and washing. WGA binds to cell surface N-acetyl-D-glucosamine and sialic acid. Toxicity reduces the WGA fluorescence as cells detach from the plastic (Figure 3.10 B and D). Anti-EBOV-

GP antibody KZ52 was included as a non-toxic inhibitor control (Figure 3.10 C and D). Note that the S-FLU virus expresses neuraminidase that cleaves off sialic acid from the cell surface, and this partially reduces WGA binding between “cell only” and “virus only” samples. Inhibition of the S-FLU virus by neutralising antibody is associated with some increase in WGA binding as the neuraminidase effect was reduced. The toxic dose of tetrandrine in our assay was 25 μM according to WGA staining, and this was confirmed by light microscopy, where much fewer cells were observed at 25 μM than lower concentrations of tetrandrine (Figure 3.11). E-S-FLU infection was completely inhibited at around 6 μM tetrandrine, whereas H5-S-FLU was not inhibited even at the toxic concentration 25 μM.

Many drug screens have been reported using wild-type EBOV or other EBOV surrogates such as EBOV virus-like particles (VLPs), EBOV-GP-pseudotyped VSV and lentivirus. There have been an increasing number of small molecules described that inhibited EBOV infection *in vitro* (Gnirß *et al.* 2012; Johansen *et al.* 2013; Gehring *et al.* 2014; Kouznetsova *et al.* 2014; Sakurai *et al.* 2015). The mechanism of inhibition of most drugs is however still not clear.

To compare our assay with those in the literature, we selected 13 drugs from different pharmacological groups that have been repeatedly shown to be EBOV inhibitors *in vitro*, and tested them for inhibition of E-S-FLU and the control H5-S-FLU. All 13 drugs inhibited E-S-FLU, and the geometric mean IC_{50}s from at least three repeated assays are summarised in Table 3.3. The IC_{50}s for different drugs inhibiting E-S-FLU were in a similar range to the IC_{50}s stated in the literature. From these 13 drugs, only niclosamide inhibited H5-S-FLU with an IC_{50} of 2.64 μM.

Table 3. 3 IC_{50} values of 13 drugs that inhibited E-S-Flu virus infection selected from the literature

Drug	Mechanism	E-S-FLU IC_{50} (μM) Geometric mean (95% CI)	IC_{50} in the literature (μM)	Virus	Reference
Amiodarone	Calcium channel inhibitor	2.04 (0.54~7.76)	0.4	Wild-type EBOV	Gehring *et al.* 2014
Verapamil		10.6 (2.75~9.8)	3.1	Wild-type EBOV	Sakurai *et al.* 2015
Tetrandrine		1.63 (0.65~4.07)	0.06	Wild-type EBOV	Sakurai *et al.* 2015
Clomiphene	Estrogen receptor antagonist	0.35 (0.23~0.55)	2.4	Wild-type EBOV	Johansen *et al.* 2013
Toremifene		0.15 (0.14~0.16)	0.2	Wild-type EBOV	Johansen *et al.* 2013
Imipramine	Anti-depressant	3.82 (2.51~5.75)	13.7	EBOV-VLPs	Kouznetsova *et al.* 2014
Clarithromycin	Antibiotics	14.0 (2.19~91.2)	4.5	EBOV-VLPs	Kouznetsova *et al.* 2014
U18666A	NPC1 phenotype inducer	2.32 (0.19~28.8)	3.0	rVSV-EBOV-GP	Carette *et al.* 2011
Arbidol	Fusion inhibitor	5.17 (0.60~43.7)	5.97	Wild-type EBOV	Pécheur *et al.* 2016
EIPA	Macropinocytosis inhibitor	17.8 (14.1~22.4)	25.0	Wild-type EBOV	Saeed *et al.* 2010
MDL28170	Calpain inhibitor	3.81 (0.85~17.0)	10.0	GP-lentivirus	Gnirß *et al.* 2012
E64	Cathepsin inhibitor	77.2 (64.6~93.3)	50.0	GP-lentivirus	Schornberg *et al.* 2006
Niclosamide	Proton Ionophore	1.69 (1.00~2.88)	2.64	Wild-type EBOV	Kouznetsova *et al.* 2014

***E-S-FLU IC_{50} (μM) Geometric mean (95% CI)**: Geometric mean of drug inhibition IC_{50} of E-S-FLU infection measured in at least three repeated assays, and the 95% confidence interval is shown in the brackets.*

3.4 GP-HA hybrid pseudotyping

We showed that we can pseudotype S-FLU with full length EBOV-GP to produce E-S-FLU, and it behaves similarly to wild-type EBOV during the entry process into cells. Although we can produce a reasonable titre of E-S-FLU without further need of concentration, the viral titre was about 100-fold lower than pseudotypes coated in various Influenza haemagglutinins including H5 (Figure 3.3 B). We therefore set out to improve this titre.

It has been shown in the literature that the transmembrane and cytoplasmic domains of Influenza HA are important for Influenza viral particle assembly. We therefore designed a GP-HA hybrid protein, which contains the extracellular domain of the EBOV-GP and the transmembrane and cytoplasmic domain of HA (Fig. 3.12) to see if this hybrid molecule might support a higher titre of the pseudotyped virus. We estimated the transmembrane domain based on the hydrophobicity plots of EBOV-GP and Influenza H1 HA (from A/PR8/34 H1N1) based on the Kyte-Doolittle scale. The N-terminal extracellular domain (amino acid 1 to 648) from *Zaire* EBOV-GP was joined with the C-terminal sequence (amino acid 521 to 566) from H1 HA to form the GP-HA hybrid domain. The join point was selected by eye to maintain a continuous gradient in the hydrophobicity plot of GP-HA protein at the transmembrane region.

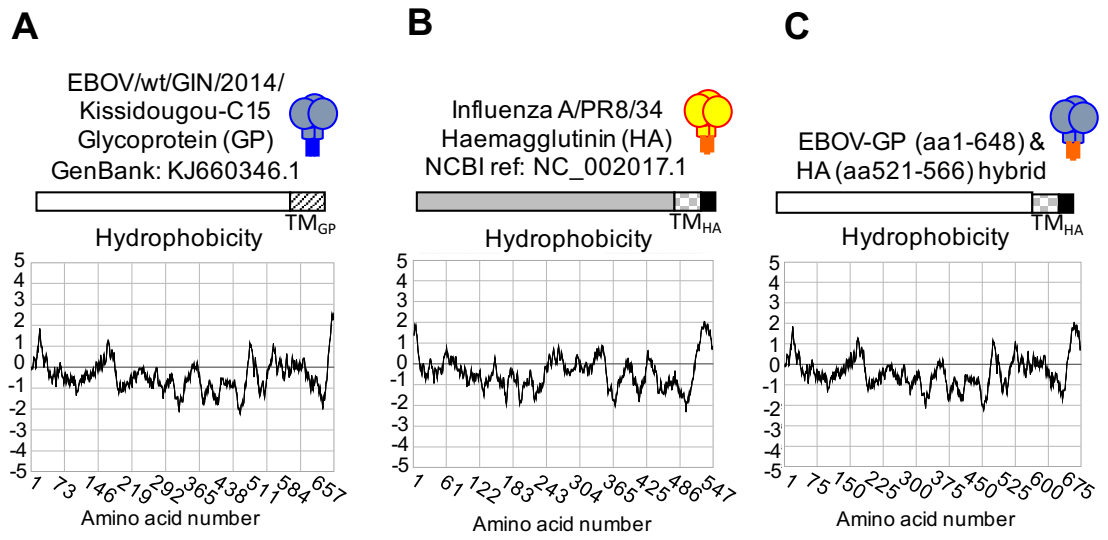


Figure 3. 12 Design of GP-HA hybrid protein

The extracellular domain of EBOV-GP was joined with the transmembrane region (TM_{HA}) and cytoplasmic domain of Influenza haemagglutinin (HA). It consists of EBOV-GP amino acid 1-648 (*Zaire ebolavirus* wt/GIN/2014/Kissidougou-C15) and HA amino acid 521-566 (Influenza H1N1 A/PR/8/34, NCBI ref: NC_002017.1), in total 694 amino acids. The hydrophobicity plots of EBOV-GP, HA and GP-HA hybrid protein were plotted based on the Kyte-Doolittle scale with a window size of 19 amino acids in order to predict the transmembrane region. The average hydrophobicity score of every 19 amino acids was plotted against the amino acid number of the first residue of the stretch (x-axis). A predicted domain structure is shown above each hydrophobicity plot. The joining point of GP and HA sequences was determined by eye to form a continuous gradient of hydrophobicity at the transmembrane region.

We then transduced MDCK-SIAT1 cells to express GP-HA hybrid protein. We detected high level of GP-HA expression at the cell surface by using anti-EBOV-GP antibody KZ52 in FACS. The expression of GP-HA was at a level similar to the full-length GP expressed in E-SIAT cells, and was stable up to at least the ninth passage after FACS sorting (Figure 3.13). We called the new cell-line EH-SIAT. We then seeded EH-SIAT cells with 1 CID_{50}/cell cloned S-FLU virus, and after 48 hours harvested the culture supernatant and titrated over indicator MDCK-SIAT1 cells. There were however no infective viral particles detected from EH-SIAT cells (Figure 3.14).

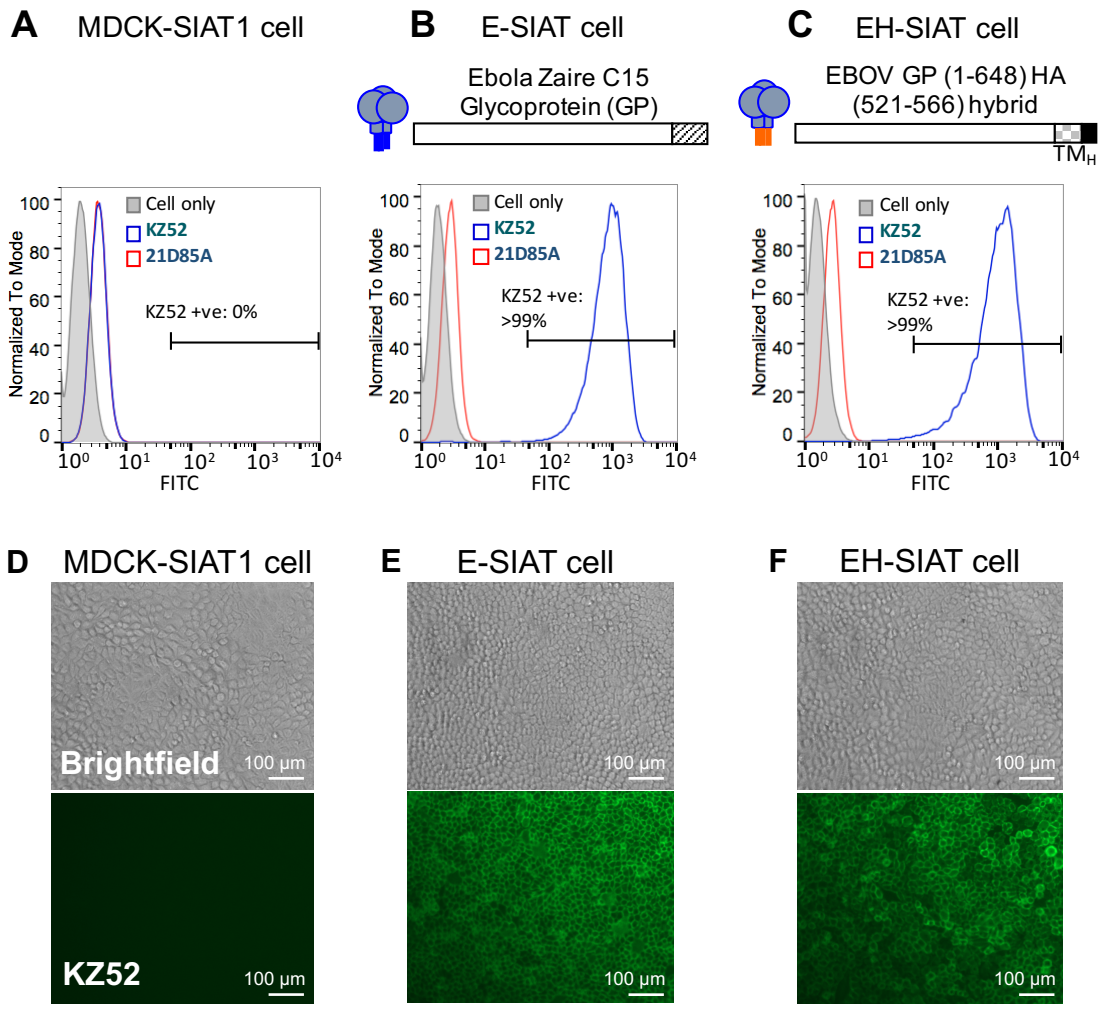


Figure 3. 13 Stable expression of EBOV-GP and GP-HA hybrid protein on the surface of transduced MDCK-SIAT1 cell-line

FACS plots of (**A**) MDCK-SIAT1, (**B**) MDCK-SIAT1 cells transduced with full-length EBOV-GP (E-SIAT), and (**C**) MDCK-SIAT1 cells transduced with GP-HA hybrid protein (EH-SIAT). Cells were stained with primary antibody KZ52 (anti-GP) or 21D85A (anti-H5), followed by a FITC-linked anti-human secondary antibody. E-SIAT and EH-SIAT cells stably express GP at the cell surface up to at least the ninth passage, which can be detected by a conformational antibody KZ52 specifically (B, C: blue). Immunofluorescence pictures showing membrane staining of MDCK-SIAT1 (D), E-SIAT (E) and EH-SIAT (F) with KZ52 (anti-GP) and FITC-linked anti-human antibody.

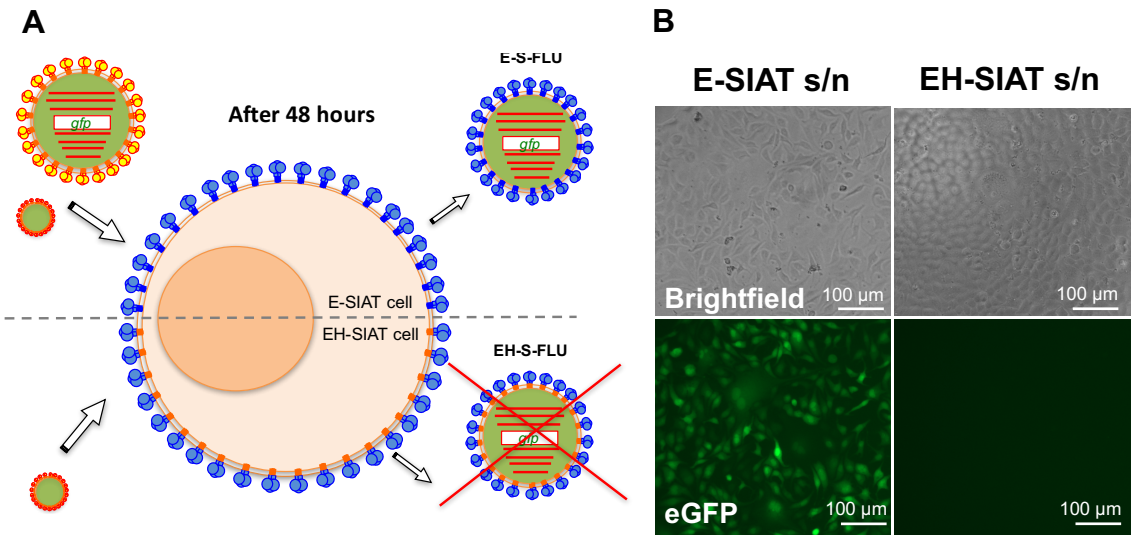


Figure 3. 14 No infective pseudotyped S-FLU produced from EH-SIAT cells
A: Schematic diagram showing the production of S-FLU pseudotyped virus. Pseudotyping S-FLU with EBOV-GP. MDCK-SIAT1 cells transduced to express full-length EBOV-GP (E-SIAT cells) or GP-HA hybrid protein (EH-SIAT cells) were seeded with S-FLU to generate EBOV-GP and GP-HA pseudotyped S-FLU viruses. Culture supernatant (s/n) harvested after 48 hours was titrated to infect MDCK-SIAT1 indicator cells for 24 hours' infection. Infected cells expressed eGFP. **B:** Fluorescence light microscopy pictures of MDCK-SIAT1 cells infected by undiluted culture supernatant harvested from E-SIAT (E-SIAT s/n) or EH-SIAT cells (EH-SIAT s/n) after 24 hours.

To detect whether there were any non-infective EH-S-FLU particles assembled and released in the culture supernatant, we carried out a virus ELISA assay. Because S-FLU particles contain neuraminidase (NA) at the viral surface, we've designed a sandwich ELISA technique using both an in-house anti-NA monoclonal antibody AF9C and an anti-EBOV-GP monoclonal antibody P6 (Figure 3.15). Similar amounts of particles co-expressing EBOV-GP and neuraminidase were detected from the supernatant harvested from E-SIAT and EH-SIAT cells but not from H5-SIAT and MDCK-SIAT1 cells. This suggested that there are pseudotyped S-FLU coated with the GP-HA hybrid protein produced, but the particles were no longer infective.

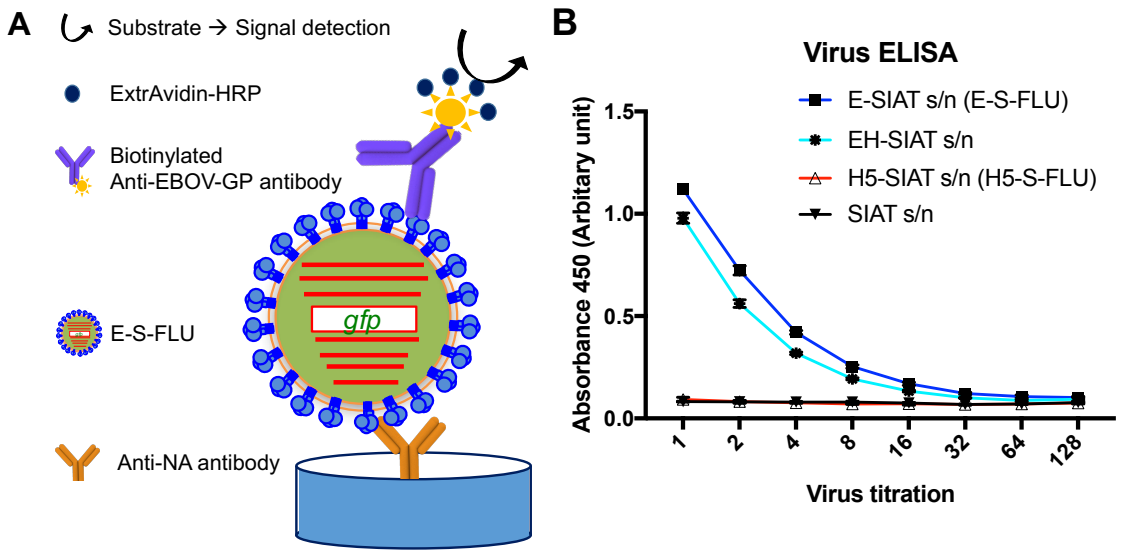


Figure 3. 15 Detection of pseudotyped S-FLU particle by virus ELISA
A: Schematic diagram demonstrating the virus sandwich ELISA set-up. 96-well Nunc® plates were coated with anti-neuraminidase (anti-NA) antibody. All S-FLU pseudotyped viruses contain neuraminidase protein at the surface, which was encoded in the S-FLU virus genome. A biotinylated anti-EBOV-GP antibody was added to detect any EBOV-GP expressing S-FLU viruses captured in the well. Horseradish peroxidase linked ExtrAvidin® (ExtrAvidin-HRP) was added to bind to the biotinylated antibody. Finally, substrate was added and we measured the absorbance at 450 nm to quantify virus particles. **B**: MDCK-SIAT1 cells, SIAT cells transduced to express full-length EBOV-GP (E-SIAT cells), hybrid GP-HA protein (EH-SIAT cells) or Influenza H5 haemagglutinin protein (H5-SIAT cells) were seeded with S-FLU to produce pseudotyped viruses. Culture supernatant (s/n) harvested from different cells after 48 hours were titrated in the ELISA plate coated with anti-NA antibody and detected by the method described in (**A**). The error bars represent the standard error of the mean calculated from technical triplicates.

3.5 Dual pseudotyped S-FLU: H7CFv3/E-S-FLU

3.5.1 Rationale of the H7CFv3/E-S-FLU design

We observed in Figure 3.3 that S-FLU replicated much more slowly in E-SIAT cells than in H5-SIAT cells. Following the first-round infection, we observed that H5-S-FLU spread uniformly to all the neighbouring cells to form a dense plaque, whereas a more diffused and smaller plaque was formed in E-SIAT cells (Figure 3.4). We hypothesised that the homologous Influenza haemagglutinin protein was better at initial cell attachment than the heterologous EBOV-GP. Hence, H5-S-FLU released from the first infected cell could infect any neighbouring cells that it

contacted efficiently. Based on this hypothesis, we decided to introduce an additional fusion-defective haemagglutinin on the surface of E-S-FLU to try and improve the viral titre of E-S-FLU. The aim was to provide a universal lectin at the viral surface, in the form of the fusion defective haemagglutinin, that would enhance the efficiency of initial cell attachment of E-S-FLU. The work presented in section 3.5 was done together by the author and a medical student Declan Pang as part of his undergraduate research project.

Holly Sadler and Alain Townsend in the lab have designed and engineered a fusion-defective HA protein: H7CFv3. H7CFv3 is a mutated version of an H7 haemagglutinin protein sourced from H7N9 Influenza (A/HK/125/2017), which is a low pathogenic avian virus that has caused human infections (Huang *et al.* 2019).

Eleven amino acid changes were introduced to abolish H7's fusion function while maintaining its binding affinity to sialic acid at the host cell surface and its antigenicity detected by a panel of monoclonal antibodies (Table 3.4). Two disulphide bonds were introduced to lock the HA head and stem in the pre-fusion state, and additional mutations were introduced in HA1 and HA2 to the cleavage site, fusion peptide, and the B loop of HA2 that undergoes a transition to an alpha helix during fusion. Each of the mutations were first introduced individually (disulphide bond mutations, and the B loop prolines, were introduced in pairs), and seven mutated sites independently prevented viral replication, the eighth had a partial effect (mutation G8A). A molecule was then constructed with all eleven mutations. All of the mutations have been described in the literature (Table 3.4), but they have never all been introduced together into one molecule.

Table 3. 4 Mutations introduced to H7 in H7CFv3

Chain: Mutation	Description	Reference
HA1: R329Q	Inhibited cleavage of the precursor HA0 into HA1 and HA2	Orlich, Linder and Rott 1995; Chen *et al.* 1998; Stech *et al.* 2005; Katsura *et al.* 2012
HA1: S212C	Inter-chain disulphide bond to lock the HA head	Godley *et al.* 1992; Lee *et al.* 2015
HA1: S216C		
HA1: T30C	Inter-chain disulphide bond to lock the HA stem	
HA2: Q47C		
HA2: F63P	A pair of prolines that together prevent the transition of the B loop of HA2 from beta sheet to alpha helix required for fusion	Gruenke *et al.* 2002
HA2: F70P		
HA2: G1Q	Mutations in the fusion peptide, inhibited fusion	Cross *et al.* 2010
HA2: L2G		
HA2: I6G		
HA2: G8A		

Haemagglutinin numbering was based on the H3 numbering system reviewed in (Burke and Smith 2014)

For dual pseudotyping, E-SIAT cells were transduced to express in addition the H7CFv3 molecule, and sorted for high expression of both EBOV-GP and H7CFv3 (Figure 3.16). We hoped that infection of these cells would result in coating of budding S-FLU with both the fusion inactive H7CFv3 protein, and the fusion active EBOV-GP. The H7CFv3 alone could not support replication (personal communication with Holly Sadler), but might act as a sialic acid binding lectin for improved attachment to the target cell plasma membrane. While the H7CFv3 should assist in cell surface attachment, all later steps should be EBOV-GP dependent.

Note that this new pseudotype design does not contain any genetic material from either H7N9 Influenza or Ebola virus, the Influenza core particle is simply coated

in proteins from these viruses. We have chosen to introduce a mutated H7 haemagglutinin, because we found that H7 haemagglutinins, including that from A/HK/125/2017, support very high titres of pseudotyped H7-S-FLU virus (>10^8 $TCID_{50}$/ml), suggesting that the H7 molecule may be very efficient at the binding and entry process.

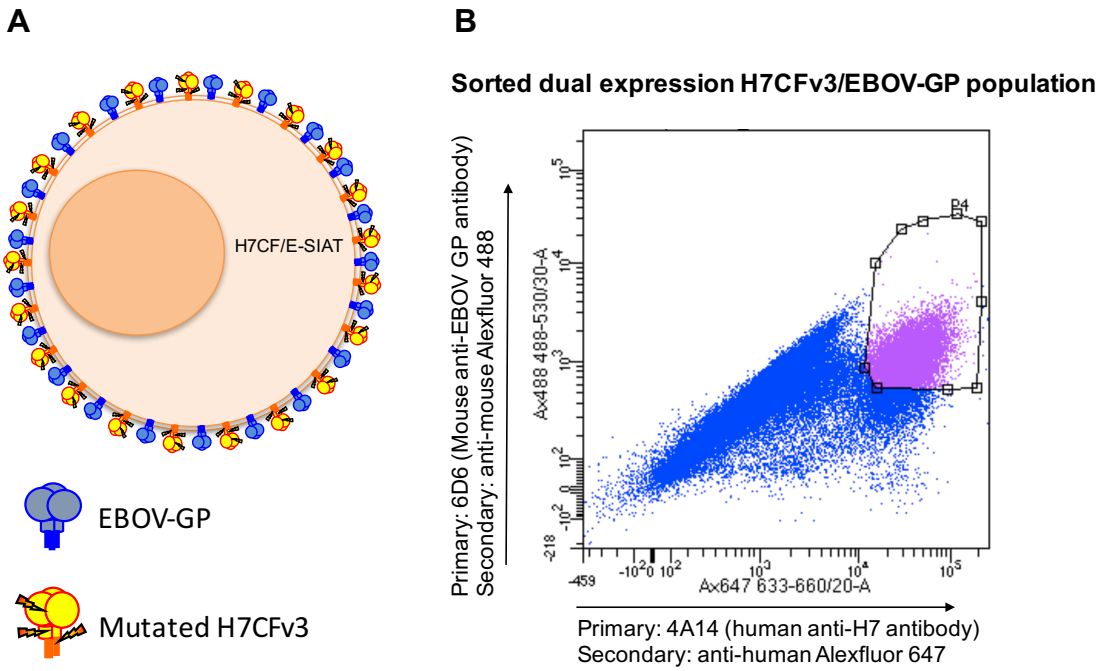


Figure 3. 16 Design and production of H7CFv3/E-SIAT cell
A: Schematic diagram showing MDCK-SIAT1 cells transduced to co-express H7CFv3 and EBOV-GP proteins. H7CFv3 is a mutated version of the H7 haemagglutinin protein from H7N9 Influenza (A/HK/125/2017), which is a low pathogenic avian virus that has caused human infections (Huang *et al.* 2019). Eleven mutations were introduced to abolish H7's fusion function while maintaining its binding affinity to sialic acid at the host cell surface and its antigenicity detected by a panel of monoclonal antibodies. **B**: Transduced cells expressing both EBOV-GP and H7CFv3 were analysed by FACS. A mouse anti-EBOV-GP antibody (6D6, Furuyama *et al.* 2016) and a human anti-H7 antibody (4A-14, Huang *et al.* 2019) were used to detect protein expression. The gated population P4 (**purple**) was bulk sorted and we named it the H7CFv3/E-SIAT cell-line.

3.5.2 H7CFv3/E-S-FLU production and titration

We transduced the sorted E-SIAT cells with a lentiviral vector containing H7CFv3 gene to co-express both EBOV-GP and H7CFv3 proteins. Cells expressing a high

level of both proteins were FACS sorted with a mouse anti-EBOV-GP antibody 6D6 (Furuyama *et al.* 2016; Milligan *et al.* 2019) and a human anti-H7 antibody 4A-14 produced in house (Huang *et al.* 2019). We called the new cell-line H7CFv3/E-SIAT cells (Figure 3.16).

We then compared the S-FLU production from E-SIAT, H7CFv3/E-SIAT, H7CFv3-SIAT and H7-SIAT cells. All cells were seeded with the same protocol and on the same day as described in section 3.2, and trypsin at 0.75 μg/ml was added to the H7-SIAT cultures (the H7 protein requires trypsin for cleavage for replication to occur).

Culture supernatants harvested after 48 hours were titrated on indicator MDCK-SIAT1 cells. All S-FLUs contain the same eGFP reporter gene. The viral titre from this batch of E-S-FLU was lower than the batch described in section 3.2, infection did not plateau when undiluted E-S-FLU was added to the cells (Figure 3.17, red). From H7CFv3/E-SIAT cells we produced H7CFv3/E-S-FLU, and the virus titre was around 32 to 64-fold higher than E-S-FLU. H7-S-FLU harvested from wild-type H7 expressing cells had around 256-fold higher titre than E-S-FLU, which is comparable to the fold difference we observed in H5-S-FLU. We did not detect any infective pseudotyped virus from the H7CFv3-SIAT culture supernatant, as expected, confirming that H7CFv3 protein alone cannot support S-FLU replication.

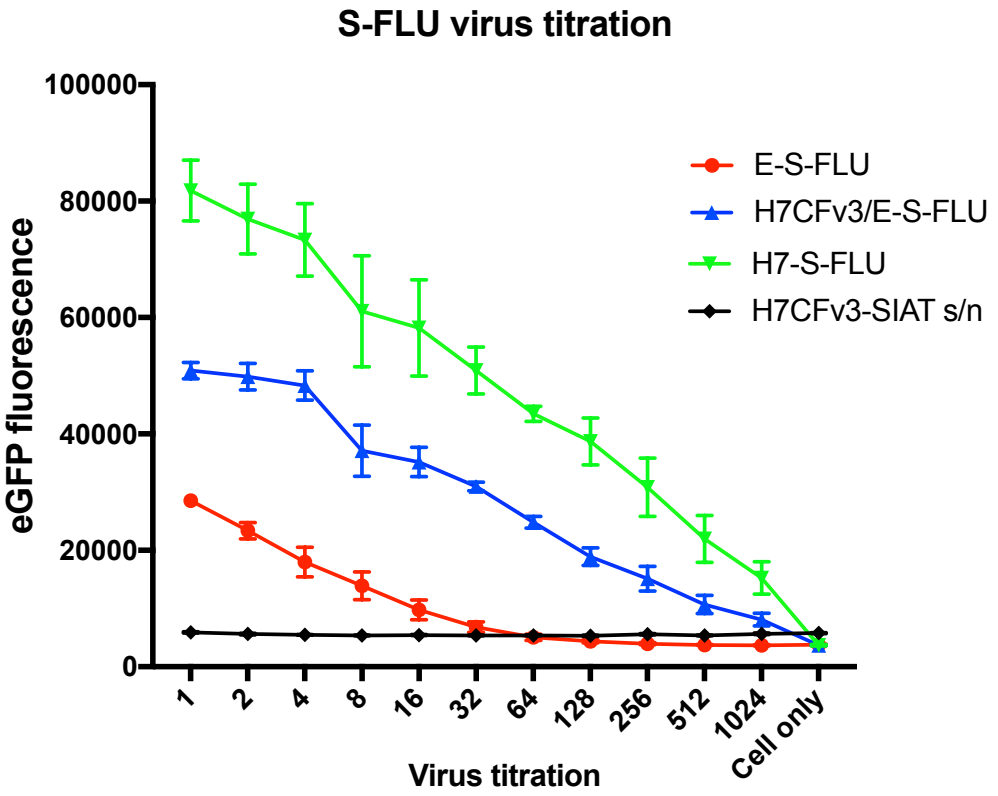


Figure 3. 17 Virus titration of H7CFv3/E-S-FLU and E-S-FLU
MDCK-SIAT1 cells were transduced to express full-length EBOV-GP (E-SIAT); wild-type H7 haemagglutinin from H7N9 Influenza (A/HK/125/2017) (H7-SIAT); mutated H7 that was fusion-defective (H7CFv3-SIAT); or both EBOV-GP and mutated H7 (H7CFv3/E-SIAT). Cells were seeded with S-FLU to produce pseudotyped viruses, culture supernatant (s/n) were harvested after 48 hours and titrated on indicator MDCK-SIAT1 cells. Infection was quantified by measuring eGFP fluorescence by a fluorescence plate reader CLARIOstar®. Average values of fluorescence were plotted with error bars representing the standard error of the mean from eight technical replicates of titrations.

3.5.3 H7CFv3/E-S-FLU infection is NPC1 dependent

NPC1 is the crucial receptor for EBOV-GP dependent infection. If dual pseudotyping had occurred, the resulting virus should still be absolutely dependent on the expression of NPC1 protein for infection of the target cells. We therefore titrated E-S-FLU, H7CFv3/E-S-FLU and H7-S-FLU for infection of wild-type HeLa and *NPC1*KO HeLa cells. Both E-S-FLU and H7CFv3/E-S-FLU infection were completely abolished in *NPC1*KO HeLa cells (Figure 3.18). By contrast, H7-S-FLU infection was not affected by the absence of NPC1 protein. This showed that

H7CFv3/E-S-FLU infection of HeLa cells was NPC1 dependent. We also observed that H7CFv3/E-S-FLU had higher viral titre than E-S-FLU in HeLa cells, and infected a higher percentage of cells at a saturating virus dose.

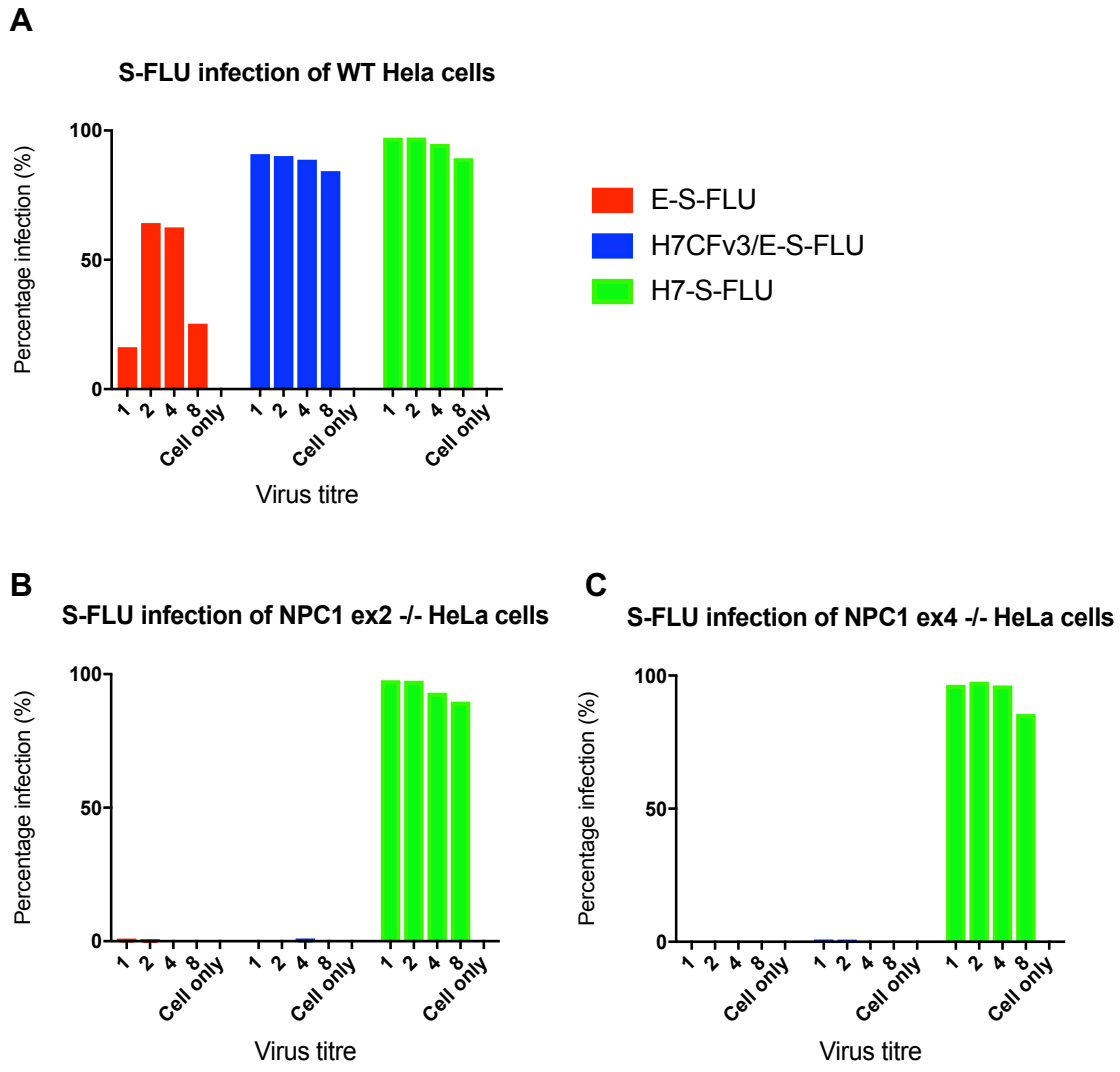


Figure 3. 18 H7CFv3/E-S-FLU requires NPC1 receptor expression for infection of HeLa cells

NPC1 protein is the key receptor for EBOV entry at the lysosomal membrane. We titrated E-S-FLU (**red**), H7CFv3/E-S-FLU (**blue**) and H7-S-FLU (**green**) for infection of wild-type HeLa cells and two clones of *NPC1*KO HeLa cells (NPC1 ex2 -/- and NPC1 ex4 -/-) (Tharkeshwar *et al.* 2017). Infected cells were analysed by FACS, the percentage of infected cells was the percentage of cells with an eGFP readout of $>10^2$ fold of uninfected "Cell only" control.

Together these results showed that dual pseudotyping of S-FLU with the inactive H7CFv3 together with EBOV-GP successfully enhanced the titre of the resulting

pseudotyped virus, while maintaining absolute dependence on the NPC1 receptor for viral entry and expression of the encoded eGFP reporter.

3.5.4 Antibody neutralisation of H7CFv3/E-S-FLU

We then compared E-S-FLU, H7CFv3/E-S-FLU and H7-S-FLU for susceptibility to neutralisation by antibodies to the H7CFv3 haemagglutinin and EBOV-GP. We have used four different monoclonal antibodies: two anti-EBOV-GP antibodies KZ52 and 66-6-3; an anti-H7 antibody 4A-14, and an anti-neuraminidase (anti-NA) antibody Z2B3. KZ52 and 66-6-3 recognise epitopes on EBOV-GP base region (Lee *et al.* 2008; Rijal *et al.* 2019). Different S-FLUs at their saturating dose (E-S-FLU 1 in 3, H7CFv3/E-S-FLU 1 in 64, H7-S-FLU 1 in 64) were pre-incubated with monoclonal antibodies. Pre-treated S-FLUs were then added to infect indicator MDCK-SIAT1 cells for 24 hours. After infection, cells were fixed and we measured the eGFP fluorescence level to quantify infection. All assays were repeated at least three times. Figure 3.19 shows a representative result.

Both anti-EBOV-GP antibodies tested (KZ52 and 66-6-3) inhibited infection by E-S-FLU and H7CFv3/E-S-FLU, but did not have any effect on infection by the H7-S-FLU control. This showed that infection of cells by E-S-FLU and H7CFv3/E-S-FLU was EBOV-GP dependent. In addition, the IC_{50} for both antibodies against these two viruses were comparable and were within 2-fold of each other. This suggested that the amount of EBOV-GP in the membranes of the two viruses, or at least the efficiency with which the EBOV GP functioned, was similar.

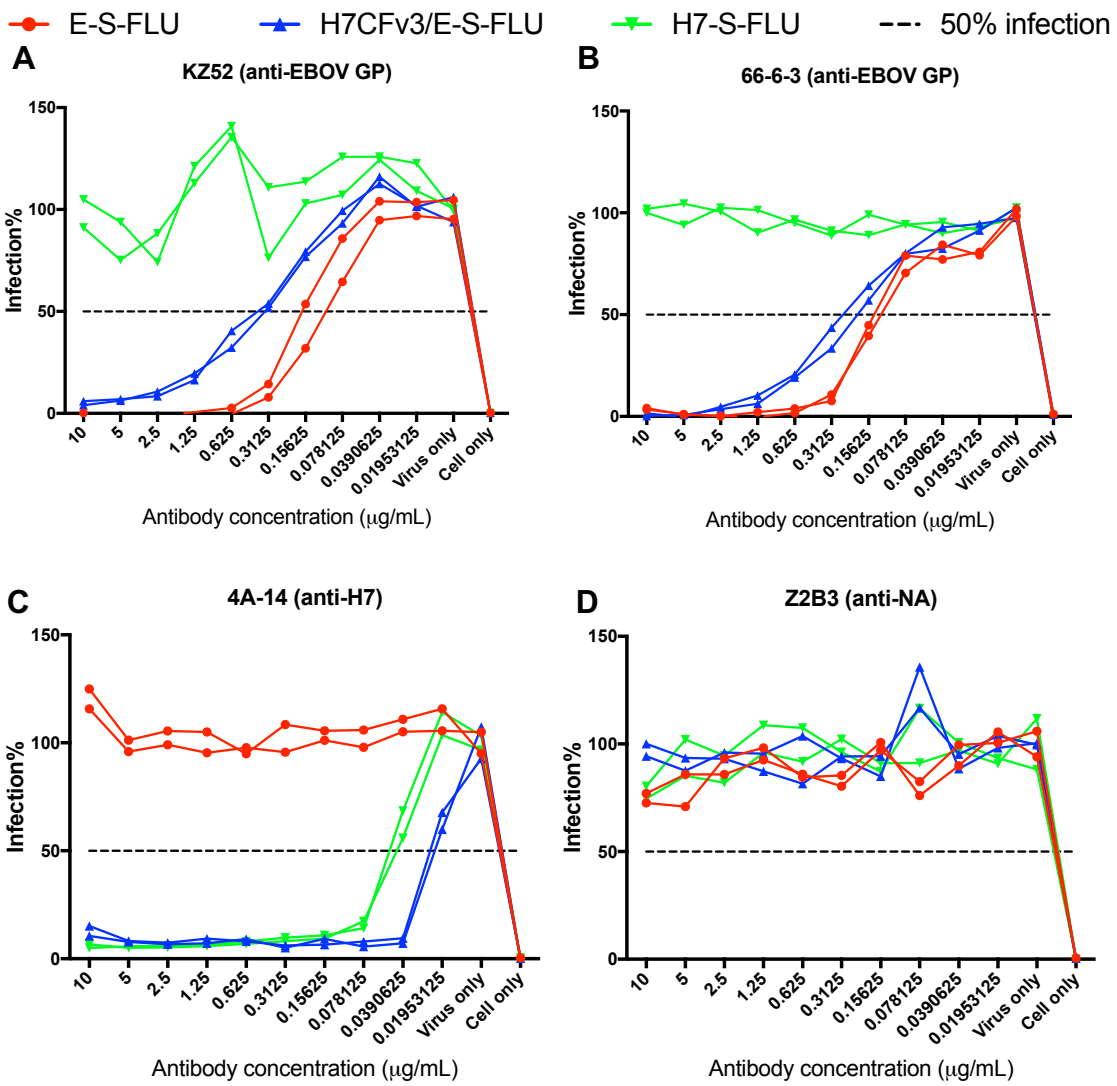


Figure 3. 19 Antibody micro-neutralisation assay of H7CFv3/E-S-FLU
We tested four monoclonal antibodies in neutralisation assay against E-S-FLU (**red**), H7CFv3/E-S-FLU (**blue**) and H7-S-FLU (**green**). KZ52 and 66-6-3 are two human anti-EBOV-GP antibodies, both recognising epitopes at the base region of EBOV-GP. 4A-14 is an anti-H7 antibody, and Z2B3 is an anti-neuraminidase (anti-NA) antibody. S-FLU viruses were pre-incubated for 2 hours with antibody before MDCK-SIAT1 indicator cells were added. Antibodies were titrated in 2-fold dilutions from 10 μg/ml. After 24 hours, percent infection was quantified by measuring eGFP expression using a fluorescence plate reader CLARIOstar®. Each antibody was titrated in technical duplicates. The broken line (50% infection) marks the 50% maximum fluorescence level.

H7-S-FLU was not inhibited by anti-EBOV-GP antibodies. In comparison, anti-H7 antibody (4A-14) did not inhibit E-S-FLU as it did not contain any H7 protein. However, 4A-14 did neutralise both H7-S-FLU and H7CFv3/E-S-FLU with similar

IC_{50} values. This result showed that the greatly enhanced titre of the H7CFv3/E-S-FLU was dependent on the mutated H7 protein. Huang *et al.* showed that the 4A-14 antibody inhibited hemagglutination by H7-S-FLU viruses, and crystal structures of 4A-14 bound to the H7 haemagglutinin reveal that the complementarity-determining region 3 (CDR3) of the antibody heavy chain occupies the sialic acid binding site (Huang *et al.* 2019). Our results are therefore consistent with the sialic acid binding function of the H7CFv3 HA being responsible for the enhanced titre of the dual pseudotype H7CFv3/E-S-FLU.

All S-FLUs contain neuraminidase (NA) at their surface, as shown by the cleavage of fetuin by S-FLUs (Powell *et al.* 2019). The anti-NA antibody (Z2B3) did not inhibit entry of any of the four S-FLUs tested, showing that the entry of these S-FLUs into cells is independent of NA, and this was included as a negative control.

3.5.5 Drug inhibition of H7CFv3/E-S-FLU

We also selected four drugs that inhibited E-S-FLU and tested their effect on H7CFv3/E-S-FLU in the drug inhibition assay. These four drugs have also been repeatedly tested in the literature, and their mechanisms of inhibitions of EBOV are relatively well understood. They are thought to act at different stages of EBOV cell entry. EIPA (5-(N-Ethyl-N-isopropyl) amiloride) is a form of amiloride, and it is known as a macropinocytosis inhibitor that blocks the initial entry of EBOV at the plasma membrane (Nanbo *et al.* 2010; Mulherkar *et al.* 2011). E64d is a derivative of E64, which inhibits cysteine proteases cathepsin B and L from digesting EBOV-GP in the endosome to a form that can bind the NPC1 receptor (Chandran *et al.* 2005; Kaletsky, Simmons and Bates 2007; Wang *et al.* 2016). Niclosamide is a

proton ionophore (Jurgeit *et al.* 2012; Johansen *et al.* 2013; Kouznetsova *et al.* 2014), which is thought to inhibit EBOV by affecting the endosomal pH, which both indirectly inhibits acidic cathepsin B/L's function in the endosome as well as blocking GP directed membrane fusion (Takada *et al.* 1997). Toremifene is a typical cationic amphiphilic drug. Its mechanism of inhibition will be discussed further in the later chapters (Chapter 4, 5, 7). In short, toremifene has two suggested mechanisms of inhibition, one is by directly binding to EBOV-GP to destabilise it at low pH environment (Zhao *et al.* 2016), the second is through a poorly understood effect on the NPC1 protein in the lysosome (Johansen *et al.* 2013; Fan *et al.* 2017). By comparing the inhibition profile of these drugs against E-S-FLU and H7CFv3/E-S-FLU, we wanted to indirectly assess whether H7CFv3/E-S-FLU still follows the same entry pathway as E-S-FLU.

Indicator MDCK-SIAT1 cells were pre-treated with drugs at different concentrations for 3 hours prior to S-FLU virus infection. Cells were fixed and analysed after 24 hours infection. All four drugs inhibited the entry of both E-S-FLU and H7CFv3/E-S-FLU at similar IC_{50} values (Figure 3.20). This suggests that the EBOV-GP was functioning as expected, and showed the usual susceptibilities to small molecule inhibitors. We have not yet tested these four molecules to inhibit H7-S-FLU infection. However, in Chapter 4, we show that for H5-S-FLU virus (coated with H5 haemagglutinin), infection was not affected by EIPA, E64d and toremifene. Niclosamide, the proton ionophore inhibited both H5-S-FLU virus (3.3 μM) and E-S-FLU virus (1.7 μM) with similar IC_{50} values.

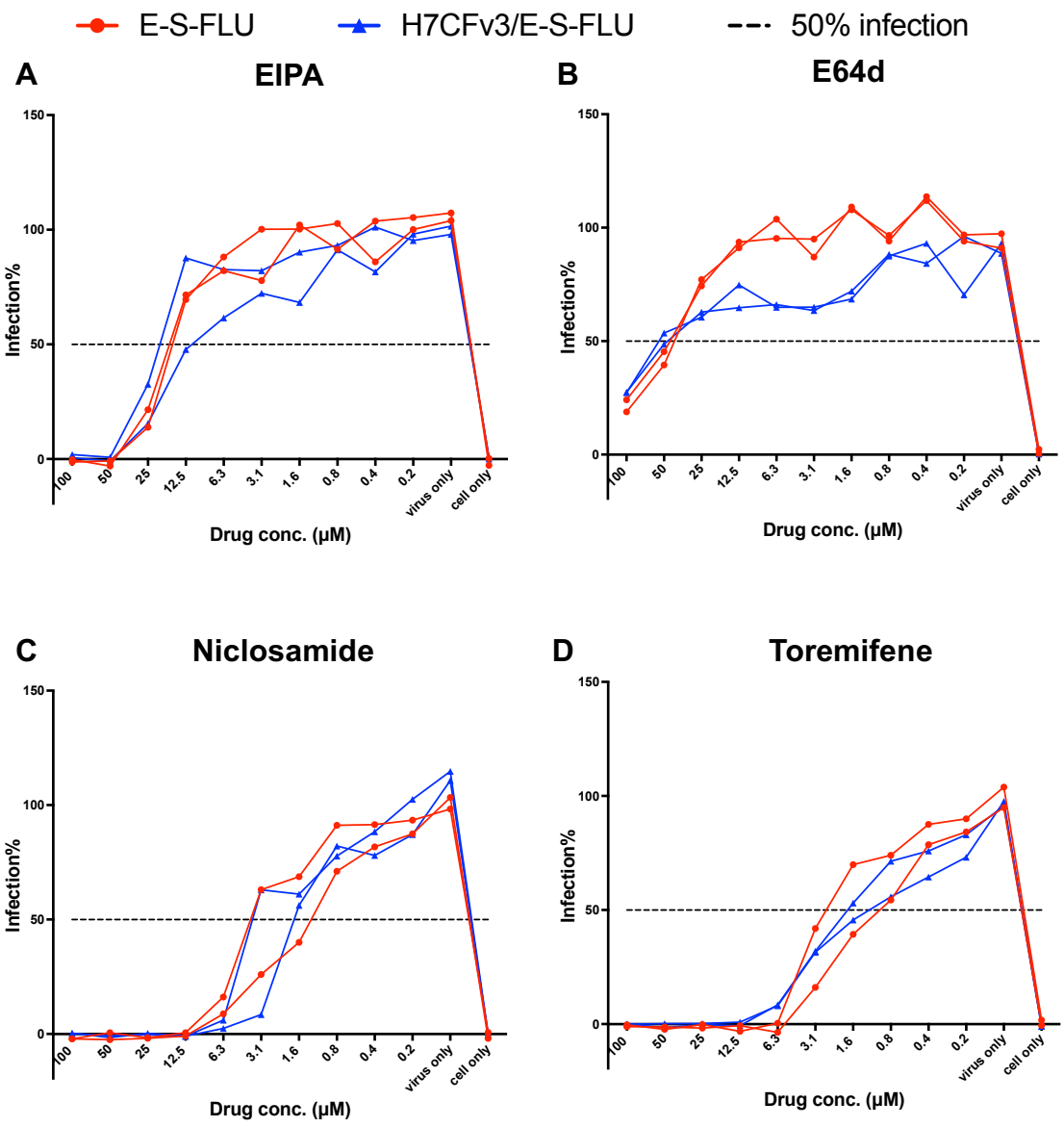


Figure 3. 20 Drug inhibition assay with the E-S-FLU and H7CFv3/E-S-FLU pseudotyped viruses

We selected four drugs that were known to inhibit EBOV entry *in vitro* to test in our drug inhibition assays. These are **A**: macropinocytosis inhibitor 5-(N-Ethyl-N-isopropyl) amiloride (EIPA); **B**: cathepsin inhibitor E64d; **C**: proton ionophore niclosamide; and **D**: cationic amphiphilic drug toremifene, which is also known to bind directly to EBOV-GP. Drugs were titrated from 100 to 0.2 μM in the drug inhibition assay against the E-S-FLU and H7CFv3/E-S-FLU viruses. Cells were pre-incubated with drugs for 3 hours and infected with virus for 24 hours. Virus infection was quantified by measuring eGFP expression with a fluorescence plate reader. Each antibody was titrated in technical duplicates, and the 50% of maximum fluorescence (50% infection) was marked out by a broken line.

3.5.6 H7CFv3/E-S-FLU infection of B lymphocytes

It was shown in the literature that EBOV does not infect B lymphocytes (Dube *et al.* 2010; Takada 2012). The suggested reason was that B lymphocytes do not have the receptors for the initial binding of EBOV to the plasma membrane. B lymphocytes should possess the lysosomal receptor NPC1, which is ubiquitously expressed. Influenza virus infects B lymphocytes very well. To test whether introducing the additional H7CFv3 molecule can facilitate E-S-FLU infection of B lymphocytes, we did a preliminary virus titration experiment comparing E-S-FLU, H7CFv3/E-S-FLU and H7-S-FLU infection on an Epstein-Barr virus (EBV) transformed B cell-line (Figure 3.21). Percentage infection was quantified by FACS analysis. In this experiment, E-S-FLU did not infect B lymphocytes (<1% eGFP positive population) whereas both H7CFv3/E-S-FLU and H7-S-FLU successfully infected B lymphocytes.

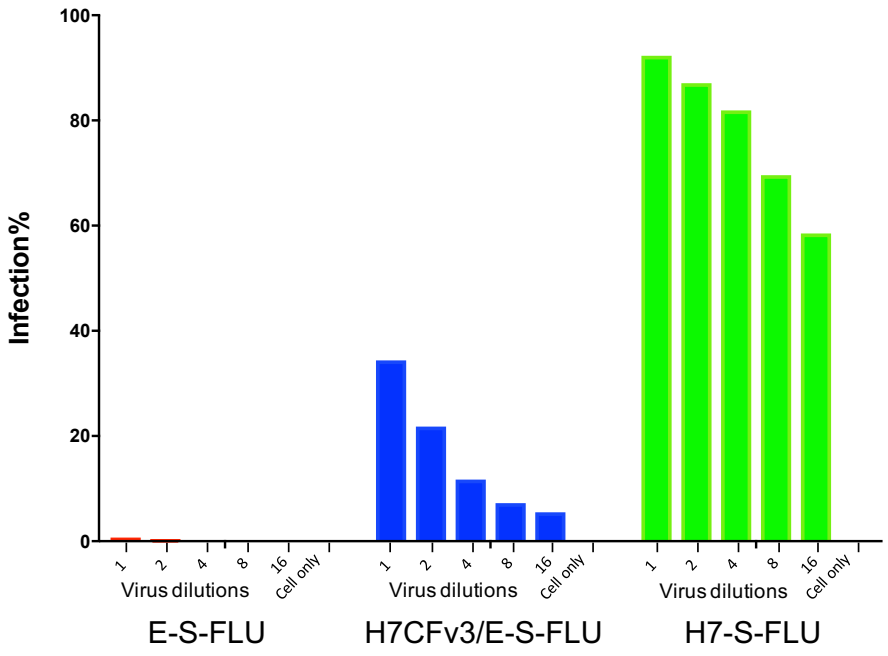


Figure 3. 21 H7CFv3/E-S-FLU infection in B lymphocytes
We titrated E-S-FLU (**red**), H7CFv3/E-S-FLU (**blue**) and H7-S-FLU (**green**) to infect an Epstein-Barr virus (EBV) transformed B cell-line. Infected cells were analysed by FACS, and the percentage of infected cells was the percentage of cells with an eGFP readout of $>10^2$ fold of uninfected "Cell only" control.

3.6 Discussion and future work

This chapter describes the design, production, characterisation and modification of a new Ebola virus glycoprotein (EBOV-GP) pseudotyped Influenza virus E-S-FLU. E-S-FLU contains no genetic material from EBOV. It is based on an Influenza A/PR/8/1934 core, in which the haemagglutinin coding sequence was replaced by an enhanced green fluorescence protein (eGFP) reporter (Powell *et al.* 2012). It is a safe surrogate for EBOV that can be used at containment level BSL-1/2. Currently there is no approved vaccines or therapeutics for EBOV, and infection leads to 50-90% fatality rate. Research with wild-type EBOV is both high in risk and cost, and it is only possible when a BSL-4 facility is available. EBOV-GP pseudotyped viruses can be very useful tools for studying EBOV biology, high-throughput screening for inhibitory small molecules and antibodies, and for diagnostic serology (Bentley *et al.* 2015).

We were able to produce E-S-FLU, that gives single-cycle infection in indicator MDCK-SIAT1 and HeLa cells. We have shown that E-S-FLU can be pseudotyped with EBOV-GP from *Zaire*, *Sudan*, *Bundibugyo* and *Taï Forest ebolavirus* species. To pseudotype S-FLU with EBOV-GP, we permanently transduced MDCK-SIAT1 cells to express full-length EBOV-GP with a lentiviral vector. We were able to express EBOV-GP at high level and the expression was stable up to at least the ninth passage.

Several papers have reported that high level expression of EBOV-GP was toxic to Vero and 293T cells (Takada *et al.* 2000; Yang *et al.* 2000; Volchkov 2001; Simmons *et al.* 2002; Alazard-Dany *et al.* 2006; Francica, Matukonis and Bates

2009; Mohan *et al.* 2015). MDCK-SIAT1 cells however, seemed to tolerate a high-level EBOV-GP expression, and cell growth and morphology were not affected. This provides a very useful tool for pseudotyping lipid-membrane viruses, including producing E-S-FLU and EBOV-GP pseudotyped VSV without the need for repeated transfection. Instead, a dose of seed H5-S-FLU virus was added to infect and replicate in the E-SIAT cells, without the need for the addition of trypsin, because EBOV-GP is cleaved into GP1 and GP2 subunits by furin protease, an endogenous proprotein convertase (Volchkov *et al.* 1998; Jeffers, Sanders and Sanchez 2002). Culture supernatant harvested after 48 hours can be directly used in assays without further concentration steps. This simple production protocol allowed us to produce a single batch of pseudotyped virus that was enough to screen a drug library from Sigma containing 1280 small molecules (Chapter 4).

E-S-FLU uses eGFP as the reporter system. Most EBOV pseudotyped viruses and virus-like particles (VLPs) use enzyme based reporter systems, such as firefly luciferase and beta-lactamase. These reporters amplify the signal from what is often a very low level infection by EBOV-GP pseudotyped lentiviruses, which may also require concentration (Takada *et al.* 1997; Wool-Lewis and Bates 1998; Johansen *et al.* 2013; Kouznetsova *et al.* 2014). Although enzymatic assays are much more sensitive than fluorescent protein reporters, they require expensive reagents for development, and cannot be easily visualised. By contrast, E-S-FLU provided saturating infection of indicator cells without concentration. In addition, eGFP allowed direct visualisation of formalin fixed infected cells under the fluorescent microscope without further manipulation, and can be measured directly in a fluorescence plate reader without additional reagents. This turned out to

provide some useful insights into the mechanism of action of some drugs (Chapter 4). Finally, if kept in the dark, the fixed indicator cells in plates retain the fluorescence signal for at least six months.

To verify and characterise E-S-FLU, we have tested it in antibody neutralisation assays using anti-EBOV-GP monoclonal antibody KZ52 (Maruyama *et al.* 1999; Lee *et al.* 2008). E-S-FLU was neutralised by KZ52, and the IC_{50} value was comparable with a control EBOV-GP lentivirus pseudotype we have tested in parallel, as well as the IC_{50} value with wild-type EBOV reported in the literature.

In parallel with my work on small molecules that inhibit EBOV infection, E-S-FLU has been used by my colleague Dr Pramila Rijal to screen human monoclonal antibodies isolated from vaccinated volunteers for neutralisation (Stanley *et al.* 2014; Ewer *et al.* 2016; Rijal *et al.* 2019). Eighty-two antibodies were isolated, and divided into cross-inhibiting groups specific for the glycan cap, receptor binding region, base and mucin-like domain. The E-S-FLU neutralisation assay successfully identified antibodies that were protective *in vivo* in the Viral Haemorrhagic Fever Immunotherapeutic Consortium (VIC) (Saphire *et al.* 2018; Rijal *et al.* 2019). Finally, E-S-FLU provided the means to collate a cocktail of four antibodies against independent epitopes that was curative for guinea pigs given treatment at day three of established EBOV infection in the BSL-4 facility at Porton Down (Rijal *et al.* 2019).

As the E-S-FLU neutralisation assay was very useful for identifying neutralising monoclonal antibodies, we have started to assess its value in measuring

neutralising antibodies in serum or plasma. We acquired 7 out of 9 plasma antibody samples tested in a study from the National Institute for Biological Standards (NIBSC) (Wilkinson *et al.* 2017). Overall, our micro-neutralisation assay with E-S-FLU showed moderate correlation with the published data on neutralisation of wild-type EBOV. This suggested that E-S-FLU may be suitable for diagnostic purposes but more validation with a bigger sample size is needed. One significant discrepancy compared to wild-type EBOV neutralisation was with sample 36, a negative plasma sample that partially neutralised E-S-FLU in our assay. Previously, we observed that E-S-FLU is highly sensitive to plasma samples prepared in heparin coated plasma tubes (personal communication with Dr Rijal). Plasma antibodies can be purified using IgG columns and eluted antibody no longer shows this inhibition effect. This however may be less practical in serology screening settings.

The comparison of neutralisation of E-S-FLU with wild-type EBOV may not offer the best correlate of immunity. Saphire *et al.* (2018), in a large collaborative study, have shown that neutralisation of EBOV-GP pseudotyped VSV actually predicted protection against EBOV disease in a murine model better than neutralisation of wild-type EBOV.

We have shown that E-S-FLU infection requires the NPC1 protein to be expressed in the target cell, which has been shown to be the key receptor for EBOV at the lysosomal membrane (Carette *et al.* 2011; Côté *et al.* 2011; Miller *et al.* 2012). In addition, we have selected 13 drugs that inhibited EBOV described in the literature and tested them in our pseudotyped system. All the drugs inhibited E-S-FLU with

similar IC_{50}s to wild-type EBOV or other EBOV-GP pseudotypes. Some of the drugs are known as EBOV entry inhibitors with defined host targets. For example, EIPA is known as a macropinocytosis inhibitor (Sandgren *et al.* 2010), E64 and MDL28170 are cathepsin B/L inhibitors (Chandran *et al.* 2005; Schornberg *et al.* 2006; Gnirß *et al.* 2012); U18666A inhibits EBOV by interacting with NPC1 (Cenedella 2009; Lu *et al.* 2015). By showing E-S-FLU was inhibited by these defined small molecules, we demonstrated that E-S-FLU behaves similarly to wild-type EBOV *in vitro*. In Chapter 4, we have shown that E-S-FLU can be a very useful tool for screening drug libraries and identifying potential therapeutics.

We have shown the production of E-S-FLU is simple with a useful yield, and can be used directly in infection and micro-neutralisation assays without further concentration steps. However, the virus titre of E-S-FLU was still about 100-fold lower than S-FLU coated in Influenza haemagglutinin, such as H5-S-FLU. This was expected as we were introducing a non-endogenous envelope protein from EBOV to Influenza. A reduced virus titre was also seen in the retrovirus and VSV pseudotypes coated with EBOV-GP (Takada *et al.* 1997; Wool-Lewis and Bates 1998).

To improve the virus titre of E-S-FLU, we first designed a hybrid protein GP-HA that combines the extracellular domain of EBOV-GP with the transmembrane domain and cytoplasmic domain of Influenza HA. GP-HA can be expressed and folded correctly as EBOV-GP on the transduced MDCK-SIAT1 cell surface, and different antigenic sites were preserved, as defined with panels of human monoclonal antibodies. However, we could not produce infective S-FLU virus

coated with the GP-HA protein. Using virus ELISA, we detected assembled particles containing GP-HA in the culture supernatant but these failed to infect MDCK-SIAT1 cells. A similar observation was made by Bukreyev *et al.* when they tried to pseudotype human parainfluenza type 3 virus (HPIV3) with EBOV-GP and they were not able to pseudotype with a hybrid protein containing the cytoplasmic domain from HPIV3 F protein (Bukreyev *et al.* 2009).

One possible explanation is that the transmembrane domain and the cytoplasmic domains of EBOV-GP are required for the fusion step. Both EBOV-GP and Influenza HA proteins belong to class I viral membrane fusion proteins. They undergo a major conformational transition during fusion and bridge the host cell membrane and virus membrane, which then leads to pore formation (White and Whittaker 2016). How the transmembrane domain and the cytoplasmic domains of EBOV-GP are involved in fusion is less studied. The transmembrane domain of HA plays a role in the later stage of fusion, i.e. from hemifusion to pore-formation (Melikyan *et al.* 1999, 2000; Webb *et al.* 2018). For EBOV, studies showed that the membrane-proximal external region (MPER), that is juxtaposed to the transmembrane domain interacts with the fusion loop to bring together lysosomal membrane and the EBOV virus membrane (Weissenhorn *et al.* 1998, 1999; Regula *et al.* 2013; Gregory *et al.* 2014; Lee *et al.* 2017).

Our GP-HA hybrid protein has kept the MPER section from EBOV-GP (up to amino acid 648). However, the transmembrane domain may play an important role in positioning the MPER section correctly, as there is a kink just between the MPER and the TM alpha helices, mediated by a short sequence containing a proline at

position 653. In our construct this short region was removed. Further work on restoring the short segment containing this proline is planned to see if this will restore infectivity to the budding pseudotyped viruses coated in the hybrid GP-HA protein.

The second approach with which we attempted to improve E-S-FLU viral titre was by introducing a fusion-defective Influenza HA protein, H7CFv3, to act as a lectin to enhance the efficiency with which E-S-FLU attaches to the target cell surface. In Figure 3.4, we visualised the S-FLU viral replication and spreading in both EBOV-GP and H5 coated MDCK-SIAT1 cells. We observed a more dispersed plaque in EBOV-GP coated cells after the initial infection, whereas a more efficient and dense spread was observed in the H5 expressing MDCK-SIAT1 cells. We proposed that this was due to the difference in efficiency at the initial attachment step. Influenza HA recognises and binds sialic acid at the cell surface. This triggers endocytosis of the virus and later fusion occurs in the early endosome.

EBOV has a wide host range and tropism, and the ubiquitous receptor for viral entry is NPC1 at the lysosomal membrane. The initial attachment step remains more controversial. Several models were proposed for the EBOV attachment step. There may not be a ubiquitous receptor that EBOV-GP uses to enter all cell types (Zapatero-Belinchón *et al.* 2019). DC-SIGN and other C-type lectins aid the attachment by interacting with N-glycans on EBOV-GP, whereas TIM-1 may bind phosphatidylserine presented at the viral lipid envelope (Alvarez *et al.* 2002; Marzi *et al.* 2004; Kondratowicz *et al.* 2011). We do not know what factors are involved in E-S-FLU attachment to our indicator cell-line MDCK-SIAT1 cell and HeLa cells.

To improve the infectivity, we introduced H7CFv3 to aid attachment. H7CFv3 protein binds sialic acid at the MDCK-SIAT1 cell surface, however mutations were introduced so it can no longer fuse like the wild-type H7. H7CFv3 acted as an additional “lectin” on the virus surface interacting with sialic acid on the target cell surface, to assist EBOV-GP in attachment.

We successfully pseudotyped S-FLU with both EBOV-GP and H7CFv3 at the same time. We called it H7CFv3/E-S-FLU. We have shown that viral titre was improved by 32 to 64-fold compared to E-S-FLU. H7CFv3/E-S-FLU infection was still NPC1 dependent and was neutralised by both anti-EBOV-GP antibody and anti-H7 antibody. We also tested it with 4 drugs that interrupt EBOV entry steps: EIPA the macropinocytosis inhibitor (Nanbo *et al.* 2010; Mulherkar *et al.* 2011); E64d the cathepsin inhibitor (Chandran *et al.* 2005; Schornberg *et al.* 2006); niclosamide the proton ionophore that affects endosomal/lysosomal pH and acid-dependent cathepsin function (Jurgeit *et al.* 2012; Kouznetsova *et al.* 2014); and toremifene the EBOV-GP binder (Zhao *et al.* 2016). All 4 drugs inhibited H7CFv3/E-S-FLU entry with a similar IC_{50} to E-S-FLU, suggesting that H7CFv3/E-S-FLU enters the cell in an EBOV-like manner. We will further characterise H7CFv3/E-S-FLU with anti-EBOV-GP antibodies recognising different epitopes. This dual-pseudotyping system can be a very useful tool for drug and antibody screening assays *in vitro*. In particular this approach may improve the titre of the *Sudan ebolavirus* GP pseudotyped E-S-FLU, which had a relatively low viral titre.

In summary, this chapter has described the new EBOV-GP pseudotyped virus, E-S-FLU and a modified version H7CFv3/E-S-FLU. Part of this chapter has been

published in Xiao *et al.* 2018. This chapter also provides the foundation for the later chapters of this thesis, as it provides us with a new safe surrogate for laboratory analysis the Ebola virus species.

(BIANK PAGE)

Chapter 4 Drug screening and mechanisms of inhibition of EBOV infection

4.1 Introduction

Since the first description in 1976, Ebola Virus Disease (EVD) has caused multiple outbreaks in the human population, mostly in West Africa (Centers for Disease Control and Prevention 2018). Ebola virus (EBOV) infection typically has a mortality rate of 50-90%. The most recent epidemic, declared by the World Health Organisation (WHO) on the 1st August 2018, is still progressing, with 1301 confirmed EVD cases and 819 deaths (WHO situation reports: 23 April 2019).

Currently there are no FDA (US Food and Drug Administration) approved therapeutics to treat EBOV infection. Patients mostly receive supportive care, such as rehydration and balancing electrolytes, maintaining oxygen supply, and blood pressure (WHO 2018a; Fowler *et al.* 2014). By itself this type of careful intensive supportive clinical care can reduce mortality considerably (Langer *et al.* 2018). During the West African outbreak in 2014-2015, the rapid spread of the disease triggered global concerns and stimulated international collaborations to find a solution. In August 2014, after a series of ethical and scientific assessments, the WHO launched a fast-track regulation for testing experimental vaccines and therapeutics for EBOV (WHO 2014a). This opened the way for testing the vaccine and drug candidates that have shown efficacy towards EBOV *in vitro,* in animal models, and in clinical trials in humans. At the same time, the FDA and the European Medicines Agency (EMA) also promoted companies who had possible

EBOV therapeutic candidates to apply for orphan designation to receive extra support to speed up the development of their candidate medicines (European Medicines Agency 2014; Harkin 2014). As a result, the safety studies of two EBOV vaccines began in December 2014, 9 months after the EBOV outbreak was first reported in Guinea. The recombinant vesicular stomatitis virus vector-based vaccine (rVSV-EBOV) (Geisbert *et al.* 2008; Agnandji *et al.* 2015; Regules *et al.* 2017) showed 100% protection in a pilot ring vaccination trial in Guinea (Henao-Restrepo *et al.* 2017). The other vaccine candidate consisted of a viral-vectored prime-boost vaccination regime with recombinant chimpanzee adenovirus type 3 vector expressing EBOV glycoprotein (GP) (ChAd3-EBOV), followed by Modified Vaccinia Ankara (MVA) also expressing EBOV-GP (Stanley *et al.* 2014; Ewer *et al.* 2016). Having passed a phase 1 safety trial, phase 2 efficacy trials are now in progress (Ledgerwood *et al.* 2017).

On the therapeutics side, the use of convalescent whole blood or convalescent plasma were prioritised for testing as an experimental treatment for EBOV (WHO 2014b). This followed the positive effect detected in the 1995 Kikwit outbreak (Mupapa *et al.* 1999), where eight EBOV infected patients received convalescent blood transfusion. Seven out of eight patients survived, and this mortality was much lower than the overall mortality rate during this epidemic (12.5% vs. 80%; Mupapa *et al.* 1999). However, some controversy arose in the larger trials conducted during the 2014-2015 EBOV outbreak. Griensven *et al.* found that patients receiving convalescent plasma transfusion treatment did not show significant improvement in survival, whereas Sahr *et al.* showed that convalescent

whole blood did reduce the viral load significantly (van Griensven *et al.* 2016; Sahr *et al.* 2017).

Several other drugs that showed good protection in mice or non-human primates were also tested in the fast-track clinical trials, or were used as experimental treatment for individual cases under compassionate usage protocols. This included ZMapp, a cocktail of three monoclonal antibodies (Qiu *et al.* 2014; Davey *et al.* 2016); a viral RNA polymerase inhibitor Favipiravir (Oestereich *et al.* 2014; Sissoko *et al.* 2016) and a small interfering RNA TKM-130803 that targets the messenger RNAs of EBOV viral protein 35 (VP35) (Dunning *et al.* 2016). The details of the clinical data are summarised in several reviews (Duraffour, Malvy and Sissoko 2017; Sweiti *et al.* 2017; Dhama *et al.* 2018). While these unregistered therapeutics have not caused severe adverse effects, none of the therapeutics tested reached statistically significant efficacy due to the small sample size. The result from use of ZMapp antibodies showed encouraging trend of therapeutic benefit, but will require further investigation to confirm its efficacy for the treatment of EBOV infection in larger sized trials (Davey *et al.* 2016).

Now four years have passed since the 2014 EBOV outbreak, and still there are no therapeutics approved for the disease. However, the huge effort and global support that were invested have greatly contributed to our knowledge of EVD, and helped in understanding how to prepare for future EBOV outbreaks. During the current 2018-2019 EBOV epidemic in the Domestic Republic of Congo (DRC), WHO updated the Monitored Emergency Use of Unregistered and Investigational Interventions (MEURI) statement for EVD (WHO 2018b). New treatment trials

began in DRC from Nov 2018 focusing on four EBOV therapeutic candidates: monoclonal antibody 114 (Corti *et al.* 2016; Misasi *et al.* 2016); antibody cocktails Remdesivir (Pascal *et al.* 2018) and ZMapp (Qiu *et al.* 2014; Davey *et al.* 2016); and an adenosine analogue GS-5734 (Warren *et al.* 2014, 2016).

In addition to developing novel drugs that specifically target EBOV infection, drug repurposing was another potential way to generate therapeutics for EVD. Drug repurposing, or drug repositioning, refers to developing old drugs for new uses (Oprea and Mestres 2012; Deotarse *et al.* 2015; Xue *et al.* 2018). It has become a common strategy used by pharmaceutical companies to find therapeutics for diseases such as Alzheimer's disease, various cancers, and sleeping sickness (Andrews, Fisher and Skinner-Adams 2014; Kim 2015; Chen *et al.* 2016; Klug, Gelb and Pollastri 2016; Hernandez *et al.* 2017; Govindaraj *et al.* 2018; Xue *et al.* 2018). There are many advantages to repurposing approved drugs as potential EVD treatments. Firstly, existing drugs have well-established clinical safety records and pharmacokinetic profiles. Their dosage range in patients and possible off-target effects are better understood. Moreover, these drugs have well-developed manufacturing and distributing lines, so they can be made available to a large number of people in a short time span. Consequently, multiple research groups have screened approved drug libraries for inhibition of EBOV infection *in vitro* (Johansen *et al.* 2013, 2015; Madrid *et al.* 2013; Gehring *et al.* 2014; Kouznetsova *et al.* 2014; Cheng *et al.* 2015; Long *et al.* 2015; Xiao *et al.* 2018).

Surprisingly, many drugs with various known pharmacological activities were found to inhibit EBOV infection *in vitro*, which we have reviewed in Chapter 3 of

this thesis (Table 3.3). Typical examples are: calcium channel inhibitors amiodarone and verapamil (Gehring *et al.* 2014; Sakurai *et al.* 2015; Salata *et al.* 2015); estrogen receptor antagonists clomiphene and toremifene (Johansen *et al.* 2013; Fan *et al.* 2017); anti-depressant imipramine (Kouznetsova *et al.* 2014; Herbert *et al.* 2015); anti-malarial drug chloroquine (Kouznetsova *et al.* 2014; Dowall *et al.* 2015; Falzarano *et al.* 2015; Madrid *et al.* 2015). Some also showed protection against EBOV infection in animal models, however, the results are preliminary (Johansen *et al.* 2013; Dowall *et al.* 2015; Falzarano *et al.* 2015; Herbert *et al.* 2015; Sakurai *et al.* 2015).

Despite the potential benefits, there are many challenges to repurposing drugs for the treatment of EBOV infection. Firstly, the mechanism of inhibition against EBOV is unknown, and it is likely that any given drug may have acted through a non-canonical target (Johansen *et al.* 2013; Fan *et al.* 2017; Penny *et al.* 2018), and therefore a much higher dose may be required to achieve this “off-target” effect. Secondly, although the safety profiles for approved drugs are better known, it may still put EVD patients at risk who are infected with EBOV and are suffering haemorrhagic fever, fluid loss and multi-organ failure. During the 2014-2015 EBOV outbreak, amiodarone was given to 65 patients in Sierra Leone on a compassionate basis, and this caused great controversy in view of the minimal pre-clinical evidence, and the potential risk of causing dangerous arrhythmias in patients with deeply disturbed electrolytes. (Turone 2014; Gupta-Wright, Lavers and Irvine 2015; Boseley 2014; Emergency International 2015).

In this chapter, we have attempted to further our understanding of drugs that inhibit EBOV infection by using our surrogate – the pseudotyped Influenza virus E-S-FLU. Previously, we demonstrated that E-S-FLU enters the cell in a similar manner to wild-type (WT) EBOV (Chapter 3). We also showed that different classes of drugs that inhibited WT EBOV also inhibited E-S-FLU with similar IC_{50} doses *in vitro* (section 3.3.4). Hence, E-S-FLU can be a useful model system for screening EBOV entry inhibitors in laboratory conditions requiring minimal biological containment.

In the first part of this chapter (section 4.2), we describe the use of E-S-FLU to screen a small drug library LOPAC®1280 (containing 1280 compounds), and compare our results with the current literature. Based on the screening result, we explored the possible mechanisms of action of the inhibitors by different biochemical analyses (section 4.3). The rationale for the techniques used in this chapter will be further introduced in each results section. In the last section (section 4.4), we began to test drug combinations for additive or synergistic effects on inhibition of EBOV infection *in vitro*. As mentioned earlier, one of the challenges of repurposing approved drugs in treating EBOV is the high dosage requirement. Finding drug combinations that can be effective with lower individual doses through additive or synergistic effects may be a solution. Additionally, drug combinations at lower dose may have fewer side effects, and if acting by different mechanisms may minimise the chance of selecting resistant virus variants.

4.2 LOPAC®1280 library screen

LOPAC®1280 (Sigma-Aldrich) is a library of 1,280 pharmacologically active molecules, which covers all major drug target classes (Figure 4.1). Using the inhibition assay described in section 3.3.4, we have screened the effect of these 1,280 molecules on E-S-FLU infection. E-S-FLU is a non-replicating Influenza virus coated with EBOV glycoprotein (EBOV-GP) and its haemagglutinin gene replaced by a reporter eGFP gene (Powell *et al.* 2012). H5-S-FLU contains the same pseudotyped S-FLU virus core, but was coated with Influenza haemagglutinin from H5N1 (Baz *et al.* 2015). H5-S-FLU was used as a control pseudotyped virus to identify any drugs that inhibited S-FLU through an effect on the Influenza core rather than the EBOV-GP coat.

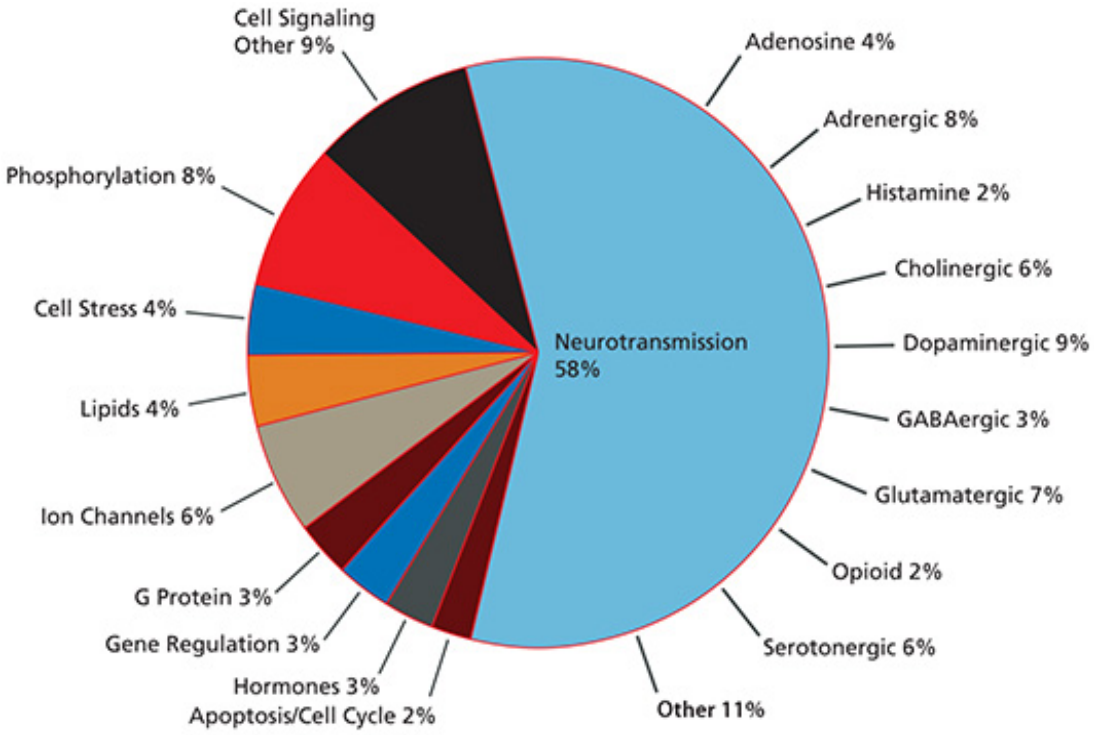


Figure 4. 1 LOPAC®1280 library drug composition
A library of 1,280 pharmacologically active compounds from Sigma-Aldrich, grouped and displayed according to their target and pharmacological classes.

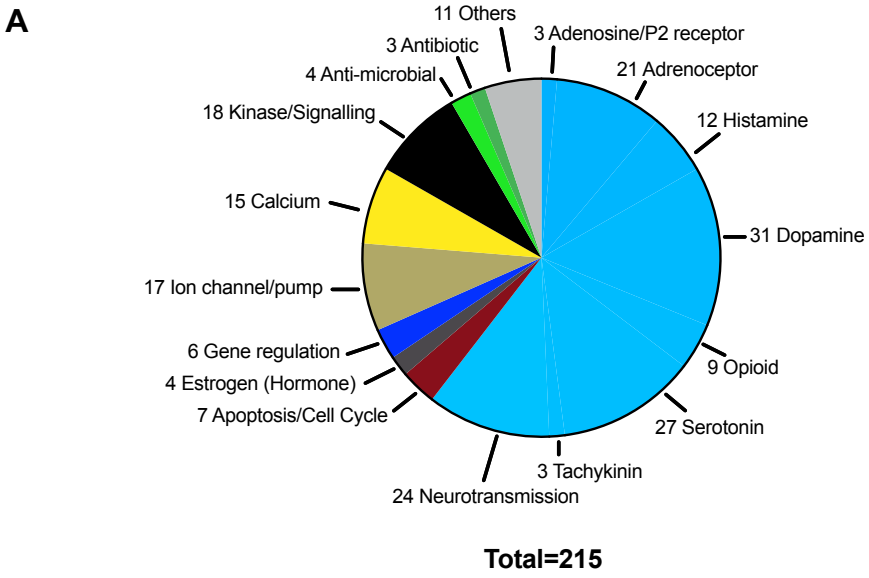
Initially, all molecules were screened at 5 μM and 100 μM in the viral inhibition assay. Indicator MDCK-SIAT1 cells were pre-treated with the drugs for 3 hours, then infected with E-S-FLU or H5-S-FLU. Selected drug candidates that inhibited E-S-FLU or H5-S-FLU infection were further titrated individually to calculate their IC_{50} values and their toxicity concentration range. IC_{50} value was defined as the concentration of drug that reduced infection of E-S-FLU or H5-S-FLU by 50%, quantified by measuring the eGFP fluorescence in infected cells encoded in the virus. Toxicity of drugs was estimated with Alexa Fluor® 647 conjugated wheat-germ agglutinin (WGA-647) staining as previously described in section 3.3.4. WGA-647 is a lectin that stains the N-acetyl-D-glucosamine and sialic acid at the cell surface (Wright 1984). Healthy MDCK-SIAT1 cells were adherent to the screening plate even after 24-hour infection by E-S-FLU or H5-S-FLU, whereas dead cells caused by toxic drug treatment detached from the plates and were washed away before we measured the fluorescence. A sharp decrease in fluorescence readout at 647 nm indicated the toxicity level of drug treatment (Chapter 3, Figure. 3.10). Drugs were counted as inhibitors if they reduced E-S-FLU or H5-S-FLU infection by at least 50% without causing toxicity. All drug inhibition assays were quantified by a fluorescence plate reader CLARIOstar®, and were verified by visual observation with the fluorescence microscope.

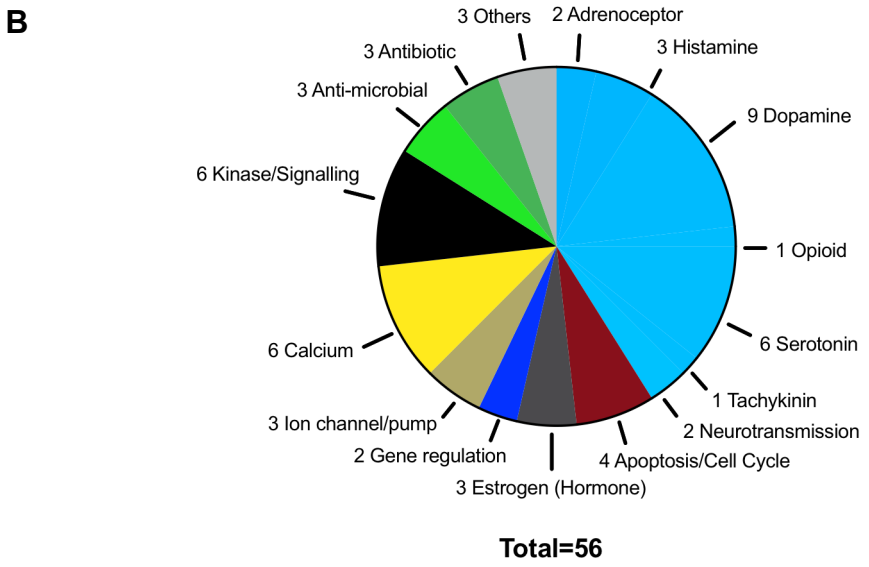
4.2.1 E-S-FLU vs. H5-S-FLU drug screening results

In total, 215 out of 1,280 molecules from the LOPAC®1280 library inhibited E-S-FLU infection to some level before reaching toxicity *in vitro* (listed in Appendix Table 4. X1). 56 of these had an IC_{50} value less than 10 μM. In contrast, only 22 molecules inhibited H5-S-FLU, 8 of which had an IC_{50} value less than 10 μM. All

of the 22 molecules that inhibited H5-S-FLU also inhibited E-S-FLU, and therefore may have acted on the core common to both.

We divided the 215 E-S-FLU inhibitors and the 56 inhibitors that had IC_{50} values less than 10 μM into pharmacological groups based on the description given by Sigma-Aldrich (Figure 4.2 A and B). Noticeably, the inhibitors came from a wide range of pharmacological groups. The detailed information on all 215 inhibitors and 13 additional drugs screened in this study are listed in the Appendix Table 4. X1 at the end of Chapter 4, with drugs ranked on E-S-FLU infection inhibition IC_{50} values. A summary of IC_{50} values for all 228 inhibitors tested in this chapter is shown in Figure 4.2 C.


A
11 Others
3 Adenosine/P2 receptor
3 Antibiotic
21 Adrenoceptor
4 Anti-microbial
12 Histamine
18 Kinase/Signalling
15 Calcium
31 Dopamine
17 Ion channel/pump
6 Gene regulation
9 Opioid
4 Estrogen (Hormone)
7 Apoptosis/Cell Cycle
27 Serotonin
3 Tachykinin
24 Neurotransmission
Total=215


B
3 Others
2 Adrenoceptor
3 Antibiotic
3 Histamine
3 Anti-microbial
9 Dopamine
6 Kinase/Signalling
1 Opioid
6 Calcium
6 Serotonin
1 Tachykinin
3 Ion channel/pump
2 Neurotransmission
2 Gene regulation
4 Apoptosis/Cell Cycle
3 Estrogen (Hormone)
Total=56

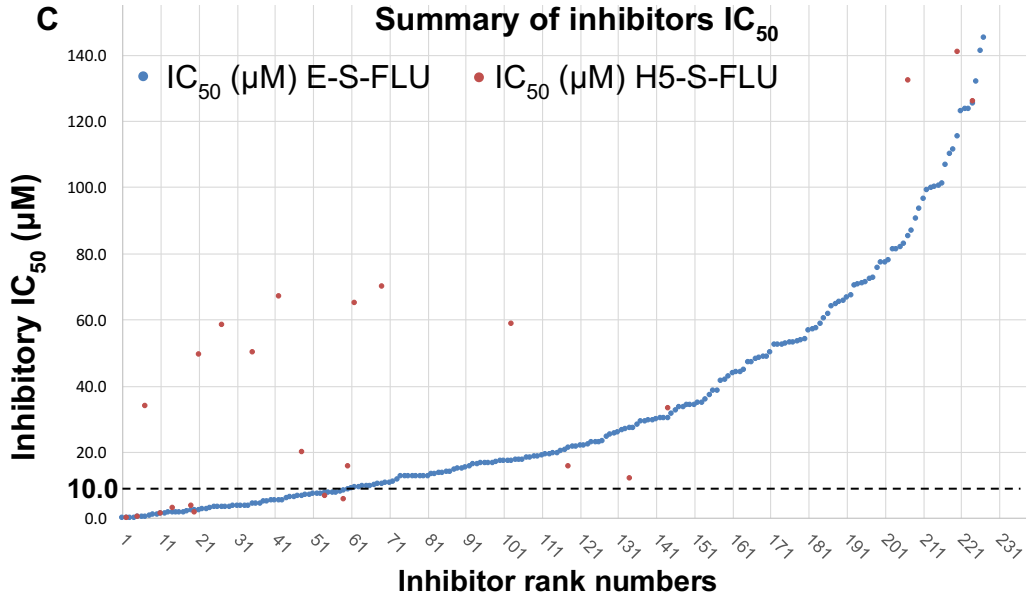

C
Summary of inhibitors IC50
IC50 (μM) E-S-FLU
IC50 (μM) H5-S-FLU
Inhibitory IC50 (μM)
140.0
120.0
100.0
80.0
60.0
40.0
20.0
10.0
0.0
1
11
21
31
41
51
61
71
81
91
101
111
121
131
141
151
161
171
181
191
201
211
221
231
Inhibitor rank numbers

Figure 4. 2 Drugs from the LOPAC®1280 library that inhibited the E-S-FLU virus

The 1,280 drugs screened, grouped according to their pharmacological activities as described in the LOPAC®1280 library (Sigma-Aldrich). 215 inhibited E-S-FLU infection (**A**), and 56 had an IC_{50} value less than 10 μM (**B**). **C**: Summary of all drugs (228 molecules) that inhibited the E-S-FLU virus in this chapter (blue dots). This includes 215 inhibitors from the LOPAC®1280 drug screen and 13 additional inhibitors tested. 24 molecules inhibited the H5-S-FLU virus (red dots), all of which also inhibited the E-S-FLU virus. The inhibitors are ranked and plotted according to their IC_{50} values in the E-S-FLU viral inhibition assay. For detailed information on the inhibitors, see Appendix Table 4. X1.

4.2.2 Comparison with the screen by Johansen *et al.*

We compared the results of our screen with those published by Johansen *et al.* (2015). We selected this study for detailed comparison because Johansen *et al.* tested a related library of 2,600 approved drugs on a category 3 containment recombinant EBOV engineered to express eGFP in infected cells. There was an overlap of 538 molecules shared between the LOPAC®1280 library and that screened by Johansen *et al.* (Table 4.1), which provided us with a gold standard for comparing E-S-FLU with EBOV. Of the 538 molecules in common, 442 gave concordant results in both screens; 23 of which inhibited both E-S-FLU and EBOV, and 419 were non-inhibitors in both studies. Of the remaining drugs, 70 inhibited E-S-FLU in our screen, but did not inhibit in Johansen's screen; 26 were inhibitors in Johansen's screen, but non-inhibitors in our hands. We performed a two-tailed Fisher's exact test for statistical analysis of the comparison, and showed the correlation between the two screens was significant ($P < 0.0001$). The 23 drugs that inhibited both E-S-FLU and eGFP-EBOV are highlighted in green in Appendix Table 4. X1.

Table 4. 1 Comparison of drugs common to both the LOPAC®1280 library and the collection of Johansen et al.

Number of drugs in the LOPAC®1280 library	Number of drugs in collection of Johansen *et al.*		
	Inhibitors	Non-inhibitors	Total
Inhibitors	23	70	93
Non-inhibitors	26	419	445
Both	49	489	538

A total of 538 drugs appeared in both our LOPAC®1280 library screening and that of Johansen et al. 2015. Associations between the two screenings were calculated by two-tailed Fisher's exact test ($P < 0.0001$).

A major difference between Johansen's screen and our screen against E-S-FLU is the range of drug concentrations tested. The highest concentration tested by Johansen *et al.* was 13 μM, whereas most of the drugs tested in our study were titrated from 100 μM, if toxicity was not reached. This may have increased the sensitivity of our screen in comparison to that of Johansen. Of the 70 drugs that selectively inhibited E-S-FLU in our screen, we have further tested ebastine (Sigma, catalogue number: E9531), imipramine (I7379), clemastine (SML0445) and verapamil (V4629) to confirm their inhibitory effects. We ordered these drugs individually from Sigma-Aldrich, and all four drugs had an inhibitory effect on the E-S-FLU virus with IC_{50} values comparable to those seen in the LOPAC®1280 screen. All four drugs were also reported as inhibitors of authentic EBOV, EBOV-GP pseudotyped lentivirus or EBOV-GP coated vesicular stomatitis virus (VSV-GP-EBOV) by other groups (Carette *et al.* 2011; Gehring *et al.* 2014; Kouznetsova *et al.* 2014; Johansen *et al.* 2015; Sakurai *et al.* 2015).

Of the 26 drugs that were positive in the screen conducted by Johansen *et al.*, but negative in our LOPAC®1280 screening, we ordered 14 individually from Sigma-

Aldrich and further tested them: auranofin (Sigma, catalogue number: A6733), bepridil (B5016), calcimycin (C7522), D609 (T8543), diphenyleneiodonium (D2926), doxylamine (D3775), linezolid (PZ0014), naproxen (M1275), nocodazole (M1404), perphenazine (P6402), rotenone (R8875), sanguinarine (S5890), serotonin (H9523), and thapsigargin (T9033).

Bepridil (a calcium channel inhibitor) and perphenazine (a cationic amphiphile) from the LOPAC®1280 library did not inhibit the E-S-FLU virus, but the individually ordered chemicals showed specific inhibition of the E-S-FLU virus (bepridil IC_{50}: 2.7 μM, perphenazine IC_{50}: 8.2 μM). This indicates that some differences in the results were due to false negatives arising from the library preparation from Sigma. D609, doxylamine, disopyramide, linezolid, naproxen, rotenone, and sanguinarine were confirmed as non-inhibitors of the E-S-FLU virus in our assay up to 100 μM. Auranofin, calcimycin, diphenyleneiodonium, nocodazole, and thapsigargin were toxic to MDCK-SIAT1 cells even at 0.2 μM, yet some cells were still infected. None of the drugs that were further tested inhibited the H5-S-FLU virus. These drugs therefore were specific inhibitors of EBOV, and presumably in the tests of Johansen *et al.* acted on target molecules in EBOV other than the EBOV-GP that is shared between E-S-FLU and authentic EBOV.

4.3 Dissecting drug inhibition mechanisms

In agreement with the current literature, we have seen that drugs from different pharmacological groups inhibited E-S-FLU entry (Johansen *et al.* 2013, 2015; Gehring *et al.* 2014; Kouznetsova *et al.* 2014; Xiao *et al.* 2018). We have shown that our screening results correlated well with a previous screen done by

Johansen's group using recombinant EBOV expressing eGFP (Johansen *et al.* 2015). However, the mechanisms by which these repurposed drugs are inhibiting EBOV remained unclear. To further investigate the inhibitors from our screen, we grouped the drugs based on common features we identified. In the following sections, we examined whether these features were crucial for the inhibitory effect on E-S-FLU. One pharmacological group that stood out from the 215 inhibitors that inhibited E-S-FLU was the subgroup of calcium channel inhibitors (15 of 215, Figure 4.2 B and C). The calcium related drugs are described and discussed separately in Chapter 6: "Calcium and EBOV entry".

4.3.1 Reduced infection vs. reduced viral gene expression

Twenty-two drugs from LOPAC®1280 library inhibited both E-S-FLU and H5-S-FLU infection, as listed in Table 4.2. We also included two additional drugs that inhibited both pseudotyped viruses. These are Favipiravir (T705) a RNA polymerase inhibitor (Oestereich *et al.* 2014; Sissoko *et al.* 2016), and U18666A an NPC1 binder (Lloyd-Evans *et al.* 2008; Lu *et al.* 2015). Of these 24 drugs, 16 showed similar IC_{50}s towards both E-S-FLU and H5-S-FLU (Table 4.2).

Our pseudotyped virus E-S-FLU used eGFP as a reporter of infection. In our drug inhibition assay, we measured the overall eGFP fluorescence level from a well of infected cells using the CLARIOstar® fluorescence plate reader. Under a fluorescence microscope, it was clear that there were two patterns of inhibition. Most inhibitors reduced the number of fluorescent cells (i.e. reduced the proportion of infected cells) as the drug concentration increased. These drugs could be thought of as reducing the probability of a cell becoming infected.

Table 4. 2 24 drugs that inhibited both E-S-FLU and H5-S-FLU

No.	Name	E-S-FLU IC_{50} (μM)	H5-S-FLU IC_{50} (μM)	Effect	Group
2	Aminopterin	0.2	0.2	dimmer	Antibiotic
5	Ouabain	0.3	0.3	reduced	Ion Pump
7	Raloxifene	0.4	33.8	reduced	Estrogen
11	Brequinar	1.3	1.4	dimmer	Gene regulation
14	Niclosamide	1.7	3.2	reduced	Antibiotic
19	Calmidazolium	2.3	3.9	dimmer	Intracellular Calcium
20	Gemcitabine	2.5	1.9	dimmer	Antitumour
21	U18666A	2.6	49.5	reduced	Biochemistry
27	Clemastine	3.4	58.4	reduced	Histamine
42	Chloroquine	5.4	67.0	reduced	Antimalarial
48	CP-100356	6.8	20.0	reduced	Signalling
54	Amsacrine	7.7	6.8	reduced	DNA topo
60	Dihydroouabain	8.3	5.7	dimmer	Ion channel
61	A-77636	8.6	15.6	reduced	Dopamine
63	*p*-Fluorohexahydro-sila-difenidol	9.3	65.0	reduced	Neurotransmission
70	LP44	10.4	70.0	reduced	Serotonin
104	Pyridostatin trifluoroacetate salt	17.4	58.8	dimmer	Gene regulation
119	PHA 767491	21.3	15.7	reduced	Kinase
135	Dequalinium	27.3	12.1	dimmer	Ion channel
145	Spironolactone	30.4	33.1	dimmer	Hormone
159	Favipiravir (T705)	39.3	67.3	dimmer	Antiviral
209	Triamterene	85.2	132.3	dimmer	Ion channel
222	Tyrphostin AG 1478	115.3	141.0	dimmer	EGFR
226	Ribavirin	125.2	125.9	dimmer	Cell cycle

No.: rank of drug in the list of 228 E-S-FLU inhibitors (Appendix Table 4. X1).
Effect: pattern of inhibition of the drugs.
Reduced: drugs reduced proportion of infected cells (blue background).
Dimmer: drugs reduced the overall fluorescence level of infected cells (grey background).

Twelve drugs however, reduced the overall fluorescence level of infected cells without reducing the number of fluorescent cells, which we call the “dimmer” effect. In Table 4.2, they are annotated as “dimmer” drugs. All twelve drugs had similar IC_{50} values for H5-S-FLU and E-S-FLU virus infection. This suggested that they

acted at a post-entry level by limiting the expression of viral proteins, and target the shared Influenza core. Favipiravir (T705), a small molecule that targets Influenza A RNA polymerase was tested to confirm the dimmer effect in our assay. Examples of the “dimmer” inhibition pattern induced by brequinar and gemcitabine under the fluorescence microscope are shown in Figure 4.3. The control in these comparisons was a monoclonal antibody that blocks the entry of H5-S-FLU by binding the H5 hemagglutinin, and reduces the proportion of infected cells without reducing their brightness.

We also examined the effect on individual cells by FACS analysis. Both brequinar and gemcitabine reduced the mean fluorescence intensity of infected cells as the drug concentration increased. In contrast, clomiphene, reduced the number of infected cells with increasing concentration, but had no effect on the fluorescence intensity of the cells that became infected (Figure 4.4).

The other twelve molecules in Table 4.2 that inhibited both E-S-FLU and H5-S-FLU viruses had a “reduced” pattern of inhibition, and reduced the proportion of cells that became infected. They may have affected both E-S-FLU and H5-S-FLU at the entry level. In general, the H5-S-FLU was much less sensitive to these drugs than E-S-FLU, indicated by a much higher IC_{50} value (Table 4.2).

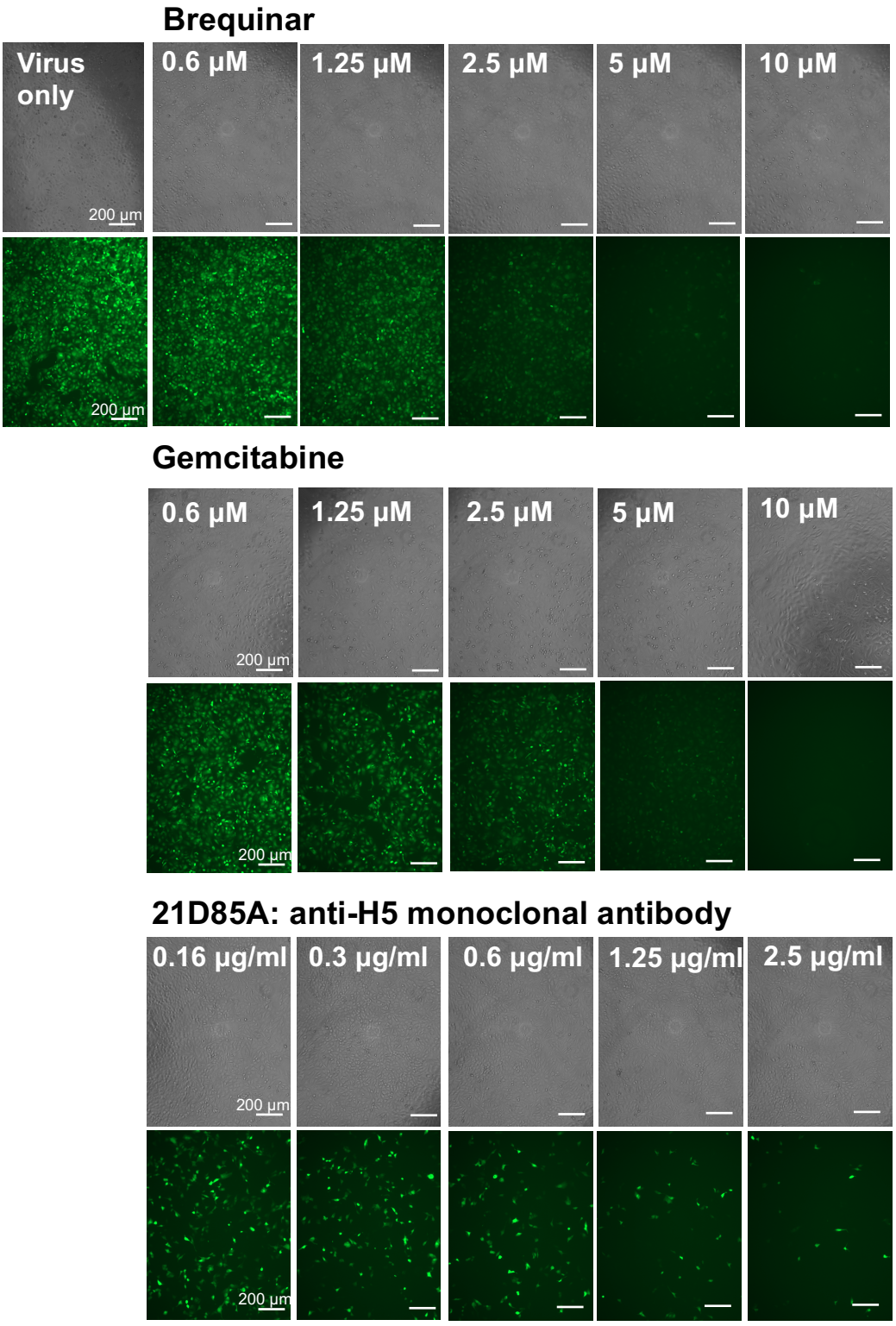


Figure 4. 3 Fluorescence microscopic images of "reduced" vs. "dimmer" inhibitors

Two dimmer effect inhibitors brequinar and gemcitabine were titrated from 10 µM to 0.6 µM to inhibit H5-S-FLU in the viral inhibition assay. Increasing concentration of drugs resulted in reduced eGFP fluorescence in infected cells. In contrast, a monoclonal antibody 21D85A that blocks H5-S-FLU entry reduced the proportion of eGFP expressing cells ("reduced" pattern inhibitor).

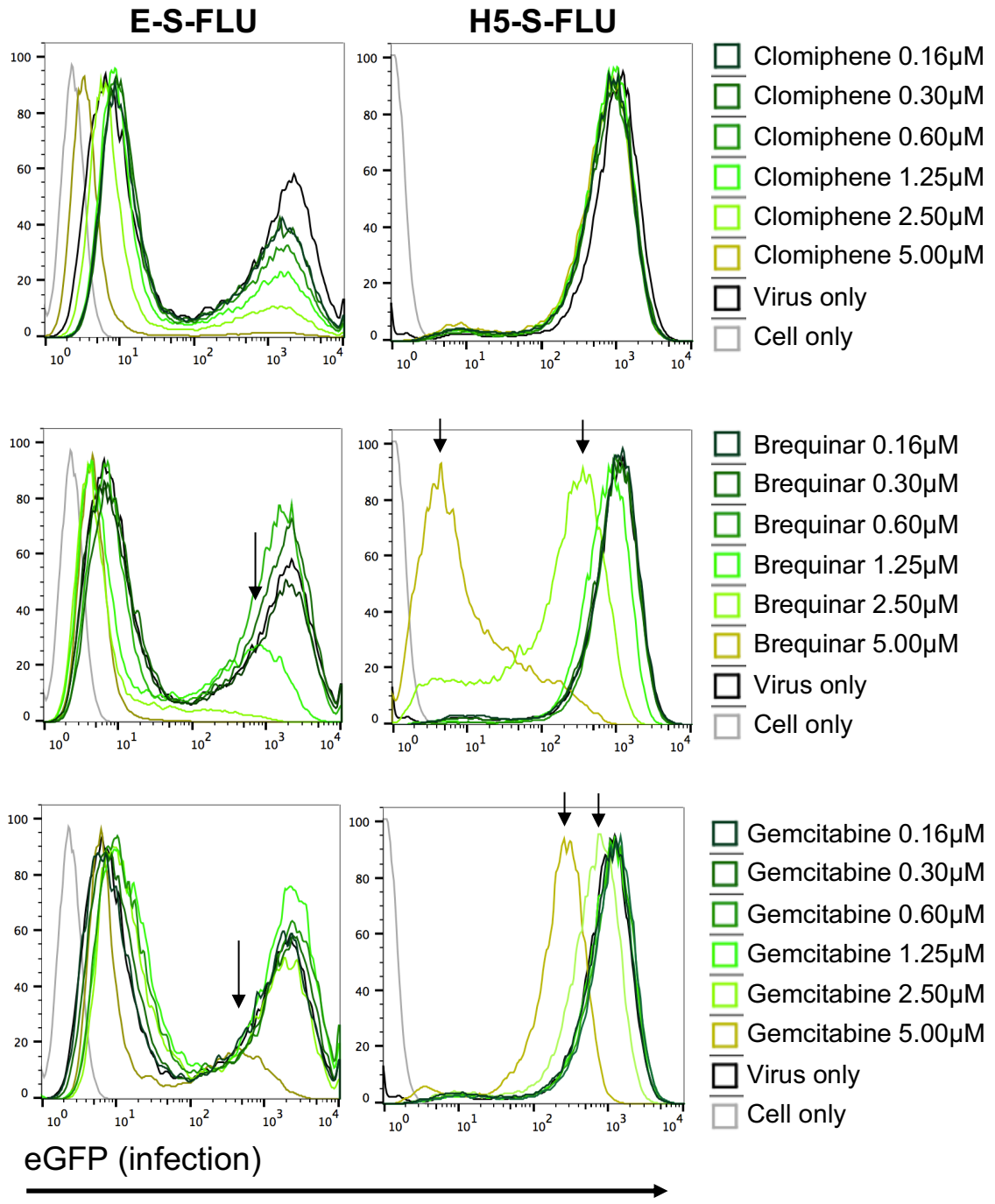


Figure 4. 4 FACS analysis pattern of drug that causes the "reduced" vs. "dimmer" inhibition

Indicator MDCK-SIAT1 cells were pre-treated for three hours with clomiphene, brequinar and gemcitabine at titrated concentrations and infected by E-S-FLU and H5-S-FLU pseudotyped virus for 24 hours. Infected cells were fixed and analysed by FACS. Overlapped histogram plots of each concentration (eGFP channel) are shown for each drug. Clomiphene gave a typical "reduced" pattern of inhibition, with a reduced proportion of eGFP +ve cells (indicating E-S-FLU infection). Clomiphene did not inhibit H5-S-FLU. By contrast, brequinar and gemcitabine reduced the mean fluorescence intensity of the eGFP +ve (infected) population (highlighted by single-headed arrows).

4.3.2 Long-QT drugs

The QT interval is a measurement of time between the Q wave and T wave on the electrocardiogram, which corresponds to the electrical depolarisation and repolarisation of the cardiac ventricles (Arunachalam *et al.* 2018). There are an increasing number of drugs reported to cause acquired prolongation of the QT interval, or long-QT syndrome. Some of these drugs were associated with cases of sudden cardiac death, presumably through life threatening ventricular dysrhythmias such as torsade de pointes. Promiscuous binding of drugs to a potassium channel called human ether-a-go-go (hERG) in cardiac myocytes has been shown to be strongly associated with induction of long-QT syndrome (De Bruin *et al.* 2005; Sanguinetti and Tristani-Firouzi 2006; Saxena *et al.* 2017).

We identified 62 out of 228 drugs that inhibited E-S-FLU (27.2%; indicated in Appendix Table 4. X1) that were either reported to have a risk of causing long-QT syndrome (CredibleMeds 2019) or were confirmed inhibitors of the hERG channel *in vitro* (De Bruin *et al.* 2005; Ayad *et al.* 2010; Foo *et al.* 2016). These drugs may have the potential side-effect of causing sudden cardiac death.

It was unclear whether the property of hERG binding and lengthening of the QT interval was related in any way to the inhibition EBOV entry. To further address this question, we tested two typical hERG binders, dofetilide (Cambridge biosciences, catalogue number: 15045) (Carmeliet *et al.* 1998; Perry 2006) and E-4031 (Cambridge biosciences, catalogue number: 15203) (Clay *et al.* 1995; Vandenberg *et al.* 2012) in the E-S-FLU drug inhibition assay. Both dofetilide and E-4031 are known to inhibit the hERG channel at the sub-micromolar range of

concentrations (Kamiya *et al.* 2006). Neither of the drugs inhibited E-S-FLU at 200 μM (Figure 4.5). We propose therefore, that hERG channel binding and lengthening of the QT interval is an undesirable off-target effect that has appeared in many E-S-FLU inhibitors. It should be possible to find inhibitors of EBOV entry that do not share this undesirable property by screening them for hERG binding.

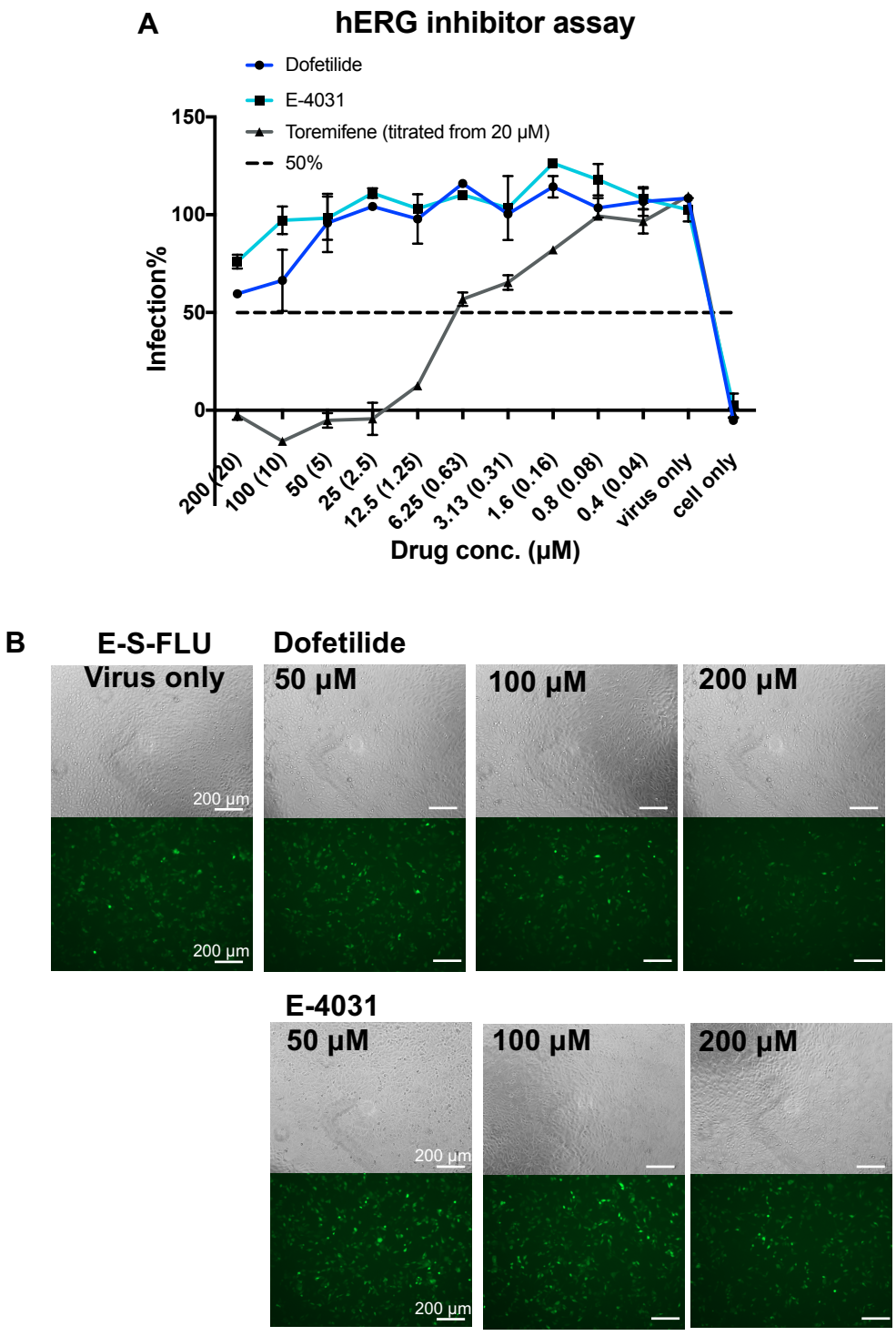


Figure 4. 5 hERG binders in the E-S-FLU drug inhibition assay

Two typical hERG (human ether-a-go-go) inhibitors dofetilide and E-4031 were titrated from 200 µM to 0.4 µM in the E-S-FLU drug inhibition assay, alongside a known E-S-FLU inhibitor toremifene (titrated from 20 µM to 0.04 µM). **A**: Percent infection was quantified by eGFP expression measured with a fluorescence plate reader. Representative titration curves are shown with error bars indicating the standard error of the mean from technical duplicates. **B**: Microscope pictures (brightfield and eGFP channel) MDCK-SIAT1 cells after treatment with 50 µM, 100 µM and 200 µM dofetilide and E-4031 and overnight E-S-FLU infection.

4.3.3 Cationic amphiphilic drugs (CADs)

Cationic amphiphilic drugs (CADs) refer to drug molecules that contain a hydrophobic ring structure on one end, and a cationic amine group on the other end. CADs are therefore weak bases with a pKa^{base} around 8, and are commonly found in various pharmacological groups. The relationship between pKa and the ratio of protonated molecules [HB^+] to unprotonated and lipid soluble drug [B] is defined by the equation: $pKa = pH + Log_{10}([HB^+]/[B])$, derived from the mass action equation. This implies that for a drug with a pKa of 8, at neutral pH, 10% of the molecules will be unprotonated and lipid soluble; but at the pH of lysosomes (~4.6) this will be reduced to 0.01%. The weak base in CADs becomes protonated when the molecule reaches acidic cellular compartments, and becomes concentrated in the lysosome as the lysosomal membrane is impermeable to positively charged molecules. Therefore, most CADs are also referred to as lysosomotropic agents (De Duve *et al.* 1974; Kaufmann and Krise 2007; Kornhuber *et al.* 2008; Nadanaciva *et al.* 2010).

Accumulation of some CADs can result in dissociation of the lysosomal membrane enzyme acid sphingomyelinase (ASM) into the lumen of the lysosome (Hurwitz, Ferlinz and Sandhofl 1994; Kölzer, Werth and Sandhoff 2004; Kornhuber *et al.* 2008). ASM is thought to bind to the lysosomal membrane through electrostatic attraction, and its dissociation caused by the accumulation of lysosomotropic drugs is associated with loss of its enzyme function (Kornhuber *et al.* 2008). Drugs with this property have therefore been referred to as Functional Inhibitors of Acid Sphingomyelinase (FIASMAs) (Kornhuber *et al.* 2008, 2010, 2011). CADs and FIASMAs usually share the physicochemical properties of a high LogP value,

which indicates the hydrophobic property; and a high basic pKa value, which refers to the weak amine base.

We noticed that many of the E-S-FLU inhibitors from the LOPAC®1280 library are CADs. We analysed the physicochemical features of the 65 most potent E-S-FLU inhibitors that had IC_{50} values less than 10 μM. The LogP and the base pKa values for these drugs are listed in Table 4.3.

Table 4. 3 Physicochemical properties of 65 most potent E-S-FLU inhibitors

No.	Drug Name	Inhibition	Effect	Group	LogP	pKa^{base}
1	Toremifene*	E	reduced	Estrogen	6.8	8.8
2	Aminopterin	E/H5	dimmer	Antibiotic	-1.8	5.5
3	PD-166285	E	reduced	Kinase	5.6	9.4
4	Tamoxifen*	E	reduced	Estrogen	7.1	8.8
5	Ouabain*	E/H5	reduced	Ion Pump	-2.0	-2.9
6	Clomiphene*	E	reduced	Estrogen	7.2	9.3
7	Raloxifene	E/H5	reduced	Estrogen	5.2	8.0
8	PD173952	E	reduced	Kinase	5.0	2.3
9	BIX 01294	E	reduced	Gene regulation	3.6	8.9
10	Triparanol	E	reduced	Biochemistry	6.5	9.3
11	Brequinar	E/H5	dimmer	Gene regulation	6.3	0.8
12	Mibefradil*	E	reduced	Calcium	5.2	9.8
13	Tetrandrine	E	reduced	Calcium	6.5	8.3
14	Niclosamide	E/H5	reduced	Antibiotic	3.9	-4.4
15	L-703,606	E	reduced	Tachykinin	6.4	9.0
16	NNC 55-0396	E	reduced	Calcium	6.1	9.8
17	Tamoxifen*	E	reduced	Estrogen	7.1	8.8
18	Amiodarone*	E	reduced	Calcium	7.6	8.5
19	Calmidazolium	E/H5	dimmer	Intracellular calcium	10.8	3.0
20	Gemcitabine	E/H5	dimmer	Antitumour	-1.4	-1.3
21	U18666A	E/H5	reduced	Biochemistry	4.7	9.4
22	Bepridil*	E	reduced	Calcium	5.2	9.2
23	Quinacrine	E	reduced	Antimalarial	5.5	10.3
24	Paroxetine*	E	reduced	Serotonin	3.6	9.8
25	Ellipticine	E	reduced	Cell Cycle	3.9	5.1
26	Terfenadine*	E	reduced	Histamine	7.1	9.0
27	Clemastine*	E/H5	reduced	Histamine	5.2	9.6
28	Methiothepin	E	reduced	Serotonin	4.7	7.8
29	Bosutinib*	E	reduced	Kinase	4.9	8.4
30	SKF525A	E	reduced	Microsomal drug metabolism	5.6	9.0
31	Prochlorperazine*	E	reduced	Dopamine	4.9	8.1
32	MDL28170	E	reduced	Cell cycle	3.4	NA

No.	Drug Name	Inhibited	Effect	Group	LogP	pKa^{base}
33	Imipramine*	E	reduced	Serotonin	4.8	9.4
34	U-73343	E	reduced	G-protein	4.7	11.0
35	Trifluoperazine*	E	reduced	Dopamine	5.0	8.4
36	GR 127935	E	reduced	Serotonin	5.4	7.4
37	Daurisoline	E	reduced	Ion channel	5.9	8.3
38	Arbidol	E	reduced	Fusion inhibitor	3.8	9.9
39	Ebastine*	E	reduced	Histamine	7.0	8.4
40	Maprotiline*	E	reduced	Adrenoceptor	5.1	10.5
41	Chloroquine *	E/H5	reduced	Antimalarial	4.6	10.1
42	CP-31398	E	reduced	Apoptosis	4.6	9.4
43	Thioridazine*	E	reduced	Calcium	5.9	9.5
44	Fiduxosin	E	reduced	Adrenoceptor	4.4	9.3
45	Rottlerin	E	reduced	Kinase	7.4	NA
46	Azithromycin*	E	reduced	Antibiotic	4.0	8.7
47	CP-100356	E/H5	reduced	Signalling	5.1	7.2
48	BNTX	E	reduced	Opioid	3.3	9.4
49	Triflupromazine	E	reduced	Dopamine	5.5	9.2
50	Fluspirilene*	E	reduced	Dopamine	5.9	9.3
51	Sertraline HCl*	E	reduced	Serotonin	5.5	9.9
52	Pimozide*	E	reduced	Calcium	6.3	8.6
53	Amsacrine*	E/H5	reduced	DNA topo	3.8	8.4
54	(±)-Octoclothepin	E	reduced	Dopamine	4.7	7.6
55	cis(Z)-Flupenthixol	E	reduced	Dopamine	4.5	8.4
56	AY9944	E	reduced	Cholesterol	5.8	9.4
57	Perphenazine*	E	reduced	Dopamine	4.2	7.9
58	Metergoline	E	reduced	Serotonin	4.0	8.7
59	Dihydroouabain	E/H5	dimmer	Ion channel	-3.1	NA
60	A-77636	E/H5	reduced	Dopamine	2.6	8.9
61	Indatraline	E	reduced	Dopamine	4.7	9.5
62	p-Fluorohexahydro-sila-difenidol	E/H5	reduced	Neurotransmission	3.5	8.8
63	Piperlongumine	E	reduced	Apoptosis	1.7	NA
64	Benztropine	E	reduced	Neurotransmission	4.5	9.5
65	Sunitinib*	E	reduced	Kinase	5.2	9.0

**: Drugs that cause long-QT effect.*
Inhibition: Drug inhibited E-S-FLU or/and H5-S-FLU.
NA: no proton acceptor atoms (base) found.
LogP values less than 2.5 and pKa^{base} values less than 6 are coloured red.

We also plotted the LogP and pKa^{base} values for all 65 strong E-S-FLU inhibitors in Figure 4.6 on the same scales as Kornhuber *et al.* plotted their set of FIASMAs (Kornhuber *et al.* 2008, Figure 2). Clearly, 53 out of 65 drugs clustered into a “high

LogP, high pKa^{base}" corner typical of CADs (LogP > 2.5; pKa^{base} > 6), and only 12 were scattered elsewhere (Figure 4.6).

Among the twelve non-CADs, five were "dimmer drugs" (hollow circles in Figure 4.6), which inhibited both E-S-FLU and H5-S-FLU at a post-entry level as described in section 4.3.1. MDL28170 is a calpain inhibitor, which is thought to block EBOV entry by inhibiting endosomal cathepsins B and L in processing EBOV-GP (Shah, Wang and Kaletsky 2010; Gnirß *et al.* 2012). Niclosamide is a proton ionophore which affects endo/lysosomal pH and consequently may affect cathepsin function (Jurgeit *et al.* 2012; Kouznetsova *et al.* 2014; Rajamuthiah *et al.* 2015). Rottlerin is a protein kinase C-delta inhibitor with broader activity towards other kinases including protein kinase A (PKA). Rottlerin has been shown to have an inhibitory effect on fluid-phase endocytosis and macropinocytosis, which may inhibit EBOV internalisation at the plasma membrane (Nanbo *et al.* 2010; Saeed *et al.* 2010). However this may be a separate activity to its kinase inhibition function, as several other PKA and PKC inhibitors did not affect cellular endocytosis (Sarkar *et al.* 2005; Mulherkar *et al.* 2011; Kindrachuk *et al.* 2014). There remain four other non-CADs: ouabain, a Na^+/K^+ ATPase inhibitor (Sandtner *et al.* 2011); PD173952 a src kinase inhibitor (Suzuki-Inoue *et al.* 2007); ellipticine, a topoisomerase II inhibitor (Stiborová *et al.* 2011); and piperlongumine, which is claimed to selectively kill cancer cells (Adams *et al.* 2012). How these drugs might have inhibited EBOV entry is not clear.

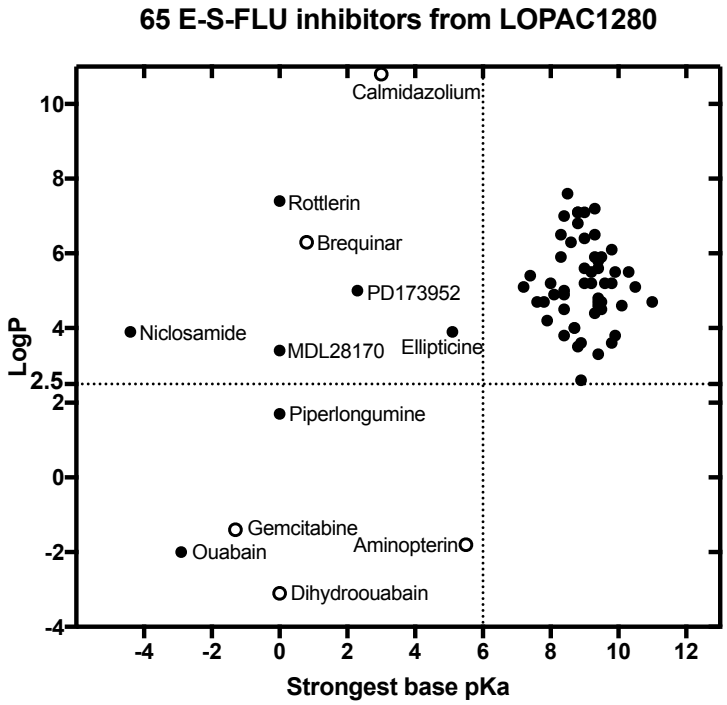


Figure 4. 6 LogP, pKa^{base} plot for 65 most potent E-S-FLU inhibitors
The physicochemical features of 65 E-S-FLU inhibitors are shown in the LogP, pKa^{base} plot. A "high LogP, high pKa^{base}" subsection (LogP > 2.5; pKa^{base} > 6) is marked out by dotted lines. Drugs that inhibited both E-S-FLU and H5-S-FLU by reducing the overall fluorescence of infected cells ("dimmer" pattern inhibitors) are shown in hollow circles, whereas drugs that reduced the proportion of infected cells ("reduced" pattern inhibitors) are shown in filled circles.

The enrichment of CADs among EBOV inhibitors has been shown in other papers (Shoemaker *et al.* 2013; Johansen *et al.* 2015), but how they are affecting EBOV remains in the realm of hypothetical models. In the following sections, we continued to investigate the CADs and their biochemical features in relation to EBOV inhibition.

4.3.4 NPC1 phenotype inducers

Niemann-Pick type C1 protein (NPC1) is a multi-pass transmembrane protein localised in the late endosomal/lysosomal membrane. Defects in NPC1 protein lead to a neurodegenerative lysosomal storage disorder called Niemann-Pick

disease type C (NPC disease) (Vanier 2010). The NPC disease phenotype consists of accumulation in acidic compartments of a broad range of lipids and lipid metabolites such as cholesterol, sphingosine, sphingomyelin, glycosphingolipids, a block in trafficking and fusion events in the endo/lysosomal system and a reduction in lysosomal calcium stores (Lloyd-Evans *et al.* 2008). A proposed sequence of disease progression is shown in Figure 4.7 based on Lloyd-Evans *et al.*

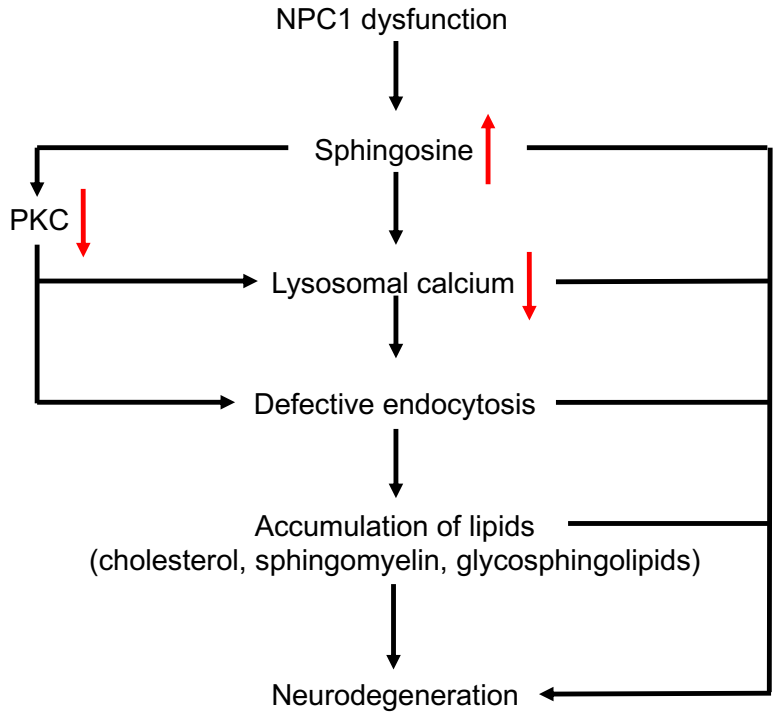


Figure 4. 7 NPC disease pathogenesis model
A proposed sequence of cellular effect and NPC disease pathogenesis caused by defective Niemann-Pick type C1 protein (NPC1), based on drug induced NPC model studied by Lloyd-Evans *et al.* 2008. PKC: protein kinase C.

NPC1 protein is also the key receptor for EBOV-GP binding and EBOV entry into the cytoplasm at the lysosomal membrane (Carette *et al.* 2011; Côté *et al.* 2011; Miller *et al.* 2012a). Some drug molecules, many of which are CADs, can induce a NPC disease-like phenotype *in vitro* (Carette *et al.* 2011; Shoemaker *et al.* 2013).

U18666A, itraconazole, astemizole and cepharanthine were shown to bind directly to NPC1 protein at the sterol-sensing domain (Lu *et al.* 2015; Head *et al.* 2017; Lyu *et al.* 2017), whereas molecules 3.47, MBX2254 and MBX2270 may compete and interrupt the binding between EBOV-GP and the NPC1 C domain specifically (Côté *et al.* 2011; Basu *et al.* 2015) (Figure 4.8). Both these sets of drugs induced lipid accumulation in lysosomes despite binding different regions of NPC1. Some CADs, while not shown to bind to NPC1 directly, inhibited EBOV entry in a NPC1-dependent manner as the IC_{50} of the drugs increased with increasing expression of NPC1 (Shoemaker *et al.* 2013). Taken together these results link the inhibition of EBOV entry by these drugs with the induction of a biochemical phenotype related to loss of NPC1 function.

It is still unclear how if the inhibition of EBOV infection by these drugs is via their interactions with NPC1 protein. On the one hand, these drugs may interact directly with NPC1 in the lysosome and interfere with binding by EBOV-GP to the domain C of NPC1. For the subset of drugs that bind the GP binding site on the NPC1 domain C this is the likely mode of action. For the drugs that bind the sterol-sensing domain (SSD) it is conceivable that they induce conformational change in the NPC1 protein to a point where the EBOV-GP can no longer bind.

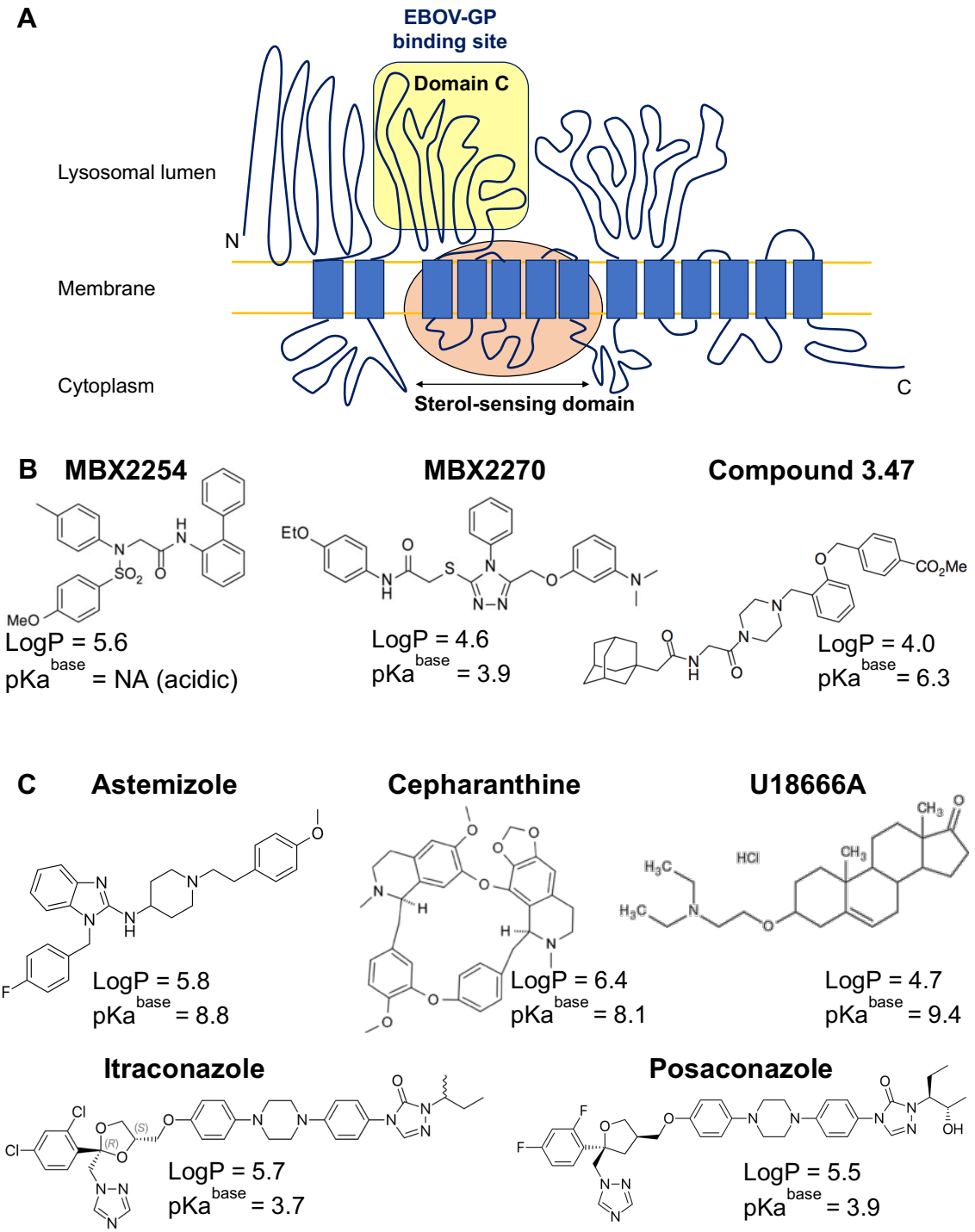


Figure 4. 8 Drugs that bind NPC1 directly

A: The schematic NPC1 protein model as proposed by Davies and Ioannou, 2000. Blue rectangles represent the putative transmembrane domains; light orange circle highlights the sterol-sensing domain; yellow square around the loop connecting second and third transmembrane helix shows the EBOV-GP binding domain C, where EBOV-GP binds. Chemical structures of compounds that bind to NPC1 domain C (**B**), or the sterol-sensing domain (**C**) are shown with their LogP and strongest base pKa values respectively.

Alternatively, the biochemical phenotype induced by the interference with NPC1 function may induce downstream effects, such as loss of calcium from the lysosome (Lloyd-Evans *et al.* 2008; Höglinger *et al.* 2015), that result in inhibition of EBOV entry. Evidence that this is unlikely came from an early observation that cells lacking NPC2 are fully susceptible to EBOV infection (Carette *et al.* 2011). NPC2 is a soluble lysosomal protein that binds cholesterol and transfers it to NPC1 (Wang *et al.* 2010). Loss of NPC2 expression is associated with an identical biochemical phenotype in the lysosome of lipid accumulation and calcium loss as that for NPC1.

In order to gain some insight into the possible interactions between the CADs and NPC1, we looked in greater detail at the biochemical phenotypes induced by the drugs compared to the classical pattern associated with NPC1 mutations. We initiated a collaboration with Professor Fran Platt's group to characterise the cellular lipid biochemistry after treatment with different drugs that inhibited E-S-FLU. We hypothesised that if the drugs interrupt NPC1 function, either via direct binding or indirectly through affecting the property of the lysosomal membrane, we would see a similar profile of lipid accumulation in drug treated and NPC1 defective cells.

Initially, we began with a panel of 20 drugs representing different drug families (Table 4.4). This included known NPC1 binders U18666A and itraconazole; standard CADs such as imipramine, toremifene, clomiphene; and calcium channel blockers that have CAD features amiodarone, verapamil, bepridil and tetrandrine; and drugs that may inhibit EBOV entry pre-NPC1 binding such as EIPA, the

macropinocytosis inhibitor; E64 and MDL28170 that inhibit cathepsin cleavage of EBOV-GP; chloroquine and niclosamide, the proton ionophores; and arbidol, a CAD and potential fusion inhibitor. In addition, we have also included quinine, which has CAD-like features, but did not inhibit E-S-FLU infection as a negative control. The biochemical analysis and the results in this section were mainly done by Frauke Fuchs and Nick Platt (Department of Pharmacology, University of Oxford). Here I have gathered and displayed some initial results and analysis.

Table 4. 4 A panel of 20 compounds tested for drug-induced NPC phenotype

Drug	Tested conc. (μM)	E-S-FLU IC_{50} (μM)	Proposed drug mechanism	LogP	pKa^{base}
Amiodarone	5	2.0	Calcium channel inhibitor	7.6	8.5
Arbidol	2	5.2	EBOV-GP binder	3.8	9.9
AY9944	2	7.8	Cholesterol synthesis inhibitor	5.8	9.4
Bepridil	5	2.7	Calcium channel inhibitor	5.2	9.2
Chloroquine	2	5.4	Proton ionophore	4.6	10.1
Clarithromycin	10	14.0	Antibiotic	3.2	8.4
Clomiphene	5	0.4	Estrogen receptor antagonist	7.2	9.3
E64	70	77.2	Cathepsin inhibitor	-1.1	11.3
EIPA	20	17.8	Macropinocytosis inhibitor	0.3	2.3
Itraconazole	1	NA	Anti-fungal	5.7	3.7
Imipramine	10	3.8	Anti-depressant	4.8	9.4
MDL28170	10	3.8	Calpain inhibitor	3.4	NA
Niclosamide	1.5	1.7	Proton ionophore	3.9	-4.4
Quinine	2	NA	Anti-malarial	3.4	9.1
Tetrandrine	2	1.6	Calcium channel inhibitor	6.5	8.3
Toremifene	5	0.2	Estrogen receptor antagonist	6.8	8.8
Triparanol	5	1.1	Cholesterol synthesis inhibitor	6.5	9.3
U18666A	0.005 (2 μg/ml)	2.6	NPC1 binder	4.7	9.4
Verapamil	20	10.6	Calcium channel inhibitor	3.8	9.7
Wortmannin	30	64.7	PI3K inhibitor	1.4	-3.2

NA in the "E-S-FLU IC_{50} (μM)" column: drugs did not inhibit E-S-FLU.
NA in the "pKa^{base}" column: no proton acceptor atoms (base) found.
Values coloured red: LogP values less than 2.5 and pKa^{base} values less than 6 (non-CAD features).

Lysotracker staining of the acid compartment

Lysotracker is a fluorescently labelled weak amine base, which stains acidic organelles in cells (Lemieux, Percival and Falgueyret 2004). Enlargement of the lysosomal compartment is a common feature of different lysosomal storage diseases including NPC disease (Platt, Boland and van der Spoel 2012), and this can be detected by lysotracker staining (Bampton *et al.* 2005; te Vruchte *et al.* 2014). J774, a murine monocyte macrophage cell-line and MDCK-SIAT1, a canine kidney cell-line were treated with 18 drugs (All drugs in Table 4.4 except niclosamide and wortmannin) at stated concentrations for 48 hours. A preliminary investigation was done to ensure that the concentration of each drug used did not significantly impact upon cell viability after 48 hours of treatment (data not shown). Cells were then stained with lysotracker and analysed by FACS. The relative lysotracker staining value is the mean fluorescence intensity (MFI) of drug treated cells divided by the MFI of untreated cells (Figure 4.9).

The positive control drugs itraconazole and U18666A caused increased lysotracker staining in both J774 and MDCK-SIAT1 cells. The effect of U18666A on MDCK-SIAT1 cells was relatively lower (1.32-fold change relative to the untreated cells) and we used it as a reference to define a positive effect in lysotracker staining. Drugs that increased lysotracker staining by more than 1.32-fold to the untreated cells were annotated as having a “+” effect in the summary Table 4.5. Suboptimal increase between 1 ~ 1.32-fold were annotated as “+/-“.

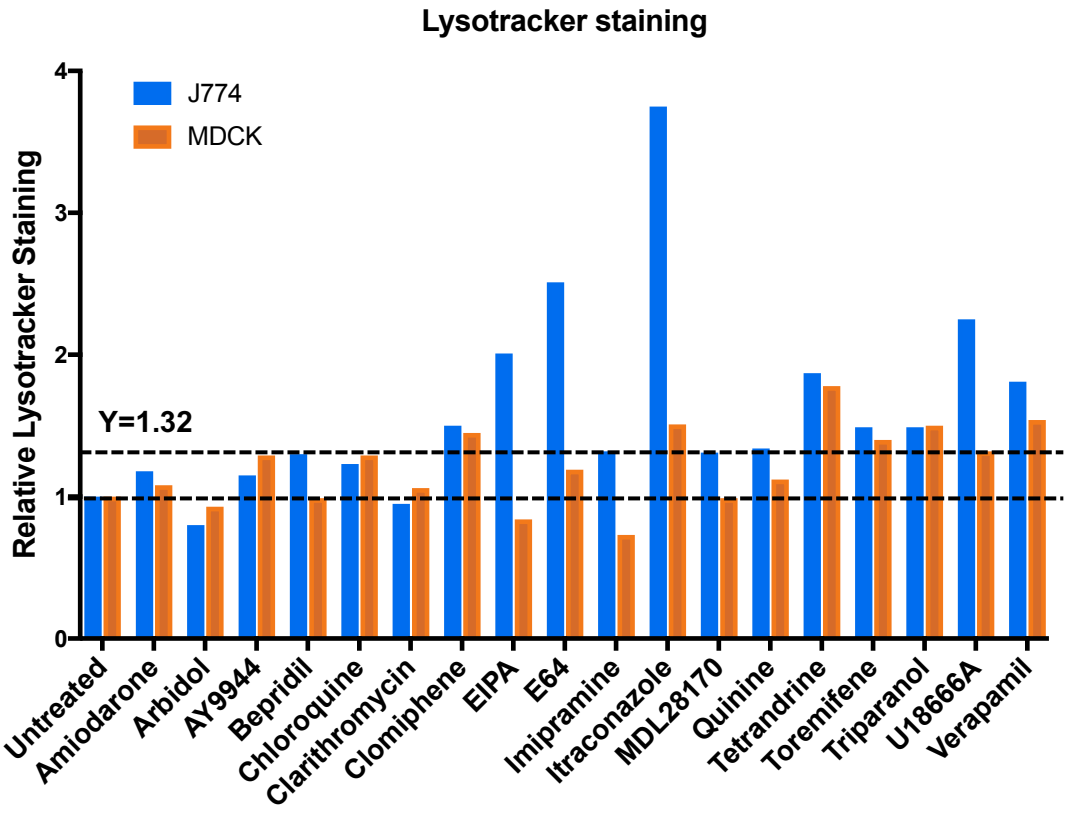


Figure 4. 9 Lysotracker staining of drug treated cells
J774, a mouse monocyte macrophage cell-line and a canine kidney MDCK-SIAT1 cell-line were treated with 18 drugs for 48 hours at a given concentration as stated in Table 4.4. Cells were then stained with GFP-conjugated lysotracker, and analysed by FACS. The relative lysotracker staining result presented in the diagram was based on the measured GFP fluorescence intensity normalised to the untreated cells control.

Filipin staining for cholesterol accumulation

Filipin is a fluorescent antibiotic that forms a stable complex with unesterified cholesterol (Pentchev *et al.* 1985; Kruth *et al.* 1986; Vanier *et al.* 1991, 2016). Accumulation of unesterified cholesterol is found in the majority of fibroblasts taken from typical NPC cases and therefore filipin staining is used as one test to diagnose NPC disease (Vanier 2010). An intense punctate staining of lysosomes by filipin is seen in NPC1 defective cells. J774 and MDCK-SIAT1 cells were treated with 20 drugs at the stated concentrations for 48 hours (Table 4.4). The cells were then washed, fixed and stained with filipin. Random fields of cells were

photographed by confocal microscope. Definite and intense punctate staining were scored as “+” and suboptimal or uncertain effect were scored as “+/-” in the summary table (Table 4.5), and representative images are shown in Figure 4.10.

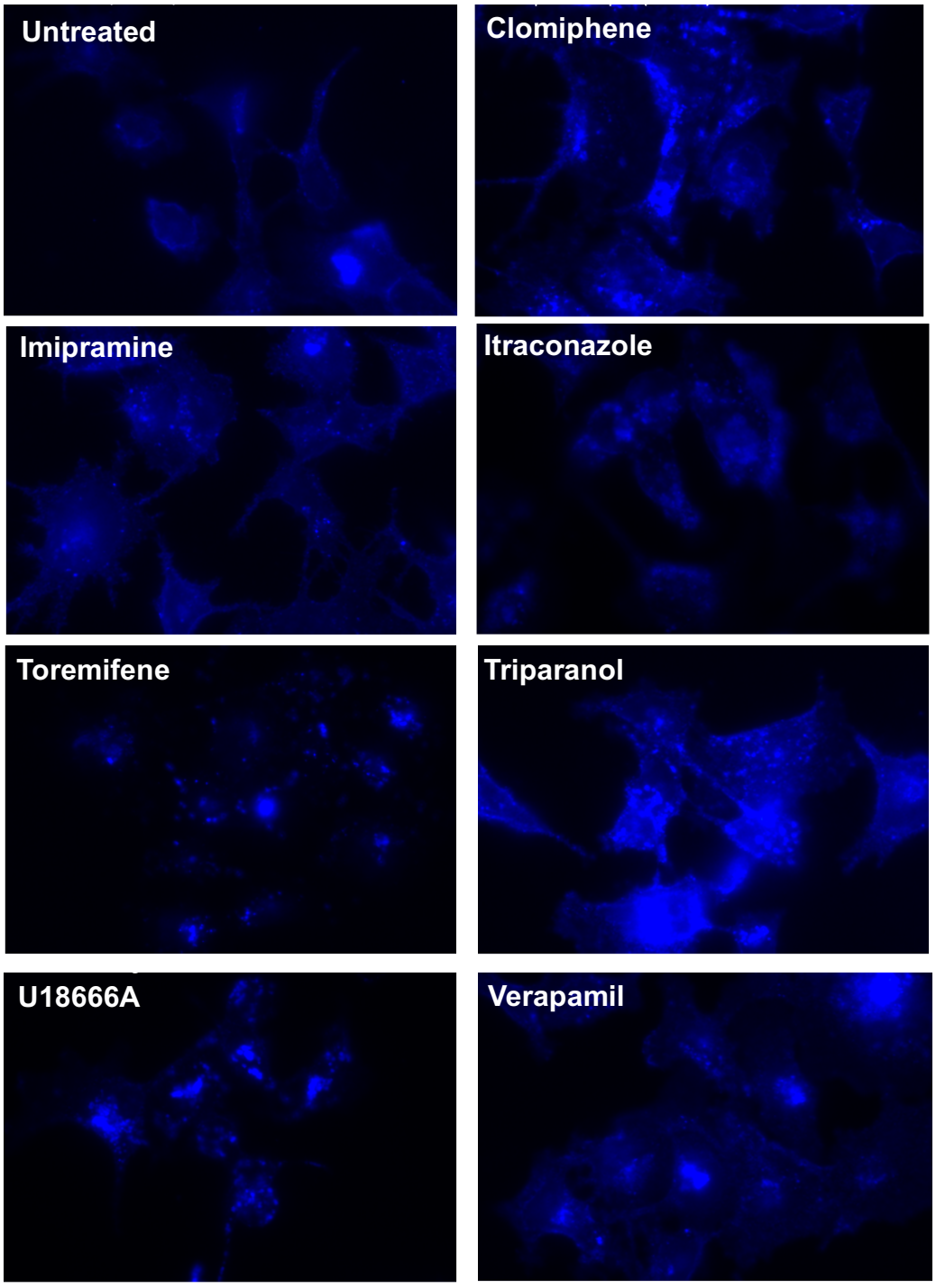


Figure 4. 10 Filipin fluorescence staining microscopy
MDCK-SIAT1 cells were treated with drugs at a constant concentration for 48 hours (concentration for the drugs are summarised in Table 4.4), and then fixed and stained with filipin. Representative confocal microscopic images are shown in the diagram.

Amplex® Red measuring for cellular cholesterol level

Amplex® Red Cholesterol Assay Kit (Invitrogen, catalogue number: A12216) was used to quantify the total cholesterol level in drug-treated cells. J774 cells were treated with the panel of 20 drugs at the stated concentrations for 48 hours (Table 4.4, Figure 4.11). Cells were then stained with the kit and quantified under a fluorescence plate reader (CLARIOstar®). Cholesterol level was calculated as µg cholesterol per mg total protein from the cells, based on a cholesterol standard curve and protein level quantified on the same day.

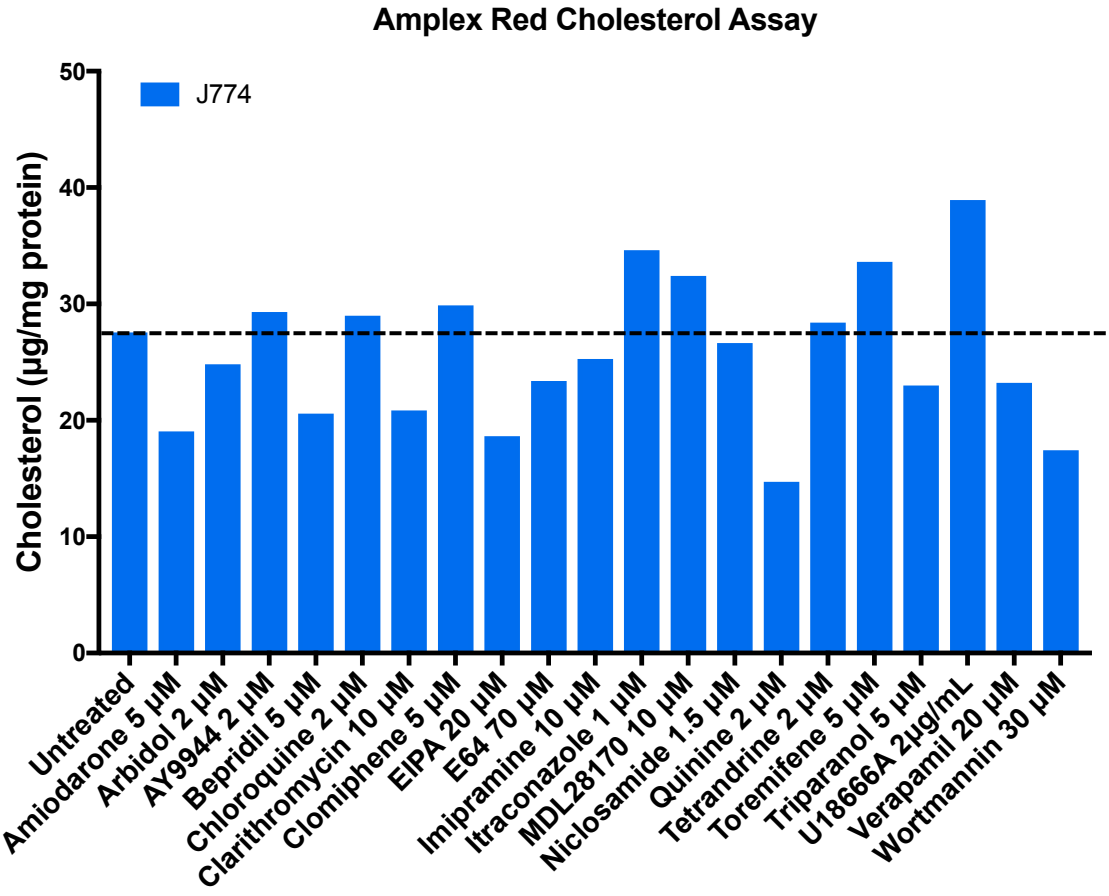


Figure 4. 11 Amplex® Red cholesterol assay
A mouse monocyte macrophage cell-line J774 was treated with 20 drugs for 48 hours at the stated concentrations. Cells were then quantified for cholesterol level by using the Amplex® Red Cholesterol Assay kit (Invitrogen), based on a fluorometric cholesterol esterase-coupled reaction. Cholesterol level was calculated as µg cholesterol per mg total protein from the cells, based on a cholesterol standard curve and protein level quantified on the same day. The broken line indicates the level of cholesterol in untreated cells.

Sphingomyelin detection by Ostreolysin A staining

Ostreolysin A (OlyA) protein binds and stains cholesterol- and sphingomyelin-rich membranes (Skočaj *et al.* 2014). J774 and MDCK-SIAT1 cells were treated with 20 drugs at stated concentrations for 48 hours (Table 4.5). After treatment, cells were washed and fixed, then stained with eGFP-linked OlyA (Skočaj *et al.* 2014) and a nuclear stain 4',6-diamidino-2-phenylindol (DAPI). Intense green punctate staining sphingomyelin accumulation in lysosomes, which is a downstream effect of defective NPC1 activity. Representative confocal microscopic images of green punctate staining by OlyA-eGFP are shown in Figure 4.12. Intense staining such as seen in U18666A treated cells are annotated as "+" in the summary Table 4.5, whereas weaker staining such as triparanol treated cells are marked as "+/-". "-" indicates no punctate staining.

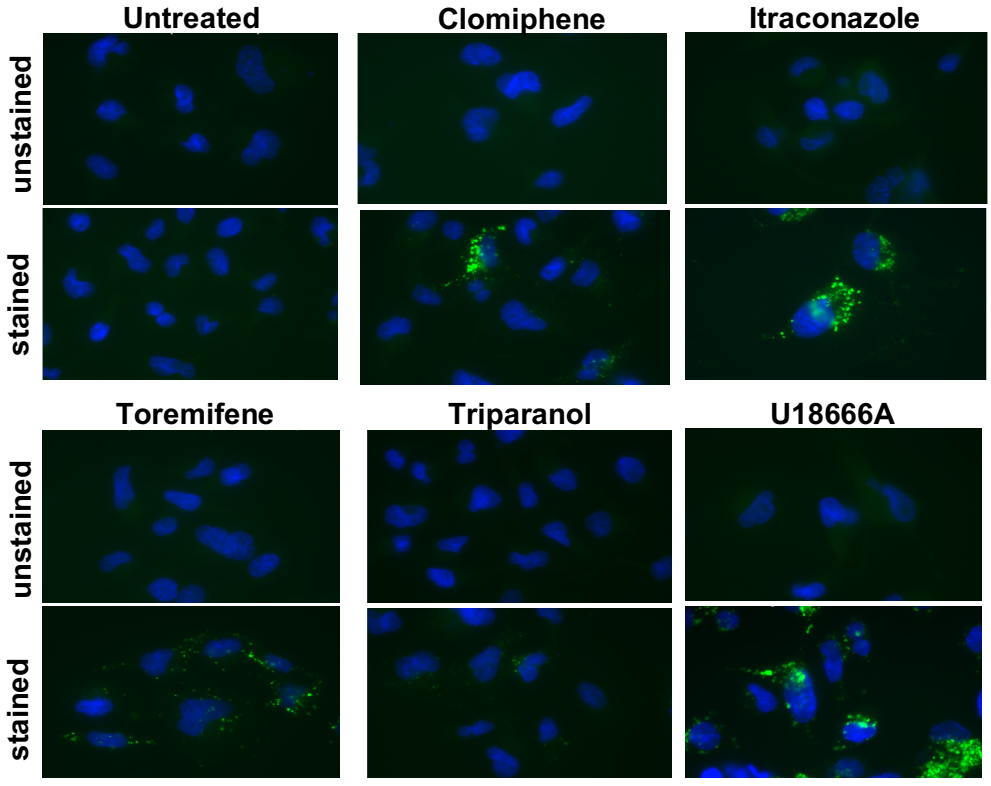


Figure 4. 12 Sphingomyelin OlyA staining
MDCK-SIAT1 cells were treated with drugs at a constant concentration for 48 hours, and then fixed and stained with DAPI (blue) and eGFP-linked Ostreolysin A (OlyA, green). Representative microscopic images are shown in the diagram.

Summary of the NPC phenotype induced by drugs

We summarised all of the assays we conducted to detect the NPC disease phenotype induced by a collection of 20 different drugs in Table 4.5. U18666A and itraconazole, the two well-established NPC1 binders showed a full NPC disease-like profile in all the assays we have done so far: increased lysotracker staining showing the enlarged acidic organelles; punctate patterned filipin and OlyA staining indicating the accumulated unesterified cholesterol and sphingomyelin in lysosomes; increased Amplex® Red staining to show the elevated total cholesterol level in cells.

Table 4. 5 Summary of biochemical phenotypes for drug treated cells

Durgs	**Lysotracker**		**Amplex® Red**	**Filipin**		**OlyA**	
	J774	MDCK	J774	J774	MDCK	J774	MDCK
Amiodarone	+/-	-	-	+	+	-	-
Arbidol	-	-	-	-	-	-	-
AY9944	+/-	+	+/-	+	+	+	+/-
Bepridil	+/-	-	-	+/-	+/-	+/-	-
Chloroquine	+/-	+	+/-	-	+/-	-	-
Clarithromycin	-	-	-	+/-	+/-	-	-
Clomiphene	+	+	+/-	+	+	+	+
EIPA	+	-	-	+	+/-	+	+/-
E64	+	+/-	-	-	-	-	-
Imipramine	+/-	-	-	+	+/-	+/-	-
Itraconazole	+	+	+	+	+	+	+
MDL28170	+/-	-	+	-	-	-	-
Niclosamide			-	-	-	-	-
Quinine	+/-	+/-	-	-	-	-	-
Tetrandrine	+	+	+/-	+/-	+/-	-	-
Toremifene	+	+	+	+	+	+	+
Triparanol	+	+	-	+	+	-	+/-
U18666A	+	+	+	+	+	+	+
Verapamil	+	+	-	+	+	-	-
Wortmannin			-		-		-

"+": drug treatment induced NPC disease-like phenotype, i.e. intense punctate staining in filipin, OlyA fluorescence microscopy or increased level of measured parameter in lysotracker staining and Amplex® Red cholesterol assays.
"+/-": drugs induced an intermediate effect.
"-": drugs showed no effect on cells compared with the untreated samples.

It is noteworthy that U18666A had a moderate IC_{50} (2.56 μM) for inhibition of E-S-FLU infection, which is much higher than the concentration at which it induced the NPC-disease phenotype (5 nM). Itraconazole did not inhibit E-S-FLU in our hands. Not all CADs showed the same profile; clomiphene, toremifene and AY9944 showed a similar "all positive" result in the NPC-disease phenotype assays to the U18666A compound, and all were strong inhibitors of E-S-FLU. We will further investigate their effect on lipid biochemistry and NPC1 in the future. In summary, there was no clear relationship revealed between the intensity of any of these staining patterns and the IC_{50} of the drugs in the E-S-FLU inhibition assay.

4.3.5 CADs that induced lysosomal membrane permeability

The interaction between CADs and the lysosomal membrane can lead to increased permeability of the membrane and leakage of lysosomal contents into the cytosol (Kroemer and Jäättelä 2005; Boya and Kroemer 2008). Ellegaard *et al.* showed that CADs can induce lysosomal cell death in cancer cells (Ellegaard *et al.* 2016). The group also showed that some of the cytotoxic CADs induced lysosomal leakage indicated by lysosomal galectin-1 puncta staining in the lysosome (Aits *et al.* 2015).

We selected the 12 most potent cytotoxic CADs reported by Ellegaard *et al.* (2016) and tested them in our E-S-FLU inhibition assay. Apart from emetine which was too toxic to our indicator MDCK-SIAT1 cells, eleven of them inhibited E-S-FLU while none inhibited H5-S-FLU (Table 4.6). This result suggested that CADs that increase lysosomal membrane permeability can block E-S-FLU infection. It is noticeable that 9 of these 12 drugs had an IC_{50} of less than 10 μM in the E-S-FLU

inhibition assay, equivalent to the most powerful 27% of the 215 drugs detected in the original screen.

Table 4. 6 CADs that induced lysosomal membrane permeability tested in E-S-FLU drug inhibition assay

Drug	Toxic concentration (μM)	E-S-FLU IC_{50} (μM)
Terfenadine	12.5	1.1
Penfluridol	12.5	4.8
Perhexiline	25	2.5
Astemizole	25	11.2
Sertindole	25	4.7
Siramesine	12.5	7.5
Mefloquine	25	2.4
Cepharanthine	25	2.1
Chlorprothixene	50	14.0
Emetine	<0.2	<0.2
Clemastine	50	4.3
Chlorpromazine	50	6.3

Drugs are listed in the order of efficacy in killing A549 lung cancer and MCF7 breast cancer cells (personal communication with Marja Jäättelä)

We then tested the panel of 20 drugs representing different drug families that we characterised for inducing NPC-disease phenotype in section 4.3.4, although at different concentrations (Table 4.7). Fourteen out of the 20 drugs have CAD features (high LogP, high pKa^{base}). We used lysosomal galactin-3 (LGAL-3) staining as an indication of drug-induced lysosomal membrane permeability in MDCK-SIAT1 cells (Aits *et al.* 2015). The LGAL-3 staining experiment was performed by our collaborator Gokhan Yilmaz (Department of Pharmacology, University of Oxford). The MDCK-SIAT1 cells were treated with drugs for 3 hours or 48 hours. The concentration of each drug tested in the LGAL-3 assay was at least 2-fold above the IC_{50} for E-S-FLU (Table 4.7). Three hours is the same incubation time we normally used in virus inhibition assays before adding E-S-FLU to infect cells. Forty-eight hours is a prolonged treatment to check additional

effects caused by the drugs. After drug treatment, cells were fixed and stained with anti-galectin-3 antibody and scored for LGAL-3 puncta using confocal microscopy. Five random regions of more than 100 cells were scored, and the percentage of cells with more than 3 puncta per cell after drug treatment was calculated (Figure. 4.13). The experiment was repeated at least three times.

Table 4. 7 Drugs and conditions used in LGAL-3 assay

Drug	LGALS-3 assay (μM)	E-S-FLU IC_{50} (μM)	Proposed drug mechanism	LogP	pKa^{base}
Amiodarone	5	2.0	Calcium channel inhibitor	7.6	8.5
Arbidol	20	5.2	EBOV-GP binder	3.8	9.9
AY9944	20	7.8	Cholesterol synthesis inhibitor	5.8	9.4
Bepridil	10	2.7	Calcium channel inhibitor	5.2	9.2
Chloroquine	20	5.4	Proton ionophore	4.6	10.1
Clarithromycin	40	14.0	Antibiotic	3.2	8.4
Clomiphene	1	0.4	Estrogen receptor antagonist	7.2	9.3
E64	140	77.2	Cathepsin inhibitor	-1.1	11.3
EIPA	40	17.8	Macropinocytosis inhibitor	0.3	2.3
Itraconazole	2	NA	Anti-fungal	5.7	3.7
Imipramine	10	3.8	Anti-depressant	4.8	9.4
MDL28170	20	3.8	Calpain inhibitor	3.4	NA
Niclosamide	6	1.7	Proton ionophore	3.9	-4.4
Quinine	4	NA	Anti-malarial	3.4	9.1
Tetrandrine	6	1.6	Calcium channel inhibitor	6.5	8.3
Toremifene	0.4	0.2	Estrogen receptor antagonist	6.8	8.8
Triparanol	4	1.1	Cholesterol synthesis inhibitor	6.5	9.3
U18666A	10	2.6	NPC1 binder	4.7	9.4
Verapamil	20	10.6	Calcium channel inhibitor	3.8	9.7
Wortmannin	130	64.7	PI3K inhibitor	1.4	-3.2

NA in the "E-S-FLU IC_{50} (μM)" column: drugs did not inhibit E-S-FLU.
NA in the "pKa^{base}" column: no proton acceptor atoms (base) found.
Values coloured red: LogP values less than 2.5 and pKa^{base} values less than 6 (non-CAD features).

After a 3-hour drug treatment, amiodarone, arbidol, AY9944, imipramine and toremifene caused LGAL-3 puncta staining in more than 40% of the cells. Again, it is noteworthy that these five drugs had IC_{50} values less than 10 μM and were in

the most powerful 27% of screened drugs. Bepridil, chloroquine, niclosamide and tetrandrine showed subtle effects. The rest of the drugs did not cause LGAL-3 puncta formation (Figure 4.13 A). The result after 48-hour drug treatment was comparable to the result after 3-hour treatment. Exceptions were AY9944 and niclosamide, which showed less LGAL-3 puncta staining after 48-hour treatment; this was due to toxicity caused by the drugs after prolonged treatment, reducing the number of cells (Figure 4.13 B).

Together these results suggested a correlation between the 50% inhibition of E-S-FLU infection at less than 10 μM, and the induction of lysosomal permeability as detected by staining of LGAL-3 puncta. Not all CADs that inhibit EBOV entry cause lysosomal membrane permeability suggesting that this is not an absolute requirement for blockade of EBOV. These results are consistent with the CADs acting through an effect at the level of the lysosomal membrane, where they are known to integrate.

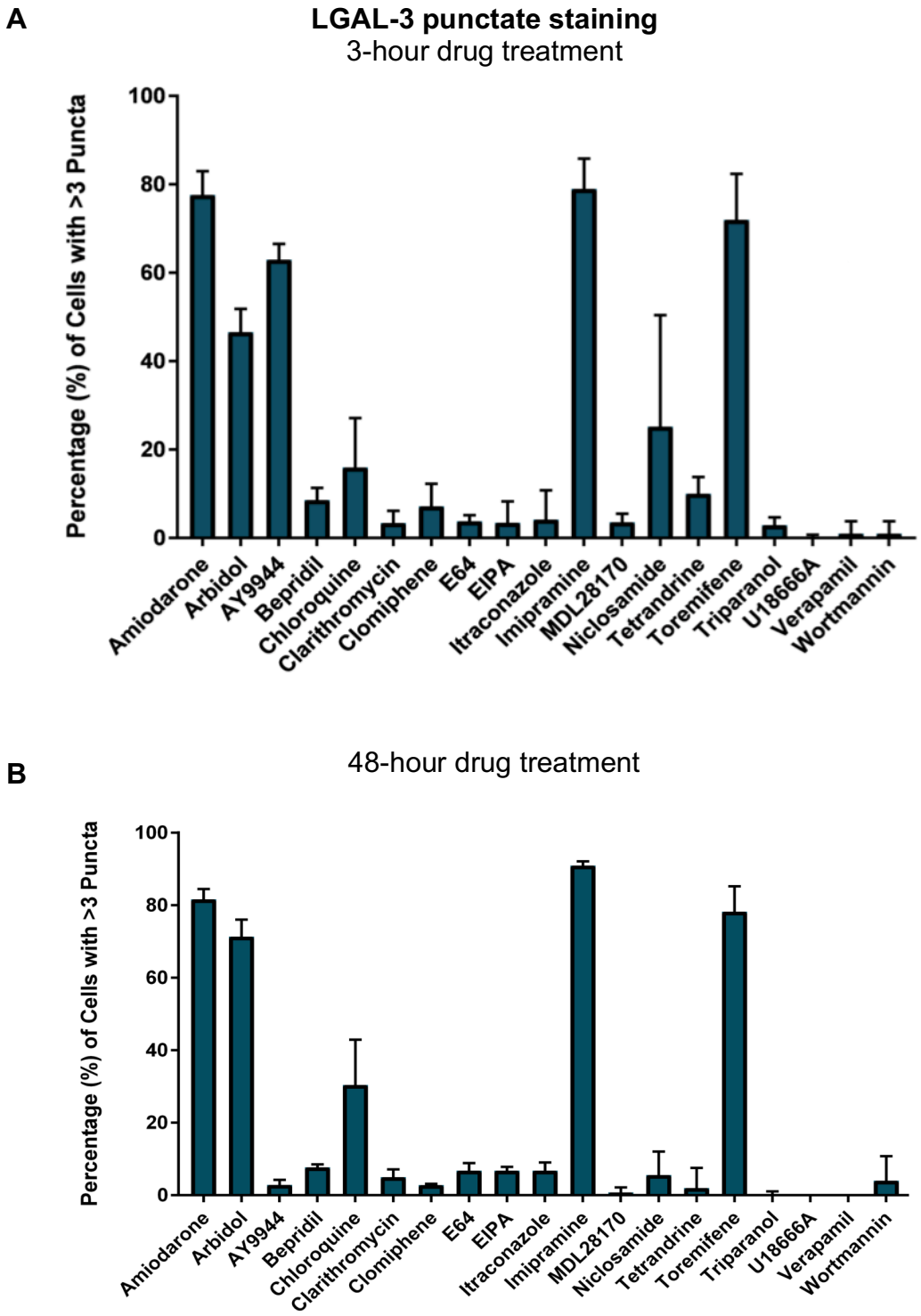


Figure 4. 13 LGAL-3 punctate staining in drug treated MDCK-SIAT1 cells
MDCK-SIAT1 cells treated with 20 drugs at concentrations stated in Table 4.7 for 3 hours (**A**) or 48 hours (**B**). Cells were fixed and stained with anti-galectin-3 antibody, followed by Alexa Fluor® 488-conjugated secondary antibody. Percentage of cells with at least 3 puncta observed was calculated from 5 random region of more than 100 cells. The experiment was repeated three times and the mean value is displayed with error bars representing the 95% confidence intervals.

4.4 Drug combinations and synergy

To investigate potential synergistic drug combinations, we tested 17 drugs in pairs: amiodarone, arbidol, AY9944, bepridil, chloroquine, clarithromycin, clomiphene, E64d (a derivative of E64), EIPA, imipramine, MDL28170, niclosamide, tetrandrine, toremifene, triparanol, U18666A and verapamil. Each drug was titrated individually for multiple times in the virus inhibition assay against E-S-FLU. Drugs were then tested in combinations of two based on the Bliss additivity method (Williams *et al.* 2012).

For each pair of drugs, e.g. drug A and drug B, drug A was held at a constant concentration [$A_{constant}$] at which E-S-FLU infection was inhibited by approximately 30%. Inhibition% by drug A alone at this constant concentration was measured as $I_{[Aconstant]}$%. Drug B was titrated to inhibit E-S-FLU in the presence or absence of drug A at concentration [$A_{constant}$]. At a given concentration of drug B [B], the measured Inhibition% by B alone was $I_{[B]}$%. The Bliss additivity equation calculates inhibition% by drug B + drug $A_{constant}$ = I^{Bliss}% = ($I_{[Bx]}$% + $I_{[Aconstant]}$%) - ($I_{[Bx]}$% X $I_{[Aconstant]}$%), assuming there was only an additive effect between the two drugs.

We then compared the experimental titration curve of drug B + drug $A_{constant}$ with the calculated predicted Bliss Additivity curve for drug B + drug $A_{constant}$. If drug A and drug B only are additive in their effects on inhibiting E-S-FLU, the experimental curve and the calculated curve would overlap. If two drugs “synergised” with each other, or had more than an additive effect in combination, there would be a difference between the two curves. In this thesis, the terms “synergy” or “synergise” were used to refer to an effect beyond addition. Figure 4.14 showed an example

of a synergic drug pair MDL28170 and chloroquine, where a shift from the calculated Bliss additivity curve to the experimental inhibition% curve was seen when either member of the pair was held constant.

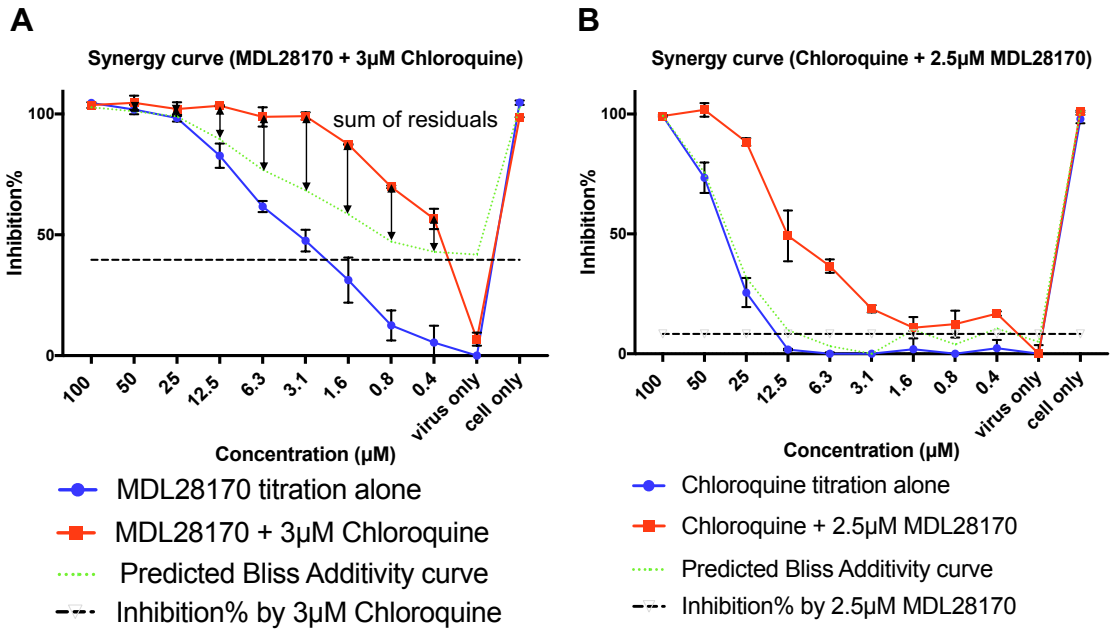


Figure 4. 14 Assay for synergy by drug combinations
A representative titration curve for a drug pair MDL28170 and chloroquine tested in the synergy drug inhibition assay. **A**: MDL28170 was titrated to inhibit E-S-FLU infection either alone (blue) or with 3 μM chloroquine (red). Drug titrations were done in technical duplicates, and the average percentage inhibition was plotted with the error bars representing the standard error of the mean. A predicted Bliss additivity titration curve (broken line, green) was calculated based on the MDL28170 titration curve and the inhibition% by 3 μM chloroquine alone. The additional inhibitory effect between the actual drug combination and the Bliss additivity curve was quantified by the sum of residuals (double headed arrows). **B**: Similar analysis was done in reverse, titrating chloroquine with (red) or without (blue) 2.5 μM MDL28170.

In total, 289 pairs were analysed using the method described above and all the pairs were tested twice. We calculated the sum of residuals by subtracting the I^{Bliss}% from the experimental measured Inhibition% of drug A + B (Figure 4.15). To select potential synergising drug pairs, we first removed the pairs that had a negative value of the sum of residuals (grey table units in Figure 4.16). For the remaining drugs, we multiplied the two sums of residuals from two synergy repeats and

applied an arbitrary synergy threshold value > 1000. Drug pairs that have shown a synergistic effect in both directions (i.e. titrating drug A with constant B and titrating drug B with constant A) repeatedly were marked out with double-headed arrows in Figure 4.16 and summarised in Table 4.8.

Table 4. 8 Potential synergistic drug combinations

Pair No.	Drug A	Drug B
1	Amiodarone	Imipramine
2	Arbidol	Toremifene
3	AY9944	Clarithromycin
4	AY9944	EIPA
5	AY9944	Imipramine
6	AY9944	Toremifene
7	AY9944	U18666A
8	Bepridil	Toremifene
9	Chloroquine	E64d
10	Chloroquine	MDL28170
11	Chloroquine	Toremifene
12	Triparanol	Toremifene
13	E64d	Tetrandrine
14	MDL28170	Tetrandrine
15	Triparanol	Tetrandrine
16	Triparanol	Clomiphene
17	Triparanol	U18666A

First synergy drug screen

Drugs	Amiodarone	Arbidol	AY9944	Bepridil	Chloroquine	Clarithromycin	Clomiphene	E64d	EIPA	Imipramine	MDL28170	Niclosamide	Tetrandrine	Toremifene	Triparanol	U18666A	Verapamil
Amiodarone	-54.5	2.5	-1.2	7.0	NA	-15.8	88.7	14.0	61.3	62.8	-19.6	31.8	NA	-18.8	-76.2	75.9	
Arbidol	38.4	3.6	7.8	39.8	NA	-70.7	97.8	-2.2	35.8	-124.4	-3.5	14.1	23.6	34.3	31.9	76.8	
AY9944	222.1	-32.6	-8.7	0.0	-27.8	167.8	115.2	17.9	54.6	25.1	167.5	-4.4	-13.3	106.0	57.0	61.4	
Bepridil	27.2	5.7	28.8	77.2	9.8	65.3	35.8	7.1	-102.0	-19.8	-98.6	-3.9	-25.4	94.6	73.3	83.9	
Chloroquine	10.4	-51.5	-10.6	14.0	2.6	72.9	-76.6	47.5	10.8	-16.9	18.8	20.0	-10.8	28.5	-54.1	32.5	
Clarithromycin	40.1	78.8	40.5	-20.0	48.9	4.2	14.5	47.5	-35.8	-66.4	-98.1	4.6	-66.6	59.3	116.3	96.7	
Clomiphene	-43.9	-70.8	49.9	-24.5	-20.9	8.9	39.4	-45.7	64.4	17.1	-50.4	-18.7	7.3	54.1	85.5	72.5	
E64d	95.2	87.5	66.2	-53.5	110.7	71.6	25.5	127.9	-66.3	-29.3	53.3	24.3	147.4	-44.8	129.4	95.6	
EIPA	202.8	-78.3	26.0	11.6	185.4	11.7	-154.4	-29.0	16.5	56.0	-89.5	22.0	-47.7	24.4	33.6	52.2	
Imipramine	57.0	-17.3	34.9	-12.3	113.4	31.8	8.1	82.2	-56.7	-37.9	-31.8	17.5	-101.9	75.1	86.7	81.2	
MDL28170	9.5	-9.7	113.7	-42.5	139.0	15.0	-102.6	43.7	-2.1	47.6	-20.6	24.4	234.2	22.5	66.2	-12.3	
Niclosamide	-5.1	6.5	-30.4	-2.3	-58.4	-28.3	-45.8	48.1	-1.2	8.6	34.7	-5.0	6.6	83.8	-8.2	-50.4	
Tetrandrine	91.5	-48.2	39.8	-9.7	72.0	58.5	24.6	39.9	55.9	68.1	158.7	7.9	52.9	18.5	75.0	110.1	
Toremifene	-24.8	23.0	74.4	70.2	51.8	3.6	-8.1	-15.2	6.5	25.1	-62.9	18.0	14.9	23.2	91.3	177.7	
Triparanol	-2.1	-39.1	21.1	-127.0	-42.8	108.8	86.2	49.4	97.2	40.5	-29.0	-15.0	72.1	57.8	-69.3	57.2	
U18666A	38.5	19.8	21.6	28.3	8.3	42.2	46.6	33.0	-3.2	21.4	26.2	10.8	105.7	26.1	62.5		
Verapamil	14.0	38.2	-136.2	33.0	17.2	-24.7	NA	83.3	86.9	86.9	19.1	14.7	-119.8	108.5	64.1	54.1	

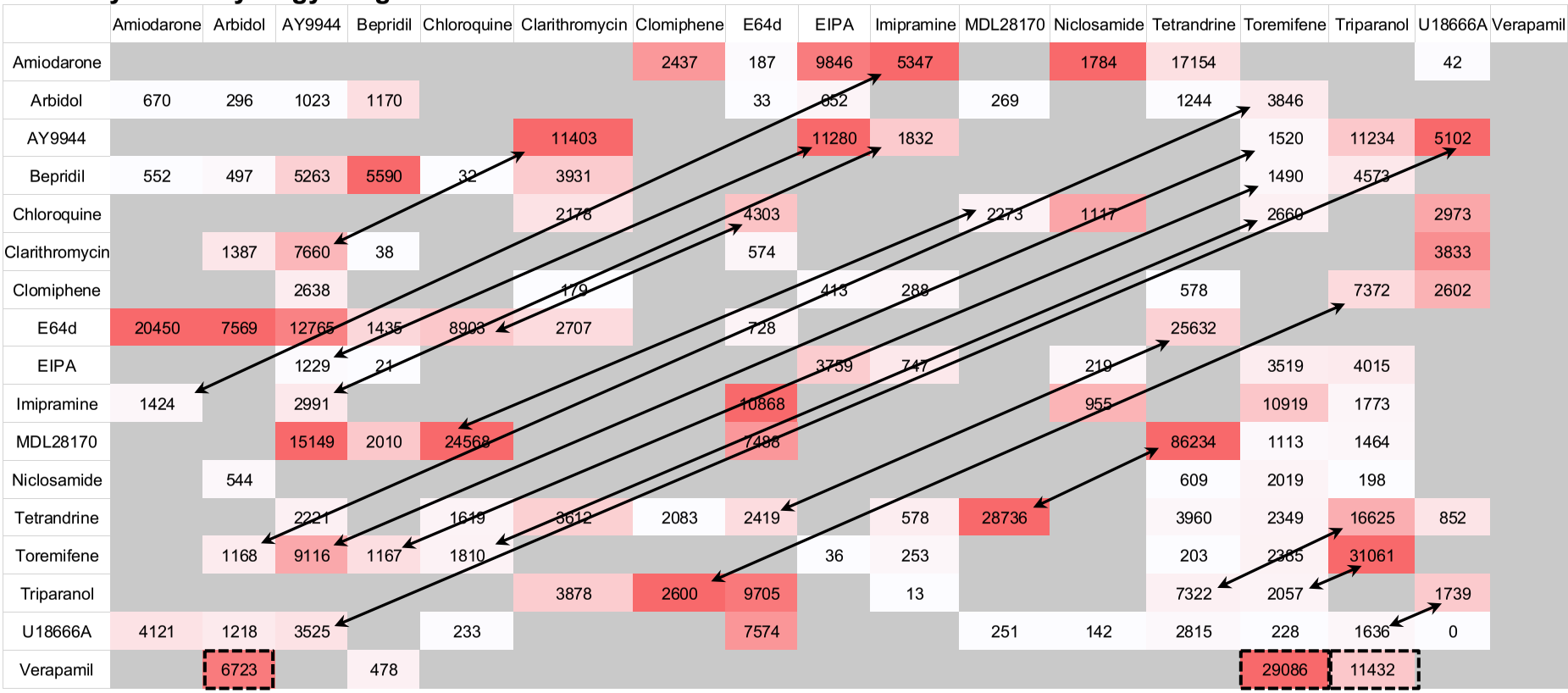
Second synergy drug screen

Drugs	Amiodarone	Arbidol	AY9944	Bepridil	Chloroquine	Clarithromycin	Clomiphene	E64d	EIPA	Imipramine	MDL28170	Niclosamide	Tetrandrine	Toremifene	Triparanol	U18666A	Verapamil
Amiodarone	-33	-50	163	-8	-126	-63	27	13	161	85	121	56	214	164	50	1	
Arbidol	17	82	132	29	-41	42	-50	-15	18	-45	-76	-74	53	112	-39	-22	
AY9944	-51	-33	100	63	-211	68	-9	-74	207	73	-49	21	174	14	NA	83	
Bepridil	20	87	183	72	3	60	-8	-70	25	-18	-127	-130	52	16	62	-7	
Chloroquine	-247	-50	-105	-17	-76	30	-84	91	-132	-25	121	56	173	93	-44	92	
Clarithromycin	-90	18	189	-2	-22	-44	-259	12	-231	-25	-76	-68	50	-16	-38	40	
Clomiphene	-135	33	53	15	-68	20	-5	-104	6	17	-49	59	79	-10	86	36	
E64d	215	87	193	-27	80	38	-114	6	-283	-129	-127	-19	174	-193	-50	-22	
EIPA	-22	-64	47	2	-141	-28	-15	-9	NA	13	20	10	169	144	119	-6	
Imipramine	25	42	86	11	-124	-59	-25	132	NA	-27	3	55	233	145	20	-72	
MDL28170	-139	55	133	-47	177	-27	-94	171	-184	-29	0	-19	368	49	22	-18	
Niclosamide	102	84	13	13	79	5	-6	-25	-54	-6	-56	62	92	24	-24	12	
Tetrandrine	-47	-19	56	8	22	62	85	61	-27	8	181	-39	75	127	222	8	
Toremifene	35	51	123	17	35	-7	83	-25	6	10	-157	-122	14	103	340	-13	
Triparanol	37	86	-4	34	-25	36	30	NA	-6	0	62	93	102	36	83	30	
U18666A	107	62	163	-11	28	-4	19	NA	26	-42	10	13	27	9	26	9	
Verapamil	-286	176	-66	14	-1	-40	-107	NA	-82	0	-66	-183	-10	268	178	-12	

Figure 4. 15 Synergy drug screen results

17 drugs were tested in 289 pairs in synergy drug inhibition assay against E-S-FLU infection. Drugs listed in the first column were titrated with or without a second drug (header row) held at a constant concentration, which alone partially inhibited E-S-FLU infection. Sum of residuals were calculated between the measured inhibition% and calculated Bliss additivity curve for each drug combination, and in two repeated screens. A continuous colour-scaled formatting was applied for each column, with red indicating higher positive values and blue the lower negative values. “NA” or empty units indicate the experimental values that are missing.

Summary of two synergy drug screens



	Amiodarone	Arbidol	AY9944	Bepridil	Chloroquine	Clarithromycin	Clomiphene	E64d	EIPA	Imipramine	MDL28170	Niclosamide	Tetrandrine	Toremifene	Triparanol	U18666A	Verapamil
Amiodarone							2437	187	9846	5347		1784	17154			42	
Arbidol	670	296	1023	1170				33	652		269		1244	3846			
AY9944						11403			11280	1832				1520	11234	5102	
Bepridil	552	497	5263	5590	32	3931								1490	4573		
Chloroquine						2178		4303			2273	1117		2660		2973	
Clarithromycin		1387	7660	38				574								3833	
Clomiphene			2638			179			413	288			578		7372	2602	
E64d	20450	7569	12765	1435	8903	2707		728					25632				
EIPA			1229	21					3759	747		219		3519	4015		
Imipramine	1424		2991					10868				955		10919	1773		
MDL28170			15149	2010	24568			7488					86234	1113	1464		
Niclosamide		544											609	2019	198		
Tetrandrine			2221		1619	3612	2083	2419		578	28736		3960	2349	16625	852	
Toremifene		1168	9116	1167	1810				36	253			203	2365	31061		
Triparanol						3878	2600	9705		13			7322	2057		1739	
U18666A	4121	1218	3525		233			7574			251	142	2815	228	1636	0	
Verapamil		6723		478										29086	11432		

Figure 4. 16 Summary of two synergy drug screens

The multiplication of corresponding sums of residual values from two synergy screens were calculated and displayed in the diagram. Negative values (i.e. no synergy effect in one or both screens) were removed and displayed as grey boxes. Drug combinations that showed a synergistic effect in both directions (> 1000 in the table) were selected and indicated by double-headed arrows. Verapamil synergy titration experimental data was incomplete and three potential synergistic pairs with verapamil are marked by broken lines.

4.5 Discussion and future work

Ebola virus (EBOV) is a filamentous virus that infects humans and causes Ebola virus disease (EVD) with a high mortality rate (Emond *et al.* 1977; Burke, Declerq and Ghysebrechts 1978; Martines *et al.* 2014; Center for Disease Control and Prevention 2018). Currently there are no FDA approved vaccines or therapeutics available to treat EBOV infection. Since 2014, the development of EBOV-specific therapeutics such as convalescent plasma (Mupapa *et al.* 1999; van Griensven *et al.* 2016; Sahr *et al.* 2017) and antibody cocktails (Qiu *et al.* 2014; Corti *et al.* 2016; Davey *et al.* 2016) has been encouraged by the WHO, and some have been put forward to test in small clinical trials to treat EBOV under the fast-track regulation and Monitored Emergency Use of Unregistered and Investigational Interventions statement (MEURI). In addition to that, many research groups have attempted to repurpose approved drugs to treat EBOV (Johansen *et al.* 2013, 2015; Shoemaker *et al.* 2013; Gehring *et al.* 2014; Kouznetsova *et al.* 2014; Cheng *et al.* 2015; Ekins and Coffee 2015; Long *et al.* 2015; Madrid *et al.* 2015; Xiao *et al.* 2018).

There are many apparent advantages of using already approved drugs, as they have better clinical and pharmacokinetics records, and they can be available quickly due to the mature production and distribution lines. On the other hand, there are also hurdles to overcome to use these “old” drugs in an EBOV epidemic. First and foremost, although many FDA approved drugs showed an inhibitory effect against EBOV *in vitro,* their mechanisms of action remain unknown. Furthermore, the dose of drugs required to protect in animal models of EBOV infection was very high (Johansen *et al.* 2013; Dowall *et al.* 2015; Falzarano *et al.* 2015; Herbert *et al.* 2015; Madrid *et al.* 2015). In this chapter, we intended to try

to find solutions to these challenges with the new EBOV-GP pseudotyped virus E-S-FLU we developed and described in the previous chapter.

4.5.1 E-S-FLU is a useful tool for drug screens

E-S-FLU is a non-replicating Influenza pseudotyped virus coated with full-length EBOV-GP. Previously, we have shown that E-S-FLU is a useful surrogate for studying EBOV in *in vitro* studies. Here, we have screened 1,280 drugs from the LOPAC®1280 library to identify pharmacologically active small molecules that inhibit cell entry of E-S-FLU. H5-S-FLU virus was tested in parallel with E-S-FLU virus to differentiate between inhibition specific to EBOV-GP and to the S-FLU virus core. We identified 215 molecules from the library that inhibit the E-S-FLU virus, whereas only 22 inhibit the H5-S-FLU virus, all of which also inhibit the E-S-FLU virus.

We compared our screening results with those of Johansen *et al.*, who screened 2,635 small molecules against eGFP-expressing EBOV (Johansen *et al.* 2015). A total of 538 small molecules were common to the two libraries (Johansen's screen versus LOPAC®1280). Out of these, 442 molecules had concordant results in the two screens. The correlation was statistically significant ($P < 0.0001$). This reassured us of the validity of using E-S-FLU in high-throughput drug screening assays.

It is noteworthy that we found at least 15 calcium flux modulators that inhibited E-S-FLU virus infection. Independent evidence exists for a possible role for calcium channels in the lysosomal membrane in viral entry (Gehring *et al.* 2014; Sakurai

et al. 2015; Simmons *et al.* 2016; Fan *et al.* 2017), perhaps through an effect on membrane fusion (Suárez *et al.* 2003; Carette *et al.* 2011). Recent studies have suggested that two-pore channel 2 (TPC2), an endo/lysosomal calcium channel, is involved in the EBOV entry process, and this could be the target of the calcium channel inhibitors (Sakurai *et al.* 2015). We further investigated the relationship between calcium channel inhibitors and EBOV infection in Chapter 6.

One advantage of our E-S-FLU pseudotyped virus is that infected cells express eGFP and fluoresce brightly. Visual inspection of cells in assay plates by fluorescence microscopy revealed that two forms of inhibition could be distinguished. In most cases, the drugs reduced the number of infected cells. All the drugs that inhibited E-S-FLU but not H5-S-FLU, belong to this category, suggesting that they prevent viral entry (Appendix Table 4. X1). In contrast, in some cases, the drugs did not reduce the number of infected cells but reduced the intensity of fluorescence expression in the infected cell population. Of the 228 inhibitors tested (215 from LOPAC®1280 library plus 13 additional inhibitors), 12 reduced the fluorescence intensity and we named this the “dimmer effect” (Table 4.2).

These drugs also inhibited H5-S-FLU virus in the same manner. In general, the IC_{50} values of these agents were similar for the E-S-FLU and H5-S-FLU viruses, which is consistent with action on functions controlled by the Influenza virus core, which is common to both. We suggest that they affect the virus at a post-entry level like Favipiravir (T-705), a specific inhibitor of RNA-dependent RNA polymerase that was initially synthesised to inhibit Influenza virus, but later found

to be effective against EBOV *in vitro* (Furuta *et al.* 2013; De Clercq 2014; Oestereich *et al.* 2014; Nagata *et al.* 2015; Sissoko *et al.* 2016). In addition, aminopterin, a dihydrofolate reductase inhibitor; brequinar, a dihydroorotate dehydrogenase inhibitor (Liu *et al.* 2000; McLean *et al.* 2001; Hoffmann *et al.* 2011; Lucas-Hourani *et al.* 2013); and ribavirin, a guanosine analogue nucleoside inhibitor (Eriksson *et al.* 1977; Adinolfi *et al.* 2003; Nguyen *et al.* 2010), may affect transcription indirectly by blocking the biosynthesis of nucleotides. It is interesting that spironolactone and triamterene both cause the “dimmer” effect. These drugs are used clinically as diuretics that block sodium channels. It is unclear how they can affect the functions of the Influenza virus core at a post-entry level.

Of the 24 drugs that inhibited both the H5-S-FLU and E-S-FLU viruses, 12 were “dimmer” drugs, and the rest reduced the number of infected cells and thus may have inhibited cell entry by both H5 HA and EBOV-GP (Table 4.2, “reduced” effect). Of these, chloroquine (also a CAD) and niclosamide may have acted by reducing the endosomal and lysosomal proton concentration, which can influence the efficiency of digestion of EBOV-GP by cathepsins that requires acidic pH to be proteolytically active (Takada *et al.* 1997; Wool-Lewis and Bates 1998; Markosyan *et al.* 2016). Niclosamide is a proton ionophore (Jurgeit *et al.* 2012; Rajamuthiah *et al.* 2015) and had similar IC_{50} values for inhibition of H5-S-FLU virus (3.3 μM) and E-S-FLU virus (1.7 μM) entry.

4.5.2 Long-QT: a side effect to watch out for in treating EBOV

We have identified 228 drugs that inhibited E-S-FLU infection *in vitro*, 215 from the LOPAC®1280 library and 13 additional drugs tested (Appendix Table 4. X1). Many

of these drugs have been found to have a risk of causing long-QT syndrome, such as amiodarone, toremifene, and clarithromycin (Ayad *et al.* 2010; Svanström *et al.* 2014). Inhibition of the potassium channel hERG (human ether-a-go-go) in cardiac myocytes is commonly associated with long-QT syndrome (Foo *et al.* 2016). By comparing the 228 drugs that inhibited the E-S-FLU virus in our studies with the hERG screening literature and the list of known long-QT drugs (De Bruin *et al.* 2005; Dennis *et al.* 2007; Ayad *et al.* 2010; Lounkine *et al.* 2012; Foo *et al.* 2016; CredibleMeds 2019), we identified 62 drugs (27.2%; indicated in Appendix Table 4. X1) that may risk causing a prolonged QT interval in patients. Most of these hERG binders are typical cationic amphiphilic drugs (CADs).

It is unclear whether the features that inhibited EBOV entry also predisposed to effect on hERG binding and lengthen the QT interval. After consulting Professor Derek Terrar (Department of Pharmacology, University of Oxford), we tested two classical hERG binders: dofetilide (Carmeliet *et al.* 1998; Perry 2006) and E-4031 (Clay *et al.* 1995; Vandenberg *et al.* 2012) in our virus inhibition assay. Dofetilide and E-4031 are known to block hERG channel at the nanomolar range of concentrations. Neither of them inhibited E-S-FLU up to a concentration of 200 μM. We therefore suggest that the long-QT feature found in EBOV inhibitors is an undesirable side-effect. This should be taken into consideration before administering drugs, such as amiodarone, to EBOV infected patients (Turone 2014; Gupta-Wright, Lavers and Irvine 2015).

4.5.3 CADs vs. EBOV: what is the target?

In agreement with the current literature on EBOV inhibitors, we found that many drugs from different pharmacological groups inhibited EBOV entry *in vitro*. The majority of them have a cationic amphiphilic feature (CADs), being hydrophobic at one end, and a weak base at the other end (high LogP and high pKa^{base}). The mechanism by which these drugs inhibit EBOV entry has not been resolved. Here we would like to discuss four main hypotheses based on our current findings and the literature in the field (Shoemaker *et al.* 2013).

The first three hypotheses suggest that the CADs are interacting with EBOV entry at the point of the lysosome. Since 1974, the term “lysosomotropic agents” has been used to describe drugs with cationic amphiphilic features that concentrate in the acidic environment of the lysosome (De Duve *et al.* 1974; Liscum, Ruggiero and Faust 1989; Marceau *et al.* 2012; Logan *et al.* 2014; Lu *et al.* 2017). The weak unprotonated base being an uncharged lipophilic molecule at pH 7, travels through the lysosomal membrane and becomes positively charged and “trapped” in the low pH lysosomal luminal membrane. It is now well-accepted that EBOV-GP binds to the NPC1 protein and fuses with the lysosomal membrane to release viral proteins and genes to the cytosol (Figure 4.17), and therefore CADs may interrupt EBOV entry at this stage.

Hypothesis 1: CADs that bind NPC1 directly or indirectly affect EBOV-GP binding to the NPC1 protein (Figure 4.18). NPC1 protein is a multi-pass transmembrane protein that locates in the late endosomal/lysosomal membrane (Higgins *et al.* 1999; Neufeld *et al.* 1999). The exact function of NPC1 is unknown. However, it is

often described as the cholesterol transporter, based on the observation that NPC1 dysfunction often leads to accumulation of unesterified cholesterol in the lysosome (Kruth *et al.* 1986; Vanier 2010). More recently, it was found that NPC1 mutations also cause accumulation of sphingosine, sphingomyelin, glycosphingolipids as well as depleting the calcium store in the lysosome (Lloyd-Evans *et al.* 2008; Höglinger *et al.* 2015).

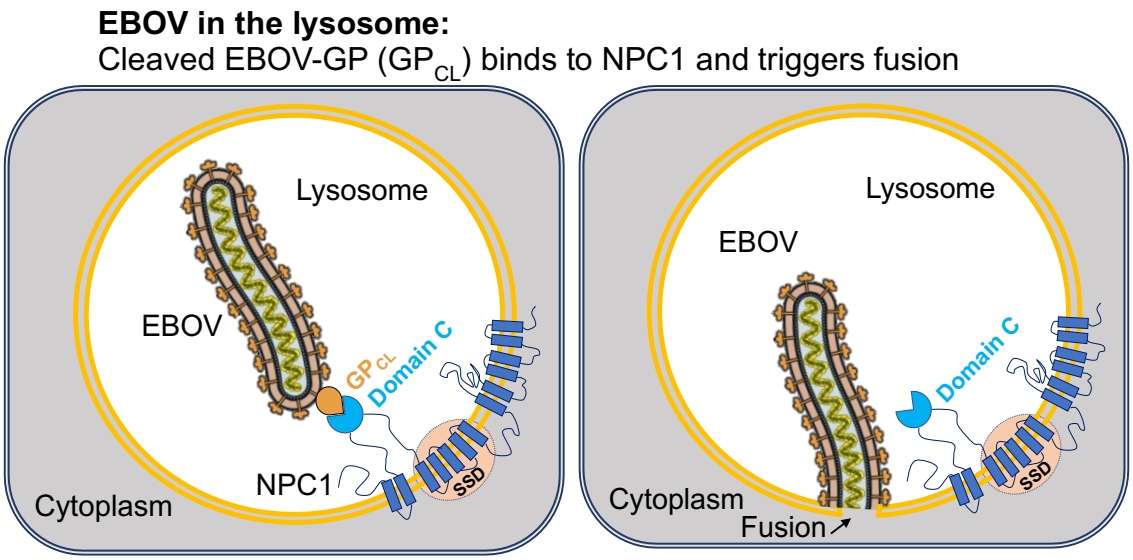


Figure 4. 17 EBOV entry in the lysosome
Schematic diagrams showing the mechanism of EBOV entry in the lysosome. The cleaved EBOV-GP (GP_{CL}) binds to the NPC1 C domain in the lysosome, and triggers membrane fusion between EBOV envelope and lysosomal membrane and subsequently the release of viral nucleocapsid to the host cytoplasm. SSD: sterol-sensing domain.

The NPC1 protein is the key receptor for EBOV entry at the lysosomal membrane (Carette *et al.* 2011; Côté *et al.* 2011; Miller *et al.* 2012a; Herbert *et al.* 2015) (Figure 4.17). There are at least two sites in NPC1 protein where drugs may interact. One site is in domain C, compounds binding here directly block NPC1 binding to EBOV-GP (Côté *et al.* 2011; Miller *et al.* 2012a; Basu *et al.* 2015; Wang *et al.* 2016). These molecules also caused punctate filipin staining, which indicates

the accumulation of unesterified cholesterol in the lysosome (Côté *et al.* 2011; Basu *et al.* 2015), suggesting that they may affect normal NPC1 function.

The other drug binding site on NPC1 is the sterol-sensing domain. Drugs that showed evidence of binding are astemizole, cepharanthine, U18666A, itraconazole and posaconazole (Lu *et al.* 2015; Head *et al.* 2017; Lyu *et al.* 2017, 2018; Trinh *et al.* 2017). Drug binding at this site may have affected NPC1 and EBOV-GP interaction indirectly. The first three drugs are CADs based on LogP > 2.5 and pKa^{base} > 6 criteria, and the two triazole drugs itraconazole and posaconazole were non-CADs (pKa^{base} ~ 4, Figure 4.8). We showed that astemizole, cepharanthine, and U18666A inhibited E-S-FLU entry, whereas posaconazole and itraconazole did not. Itraconazole was also tested by Johansen *et al.*, and it did not inhibit a recombinant GFP expressing EBOV (Johansen *et al.* 2015). Posaconazole, on the other hand, inhibited the entry of EBOV virus-like particles (VLPs) reported by Kouznetsova *et al.* (Kouznetsova *et al.* 2014; Sun *et al.* 2017).

The IC_{50} of U18666A for inhibition of EBOV entry was about 1000-fold higher than its binding affinity to NPC1 (μM vs. nM) (Cenedella 2009; Carette *et al.* 2011; Lu *et al.* 2015). This also suggested that drug binding to the NPC1 sterol-sensing domain may not be sufficient for blocking EBOV entry. Moreover, the NPC1 C domain can be expressed in isolation and still provides a receptor function for EBOV entry (Miller *et al.* 2012a). It would be interesting to see if cells expressing the isolated C domain, without the sterol-sensing domain, are still susceptible to

the action of CADs, particularly those that are known to bind the sterol-sensing domain.

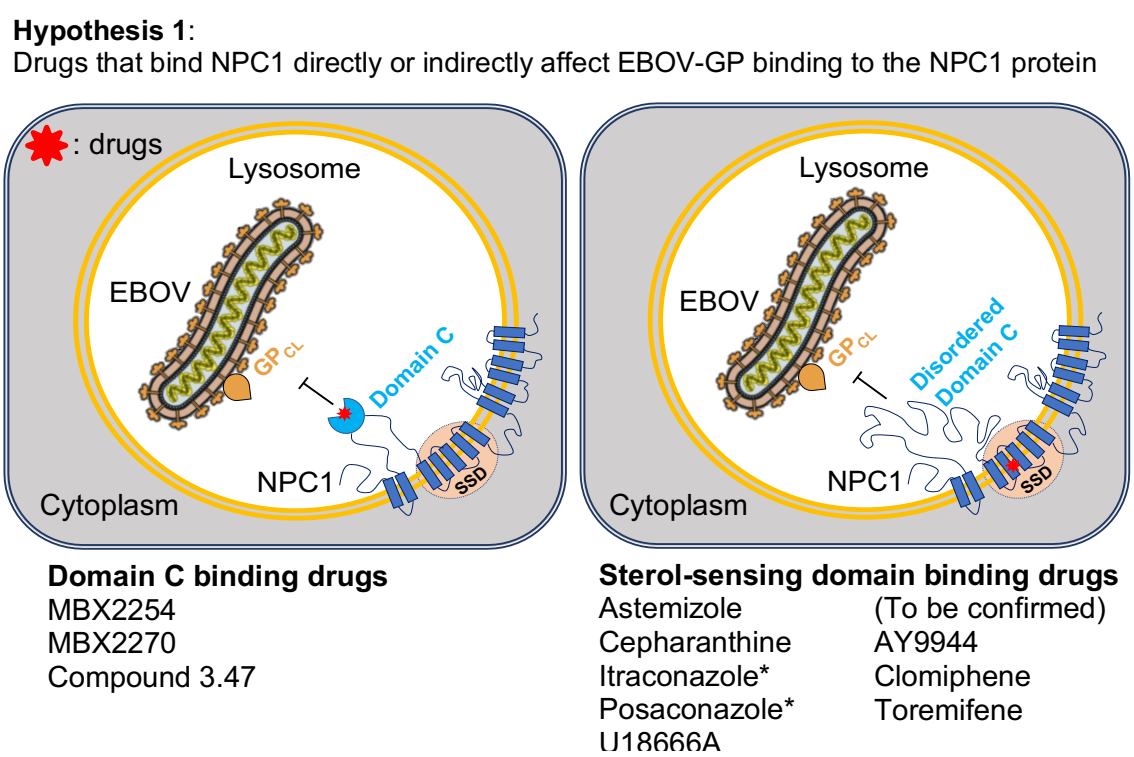


Figure 4. 18 Drug inhibition mechanism 1: NPC1 binding drugs
Schematic diagram showing the potential mechanism of NPC1-binding drugs inhibiting EBOV entry. Drugs that bind to NPC1 protein domain C block cleaved EBOV-GP (GP_{CL}) binding directly (left panel). Drugs that bind to NPC1 sterol-sensing domain (SSD) may indirectly alter the conformation of domain C and inhibit EBOV-GP binding (right). Drugs that are known NPC1 binders are listed below the diagrams. *: itraconazole and posaconazole did not inhibit E-S-FLU infection. We demonstrated that AY9944, clomiphene and toremifene induced a similar NPC phenotype profile as U18666A and itraconazole in this study, suggesting that they may be NPC1 binding drugs.

Hitherto, all of the NPC1 binding drugs also induced an NPC disease-like phenotype in cells *in vitro*. Several groups showed that other EBOV inhibiting CADs may also induce the NPC phenotype, but most of them were only shown to elevate the level of cellular or lysosomal cholesterol (Rodriguez-Lafrasse *et al.* 1990; Carette *et al.* 2011; Shoemaker *et al.* 2013; Fan *et al.* 2017; Sun *et al.* 2017). However, drugs can induce cholesterol accumulation independently from NPC1, and hence it is insufficient to draw the link between CADs and NPC1 on this test

alone. To better establish the relationship among CADs, NPC1 and EBOV infection, we began to build up a more complete NPC-related biochemical profile for a panel of drugs that inhibited EBOV, including accumulation of sphingosine, sphingomyelin, unesterified cholesterol and calcium storage, based on Lloyd-Evans *et al.* (2008). This work was done in collaboration with Fran Platt, Antony Galione and Doris Höllinger's group and is ongoing.

Some typical CADs that inhibited E-S-FLU entry such as imipramine, amiodarone, verapamil and chloroquine scored positive in the filipin staining but did not show a full NPC phenotype profile. We therefore suggested that not all CADs interacted directly with NPC1. Five drugs did induce the full NPC disease phenotype, of which four are typical CADs: AY9944, clomiphene, U18666A and toremifene, and one itraconazole is not a CAD. U18666A is the best characterised NPC phenotype inducer (Lloyd-Evans *et al.* 2008) and both U18666A and itraconazole were shown to bind NPC1 protein at the sterol-sensing domain (Lu *et al.* 2015; Head *et al.* 2017). It is noteworthy that itraconazole, the only non-CAD of these five drugs, despite inducing a complete NPC phenotype, did not inhibit E-S-FLU infection. We conclude that direct binding of drugs to the NPC1 sterol sensing domain does not correlate well with inhibition of E-S-FLU infection.

Hypothesis 2: CADs concentrate in the lysosome and target other host proteins that are essential for EBOV entry (Figure 4.19). The lysosome contains many proteins that are involved in digesting macromolecules and transporting them within the cell. Accumulation of CADs in the lysosomal membrane creates stress and affects lysosome homeostasis (Liscum, Ruggiero and Faust 1989; Marceau

et al. 2012; Kuzu *et al.* 2017; Lu *et al.* 2017). In addition to NPC1, there may be other proteins that are required for EBOV cell entry. One candidate is acid sphingomyelinase (ASM). Charged CADs that are trapped in the luminal side of the lysosomal membrane, inhibit ASM by dissociating it from the membrane. These CADs were described by Kornhuber *et al.* as Functional Inhibitors of Acid SphingoMyelinase (FIASMAs) (Kornhuber *et al.* 2008, 2010; Miller *et al.* 2012b; Johansen *et al.* 2013; Fan *et al.* 2017). Another candidate is an endo/lysosomal calcium channel two-pore channel 2 (TPC2) (Sakurai *et al.* 2015; Simmons *et al.* 2016; Penny *et al.* 2018). We further studied these candidates in detail in Chapter 5 and 6 through a genetic knockout approach.

Hypothesis 2:
CADs concentrate in the lysosome and target other host proteins that are essential for EBOV entry

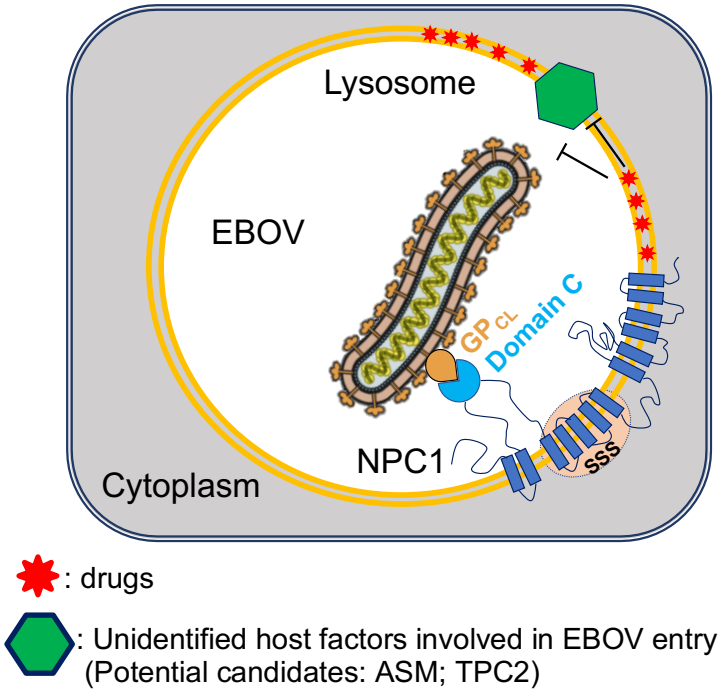


Figure 4. 19 Drug inhibition mechanism 2: additional host target
Cationic amphiphilic drugs are known to concentrate in the lysosomal membrane. This affects lysosome homeostasis and inactivates host factors that may be essential for EBOV-GP dependent entry. Potential host factors involved are acid sphingomyelinase (ASM) and calcium channel two-pore channel 2 (TPC2) that are localised in the late endosome/lysosome. GP_{CL}: cathepsin cleaved GP; SSD: sterol-sensing domain.

Hypothesis 3: CADs inhibit EBOV entry through an effect on the lysosomal membrane (Figure 4.20). In the field of cancer research, CADs are repurposed to be potential chemotherapeutics, as some cancer cells are sensitive to cytotoxic lysosomotropic agents (Ostenfeld *et al.* 2008; Jahchan *et al.* 2013; Petersen *et al.* 2013; Sukhai *et al.* 2013; Shchors, Massaras and Hanahan 2015; Dielschneider *et al.* 2016; Kuzu *et al.* 2017). Our collaborator Marja Jäättelä (Danish Cancer Society Research Centre) showed that a group of antihistamine CADs, which induced lysosomal cell death in non-small cell lung cancer (NSCLC) also caused increased lysosomal membrane permeability (Ellegaard *et al.* 2016).

We tested the link between EBOV inhibiting CADs and lysosomal membrane permeability in two approaches. First and foremost, we selected the 12 most cytotoxic antihistamine CADs based on Jäättelä̈'s experiment with cancer cells (personal communication) and tested them to inhibit E-S-FLU infection. Eleven of 12 inhibited E-S-FLU, but not H5-S-FLU *in vitro* (emetine was too toxic to test). Some of them have never before been described as EBOV inhibitors, such as sertindole, penfluridol and siramesine, and they all had IC_{50} values less than 10 μM. Notice that astemizole and cepharanthine, the two recently described NPC1 binders are also in the list of drugs causing lysosomal membrane permeability (Lyu *et al.* 2017, 2018).

Secondly, we tested a list of EBOV inhibiting CADs for their effect on inducing lysosomal membrane permeability by galectin-3 puncta staining assay (Aits *et al.* 2015; Ellegaard *et al.* 2016). Six out of 14 CADs tested induced lysosomal membrane permeabilisation to some level: amiodarone, arbidol, AY9944,

chloroquine, imipramine and toremifene. While these results are not definitive, it is clear that CADs that increase lysosomal membrane permeability are very likely to inhibit E-S-FLU entry.

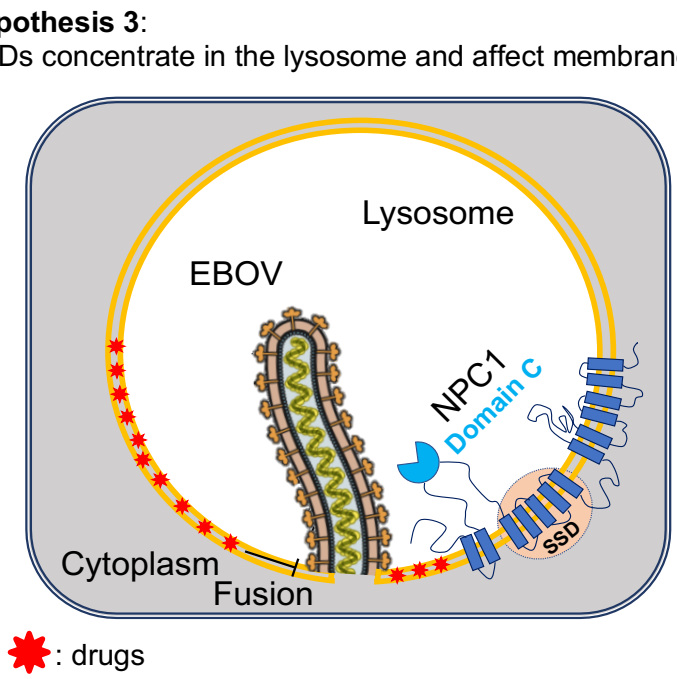


Figure 4. 20 Drug inhibition mechanism 3: target membrane fusion
Lysosomotropic CADs affect EBOV-GP membrane fusion by altering membrane electrostatic environment and disrupting membrane integrity. This effect could independently inhibit other proteins associated with the lysosomal membrane, such as NPC1, two-pore channels (TPCs) and acid sphingomyelinase (ASM). SSD: sterol-sensing domain.

Hypothesis 4: CADs bind to the luminal domain of EBOV-GP to destabilise the viral protein before fusion. David Stuart's group (Division of Structural Biology, University of Oxford) has identified a potential binding site for drugs in the EBOV-GP in a co-crystal structure with toremifene (Zhao *et al.* 2016). Since then, the group has also found evidence for several other CADs binding directly to EBOV-GP (Ren *et al.* 2018; Zhao *et al.* 2018; Shaikh *et al.* 2019). The pocket in EBOV-GP could accommodate different hydrophobic structures, and this opens up a possible new explanation for how drugs inhibit EBOV entry. We will describe our

collaboration with Stuart's group in studying EBOV-GP binding drug mechanisms in Chapter 7.

4.5.4 Synergistic drug combinations for treating EBOV

It is very common to use drug combinations to treat infectious diseases in the clinic (Worthington and Melander 2013; Abramowicz, Zuccotti and Pflomm 2015; Cui *et al.* 2015; Samuel, Winston and Peters 2015). It lowers the chance of selecting drug resistant mutants, as well as often reducing the drug doses needed to give the same efficacy. Right now, there are more than 10,000 FDA ongoing clinical trials testing drug combinations for various diseases (Nature Medicine 2017). Often drug combinations are found by random high-throughput screening. However, the more we understand the drug mechanisms, the more rationale design we can do.

In the current literature, two groups have conducted synergy drug screens to inhibit EBOV. Sun *et al.* identified two sets of three-drug combinations: 1. toremifene – mefloquine – posaconazole; 2. toremifene – clarithromycin – posaconazole (Sun *et al.* 2017). Dyall *et al.* identified 4 highly synergistic pairs: 1. aripiprazole – piperacetazine; 2. sertraline – toremifene; 3. sertraline – bepridil; and 4. amodiaquine - clomiphene (Dyall *et al.* 2018). These drugs are all CADs, and most of them have the undesirable long-QT side effect. We sought to identify drug combinations acting through more diverse mechanisms.

We selected 17 drugs likely to involve different inhibitory mechanisms and began to test for drug combinations that may have better EBOV inhibition efficacy than single drug treatment *in vitro*. After the initial screening, we identified 17 synergistic

drug pairs that showed more than additive effect based on Bliss additivity theory (Williams *et al.* 2012).

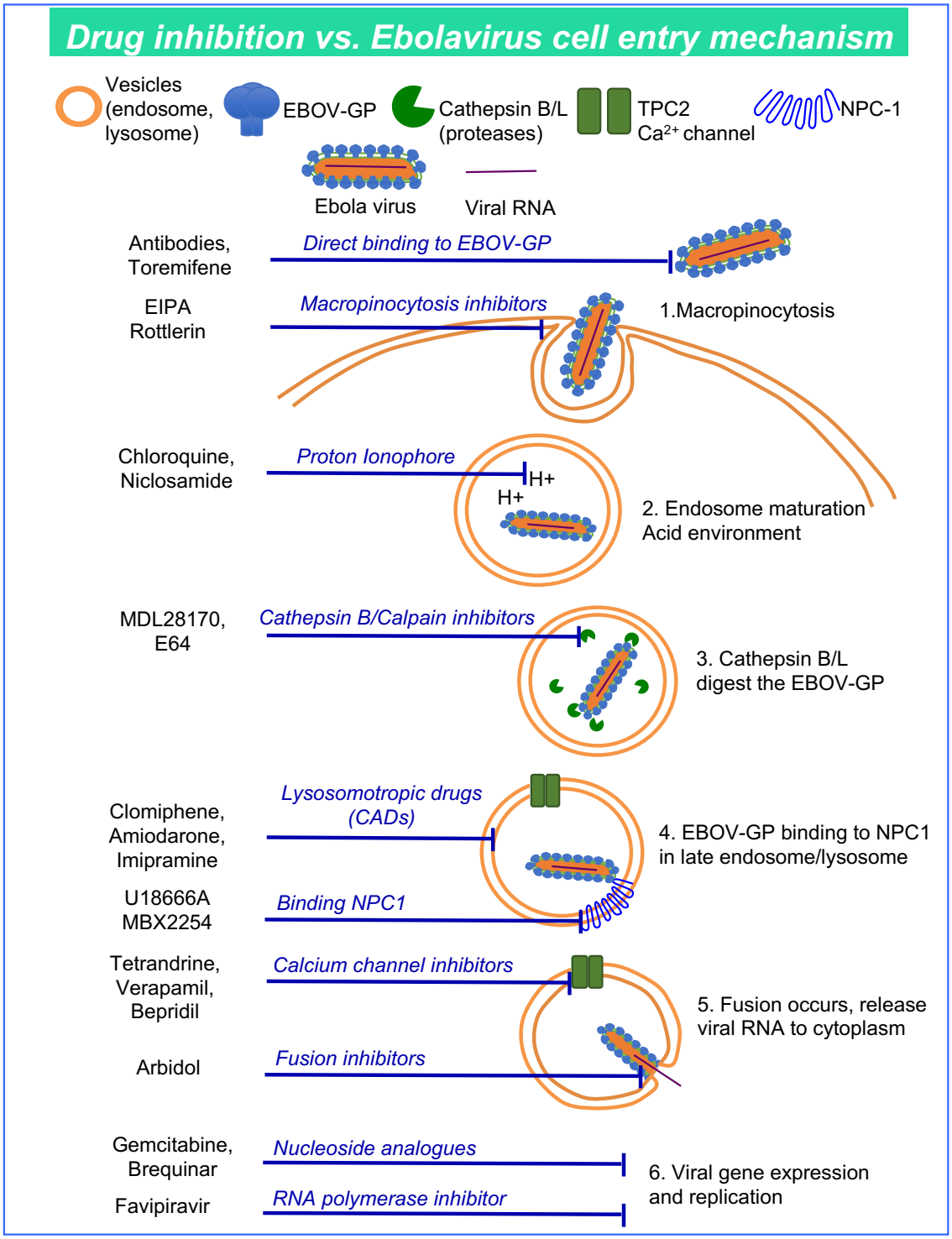


Figure 4. 21 EBOV cell entry mechanism and potential drug modes of action

While we will continue analysing these results, we would like to highlight the combination of chloroquine, toremifene and the cathepsin inhibitors E64d and MDL28170. Chloroquine is a lysosomotropic CAD and it increases the endosomal and lysosomal pH. This may indirectly affect the activity of cathepsin B/L in digesting EBOV-GP, and therefore synergise with cathepsin inhibitors (Chandran *et al.* 2005; Schornberg *et al.* 2006; Kouznetsova *et al.* 2014; Linden *et al.* 2016). Chloroquine also synergised with toremifene, the most powerful single inhibitor that is known to bind and destabilise EBOV-GP (Zhao *et al.* 2016)

Chloroquine is the most studied repositioned drug for treating EBOV in animal models (Kouznetsova *et al.* 2014; Dowall *et al.* 2015; Falzarano *et al.* 2015; Madrid *et al.* 2015). The biggest challenge was the very high dose of chloroquine required to protect animals from infection. This could be solved if the synergistic effect of chloroquine, cathepsin inhibitors, and toremifene can be repeated *in vivo*. Toremifene has been demonstrated to provide *in vivo* protection against EBOV challenge in at least some experiments (Johansen *et al.* 2013). In addition, the cathepsin inhibitors have been optimised for inhibition of EBOV (Linden *et al.* 2016). Therefore, some combinations of chloroquine with a cathepsin inhibitor, and an EBOV-GP binding CAD-like toremifene may be a logical combination to reduce the dosage needed to reach adequate efficacy to prevent EBOV infection.

Appendix Table 4. X1 228 small molecules that has inhibited E-S-FLU in this study.

No.	228 inhibitors are ranked by their IC_{50} (concentration at 50% inhibition) for E-S-FLU.
	Drugs tested and **inhibited** Ebolavirus in Johansen *et al.* 2015.
	Drugs tested but **did not inhibit** Ebolavirus in Johansen *et al.* 2015.
Drug name*	62 drugs that have inhibited hERG receptor/Long-QT drugs.
Plate No.	Plate position of the molecule in LOPAC®1280 library.)
	Inhibitors that have no "plate No." are extra molecules being tested in this study (e.g. No.1 Toremifene), chosen from the published literature.
Highest conc	Highest concentration tested in virus inhibition assay. For "Highest conc" < 100 µM, the drugs are not toxic up to the stated concentration.
IC_{50}-E/H5	Concentration at which 50% of the infection is inhibited (E-S-FLU/H5-S-FLU).
Effect	"Reduced": inhibitors reduced the number of cells infected; "Dimmer": inhibitors reduced the expression of reporter eGFP in infected cells.
Description	Pharmacological groups the drugs belong to and the description of their known mechanism in the current literature.

No.	Plate No.	Cat. Number	Name	Highest conc (µM)	E-S-FLU IC_{50} (µM)	H5-S-FLU IC_{50} (µM)	Effect	Group	Description
1		T7204	**Toremifene***	100	0.15	NA	reduced	Estrogen	Selective estrogen receptor modulator (SERM)
2	01-D5	A1784	Aminopterin	100	0.20	0.2	**dimmer**	Antibiotic	Dihydrofolate reductase inhibitor
3	14-B11	PZ0116	PD-166285 hydrate	5	0.20	NA	reduced	Kinase	Broad spectrum protein tyrosine kinase inhibitor; Src and FGFR kinase inhibitor
4	16-A4	T9262	**Tamoxifen citrate***	50	0.20	NA	reduced	Estrogen	Anti-estrogen; relatively selective protein kinase C inhibitor
5	12-G4	O3125	**Ouabain***	1.5	0.28	0.3	reduced	Ion Pump	Blocks movement of the H5 and H6 transmembrane domains of Na+-K+ ATPases
6		C6272	**Clomiphene***	25	0.35	NA	reduced	Estrogen	Selective estrogen receptor modulator (SERM)
7	14-B2	R1402	Raloxifene HCl	50	0.40	33.8	reduced	Estrogen	Estrogen receptor modulator; anti-estrogenic drug
8	13-C4	PZ0113	PD173952	6.25	0.60	NA	reduced	Kinase	PD173952 is a Src family kinase inhibitor.
9	15-A9	B9311	BIX 01294 trihydrochloride hydrate	25	1.00	NA	reduced	Gene regulation	Selective histone methyl transferase inhibitor.
10		T5200	Triparanol	6	1.13	NA	reduced	Biochemistry	Inhibits cholesterol biosynthesis in lipid rafts. 3β-hydroxysterol-Δ24-reductase inhibitor
11	02-C11	SML0113	Brequinar sodium salt hydrate	100	1.30	1.4	**dimmer**	Gene regulation	inhibits DHODH in de novo pyrimidine biosynthesis.
12	10-C9	M5441	**Mibefradil dihydrochloride***	25	1.30	NA	reduced	Calcium	T-type Ca2+ channel blocker
13		T2695	Tetrandrine	25	1.63	NA	reduced	Calcium	Tetrandrine blocks voltage-dependent Ca2+ and Ca(+)-activated K+ channels.
14	11-G7	N3510	Niclosamide	25	1.69	3.2	reduced	Antibiotic	Protonophoric anthelmintic; uncouples oxidative phosphorylation
15	10-D3	L119	L-703,606 oxalate salt hydrate	25	1.70	NA	reduced	Tachykinin	Potent and selective non-peptide NK-1 tachykinin receptor antagonist
16	09-B11	N0287	NNC 55-0396	12.5	1.80	NA	reduced	Calcium	Selective T-type calcium channel inhibitor
17	07-B5	T5648	**Tamoxifen***	50	1.80	NA	reduced	Estrogen	Protein kinase C inhibitor; selective estrogen response modifiers (SERMs)
18	02-E3	A8423	**Amiodarone hydrochloride***	12.5	2.04	NA	reduced	Calcium	L-type Calcium trannel inhibitor; α/β adrenoceptor agonist
19	04-D3	C3930	Calmidazolium chloride	6.25	2.30	3.9	**dimmer**	Calcium	Potent inhibitor of calmodulin-dependent phosphodiesterase and Ca2+-ATPase
20	03-D6	G6423	Gemcitabine hydrohloride	100	2.50	1.9	**dimmer**	Antitumour	Antineoplastic agent and antimetabolite
21		U3633	U18666A	100	2.56	49.5	reduced	Biochemistry	Niemann-Pick Disease Type C (NPC) phenotype inducer
22	03-G3	B5016	**Bepridil***	25	2.68	NA	reduced	Calcium	Non-selective Ca2+ channel blocker
23	13-A11	Q3251	Quinacrine dihydrochloride	25	2.91	NA	reduced	Antimalarial	Monoamine oxidase (MAO) inhibitor; antimalarial
24	02-B6	P9623	**Paroxetine HCl hemihydrate***	50	3.00	NA	reduced	Serotonin	Selective serotonin reuptake inhibitor; antidipressant

No.	Plate No.	Cat. Number	Name	Highest conc (μM)	E-S-FLU IC50 (μM)	H5-S-FLU IC50 (μM)	Effect	Group	Description
25	07-F2	E3380	Ellipticine	12.5	3.30	NA	reduced	Cell Cycle	Cytochrome P450 (CYP1A1)and DNA topoisomerase II inhibitor
26	16-B4	T9652	**Terfenadine***	25	3.37	NA	reduced	Histamine	Non-sedating H1 histamine receptor antagonist
27	04-B11	C8903	**Clemastine fumarate salt***	100	3.40	58.4	reduced	Histamine	H1 Histamine receptor antagonist
28	11-A5	M149	Methiothepin	25	3.40	NA	reduced	Serotonin	5-HT1 Serotonin receptor antagonist; blocks serotonin autoreceptors
29	01-E4	PZ0192	**Bosutinib***	25	3.53	NA	reduced	Kinase	dual Src/Abl tyrosine kinase inhibitor with potent antiproliferative activity
30	12-C7	P1061	SKF525A HCl	100	3.60	NA	reduced	Microsomal drug	Inhibitor of microsomal drug metabolism
31	13-H5	P9178	**Prochlorperazine dimaleate***	25	3.70	NA	reduced	Dopamine	Antipsychotic agent; used in the treatment of spastic gastrointestinal disorders
32	10-A11	M6690	MDL 28170	200	3.81	NA	reduced	Cell cycle	Cell permeable calpain I and II inhibitor
33	09-G3	I7379	**Imipramine HCl***	100	3.82	NA	reduced	Serotonin	Tricyclic antidepressant; blocks reuptake of serotonin and norepinephrine
34	09-B8	U6881	U-73343	50	3.90	NA	reduced	G-protein	Inactive analog of U73122 (Rack 16, Well D06)
35		SML0445	**Clemastine***	50	4.30	50.0	reduced	Histamine	H1 Histamine receptor antagonist
36	16-D3	T8516	**Trifluoperazine dihydrochloride***	50	4.40	NA	reduced	Dopamine	Calmodulin antagonist; dopamine receptor antagonist; antipsychotic; sedative
37	10-G11	G5793	GR 127935 HCl hydrate	25	4.50	NA	reduced	Serotonin	Selective 5-HT1B/1D serotonin receptor antagonist
38	14-F5	SML0597	Daurisoline	50	5.10	NA	reduced	Ion channel	Antiarrythmic, anti-inflammatory, neuron-protective and blocks hERG channels
39		SML0860	Arbidol	125	5.17	NA	reduced	Fusion inhibitor	Broad-spectrum antiviral, fusion inhibitor
40	05-E2	E9531	**Ebastine***	12.5	5.33	NA	reduced	Histamine	Nonsedating histamine H1 receptor antagonist without cardiac side effect
41	11-B3	M9651	**Maprotiline HCl***	100	5.40	NA	reduced	Adrenoceptor	Selective norepinephrine reuptake inhibitor
42	04-F7	C6628	**Chloroquine diphosphate***	200	5.44	67.0	reduced	Antimalarial	Antimalarial; anti-amoebic; anti-inflammatory; binds strongly to dsDNA
43	16-H5	PZ0115	CP-31398 dihydrochloride hydrate	50	5.50	NA	reduced	Apoptosis	CP-31398 dihyrochloride hydrate is a p53 stabilizer; apoptosis inducer
44	16-F3	T9025	**Thioridazine hydrochloride***	50	6.00	NA	reduced	Calcium	Dopamine receptor antagonist; Ca2+ channel antagonist; antipsychotic
45	07-E6	F4303	Fiduxosin hydrochloride	50	6.25	NA	reduced	Adrenoceptor	alpha1-Adrenoceptor antagonist
46	14-B3	R5648	Rottlerin	50	6.25	NA	reduced	Kinase	PKC and CaM kinase III inhibitor
47	02-A10	PZ0007	**Azithromycin***	100	6.70	NA	reduced	Antibiotic	Macrolide antibiotic, azalide subclass. It inhibits protein synthesis in bacterial cells
48	03-B7	PZ0171	CP-100356 monohydrochloride	50	6.80	20.0	reduced	Signalling	Specific inhibitor of MDR1 (P-Gp) protypical ABC transporter; prazosin transport inhibitor
49	08-C9	B8312	BNTX maleate salt hydrate	12.5	6.90	NA	reduced	Opioid	Selective d1 non peptide opioid receptor antagonist.
50	15-C7	T2896	Triflupromazine hydrochloride	25	7.10	NA	reduced	Dopamine	D2 dopamine receptor antagonist; phenothiazine antipsychotic
51	07-D9	F100	**Fluspirilene***	25	7.40	NA	reduced	Dopamine	Dopamine receptor antagonist; antipsychotic
52	11-G11	S6319	**Sertraline HCl***	25	7.40	NA	reduced	Serotonin	Selective serotonin reuptake inhibitor; antidepressant
53	12-G7	P1793	**Pimozide***	25	7.50	NA	reduced	Calcium	Ca2+ channel antagonist; antipsychotic; D2 dopamine receptor antagonist
54	02-H5	A9809	**Amsacrine hydrochloride***	25	7.68	6.76	reduced	DNA topo	DNA topoisomerase II inhibitor
55	12-A6	O111	(±)-Octoclothepin maleate	50	7.70	NA	reduced	Dopamine	D2 Dopamine receptor antagonist; serotonin receptor antagonist
56	07-E9	F114	cis(Z)-Flupenthixol dihydrochloride	50	7.80	NA	reduced	Dopamine	Dopamine receptor antagonist; antipsychotic
57		190080	AY9944	50	7.81	NA	reduced	Cholesterol	Cholesterol synthesis inhibitor
58	12-E11	P6402	**Perphenazine***	50	8.18	NA	reduced	Dopamine	D2 dopamine receptor antagonist; sigma receptor agonist; phenothiazine antipsychotic
59	10-A7	M3668	Metergoline	50	8.20	NA	reduced	Serotonin	5-HT1/5-HT2 Serotonin receptor antagonist; analgesic; antipyretic
60	05-D6	D0670	Dihydroouabain	25	8.30	5.7	**dimmer**	Ion channel	Sodium-potassium pump inhibitor
61	02-E10	A255	A-77636 hydrochloride	25	8.60	15.6	reduced	Dopamine	Potent, orally active D1 dopamine receptor agonist
62	09-E5	I119	Indatraline HCl	25	9.10	NA	reduced	Dopamine	Potent inhibitor of dopamine, norepinephrine and serotonin reuptake
63	08-E9	H127	Hexahydro-sila-difenidol hydrochloride, p-fluoro analog	100	9.30	65.0	reduced	Neurotransmission	High affinity muscarinic acetylcholine receptor antagonist

No.	Plate No.	Cat. Number	Name	Highest conc (μM)	E-S-FLU IC50 (μM)	H5-S-FLU IC50 (μM)	Effect	Group	Description
64	11-A6	SML0221	Piperlongumine	12.5	9.50	NA	reduced	Apoptosis	Selectively kills cancer cells without harming normal cells
65	03-D5	B8262	Benztropine mesylate	100	9.60	NA	reduced	Neurotransmission	Muscarinic acetylcholine receptor antagonist
66	07-D5	PZ0012	**Sunitinib malate***	25	9.70	NA	reduced	Kinase	Sunitinib malate is a receptor tyrosine kinase inhibitor, and an anticancer drug.
67		SML0847	Benztropine	100	9.76	NA	reduced	Neurotransmission	Muscarinic acetylcholine receptor antagonist
68	15-D7	T3146	**Trimipramine maleate***	100	10.10	NA	reduced	Serotonin	Serotonin reuptake inhibitor that also blocks norepinephrine reuptake; antidepressant.
69	08-D9	M7320	N-methylhistaprodifen dioxalate salt	100	10.30	NA	reduced	Histamine	H1 histamine receptor agonist.
70	12-E7	L9793	LP44	100	10.40	70.0	reduced	Serotonin	A high affinity 5-HT7 receptor agonist.
71		PHR1131	**(±)-Verapamil hydrochloride***	100	10.57	NA	reduced	Calcium	α1-adrenoceptor antagonist; L-type calcium channel blocker.
72	15-G11	A7606	Aprindine hydrochloride	100	10.60	NA	reduced	Ion channel	Class Ib antiarrhythmic and hERG channel blocker
73	13-D8	G9048	GANT61	100	11.00	NA	reduced	Gene regulation	GANT61 blocks hedgehog pathway signaling by inhibiting the transcripional activity
74	05-B3	C106	CGS-12066A maleate	50	11.80	NA	reduced	Serotonin	5-HT1B Serotonin receptor agonist
75	03-A11	C1671	Chlorprothixene hydrochloride	50	12.60	NA	reduced	Dopamine	D2 dopamine receptor antagonist; blocks a subset of GABA-A receptors
76	11-G9	N7261	**Nortriptyline HCl***	50	12.60	NA	reduced	Adrenoceptor	Tricyclic antidepressant
77	05-C8	C3993	**Carvedilol***	50	12.70	NA	reduced	Adrenoceptor	Antihypersensive; cardioprotective, selective to alpha1/beta
78	07-H11	SML0634	CID2858522	50	12.70	NA	reduced	Kinase	CID2858522 specifically inhibits NF-kB activation downstream of protein kinsase C
79	11-H4	E5406	Ethopropazine HCl	100	12.70	NA	reduced	Neurotransmission	Butyrylcholinesterase inhibitor; antiparkinsonian
80	15-E10	B9685	BAY 61-3606 hydrochloride hydrate	200	12.80	NA	reduced	Kinase	Spleen tyrosine kinase (Syk) inhibitor; anti-inflammatory
81	15-C8	K4144	KB-R7493	100	12.80	NA	reduced	Calcium	KB-R7943 inhibits the reversed Na(+)/Ca(2+) exchanger, NCX. In cardiomyocytes
82	13-D11	L3169	LP12 HCl hydrate	50	13.30	NA	reduced	Serotonin	5-HT7 receptor agonist displaying selectivity over D2, 5-HT1A and 5-HT2A receptors
83	08-G11	I2279	IMID-4F hydrochloride	100	13.40	NA	reduced	Ion channel	Imidazoline-based K(ATP) channel blocker
84	07-H6	F4765	**Fluphenazine dihydrochloride***	50	13.60	NA	reduced	Dopamine	Dopamine receptor antagonist; antipsychotic
85	13-B5	P8813	**Protriptyline HCl***	100	13.80	NA	reduced	Adrenoceptor	Norepinephrine reuptake blocker
86	04-G8	C7291	**Clomipramine hydrochloride***	50	13.90	NA	reduced	Serotonin	Serotonin reuptake inhibitor; antidepressant
87		A3487	**Clarithromycin***	100	14.03	NA	reduced	Antibiotic	Clarithromycin is a macrolide antibiotic that interferes with bacterial protein synthesis.
88	13-F7	B5063	BMS-193885	50	14.70	NA	reduced	Neurotransmission	Potent, selective Y1 antagonist that is active in animal models of food intake
89	07-E8	F8257	**Flunarizine dihydrochloride***	25	15.00	NA	reduced	Ion channel	Ca2+/Na+ channel blocker; vasodilator
90	13-A2	P6656	Promazine HCl	200	15.00	NA	reduced	Dopamine	D2 dopamine receptor antagonist; phenothiazine antipsychotic
91	13-D3	P7780	Propionyl promazine HCl	100	15.30	NA	reduced	Dopamine	D2 dopamine receptor antagonist; phenothiazine antipsychotic
92	06-E7	D052	GBR-12909 dihydrochloride	25	15.70	NA	reduced	Dopamine	Selective dopamine reuptake inhibitor
93	12-A5	O3752	**Orphenadrine HCl***	100	16.20	NA	reduced	Neurotransmission	Muscarinic acetylcholine receptor antagonist; H1 histamine receptor antagonist
94	14-E4	R103	Ritanserin	50	16.20	NA	reduced	Serotonin	Potent 5-HT2 serotonin receptor antagonist which passes the blood-brain barrier
95	11-G8	A6605	AMN082	25	16.50	NA	reduced	Neurotransmission	Selective allosteric mGluR7 receptor agonist.
96	02-C5	A9561	5-(N,N-hexamethylene) amiloride	50	16.70	NA	reduced	Ion channel	Na+/H+ antiport inhibitor
97	09-G9	L4762	**Loperamide HCl***	100	16.80	NA	reduced	Calcium	Meperidine congener which binds to opioid receptors; Ca2+ channel antagonist
98	15-B2	S8688	SR 59230A oxalate	100	16.80	NA	reduced	Adrenoceptor	beta3-Adrenoceptor antagonist
99	09-H10	L8539	L-687,384 HCl	100	17.00	NA	reduced	Opioid	Putative sigma-1 receptor agonist
100	03-A5	B7651	Brefeldin A from Penicillium brefeldianum	50	17.20	NA	reduced	Cytoskeleton and ECM	Fungal metabolite that disrupts the structure and function of the Golgi apparatus
101	04-A10	C8138	**Chlorpromazine hydrochloride***	50	17.30	NA	reduced	Dopamine	Dopamine receptor antagonist; anti-emetic; antipsychotic

No.	Plate No.	Cat. Number	Name	Highest conc (μM)	E-S-FLU IC50 (μM)	H5-S-FLU IC50 (μM)	Effect	Group	Description
102	04-A7	C6022	Cyproheptadine hydrochloride	100	17.40	NA	reduced	Serotonin	5-HT2 serotonin receptor antagonist
103	13-B10	SML0678	Pyridostatin trifluoroacetate slt	200	17.40	58.8	**dimmer**	Gene regulation	Pyridostatin stabilizes G-quadruplexes, inducing DNA damage and cell-cycle arrest.
104	06-E9	D5676	N-Desmethylclozapine	100	17.50	NA	reduced	Neurotransmission	5-HT2 serotonin receptor antagonist; allosteric potentiator of M1 muscarinic receptors
105	07-H5	F1553	**S-(+)-Fluoxetine hydrochloride***	50	17.50	NA	reduced	Serotonin	Selective serotonin reuptake inhibitor
106	01-E6	A3085	5-(N-Ethyl-N-isopropyl) amiloride (EIPA)	100	17.80	NA	reduced	Ion channel	Selective blocker of Na+/H+ antiport
107	02-E9	O5889	Opipramol dihydrochloride	100	18.30	NA	reduced	Dopamine	Sigma1, sigma2 receptor agonist; antagonist at D2, 5HT2, and H1 receptors
108	12-D10	P4670	**Propafenone HCl***	100	18.40	NA	reduced	Ion channel	Blocks hKv1.5 and ATP-sensitive K+ channels; beta-adrenoceptor antagonist
109	02-D7	A129	**Amoxapine***	100	18.60	NA	reduced	Adrenoceptor	Tricyclinc antidepressant; inhibits neuronal uptake of norepinephrine
110	02-D3	A8404	**Amitriptyline hydrochloride***	100	18.80	NA	reduced	Adrenoceptor	Tricyclic antidepressant
111	10-A5	SML0667	PF-429242 dihydrochloride	100	19.10	NA	reduced	Gene regulation	Inhibitor of proprotein convertase sterol regulatory element-binding protein S1 protease
112	16-E6	S5317	SKF 95282 dimaleate	100	19.20	NA	reduced	Histamine	H2 Histamine receptor antagonist.
113	05-D9	D3900	**Desipramine hydrochloride***	100	19.40	NA	reduced	Adrenoceptor	Antidepressant
114	11-A8	PZ0111	PD-407824	50	19.60	NA	reduced	Kinase	PD-407824 is a Wee1/Chk1 inhibitor
115	13-E3	P7791	**Prazosin HCl***	50	19.80	NA	reduced	Adrenoceptor	Peripheral alpha1 adrenoceptor antagonist
116	04-G4	C4542	Cyclobenzaprine hydrochloride	100	20.30	NA	reduced	Serotonin	5-HT2 serotonin receptor antagonist
117	03-E10	C1172	ML-9	100	20.60	NA	reduced	Kinase	Myosin light chain kinase (MLCK) inhibitor
118	02-C7	PZ0178	PHA 767491 hydrochloride	25	21.30	15.7	reduced	kinase	selective ATP-competitive dual inhibitor cdc7/cdk9
119	09-A2	I2764	ML-7	50	21.60	NA	reduced	Kinase	Selective myosin light chain kinase (MLCK) inhibitor
120	07-A5	E101	S-(-)-Eticlopride hyrrochloride	100	21.60	NA	reduced	Dopamine	Potent and selective D2 dopamine receptor antagonist
121	08-F11	G0419	GR55562 dihydrobromide	100	21.80	NA	reduced	Serotonin	Selective 5-HT1B/1D serotonin receptor antagonist.
122	16-C8	V1377	Vinblastine sulfate salt	50	22.00	NA	reduced	Microtubule	Inhibitor of microtubule assembly
123	10-E2	B175	BW723C86	100	22.40	NA	reduced	Serotonin	5-HT2B serotonin receptor agonist.
124	12-B10	P4651	**Promethazine HCl***	100	22.80	NA	reduced	Histamine	H1 Histamine receptor antagonist; anticholinergic
125	02-E7	A138	Aminobenztropine	100	23.00	NA	reduced	Neurotransmission	high affinity muscarinic acetylcholine receptor ligand
126	13-A4	PZ0112	PD-184161	100	23.00	NA	reduced	Kinase	PD-184161 is a MEK inhibitor
127	02-F11	T6951	TBB2	25	23.20	NA	reduced	Kinase	Cell-permeable casein kinase 2 (CK2) inhibitor
128	16-G9	A7111	Acepromazine maleate	100	24.60	NA	reduced	Neurotransmission	Acepromazine is a phenothiazine antipsychotic comonly used as a veterinary drug
129	10-B11	M6760	Myricetin	50	25.30	NA	reduced	Kinase	Casein Kinase II inhibitor
130	06-D6	D027	R(-)-Propyl norapomorphine hydrochloride	50	25.60	NA	reduced	Dopamine	Highly potent and selective D2 dopamine receptor agonist
131	04-D7	C6305	**Clozapine***	100	26.10	NA	reduced	Dopamine	Atypical neuroleptic agent, displays greater affinity for the D4 dopamine receptors
132	01-F5	A1895	Aurintricarboxylic acid	100	26.60	NA	reduced	DNA topo	DNA topoisomerase II inhibitor
133	01-H6	D033	(+)-Butaclamol hydrochloride	100	27.00	NA	reduced	Dopamine	Dopamine receptor antagonist
134	05-B9	D3768	Dequalinium chloride hydrate	100	27.30	12.1	**dimmer**	Ion channel	Selective blocker of apamin-sensitive K+ channels
135	03-C8	B168	(±)-Butaclamol hydrochloride	100	27.40	NA	reduced	Dopamine	Dopamine receptor antagonist; selective for D2 over D1
136	11-A10	N7510	**Nicardipine HCl***	50	28.30	NA	reduced	Calcium	L-type Ca2+ channel antagonist; antihypertensive
137	13-E11	Q109	Quipazine, 6-nitro, maleate	200	29.20	NA	reduced	Serotonin	Potent and selective serotonin reuptake inhibitor
138	16-A3	T7947	Tomoxetine	200	29.40	NA	reduced	Adrenoceptor	Norepinephrine reuptake blocker
139	15-B9	PZ0136	CP-100263 dihydrochloride hydrate	200	29.70	NA	reduced	Tachykinin	CP-100263 is an NK-1 neurokinin receptor antagonist
140	07-H9	F132	**Fluoxetine hydrochloride***	100	29.70	NA	reduced	Serotonin	Selective serotonin reuptake inhibitor

No.	Plate No.	Cat. Number	Name	Highest conc (μM)	E-S-FLU IC50 (μM)	H5-S-FLU IC50 (μM)	Effect	Group	Description
141	02-E8	A164	Alaproclate hydrochloride	100	30.00	NA	reduced	Serotonin	Potent and selective serotonin reuptake inhibitor
142	15-G7	SML0824	Lubeluzole dihydrochloride	100	30.20	NA	reduced	Neurotransmission	Lubeluzole is an NMDA glutamate receptor antagonist.
143	05-D8	D2763	Dihydro ergotamine methanesulfonate	100	30.30	NA	reduced	Serotonin	Serotonin receptor antagonist; partial α adrenoceptors, D2 dopamine receptors agonist
144	14-C9	S3378	**Spironolactone***	100	30.40	33.1	**dimmer**	Hormone	Competitive antagonist of the cytoplasmic aldosterone receptor; diuretic
145	16-D8	V4629	**(±)-Verapamil hydrochloride***	100	31.60	NA	reduced	Calcium	L-type Ca2+ channel modulator; adrenoceptor antagonist; antiarryhthmic
146	11-F11	N115	Naltrindole HCl	100	32.70	NA	reduced	Opioid	Highly selective, non-peptide delta opioid receptor antagonist
147	06-D3	D7909	Dicyclomine hydrochloride	100	33.63	NA	reduced	Neurotransmission	Competitive mucarinic acetylcholine receptor antagonist
148	13-H2	P7340	PDMP HCl	100	33.70	NA	reduced	Lipid	Inhibits formation of glucosylceramide from ceramide by glucosylceramide synthase
149	05-E10	D5294	Dilazep Dihydrochloride	100	34.10	NA	reduced	Adenosine	Adeosine uptake inhibitor
150	14-B7	SML0752	(+)-CP-99994 dihydrochloride	200	34.20	NA	reduced	Tachykinin	(+)-CP-99994 is a selective neurokinin (NK)-1 tachykinin antagonist.
151	03-A6	B9308	BP 897	100	34.30	NA	reduced	Dopamine	Partially selective D3 dopamine receptor agonist
152	16-B9	A2731	AMG 9810	50	34.80	NA	reduced	Ion channel	Potent, non-vanilloid, antagonist of the TRPV1 receptor.
153	03-F8	B5311	Biperiden hydrochloride	100	34.80	NA	reduced	Neurotransmission	Non-selective muscarinic acetylcholine receptor antagonist; antiparikinsonian
154	16-E8	SML0776	Galloflavin potassium	50	36.00	NA	reduced	Cell Stress	Galloflavin is an inhibitor of lactate dehydrogenase (LDH).
155	15-A6	T1516	Trihexyphenidyl hydrochloride	200	37.30	NA	reduced	Neurotransmission	Muscarinic acetylcholine receptor antagonist; centrally acting anticholinergic
156	05-B10	D4526	**Doxepin hydrochloride***	100	38.50	NA	reduced	Adrenoceptor	Antidepressant; antipuritic
157	14-B10	S7389	SB 269970 HCl	200	38.50	NA	reduced	Serotonin	Selective 5-HT7 serotonin receptor antagonist
158		2778-5 (Ca	Faviparivir (T705)	500	39.30	67.3	**dimmer**	Antiviral	Sselective inhibition of viral RNA-dependent RNA polymerase
159	03-G7	B138	BTCP hydrochloride	100	41.40	NA	reduced	Dopamine	Selective blocker of dopamine reuptake
160	13-B4	P8293	Protoporphyrin IX	200	42.00	NA	reduced	Guanylyl cyclase	Activates soluble guanylyl cyclase
161	06-H5	D9815	**Doxazosin mesylate***	100	42.90	NA	reduced	Adrenoceptor	alpha1 adrenoceptor blocker
162	01-C3	861804	TMB-8 hydrchloride	100	43.90	NA	reduced	Calcium	Intracellular Ca2+ antagonist, inhibits calmodulin-sensitive Ca2+-ATPase and PKC
163	13-D9	P203	Phenamil methanesulfonate	200	44.00	NA	reduced	Ion channel	Irreversible inhibitor of amiloride-sensitive Na+ channels; derivative of amiloride
164	16-H9	PZ0121	CP-135807	200	44.30	NA	reduced	Serotonin	CP-135807 is a selective 5-HT1D agonist
165	07-B6	F2802	**Fluvoxamine maleate***	100	44.90	NA	reduced	Serotonin	Selective serotonin reuptake inhibitor
166	13-G8	A1980	A3 hydrochloride	200	47.00	NA	reduced	Kinase	Non-selective casein kinase (CK) inhibitor
167	05-B8	D2531	Dextromethorphan hydrobromide monohydrate	100	47.20	NA	reduced	Neurotransmission	Allosteric antagonist at NMDA-controlled ion channels
168	04-H4	C4662	Carbetapentane citrate	100	48.00	NA	reduced	Opioid	Opioid receptor ligand with high affinity toward sigma 1 sites; antitussive
169	12-E4	O2881	Oxybutynin Chloride	100	48.50	NA	reduced	Neurotransmission	Muscarinic acetylcholine receptor antagonist
170	10-B10	M6383	2-methoxy estradiol	200	48.80	NA	reduced	Estrogen	Inhibitor of angiogenesis and endothelial cell proliferation
171	16-E4	T103	Trifluperidol hydrochloride	200	48.90	NA	reduced	Dopamine	Dopamine receptor antagonist; antipsychotic
172	10-A2	T5576	TMPH HCl	200	50.00	NA	reduced	Neurotransmission	Potent inhibitor of neuronal nicotinic receptors. Alpha 3/4 and beta 2/4 subtype specific
173	06-C8	D122	Doperidone	200	52.30	NA	reduced	Dopamine	Peripherall dopamine receptor antagonis; anti-emetic
174	14-C10	S7395	Spiperone	100	52.40	NA	reduced	Dopamine	Selective D2 dopamine receptor antagonist
175	10-F9	M5644	(±)-Methoxyverapamil HCl	200	52.50	NA	reduced	Calcium	L-type Ca2+ channel antagonist
176	16-G7	U111	(-)-trans-(1S,2S)-U-50488 hydrochloride	200	52.90	NA	reduced	Opioid	Selective kappa opioid receptor agonist.
177	13-E9	PZ0210	PF-04885614	200	53.00	NA	reduced	Ion channel	PF-04885614 is a potent and selective Nav1.8 inhibitor.
178	14-B8	S2812	SNC80	200	53.20	NA	reduced	Opioid	delta Opioid receptor
179	04-H3	C4238	CNS-1102	100	53.30	NA	reduced	Neurotransmission	Noncompetitive NMDA glutamate receptor antagonist

No.	Plate No.	Cat. Number	Name	Highest conc (μM)	E-S-FLU IC50 (μM)	H5-S-FLU IC50 (μM)	Effect	Group	Description
180	16-E2	P0115	PAC-1	100	53.80	NA	reduced	Apoptosis	Caspase 3 activator; apoptosis inducer
181	16-G10	X6000	Xylometazoline hydrochloride	200	54.20	NA	reduced	Adrenoceptor	alpha-Adrenoceptor agonist; imidazoline binding site ligand
182	12-A11	P5514	**Pyrilamine maleate***	200	56.80	NA	reduced	Histamine	H1 Histamine receptor antagonist
183	10-C3	L135	L-741,626	100	57.10	NA	reduced	Dopamine	Selective D2 dopamine receptor antagonist
184	12-C2	N151	Nisoxetine HCl	200	57.40	NA	reduced	Adrenoceptor	Potent and selective norepinephrine reuptake blocker
185	10-C5	M2525	**Mianserin HCl***	200	58.90	NA	reduced	Serotonin	Serotonin receptor antagonist
186	01-H7	A4393	**Apomorphine HCl hemihydrate***	100	60.40	NA	reduced	Dopamine	Non-selective dopamine receptor agonist
187	03-G6	B016	Benoxathian hydrochloride	100	61.70	NA	reduced	Adrenoceptor	Selective alpha1 adrenoceptor antagonist
188	09-F6	I160	3-(1H-Imidazol-4-yl)propyldi(p-fluorophenyl)methyl ether Cl	200	64.20	NA	reduced	Histamine	H3 Histamine receptor antagonist
189	16-E9	W1628	Wortmannin from Penicillium funiculosum	500	64.70	NA	reduced	Phosphorylation	Potent and specific phosphatidylinositol 3-kinase (P13-K) inhibitor
190	12-G2	N158	Naftopidil dihydrochloride	100	65.50	NA	reduced	Adrenoceptor	alpha1 Adrenoceptor antagonist; antihypertensive
191	14-B5	R115	Reactive Blue 2	200	65.80	NA	reduced	P2 receptor	P2Y receptor antagonist; most potent antagonist for ATP-activated channels
192	09-C2	I2892	Ifenprodil tartrate	200	66.80	NA	reduced	Neurotransmission	Blocks the polyamine binding site associated with the NMDA glutamate receptor
193	01-G6	A3145	Apigenin	200	67.40	NA	reduced	Cell Cycle	Arrests cell cycle at G2/M phase
194	10-B7	U106	(-)-cis-(1S,2R)-U-50488 tartate	200	70.40	NA	reduced	Neurotransmission	Potent sigma receptor ligand.
195	08-C4	H1512	**Haloperidol***	200	70.80	NA	reduced	Dopamine	Dopamine receptor antagonist; antipsychotic
196	08-B3	G133	GR-89696 fumarate	200	71.00	NA	reduced	Opioid	kappa Opioid receptor agonist
197	16-F11	C1119	Caroverine hydrochloride	200	71.30	NA	reduced	Neurotransmission	Nonselective NMDA and AMPA glutamate receptor antagonist.
198	09-G7	K2628	Ketotifen tumarate	200	72.20	NA	reduced	Histamine	H1 Histamine receptor antagonist
199	06-H3	D8040	(±)trans-U-50488 methanesulfonate	200	72.60	NA	reduced	Opioid	Selective kappa opioid receptor agonist
200	15-B3	S009	PAPP	200	75.50	NA	reduced	Serotonin	Selective 5-HT1A serotonin receptor agonist
201	06-H11	E3132	E64	100	77.17	NA	reduced	Biochemistry	Irreversible inhibitor of cysteine proteases
202	09-C7	K1003	**Ketoconazole***	100	77.30	NA	reduced	antifungal	Potent inhibitor of cytochrome P450c17 enzyme; antifungal agent
203	16-C2	T7540	Tyrphostin 47	200	77.80	NA	reduced	Kinase	EGFR tyrosine kinase inhibitor
204	13-E10	Q0875	**Quinidine sulfate***	200	81.30	NA	reduced	Ion channel	Na+ channel blocker and Class I antiarrythmic
205	08-H4	H2380	6-Hydroxy-DL-DOPA	200	81.40	NA	reduced	Adrenoceptor	Precursor of the catecholaminergic neurotoxin, 6-hydroxydopamine
206	03-D4	B5683	Betaxolol hydrochloride	100	81.80	NA	reduced	Adrenoceptor	Selective beta1 adrenoceptor antagonist
207	15-G3	S2671	Suramin sodium salt	200	83.00	NA	reduced	P2 receptor	P2X and P2Y receptor antagonist; antiparasitic; anti-tumor agent
208	15-H7	T4143	Triamterene	200	85.20	132.3	**dimmer**	Ion channel	Na+ channel blocker; diuretic
209	12-H2	B2185	Bisoprolol hemifumarate	200	86.90	NA	reduced	Adrenoceptor	Cardioselective Beta1-adrenoceptor antagonist. Actual molecular weight is 383.48
210	03-F7	B135	R(+)-6-Bromo-APB hydrobromide	100	90.40	NA	reduced	Dopamine	D1 Dopamine receptor agonist
211	02-C6	A9899	Antozoline hydrochloride	100	93.60	NA	reduced	Histamine	Imidazoline agonist; H1 histamine receptor antagonist
212	09-F5	I120	Iofetamine HCl	200	96.60	NA	reduced	Neurotransmission	Reference standard; radio-iodinated iofetamine is used to image brain blood flow
213	12-F2	N156	Naltriben methanesulfonate	200	99.10	NA	reduced	Opioid	Highly selective delta2 opioid receptor antagonist
214	12-B7	P0884	**(±)-Propranolol HCl***	200	99.80	NA	reduced	Adrenoceptor	beta Adrenoceptor antagonist; cardiac depressant (anti-arrhythmic)
215	05-C3	C108	2-Cycloocytyl-2-hydroxyethylamine hydrochloride	200	100.00	NA	reduced	Neurotransmission	Inhibitor of Phenylethanolamine N-methyltransferase (PNMT)
216	09-H11	L106	Loxapine succinate	200	100.50	NA	reduced	Dopamine	Dibenzoxazepine antipsychotic agent

No.	Plate No.	Cat. Number	Name	Highest conc (μM)	E-S-FLU IC50 (μM)	H5-S-FLU IC50 (μM)	Effect	Group	Description
217			Ned19	267	101.00	NA	reduced	Calcium	Inhibits nicotinic acid adenine dinucleotide phosphate-mediated Ca2+ release
218	09-E4	C1618	**Cibenzoline succinate***	200	106.80	NA	reduced	Ion channel	Blocks ATP-sensitive K channels in heart and pancreatic cells; class IA antiarrhythmic
219	04-E5	C5040	Clemizole hydrochloride	200	110.00	NA	reduced	Histamine	H1 Histamine receptor antagonist
220	14-E3	R7150	Ro 25-6981 HCl	200	111.30	NA	reduced	Neurotransmission	NR2B-selective, NMDA glutamate receptor antagonist
221	15-A8	T4182	Tyrphostin AG 1478	200	115.30	141.0	**dimmer**	EGFR	Selective inhibitor of epidermal growth factor receptor (EGFR) protein
222	14-E2	R3255	13-cis-retinoic acid	200	123.00	NA	reduced	Gene regulation	Anti-inflammatory and antitumor actions mediated through RAR-α and RAR-β receptors
223	15-A11	T6764	Triprolidine hydrochloride	200	123.70	NA	reduced	Histamine	Potent H1 histamine receptor antagonist
224	16-B2	T7508	Tetracaine hydrochloride	200	123.80	NA	reduced	Ion channel	Local anesthetic
225	14-C4	R9644	Ribavirin	200	125.20	125.9	**dimmer**	Cell cycle	Antiviral agent
226	15-C4	S168	(±)-SKF 38393, N-allyl-, hydrobromide	200	132.10	NA	reduced	Dopamine	D1 Dopamine receptor agonist
227	14-D2	R2751	Ruthenium red	200	141.10	NA	reduced	Calcium	Inhibits mitchondrial Ca2+ uniporter; capsaicin antagonist
228	04-E3	G5918	GR 113808	200	145.20	NA	reduced	Serotonin	5-HT4 serotonin receptor antagonist.

Chapter 5 Niemann-Pick Type C 1/2 Proteins, Acid Sphingomyelinase and EBOV Infection

5.1 Introduction

Previously in Chapter 4, we used our EBOV-GP pseudotyped virus E-S-FLU in a drug screening assay. We showed that many drugs from different drug families inhibited EBOV-GP dependent cell entry, in agreement with the current literature (Johansen *et al.* 2013, 2015; Gehring *et al.* 2014; Kouznetsova *et al.* 2014). However, the mechanism by which these drugs are inhibiting EBOV is still unknown. We identified most of these drugs as cationic amphiphilic drugs (CADs), which are very likely to concentrate in lysosomes (De Duve *et al.* 1974; Kornhuber *et al.* 2008; Nadanaciva *et al.* 2010; Salata *et al.* 2017). We began to characterise the effect of selected EBOV inhibitors on target cell lysosomes by measuring lysosomal membrane permeability and the level of unesterified cholesterol and sphingomyelin in the lysosome (Chapter 4 section 4.3.4 and 4.3.5). Based on our results and the current literature, we presented four hypotheses to explain how CADs may inhibit EBOV entry, and three of these involved effects in the lysosome (section 4.5.3) (Shoemaker *et al.* 2013). It is often very difficult to tease apart the mechanisms of small molecules which may have multiple actions.

In this chapter, we will study the effect of specific lysosomal proteins that may be targets for these drugs by genetically knocking out selected genes. We created

two genetically modified HeLa cell-lines by CRISPR/Cas 9 technique: Niemann-Pick C2 protein gene knockout (*NPC2*KO) and sphingomyelinase phosphodiesterase/ acid sphingomyelinase protein gene knockout (*SMPD1*KO). The design and verification of the guide sgRNAs used in this chapter were carried out by Dr Philip Hublitz from the Genome Editing Service at the Weatherall Institute of Molecular Medicine.

Niemann-Pick C2 protein (NPC2) is a soluble protein found in the lysosomal lumen. The exact function of NPC2 protein is unknown, but it is suggested to work together with the NPC1 protein in endocytic transport and regulation of cholesterol and lipid levels in the late endosome/lysosome compartment (Liscum 2000; Ko *et al.* 2001; Babalola *et al.* 2007; Lloyd-Evans *et al.* 2008). Mutations and dysfunction in NPC1 and NPC2 proteins both lead to the neurodegenerative lysosomal storage disease, Niemann-Pick type C (NPC) disease (Vanier 2010). The biochemical phenotypes of NPC1 and NPC2 mutants are indistinguishable (Vanier and Millat 2004), which include accumulation of sphingosine, sphingomyelin, cholesterol, and glycosphingolipids in lysosomes, as well as calcium depletion in these acidic organelles (Lloyd-Evans *et al.* 2008). The clinical phenotypes of individuals with mutations in either NPC1 or NPC2 are also very similar, and 95% of the clinical cases are due to mutations in NPC1, the rest are caused by mutations in NPC2. These observations suggest that the two proteins may function in the same pathway.

Some CADs have been reported to induce an NPC disease-like phenotype in cells (Carette *et al.* 2011; Côté *et al.* 2011; Shoemaker *et al.* 2013; Sun *et al.* 2017),

namely accumulation of unesterified cholesterol in the lysosome detected by filipin staining. Drugs including U18666A, itraconazole, astemizole, cepharanthine, and small molecules 3.0 and 3.47, MBX2254 and MBX2270, were found to bind directly to the NPC1 protein (Côté *et al.* 2011; Basu *et al.* 2015; Lu *et al.* 2015; Head *et al.* 2017; Lyu *et al.* 2017, 2018). Are all the CADs that inhibited EBOV infection binding directly to NPC1, and thereby blocking binding of EBOV-GP to its receptor site? Or is the accumulation of cholesterol and sphingolipids, and the subsequent effects this has on lysosomal functions, influencing EBOV entry indirectly? Or finally, are the CADs inhibiting EBOV entry by some other mechanisms, and the effects on NPC1 are simply coincidental?

It is unlikely that the NPC biochemical phenotype is responsible for inhibition of EBOV infection as several papers have demonstrated that NPC2 is not essential for EBOV entry into target cells by siRNA knockdown studies, infection in NPC2 deficient mice, and infection of fibroblasts from patients with classical lipid storage diseases (Carette *et al.* 2011; Côté *et al.* 2011; Herbert *et al.* 2015). In each of these scenarios, EBOV was able to infect cells with lysosomal lipid accumulation. In addition, we found that the drug itraconazole, that is known to bind the sterol sensing domain on NPC1, and induce a complete NPC biochemical phenotype, failed to block entry of E-S-FLU (Chapter 4). We have generated a *NPC2*KO human HeLa cell-line to confirm these findings and provide a control for other gene knockout experiments.

CADs contain both a lipophilic end and a weak basic end formed by a secondary or tertiary amine. The base pKa of CADs, determined by the weakly basic amine

group, is usually in the range of 8. The pKa^{base} is defined by the relationship $pKa^{base} = pH + Log_{10}([HBase^{+}]/[Base]$, which is derived from the association constant for protonation of the base of a weak base: $Base + H^{+} \rightleftharpoons HBase^{+}$. In a neutral state at pH ~ 7, this relationship predicts that around 10% of the CAD molecules are unprotonated and therefore uncharged and lipid soluble. They can freely diffuse across the lipid membrane but become protonated and positively charged in the acidic lumen of lysosome (pH ~ 4.6), where fewer than 0.1% remains lipid soluble. The positively charged CADs can no longer pass through the hydrophobic lipid membrane and therefore are trapped and concentrated at the luminal side of lysosomal membrane.

Some CADs can functionally inhibit ASM by competing for the electrostatic charge that is thought to associate the ASM with the lysosomal membrane (Kornhuber *et al.* 2008, 2010b, 2011). ASM is a lysosomal enzyme that catalyses the hydrolysis of sphingomyelin to phosphorylcholine and ceramide (Schuchman *et al.* 1991; Jenkins, Canals and Hannun 2009). After dissociation from the membrane into the lumen of the lysosome, ASM is degraded by proteases. Kornhuber *et al*. (2010) named these drugs FIASMAs (Functional Inhibitors of Acid SphingoMyelinAses).

As a result, ASM and FIASMAs frequently feature in proposed mechanisms by which CADs inhibit EBOV infection (Johansen *et al.* 2015; Fan *et al.* 2017; Sun *et al.* 2017). ASM deficiency underlies the clinical conditions Niemann-Pick Type A and Type B in which sphingomyelin accumulates (Platt *et al.* 2018). Miller *et al*. (2012) showed that ASM is necessary for EBOV infection by an siRNA knockdown experiment in HeLa cells (Miller *et al.* 2012b). However, since 2012 there have

been no follow up studies on the relationship between ASM and EBOV infection. In this chapter, we specifically knocked out *SMPD1* gene that encodes for ASM to see if the protein is required for EBOV entry.

In the final part of this chapter, we turn our focus back to the NPC1 protein, the key receptor for EBOV entry at the late endosomal/lysosomal membrane (Carette *et al.* 2011; Côté *et al.* 2011; Miller *et al.* 2012a; Herbert *et al.* 2015). We developed an *in vitro* system to test the effect of single-residue changes in NPC1 on EBOV entry. We then collaborated with Dr Mary Carrington from the National Institutes of Health (NIH) to investigate the relationship between single nucleotide polymorphisms (SNPs) in the human *NPC1* gene and the survival rate in the West African population during 2014-2015 EBOV outbreak.

5.2 EBOV infection in NPC2 deficient cells

5.2.1 *NPC2* knockout design

Niemann-Pick C2 protein (NPC2) is a soluble lysosomal protein (Blom *et al.* 2003; Zhang *et al.* 2003; Kirchhoff, Osterhoff and L. 2005). Mature human NPC2 protein contains 132 amino acids after the first 19-residue signal post-translationally cleaved, and it folds into a single-domain β-sandwich structure (Figure 5.1 A). The crystal structure of bovine NPC2 revealed a hydrophobic pocket that binds cholesterol with sub-micromolar affinity (Friedland *et al.* 2003; Ko *et al.* 2003; Kirchhoff, Osterhoff and L. 2005) (Figure 5.1 B). NPC2 is encoded by the *NPC2* gene that is located on chromosome 14q24.3 in the human genome, and its transcript contains 5 exons (Naureckiene *et al.* 2000; Vanier and Millat 2004). To knockout the *NPC2* gene expression in a HeLa cell-line, we targeted exon 3 (173

base pairs) for deletion by using CRISPR/Cas 9 technology (Ran *et al.* 2013). Removing exon 3 would prevent translation of three fifths of the NPC2 C terminus, leaving the N-terminus incapable of folding and binding cholesterol. Deletion would also introduce a frameshift, which may the mRNA to nonsense-mediated decay (Figure 5.2).

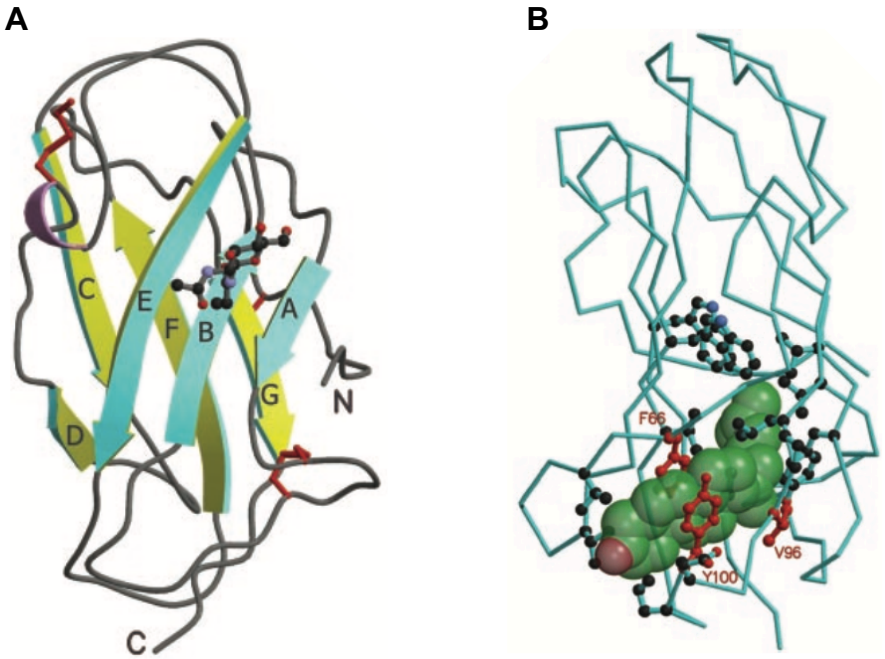


Figure 5. 1 Structure of bovine NPC2 protein
Figure is adapted from Friedland *et al.* 2003. **A**: Crystal structure of bovine NPC2 protein (PDB ID code 1NEP) shown in cartoon representation. Three disulphide bonds are shown in red and an N-glycosylation site at position Asn39 is shown in ball-and-stick representation. **B**: Space-filling model of cholesterol (green) docked in the proposed binding cavity in bovine NPC2 (ribbon representation). The side chains of amino acid residues that are involved in cholesterol binding (F66, V96, Y100) are shown in red.

HeLa cells are known to have a high level of aneuploidy (Landry *et al.* 2013) so we applied a dual sgRNAs strategy (Ran *et al.* 2013; Lonowski *et al.* 2017). We designed two sgRNAs directing the Cas 9 nuclease enzyme to cut at both 5' and 3' intronic regions flanking the target exon 3 (Figure 5.2). When both sites are cut simultaneously, there is a chance that the whole exon is deleted and re-joined by non-homologous end joining (NHEJ).

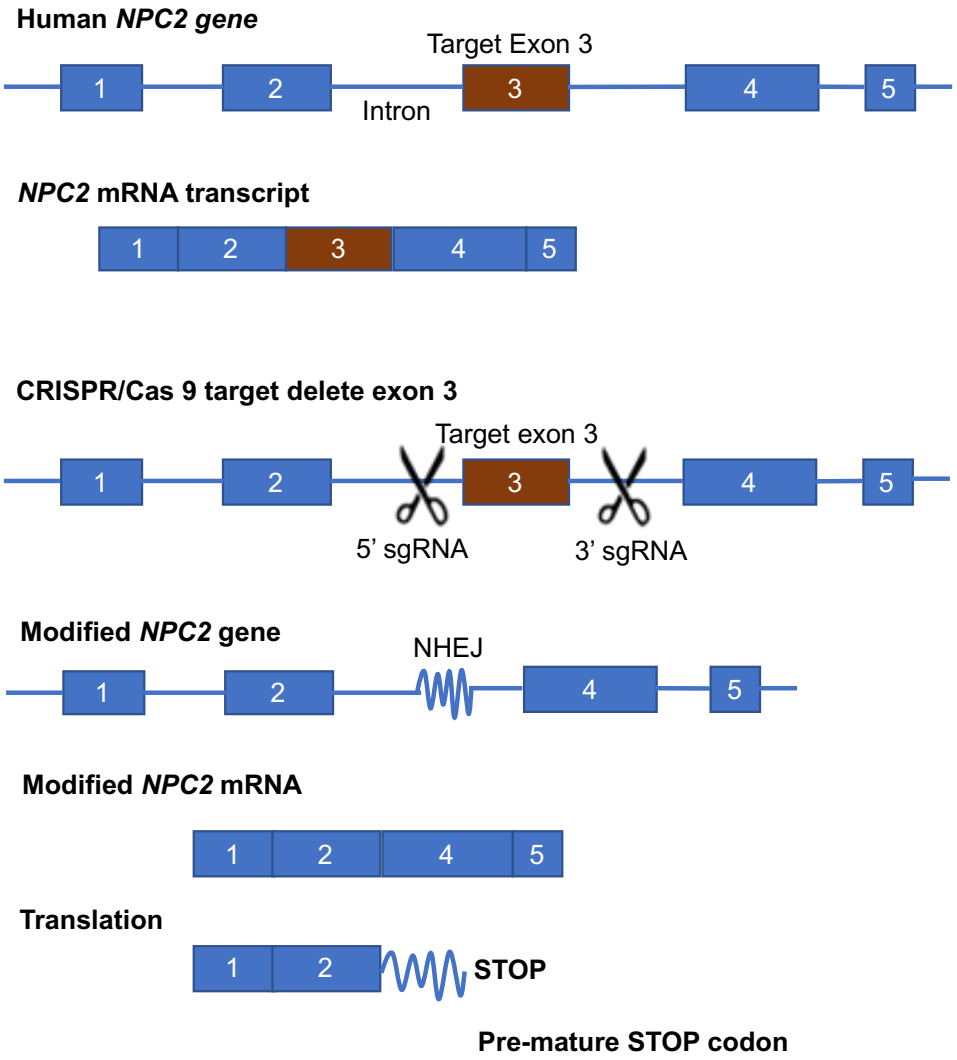


Figure 5. 2 Schematic diagram of NPC2 exon 3 knockout by CRISPR/Cas 9
Gene organisation and mRNA transcript of WT and exon 3 deleted *NPC2* gene. The 5' and 3' sgRNAs guided Cas 9 nuclease to cleave at intronic regions flanking the target exon 3 (scissors), which may lead to a complete deletion of the fragment between two sgRNAs' annealing sites. Double-stranded break in DNA is then repaired by non-homologous end joining (NHEJ). Modified *NPC2* transcript contains a pre-mature STOP codon.

Philip Hublitz designed the sgRNAs and validated them in 293T cells by the surveyor nuclease assay, described in Chapter 2 (Ran *et al.* 2013). Individual sgRNA was transfected with Cas 9 nuclease enzyme into 293T cells to introduce a double-strand break in the genomic DNA at the annealed site. An efficient sgRNA would result in a cut followed by NHEJ DNA repair with mutations and indels (insertions and deletions) introduced. The sgRNA target site was then

amplified by PCR and subjected to reannealing (denatured to 95 °C and slowly cooled down). As the result, heteroduplex DNA were formed i.e. DNA paired up with mis-matches. Surveyor nuclease cleaved DNA specifically at mis-matched regions and a shorter size band on the gel suggested that the tested sgRNA successfully introduced target site modification. Based on the result from the surveyor assay we selected sgRNA-npc2-5' #2 and sgRNA-npc2-3' #6 (Figure 5.3).

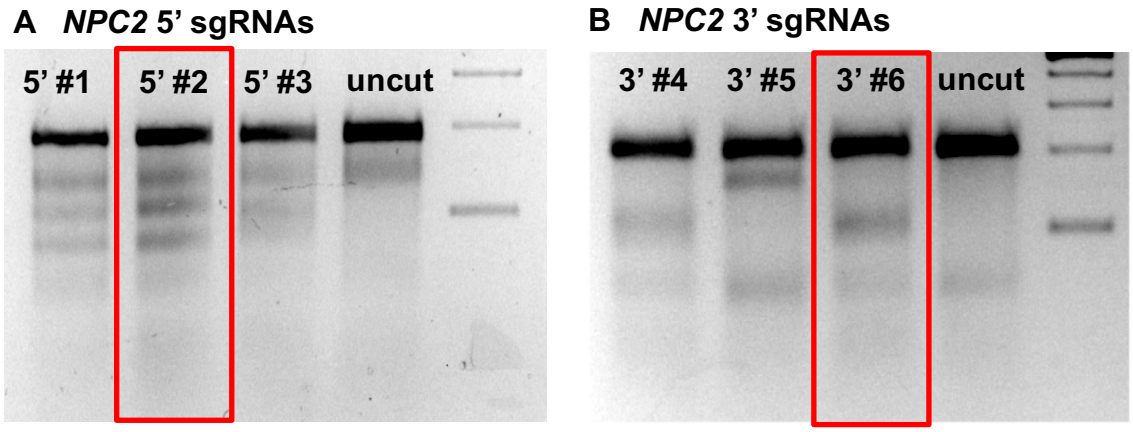


Figure 5. 3 NPC2 specific sgRNAs tested in the surveyor assays
293T gDNA has been treated with **A:** *NPC2* specific 5' sgRNAs (#1, #2 and #3); **B**: *NPC2* specific 3' sgRNAs (#4, #5 and #6) respectively. "Uncut" lane: gDNA isolated from cells that have been transfected only with Cas 9, without sgRNA or with a mutated unmatched sgRNA. Shorter fragments obtained in sgRNA treated gDNA samples compared to the uncut control indicated successful Cas 9 cutting. Selected sgRNA used in subsequent experiments are marked by a red rectangle.

The 5' and 3' sgRNAs were vectored in separate plasmids which carried different fluorescence gene reporters (mRuby and GFP) as well as the CRISPR/Cas 9 gene. Co-transfected HeLa cells with both sgRNAs were then single-cell sorted by FACS selecting for mRuby and GFP double positive cell population. Single-cell clones were stored and later screened for *NPC2* exon 3 deletion.

5.2.2 Genetic confirmation of *NPC2*KO HeLa cells

We screened the HeLa single-cell clones for *NPC2*KO using genomic DNA (gDNA) polymerase chain reaction (PCR). For gDNA PCR, we used primer pairs JX93, JX94 that were designed to anneal just outside of the sgRNA directed cut sites, schematically demonstrated in Figure 5.4. With wild-type (WT) HeLa gDNA, JX93/94 PCR gave an 840 base pair (bp) product, and for exon 3 deleted gDNA, the expected PCR product size is 318 bp. Because PCR preferably amplifies shorter DNA fragments, we ran two additional gDNA PCR with internal primers that anneal to the deleted exon region (primer JX95 and JX96), which should give a negative result if the target exon has been removed from the genome.

The gDNA PCR result for two selected *NPC2*KO clones H12 and H187 on 1% agarose gel is shown in Figure 5.4. From gDNA PCR reaction 1, both H12 and H187 had a single intense band at around 300 bp position. DNA was isolated from the gel band and sent for Sanger sequencing and the result confirmed the deletion of targeted fragment between the two sgRNAs. From reaction 2 and 3, there was no specific PCR product amplified from H12 and H187's gDNA. We further verified the knockout clones with reverse transcriptase PCR (RT-PCR) at the mRNA level, results are shown in Figure 5.5. We therefore confirmed that we successfully generated two *NPC2*KO HeLa cell-lines based on the genetic evidence.

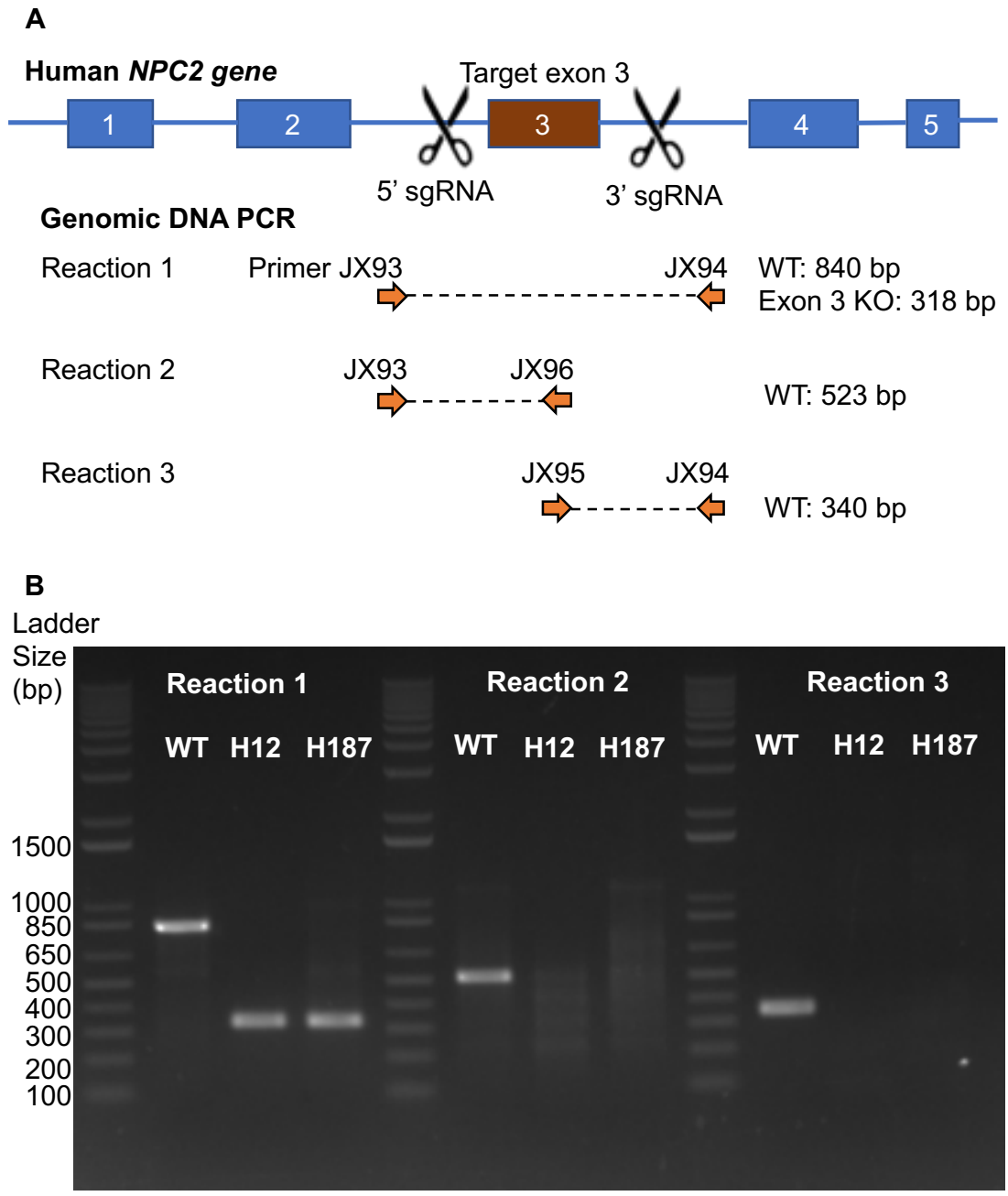


Figure 5. 4 NPC2KO HeLa genomic DNA PCR verification
We isolated genomic DNA (gDNA) from genetically modified HeLa clones (H12 and H187) and screened for target exon 3 deletion in the *NPC2* gene **A**: Schematic diagram showing the primer annealing sites (orange arrows) in respect of the target exon position and the sgRNAs cut sites (scissors). **B**: Reaction 1, 2 and 3 gDNA PCR were used to screen for successful modification of the *NPC2* gene. PCR products were separated on 1% agarose gel. Lanes for WT gDNA and gDNA isolated from selected *NPC2*KO clone H12 and H187 are shown.

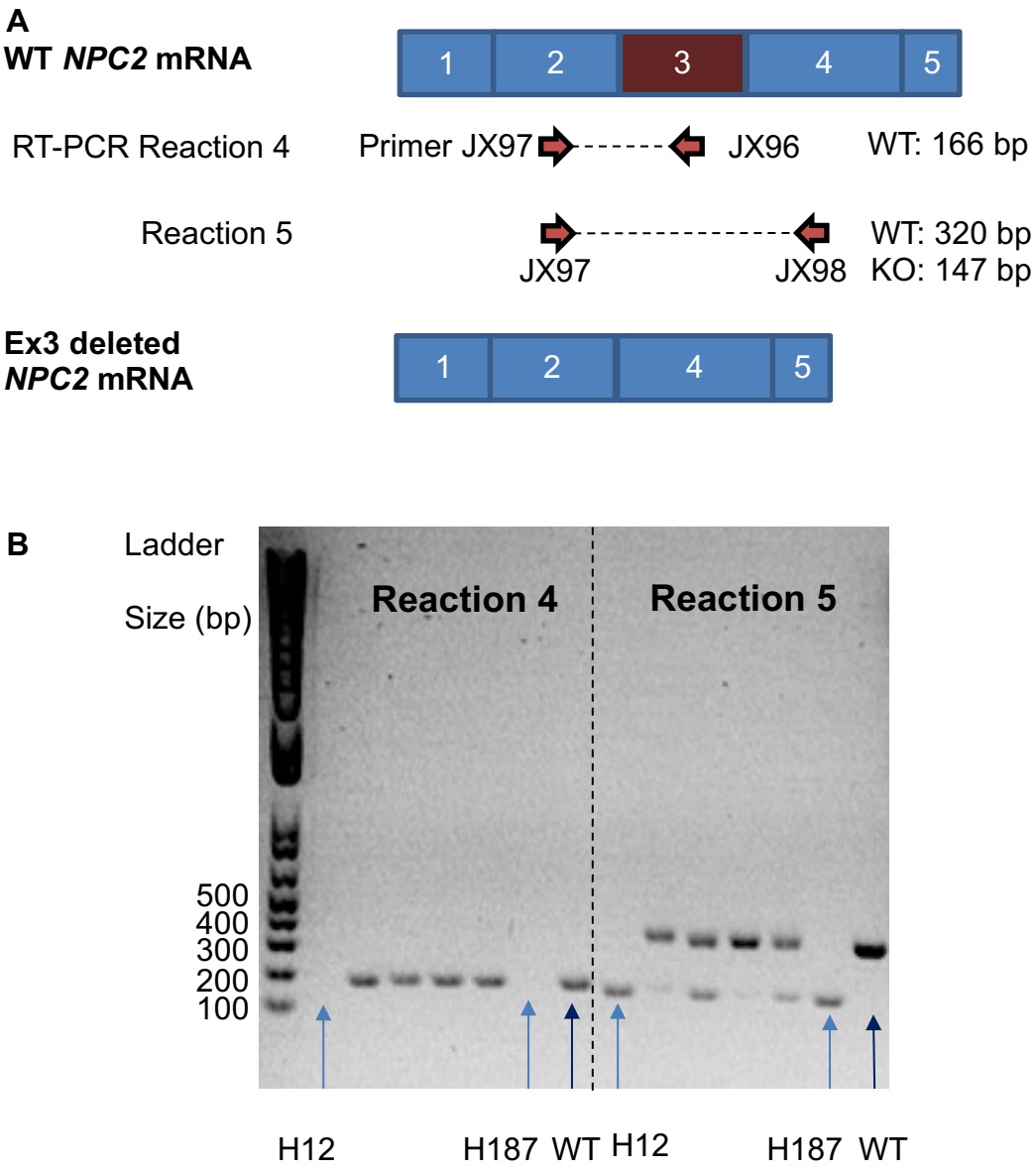


Figure 5. 5 RT-PCR characterising NPC2KO HeLa clones
A: Schematic diagram showing the annealing sites of RT-PCR primers in respect of *NPC2* exons in the WT *NPC2* mRNA transcript. **B**: Picture of 1% agarose gel for RT-PCR product of *NPC2* RT-PCR reaction 4 (primer JX97/JX96) and reaction 5 (primer JX97/JX98) amplified from WT and selected *NPC2*KO clones (H12 and H187) mRNA. Successful deletion of *NPC2* exon 3 resulted in the absence of an amplified product in reaction 4 and a shorter sized band in reaction 5. DNA purified from individual bands were sent for Sanger sequencing.

5.2.3 Functional assays of *NPC2*KO HeLa cells

Niemann-Pick type C disease is a neurodegenerative lysosomal storage disorder. Mutations in the NPC2 protein account for 5% of identified NPC disease cases and the rest are caused by NPC1 dysfunction (Vance and Karten 2014). The

cellular phenotype of NPC1 and NPC2 dysfunctional cells are the same and include accumulation of sphingosine, glycosphingolipids, sphingomyelin and cholesterol, as well as altered lysosomal calcium homeostasis (Babalola *et al.* 2007; Lloyd-Evans *et al.* 2008). In a drug-induced NPC disease-like model, sphingosine accumulation occurred first and is thought to be one of the initial factors for NPC disease pathogenesis (Lloyd-Evans *et al.* 2008). We therefore performed two sphingosine-based functional assays on our *NPC2*KO cells and tested them in parallel with both the parental WT HeLa cells and the control *NPC1*KO HeLa cells (ex2 and ex4) we obtained from our collaborator (Tharkeshwar *et al.* 2017).

We quantified the total amount of cellular sphingosine using high performance liquid chromatography (HPLC) (He *et al.* 2005). We showed that the sphingosine level was increased by around two-fold in both the *NPC1*KO and *NPC2*KO cells (H12 and H187) compared to their parental WT HeLa cells respectively (Figure 5.6) The sphingosine HPLC experiment was repeated twice and was supervised by Mylene Huebecker (Platt lab, Department of Pharmacology, University of Oxford). Further repeats will be required to draw statistical significance.

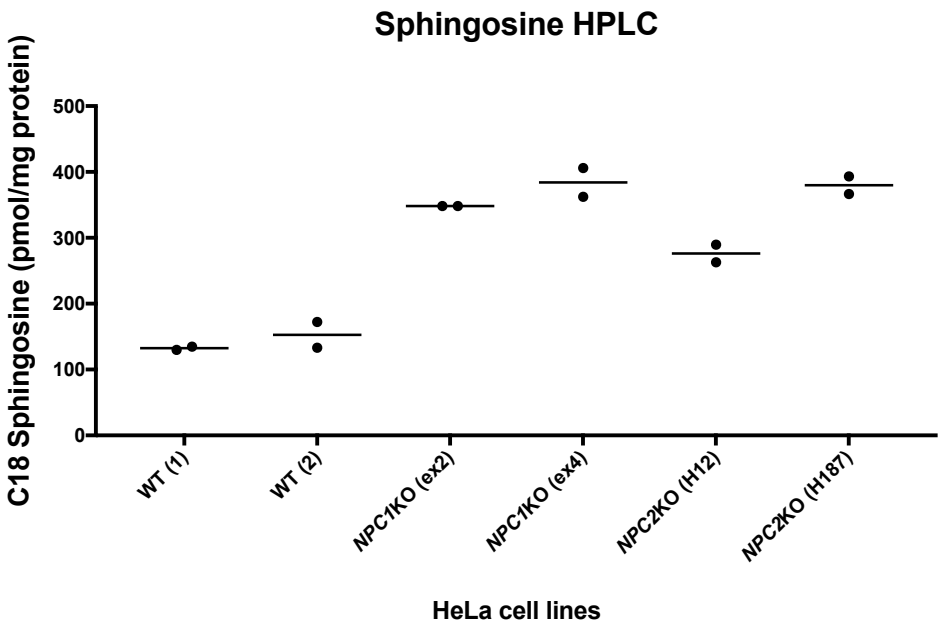


Figure 5. 6 Sphingosine level in NPC1KO and NPC2KO cells
C18 sphingosine concentration (pmol per mg protein) in HeLa cells was quantified by high performance liquid chromatography (HPLC). WT (1) is the parental wild-type HeLa used to generate the two tested *NPC1*KO clones (ex2 and ex4; Tharkeshwar *et al.* 2017). WT (2) is the parental HeLa cell-line used to generate the *NPC2*KO HeLa clones (H12 and H187). Results from technical duplicates are shown in the diagram with the horizontal line representing the average value.

In addition, we sent the *NPC1*KO and *NPC2*KO cells to our collaborator Doris Höglinger (Heidelberg University) to measure sphingosine trafficking in live cells by using a photo-crosslinkable and clickable trifunctional sphingosine (pacSph) (Höglinger *et al.* 2017). HeLa cells were pulse-labelled with pacSph for 5 min, and chased for 0 min, 10 min or 30 min. Upon UV irradiation, pacSph crosslinked with interacting protein in the cell. Cells were fixed and imaged using confocal microscopy (Figure 5.7 A). As shown in Figure 5.7 B, sphingosine co-localised with the lysosomal marker LAMP-1 initially (0 min). In WT HeLa cells, sphingosine began to be released to the cytoplasm within 10 min of chasing and the majority had reached the cytoplasm after 30 min.

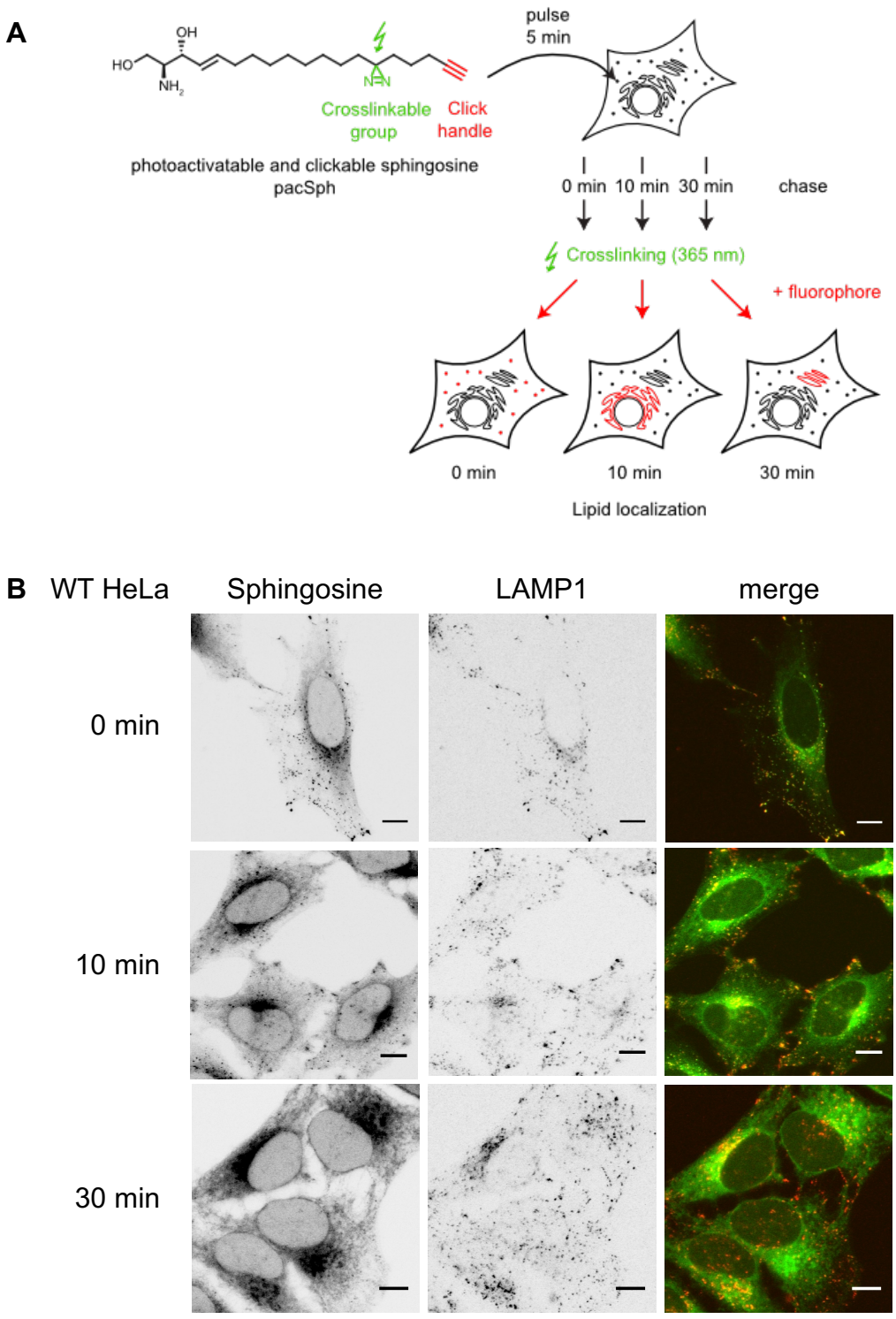


Figure 5. 7 Pulse-chase photo-crosslinkable sphingosine in HeLa cells
A: Schematic diagram showing the mechanism of photoactivatable and clickable sphingosine (pacSph) (Höglinger *et al*. 2017). HeLa cells were pulsed with pacSph for 5 min and subsequently chased for 0, 10 and 30 min. UV irradiation then activated the pacSph to crosslink with interacting proteins in the cell. **B**: Confocal images of WT HeLa cells during the pacSph pulse-chase experiment. Sphingosine was stained with Alexa Fluor® 488 conjugated-azide (green) and lysosomal marker LAMP1 was stained with rabbit anti-LAMP1 antibody and Alexa Fluor® 555 conjugated anti-rabbit second layer (red). (Scales bar, 20 μm).

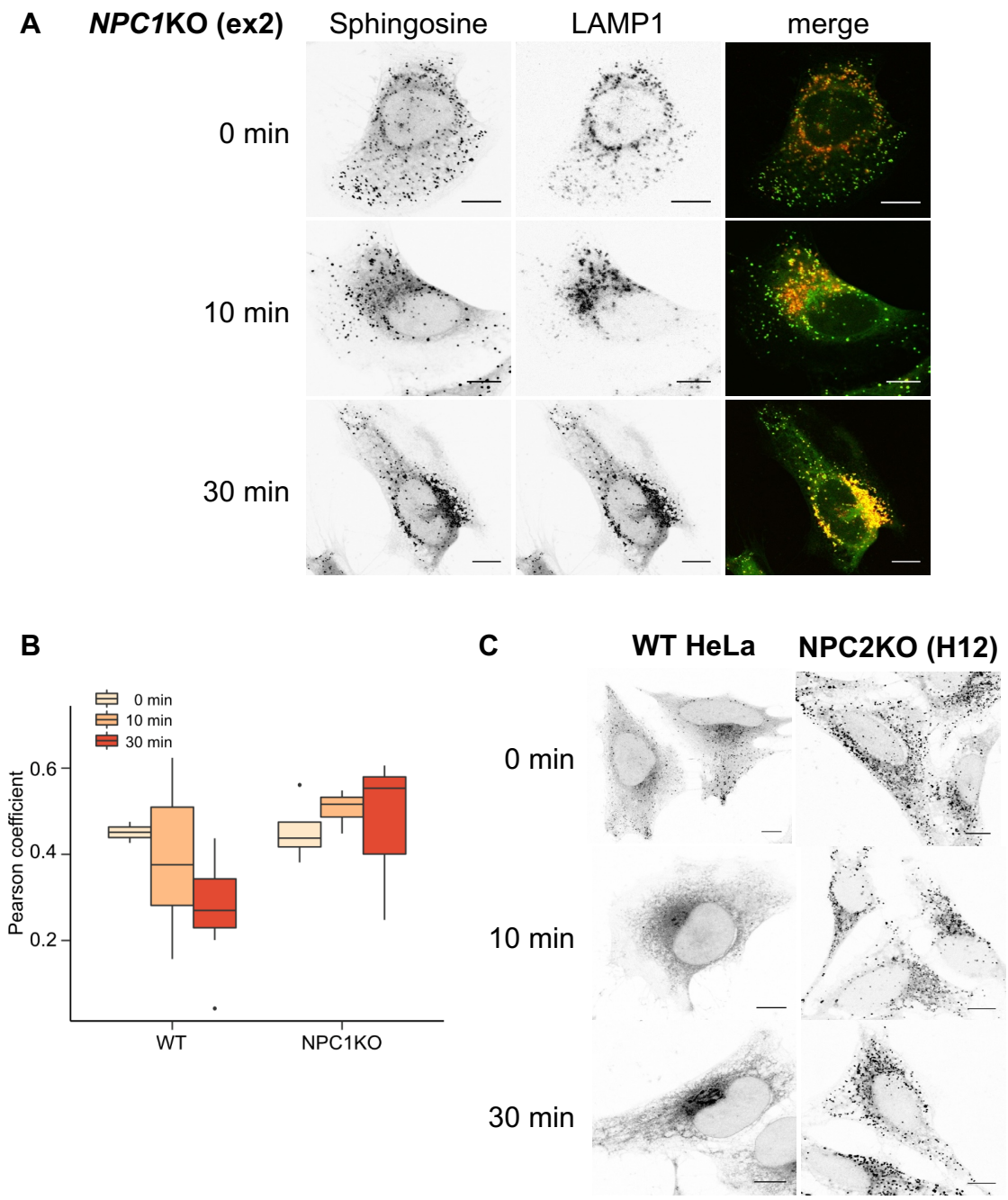


Figure 5. 8 Sphingosine localisation and trafficking in NPC1/2KO HeLa cells
A: Confocal images of *NPC1*KO HeLa cells (ex2 clone, Tharkeshwar *et al.* 2017). Pulse−chase experiments were performed by varying the time between uncaging and cross-linking from 0 min to 30 min. Sphingosine was stained with Alexa Fluor® 488 conjugated-azide (green) and lysosomal marker LAMP1 stained with rabbit anti-LAMP1 antibody and Alexa Fluor® 555 conjugated anti-rabbit second layer (red) (scale bars, 20 μm). **B**: Co-localisation of sphingosine with lysosomal marker LAMP1 in WT and *NPC1*KO HeLa cells was quantified by automated image analysis, represented as Pearson's correlation coefficient for >6 cells in each condition. **C**: Confocal images of *NPC2*KO HeLa cells (H12 clone) after pulse-chase experiments performed with cross-linkable sphingosine, uncaging from 0 min to 30 min. Sphingosine was stained with Alexa Fluor 555 conjugated-azide (scale bars, 20 μm).

In contrast, sphingosine trafficking was impaired in both *NPC1*KO (ex2 clone) and *NPC2*KO cells (clone H12 tested) (Figure 5.8). Sphingosine remained concentrated in the lysosome up to 30 minutes after uncaging. With these two sphingosine-based functional assays, we are confident that there was no residual functional NPC2 protein in the cells. In the future, we plan to characterise the knockout cells with anti-NPC2 antibody in Western blotting and measure other hallmarks of NPC disease phenotype such as cholesterol and sphingolipid accumulation, and calcium levels in the lysosomes.

5.2.4 EBOV-GP pseudotyped virus infection in NPC2 deficient cells

We then infected *NPC2*KO HeLa cells with our EBOV-GP pseudotyped virus E-S-FLU, developed and characterised in Chapter 3. E-S-FLU expresses a reporter eGFP gene after successful cell entry. Previously we showed that E-S-FLU does not infect *NPC1*KO cells (Chapter 3, Figure 3.5 and Figure 3.18). We infected two *NPC2*KO HeLa clones (H12 and H187) and their parental WT HeLa cell-line with E-S-FLU and control H7-S-FLU for 24 hours. H7-S-FLU contains the same pseudotyped virus core as E-S-FLU but differs only by its coating protein, which is H7 hemagglutinin. Infection was quantified by FACS analysis, and the level of infection by both E-S-FLU and H7-S-FLU was similar between WT HeLa and *NPC2*KO cells (Figure 5.9). The experiment was repeated three times.

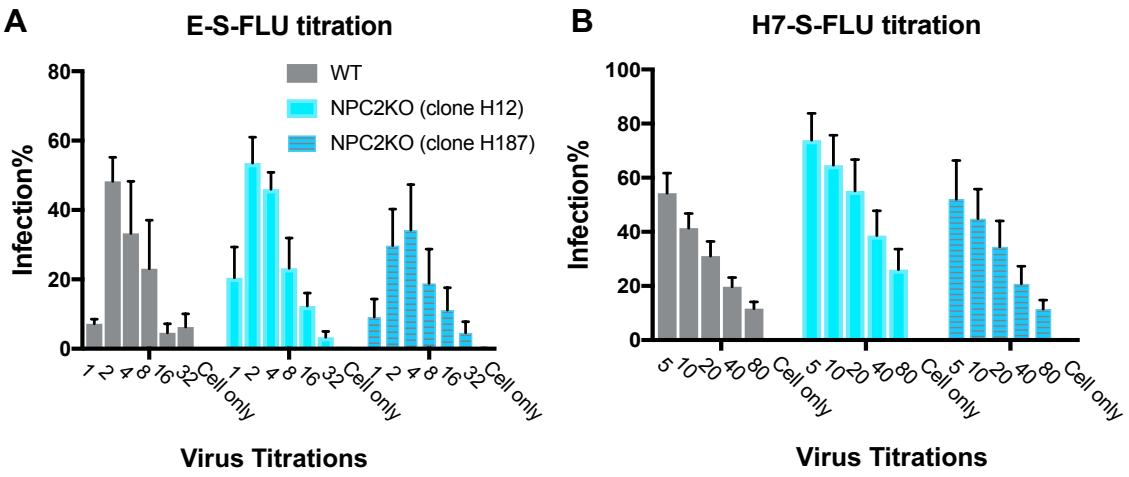


Figure 5. 9 E-S-FLU infection in NPC2KO HeLa cells
We titrated EBOV-GP pseudotyped E-S-FLU (**A**) and control H7-S-FLU (**B**) to infect WT and *NPC2*KO HeLa cells (H12 and H187 clones). Cells were infected for 24 hours then fixed and analysed by FACS. The infection% was the percentage of cells with an eGFP readout of $>10^2$ fold more than the uninfected "Cell only" control. Average infection% from three experimental repeats are shown with error bars representing the standard error of the mean (SEM).

*NPC2*KO cells were then infected with EBOV-GP pseudotyped lentivirus (GP-lentivirus), kindly provided by our collaborator Edward Wright (University of Sussex). GP-lentivirus carries a firefly luciferase reporter gene. GP-lentivirus was titrated and incubated with *NPC2*KO cells were for 48-hour infection. Cells were then lysed and analysed with Bright-Glo™ Luciferase Assay System kit. Both *NPC2*KO clones (H12 and H187) were permissive to GP-lentivirus infection, which gave up to 1000-fold greater luminescence than uninfected (Figure 5.10).

The average luminescence of infected *NPC2*KO cells was reduced to approximately one-third that of infected HeLa cells. We also performed the same assay with *NPC1*KO HeLa cells. Post-infection luminescence readout in *NPC1*KO cells were reduced by more than 20-fold compared to WT cell-line. Combining the results of E-S-FLU and GP-lentivirus infection, we conclude that NPC2 was not

necessary for infection of EBOV pseudotyped viruses but may have a subtle negative effect on GP-lentivirus infection, which requires further investigation.

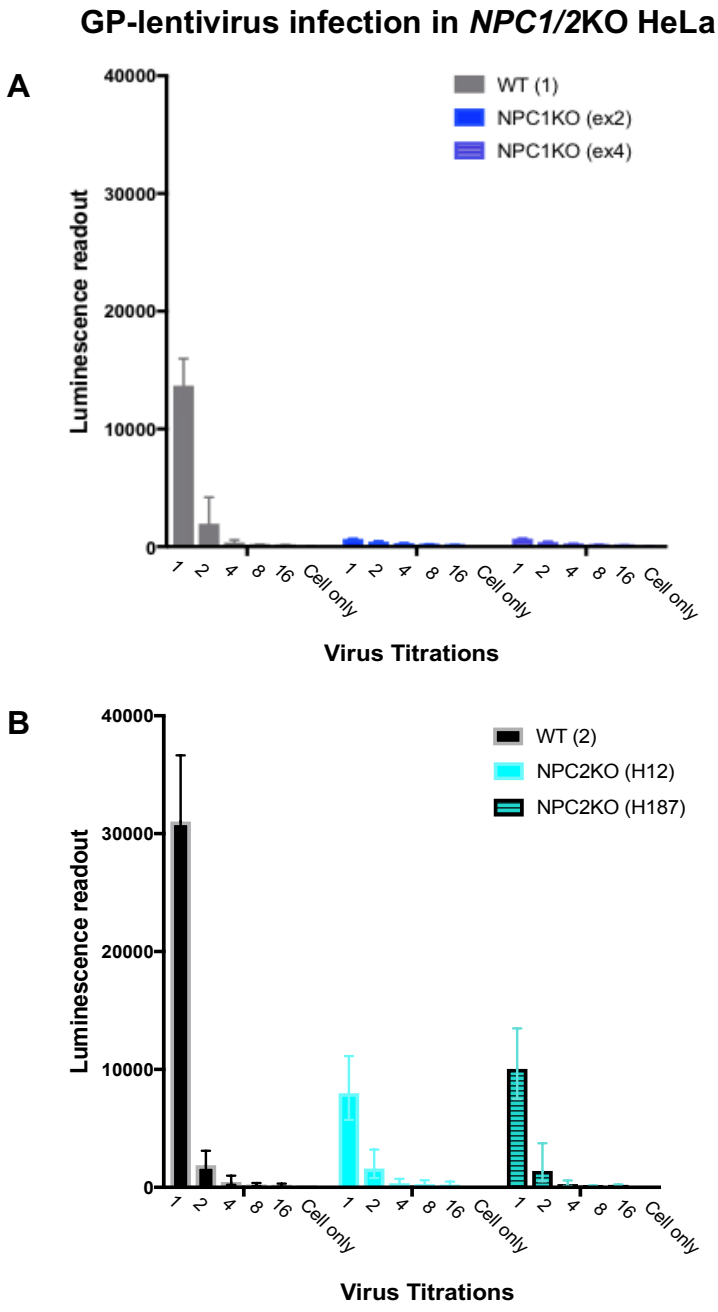


Figure 5. 10 GP-lentivirus infection of NPC1KO and NPC2KO HeLa cells
EBOV-GP pseudotyped lentivirus (GP-lentivirus) was titrated to infect *NPC1*KO (ex2 and ex4) and *NPC2*KO (H12, H187) HeLa cells with their parental WT HeLa cells respectively. GP-lentivirus carries a firefly luciferase reporter gene. Cells were infected for 48 hours. After infection, cells were lysed and reacted with luciferase substrate (Glo-lysis kit, Promega), and infection was quantified by measuring the luminescence level. The experiment was repeated three times, and the mean luminescence readout was plotted with error bars representing the standard error of the mean (SEM).

5.3 EBOV infection in ASM deficient cells

5.3.1 *SMPD1*KO design

Acid Sphingomyelinase (ASM) belongs to the family of sphingomyelinases (SMase), enzymes which catalyse the hydrolysis of sphingomyelin to ceramide and phosphorylcholine (Goñi and Alonso 2002; Jenkins, Canals and Hannun 2009) (Figure 5.11). ASM has an optimal activity in an acidic environment (pH ~ 5, Goñi and Alonso 2002). There are two forms of ASMs: lysosomal and secretory ASM (Tardy *et al.* 2006), both coded by *SMPD1* gene (sphingomyelinase phosphodiesterase 1). We used CRISPR/Cas 9 technology to modify the *SMPD1* gene at the genomic level to abolish the expression of both forms of ASM.

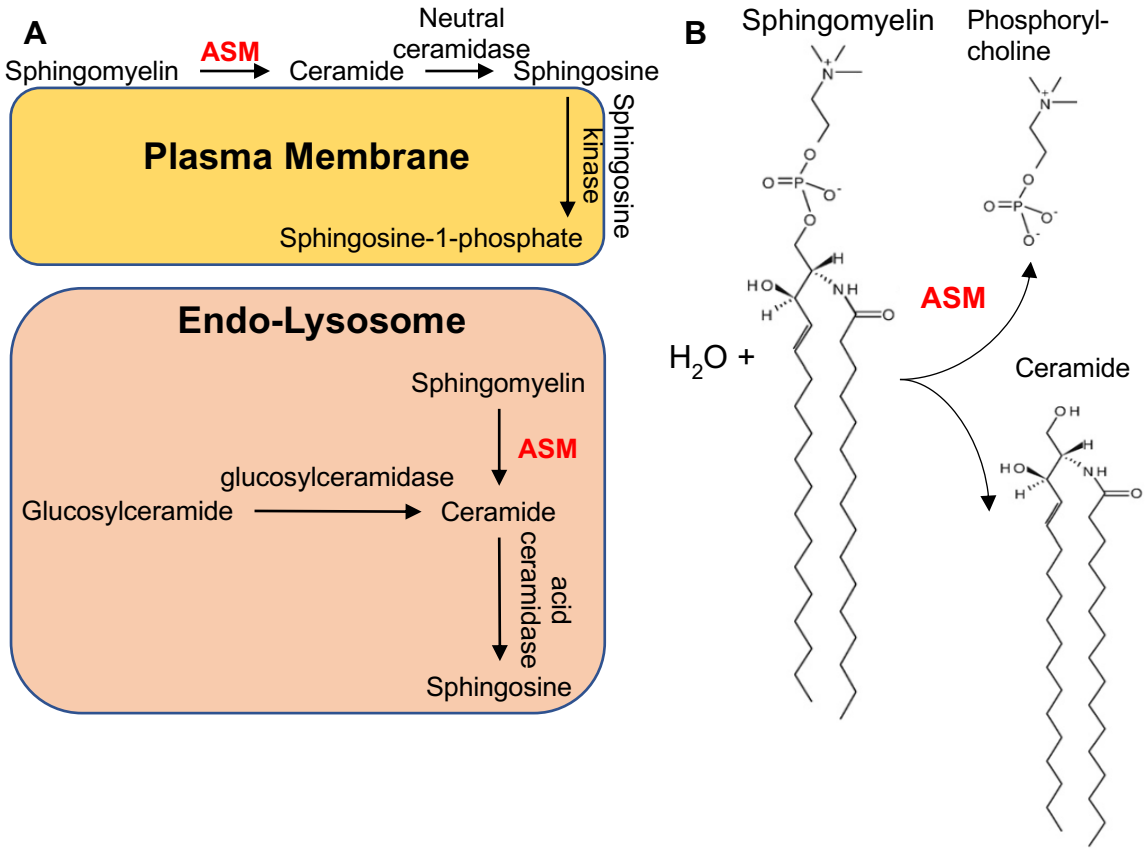


Figure 5. 11 Sphingolipid metabolism and sphingomyelinase pathway
Figure adapted from Jenkins *et al.* 2009. **A**: The breakdown of sphingomyelin by acid sphingomyelinase (ASM) within the endo-lysosomal compartment and at the outer leaflet of the plasma membrane. **B**: Sphingomyelinase reaction. Sphingomyelin is hydrolysed into ceramide and phosphorylcholine catalysed by acid sphingomyelinase (ASM).

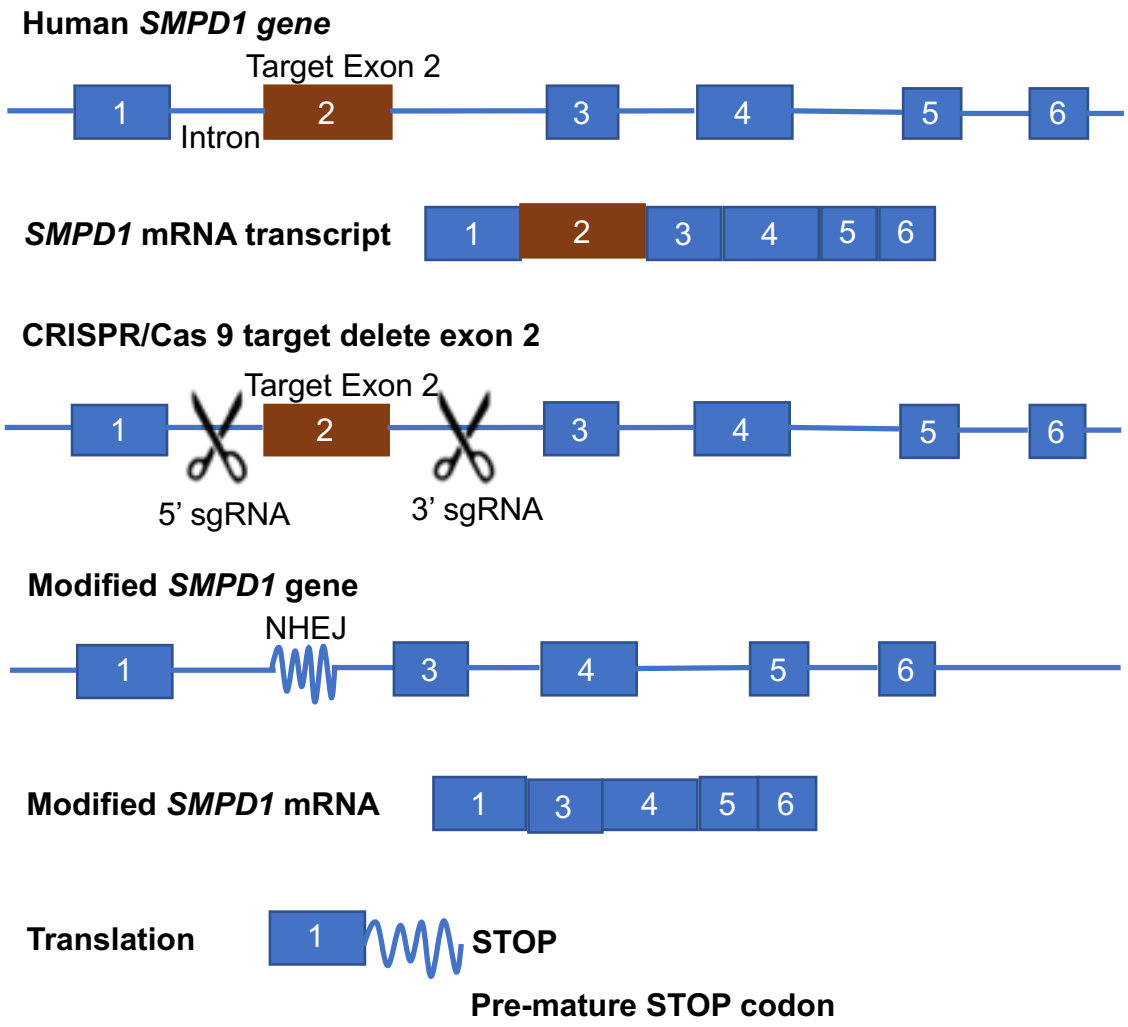


Figure 5. 12 Schematic diagram of SMPD1 gene exon 2 knockout design by CRISPR/Cas 9

Gene organisation and mRNA transcript of WT and exon 2 deleted *SMPD1* gene. Exons are represented by rectangular blocks and introns by lines. 5' and 3' sgRNAs guided Cas 9 nuclease to cleave (scissors) at intronic regions flanking the target exon 2, which may lead to a complete deletion of the fragment between two sgRNAs' annealing sites. DNA break was repaired by non-homologous end joining (NHEJ). Modified *SMPD1* transcript has a frameshift and a pre-mature STOP codon introduced.

The *SMPD1* gene is located on human chromosome 11p15.1 and spans around 6 kb. The gene contains 6 exons and 5 introns. The functional transcript is 1,890 base pairs (bp) long, encoding for a 629-residue polypeptide (da Veiga Pereira *et al.* 1991; Schuchman *et al.* 1991, 1992). Mature ASM starts from residue 66 after post-translational modification (Jenkins, Canals and Hannun 2009). We targeted

to delete *SMPD1* exon 2 with the dual sgRNAs strategy as described earlier in section 5.2.1 (NPC2 knockout design). *SMPD1* gene exon 2 is 773 bp long, deletion of which results in the removal of more than 80% of the coding region and introduces a frame-shift with a premature termination of translation (Figure 5.12). The remaining exon 1 encodes for the first 106 amino acids, 65 of which are removed (the signal peptide) in post-translational modification, and the rest runs into half of the first functional domain (saposin-like domain, amino acid 89 – 165), which is most likely to be misfolded, non-functional and degraded (Gorelik *et al.* 2016; Xiong *et al.* 2016).

Philip Hublitz designed the sgRNAs directing the Cas 9 protein to cut at both 5' and 3' intronic regions flanking *SMPD1* exon 2. He also validated the sgRNAs in 293T cells by the surveyor nuclease assay (Figure 5.13). Based on the results we selected sgRNA-smpd1-5' #3 and sgRNA-smpd1-3' #5. We then co-transfected both sgRNAs into HeLa cells to modify its genome, and selected single cell clones for knockout verifications.

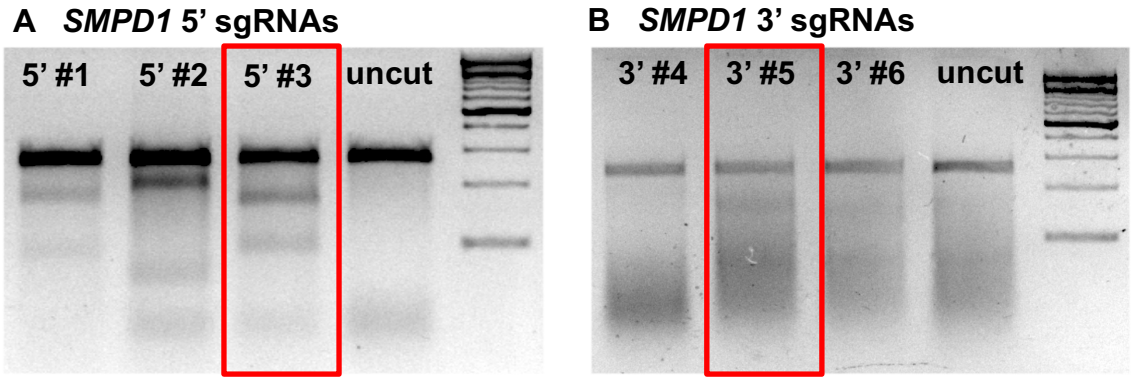


Figure 5. 13 SMPD1 specific sgRNAs tested in surveyor assays
293T gDNA has been treated with **A:** *SMPD1* specific 5' sgRNAs (#1, #2 and #3); **B**: *SMPD1* specific 3' sgRNAs (#4, #5 and #6) respectively. "Uncut" lane: gDNA isolated from cells that have been transfected only with Cas9 without sgRNA or with a mutated unmatched sgRNA. Shorter fragments obtained in sgRNA treated gDNA samples compared to the uncut control indicated successful Cas 9 cutting. Selected sgRNAs used in subsequent experiments are marked by a red rectangle.

5.3.2 Genetic confirmation of *SMPD1*KO cells

*SMPD1*KO clones were selected based on the genomic DNA (gDNA) PCR result, using primer pair JX99/JX100 which amplified the genetically modified region (Figure 5.14 Reaction 1). The expected PCR product size was 1,310 bp for the WT gDNA, and 250 bp for exon 2 deleted gDNA. We also ran additional gDNA PCR reactions 2 and 3 with internal primers (primer JX101 and JX102) that annealed to the target deleted region (Figure 5.14 Reaction 2, 3).

The result from PCR reaction 2 and 3 showed that clones I16, I93 and I147 no longer have any specific PCR product, suggesting that deletion of the target exon 2 was complete. However, the 1,310 bp band was still seen in PCR reaction 1 in these clones. We purified DNA from the excised gel bands and sent it for Sanger sequencing. The result revealed that the cleaved fragment was flipped and re-inserted back to the same site, which was confirmed by PCR reaction 1X using two forward primers JX99 and JX101 demonstrated in 5.15. Clone I7 still had a trace of an unmodified *SMPD1* copy remaining. We further confirmed the three knockout clones (I16, I93 and I147) with reverse transcriptase PCR (RT-PCR) at the mRNA level, as shown in Figure 5.16. We therefore concluded that we had successfully generated three *SMPD1*KO HeLa cell-lines based on the genetic evidence.

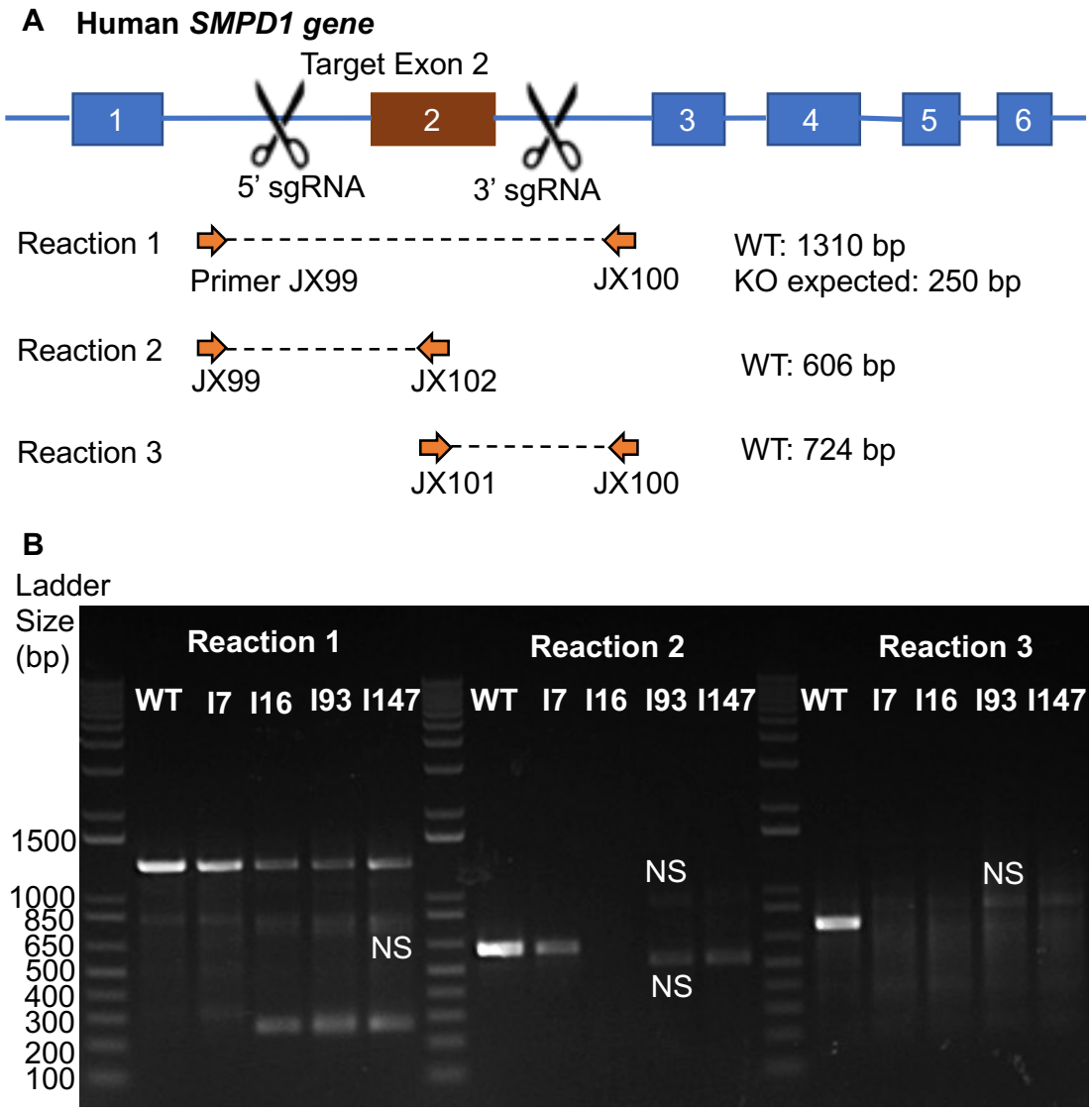
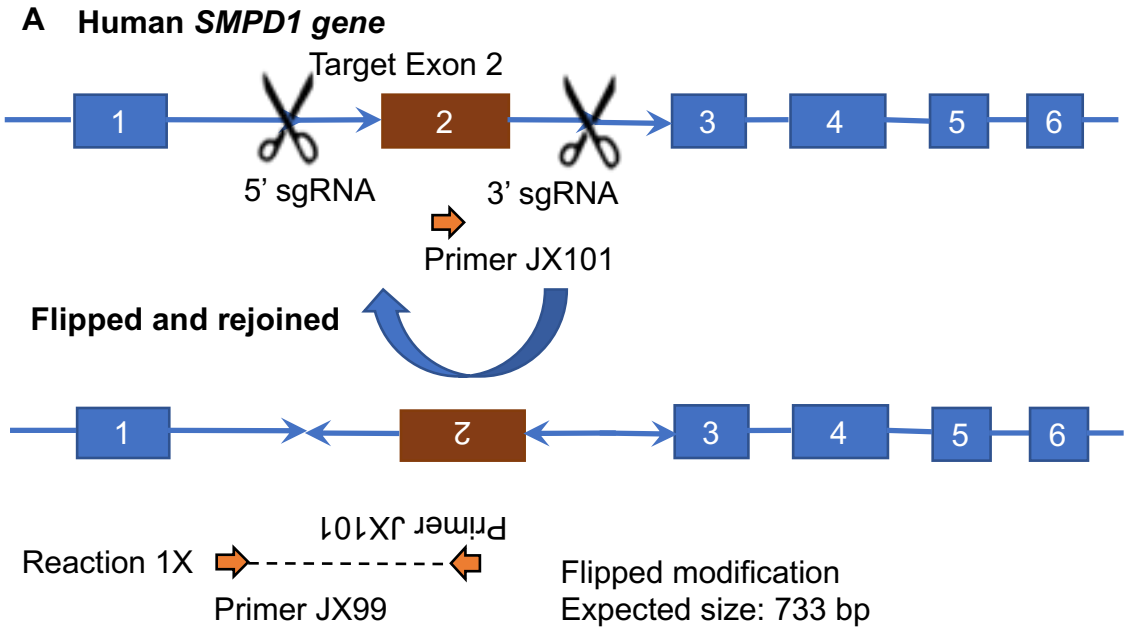


Figure 5. 14 SMPD1KO HeLa genomic DNA PCR verification

We isolated genomic DNA (gDNA) from genetically modified HeLa clones (I7, I16, I93 and I147), and screened for target exon 2 deletion in the *SMPD1* gene. **A**: Schematic diagram showing the primer annealing sites (orange arrows) in respect of the target exon position and the sgRNAs recognition sites (scissors). **B**: Reaction 1, 2 and 3 gDNA PCR was used to screen for successful modification of the *SMPD1* gene. PCR products were analysed on a 1% agarose gel. Lanes for WT gDNA and gDNA isolated from selected *SMPD1*KO clone I7, I16, I93 and I147 are shown. DNA was isolated from specific gel bands and sent for sequencing. NS labels the non-specific bands that showed no alignment with gDNA sequence in *SMPD1* gene region.



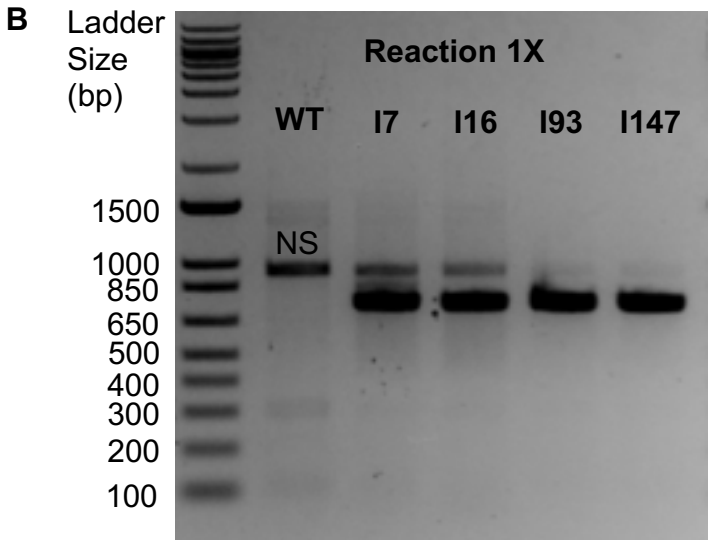


Figure 5. 15 Genetic modification of SMPD1 with exon 2 flipped and reinserted

A: Schematic diagram illustrating the flipped and re-inserted genetic modification in the *SMPD1* gene. The 5' and 3' sgRNA cleaved fragment was re-inserted into the same position but with inverted orientation. **B**: PCR reaction 1X using primer pair JX 99/101 gave an intense band at position 733 bp from *SMPD1* modified clones (I7, I16, I93 and I147). NS: non-specific band amplified and sequenced by Sanger sequencing.

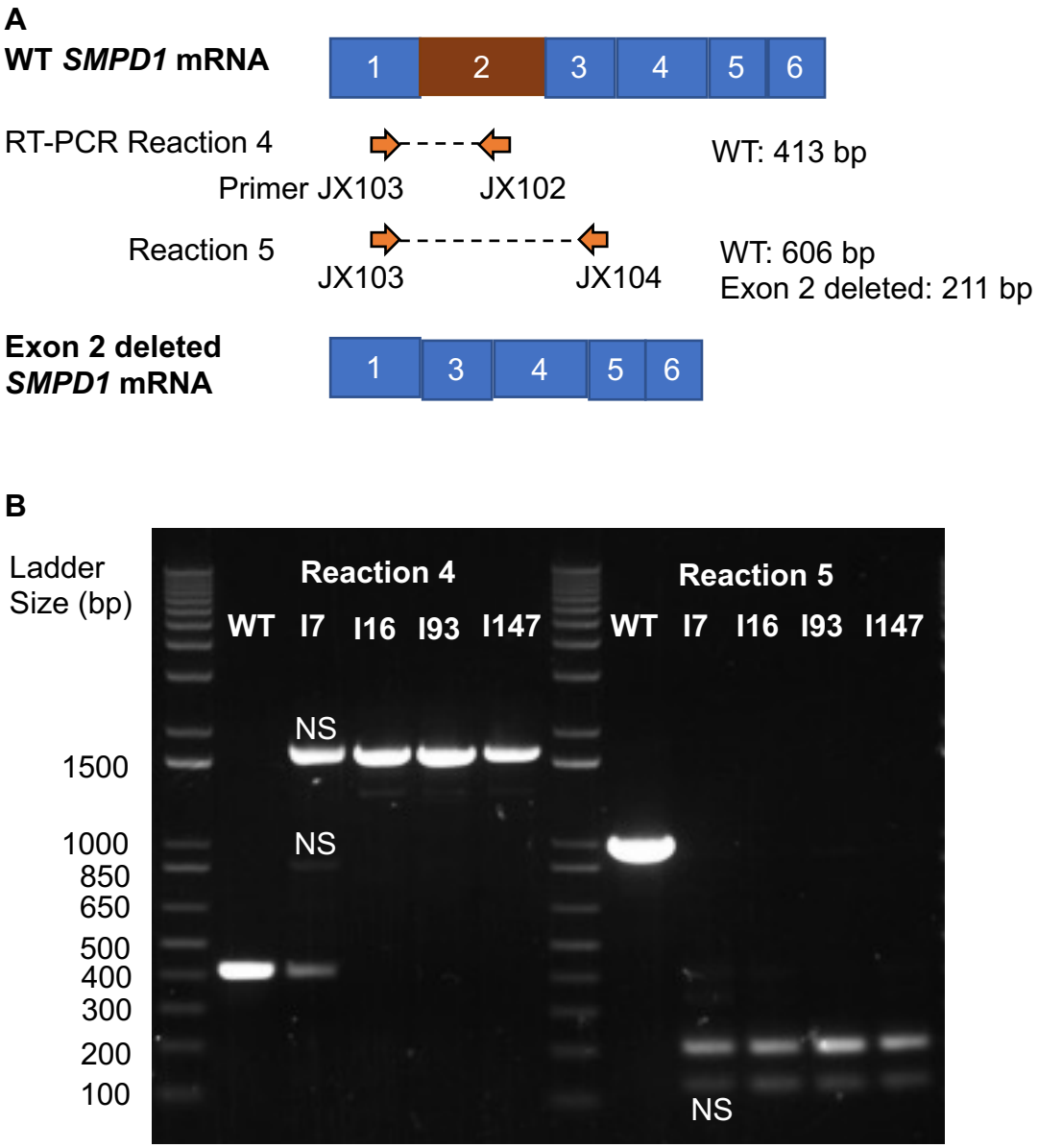


Figure 5. 16 RT-PCR characterisation of SMPD1KO HeLa clones

A: Schematic diagram showing the annealing sites of RT-PCR primers in respect of *SMPD1* exons in the WT mRNA transcript. **B**: Picture of 1% agarose gel loaded with product of *NPC2* RT-PCR reaction 4 (primer JX103/JX102) and reaction 5 (primer JX103/JX104) amplified from WT and selected *SMPD1*KO clones (I7, I16, I93 and I147) mRNA. Successful deletion of *SMPD1* exon 2 resulted in no amplified product from RT-PCR reaction 4 and a shorter sized band in reaction 5 (size: 211 bp). DNA purified from individual bands were confirmed by Sanger sequencing. NS indicates non-specific bands amplified with no sequence alignment to the *SMPD1* gene.

5.3.3 Functional assays of *SMPD1*KO cells

ASM catalyses the hydrolysis of lysosomal sphingomyelin to ceramide and phosphorylcholine. Subsequently, ceramide can further be hydrolysed by acid

ceramidase to yield sphingosine (Figure 5.11). Deficiency of ASM is the cause of Niemann-Pick disease types A and B (Schuchman 2007). In ASM deficient cells, sphingomyelin accumulates and less ceramide is produced in the lysosome, which results in less sphingosine from the breakdown of ceramide. As an indirect functional measurement, we quantified the level of naturally occurring C18 sphingosine in our *SMPD1*KO cells by using HPLC (He *et al.* 2005). Two repeated measurements showed that all three clones of *SMPD1*KO cells (clone I16, I93 and I147) had reduced sphingosine level to one-third in comparison to WT HeLa cells (Figure 5.17). In the future, we plan to further characterise these *SMPD1*KO cells with more specific functional assays, such as western-blotting using anti-ASM antibody and measuring cellular ASM activities.

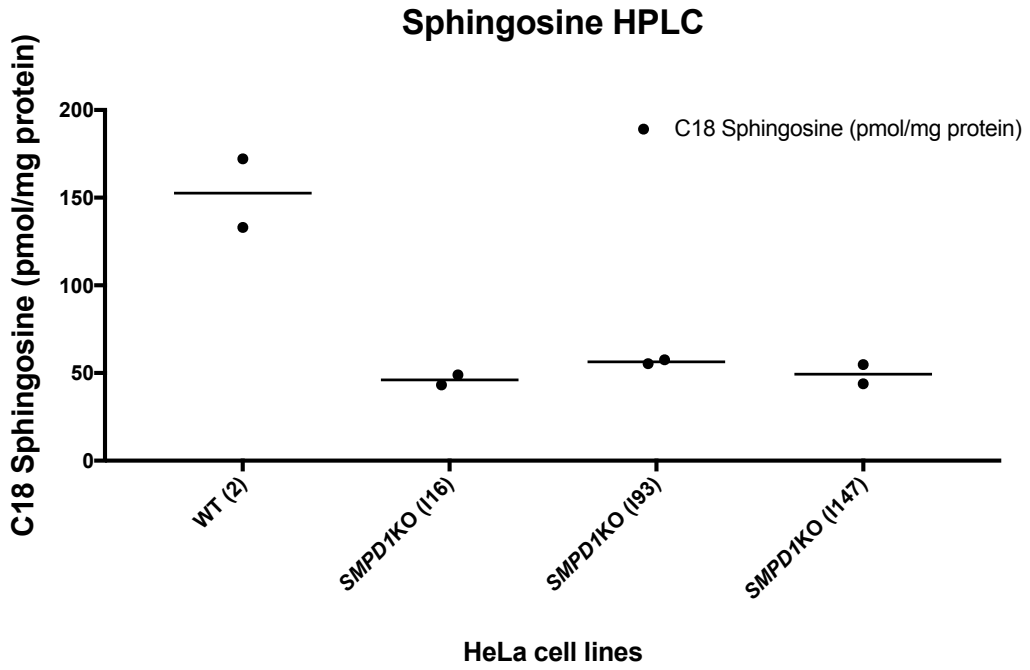
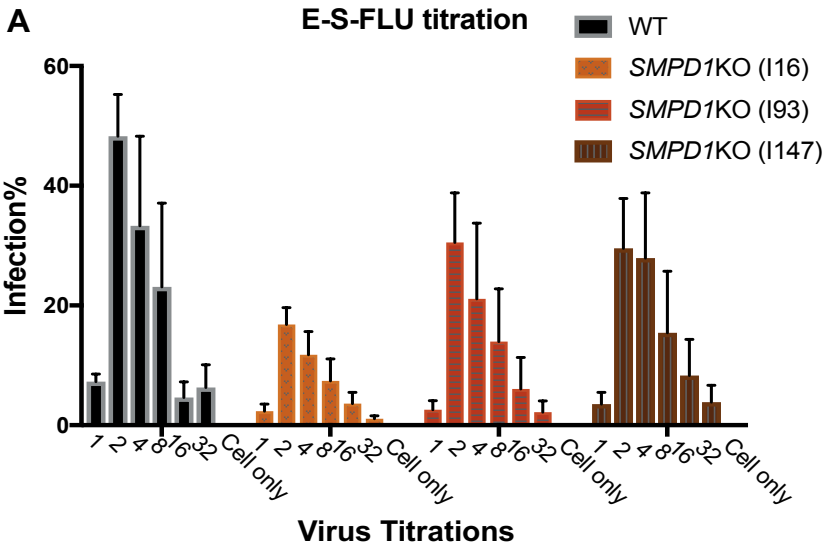


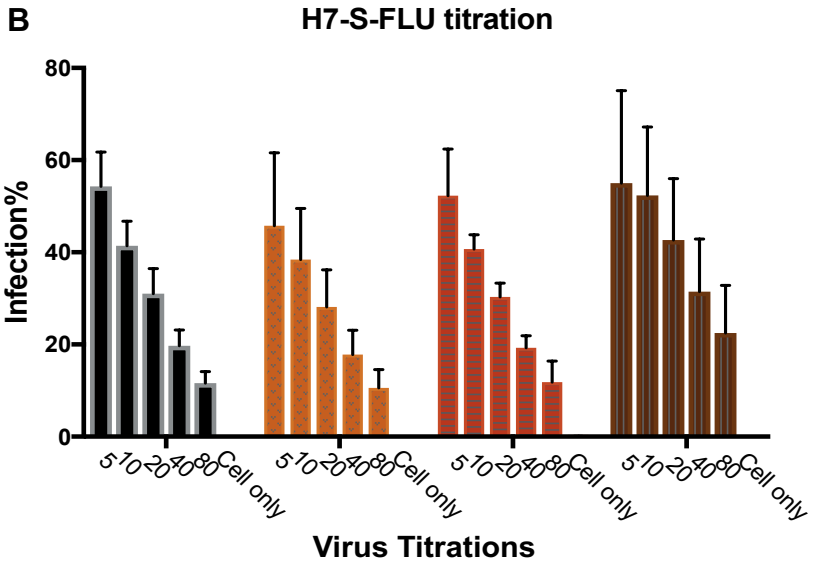
Figure 5. 17 Sphingosine level in SMPD1KO cells
C18 sphingosine concentration (pmol per mg protein) in HeLa cells was quantified by high performance liquid chromatography (HPLC). WT (2) is the parental HeLa cell-line used to generate the *SMPD1*KO HeLa clones (I16, I93 and I147). Results from technical duplicates are shown in the diagram with the horizontal line representing the mean value.

5.3.4 EBOV-GP pseudotyped virus infection in ASM deficient cells

We next compared the ASM deficient cells with WT HeLa cells in EBOV-GP pseudotyped virus infection assays. We titrated E-S-FLU and control H7-S-FLU for infection of the HeLa cells for 24 hours, and quantified percentage infected cells by FACS. E-S-FLU did not reach saturation when infecting HeLa cells, and we saw quite a range of variation in percentage infection between independent experimental repeats, indicated by the big error bars representing the standard error of the mean (SEM). All three clones of *SMPD1*KO cells were infected by E-S-FLU, but the percentage infection of E-S-FLU was slightly lower in clone I16 (Figure 5.18 A). The control H7-S-FLU virus had the same level of infection in both the *SMPD1*KO cells and WT HeLa cells (Figure 5.18 B).

We also infected the *SMPD1*KO cells with EBOV-GP pseudotyped lentivirus, which carries a firefly luciferase reporter gene. All three clones were infected by GP-lentivirus; however, a significant reduction of luminescence signal was found in clone I93, which may be caused by clonal variation (Figure 5.18 C). The results suggested that *SMPD1*KO may have had a modest inhibitory effect on infection by viruses pseudotyped with EBOV-GP, but ASM was not essential for EBOV-GP dependent entry. Further work is needed to find out if the minor variation in infection that we observed is independent clonal variation in HeLa cells in the expression of the surface binding molecules used by the GP, or a genuine effect on the efficiency of infection caused by loss of ASM expression.


A
E-S-FLU titration
WT
SMPD1KO (I16)
SMPD1KO (I93)
SMPD1KO (I147)
Infection%
60
40
20
0
1 2 4 8 16 32 Cell only
Virus Titrations


B
H7-S-FLU titration
Infection%
80
60
40
20
0
5 10 20 40 80 Cell only
Virus Titrations

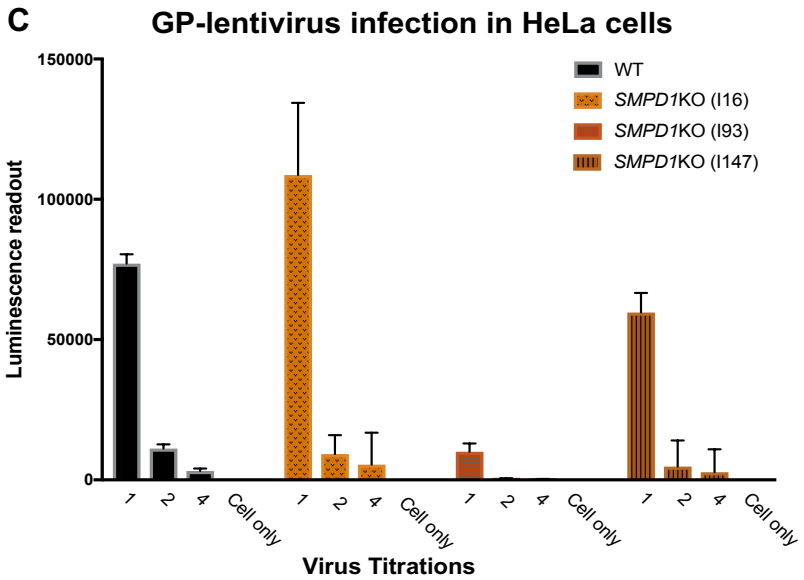

C
GP-lentivirus infection in HeLa cells
WT
SMPD1KO (I16)
SMPD1KO (I93)
SMPD1KO (I147)
Luminescence readout
150000
100000
50000
0
1 2 4 Cell only
Virus Titrations

Figure 5. 18 EBOV-GP pseudotyped virus infection in SMPD1KO HeLa cells
(**A**) EBOV-GP pseudotyped E-S-FLU, (**B**) control H7-S-FLU and (**C**) EBOV-GP pseudotyped lentivirus (GP-lentivirus) were titrated to infect WT and *SMPD1*KO HeLa cells (clone I16, I93 and I147). (**A** and **B**) E-S-FLU and H7-S-FLU viruses carry an eGFP reporter gene. Cells were infected for 24 hours, then fixed and analysed by FACS. The infection% was the percentage of cells with an eGFP readout of $>10^2$ fold more than the uninfected "Cell only" control. Average infection% from three experimental repeats are showed with error bars representing the standard error of the mean (SEM). (**C**) GP-lentivirus carries a firefly luciferase reporter gene. HeLa cells were infected for 72 hours. After infection, cells were lysed and reacted with luciferase substrate (Glo-lysis kit, Promega), and infection was quantified by measuring the luminescence level. The experiment was repeated three times, and the mean luminescence readout was plotted with error bars representing the standard error of the mean (SEM).

5.4 NPC1 polymorphism and EBOV infection

The NPC1 protein is the key receptor for EBOV entry via the lysosome. Cathepsin cleaved EBOV-GP binds to the domain C of the NPC1 protein, and this is thought to trigger a conformational change in GP2 that induces membrane fusion (Figure 5.19 A) (Weissenhorn *et al.* 1998, 2002; Malashkevich *et al.* 1999; Gregory *et al.* 2011; Miller *et al.* 2012a; Gong *et al.* 2016; Wang *et al.* 2016).

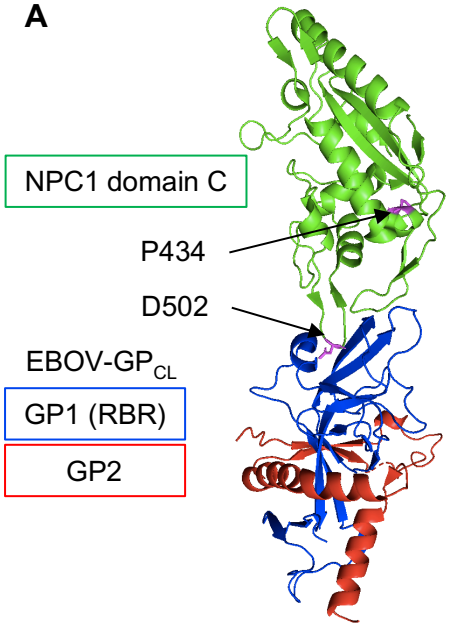
Together with our collaborator Mary Carrington (National Institutes of Health), we were interested in testing single nucleotide polymorphisms (SNPs) in the *NPC1* gene and their effect on susceptibility to EBOV infection and survival rate in humans. Mary began to genotype the *NPC1* gene from Ebola disease patients from the 2014-2015 West African outbreak. There are 4 non-synonymous SNPs found in the *NPC1* gene that have a frequency of 4% or greater in the West African population, based on the 1000 genomes database (Figure 5.19 B). SNP rs61731962 causes a change from proline to serine at position 434 in the NPC1 protein domain C. Although residue 434 is not in direct contact with bound EBOV-GP in the crystal structure (Wang *et al.* 2016), we reasoned that alteration from a

proline close to the binding site might alter the orientation of the binding loops and thus interfere with GP binding.

The other three SNPs correspond to amino acid residues outside of domain C (Figure 5.19 C) and therefore seemed less likely to influence EBOV entry. We initially tested the effect of P434S in our *in vitro* infection assay and the mutation D502F as a control NPC1 variant. NPC1 position 502 is in direct contact with cleaved EBOV-GP, as demonstrated in the crystal structure (Figure 5.19 A) (Gong *et al.* 2016; Wang *et al.* 2016). The NPC1 from African straw-coloured fruit bats (*Eidolon helvum*) has phenylalanine instead of aspartic acid (human NPC1) at position 502, and this was found to be a critical factor in resisting EBOV infection in this species (Ng *et al.* 2015).

Using mutagenesis PCR, we introduced mutation P434S and D502F into a mCherry-tagged human NPC1 cDNA. During the cloning stage, we observed that plasmids containing NPC1 cDNA were very unstable and resulted in high frequencies of genetic rearrangement after transformation of bacteria. After communicating with Feiran Lu (Lu *et al.* 2015), we solved this problem by using low salt LB medium (Sigma L3397, 0.5 g/L NaCl) and growing the bacteria culture at 30 ^{o}C instead of the 37 ^{o}C in the standard method.

A



B

Polymorphism in human *NPC1* gene

SNP	MAF	DNA	Exon	Protein
rs1788799	0.0417	G/C	12	M642I
rs61731962	0.0463	C/T	8	P434S
rs1805082	0.2778	A/G	16	I858V
rs1805084	0.287	G/A	25	R1266Q

SNP: single nucleotide polymorphism
MAF: minor allele frequency in African population

C

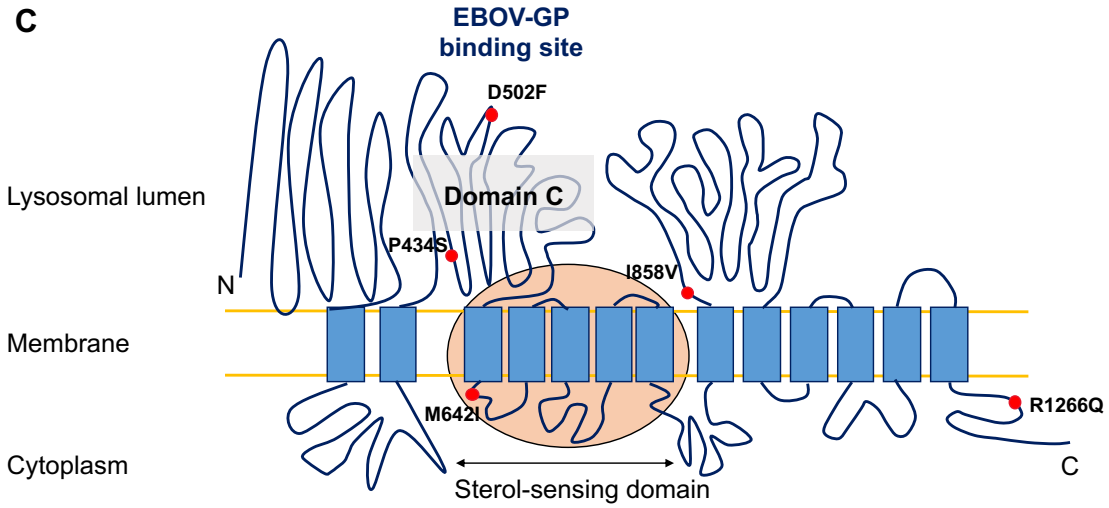


Figure 5. 19 NPC1 polymorphism and domain structure
A: Crystal structure of NPC1 domain C (green) in complex with cleaved EBOV-GP (PDB: 5F1B, Wang *et al*. 2016). GP1 with the receptor binding site (RBR) is coloured blue and GP2 is coloured red. The side chains of proline 434 (P434) and aspartate 502 (D502) are coloured in magenta. **B**: Summary of four single nucleotide polymorphisms (SNPs) found in human *NPC1* gene with the minor allele frequency (MAF) greater than 0.04 in the African population, based on the 1000 genome database. **C**: The schematic NPC1 protein model is drawn as proposed by Davies and Ioannou (2000). Blue rectangles represent the putative transmembrane domains. 4 non-synonymous SNPs (P434S, M642I, I858V and R1266Q) and the bat mutation D502F are indicated by red spots showing their predicted positions in the NPC1 protein.

We then cloned the mCherry-tagged WT and mutated NPC1 cDNA into a lentiviral vector, and transduced two clones of *NPC1*KO HeLa cells (ex2 and ex4)

(Tharkeshwar *et al.* 2017) to express three different NPC1-mCherry proteins (WT, D502F, P434S). Transduction was not 100% efficient and this resulted in populations of HeLa cells expressing different levels of NPC1-mCherry protein. Experiments have shown that the efficiency of infection by EBOV is dependent on the level of NPC1 protein expressed (Shoemaker *et al.* 2013; Herbert *et al.* 2015). The effect of NPC1 mutations on EBOV infection may thus be masked by over-expressing the protein.

To prevent this from happening, we continued our study with unsorted NPC1-mCherry transduced cells expressing different levels of NPC1 variants. We titrated E-S-FLU to infect the unsorted NPC1-mCherry transduced *NPC1*KO HeLa cells, and compared the mCherry fluorescence (NPC1-mCherry level) in the infected and uninfected cells (eGFP +ve/-ve). We reasoned that if only cells with high levels of NPC1 expression became infected we could suggest that the mutation had had an inhibitory effect on EBOV-GP dependent infection.

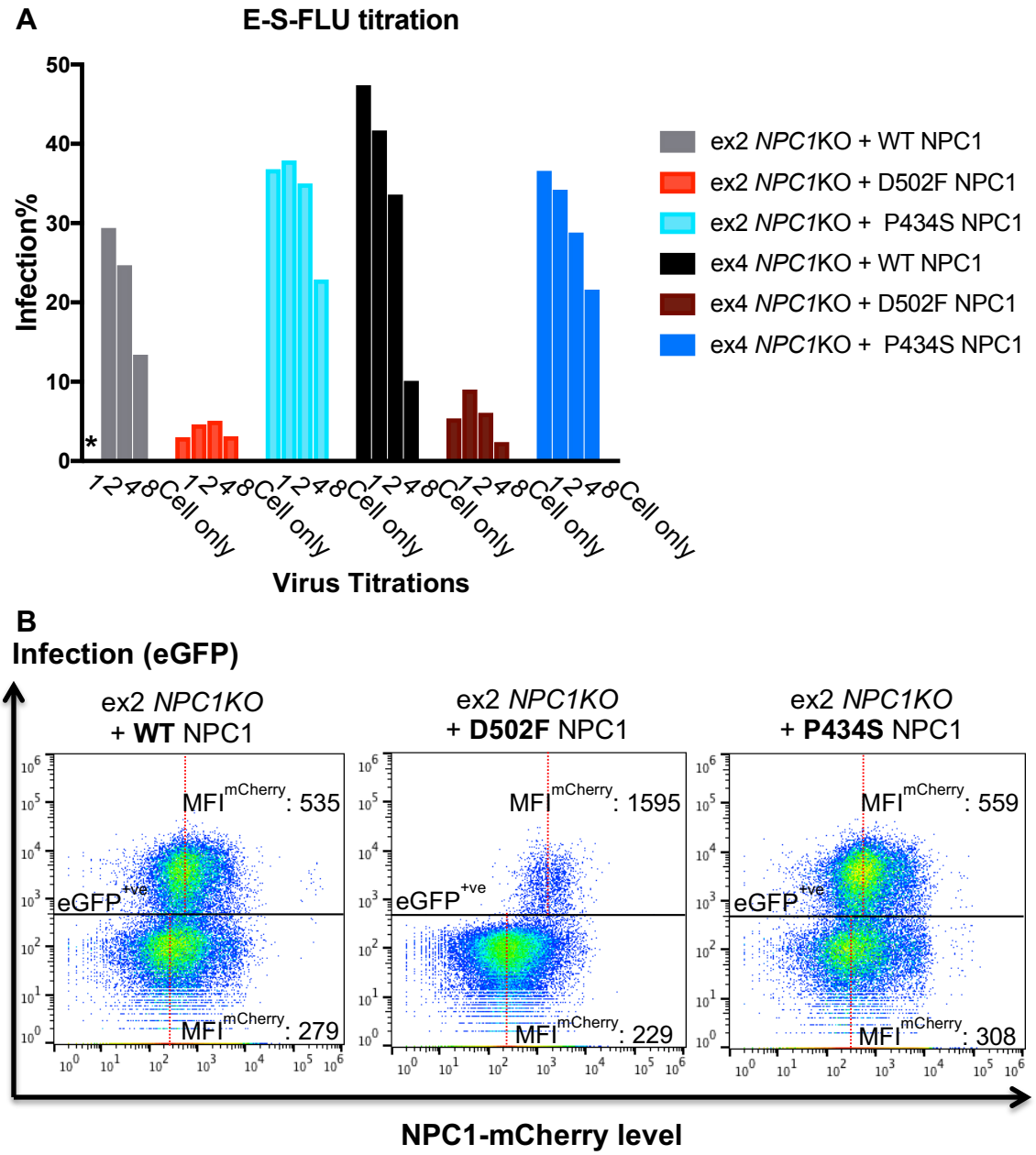


Figure 5. 20 E-S-FLU infection in HeLa cells expressing NPC1 variants
Two clones of *NPC1*KO cells were transduced to express WT, D502F and P434S variants of NPC1-mCherry. We infected the transduced cell population (unsorted) with E-S-FLU for 24 hours, and cells were then fixed and analysed by FACS. **A**: Infection% was the overall percentage of cells with an eGFP readout of $>10^2$ fold relative to the uninfected "Cell only" control. *****: E-S-FLU was titrated from dilution 1 in 2 instead of 1 in 1 (undiluted) for "ex2 *NPC1*KO + WT NPC1" cells. **B**: Representative FACS dot plots for ex2 *NPC1*KO cell transduced with WT, D502F and P434S NPC1-mCherry after E-S-FLU infection (virus diluted 1 in 2). The level of eGFP indicates E-S-FLU infection, whereas the mCherry fluorescence represents the expression level of transduced NPC1-mCherry in the infected and uninfected cells. Median fluorescence intensity ($MFI^{mcherry}$) of mCherry was calculated for $eGFP^{+ve}$ (infected) and $eGFP^{-ve}$ (uninfected) sub-populations, and indicated by red broken lines.

As shown in Figure 5.20 A, E-S-FLU infected HeLa cells expressing WT and P434S-NPC1-mCherry at similar levels (up to 30-35%), whereas infection was less than 5% in D502F-NPC1-mCherry transduced cells. We also showed that E-S-FLU infected cells (eGFP +ve population) had a higher median mCherry fluorescence intensity ($MFI^{mCherry}$, Figure 5.20 B) than the uninfected cells, indicating that infection was NPC1-mCherry dependent. In D502F-NPC1-mCherry transduced cells, infected cells had about three-fold higher mCherry MFI compared to WT and P434S-NPC1 expressing cells. This suggested that D502F-NPC1 resisted E-S-FLU entry, and efficient infection required a higher level of the D502F-NPC1 expression. The P434S mutant, which corresponded to the SNP we would like to test, did not show an obvious effect on the efficiency of E-S-FLU infection.

We further investigated whether the D502F and P434S mutations in NPC1 affected its normal physiological function. We bulk-sorted HeLa cells with high level expression of NPC1-mCherry (WT, D502F and P434S) and sent them to our collaborator Doris Höglinger (Heidelberg University). As described in section 5.2.3, Doris' assay measures the real-time trafficking of sphingosine from lysosome to cytosol in live cells (Höglinger *et al.* 2017). Defective sphingosine trafficking and subsequent accumulation of sphingosine in the lysosome has been shown as the earliest event in the drug-induced NPC disease model, and is a more specific hallmark than cholesterol accumulation (Lloyd-Evans *et al.* 2008). As shown in Figure 5.21, sphingosine trafficking was restored in *NPC1*KO cells by overexpression of all three NPC1 variants (WT, D502F and P434S). This

confirmed that the point mutations we introduced did not affect the function of NPC1 in sphingosine trafficking from lysosome to cytosol.

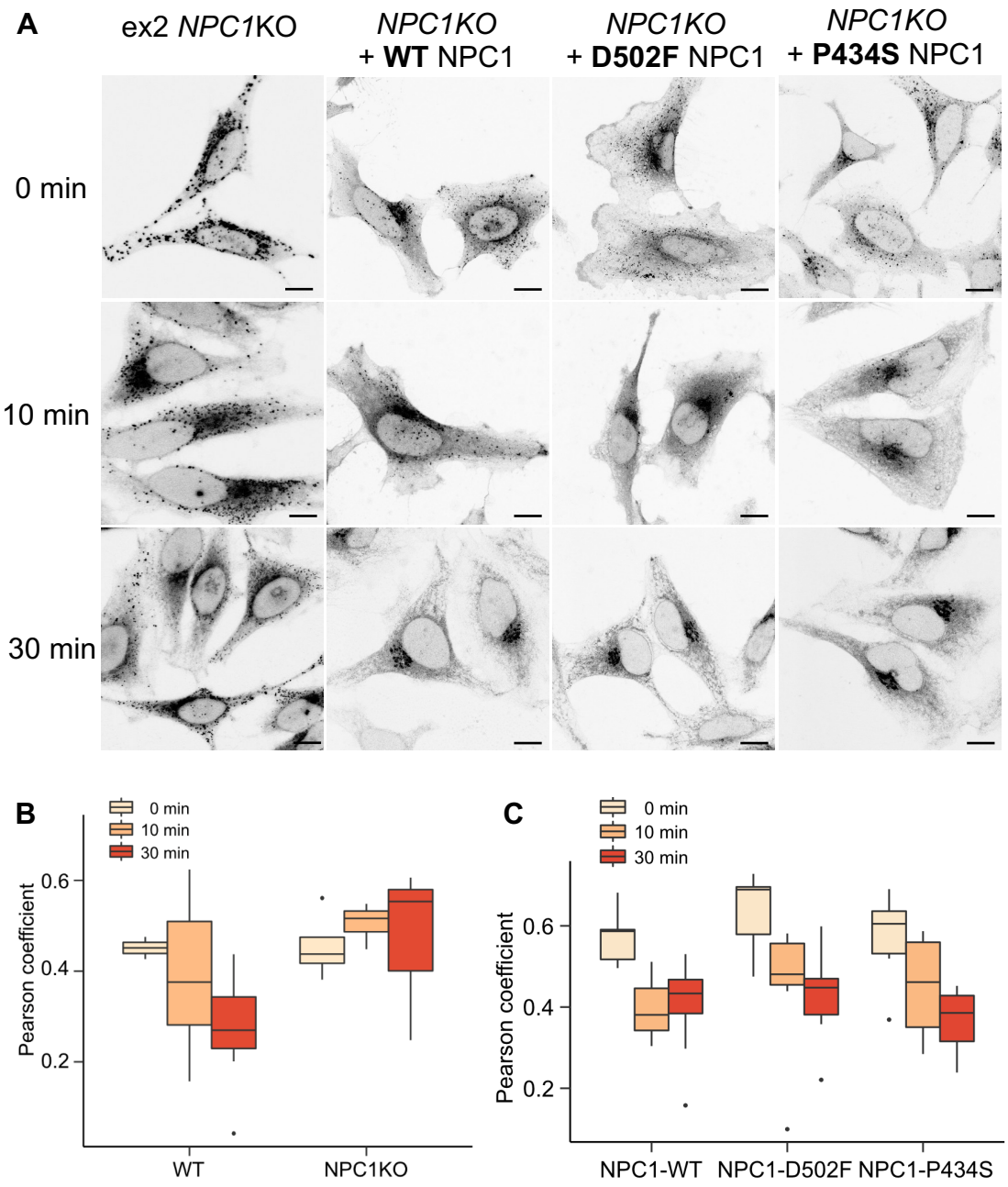


Figure 5. 21 Sphingosine transport in NPC1 variant expressing HeLa cells
A: Confocal images of *NPC1*KO HeLa cells (ex2 clone, Tharkeshwar *et al.* 2017) and *NPC1*KO transduced to overexpress WT, D502F and P434S NPC1-mCherry. Pulse−chase experiments were performed by varying the time between uncaging and cross-linking from 0 min to 30 min. Sphingosine was stained with Alexa Fluor® 488 conjugated-azide (scales bar, 20 µm). **B**: Co-localisation of sphingosine with lysosomal marker LAMP1 in WT, *NPC1*KO HeLa and *NPC1*KO overexpressing WT, D502F and P434S NPC1 were quantified by automated image analysis, represented as Pearson's correlation coefficient for >6 cells in each condition (the dots represent the outlier values).

5.5 Discussion and future work

In this chapter, we studied three lysosomal proteins: NPC1, NPC2 and ASM for their roles in the entry pathway of EBOV. Mutations that destroy the function of NPC1 or NPC2 lead to the lysosomal storage disease Niemann Pick type C (NPC), whereas ASM deficiency underlies the clinical conditions Niemann-Pick type A and B in which sphingomyelin accumulates (Platt *et al.* 2018).

We investigated a panel of genetically modified HeLa cells for their susceptibility to infection by EBOV-GP pseudotyped virus E-S-FLU, and compared this with their biochemical phenotype (characterised by measuring cellular sphingosine level and sphingosine trafficking). (Summarised in Table 5.1).

Table 5. 1 Summary of sphingosine profile and susceptibility to E-S-FLU infection for cells studied in this chapter

	Sphingosine HPLC	**Sphingosine trafficking**	**E-S-FLU infection**
WT HeLa	Normal	Normal	Yes
*NPC1*KO	Increased	Blocked	No
*NPC1*KO + WT NPC1-mCherry	-	Normal	Yes
*NPC1*KO + D502F NPC1-mCherry	-	Normal	Reduced
*NPC1*KO + P434S NPC1-mCherry	-	Normal	Yes
*NPC2*KO	Increased	Blocked	Yes
*SMPD1*KO (ASM deficient)	Decreased	-	Yes

KO: genetic knockout by CRISPR/Cas 9 technique
-: assay not yet completed.

We know that NPC1 deletion completely abrogates EBOV infection, and creates a downstream accumulation of sphingolipids. Here we demonstrated that NPC2 and ASM, however, are not required for EBOV-GP dependent viral entry. Both are

factors involved in lysosomal storage diseases, and the *NPC2*KO and *SMPD1*KO HeLa cells differed in their levels of sphingosine. Nevertheless, both were still infected by E-S-FLU.

In addition, we re-introduced WT or mutated NPC1 into the *NPC1*KO HeLa cells by lentiviral transduction, and showed that sphingosine trafficking was restored in the knock-in cells. Interestingly, a point mutation at the domain C of NPC1 (D502F), greatly reduced infection by EBOV without affecting the NPC1 function.

5.5.1 NPC2 and EBOV-GP dependent infection

In the previous chapters, we developed a new EBOV-GP pseudotyped virus E-S-FLU and showed that it mimicked wild-type EBOV in the cell entry process (Chapter 3). We showed that small molecules that inhibited WT EBOV at known targets involved in EBOV entry e.g. E64 that inhibited cathepsin cleavage of EBOV-GP, also inhibited E-S-FLU with a comparable IC_{50} value (Chandran *et al.* 2005; Schornberg *et al.* 2006; Shah, Wang and Kaletsky 2010; Gnirß *et al.* 2012; Xiao *et al.* 2018). However, the mechanisms of most inhibitors we identified in Chapter 4 after a drug screen remain unknown and the majority of them are cationic amphiphilic drugs (CADs).

Some CADs that inhibited EBOV entry were shown to induce a NPC disease-like phenotype, such as U18666A, imipramine and amiodarone (Carette *et al.* 2011; Shoemaker *et al.* 2013; Herbert *et al.* 2015). The NPC disease-like phenotype refers to a lysosomal storage dysfunction and the accumulation of a range of lipids and cholesterol as the result of mutations in the NPC1 and NPC2 proteins (Vanier

2010). The CADs are thought to inhibit the function of NPC1 although the mechanism is still unclear for many of them.

Several papers have shown that NPC2 defective cells or mice are still susceptible to EBOV infection, despite having the same lipid storage phenotype in lysosomes as in NPC1 defective cells (Carette *et al.* 2011; Côté *et al.* 2011; Herbert *et al.* 2015). These experiments suggested that the downstream cholesterol and lipid accumulations induced by CADs are “side-effects” rather than causing inhibition of EBOV entry.

To confirm this statement, we generated *NPC2*KO HeLa cells by CRISPR/Cas 9 technology, which were confirmed at the genomic and transcription levels. We also showed that the *NPC2*KO cells had a defect in sphingosine trafficking and accumulated sphingosine in the lysosome, which is the hallmark of NPC disease (Lloyd-Evans *et al.* 2008). We then showed that *NPC2*KO cells were still susceptible to infection by two EBOV-GP pseudotyped viruses: E-S-FLU and EBOV-GP pseudotyped lentivirus. We concluded that NPC2 is not required for EBOV entry, and that the NPC-like phenotype caused by NPC2 loss and induced by CADs is unlikely to be the cause of the inhibition of EBOV infection by these drugs.

5.5.2 ASM and EBOV-GP dependent infection

Acid sphingomyelinase (ASM) is a lysosomal enzyme that catalyses the hydrolysis of sphingomyelin to phosphorylcholine and ceramide in the late endosome/lysosome (Figure 5.11) (Jenkins, Canals and Hannun 2009). ASM is

normally localised in the lysosomal membrane, but it is translocated to the plasma membrane in response to ASM activating stimuli such as reactive oxygen species, stress stimuli or infection etc. (Beckmann *et al.* 2014). After translocated to the plasma membrane (many times also referred as “ASM activation”), ASM breaks down sphingomyelin to ceramide at the outer leaflet, resulting in a ceramide-enriched microdomain at the cell surface. The formation of ceramide-enriched lipid rafts can subsequently promote receptor clustering, alter membrane signalling and membrane fusion (Gulbins *et al.* 2004; Beckmann *et al.* 2014). ASM has been shown to be involved in infection by several pathogens including Measles virus, *Pseudomonas aeruginosa*, and *Neisseria gonorrhoeae*. (Jan, Chatterjee and Griffin 2002; Gulbins *et al.* 2004; Grassmé *et al.* 2005; Avota, Gulbins and Schneider-Schaulies 2011; Beckmann *et al.* 2014; Zhang *et al.* 2014). Some pathogens that prefer ceramide-rich rafts for entry, including Measles virus, stimulate host ASM expression to enhance infection (Avota, Gulbins and Schneider-Schaulies 2011). Sindbis virus, however, requires sphingomyelin for virus fusion and entry. Deletion of ASM accumulated sphingomyelin and resulted in increased viral infection and encephalomyelitis (Ng and Griffin 2006).

Whether or how ASM is involved in EBOV-GP dependent infection is less established. Miller *et al.* (2012) showed that plasma membrane sphingomyelin promoted EBOV entry. However, knockdown of the ASM/SMPD1 gene, which should have resulted in an increase in the sphingomyelin level in membranes, actually reduced EBOV infection (Miller *et al.* 2012b). In contrast, Côté showed that knockdown of ASM by siRNA did not affect EBOV infection (Côté *et al.* 2011).

The other evidence suggesting that EBOV requires ASM is based on drug inhibition studies. As we showed in Chapter 4, many EBOV entry inhibitors share a cationic amphiphilic feature (CAD). Kornhuber *et al.* showed that some CADs can functionally inhibit ASM by concentrating to the inner membrane of the lysosome and changing the electrostatic environment, resulting in detachment of ASM and with subsequent inhibition (Kornhuber *et al.* 2008, 2010a). Kornhuber named these drugs as FIASMA (Functional Inhibitors of Acid SphingoMyelinAse), and this theory is often used to explain the inhibitory effect of CADs on EBOV (Johansen *et al.* 2015; Fan *et al.* 2017; Sun *et al.* 2017).

Fan *et al.* showed that treating cells with estrogen receptor modulators tamoxifen and clomiphene (both are CADs), reduced the cellular level of sphingosine and reduced lysosomal calcium release. They suggested that this secondary effect on lysosomal calcium release was responsible for the inhibition of EBOV infection (Figure 5.22) (Höglinger *et al.* 2015; Sakurai *et al.* 2015). However, the control drug U18666A, a well characterised NPC1 inhibitor that is known to induce sphingosine accumulation (Lloyd-Evans *et al.* 2008), also reduced sphingosine in their assay, which made the findings difficult to interpret (Fan *et al.* 2017). In addition, if secondary effects on lysosomal Ca^{2+} trafficking were responsible for the inhibition of EBOV entry by CADs, the *NPC2*KO cells which have reduced lysosomal Ca^{2+} storage (Lloyd-Evans *et al.* 2008), should have been resistant to EBOV-GP dependent infection, but we have shown that they were fully permissive.

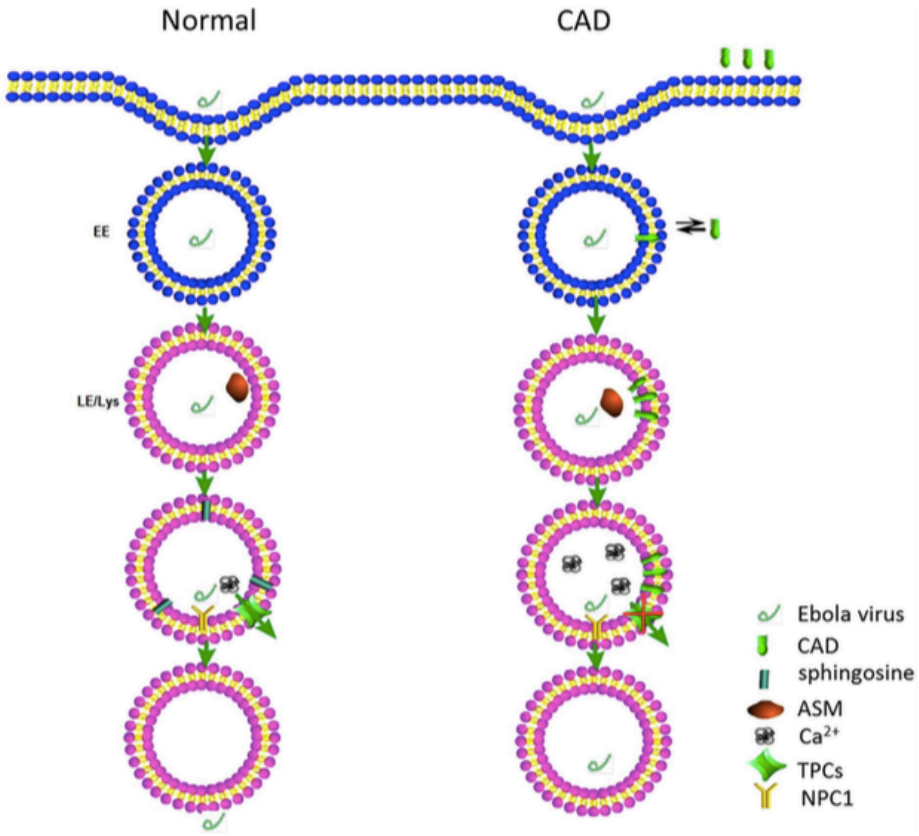


Figure 5. 22 Fan's model of drugs inhibiting EBOV via ASM
Figure adapted from Fan *et al.* 2017. A proposed mechanism of cationic amphiphilic drugs (CADs) inhibiting EBOV entry. Fan *et al.* suggested that CADs concentrated to the lysosomal luminal membrane and inactivated acid sphingomyelinase (ASM). Loss of ASM function caused a reduction in lysosomal sphingosine and subsequent blocking of calcium ion release through two pore channels (TPCs). Calcium flux may be required for EBOV-GP fusion, and hence CADs inhibited EBOV entry.

To specifically address whether ASM is involved in EBOV infection, we knocked out the *SMPD1* gene from the human HeLa cell-line by using CRISPR/Cas 9 technology. We verified the knockout clones at genomic and transcriptional levels and showed that the cellular sphingosine level was reduced in three independent *SMPD1*KO clones. We then showed that both E-S-FLU and EBOV-GP pseudotyped lentivirus infected the knockout cells. There may have been some slight reduction in infection in individual clones, and further analysis is needed to confirm whether this is due to clonal variation.

Previously, we showed that all inhibitory CADs could block E-S-FLU entry completely. Therefore, CADs are unlikely to be acting mainly via the FIASMA route, even if this is contributing a minor inhibitory effect. The partial reduction of EBOV pseudotyped virus in ASM deficient cells may also be caused by reduced ceramide in lipid rafts and reduced entry at the plasma membrane level.

Although we still cannot pinpoint the target of CADs in suppression of EBOV infection, we interpret our results to show that it is unlikely to be directly connected with the biochemical NPC disease-like phenotype induced by these drugs, nor via inhibition of ASM. The most likely explanation is that integration of the CADs in the lysosomal membrane directly interferes with the binding of EBOV-GP and NPC1 or affects the insertion of EBOV-GP into the target host membrane and the subsequent fusion function of EBOV-GP. The virus inhibitory effect of CADs is likely to be independent from their actions on the transport function of NPC1/2 and the enzyme action of ASM.

5.5.3 EBOV and NPC1 polymorphism

EBOV infection in humans leads to a mortality rate between 50% and 90% (Martines *et al.* 2014), although asymptomatic cases have been reported (Leroy *et al.* 2000; Kuhn and Bavari 2017). Are there any host factors affecting survival rate of EBOV infection? NPC1 is the key receptor for EBOV-GP dependent virus entry, and both homozygous and heterozygous NPC1 deficient mice showed a survival advantage compared to WT mice when challenged with lethal dose of EBOV infection (Herbert *et al.* 2015). This leads us to the hypothesis that

polymorphisms affecting the sequence or level of expression of the NPC1 receptor may affect host susceptibility to EBOV infection.

Our collaborator, Mary Carrington (National Institutes of Health), began to genotype NPC1 genes from a small cohort of African patients who died or survived EBOV infection after the 2014-2015 outbreak. NPC1 is the best characterised host factor that is involved in EBOV infection. It is the essential receptor for EBOV binding and entry (Carette *et al.* 2011; Côté *et al.* 2011; Miller *et al.* 2012a). Recent structural data further revealed the specific interaction between the cathepsin cleaved EBOV-GP (GP_{CL}) and the NPC1 C domain (Gong *et al.* 2016; Wang *et al.* 2016). However, because of the small sample size and the limitation of typing asymptomatic patients, it has been difficult to draw a conclusion from the genotyping data. We therefore designed an *in vitro* functional test to investigate potentially protective NPC1 SNPs. We introduced mutated NPC1 tagged with mCherry to *NPC1*KO HeLa cells and tested their susceptibility to E-S-FLU virus.

The SNP rs61731962 occurs in around 4.6% of the Youraban population (West African), and is a non-synonymous change from proline to serine at residue 434. P434S is located in the NPC1 domain C region that contains the EBOV-GP binding site, but it is not directly in contact with EBOV-GP_{CL} (Wang *et al.* 2016). We did not see any apparent reduction in E-S-FLU infection comparing P434S with WT NPC1 expressing cells.

Two papers have shown that NPC1 from African straw-coloured fruit bats (*Eidolon helvum*) and Russell's viper (*Daboia russellii*) can resist EBOV entry. Sequence

variation at sites 502 and 503 were especially important for the resistance (Ng *et al.* 2015; Ndungo *et al.* 2016). As a control, we generated D502F NPC1 expressing HeLa cells and showed that E-S-FLU infection was greatly reduced. Neither P434S nor the D502F NPC1 variant affected the physiological function of NPC1 detected by measuring sphingosine trafficking. Our confirmation that the D502F variant is fully functional biochemically suggests that humans carrying this type of mutation would be healthy, and likely to resist EBOV infection.

A recently published paper tested 10 other missense SNPs in NPC1 and showed that three of them: P424A, D502E, D508N, influenced Filovirus entry detected by EBOV-GP pseudotyped vesicular stomatitis virus (VSV) (Kondoh *et al.* 2018). All three of them sit right at the interacting face between NPC1 and EBOV-GP. However, these SNPs are seen in less than 0.01% of the African population (NCBI SNP library: https://www.ncbi.nlm.nih.gov/snp/). There are three other non-synonymous NPC1 SNPs which are found in more than 4% of the West African population (M642I, I858V and R1266Q). Although they are positioned outside of the NPC1 domain C, they may have an indirect effect on EBOV-GP binding. We will test their effect on EBOV entry by using the tool we have developed.

Chapter 6 Calcium and EBOV Infection

6.1 Introduction

In Chapter 4, we described screening a small library of 1,280 drug molecules for inhibition of infection by our EBOV-GP pseudotyped Influenza virus. This library contained molecules from various pharmacological groups (Sigma LOPAC®1280; section 4.2). Surprisingly, 215 drugs with different known targets inhibited the infection of our EBOV-GP pseudotyped virus E-S-FLU, and this agreed with the current literature where other groups have screened FDA approved drugs to inhibit wild-type EBOV or other EBOV pseudotyped viruses (Johansen *et al.* 2013, 2015; Shoemaker *et al.* 2013; Gehring *et al.* 2014; Kouznetsova *et al.* 2014).

The mechanisms by which these drugs were influencing EBOV infection may have differed from their canonical activities. For instance, the estrogen receptor modulators clomiphene and toremifene inhibited EBOV infection in cells that lacked the estrogen receptor (Johansen *et al.* 2013). We identified and investigated some of the shared biochemical features of the EBOV blockers in our screen, such as cationic amphiphilic physicochemistry, lysosomotropic tendency, effect on lysosomal membrane permeability, and induction of cholesterol and sphingolipids accumulation in lysosomes (Chapter 4, section 4.3). In this chapter, we will focus on the sub-group of drugs that are known to influence calcium fluxes, and study the mechanisms by which they inhibit E-S-FLU infection.

In recent years, evidence has accumulated for the involvement of lysosomal calcium channels in the EBOV entry process. Several studies showed that various

calcium channel blockers such as amiodarone, verapamil and bepridil inhibited EBOV infection (Gehring *et al.* 2014; Kouznetsova *et al.* 2014; Johansen *et al.* 2015). Other studies linked EBOV infection with the two-pore channels (TPCs), but were indirect. Simmons *et al.* showed that EBOV fusion takes place in the late endosomal/lysosomal vesicles, where NPC1 and TPC2 co-localised (Simmons *et al.* 2016). Others focused on drawing a correlation between the inhibitory effects of drugs on EBOV infection and their specificity as calcium channel modulators, or on computer generated models predicting drug binding specificity for the TPCs (Rahman *et al.* 2014; Fan *et al.* 2017; Penny *et al.* 2018).

The most influential study was by Sakurai *et al.* in 2015, which provided the first direct evidence that the two-pore channels 1 and 2 (TPC1/2) in the endo/lysosomal membrane may be the factors targeted by these drugs (Sakurai *et al.* 2015). The authors showed that EBOV infection was reduced *in vitro* in embryonic fibroblast cells taken from mice in which TPC1 or TPC2 expression was disrupted by a Cre-LoxP recombination based method (Arndt *et al.* 2014; Grimm *et al.* 2014), as well as in a HeLa cell-line treated with specific siRNA to reduce *TPC1* and *TPC2* gene expression (Sakurai *et al.* 2015). They also showed that tetrandrine, an L-type calcium channel blocker and trans-Ned19, an inhibitor of nicotinic acid adenine dinucleotide phosphate (NAADP)-induced Ca^{2+} release from endo/lysosomes, inhibited EBOV infection. Finally, they established that treatment with 30 mg/kg per day of tetrandrine protected mice from a lethal dose challenge with mouse-adapted EBOV infection.

In this chapter, we have explored the relationship between calcium flux and EBOV entry from two angles. First, we carefully analysed all of the calcium channel modulators screened in our assays, both the E-S-FLU inhibitors and non-inhibitors, by comparing their physicochemical properties. Secondly, we decided to repeat the genetic studies from Sakurai *et al.* by testing our EBOV-GP pseudotyped virus E-S-FLU for infection either of embryo fibroblasts from *Tpcn1/2* knockout mice (Calcraft *et al.* 2009; Arndt *et al.* 2014; Grimm *et al.* 2014; Ruas *et al.* 2014, 2015) or human HeLa cells in which expression of the TPC1 and TPC2 had been abrogated by the CRISPR/Cas 9 technique.

Although E-S-FLU as a pseudotyped Influenza virus differs biologically from wild-type EBOV, we showed in Chapter 3 that infection by E-S-FLU was absolutely NPC1 dependent, and was prevented by a characteristic set of drugs that inhibit infection by wild-type EBOV. These preparatory studies gave us confidence in using E-S-FLU as a BSL-1/2 surrogate for studying EBOV infection, and investigating the involvement of specific host factors.

6.2 Drugs that affect Ca^{2+} flux and EBOV inhibition

From the small drug library screen we performed in Chapter 4, we observed an enrichment of Ca^{2+} channel blockers in the list of E-S-FLU inhibitors (Appendix Table 4. X1). There are 38 out of 1,280 drugs in the library that have functions related to Ca^{2+} ion flux, listed in the Sigma LOPAC®1280 library literature. Of these 38, 15 inhibited E-S-FLU infection of MDCK-SIAT1 cells (out of 215 total inhibitors from the LOPAC®1280 library). An additional 6 calcium channel inhibitors were added from the recent literature to give a total of 44 Ca^{2+} drugs listed in Table 6.1.

Table 6. 1 44 calcium related drugs screened in this study

Drug name	LogP	pKa^{base}	E-S-FLU IC_{50} (μM)	H5-S-FLU IC_{50} (μM)	Drug description
8-Methoxymethyl-IBMX	0.4	-1.8	NA	NA	Selective inhibitor of Ca^{2+}-calmodulin-dependent phosphodiesterase
A-315456	2.3	6.5	NA	NA	TPCs inhibitor; selective alpha 1D-adrenoceptor antagonist
Amiodarone HCl	7.2	8.5	2.0	NA	Inhibits binding of 1,4-dihydropyridine to L-type Ca^{2+} channels; coronary vasodilator; α/β adrenoceptor agonist
Bay K 8644	2.2	0	NA	NA	L-type Ca^{2+} channel agonist
Benidipine HCl	4.3	7.9	NA	NA	Calcium channel blocker
Benzamil HCl	1.5	7.5	NA	NA	Selective and potent blocker of Na^+/H^+ and Na^+/Ca^{2+} channels
Bepridil HCl	5.3	9.2	2.7	NA	Non-selective Ca^{2+} channel blocker which stimulates the binding of 1,4-dihydropyridine-based drugs to Ca^{2+} channels
Calcimycin	5.4	1.7	NA (too toxic)	NA	Ca^{2+} ionophore used to potentiate responses to NMDA, but not quisqualate glutamate receptors
Calmidazolium chloride	10.8	3.0	2.3	3.9	Potent inhibitor of calmodulin activation of phosphodiesterase; strongly inhibits calmodulin-dependent Ca^{2+}-ATPase
Cilnidipine	4.1	-4.1	NA	NA	Slow-acting Ca^{2+} channel blocker; antihypertensive; vasodilator
Cinnarizine	5.8	8.4	NA	NA	Ca^{2+} channel blocker; central and peripheral vasodilator
Dantrolene sodium	2.1	-0.6	NA	NA	Inhibits intracellular Ca^{2+} release from the sarcoplasmic reticulum
Diltiazem HCl	3.1	8.2	NA	NA	Ca^{2+} channel antagonist selective for slow, or L-type, channels; stimulates 1,4-dihydropyridine binding to Ca^{2+} channels; blocks NAADP-evoked Ca^{2+} release
Felodipine	3.9	-6.6	NA	NA	L-type calcium channel blocker
Flunarizine diHCl	5.3	7.6	15	NA	Ca^{2+}/Na^+ channel blocker; vasodilator
FPL 64176	5.0	0	NA	NA	Potent L-type Ca^{2+} channel activator
Gabapentin	-1.1	9.9	NA	NA	Anticonvulsant that may modulate certain types of Ca^{2+} channel currents; analgesic
KB-R7943	3.8	10.6	12.8	NA	Inhibits the reversed Na^+/ Ca^{2+} exchanger in cardiomyocytes
Lercanidipine	6.4	9.4	NA	NA	L-type vascular calcium channel antagonist
Loperamide HCl	4.4	9.4	16.8	NA	Ca^{2+} channel antagonist; Meperidine congener which binds to opioid receptors
LY-310762	4.0	7.2	NA	NA	TPCs inhibitor; potent, selective 5-HT 1D serotonin receptor antagonist
Methoxyverapamil	3.8	9.0	52.5	NA	L-type Ca^{2+} channel antagonist
Mibefradil diHCl	5.3	9.8	1.3	NA	T-type Ca^{2+} channel blocker

Drug name	LogP	pKa^{base}	E-S-FLU IC_{50} (μM)	H5-S-FLU IC_{50} (μM)	Drug description
Naringenin	2.5	-3.9	NA	NA	TPCs inhibitor; antioxidant; free radical scavenger; anti-inflammatory, carbohydrate metabolism promoter, immunity system modulator
Nemadipine-A	3.3	0	NA	NA	L-type calcium channel alpha1-subunit antagonist.
Nicardipine HCl	3.8	8.2	28.3	NA	L-type Ca^{2+} channel antagonist; antihypertensive
Nifedipine	2.2	5.3	NA	NA	L-type Ca^{2+} channel blocker; vasodilator
Nimodipine	3.0	5.4	NA	NA	Potent L-type Ca^{2+} channel antagonist
Nitrendipine	2.9	5.4	NA	NA	Ca^{2+} channel blocker; antihypertensive
NNC 55-0396	6.1	9.8	1.8	NA	Selective T-type calcium channel inhibitor
PDMP HCl	5.2	6.7	33.7	NA	Glucosylceramide synthase inhibitor
Phloretin	3.9	0	NA	NA	Blocks L-type Ca^{2+} channels
Pimozide	6.3	8.4	7.5	NA	Ca^{2+} channel antagonist; antipsychotic; D2 dopamine receptor antagonist
Praziquantel	2.5	-0.2	NA	NA	Ca^{2+} Ionophore; anthelmintic
Ruthenium red	0	0	145.2	NA	Inhibits mitochondrial Ca^{2+} uniporter; capsaicin antagonist
Tetrandrine	6.5	8.4	1.6	NA	Voltage-dependent Ca^{2+} channel blocker
Thapsigargin	4.4	0	NA	NA	Potent, cell-permeable, IP_3-independent intracellular calcium releaser
Thio-NADP sodium	5.5	8.9	NA	NA	Blocks (NAADP)-induced Ca^{2+} release
Thioridazine HCl	5.9	9.5	6.0	NA	Ca^{2+} channel antagonist; Dopamine receptor antagonist; antipsychotic
TMB-8 HCl	4.6	10.3	43.9	NA	Intracellular Ca^{2+} antagonist; inhibits calmodulin-sensitive Ca^{2+}-ATPase activity; PKC inhibitor
trans-Ned19	5.6	8.3	101.0	NA	Inhibits NAADP-mediated Ca^{2+} release
Verapamil HCl	3.8	8.9	10.6	NA	L-type Ca^{2+} channel modulator; adrenoceptor antagonist; antiarrhythmic; cardiac depressant; coronary vasodilator
Vinpocetine	4.4	6.9	NA	NA	Ca^{2+} /calmodulin-dependent phosphodiesterase1 (PDE1) inhibitor
YS-035 HCl	3.6	9.6	NA	NA	L-type Ca^{2+} channel blocker; verapamil derivative

Orange background: drugs that inhibited E-S-FLU;
Yellow background: drugs that inhibited GFP-EBOV in Johansen et al. 2015;
Blue background: drugs that inhibited GFP-EBOV in Sakurai et al 2015.

Sakurai *et al*. observed that L-type Ca^{2+} channel blockers including verapamil, nimodipine, diltiazem and tetrandrine, and the specific TPCs inhibitor trans-Ned19, inhibited EBOV infection (Sakurai *et al.* 2015), and they suggested that the drugs were acting via TPC1/2. We tested these Ca^{2+} channel blockers for inhibition of E-S-FLU, either as part of the LOPAC®1280 screen or as individually acquired drugs. Verapamil, tetrandrine and trans-Ned19 (Table 6.1) inhibited E-S-FLU in our drug inhibition assay, and the IC_{50} values were comparable with the data showed in Sakurai's study, where they used a GFP-labelled recombinant EBOV in the assay. However, nimodipine and diltiazem failed to inhibit E-S-FLU infection.

Recently, two papers described new inhibitors of the TPCs (Pafumi *et al.* 2017; Gunaratne *et al.* 2018a). Pafumi *et al.* found that naringenin at the high dose of 1000 μM inhibited TPC2. We tested naringenin (up to 100 μM) in our virus inhibition assay but it did not inhibit E-S-FLU infection in our hands. Gunaratne *et al.* screened the LOPAC®1280 library and 250 additional small molecules for inhibition of NAADP-induced calcium release, which is thought to be TPCs-dependent. They showed that seven small molecules inhibited NAADP-induced calcium release both in the sea urchin egg system and in mammalian cells, without showing evidence for lysosomotropism (PF-543, SKF 96,365, racecadotril, A-315456*, LY-310,762*, PDMP* and salmeterol xinafolate). Three of these (marked with *) were from the LOPAC®1280 library that we screened. PDMP inhibited E-S-FLU, but the other two (A-315456 and LY-310,762) did not.

In Table 6.2, we summarise a subgroup of 18 of the 44 calcium-related drugs that showed an inhibitory effect towards TPCs reported in the literature, experimentally

determined in the sea urchin egg homogenate and mammalian cells (Pafumi *et al.* 2017; Gunaratne *et al.* 2018a).

Table 6. 2 18 two-pore channels inhibiting drugs

Drug name	LogP	pKa^{base}	E-S-FLU IC_{50} (μM)	H5-S-FLU IC_{50} (μM)	TPCs inhibition reference
A-315456	2.3	6.5	NA	NA	Gunaratne *et al.* 2018a
Bepridil HCl	5.3	9.2	2.7	NA	Penny *et al.* 2018
Diltiazem HCl	3.1	8.2	NA	NA	Rahman *et al.* 2014
Felodipine*	3.9	-6.6	NA	NA	Rahman *et al.* 2014
LY-310762	4.0	7.2	NA	NA	Gunaratne *et al.* 2018a
Naringenin	2.5	-3.9	NA	NA	Pafumi *et al.* 2017
Nicardipine HCl*	3.8	8.2	28.3	NA	Rahman *et al.* 2014
Nifedipine	2.2	5.3	NA	NA	Rahman *et al.* 2014
Nimodipine*	3.0	5.4	NA	NA	Rahman *et al.* 2014
Nitrendipine*	2.9	5.4	NA	NA	Rahman *et al.* 2014
PDMP HCl	5.2	6.7	33.7	NA	Gunaratne *et al.* 2018a
Pimozide	6.3	8.4	7.5	NA	Penny *et al.* 2018
Tetrandrine	6.5	8.4	1.6	NA	Gunaratne *et al.* 2018a
Thio-NADP sodium	5.5	8.9	NA	NA	Gunaratne *et al.* 2018a
Thioridazine HCl	5.9	9.5	6.0	NA	Gunaratne *et al.* 2018a
TMB-8 HCl	4.6	10.3	43.9	NA	Gunaratne *et al.* 2018a
trans-Ned19	5.6	8.3	101.0	NA	Naylor *et al.* 2009
Verapamil HCl	3.8	8.9	10.6	NA	Rahman *et al.* 2014

Orange background: drugs inhibited E-S-FLU;
Blue background: drugs inhibited GFP-EBOV in Sakurai et al 2015;
**: Predicted TPCs inhibitors by molecular docking simulations.*

In Chapter 4, we suggested that many drugs that inhibited E-S-FLU infection shared a cationic amphiphilic feature (high LogP, high pKa^{base}), despite coming from different drug groups. This included calcium channel inhibitors such as amiodarone, bepridil, tetrandrine and verapamil. Therefore, we further analysed the physicochemical properties of the 44 calcium-related drugs (listed in Table 6.1), 38 of which were defined as calcium-channel inhibitors by Sigma-Aldrich, and the other six compounds were experimentally determined as TPC blockers by Gunaratne *et al.* (PDMP, A-315456 and LY-310,762), Sakurai *et al.* (tetrandrine, Ned19) and Pafumi *et al.* (naringenin). All of these 44 drugs have been titrated for inhibition of E-S-FLU and H5-S-FLU (IC_{50} summarised in Table 6.1).

For each molecule, we obtained the partition coefficient LogP value as an indicator of the hydrophobicity, and the strongest basic pKa value (pKa^{base}), to identify a potential site of protonation. The LogP and pKa^{base} values either came from the Drugbank dataset (https://www.drugbank.ca), or were calculated by the Chemicalize online platform based on chemical structures of drugs (https://chemicalize.com/). We plotted the LogP/pKa^{base} values for the 44 calcium-related drugs in Figure 6.1 (upper panel), with the filled circles indicating drugs that inhibited E-S-FLU, and hollow circles as the non-inhibitors.

We noticed that drugs that inhibited E-S-FLU focused to the upper right corner of the plot with high LogP and high pKa^{base} (Figure 6.1), which are characteristics of cationic amphiphilic drugs (CADs) (De Duve *et al.* 1974; Kornhuber *et al.* 2008, 2010b; Nadanaciva *et al.* 2010; Kornhuber *et al.* 2011). Two potential exceptions, calcimycin and thapsigargin, were reported by Johansen *et al.* as inhibitors of eGFP-EBOV entry (Johansen *et al.* 2015). We ordered these two drugs individually from Sigma (calcimycin C7522; thapsigargin T9033) and tested them in our E-S-FLU inhibition assay. However, both drugs were highly toxic to the indicator MDCK-SIAT1 cells (toxicity < 0.2 μM). We also acquired and tested fresh nimodipine (Sigma, PHR1293), which showed an inhibitory effect in Sakurai's study (Sakurai *et al.* 2015), but it did not inhibit E-S-FLU infection.

We plotted separately the subgroup of 18 drugs that are known to block the TPCs, of which 9 blocked E-S-FLU infection. Again we saw the same pattern, with the inhibitors of E-S-FLU clustering in the group with high LogP and pKa^{base}. Moreover, of the six TPCs inhibitors described recently, (A-315456, LY-310,762,

PDMP, tetrandrine, Ned-19, naringenin) (Sakurai *et al.* 2015; Pafumi *et al.* 2017; Gunaratne *et al.* 2018a), only PDMP, tetrandrine and Ned-19 blocked E-S-FLU infection, and they all have high LogP and pKa^{base} values (Figure 6.1 lower panel).

Rahman *et al.* (2014) found that in computer-generated models, the family of dihydropyridine L-type calcium channel blockers (with names ending in "–pine") were predicted to bind and block the pore of the TPCs. They then confirmed these predictions with measurements of inhibition of NAADP-induced Ca^{2+} release in sea urchin egg homogenate and eukaryotic cells (SKBR3 human breast cancer cell-line) that overexpressed TPC1 (Rahman *et al.* 2014). In our collection, nine dihydropyridines were titrated for inhibition of E-S-FLU (Table 6.1, lercanidipine, nicardipine, benidipine, nitrendipine, nimodipine, nifedipine, nemadipine-A, cilnidipine, and felodipine). Of these only nicardipine, which has a high LogP and high pKa^{base}, inhibited E-S-FLU infection. Two additional drugs, verapamil and diltiazem, were shown to block the TPCs (Rahman *et al.* 2014). Verapamil (high LogP and pKa^{base}) blocked E-S-FLU, but diltiazem did not.

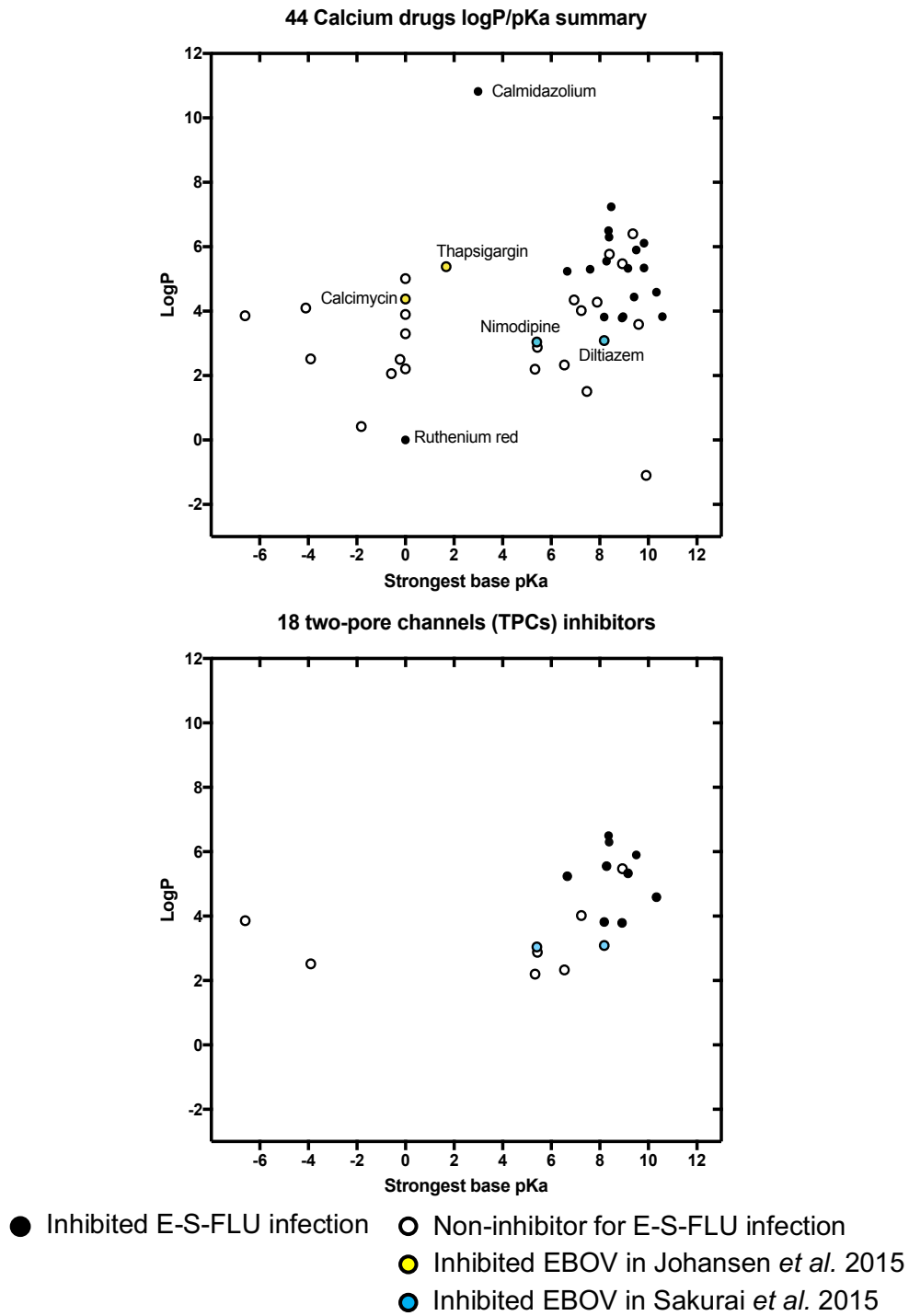


Figure 6. 1 LogP/pKa^{base} diagram for calcium-related drugs

Upper panel: the partition coefficient LogP and pKa^{base} values of 44 calcium-related drugs were obtained either from the Drugbank dataset, or calculated by the Chemicalize online platform based on their chemical structures. Each dot represents a drug, corresponding to Table 6.1. The filled circles indicate drugs that have inhibited E-S-FLU in the virus inhibition assay, whereas hollow circles are the non-inhibitors. The coloured/hollow circles are drugs that did not inhibit E-S-FLU, but inhibited eGFP-EBOV reported in Johansen *et al.* 2015 (yellow: thapsigargin, calcimycin) or Sakurai *et al.* 2015 (blue: nimodipine, diltiazem). Lower panel: a subset of 18 drugs that are known to inhibit TPCs (Table 6.2).

As a control, we screened these 44 Ca^{2+} flux modulating drugs for inhibition of the H5-S-FLU virus, but none of them blocked H5-S-FLU infection except calmidazolium chloride (IC_{50} = 3.9 μM; Appendix Table 4. X1). Calmidazolium chloride was one of the "dimmer" drugs (Chapter 4), which reduced eGFP expression in infected cells rather than reducing the number of infected cells. This suggested that it inhibited E-S-FLU and H5-S-FLU at a post-entry level and acted on the Influenza core. Calmidazolium has a wide variety of Ca^{2+} dependent effects through binding and inhibition of calmodulin (El-Saleh and Solaro 1987; Sunagawa *et al.* 2000; Tseng *et al.* 2004; Lee *et al.* 2016).

In conclusion, we tested 44 Ca^{2+} channel blockers in our pseudotyped virus inhibition assay, and compared their virus inhibition activity with their physicochemical features. The 17 molecules that blocked E-S-FLU entry all shared a cationic amphiphilic feature (Figure 6.1 upper panel, except the inorganic drug ruthenium red). Within these 44 drugs, 18 are known to block TPCs, again only the subgroup of 9 TPC inhibitors that have high LogP and pKa^{base}, prevented E-S-FLU infection (Table 6.2, Figure 6.1 lower panel).

These results showed that the Ca^{2+} channel inhibitory activity of these drugs did not correlate with inhibition of infection by E-S-FLU. In addition, the specificity for blockade of TPCs, may not be the critical function required for these drugs to prevent EBOV entry. By contrast, the inhibitory activity on E-S-FLU infection clearly segregated with their cationic amphiphilic chemistry. Cationic amphiphilic drugs can exert multiple actions through integration in the lysosomal membrane

as described in Chapter 4, and discussed by Kornhuber *et al.* (Kornhuber *et al.* 2008, 2010a, 2010b, 2011).

6.3 EBOV infection of embryonic fibroblasts from *Tpcn1/2* knockout mice

In a recent published paper, Sakurai *et al.* suggested that the two-pore channel proteins TPC1 and TPC2 are required by EBOV for the cell entry process (Sakurai *et al.* 2015). One of their key experiments showed a reduction of EBOV infection in embryonic fibroblasts (MEF) isolated from TPC1 and TPC2 deficient mice (Arndt *et al.* 2014; Grimm *et al.* 2014). To confirm this result, we infected *Tpcn1* knockout (KO) and *Tpcn2*KO MEF cells with two EBOV-GP pseudotyped viruses: E-S-FLU and EBOV-GP pseudotyped lentivirus (GP-lentivirus) (Long *et al.* 2015; Xiao *et al.* 2018). Our collaborator Professor Antony Galione (Department of Pharmacology, University of Oxford) kindly provided us two sets of MEF cells. One set of MEF cells were generated and verified by the Galione group (later referred as AG-MEF cells), which includes wild-type MEF, *Tpcn1*KO (Ruas *et al.* 2014), *Tpcn2*KO (Calcraft *et al.* 2009) and *Tpcn1/2* double knockout (DKO) MEF cells (Ruas *et al.* 2015). Another set of MEF cells were separately generated by the Wahl-Schott group (Department of Pharmacy, Ludwig-Maximilians-Universität), which contains wild-type MEF, *Tpcn1*KO (Arndt *et al.* 2014) and *Tpcn2*KO MEF cells (Grimm *et al.* 2014), later referred as CW-MEF cells. CW-MEF cells were used by Sakurai's group to test EBOV infection (Sakurai *et al.* 2015).

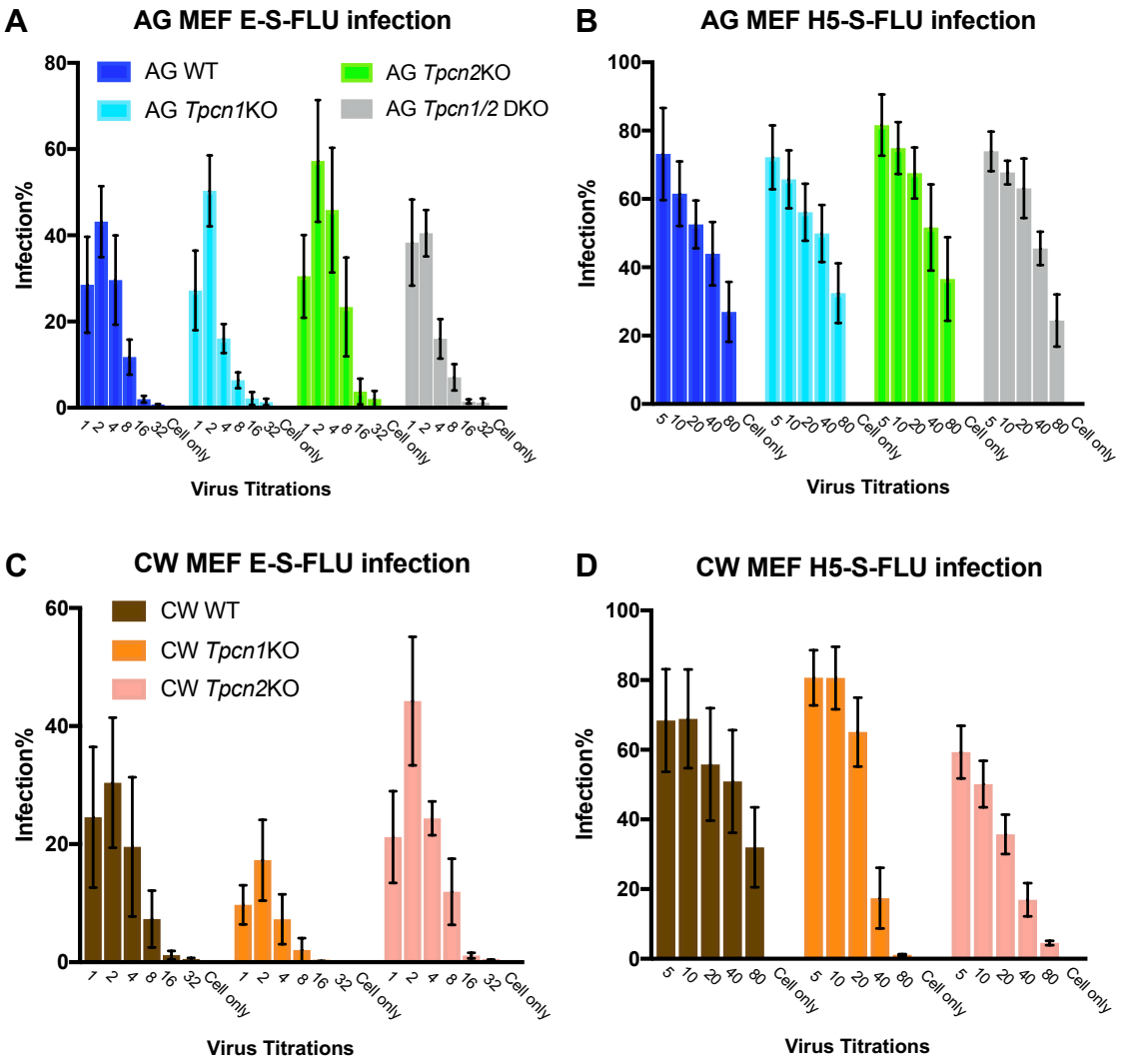


Figure 6. 2 E-S-FLU infection of Tpcn1/2KO mice embryonic fibroblast (MEF)
Two sets of independently generated *Tpcn1* or *Tpcn2* knockout MEFs (*Tpcn1*KO, *Tpcn2*KO) were tested for infection by EBOV-GP pseudotyped E-S-FLU and the control H5-S-FLU virus: AG MEF (**A, B**) and CW MEF (**C, D**). We titrated E-S-FLU in PBS and titrated H5-S-FLU in virus growth medium (VGM) to infect MEF cells for 24 hours. Infected cells were fixed and analysed by FACS. Infection% was the percentage of cells with an eGFP fluorescence >10^2 fold change relative to the uninfected cells. Average infection% from four experimental repeats are shown with error bars representing the standard error of the mean (SEM).

We titrated E-S-FLU and control H5-S-FLU pseudotyped viruses for infection of AG-MEF cells and CW-MEF cells. H5-S-FLU contains the same viral core as E-S-FLU, and differs only at the coating glycoprotein, and both S-FLUs express eGFP as a fluorescent protein reporter. Cells were infected for 24 hours, and analysed by FACS, counting eGFP expressing cells. Virus titration was repeated four times,

and the mean percentage infection was plotted with error bars representing the standard error of the mean (SEM). For AG-MEF cells, both E-S-FLU and H5-S-FLU infected wild-type (WT) MEF, *Tpcn1*KO and *Tpcn2*KO MEF cells at similar levels (Figure 6.2 A, B). *Tpcn1/2* DKO cells were also infected with no obvious reduction in percentage infection. For CW-MEF cells, E-S-FLU infected a similar percentage of WT MEF and *Tpcn2*KO MEF cells, but infection was slightly reduced in *Tpcn1*KO CW-MEF cells (Figure 6.2 C). In comparison, H5-S-FLU infection in WT CW-MEF cells was comparable to infection in *Tpcn1*KO and *Tpcn2*KO at lower virus titrations, but infection% dropped quicker when titrated in the knockout cells, with the biggest difference seen at virus titrations below 1 in 40 (Figure 6.2 D).

We then titrated a different pseudotyped virus, EBOV-GP coated lentivirus (GP-lentivirus) for infection of both AG-MEF and CW-MEF cells. GP-lentivirus carries a firefly luciferase reporter. The *Tpcn1*KO, *Tpcn2*KO and *Tpcn1/2* DKO MEF cells from both AG and CW-MEFs were infected by the GP-lentivirus, with a similar level to their corresponding WT MEF cells (Figure 6.3). All virus titration experiments were repeated at least three times, and the mean luminescence readout are shown with error bars indicating the standard error of the mean.

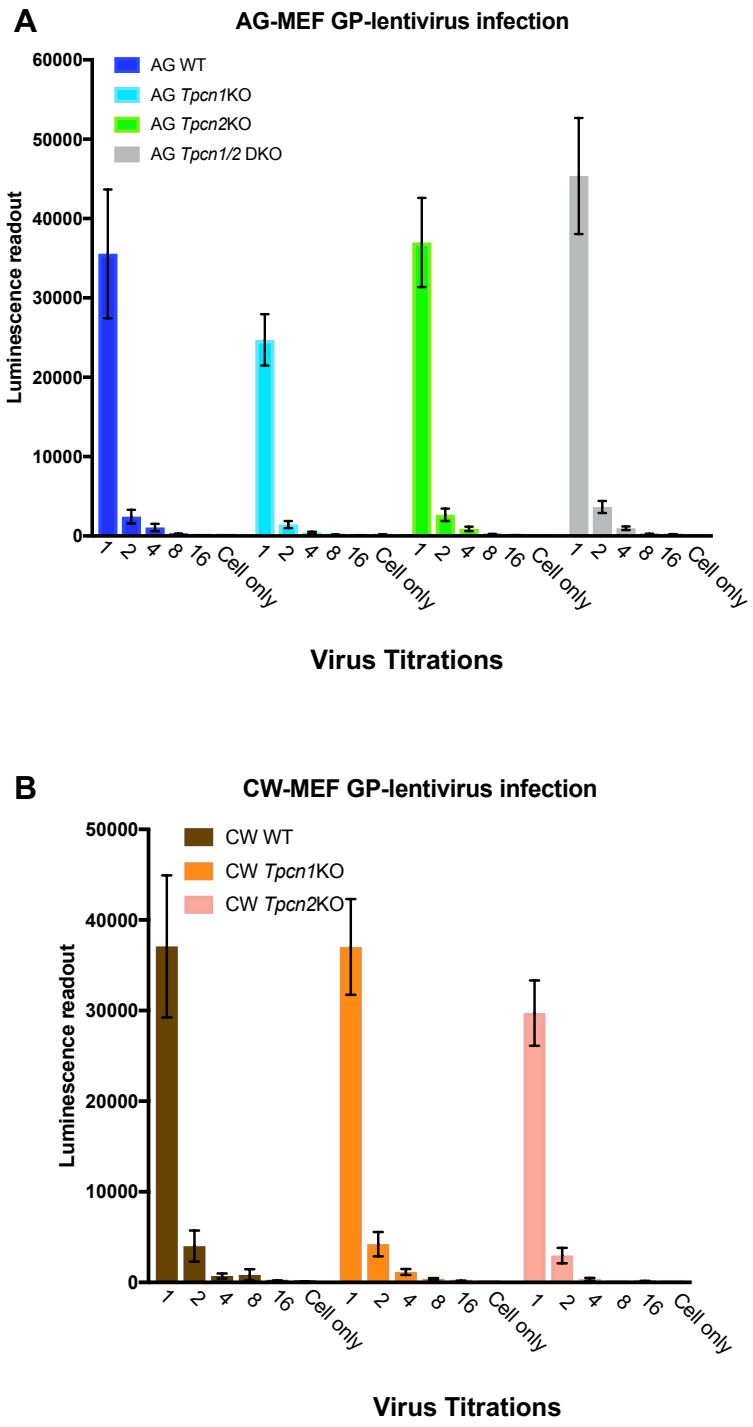


Figure 6. 3 GP-lentivirus infection of Tpcn1/2KO MEF cells

We titrated EBOV-GP pseudotyped lentivirus (GP-lentivirus) to infect two sets of TPC1/2 deficient mice embryonic fibroblast cells (MEF): AG-MEF (WT, *Tpcn1*KO, *Tpcn2*KO and *Tpcn1/2* double knockout DKO) and CW-MEF (WT, *Tpcn1*KO and *Tpcn2*KO). GP-lentivirus carries a firefly luciferase reporter gene. Cells were infected for 48 to 72 hours. After infection, cells were lysed and reacted with luciferase substrate Glo-lysis kit (ordered from Promega), and infection was quantified by measuring the luminescence level. Experiment was repeated three times, and the mean luminescence readout was plotted with error bars representing the standard error of the mean (SEM).

6.4 EBOV infection in *TPCN1/2* knockout HeLa cells

To further investigate the involvement of TPC1 and TPC2 proteins in EBOV entry, we decided to specifically knockout *TPCN1* and *TPCN2* genes from human HeLa cells by using the CRISPR/Cas 9 technique. TPCs are voltage-gated ion channels found in acidic organelles such as plant cells vacuoles and endo/lysosomes in animal cells (Ishibashi, Suzuki and Imai 2000; Furuichi, Cunningham and Muto 2001). Some organisms express three isoforms of TPCs (TPC1, 2, and 3), whereas only TPC1 and TPC2 are found in humans, mice and rats (Zhu *et al.* 2009; Brailoiu *et al.* 2010; Galione *et al.* 2010). TPCs function as dimers (Rietdorf *et al.* 2011), and each polypeptide chain has 12 transmembrane helices forming two homologous structural domains. Each domain contains 6 transmembrane helices and 2 pore helices on the luminal side, which may function as a selective funnel. This is confirmed by recent structural studies (Guo *et al.* 2016; Kintzer and Stroud 2016; She *et al.* 2018). Increasing evidence suggests that TPCs function as non-selective cation channels permeable to Ca^{2+} ions, in particular they are involved in nicotinic acid adenine dinucleotide phosphate (NAADP)-regulated Ca^{2+} release from acidic Ca^{2+} stores to the cytoplasm (Brailoiu *et al.* 2009; Calcraft *et al.* 2009; Zong *et al.* 2009; Ruas *et al.* 2015; Patel and Kilpatrick 2018). However, some hold a different view that TPCs are Na^+ channels regulated by phosphatidylinositol 3,5-biphosphate ($PI(3, 5)P_2$). (Wang *et al.* 2012; Cang, Bekele and Ren 2014; Morgan and Galione 2014).

6.4.1 TPCN1 and *TPCN2* knockout design

In consultation with Dr Philip Hublitz (Weatherall Institute of Molecular Medicine, Genome Engineering Service), we designed CRISPR/Cas 9 constructs to

specifically modify *TPCN1* and *TPCN2* genes in HeLa cells to abolish the protein expression of TPCs. Because HeLa cells are more than diploid in many chromosomal regions, we decided to use the double sgRNA approach to delete the targeted exon. We designed sgRNAs that direct Cas 9 nuclease enzyme to cut at both 5' and 3' intronic regions flanking the selected exon, so the whole exon will be deleted and DNA re-joined by non-homologous end joining (NHEJ).

The *TPCN1* gene that encodes TPC1 protein is located on human chromosome 12, and it encodes multiple transcriptional variants. The exon numbering used in this chapter is based on the *TPCN1* transcript variant 1 (NCBI code: NM_001143819.2), which contains 29 exons and encodes for human TPC1 isoform 1 (888 amino acids, NCBI reference sequence: NP_001137291.1). It has been reported that the TPC1 protein has multiple isoforms, and the TPC1B isoform has its first 69 amino acids truncated from the N-terminus compared to the TPC1A isoform (Ruas *et al.* 2014). We decided to knock out exon 7, which is an early exon present in all confirmed and predicted *TPCN1* transcriptional variants. Exon 7 contains 131 nucleotides, and deletion of this exon will result in a frameshift in transcription, followed by the translation of 38 nonsense-coding amino acids and a premature STOP codon. The first 176 residues from the N-terminus coded by exon 1 to exon 6 may still be translated and form the first 2 transmembrane helices of the TPC1 protein. However, with the latter 10 transmembrane helices and the pore forming helices deleted, it is most likely to be non-functional (Figure 6.4).

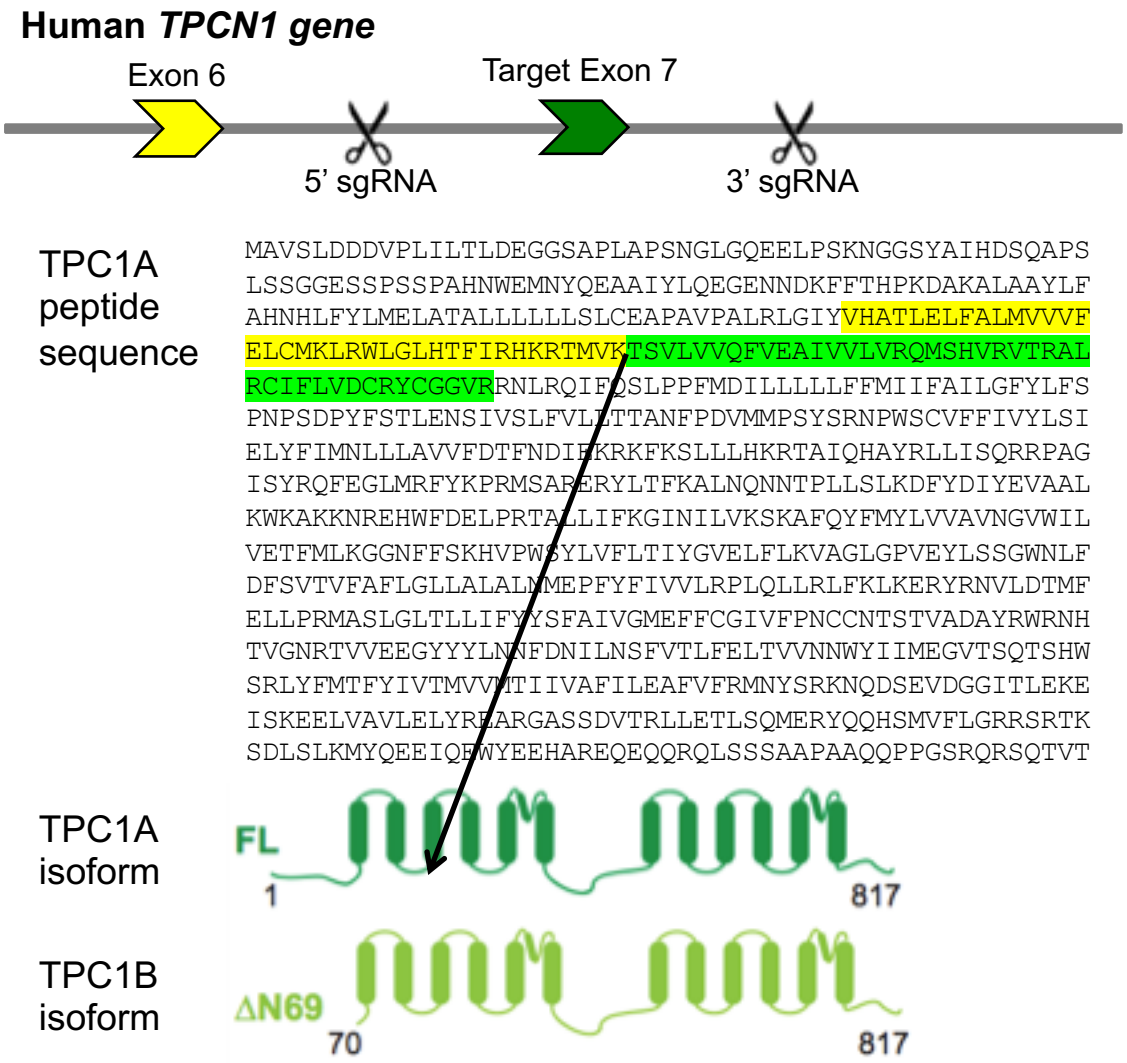


Figure 6. 4 Human TPCN1 gene and the corresponding peptide sequence
Schematic diagram showing the CRISPR/Cas 9 knockout strategy used to modify *TPCN1* gene in HeLa cells. Two sgRNAs guided Cas 9 nuclease enzyme to cleave at both 5' and 3' intronic region flanking the target exon 7 (green). Amino acids encoded by exon 6 and exon 7 are coloured yellow and green respectively in the full-length TPC1A peptide sequence. The arrow marks the position of the beginning of exon 7 in a predicted TPC1A protein domain diagram, with transmembrane helices represented by vertical blocks (adapted from Ruas *et al.* 2014). TPC1 has two isoforms reported by Ruas *et al.* (2014): the full-length (FL) TPC1A isoform and the shorter TPC1B isoform, in which the first 69 amino acids from the N-terminus are truncated (ΔN69) in comparison to TPC1A.

The *TPCN2* gene is located on human chromosome 11, and there is only one protein-coding transcript reported (NCBI code: NM_139075.4). The *TPCN2* gene contains 25 exons and encodes the 752 amino acids length TPC2 protein

(NP_620714.2). We selected to delete exon 2, which contains 65 nucleotides. Deleting exon 2 will result in removal of part of the first transmembrane helix of TPC2 and introduces a long non-sense translation (98 nonsense amino acids) before reaching the first premature STOP codon (Figure 6.5).

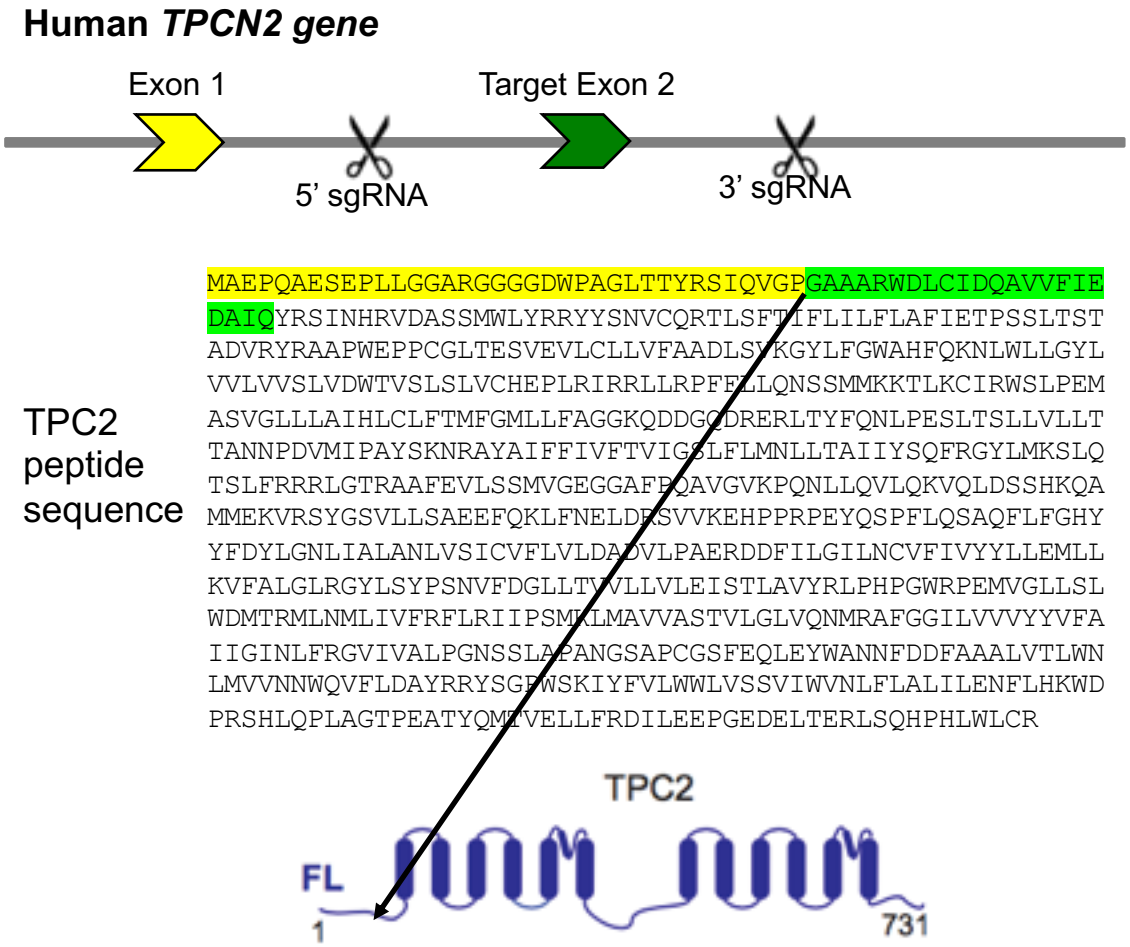


Figure 6. 5 Human TPCN2 gene and corresponding peptide sequence
Schematic diagram showing the CRISPR/Cas 9 knockout strategy used to modify *TPCN2* gene in HeLa cells. Two sgRNAs guided Cas 9 enzyme to cleave at both 5' and 3' intronic region flanking the target exon 2 (green). Amino acids encoded by exon 1 and exon 2 are coloured yellow and green respectively in the TPC2 peptide sequence. The arrow marks the position of the beginning of exon 2 in a predicted TPC2 protein domain diagram. Transmembrane helices are represented by vertical blocks (figure adapted from Ruas *et al.* 2015).

Philip Hublitz designed the sgRNAs that target the deletion of *TPCN1* exon 7 and *TPCN2* exon 2. He validated them in 293T cells by the surveyor assay (Figure 6.6). Individual sgRNA was transfected together with Cas 9 enzyme into 293T cells

to introduce a double-stranded break in DNA at a specific site. Efficient sgRNA will result in a cut that is later repaired by NHEJ with mutations and indels (insertions and deletions) introduced. The sgRNA target site is then amplified by PCR and subjected to reannealing, forming heteroduplex DNA. Surveyor nuclease cleaved DNA specifically at mismatched regions. Therefore, a shorter-sized cut band on the gel suggested that the tested sgRNA successfully introduced target site modification.

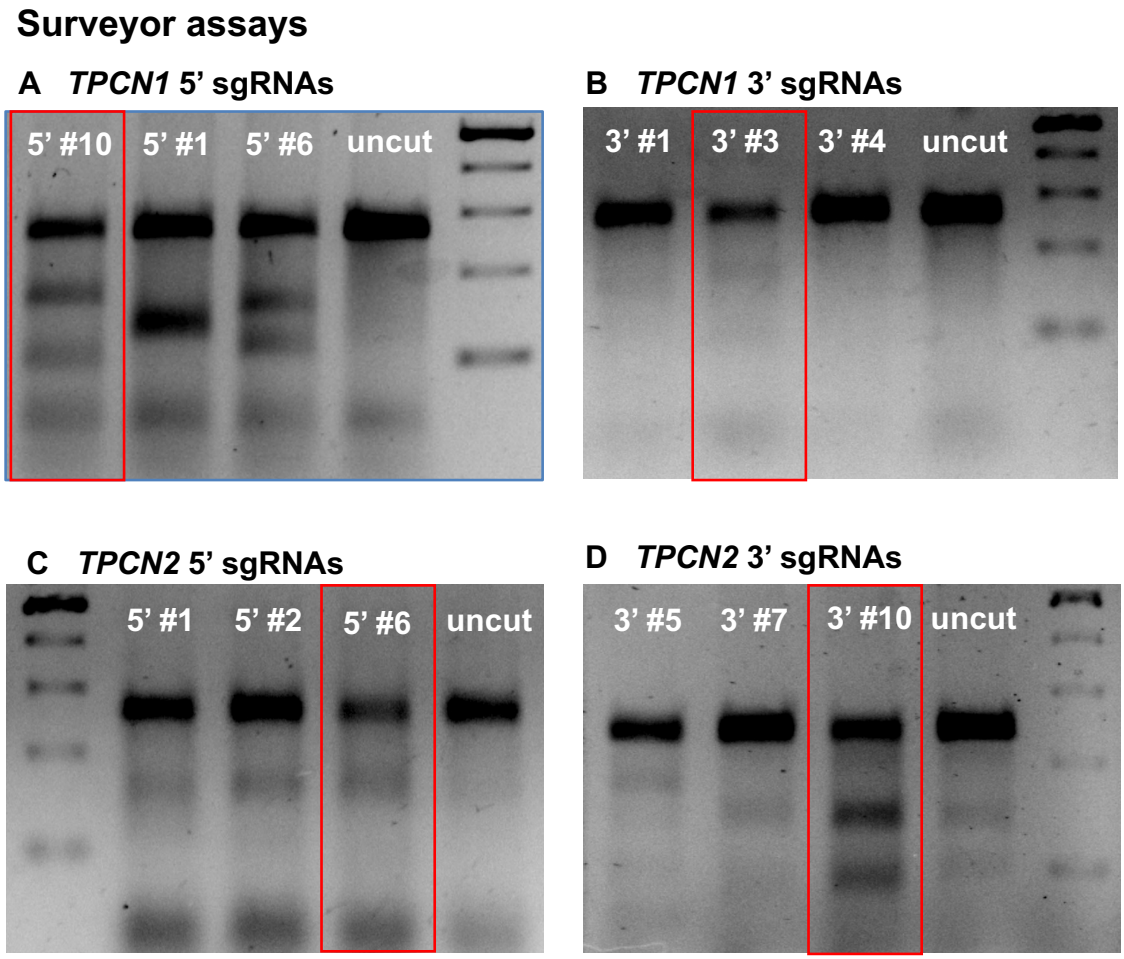


Figure 6. 6 TPCN1 and TPCN2 specific sgRNAs tested in surveyor assays
293T gDNA has been treated with **A:** *TPCN1* specific 5' sgRNAs (#10, #1 and #6); **B**: *TPCN1* specific 3' sgRNAs (#1, #3 and #4); **C**: *TPCN2* specific 5' sgRNAs (#1, #2 and #6); **D**: *TPCN2* specific 3' sgRNAs (#5, #7, #10). "Uncut" lane: gDNA isolated from cells that have been treated only with transfected Cas 9 without any sgRNA or with a mutated unmatched sgRNA. Shorter fragments obtained in treated gDNA samples compared to the uncut control indicated successful Cas 9 cutting guided by sgRNAs. The sgRNAs selected for subsequent experiments are highlighted by red rectangles.

Based on this result, we selected sgRNA-tpcn1-5' #10 and sgRNA-tpcn1-3' #3 to knock out *TPCN1* exon 7, and sgRNA-tpcn2-5' #6 and sgRNA-tpcn2-3' #10 to knock out *TPCN2* exon 2 from HeLa cells. We co-transfected HeLa cells with 5' and 3' sgRNAs for each gene, and cultured single-cell clones. Selected clones were stored and characterised in the later sections.

6.4.2 Genetic confirmation of *TPCN1*KO and *TPCN2*KO cells

We screened the single-cell HeLa clones for *TPCN1*KO and *TPCN2*KO using genomic DNA (gDNA) PCR and RT-PCR for mRNA. At least three independent clones were generated to ensure that any effects we detect is specific to the gene we targeted, and to avoid random clonal variations. For gDNA PCR, we designed primers that anneal just outside of the sgRNA cut sites. Figure 6.7 A and Figure 6.8 A showed the schematic design for primers used in gDNA PCR, and the expected size of amplified DNA fragments from WT, *TPCN1*KO and *TPCN2*KO HeLa cells. Cells with the targeted exon removed will have a shortened gDNA PCR product (Figure 6.7 B; Figure 6.8 B). There may be more than two copies of *TPCN1* and *TPCN2* genes in HeLa cells due to its nature of aneuploidy, and the sgRNAs may modify each copy differently. We aimed for complete knockout of the gene.

Because PCR preferably amplifies shorter DNA fragments, we designed an additional internal primer that anneals to the deleted region, to make sure that there were no copies of the target exon left in the KO clones (Figure 6.7 C; Figure 6.8 C and D). The gDNA PCR results were analysed on 1% agarose gel, and DNA was isolated from the gel bands for Sanger sequencing.

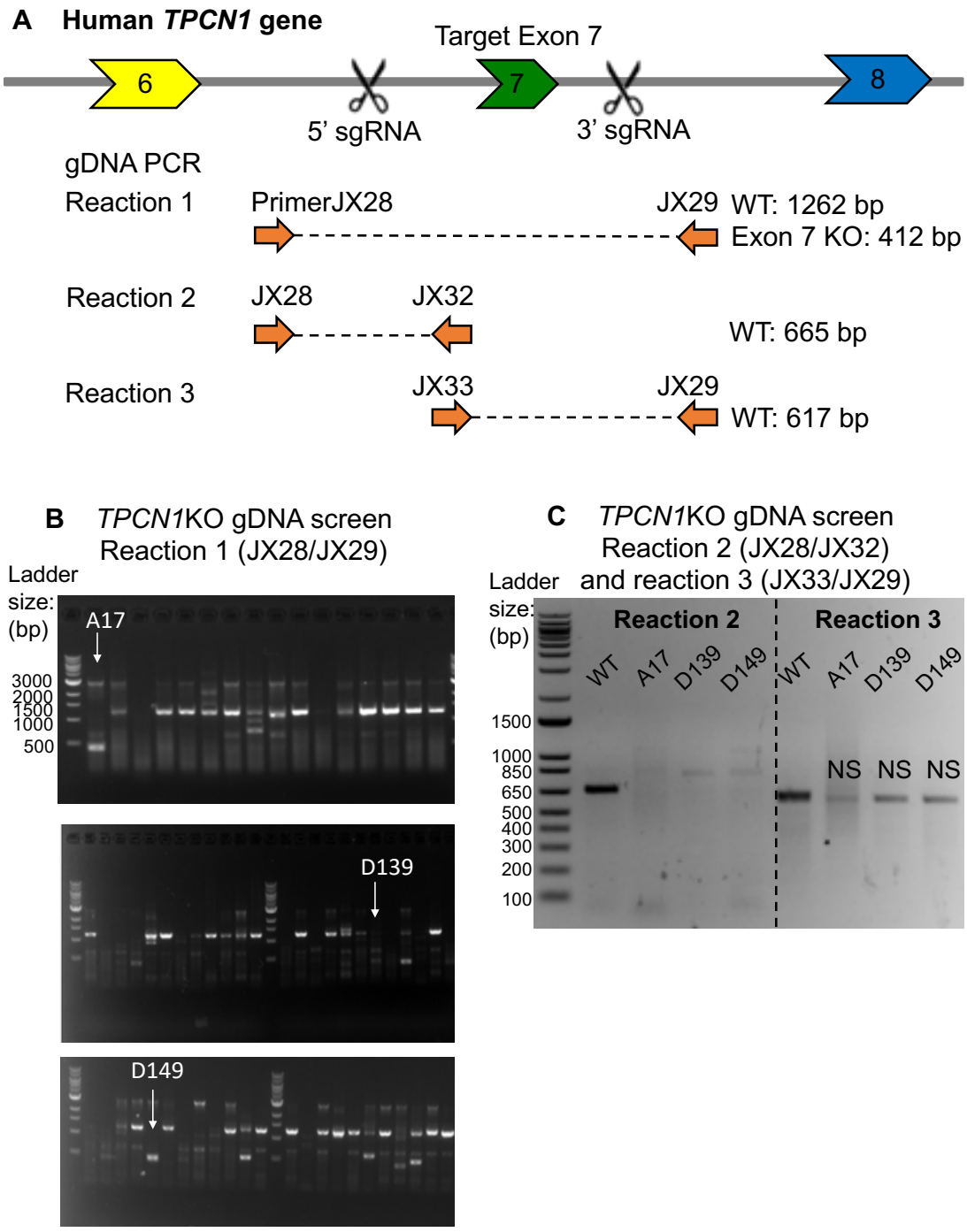


Figure 6. 7 TPCN1KO HeLa genomic DNA PCR verification

We isolated genomic DNA (gDNA) from genetically modified HeLa clones and screened for deletion of the targeted *TPCN1* exon 7. **A**: Schematic diagram showing the primer annealing sites (orange arrows) in respect of the target exon position and the sgRNA cut sites (scissors). Reaction 1 (**B**), 2 and 3 (**C**) gDNA PCR were used to screen for successful modification of *TPCN1* gene. PCR products were separated on 1% agarose gel and the PCR product amplified from WT gDNA and gDNA isolated from selected *TPCN1*KO clones (A17, D139, D149) are labelled in the diagram. "NS" marks the non-specific bands that showed no sequence alignment with *TPCN1* gDNA by Sanger sequencing.

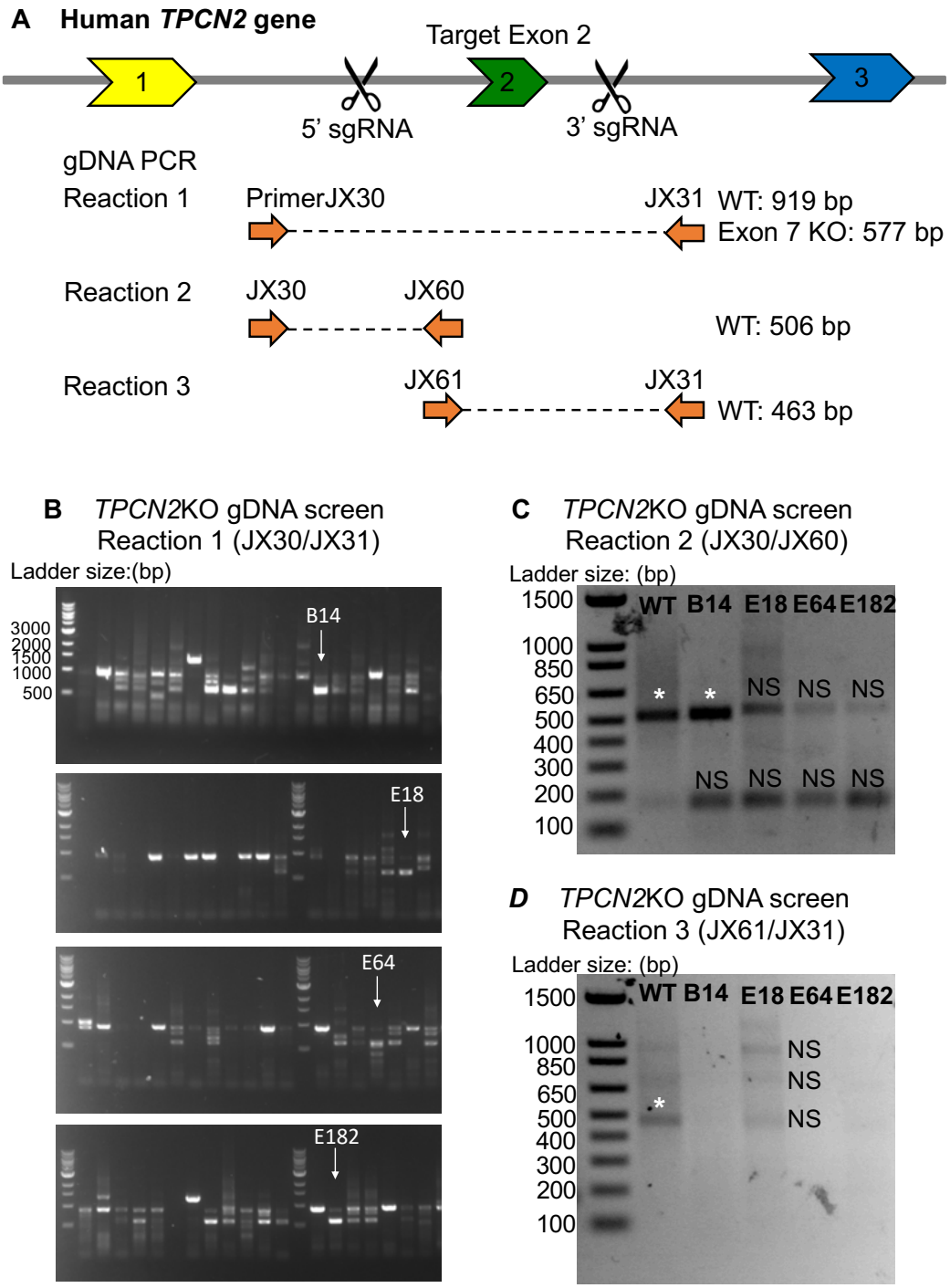


Figure 6. 8 TPCN2KO HeLa genomic DNA PCR verification

We isolated genomic DNA (gDNA) from genetically modified HeLa clones and screened for deletion of the targeted *TPCN2* gene exon 2. **A**: Schematic diagram showing the primer annealing sites (orange arrows) in respect of the target exon position and the sgRNA cut sites (scissors). Reaction 1 (**B**), 2 (**C**) and 3 (**D**) gDNA PCR were used to screen for successful modification of *TPCN2* gene. PCR products were separated on 1% agarose gel. Lanes for WT gDNA and gDNA isolated from four selected *TPCN2*KO clones (B14, E18, E64, E182) are labelled. "NS" marks the non-specific bands that showed no sequence alignment with *TPCN2* gDNA after Sanger sequencing. * labelled bands which contained part of the WT *TPCN2* sequence.

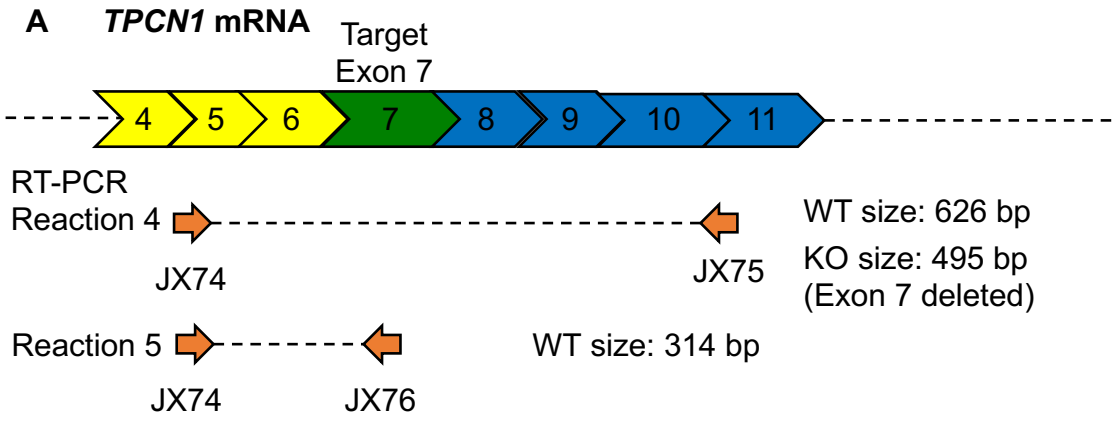
We isolated gDNA from three *TPCN1*KO HeLa clones (A17, D139, D149). All three clones had a shortened band for gDNA PCR reaction 1 compared to the PCR product amplified from WT gDNA (Figure 6.7 A), and no specific bands identified from reaction 2 and 3 (Figure 6.7 B, C). We isolated DNA from the gel bands and sent for Sanger sequencing. The result confirmed that *TPCN1* gene was modified as we expected, with the block between 5' and 3' sgRNAs deleted.

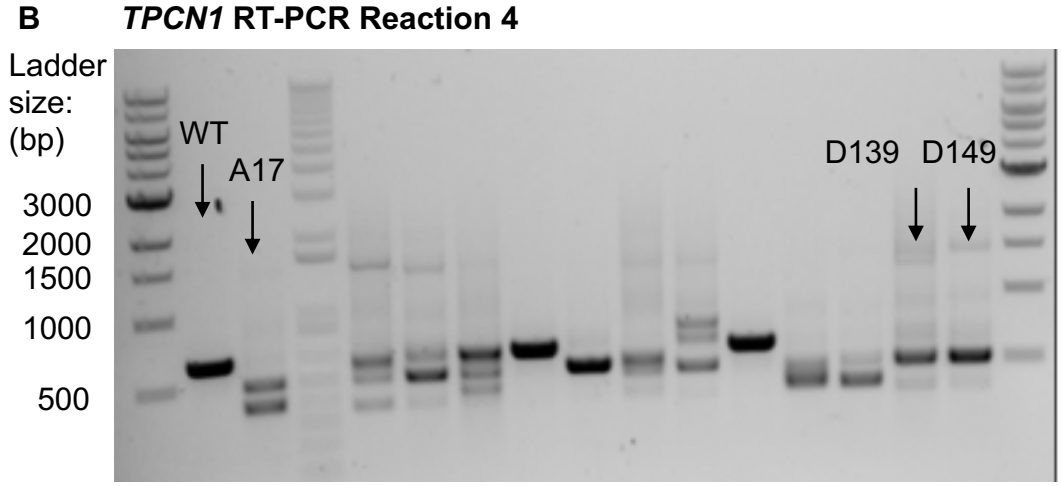
We also isolated four *TPCN2*KO HeLa clones (B14, E18, E64 and E182), and all of them had a shorter band in gDNA PCR reaction 1, as expected result from the deletion of exon 2 (Figure 6.8 B). For reaction 2 and 3, clone E18, E64 and E182 no longer had any specific PCR product, suggesting that deletion of the target exon was complete (Figure 6.8 C, D). For clone B14, however, a contradictory result was seen: no specific band amplified from reaction 3 but WT sequence was identified from PCR reaction 2 (Sanger sequencing). The reverse primer for reaction 2 (primer JX60) anneals at an intronic region upstream to exon 2, and therefore the amplified WT sequence did not include exon 2 sequence. We decided to further characterise this clone at mRNA level to confirm the genetic modification.

We further characterised the *TPCN1*KO and *TPCN2*KO HeLa clones at mRNA level by RT-PCR. The design of primers used in the assay and the results are shown in Figure 6.9 and Figure 6.10. We isolated the gel bands and sequenced the DNA fragment from the RT-PCR reaction. For *TPCN1*KO cells, D139 and D149 clones had their exon 7 deleted (131 bp), and the remaining exon 6 joined with exon 8 as we expected (primer pair JX74/75 amplified 495 bp fragment). The A17

clone however, had two shortened bands with different sizes. After sequencing the DNA isolated from these bands, we found that one band had exon 7 deleted, the other had both exon 6 and exon 7 deleted (245 bp deletion), and exon 5 was joined with exon 8 (JX74/75 amplified 381 bp). This will still introduce a frameshift to the altered transcript.

For *TPCN2*KO cells, all 4 clones including clone B14 had a shorter band amplified than WT from reaction 4, but the band size was shorter than expected (RT-PCR with primers JX77/JX82). If only the target exon 2 (65 bp) was removed, the expected amplification size was 297 bp, but the gel band size was closer to the 200 bp ladder marker. We sequenced the bands and showed that in addition to deleting exon 2, part of exon 3 was deleted, resulting in removal of 142 bp fragment, but still introducing a frameshift.





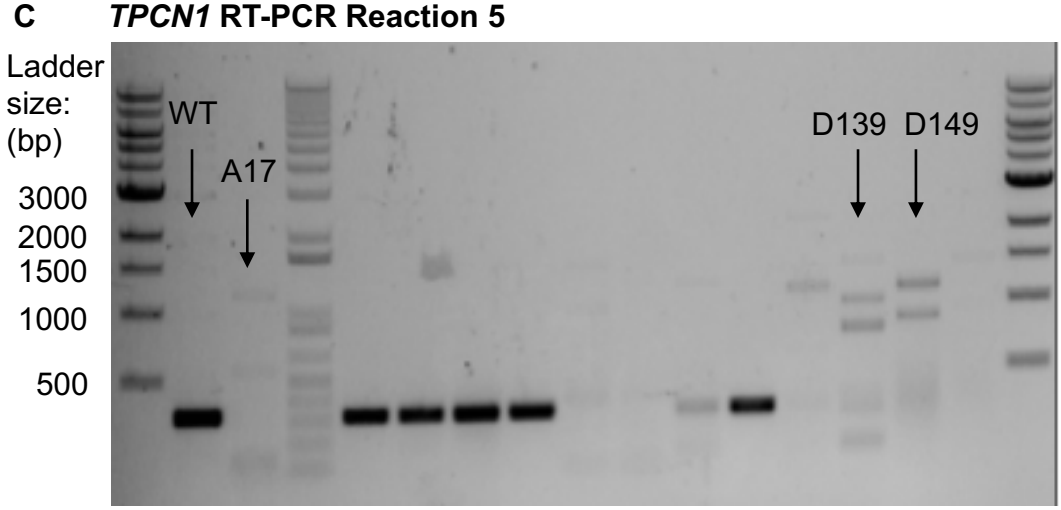


Figure 6. 9 RT-PCR characterising TPCN1KO HeLa clones

A: Schematic diagram showing the annealing sites of RT-PCR primers in respect of *TPCN1* exons in mRNA transcript. **B**, **C**: 1% agarose gel picture for RT-PCR product of *TPCN1* RT-PCR reaction 4 (primer JX74/JX75) and reaction 5 (primer JX74/JX76) amplified from mRNA isolated from WT and selected *TPCN1*KO clones (A17, D139, D149). Successful deletion of *TPCN1* exon 7 resulted in a shorter band in reaction 4 and no amplified product in reaction 5. DNA purified from individual bands were sent for Sanger sequencing.

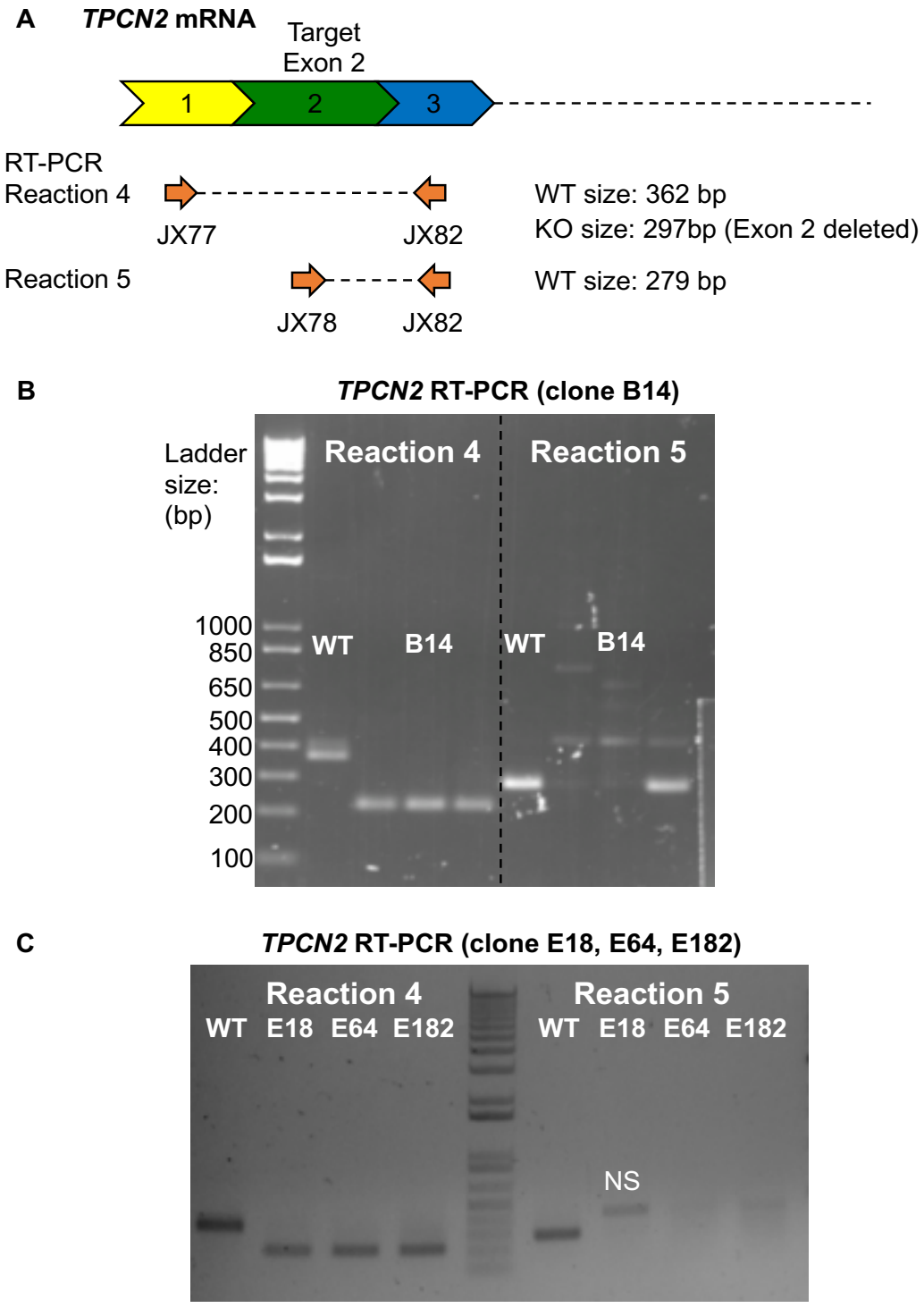


Figure 6. 10 RT-PCR characterising TPCN1KO HeLa clones

A: Schematic diagram showing the annealing sites of RT-PCR primers in respect of *TPCN2* exons in mRNA transcript. **B**, **C**: 1% agarose gel picture for RT-PCR product of *TPCN2* RT-PCR reaction 4 (primer JX77/JX82) and reaction 5 (primer JX78/JX82) amplified from WT and selected *TPCN2*KO clones (B14, E18, E64, E182) mRNA. Successful deletion of *TPCN2* exon 2 resulted in a shorter sized band in reaction 4 and no specifically amplified product in reaction 5. DNA purified from individual bands were sent for Sanger sequencing. “NS” labels the non-specific bands that showed no sequence alignment with WT *TPCN2* mRNA.

6.4.3 Functional assays of TPCN1KO and TPCN2KO HeLa cells

We have had time for only limited characterisation of the *TPCN1*KO and *TPCN2*KO HeLa cells at phenotypic level. We have not found any specific antibodies for TPC1 or TPC2. We ordered a few from Abcam and tested them in western blotting and confocal microscopy but detected only non-specific binding.

TPCs are reported as NAADP-regulated calcium permeable channels. Our collaborator Antony Galione's group is currently waiting for a robust cell-permeant NAADP analogue in order to test the *TPCN1/2*KO clones for NAADP-induced Ca^{2+} release from endo/lysosomal calcium stores. As an alternative, Anthony Morgan from the Galione group transfected HeLa cells with fluorescently-tagged mouse cholecystokinin receptor-A (CCKR-A), which responds to cholecystokinin stimulation (CCK) and is known to couple to NAADP-evoked Ca^{2+} release from acidic organelles in pancreatic acinar cells (Cancela, Churchill and Galione 1999; Yamasaki *et al.* 2004). HeLa cells did not respond to CCK unless heterologously expressing CCKRs. After transfection, cells were stimulated with 100 pM CCK and loaded with a fluorescence Ca^{2+} dye (Calbryte-520/AM) to image and measure the Ca^{2+} signals by confocal microscopy (Figure 6.11).

We tested one *TPCN1*KO clone (D149) and one *TPCN2*KO clone (E64) in comparison to WT HeLa in this assay. We observed a significant decrease in oscillatory amplitude (Ca^{2+} signals) and a slower rate of rise for the first three spikes in both KO cells than WT, stimulated by CCK (Figure 6.11). At the same time, the spikes were wider in KO cells, indicating a smaller and slower response in Ca^{2+} signalling.

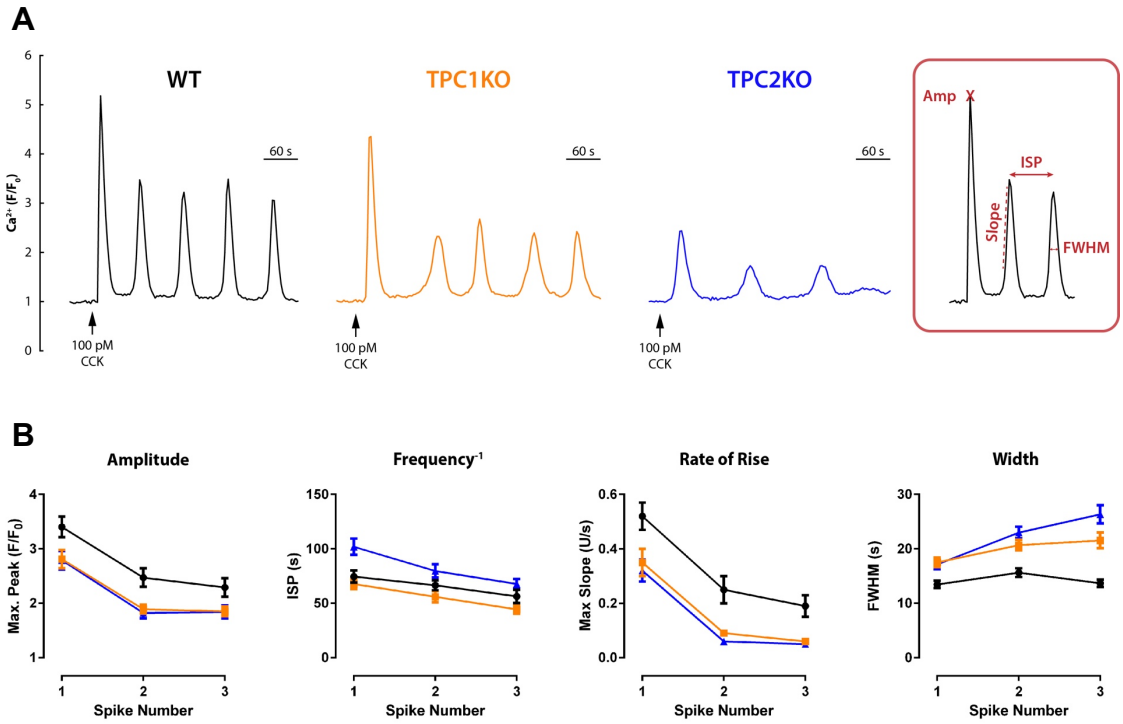


Figure 6. 11 Effect of TPC knockout on Ca^{2+} signals

A: Representative single-cell Ca^{2+} traces of HeLa cells stimulated by cholecystokinin (CCK). WT HeLa (black), *TPCN1*KO clone D149 (orange) and *TPCN2*KO clone E64 (blue) were tested respectively. All traces are normalised to the initial fluorescence (F/F_0) to account for loading variation. HeLa cells were transiently transfected overnight with the mouse cholecystokinin receptor A (CCKR-A) tagged with mTagBFP2 fluorescence protein on its C-terminus. Cells were loaded with a Ca^{2+} dye, 2 μ M Calbryte-520/AM and imaged on a Nikon A1R confocal microscope. Only those cells positive for mTagBFP2 were included in the analysis and, of these, only cells that responded to 100 pM CCK were included. The inset on the right (bordered by a red square) shows a cartoon of the four spike parameters depicted in the summary charts **B**, where Amp = the amplitude of each spike; Slope = the maximum rate of rise; ISP = interspike period; FWHM = the full-width at half-maximum height. Data are mean ± SEM of 43 - 90 cells performed on 3 different days.

The residual spikes are most likely due to Ca^{2+} released from the endoplasmic reticulum (ER) calcium store (personal communication with Anthony Morgan; Morgan 2016). The notably more sluggish and blunted Ca^{2+} oscillations in *TPCN1*KO and *TPCN2*KO clones imply that TPC1 and 2 function was affected in our knockout cells. We will further carry out the protein level characterisations.

6.4.4 EBOV-GP pseudotyped virus infection in TPC1/2 deficient cells

We titrated E-S-FLU and the control H5-S-FLU pseudotyped virus to infect WT, *TPCN1*KO and *TPCN2*KO HeLa cells, and quantified percentage infection by using FACS to count the eGFP expressing cells. Both E-S-FLU and H5-S-FLU infected *TPCN1*KO and *TPCN2*KO cells at a similar level compared to WT HeLa cells (Figure 6.12, Figure 6.13).

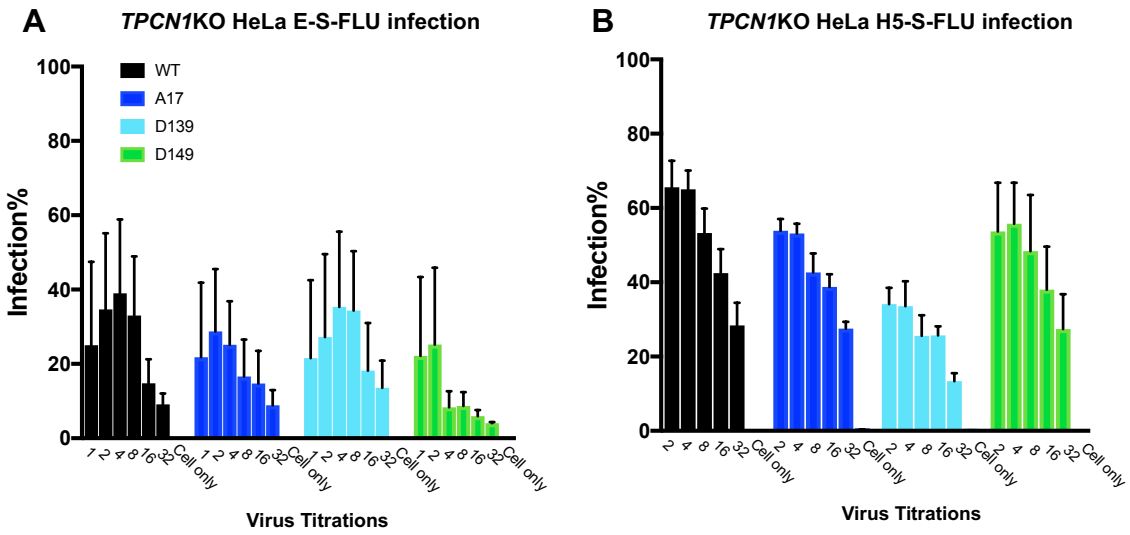


Figure 6. 12 E-S-FLU infection in TPCN1KO HeLa cells
We titrated EBOV-GP pseudotyped E-S-FLU (**A**) and control H5-S-FLU (**B**) to infect WT and *TPCN1*KO HeLa cell-lines (A17, D139 and D149 clones). Cells were infected for 24 hours then fixed and analysed by FACS. The infection% was the percentage of cells with an eGFP readout of $>10^2$ fold more than the uninfected "Cell only" control. Average infection% from four experimental repeats are shown with error bars representing the standard error of the mean (SEM).

We observed a big variation in percentage infection of E-S-FLU in HeLa cells between independent experimental repeats, hence the relatively big error bars (standard error of the mean) displayed in E-S-FLU infection figures (Figure 6.12 A, 6.13 A). However, the changes were consistent across WT and *TPCN1*KO, *TPCN2*KO cell-lines and did not reveal a reduction of infection in the TPC1 or 2 deficient cells. All experiments were repeated 4 times. In the *Tpcn*1/2KO MEF cell section (section 6.3), we used two EBOV-GP pseudotyped viruses, E-S-FLU and

GP-lentivirus. We plan to infect *TPCN*1/2 KO HeLa cells with GP-lentivirus in future experiments.

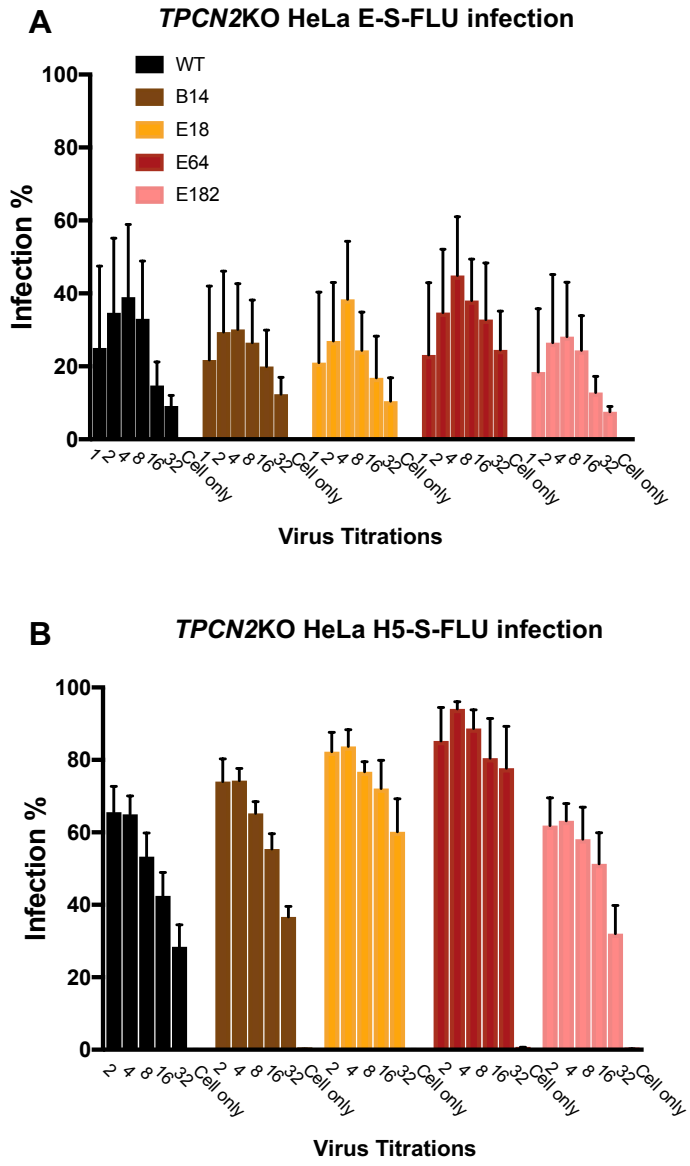


Figure 6. 13 E-S-FLU infection in TPCN2KO HeLa cells
We titrated EBOV-GP pseudotyped E-S-FLU (**A**) and control H5-S-FLU (**B**) to infect WT and four *TPCN2*KO HeLa cell-lines (B14, E18, E64 and E182 clones). Cells were infected for 24 hours then fixed and analysed by FACS. The infection% was the percentage of cells with an eGFP readout of $>10^2$ fold more than the uninfected "Cell only" control. Average infection% from four experimental repeats are showed with error bars representing the standard error of the mean (SEM).

We noticed a confounding issue of a prozone effect of E-S-FLU infection, where exposure to the higher concentrations of pseudotyped virions resulted in a lower

percentage infection (Figure 6.12 A, 6.13 A). Our pseudotyped viruses culture supernatant was harvested directly from production cells without purification procedures (Chapter 3, section 3.2). We suggest that this is likely to be a tissue culture artefact, where some unknown factors in the virus growth medium (VGM: Dulbecco's modified Eagle's medium (DMEM) with 0.1% bovine serum albumin, 10 mM HEPES, 2 mM glutamine, 100 U/ml penicillin, and 100 µg/ml streptomycin) may be inhibiting E-S-FLU attachment or infection *in vitro*. When we titrated E-S-FLU with VGM in the HeLa infection assay, percentage infection was reduced to less than 1% at a dilution of 1 in 2 (data not shown). To overcome this problem, we titrated E-S-FLU with PBS in the HeLa infection experiments. Surprisingly, even at 1 in 32 dilution, enough HeLa cells survived during the 24-hour infection period for FACS analysis (>1000 cells), feeding on the limited medium from the virus culture supernatant. The false inhibitory effect from medium was not seen in H5-S-FLU titration and therefore titrations were done in VGM.

An alternative method to overcome the relatively inefficient infection of HeLa cells with E-S-FLU is to add a lectin in the form of inactivated haemagglutinin to the pseudotype membrane to increase the initial cell attachment, as described in Chapter 3 (section 3.5). These experiments are planned.

6.5 Overexpression of pore-mutants of TPC2 and E-S-FLU infection

Sakurai's group transduced WT HeLa cells with a lentiviral vector to express a dominant mutant version of human TPC2 with a change from leucine to proline at position 265 ($TPC2^{L265P}$) (Brailoiu *et al.* 2010; Sakurai *et al.* 2015). They showed that introducing GFP-tagged $TPC2^{L265P}$ in WT HeLa cells significantly reduced

EBOV infection. The TPC2 protein has 12 transmembrane helices forming two homologous structural domains, and it dimerises to form the cation channel complex. The L265P mutation lies in the pore-forming region, at the first luminal pore helix between transmembrane helices 5 and 6 (Brailoiu *et al.* 2010). Overexpressing the pore-mutant $TPC2^{L265P}$ subunits impaired the NAADP-evoked Ca^{2+} signal, likely by pairing with WT TPC2 subunits forming defective channel dimers. From our collaborator, Antony Galione, we had access to two similar pore-mutant murine TPC2 cDNAs. These were $TPC2^{N257A}$ and $TPC2^{E643A}$ (Ruas *et al.* 2015). The N257A mutation locates at the same region as the L265P mutation, whereas E643A mutation lies at the equivalent site in the second homologous domain, between transmembrane helices 11 and 12 (Figure 6.17).

Although $TPC2^{N257A}$ and $TPC2^{E643A}$ were from mice, the TPC2 protein is highly conserved between human and mouse species (75% identity), and the N-terminal di-leucine endo/lysosomal targeting sequence motif is identical in mouse and human TPC2 (Brailoiu *et al.* 2010). Ruas *et al*. previously showed that expression of $TPC2^{N257A}$ and $TPC2^{E643A}$ were unable to restore NAADP-regulated Ca^{2+} signal in *Tpcn2*KO mice embryonic cells (MEF) confirming their pore-mutant properties (Ruas *et al.* 2015).

We transduced WT HeLa cells to express mCherry-tagged mouse $TPC2^{WT}$, $TPC2^{N257A}$ and $TPC2^{E643A}$ using a lentiviral vector. We bulk-sorted the cells expressing high level of TPC2-mCherry. The sorted cells showed perinuclear punctate fluorescence when viewed under the fluorescence microscope (Figure 6.14 C), suggesting that the transduced TPC2-mCherry proteins were correctly

localised to the endo/lysosomal compartment. Next, we titrated E-S-FLU and control H5-S-FLU pseudotyped virus to infect HeLa cells or HeLa transduced with mouse TPC2 variants. As shown in Figure 6.15, E-S-FLU infection did not differ in HeLa cells overexpressing WT TPC2 or pore-mutant $TPC2^{N257A}$ and $TPC2^{E643A}$. We plan to contact Brailoiu *et al.* to request the human version of pore-mutant $TPC2^{L265P}$ to repeat this experiment. We will also test the TPC2 function in the transduced cells we have made for responses to NAADP in due course.

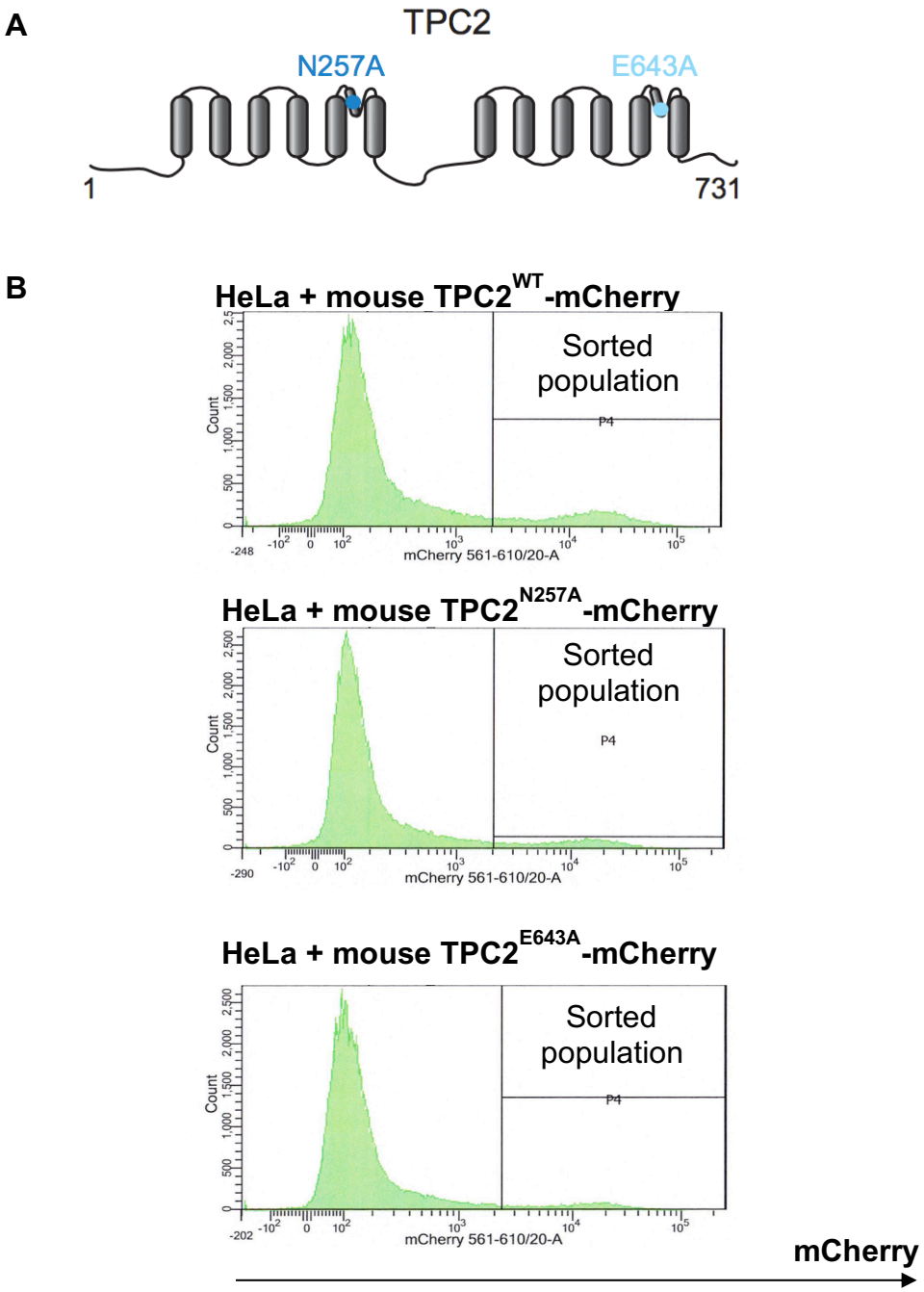

A
TPC2
N257A
E643A
1
731
B
HeLa + mouse TPC2WT-mCherry
Sorted population
P4
Count
mCherry 561-610/20-A
HeLa + mouse TPC2N257A-mCherry
Sorted population
P4
Count
mCherry 561-610/20-A
HeLa + mouse TPC2E643A-mCherry
Sorted population
P4
Count
mCherry 561-610/20-A
mCherry
C
HeLa + WTtpc2 mCherry
Brightfield
mCherry

Figure 6. 14 HeLa transduced to express pore-mutants of TPC2
A: Predicted domain structure of mouse TPC2 with N257A and E643A mutations labelled. The vertical blocks represent transmembrane helices and the numbers represent amino acid residues. **B**: FACS histogram showing the mCherry fluorescence level of HeLa transduced with WT, N257A or E643A mCherry-tagged mouse TPC2. Cells with high-level mCherry fluorescence were bulk sorted as TPC2 overexpressing cells. **C**: Microscope picture of sorted HeLa transduced with mCherry-tagged WT TPC2. Perinuclear punctate staining suggested the TPC2-mCherry were correctly localised to the endo/lysosomal compartment.

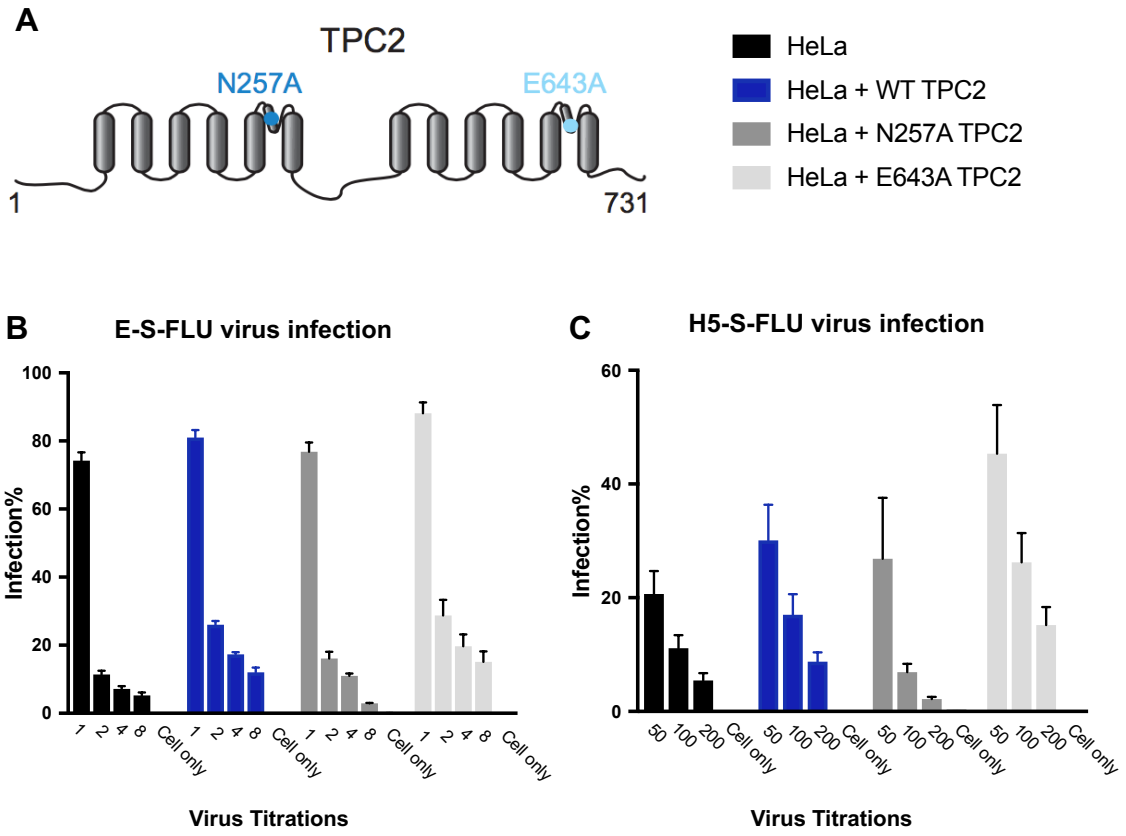


Figure 6. 15 E-S-FLU infection of HeLa overexpressing pore-mutants of TPC2
We titrated EBOV-GP pseudotyped E-S-FLU and control H5-S-FLU to infect HeLa cells overexpressing WT TPC2-mCherry or pore-mutant versions of TPC2-mCherry (N257A, E643A). Cells were infected for 24 hours then fixed and analysed by FACS. Cells with high-level mCherry expression were gated for analysis. The infection% was the percentage of cells with an eGFP readout of $>10^2$ fold more than the uninfected "Cell only" control. Average infection% from two experimental repeats are shown with error bars representing the standard error of the mean (SEM).

6.6 Discussion and future work

Calcium plays an important role in intracellular signalling, regulating enzyme activities, lysosome biogenesis and vesicle membrane fusion (Morgan *et al.* 2011; Luzio *et al.* 2014). While the endoplasmic reticulum (ER) is the major Ca^{2+} store in the cell with a neutral pH environment (Kim *et al.* 1998; Kneen *et al.* 1998; Foyouzi-Youssefi *et al.* 2000), the endosomes and lysosomes are recognised as additional crucial acidic stores for Ca^{2+} ions (Patel and Cai 2015). Elevation of cytoplasmic Ca^{2+} released from endo/lysosomes can subsequently trigger the opening of ER Ca^{2+} channels, which is known as Ca^{2+}-induced Ca^{2+} release (Berridge, Lipp and Bootman 2000; Bootman, Berridge and Roderick 2002; Morgan 2016).

Endo/lysosomal Ca^{2+} homeostasis and regulation are a new and growing field. The exact ion pump used for uptake of Ca^{2+} into the lysosomal lumen has yet to be identified, and it may be coupled to H^+ or/and Na^+ ion exchange (Morgan *et al.* 2011). Several cation channels have been described as endo/lysosomal Ca^{2+} release channels in the last decades, such as two-pore channels (TPCs) (Brailoiu *et al.* 2009; Calcraft *et al.* 2009; Schieder *et al.* 2010; Ruas *et al.* 2015), ryanodine receptor (RyR) (Dammermann and Guse 2005; Gerasimenko *et al.* 2006); and transient receptor potential-mucolipins (TRPML1, 2, 3) (Abe and Puertollano 2011; Venkatachalam, Wong and Zhu 2015; Rinkenberger and Schoggins 2018). TPC1 and TPC2 are widely accepted as nicotinic acid adenine dinucleotide phosphate (NAADP)-regulated Ca^{2+} channels with some controversial claims that they are phosphatidylinositol 3,5-bisphosphate ($PI(3,5)P_2$)-regulated Na^+ channels

(Morgan *et al.* 2011; Wang *et al.* 2012; Cang, Bekele and Ren 2014; Patel and Kilpatrick 2018).

There have been increasing claims that the endo/lysosomal Ca^{2+} and calcium channels are required for the EBOV entry process, but the mechanism by which they are involved has not been explained (Suárez *et al.* 2003; Sakurai *et al.* 2015; Simmons *et al.* 2016; Penny *et al.* 2018). Our current understanding of EBOV cell entry is that the virus is engulfed into endosomes by macropinocytosis, and passes with the maturation of the endosome into the late endosome/lysosome, where EBOV-GP is cleaved by host cathepsin B/L to expose the receptor binding region. EBOV-GP then binds to the lysosomal protein NPC1, which finally leads to fusion of the viral and lysosome membranes and ejection of the viral nucleocapsid into the cytosol (Aman 2016; Xiao *et al.* 2018). Calcium-dependent processes are involved in trafficking and fusion of intracellular vesicles (Pryor *et al.* 2000; Luzio, Bright and Pryor 2007; Pryor and Luzio 2009), and this clearly does play a role in the process of infection by some viruses such as Middle East respiratory syndrome coronavirus (MERS-CoV) (Gunaratne *et al.* 2018b).

In this chapter, we aimed to investigate whether Ca^{2+} channels are involved in EBOV infection, by drug inhibition assays and genetic knockout studies. We have demonstrated in Chapter 3 and 4 that our EBOV-GP pseudotyped virus E-S-FLU mimics WT EBOV during the entry process, hence is a suitable surrogate for the study.

6.6.1 TPC1/2 and EBOV-GP dependent infection

We became interested in the relationship between TPCs and EBOV for three reasons. Firstly, we and other groups have seen that several Ca^{2+} channel blockers such as amiodarone, verapamil and bepridil inhibited EBOV entry (Gehring *et al.* 2014; Johansen *et al.* 2015; Sakurai *et al.* 2015; Xiao *et al.* 2018). Secondly, TPCs are localised on the EBOV entry pathway, with TPC1 more towards the early and late endosomes and TPC2 in the late endosome/lysosome, co-localising with the receptor NPC1 protein and the cleaved EBOV-GP (Calcraft *et al.* 2009; Brailoiu *et al.* 2010; Simmons *et al.* 2016). Thirdly, we noted the description of reduced EBOV infection in cells that either lacked TPC1/2 expression after gene removal, or knockdown with siRNA, published by Sakurai *et al.* (2015).

We attempted to replicate these experiments by using two well-characterised EBOV-GP pseudotyped viruses: E-S-FLU (Xiao *et al.* 2018) and GP-lentivirus (Wool-Lewis and Bates 1998; Long *et al.* 2015). Our collaborator Professor Antony Galione kindly provided us with two sets of independently generated TPC1 and TPC2 knockout (KO) mice embryonic fibroblast cells (MEFs) (Calcraft *et al.* 2009; Arndt *et al.* 2014; Grimm *et al.* 2014; Ruas *et al.* 2014, 2015). However, we did not see any reduction of infection by EBOV-GP pseudotyped virus in cells modified to prevent TPC1/2 expression. Especially the TPC1/2 double knockout cells, which were shown to have completely depleted NAADP-induced Ca^{2+} signal (Ruas *et al.* 2015), were still infected at a comparable level to WT MEFs.

We then developed our own human *TPCN1*KO and *TPCN2*KO cell-lines (HeLa) by using CRISPR/Cas 9 technique. We confirmed our knockout cells at both genomic and transcriptional levels, and detected reduced NAADP-dependent Ca^{2+} signalling in an indirect assay with cholecystokinin receptor-A (CCKR-A) transduced cells. However, we still were unable to detect a difference in infection in the TPC knockout cells.

Sakurai's group showed that overexpressing a dominant pore-mutant $TPC2^{L265P}$ in HeLa cells reduced EBOV infection. In preliminary work, we transduced HeLa cells with two mouse pore-mutants $TPC2^{N257A}$ and $TPC2^{E643A}$, but they did not reduce E-S-FLU infection. We plan to contact the group to acquire and test the human pore-mutant $TPC2^{L265P}$ in our system (Brailoiu *et al.* 2010; Sakurai *et al.* 2015), and also to characterise our cells for Ca^{2+} flux responses to NAADP.

With the evidence we have generated, while still not complete, we would like to put a question mark on the involvement of TPCs in the EBOV entry process, and we hope to encourage other groups to explore the discrepancy. Certainly, EBOV-GP pseudotyped viruses such as E-S-FLU and GP-lentivirus are virologically different from wild-type EBOV. To carry forward the current findings, we will contact our collaborator Peter Halfmann (University of Wisconsin) to test the TPC1/2KO MEFs and HeLa cells for infection with a recombinant GFP-EBOV virus (Halfmann *et al.* 2008).

In addition, Jack Tan from our lab has developed an *in vivo* version of single-cycle E-S-FLU, expressing a firefly luciferase reporter instead of eGFP. Infection in a

live mouse by intravenous injection localises to the liver, the main target organ for EBOV (Ellis *et al.* 1978; Zaki and Goldsmith 1999; Martines *et al.* 2014). Infection could be quantified by luminescence camera and he showed that E-S-FLU^{luciferase} infection was blocked by EBOV-GP specific antibody KZ52 (data unpublished). In collaboration with Nick Platt and Fran Platt, we are planning to test infection by E-S-FLU^{luciferase} in *TPCN2*KO mice using *NPC1*KO and WT mice as controls.

6.6.2 Calcium channel blockers and EBOV-GP dependent infection

In Chapter 4, we screened a drug library LOPAC®1280 (Sigma) and some additional small molecules in our virus inhibition assay. In total, we have tested 44 drugs that have calcium-related functions based on the Sigma description and the current literature (Naylor *et al.* 2009; Sakurai *et al.* 2015; Bhagya and Chandrashekar 2016; Pafumi *et al.* 2017; Gunaratne *et al.* 2018a). Eighteen of them inhibited E-S-FLU infection.

Seventeen of eighteen were specific for E-S-FLU and failed to inhibit the control H5-S-FLU, which is composed of the Influenza core coated in Influenza H5 haemagglutinin. One drug calmidazolium, inhibited infection by both E-S-FLU and H5-S-FLU. Calmidazolium is a blocker of calmodulin and has very widespread effects and will not be considered further (El-Saleh and Solaro 1987; Sunagawa *et al.* 2000; Lee *et al.* 2016).

Amiodarone, bepridil, verapamil, tetrandrine and trans-Ned19 have been reported by other groups as EBOV entry inhibitors (Gehring *et al.* 2014; Kouznetsova *et al.* 2014; Johansen *et al.* 2015; Sakurai *et al.* 2015), which we confirmed. Sakurai *et*

al. stressed the importance of L-type calcium channel blockers and suggested that they were acting by blocking TPCs. Tetrandrine successfully protected mice from EBOV challenge at the dose of 30 mg/kg (Sakurai *et al.* 2015). Tetrandrine is known to block TPC2, however it also acts on other signalling pathways and is a lysosomotropic CAD with high LogP and pKa^{base} features (Bhagya and Chandrashekar 2016; Penny *et al.* 2018).

Rahman *et al.* showed by computer modelling that the dihydropyridine family of L-type Ca^{2+} channel blockers can bind into the pore of the TPCs (Rahman *et al.* 2014). They then confirmed that several dihydropyridines blocked NAADP-induced Ca^{2+} release in the sea urchin egg homogenate as well as in a mammalian cell-line. There were nine dihydropyridines in our collection of 44 Ca^{2+} channel inhibitors. Of these only nicardipine, which has a high LogP and pKa^{base}, inhibited E-S-FLU infection. In our assay, not only L-type channel inhibitors, but also T-type channel inhibitors such as mibefradil and NNC 55-0396; Ca^{2+}/Na^{+} exchanger inhibitor KB-R7943 and flunarizine also inhibited E-S-FLU infection, but all the inhibitors had the characteristic high LogP and pKa^{base}. Taken together these results hinted that drug selectivity towards L-type channel blockers, or indeed any calcium channel, may not be essential for inhibition of EBOV entry.

In Chapter 4, we showed that the majority of the strong E-S-FLU inhibitors were cationic amphiphilic drugs (CADs), which will concentrate in the lysosomal membrane (De Duve *et al.* 1974). After analysing the LogP and pKa^{base} values for the 44 calcium-related drugs, we identified a new pattern. All of the specific E-S-FLU inhibitors, except the inorganic ruthenium red, were CADs (high LogP, high

pKa^{base}). Is the CAD feature key to inhibiting EBOV entry while the calcium channel blocking character is disposable? It is difficult to confirm the effect of lysosomotropism experimentally. A recent study tried to dissect the effect of TPCs inhibition and the non-specific effect of lysosomotropism. The group identified seven specific TPCs inhibitors (three are from the LOPAC®1280 library), which blocked NAADP-evoked Ca^{2+} release without affecting the endo/lysosomal pH and acidic Ca^{2+} store (Gunaratne *et al.* 2018a). From their list, PDMP (LogP = 5.24, pKa^{base} = 6.66) inhibited E-S-FLU with IC_{50} = 33.7 μM, whereas A-315456 (LogP = 2.33, pKa^{base} = 6.54) and LY-310,762 (LogP = 4.02, pKa^{base} = 7.24) were non-inhibitors. We will test all these seven TPCs specific inhibitors, especially the ones that are non-CADs, in both WT and *TPCN1/2*KO cells to examine the effect of calcium channel blocking and EBOV entry inhibition. We will control these measurements by confirming TPCs inhibition efficacy in the sea urchin egg homogenate assay (Galione *et al.* 2014).

How are the CADs inhibiting EBOV? As we discussed at the end of Chapter 4 and 5, it remains unclear. Using a genetic knockout technique, we ruled out the participation of acid sphingomyelinase (ASM) (Chapter 5) and in this chapter, the TPCs. We learned the lesson that although drugs that inhibited EBOV may share a common pharmacological feature, the known drug target is perhaps not required for EBOV entry. As a result, more careful investigation is needed before mining calcium channel blockers as potential EBOV entry inhibitor treatment as suggested by others (Fan *et al.* 2017; Penny *et al.* 2018), especially if the calcium channel blocking activity turns out to be a “side-effect”. Many L-type calcium channel blockers have prominent cardiac actions (Fermini *et al.* 2017), and some

have the risk of causing long-QT syndromes, which may lead to sudden cardiac death (e.g. verapamil and amiodarone). EBOV infected patients suffering from haemorrhagic fever have unbalanced body fluid electrolytes, and they may be more prone to the cardiac side-effects (Turone 2014; Gupta-Wright, Lavers and Irvine 2015).

Our conclusion from the work described in this and earlier chapters is that for small molecules the physicochemical property of high LogP and pKa^{base} has strongest correlation with specific inhibition of E-S-FLU infection. It could be argued that drugs with high LogP and pKa^{base}, which concentrate in the lysosome, might require this concentrating effect to work efficiently on target molecules such as TPCs that are present in the lysosomal membrane. Further work on a range of known TPC inhibitors with varying LogP and pKa^{base}, controlled by measurements of TPCs mediated Ca^{2+} release in the mammalian cells we are studying, may shed light on this issue.

Taking our data at face value, the known molecular targets of the drugs appear to be coincidental to their inhibitor effect on EBOV-GP mediated infection. Cationic amphiphilic molecules accumulate in the lysosome, insert their hydrophobic tail in the membrane and dispose positive charges locally on the luminal side of the lysosome by concentrating their protonated secondary or tertiary amine groups (De Duve *et al.* 1974; Kaufmann and Krise 2007; Kornhuber *et al.* 2010b). It is well-described that this activity can interfere with the functions of several molecules in the membrane of the lysosome including NPC1, ASM, TPCs and affect membrane permeability (Kornhuber *et al.* 2010a; Shoemaker *et al.* 2013).

However, we have shown that none of these effects can explain the inhibition of EBOV-GP dependent viral entry.

There remain two ways CADs could inhibit EBOV entry. First, we suggest that the presence of the CADs in the lysosomal membrane may directly inhibit the fusion sequence initiated by binding of cathepsin-cleaved GP to NPC1. Fusion induced by EBOV-GP is not well-studied but as with similar fusion proteins the GP must release a hydrophobic region that inserts into the lysosomal membrane, followed by conformational changes that bring the viral and lysosomal membranes together until they fuse (Malashkevich *et al.* 1999; Gregory *et al.* 2014; White and Whittaker 2016; Lee *et al.* 2017). It seems reasonable to suggest that this sequence could be interrupted by the presence of high concentrations of positively charged CADs in the lysosomal membrane.

A second possibility has come to light recently with the observation that some inhibitors can bind into a pocket in the membrane distal head of the GP, and destabilise the molecule as detected *in vitro* by reduced melting temperatures (Zhao *et al.* 2016, 2018; Ren *et al.* 2018; Shaikh *et al.* 2019). We will investigate this possibility in the following final data chapter (Chapter 7).

(BLANK PAGE)

Chapter 7 Drugs that bind EBOV-GP

7.1 Introduction

There is currently no approved treatment for EBOV infection. However, as we and others have shown, many FDA approved drugs from various pharmacological groups inhibited EBOV infection *in vitro*, although the mechanisms remain unknown (Kouznetsova *et al.* 2014; Johansen *et al.* 2015; Xiao *et al.* 2018). One simple answer could be that there is a common target on which all of these drugs are acting in a manner independent of their primary activities. In the last two chapters, we were seeking “the target” in the host, but the progress so far has been frustrating.

We showed that many EBOV inhibitors share a cationic amphiphilic feature but had not identified a specific host protein factor that the drugs were acting through. Previously, it had been suggested that these drugs were acting on the lysosomal calcium channels known as the two-pore channels 1 and 2 (TPC1/2) (Sakurai *et al.* 2015; Simmons *et al.* 2016; Penny *et al.* 2018), or on acid sphingomyelinase (ASM) (Miller *et al.* 2012b; Fan *et al.* 2017). We specifically knocked out TPC1/2 and ASM expression in HeLa cells, but did not see any reduction in pseudotyped EBOV infection. We therefore concluded that while these drugs may have inhibited the TPC1/2 or ASM, this action was not responsible for the inhibition of EBOV entry into cells *in vitro*.

In this chapter, we are turning our interest to the virus itself. EBOV-GP is the only protein expressed at the EBOV surface (Lee and Saphire 2009). It is essential for

cell attachment, receptor binding and fusion during virus entry. EBOV-GP functions as a trimer, and each monomer consists of GP1 and GP2 subunits (Figure 7.1 A). The glycan cap (the most membrane distal part of the GP), receptor binding region and the mucin-like domain are encoded by GP1 (Lee *et al.* 2008; Zhao *et al.* 2016). The N-terminus of GP1 is connected to GP2 by a disulphide bond, and together they form the base of the protein. The GP2 subunit also contains the fusion loop, the transmembrane region and a short cytoplasmic tail. The GP2 subunit undergoes a major conformational change and rearrangement during the fusion step, inserting the fusion loop into the lysosomal membrane, and bringing the viral membrane and the lysosomal membranes together (Weissenhorn *et al.* 1998; Gregory *et al.* 2011; Lee *et al.* 2017).

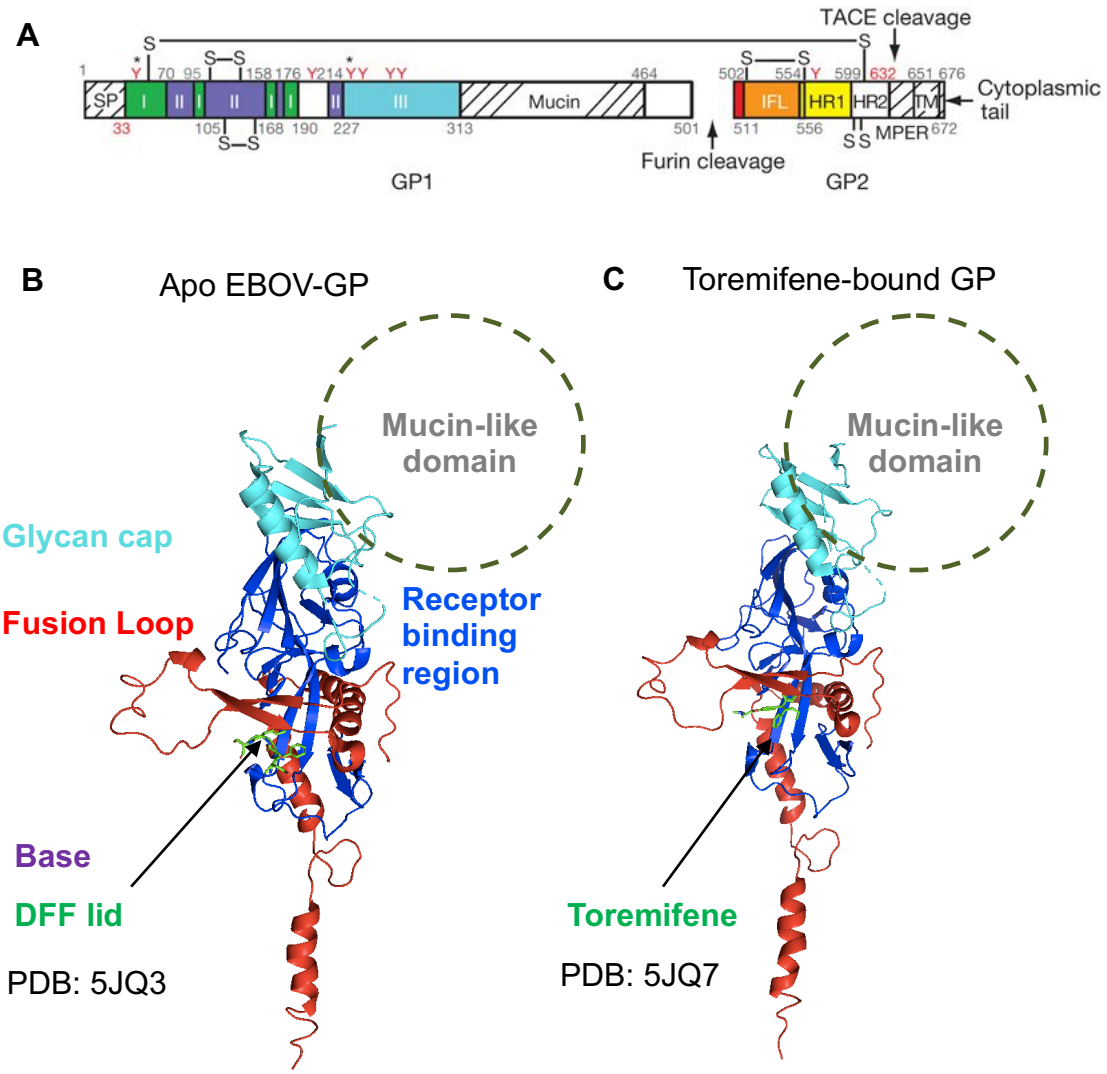


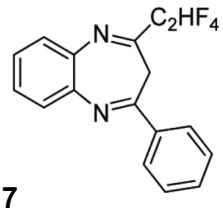
Figure 7. 1 EBOV-GP structure and the drug binding pocket
A: Figure was taken from Lee *et al.* 2008. Schematic diagram for EBOV-GP domains. SP, signal peptide; S-S: disulphide bond; I, GP1 base; II, GP1 head; III, GP1 glycan cap; mucin, mucin-like domain (MLD); IFL: internal fusion loop; HR: heptad repeat; MPER: membrane-proximal external region; TM: transmembrane domain; red Y: predicted N-linked glycosylation sites. **B**: Crystal structure of apo form of EBOV-GP(1,2) monomer in cartoon representation (PDB file: 5JQ3). **C**: Crystal structure of toremifene bound EBOV-GP (PDB file: 5JQ7).

Basu *et al.* formerly predicted that drugs can directly bind to EBOV-GP (Basu *et al.* 2011). They showed that benzodiazepine derivatives (Figure 7.2 compound 7 and 12) inhibited EBOV-GP pseudotyped lentivirus infection when added before or during the virus adsorption step, but were not effective if added 1 hour post virus entry. With computational modelling on the GP structure, they suggested a

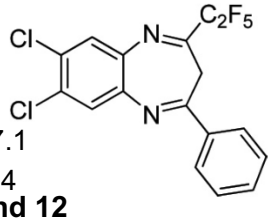
potential hydrophobic drug binding site clamped between the GP1 base subdomain and the GP2 fusion loop, and they verified it with site-directed mutagenesis experiments. Pseudotyped virus expressing GP with mutations introduced to the putative drug binding pocket was no longer inhibited by compound 7, suggesting direct interaction between the drug and the amino acids at this region (Basu *et al.* 2011).

Recent studies from David Stuart's group confirmed that several drugs can bind directly to EBOV-GP by X-ray crystallography (Zhao *et al.* 2016, 2018; Ren *et al.* 2018; Shaikh *et al.* 2019). They identified the same hydrophobic cavity as previously modelled by Basu *et al.*, with a volume of ~1000 $Å^3$ at the interface between the GP1 and GP2 subunits (Figure 7.1 B). So far, 11 crystal structures with drugs bound to EBOV-GP have been published (drug structures summarised in Figure 7.2). Seven structures had one drug molecule bound per GP monomer, and four molecules bound with a stoichiometry of two per monomer (imipramine, benztropine, 118 and 118a) (Ren *et al.* 2018; Zhao *et al.* 2018; Shaikh *et al.* 2019).

Basu *et al.* 2011

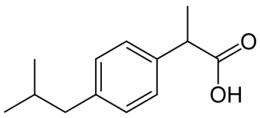


LogP : 5.5
pKa^{base}: 0.9
Compound 7

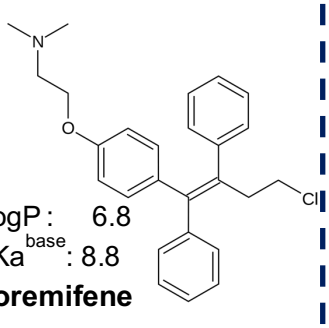


LogP : 7.1
pKa^{base}: 0.4
Compound 12

Zhao *et al.* 2016

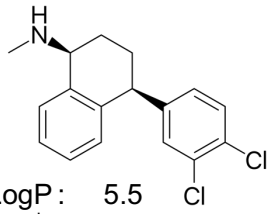


LogP : 4.0
pKa^{base}: NA (acidic)
Ibuprofen

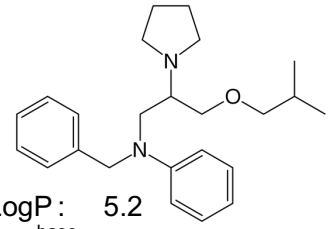


LogP : 6.8
pKa^{base}: 8.8
Toremifene

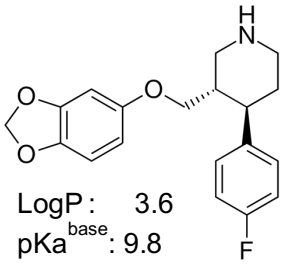
Ren *et al.* 2018



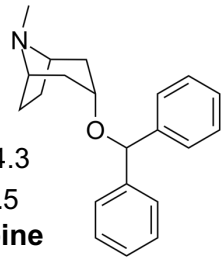
LogP : 5.5
pKa^{base}: 9.9
Sertraline



LogP : 5.2
pKa^{base}: 9.2
Bepridil

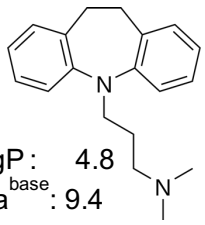


LogP : 3.6
pKa^{base}: 9.8
Paroxetine

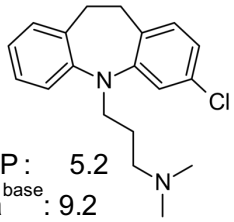


LogP : 4.3
pKa^{base}: 9.5
Benztropine

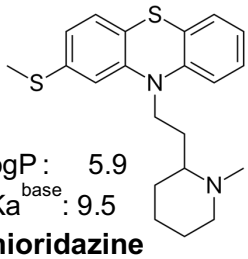
Zhao *et al.* 2018



LogP : 4.8
pKa^{base}: 9.4
Imipramine

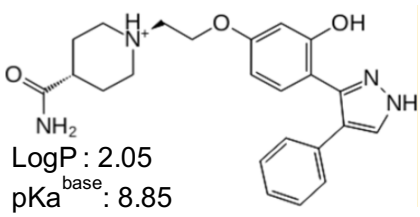


LogP : 5.2
pKa^{base}: 9.2
Clomipramine

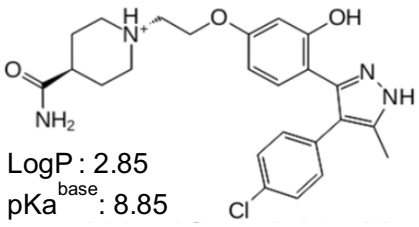


LogP : 5.9
pKa^{base}: 9.5
Thioridazine

Shaikh *et al*. 2019



LogP : 2.05
pKa^{base}: 8.85
Compound 118



LogP : 2.85
pKa^{base}: 8.85
Compound 118a

Figure 7. 2 Drugs that bind EBOV-GP
Thirteen compounds have been reported to bind directly to EBOV-GP, eleven were determined by X-ray crystallography and two were based on EBOV-GP mutagenesis and computational modelling (Basu *et al.* 2011). The partition coefficient LogP and acid/base pKa are displayed next to the corresponding compounds.

Of the eleven molecules with crystal structures, ten are also cationic amphiphilic drugs (high LogP, high pKa^{base}). The hydrophobic side of the drugs sits nicely in the GP pocket surrounded by non-polar protein side chains. The cationic tertiary amine end is either sticking out towards the solvent, or is accommodated at the mouth of the pocket where negatively charged amino acids D522 and E100 are available to interact with the partially protonated amine. In some drug-bound GP structures, the amine exploits the spacious cavity without apparently interacting with the protein. Therefore, the amine group common to the cationic amphiphiles does not seem to be playing any particular role in binding the GP pocket, whereas it may play a key role in promoting concentration of these molecules in the lysosome (De Duve *et al.* 1974; Kornhuber *et al.* 2011; Logan *et al.* 2014). The protein residues with proximity to the drug binding site are highly conserved across all five *ebolavirus* species (Zhao *et al.* 2016).

How do GP-binding drugs inhibit virus entry? We don't know. Stuart's group followed up their crystal structure observations with a thermal shift assay, where they showed that incubation of purified EBOV-GP with these drugs resulted in destabilisation of the uncleaved GP as measured by a reduced melting temperature at low pH. The biggest shift seen was with toremifene, which reduced GP melting temperature by up to 14 ^{o}C at pH 5.2, and toremifene was the most potent CAD (cationic amphiphilic drug) that inhibited E-S-FLU in our drug screen

(Zhao *et al.* 2016; Xiao *et al.* 2018). The low pH mimics the acidic environment of the lysosome, where EBOV-GP is cleaved by cathepsin B and L (Chandran *et al.* 2005; Schornberg *et al.* 2006) to expose the receptor binding region (Côté *et al.* 2011; Miller *et al.* 2012a; Wang *et al.* 2016).

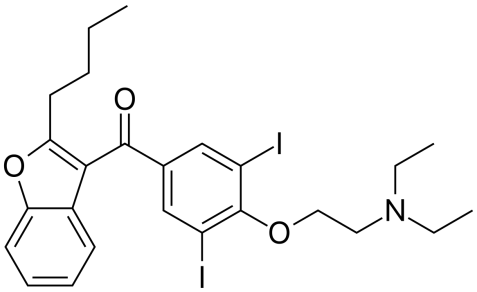
In the unbound GP structure, the drug binding pocket is occupied by a short loop from GP1 with amino acids D192, F193, F194, referred as the "DFF" lid (representing the single letter code for these three amino acids). The DFF lid is near the predicted cathepsin cleavage site close to the glycan cap (Dube *et al.* 2009; Hood *et al.* 2010). Stuart *et al.* speculated that drug binding to GP affects the local conformation and hence prevents correct GP cleavage from taking place, which subsequently affects the receptor binding region on GP or its capacity to fuse. We have tested that idea in this chapter.

After our LOPAC®1280 screen, we came across the toremifene-bound EBOV-GP structure in the literature (Zhao *et al.* 2016), and initiated a collaboration with David Stuart's group to test some of the drugs which inhibited EBOV entry in our assay. From the drugs we tested in collaboration, imipramine bound to the EBOV-GP crystal and also destabilised GP in the thermal shift assay (melting temperature reduced by 3 ^{o}C, Kd = 584 μM). This part of the study has been published recently in Zhao *et al.* 2018. In addition, arbidol (Figure 7.3), a fusion inhibitor of Influenza haemagglutinin (Leneva *et al.* 2009) also destabilised GP in the thermal shift assay (data not shown, personal communication with Stuart's group). It is not clear what biological significance these very small changes in stability might have.

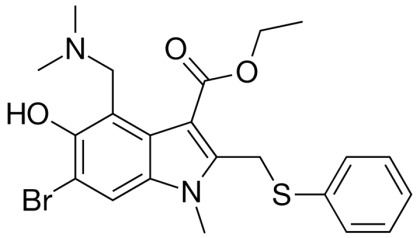
In the first part of this chapter, I summarise the work done in collaboration with Stuart's group. Next, to try and link the GP-binding feature of drugs to their virus inhibitory effect, we introduced mutations to EBOV-GP at the drug binding pocket based on the structural data, and produced pseudotyped viruses containing the mutations. Finally, we selected EBOV mutants resistant to inhibition by toremifene and arbidol in collaboration with Peter Halfmann's group (University of Wisconsin). Most of the work mentioned in this chapter is still ongoing. We will present the preliminary data we have at this point and discuss our current understanding of the relevance of GP binding for the inhibition of EBOV infection.

7.2 EBOV-GP binding drugs

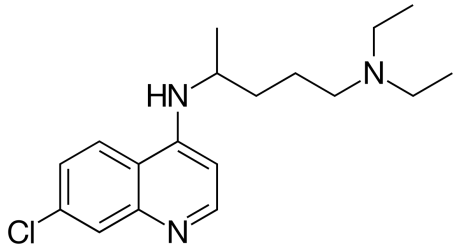
In collaboration with David Stuart's group, we tested four drugs for their ability to bind to EBOV-GP: amiodarone, arbidol, chloroquine and imipramine (Figure 7.3). All four drugs are cationic amphiphiles (high LogP, high pKa^{base}) that inhibited E-S-FLU in our assay and have also been reported as EBOV inhibitors by other groups in the literature (Gehring *et al.* 2014; Herbert *et al.* 2015; Johansen *et al.* 2015; Madrid *et al.* 2015; Pécheur *et al.* 2016; Xiao *et al.* 2018). The crystallography and thermal shift assay experiments were done by Dr Jingshan Ren and Dr Yuguang Zhao from the Stuart group. Crystallised EBOV-GP from the *Zaire ebolavirus* (1976 Mayinga strain) was soaked in a high concentration of drug (10 mM in DMSO) and immediately fished out, snap-frozen in liquid nitrogen and sent for diffraction.



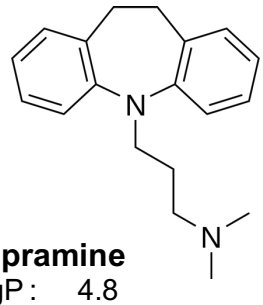
Amiodarone
LogP : 7.6
pKa^{base}: 8.5
E-S-FLU IC_{50} = 2.04 μM



Arbidol
LogP : 3.8
pKa^{base}: 9.9
E-S-FLU IC_{50} = 5.17 μM



Chloroquine
LogP : 4.6
pKa^{base}: 10.1
E-S-FLU IC_{50} = 5.44 μM



Imipramine
LogP : 4.8
pKa^{base}: 9.4
E-S-FLU IC_{50} = 3.82 μM

Figure 7. 3 Drugs tested in GP crystal soaking assay
Four drugs were tested in collaboration with the Stuart group for their ability to bind to EBOV-GP by crystal soaking assay. Their chemical structures, LogP and pKa^{base} values and the IC_{50} concentration of the drugs inhibited E-S-FLU *in vitro* are shown in the diagram.

Two imipramine molecules bound to GP in the same pocket as toremifene had bound (annotated as imipramine A and B in Figure 7.4). The hydrophobic side of imipramine A was buried deeper in the pocket, surrounded by amino acids L186, M548, L558, I38 and I43, and the polar dimethyl-propanamine group was pointing to the solvent. Imipramine B sat closer to the mouth of the tunnel. One of B's benzene rings was stacking with the side chain of Y517 as well as interacting with residue A101 and M548, and the dimethyl-propanamine end was also protruding out to the solvent.

By contrast, although the amiodarone and chloroquine soaked crystals diffracted well, the resulting GP structure remained in the unbound state. This result established that typical CADs that fail to bind in the defined pocket in EBOV-GP, can still inhibit E-S-FLU entry, with IC_{50} in the micromolar range.

We have not yet tested arbidol in this GP crystal soaking experiment. Both imipramine (ΔTm = 2 ºC, Kd 584 μM) and arbidol slightly reduced EBOV-GP melting temperature in the thermal shift assay (personal communication with Ren Jinshan, Stuart's group).

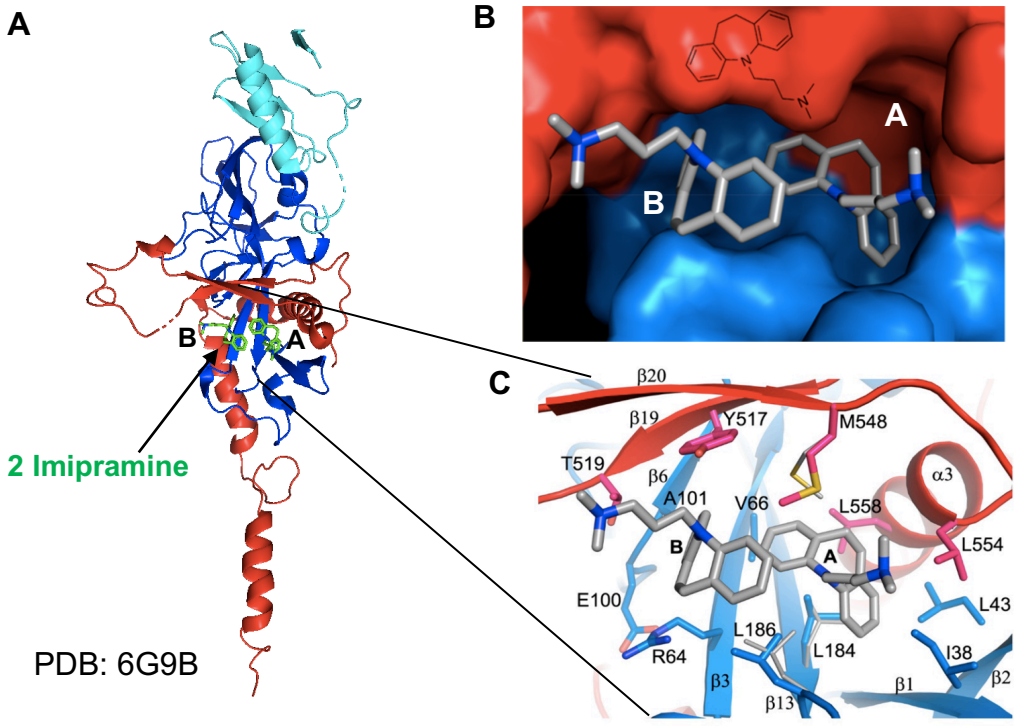


Figure 7. 4 Imipramine-bound EBOV-GP structure
The monomeric structure of EBOV-GP in cartoon representation, with two imipramine molecules (A and B) bound in the hydrophobic drug binding pocket. Structure was published by Zhao *et al.* 2018, PDB file 6G9B. GP1 is coloured blue, GP2 is coloured red, and the glycan cap is coloured cyan. The close-up view of two imipramine molecules in the drug binding pocket shown in a surface representation (**B**) and a cartoon representation (**C**). Amino acid residues in close contact with the bound imipramine molecules are labelled in (**C**).

Nine out of 11 reported EBOV-GP binding molecules have been tested in our pseudotyped virus inhibition assay (toremifene, ibuprofen, imipramine, clomipramine, thioridazine, bepridil, benztropine, sertraline, paroxetine), and all except ibuprofen inhibited E-S-FLU infection. Ibuprofen does not have a CAD structure.

We further tested two recently published GP-binding molecules 118 and 118a in the virus inhibition assay (Shaikh *et al.* 2019). Both compound 118 and 118a inhibited E-S-FLU infection. Despite the similarity in structure, compound 118a (IC_{50} = 0.11 μM) was about 300-fold more potent than compound 118 (IC_{50} = 36.5 μM) (Figure 7.5). This confirmed the results of Shaikh *et al.* on the inhibition of a EBOV-GP pseudotyped lentivirus.

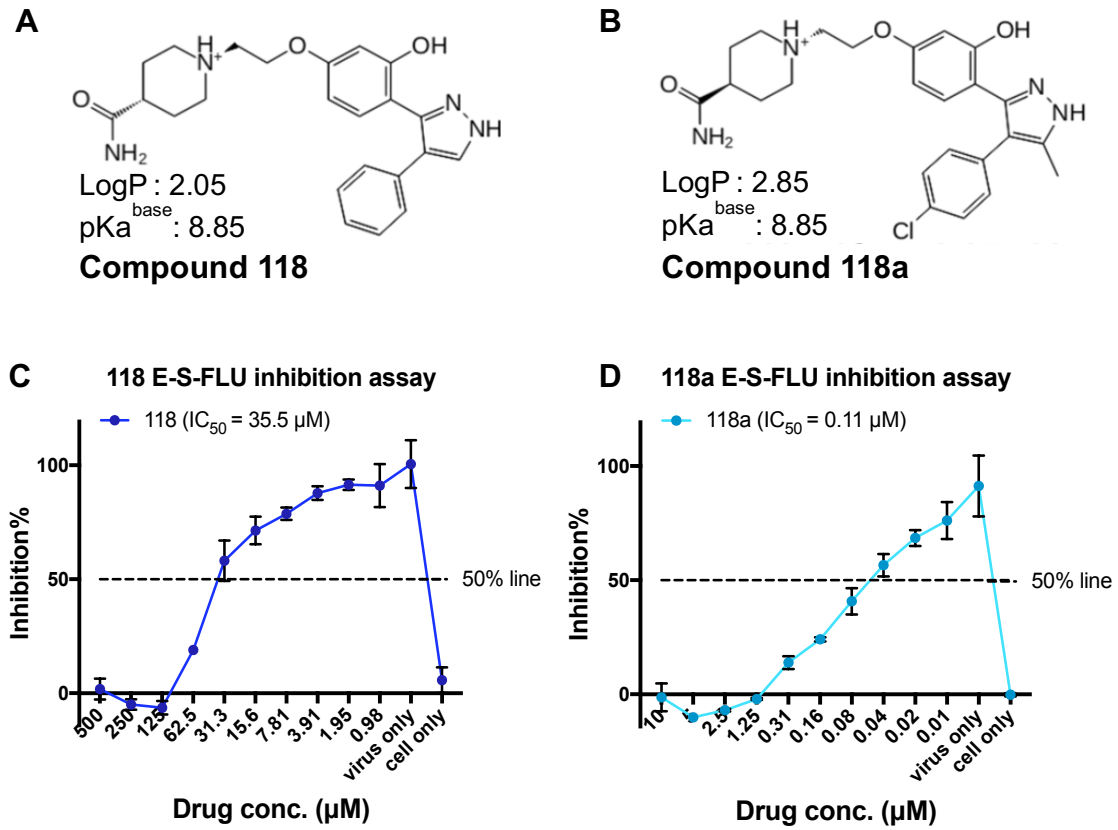


Figure 7. 5 Compound 118 and 118a virus inhibition assay

Compound 118 and 118a are recently published EBOV-GP crystal binding compounds (Shaikh *et al.* 2019). **A**, **B**: Chemical structures of 118 and 118a. The LogP and pKa^{base} values of the two compounds were calculated by Chemicalize.com based on their chemical structures. **C**, **D**: Representative titration curves of compound 118 and 118a in E-S-FLU inhibition assay, with the error bars representing the standard error of the mean from technical duplicates. Indicator MDCK-SIAT1 cells were pre-incubated with 118 or 118a for 3 hours and infected with E-S-FLU for 24 hours. Virus infection was quantified by measuring eGFP expression with a fluorescence plate reader CLARIOstar®. 50% of maximum fluorescence (50% line) was marked out by a broken line. IC_{50} is the drug concentration at which 50% of the virus infection was inhibited, and it was calculated by linear interpolation.

7.3 Drug inhibition of thermolysin treated E-S-FLU

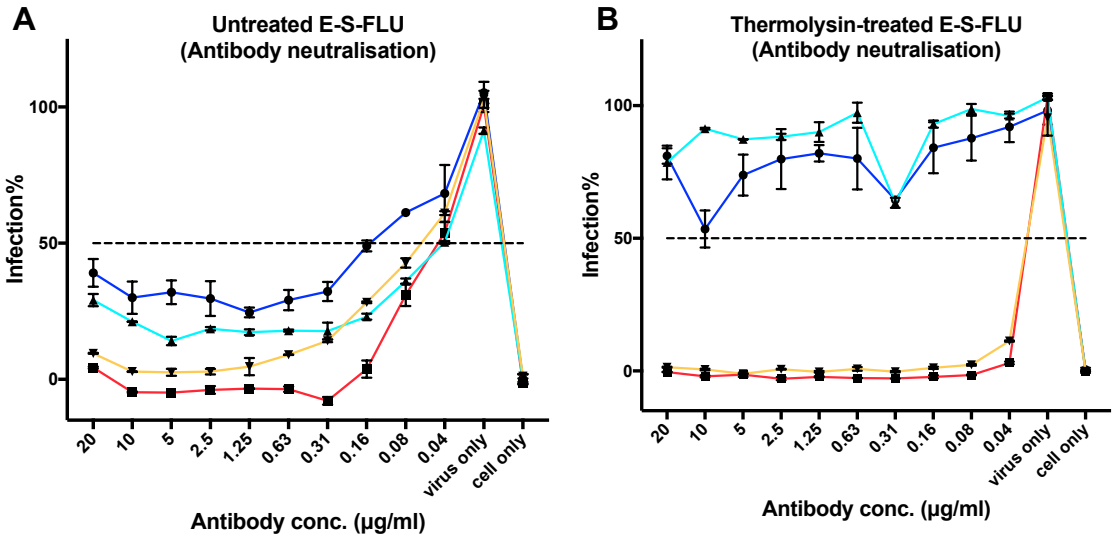
One hypothesis based on the structural studies is that drug binding to GP affects the local conformation of the DFF lid, which subsequently inhibited cathepsin processing of the protein (Zhao *et al.* 2016). The bacterial protease thermolysin has been shown to mimic cathepsin cleavage of EBOV-GP, removing the mucin-like domain and the glycan cap (Chandran *et al.* 2005; Hashiguchi *et al.* 2015;

Wang *et al.* 2016). To determine whether GP-binding drugs are acting before or after the cathepsin cleavage step, we digested E-S-FLU with thermolysin and tested it in antibody neutralisation and drug inhibition assays. To show that thermolysin treatment successfully removed the glycan cap epitope, we titrated four monoclonal antibodies that recognise different epitopes of EBOV-GP (Figure 7.6; Table 7.1) including the glycan cap that should be removed by thermolysin.

Table 7. 1 Monoclonal antibodies used in this chapter

mAb	Target protein	Epitope	Reference
KZ52	EBOV-GP	Base	Lee *et al.* 2008
100	EBOV-GP	Base	Misasi *et al.* 2016
66-6-3	EBOV-GP	Base	Rijal *et al.* 2019
P6	EBOV-GP	Glycan cap	Rijal *et al.* 2019
125	EBOV-GP	Glycan cap	Rijal *et al.* 2019
66-4-A8	EBOV-GP	Mucin-like domain	Rijal *et al.* 2019
114	EBOV-GP	Receptor binding region	Misasi *et al.* 2016
C13C6	EBOV-GP	Receptor binding region	Murin *et al.* 2014
MR78	Marburg GP	Receptor binding region	Hashiguchi *et al.* 2015
21D85A	Haemagglutinin	Head	Not published
Z2B3	Neuraminidase	Active site	Not published

All four antibodies neutralised the untreated E-S-FLU. After thermolysin treatment, the glycan cap antibodies (P6, 125) no longer neutralised the digested E-S-FLU, whereas antibodies that bind the receptor binding region (114) and GP base (66-6-3) neutralised the post-treated E-S-FLU better than the untreated virus.



C

	Untreated E-S-FLU	Post-treated E-S-FLU
66-6-3 (Base)	IC_{50} : 44 ng/ml	IC_{50} : <40 ng/ml
114 (receptor binding region)	IC_{50} : 60 ng/ml	IC_{50} : <40 ng/ml
P6 (Glycan cap)	IC_{50} : 149 ng/ml	IC_{50} : NA
125 (Glycan cap)	IC_{50} : 40 ng/ml	IC_{50} : NA
50% line		

Figure 7. 6 Antibody neutralisation assay of thermolysin treated E-S-FLU
E-S-FLU was treated with thermolysin protease to remove mucin-like domain and the glycan cap from the GP1 subunit. Untreated E-S-FLU control (**A**) and thermolysin-treated E-S-FLU (**B**) were incubated with monoclonal antibodies for 2 hours and then added to infect indicator MDCK-SIAT1 cells for 24 hours. Infection was quantified by measuring the eGFP fluorescence by a fluorescence plate reader CLARIOstar®, and normalised to infection% in relation to the fluorescence measured from wells in which cells were infected without drug treatment. Error bars represent the standard error of the mean of technical duplicates of titration. 50% infection is marked by a broken line. **C**: Summary of antibody IC_{50} values in the neutralisation assay. IC_{50} was the antibody concentration at which infection of E-S-FLU was reduced to 50%, and was calculated by linear interpolation.

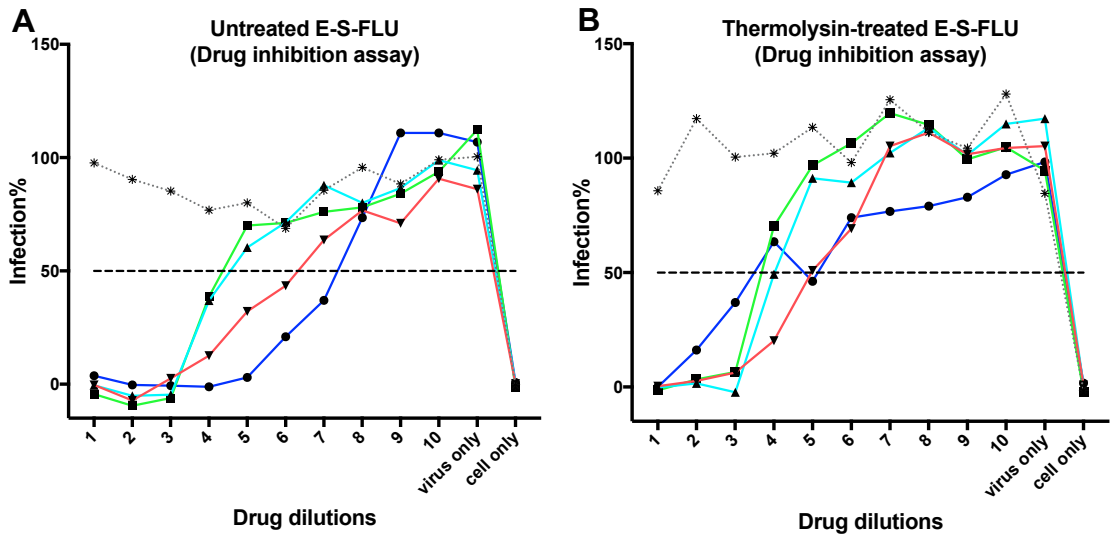
We then titrated four drugs for inhibition of the same batch of untreated and thermolysin treated E-S-FLU (Figure 7.7). In addition to the EBOV-GP binding drug toremifene, we included EIPA (5-(N-Ethyl-N-isopropyl) amiloride) a macropinocytosis inhibitor that blocks the initial entry of EBOV at the plasma membrane (Nanbo *et al.* 2010; Mulherkar *et al.* 2011) and E64 a broad-spectrum cysteine proteases inhibitor (Chandran *et al.* 2005; Kaletsky, Simmons and Bates

2007; Wang *et al.* 2016). MDL28170 is a calpain inhibitor that also inhibits cathepsin B and L (Mehdi 1991; Simmons *et al.* 2005; Gnirß *et al.* 2012). An antibody to Influenza HA, 21D85A was tested in parallel as a negative control.

All four drugs inhibited both untreated and treated E-S-FLU, with the IC_{50} value slightly higher for the thermolysin-treated E-S-FLU. MDL28170 had the biggest increase in IC_{50} (untreated: 1.22 µM, treated 17.8 µM), suggesting that the cleaved E-S-FLU was less dependent on cathepsin activity. However, the cleaved E-S-FLU was still inhibited by MDL28170 and E64. This agrees with the current literature, which suggests that there may be further trigger factors for EBOV entry that require protease activities in addition to removal of the GP glycan cap by cathepsins (Schornberg *et al.* 2006; Wong *et al.* 2010; Spence *et al.* 2016). Toremifene remained a potent inhibitor of thermolysin treated E-S-FLU (IC_{50} = 0.64 µM). This implies that its main target is conserved after cathepsin has cleaved the GP. This experiment was done only once, and further repeats are needed to determine statistical significance.

These and earlier experiments with CADs can be summarised by stating that 1) Not all CAD-like EBOV entry inhibitors can be shown to bind the defined pocket in the EBOV-GP. 2) Inhibitors that do bind may have minimal effects on melting temperature. 3) Ten of the eleven binders identified by crystallography are also CADs. 4) The two most powerful E-S-FLU inhibitors we studied, toremifene and compound 118a (IC_{50} ~ 100 nM), are EBOV-GP binders. 5) Minor changes in the structure of compound 118 by the introduction of a chlorine and a methyl group to form 118a enhanced the inhibitory activity for E-S-FLU by at least 100-fold. 6)

Toremifene is able to act on GP after removal by protease digestion of the glycan cap and mucin-like domains.



C	Untreated E-S-FLU	Post-treated E-S-FLU
EIPA (from 100 μM)	IC_{50} : 8.49 μM	IC_{50} : 12.3 μM
E64 (from 500 μM)	IC_{50} : 48.6 μM	IC_{50} : 77.9 μM
MDL28170 (from 100 μM)	IC_{50} : 1.22 μM	IC_{50} : 17.8 μM
Toremifene (from 10 μM)	IC_{50} : 0.25 μM	IC_{50} : 0.64 μM
21D85A (-ve control, from 10 μg/ml)	IC_{50}: NA	IC_{50}: NA
50% line		

Figure 7. 7 Drug inhibition assay of thermolysin treated E-S-FLU
E-S-FLU was treated with the protease thermolysin to remove the mucin-like domain and the glycan cap from the GP1 subunit. Untreated E-S-FLU control (**A**) and thermolysin-treated E-S-FLU (**B**) were added to infect indicator MDCK-SIAT1 cells that had been pre-treated with drugs for 3 hours. After 24 hours, cells were fixed and infection was quantified by measuring the eGFP fluorescence by CLARIOstar® fluorescence plate reader, and normalised to infection% in relation to the fluorescence measured from wells in which cells were infected without drug treatment. A broken line marks the 50% infection. The experiment was performed once. **C**: Summary of drug IC_{50} values in the inhibition assay. IC_{50} is the concentration at which a drug reduced eGFP fluorescence by 50% as the result of reduced E-S-FLU entry, and was calculated by linear interpolation.

7.4 Site-directed mutagenesis of the drug binding pocket

Based on the published crystal structures of drug-bound EBOV-GP (Zhao *et al.* 2016, 2018; Ren *et al.* 2018), and consultation with Jingshan Ren from the Stuart

group, we designed 11 point mutations at 8 residues within the drug-binding pocket (Table 7.1, Figure 7.8). Most residues in the pocket have large and hydrophobic side chains (e.g. Y517, M548, L184), with a few charged residues at the mouth of the pocket (e.g. D522, R64). We mutated the residues either to reduce the size to weaken the hydrophobic interaction (e.g. L184A, L186A mutations; Figure 7.8 B); or to increase the size to introduce unfavourable steric hindrance (e.g. V66M, L184M); or to change the charge on the residues (A101E, R64A). The mutated residues are mapped to the full-length EBOV-GP sequence alignment in Figure 7.9.

Table 7. 2 Mutations introduced to EBOV-GP

No.	GP mutations	Mutated GP E-SIAT	Mutated E-S-FLU
1	R64A	GP(R64A) E-SIAT	E(R64A)-S-FLU
2	V66M	GP(V66M) E-SIAT	E(V66M)-S-FLU
3	A101E	GP(A101E) E-SIAT	E(A101E)-S-FLU
4	L184M	GP(L184A) E-SIAT	E(L184A)-S-FLU
5	L184A	GP(L184M) E-SIAT	E(L184M)-S-FLU
6	L186A	GP(L186A) E-SIAT	E(L186A)-S-FLU
7	Y517A	GP(Y517A) E-SIAT	E(Y517A)-S-FLU
8	Y517V	GP(Y517V) E-SIAT	E(Y517V)-S-FLU
9	D522A	GP(D522A) E-SIAT	E(D522A)-S-FLU
10	M548A	GP(M548A) E-SIAT	E(M548A)-S-FLU
11	M548V	GP(M548V) E-SIAT	E(M548V)-S-FLU

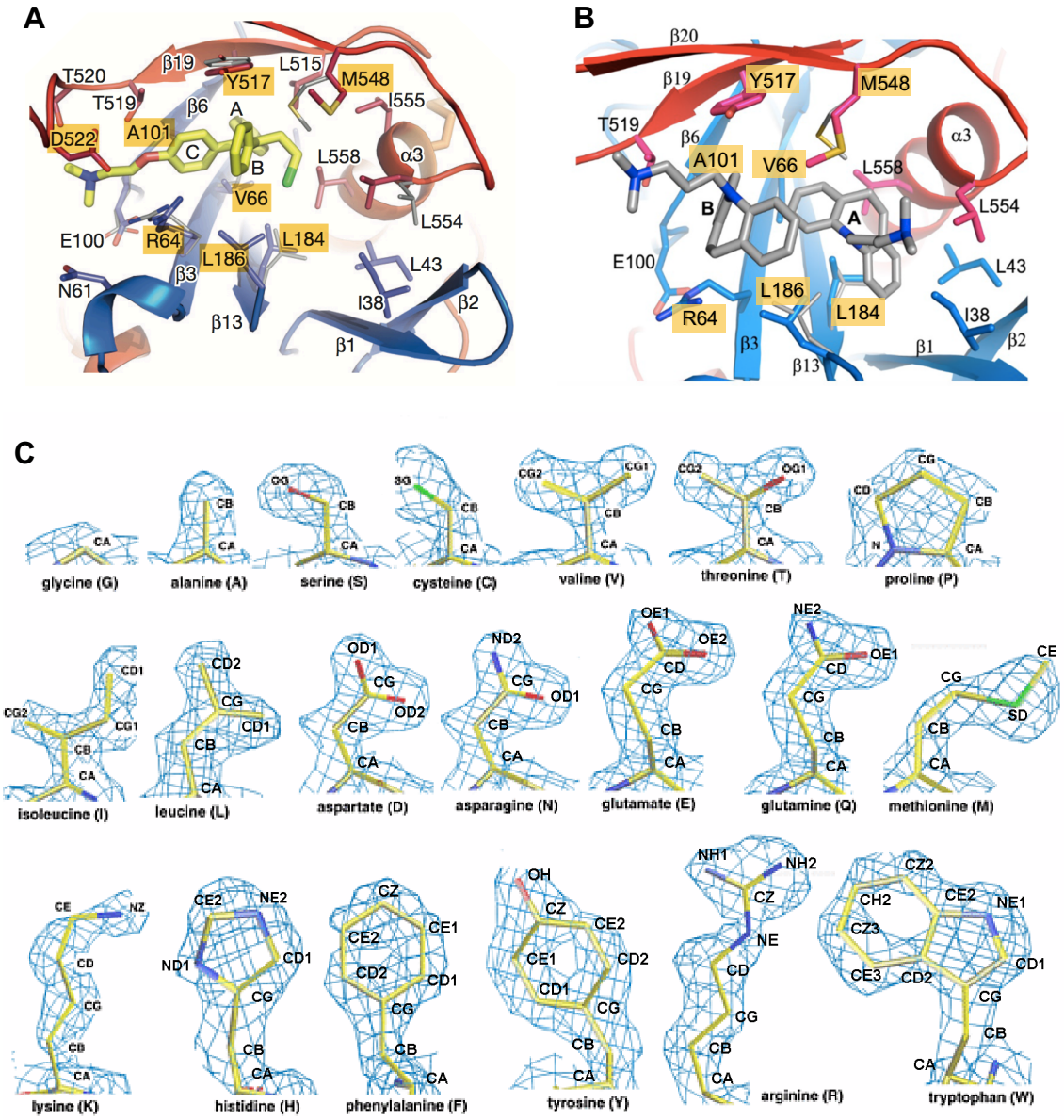
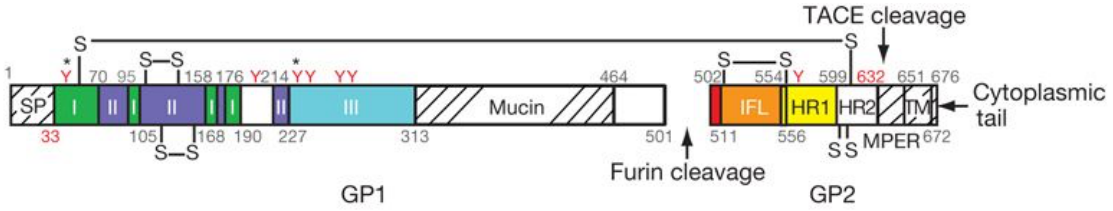
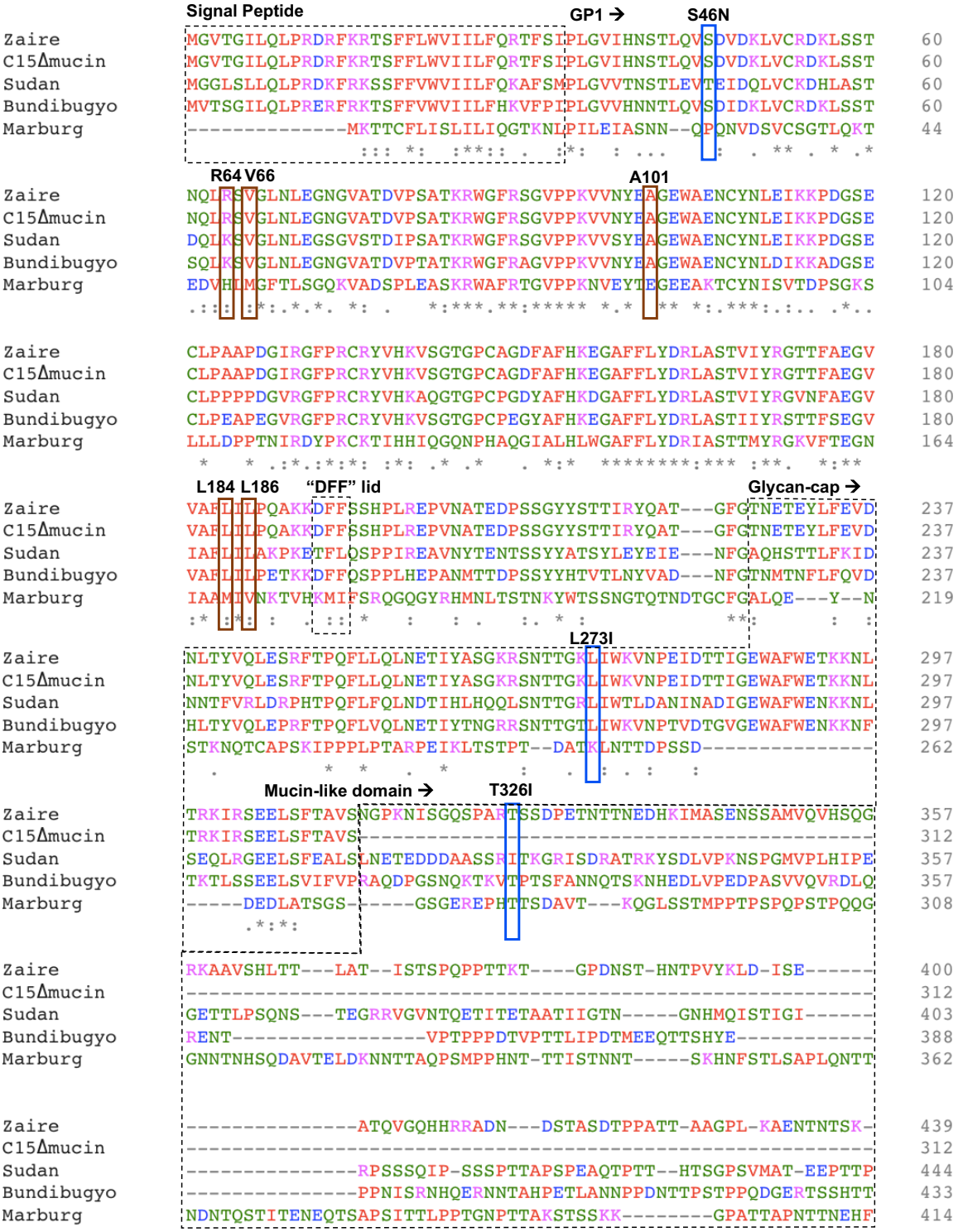


Figure 7. 8 Mutations introduced to EBOV-GP drug-binding site

We introduced mutations to eight residues in the GP drug-binding site (listed in Table 7.2). Close-up view of toremifene-bound (**A**) and imipramine-bound (**B**) GP structure in cartoon representation with mutated residues highlighted. (Figure adapted from Zhao *et al.* 2016, PDB file: 5JQ7; Zhao *et al*. 2018, PDB file: 6G9B). **C**: Amino acid side chain electron densities, arranged in order of increasing size, based on experimental electron density map calculated at 1.5 Å resolution (adapted from online resource, Molecular Biology Institute, UCLA).


TACE cleavage
SP
Mucin
IFL
HR1
HR2
TM
Cytoplasmic tail
MPER
Furin cleavage
GP1
GP2


Signal Peptide
GP1 →
S46N
R64
V66
A101
L184
L186
"DFF" lid
Glycan-cap →
L273I
Mucin-like domain →
T326I
Zaire
C15Δmucin
Sudan
Bundibugyo
Marburg

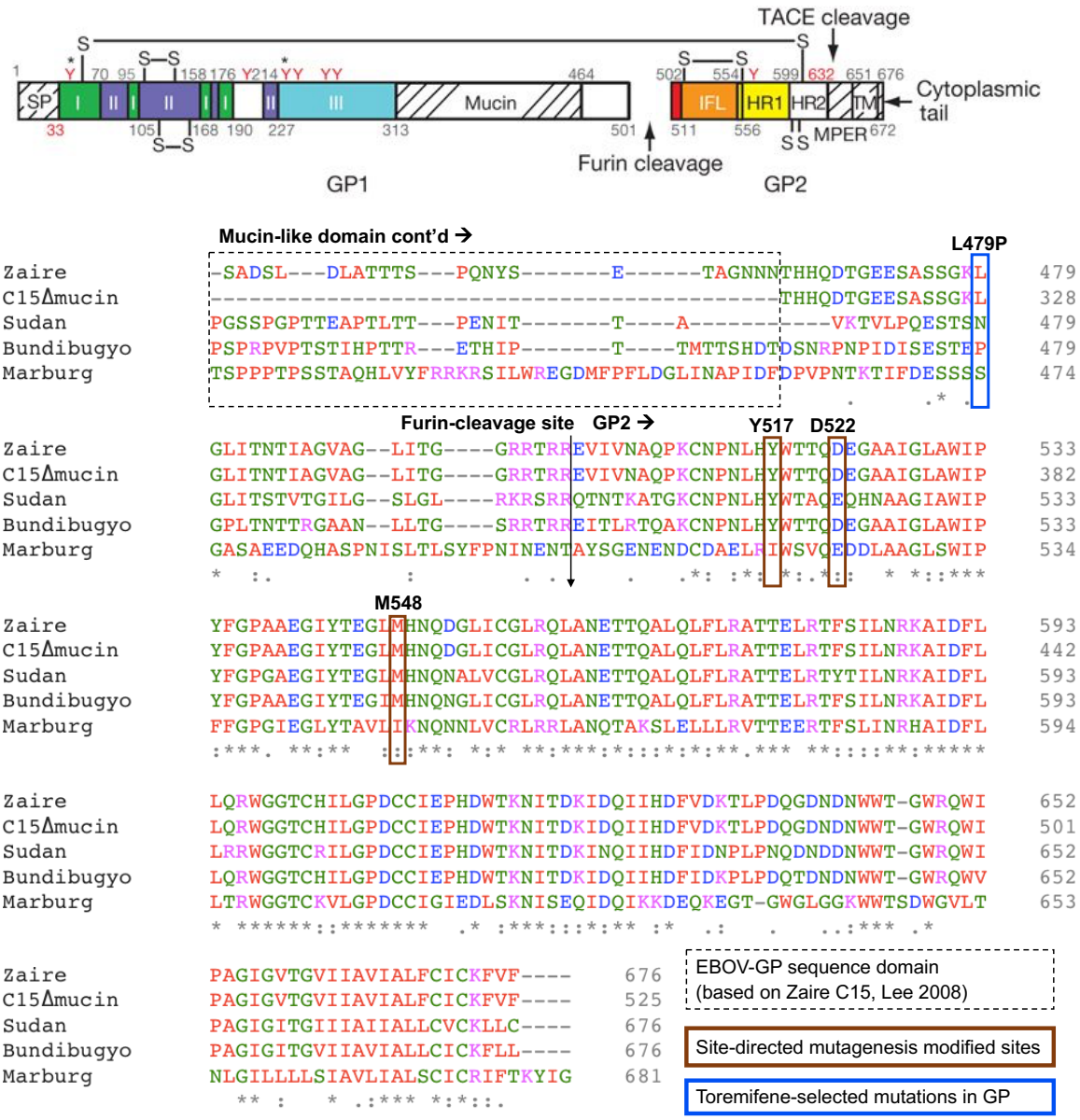


Figure 7. 9 Sequence alignment of GP from ebolavirus and marburgvirus
The alignment of amino acid sequences of glycoprotein (GP) from *Zaire* (2014 Makona C15 strain), *Sudan* and *Bundibugyo ebolavirus*, *marburgvirus*, and *Zaire* GP with mucin-like domain deleted (C15Δmucin). Domain structures are assigned based on Lee *et al.* 2008 (signal peptide region, GP1 subunit, GP2 subunit, furin-cleavage site, mucin-like domain, DFF lid). (*) denotes identical residues; (:) and (.) denote amino acids with similar function groups. Brown boxes highlight the residues that were mutated by site-directed mutagenesis in this study. The blue boxes mark the four residues that were identified in toremifene-selected escape mutants (section 7.5).

The workflow for producing mutated E-S-FLU is summarised in Figure 7.10. We introduced mutations to EBOV-GP gene cloned in *E. coli* plasmids, and lentiviral transduced the mutated GP to MDCK-SIAT1 cells to produce $E_{mutation}$-SIAT cells

(Figure 7.11). We then sorted the $E_{mutation}$-SIAT cells with GP specific antibodies P6 or KZ52 (Figure 7.12) (Lee *et al.* 2008; Rijal *et al.* 2019), and checked whether different GP epitopes were maintained on the $E_{mutation}$-SIAT cells by using different monoclonal antibodies in immunofluorescence assay (Figure 7.13). Finally, we seeded $E_{mutation}$-SIAT with S-FLU to produce $E_{mutation}$-S-FLU containing the introduced GP mutations. We detected $E_{mutation}$-S-FLU by titrating to infect indicator MDCK-SIAT1 cells, and by sandwich ELISA on the virus (Figure 7.14).

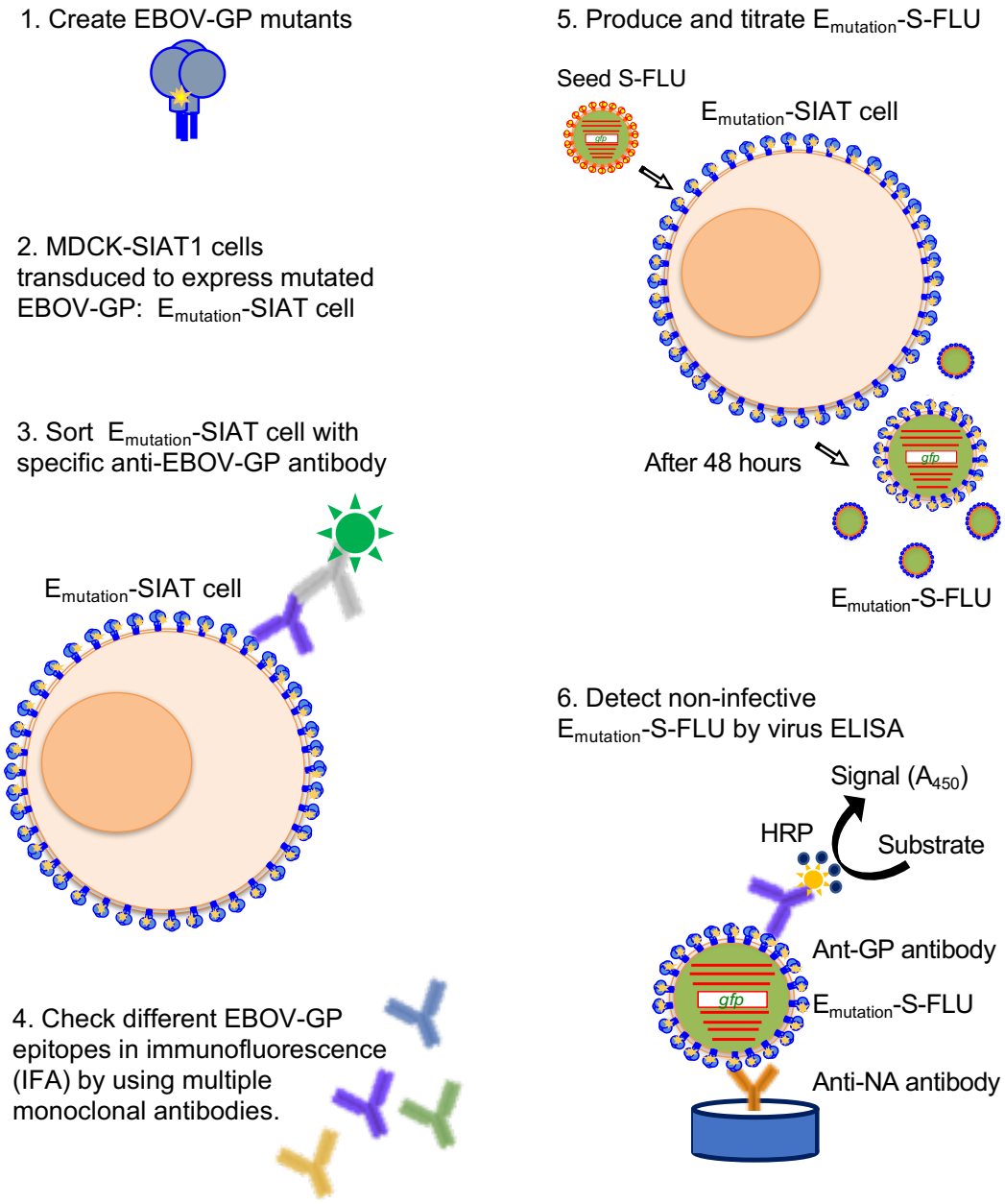


Figure 7. 10 Workflow for producing mutated GP pseudotyped E-S-FLU

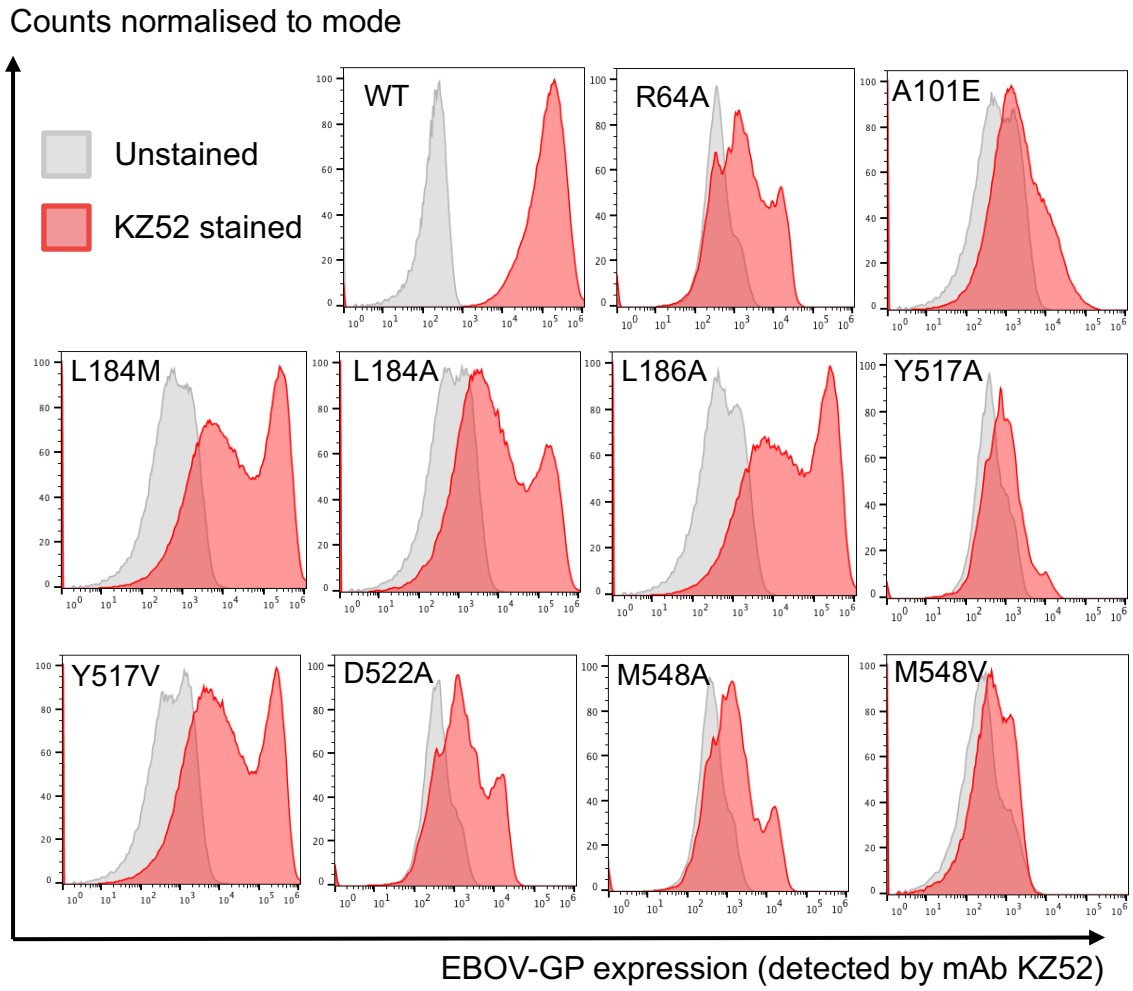


Figure 7. 11 Expression of mutated EBOV-GP on the surface of transduced MDCK-SIAT1 cells

FACS plots of sorted E-SIAT cells expressing the full-length wild-type EBOV-GP (WT), and MDCK-SIAT1 cells transduced with mutated EBOV-GP (10 mutations, V66M was not analysed in this panel) before sorting. Cells were stained with primary antibody KZ52 (anti-GP), followed by a FITC-linked anti-human secondary antibody. Unstained controls were incubated with secondary antibody only (grey).

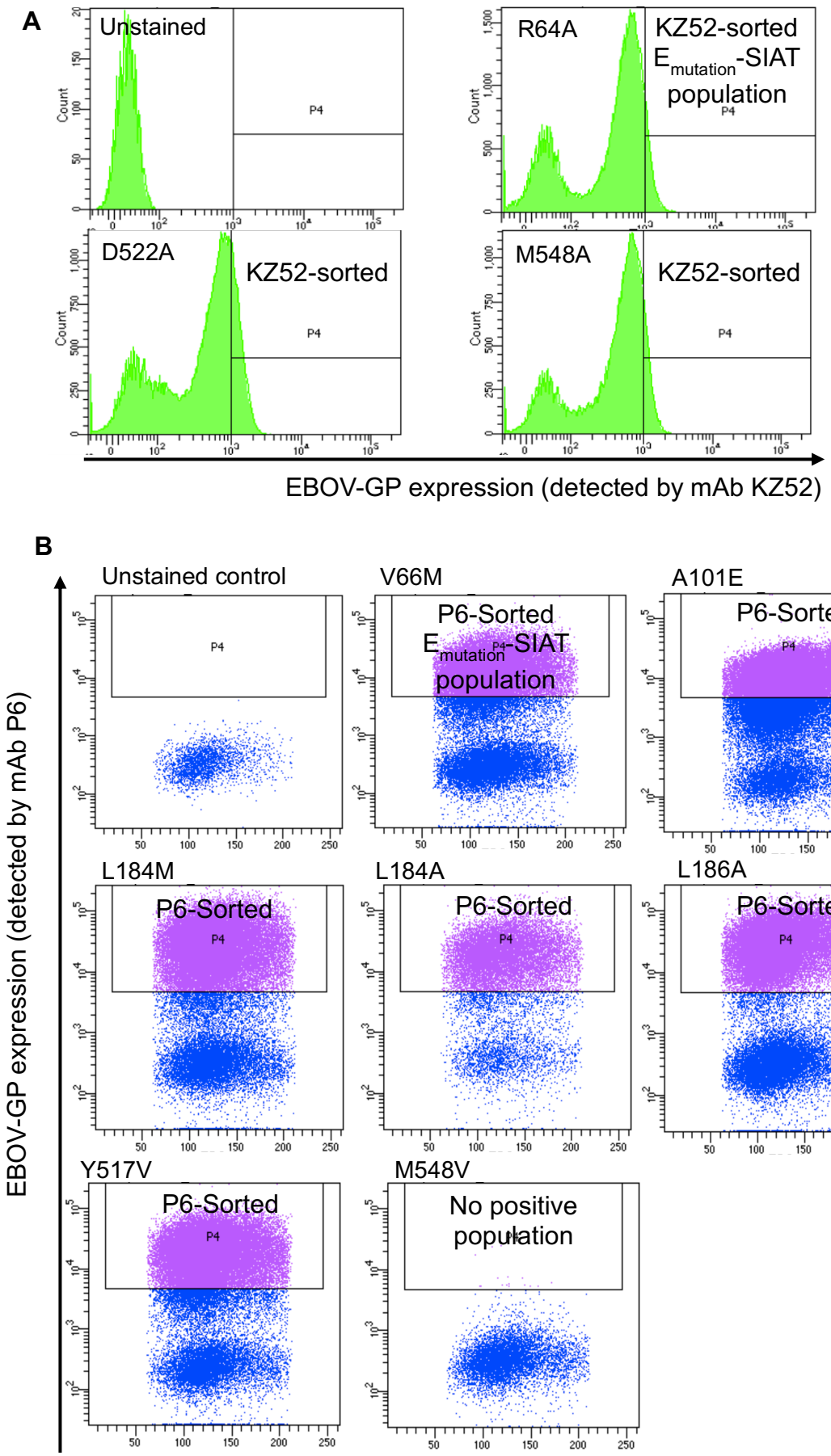

A
Unstained
P4
R64A
KZ52-sorted
E mutation -SIAT
population
D522A
KZ52-sorted
M548A
KZ52-sorted
Count
EBOV-GP expression (detected by mAb KZ52)
B
EBOV-GP expression (detected by mAb P6)
Unstained control
V66M
P6-Sorted
E mutation -SIAT
population
A101E
P6-Sorted
L184M
P6-Sorted
L184A
P6-Sorted
L186A
P6-Sorted
Y517V
P6-Sorted
M548V
No positive
population

Figure 7. 12 FACS sorting of cells with high level expression of GP
Transduced MDCK-SIAT1 cells expressing mutated EBOV-GP were analysed and sorted by FACS. Human anti-EBOV-GP monoclonal antibody KZ52 (base epitope, Lee *et al.* 2008) (**A**) or P6 (glycan cap epitope, Rijal *et al*. 2019) (**B**) were used to detect GP protein expression. The gated population "KZ52-sorted" in (**A**) or "P6-sorted" in (**B**) were bulk-sorted and stored as $E_{mutation}$-SIAT cell-lines. GP expression was not detected by FACS in cells transduced with M548V and Y517A mutated GP.

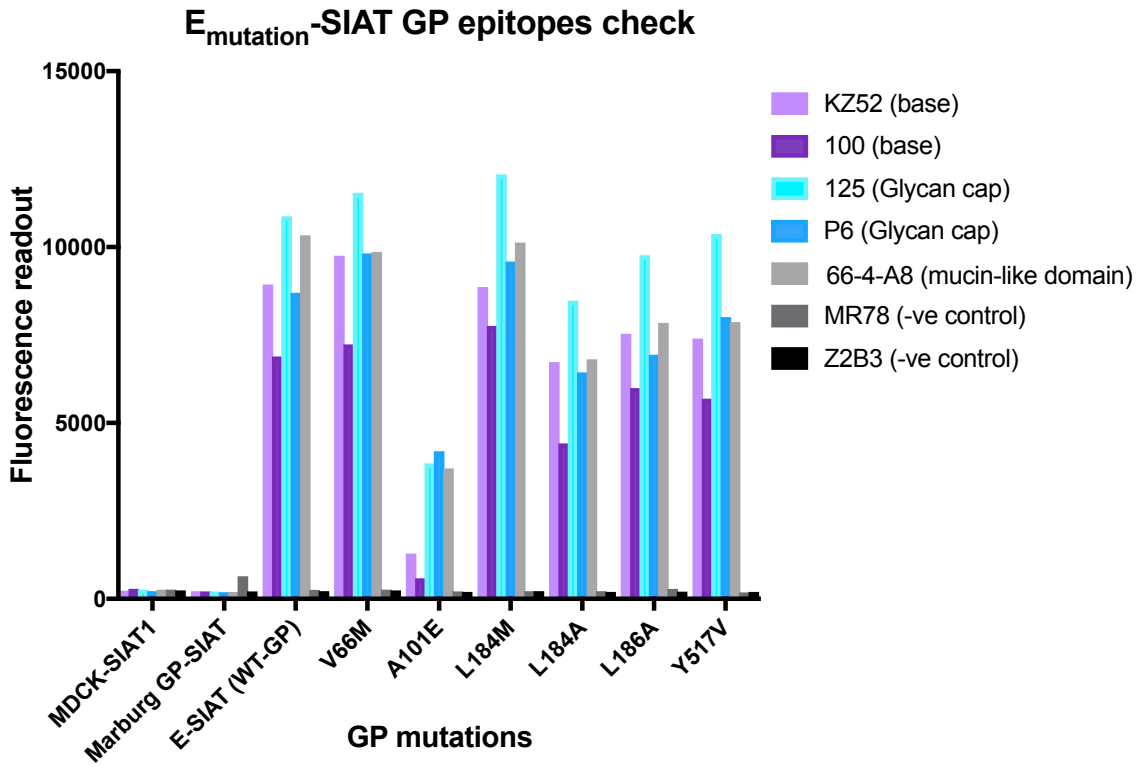


Figure 7. 13 Epitopes check for mutated EBOV-GP expressed at the cell surface
Six sorted $E_{mutation}$-SIAT cells expressing GP with mutation V66M, A101E, L184M, L184A, L186A or Y517V respectively were tested for their epitope integrity by immunofluorescence assay (IFA). E-SIAT cells expressing the WT EBOV-GP were included as positive control; the untransduced MDCK-SIAT1 cells and SIAT cells coated with *marburgvirus* GP were used as negative controls. Cells were stained with human anti-GP monoclonal antibodies or negative control antibodies (MR78 and Z2B3), followed by an Alexa Fluor® 647 conjugated anti-human second layer. After staining, cells were washed, fixed and analysed using a fluorescence plate reader CLARIOstar®.

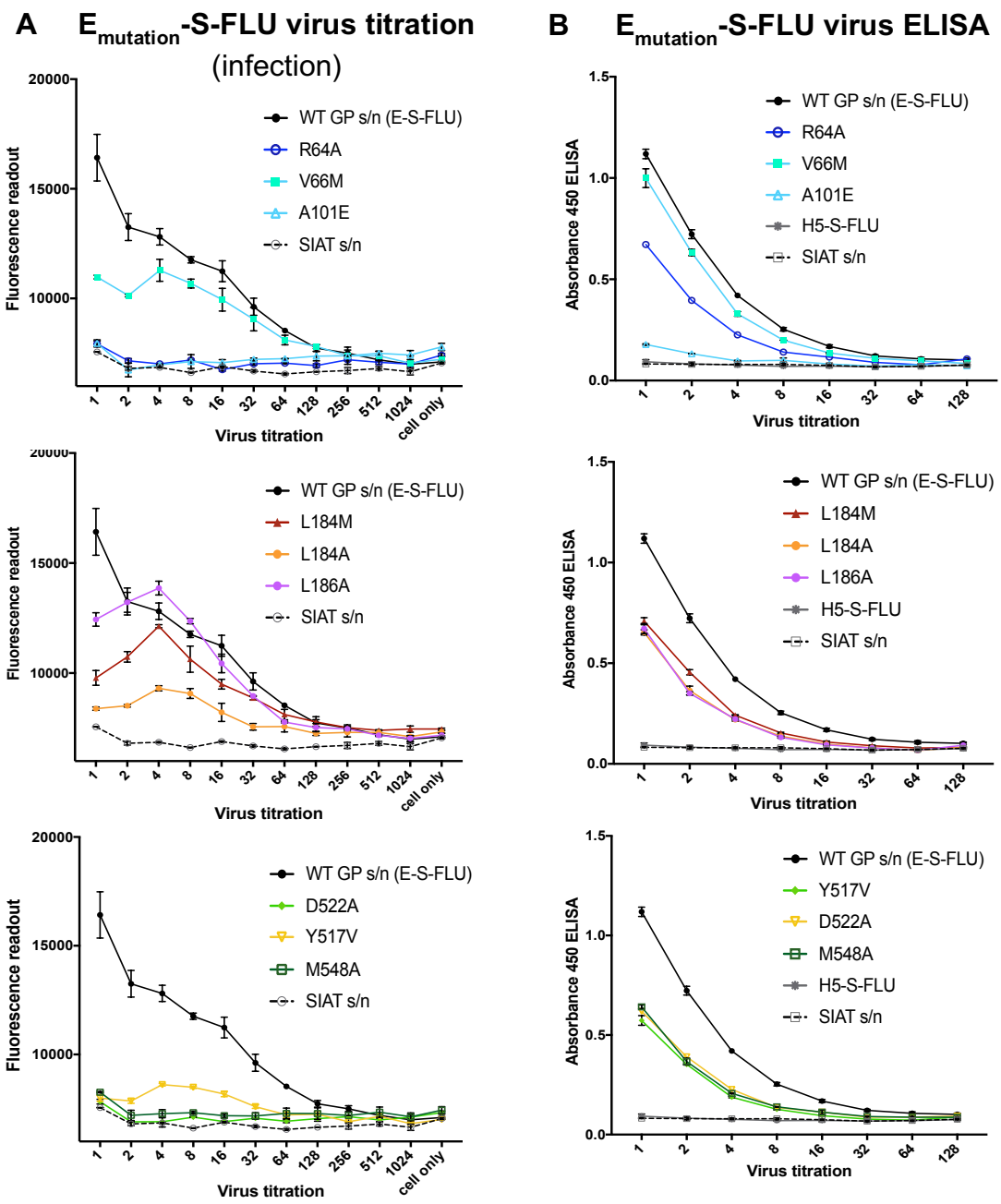


Figure 7. 14 Virus titration and ELISA for $E_{mutation}$-S-FLUs

A: Nine different $E_{mutation}$-SIAT cells were seeded with S-FLU to produce viruses pseudotyped with mutated EBOV-GP. E-SIAT expressing WT EBOV-GP and untransduced MDCK-SIAT1 cells were included as controls. Culture supernatant (s/n) were harvested 48 hours after seeding and titrated on indicator MDCK-SIAT1 cells. Infection was quantified by measuring eGFP fluorescence by a fluorescence plate reader CLARIOstar®. **B**: Harvested culture supernatants were titrated in a virus sandwich ELISA. 96-well Nunc® plates were coated with anti-NA antibody AF9C. All S-FLU pseudotyped viruses contain neuraminidase (NA) protein at the surface, which is encoded in the S-FLU virus genome. A biotinylated anti-EBOV-GP antibody (C13C6) was added to detect any EBOV-GP expressing S-FLU virions captured in the well. Horseradish peroxidase linked ExtrAvidin® (ExtrAvidin-HRP) was added to bind to the biotinylated antibody. Finally, substrate was added and we measured the absorbance at 450 nm to quantify virus particles. (Error bars: standard error of the mean from titration duplicates).

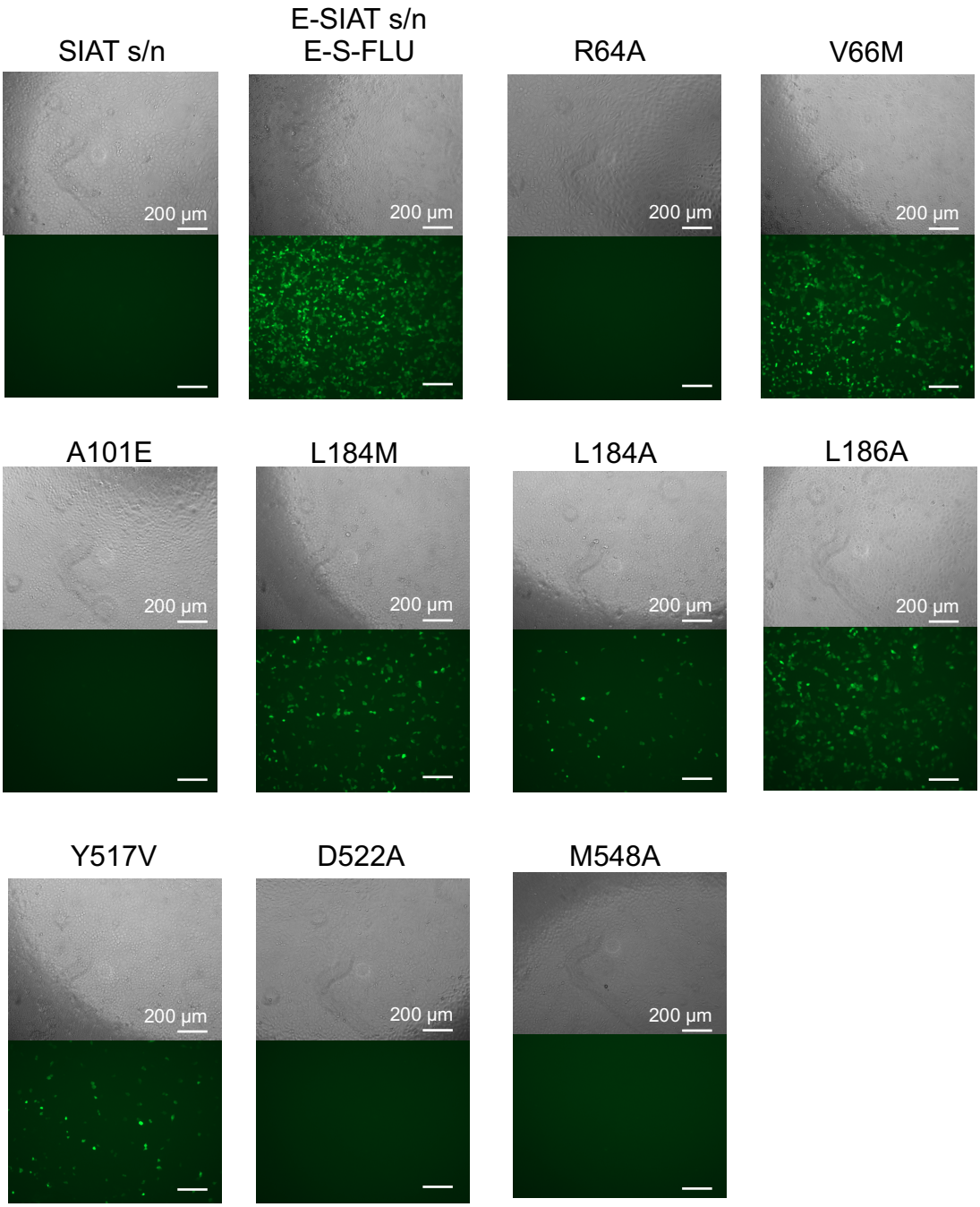


Figure 7. 15 Fluorescence microscopic images of $E_{mutation}$-S-FLU infection
Representative microscopic images (10X objective) of MDCK-SIAT1 cells infected by $E_{mutation}$-S-FLU. $E_{mutation}$-SIAT were seeded with S-FLU to produce pseudotyped virus. Undiluted culture supernatant harvested from the cells were added to infect MDCK-SIAT1 cells for 24 hours. Infected cells expressed eGFP, shown as green cells. Fluorescence microscopic pictures were taken in brightfield and eGFP channels after infection and fixation.

Of the eleven single mutations we introduced, GP(Y517A) and GP(M548V) were not detectable by anti-GP antibodies in transduced E-SIAT cells, suggesting the point-mutation abolished correct GP folding or expression at the cell surface. GP(A101E) E-SIAT could be sorted by using an anti-GP antibody, but most epitopes showed decreased binding in immunofluorescence assay (Figure 7.13). The other 8 mutations successfully generated $E_{mutation}$-SIAT cells with high level GP expression and with no obvious loss of epitopes detected by a set of MAbs (Figure 7.13).

Table 7. 3 Summary of $E_{mutation}$-S-FLU production

GP mutations	Transduced E-SIAT (KZ52)	Sorted E-SIAT (KZ52/P6)	Sorted E-SIAT epitopes check	E-S-FLU produced	Virus ELISA (c13b)
WT GP	✓	✓	✓	✓	✓
R64A	✓	✓	(✓)	×	✓
V66M		✓	✓	✓	✓
A101E	✓/×	✓	✓/×	×	×
L184M	✓	✓	✓	✓	✓
L184A	✓	✓	✓	✓/×	✓
L186A	✓	✓	✓	✓	✓
Y517A	×	×		×	×
Y517V	✓	✓	✓	✓/×	✓
D522A	✓	✓	(✓)	×	✓
M548A	✓	✓	(✓)	×	✓
M548V	×	×	×	×	×

✓: epitope detected; infectious virus produced; virus detected in the supernatant.
(✓): Not yet characterised with full panel of antibodies, but detected by KZ52 recognising the base epitope.
✓/×: epitope partially detected.
×: epitope lost; no virus production.

However, several mutations were associated with loss of infectivity of the resulting $E_{mutation}$-S-FLU. We could not detect infective E-S-FLU coated with GP(R64A), (D522A) and (M548A), despite virus particles co-expressing NA and GP being detected by the sandwich virus ELISA (Figure 7.14). GP(V66M), (L184M) and (L186M) produced infectious $E_{mutation}$-S-FLU, whereas (Y517V) and (L184A)

yielded only low viral titres (summarised in Table 7.3). We will test these mutant E-S-FLU in drug inhibition assays using GP-binding drugs for the next step.

7.5 Drug-resistant EBOV mutants

We collaborated with Peter Halfmann (University of Wisconsin-Madison) to select escape mutant EBOV viruses in the presence of GP-binding drugs. Recombinant EBOV with its VP30 gene replaced by a GFP reporter gene (EBOVΔVP30-GFP) was passaged to grow in VP30 transduced Vero cells (VeroVP30) in the presence of 5 μM toremifene (Halfmann *et al.* 2008). After eight days, the harvested culture supernatant was diluted to infect VeroVP30 cells, and virus clones were isolated and expanded from individual focus-forming units (FFU). So far, we have identified three mutant viruses for which the GP has been sequenced: mutant 1 (GP mutation S46N, T326I); mutant 3 (GP mutation S46N, L273I); mutant 5 (S46N, L479P). 5 μM Toremifene inhibited EBOVΔVP30-GFP virus growth by 4 log units measured on day 3 and day 6 of growth (Figure 7.16 A). The mutant viruses were not affected by toremifene.

Peter also tested the toremifene-selected escape mutant viruses for their growth in the presence of 10 μM arbidol, another putative GP-binding drug. At day 3 there was no detectable WT EBOV from the culture supernatant, and at day 6, arbidol reduced WT EBOV growth by 3 log units. The growth of toremifene-selected mutants (1, 3, 5) was reduced only by 1 log unit at day 6 compared to the virus grown in the DMSO only control medium (Figure 7.16 B). Notice that these three mutant viruses grew better compared to WT EBOV without any drug added. We plan to test the mutant viruses with non-GP-binding drugs such as cathepsin

inhibitor E64d to see whether these mutations are escaping the drugs by affecting the drug binding or by improved viral growth in general.

It is also possible that toremifene resistance involves mutations elsewhere in the genome. Therefore, Peter's group plan to sequence the whole virus genome for the escape mutants. Meanwhile, we will introduce the known GP mutations individually into our pseudotyped virus E-S-FLU to study the effect of the mutations on sensitivity to the drugs.

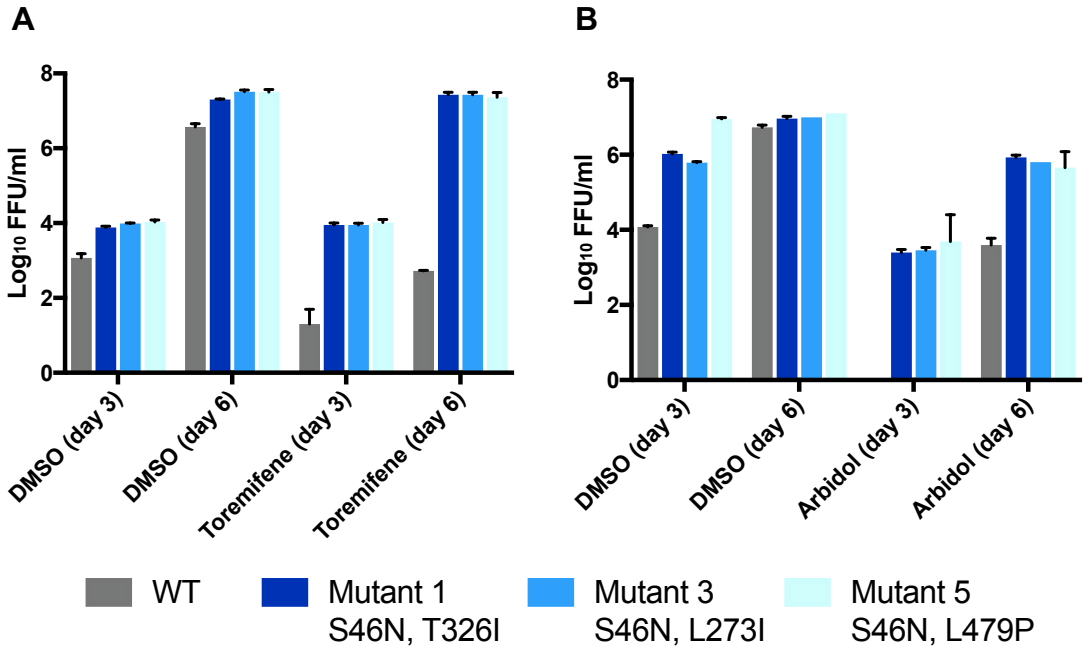


Figure 7. 16 Toremifene-selected mutant EBOV growth
Three toremifene-selected EBOV mutants (1, 3, 5) were passaged to infect VP30Vero cells and were measured for growth kinetics in the presence of 5 μM toremifene or 10 μM arbidol in comparison to the control DMSO-containing medium. On day 3 and day 6, culture supernatant was harvested and virus titres (focus-forming units) were determined and represented in common logarithm (Log_{10} FFU/ml). The geometric mean value of experimental triplicates with geometric standard deviation error bars are presented here.

We mapped the mutations identified in toremifene-selected EBOV mutants to the GP peptide sequence (Figure 7.9, blue squares). S46N may be a tissue culture

adaptation mutation as it appeared in unselected viruses (Halfman personal communication). L273I sits in the glycan cap region while T326I is in the mucin-like domain. L479P is at the C-terminus of GP1 subunit, between the predicted mucin-like domain and the furin cleavage site, which separates GP1 and GP2 subunits. It is noteworthy that none of these mutations locates in the putative drug binding pocket defined by crystallography.

The L479P mutation naturally occurs in *Bundibugyo ebolavirus* BDBV-GP, whereas T326I mutation is present in *Sudan ebolavirus* SUDV-GP. We therefore titrated toremifene for inhibition of *Zaire*, *Sudan*, *Bundibugyo* E-S-FLU, as well as a mucin-deleted *Zaire* E(Δmucin)-S-FLU. The E(Δmucin)-S-FLU was pseudotyped with *Zaire ebolavirus* GP (Makona 2014 strain) with residue 313 to 463 deleted, designed based on the published literature (Lee *et al.* 2008). Toremifene inhibited all of the E-S-FLUs, however the IC_{50} concentration inhibiting *Sudan* and *Bundibugyo* E-S-FLU was at least 10-fold higher than the IC_{50} inhibiting *Zaire* E-S-FLU, both full-length and mucin-deleted versions (Figure 7.17). This drug titration assay was only done once and will need further repeats to determine statistical significance. In the future, we will test the effect of S46N, L273I, T326I and L479P mutations on E-S-FLU infection and toremifene inhibition titre by site-directed mutagenesis using the workflow we described in Figure 7.10.

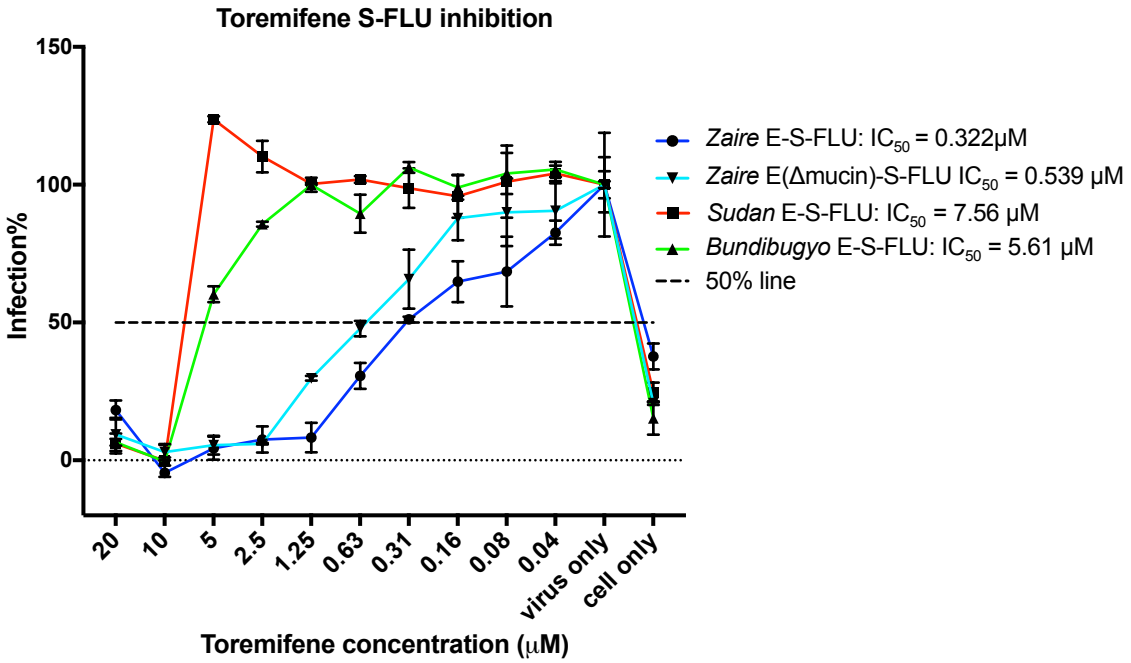


Figure 7. 17 Toremifene inhibition assays with different species E-S-FLU
Toremifene was titrated from 20 to 0.04 μM in the drug inhibition assay against E-S-FLU pseudotyped with GP from different *ebolavirus* species (*Zaire*; *Sudan*; *Bundibugyo*) and with mucin-like domain deleted GP E(Δmucin)-S-FLU. Indicator MDCK-SIAT1 cells were pre-incubated with toremifene for 3 hours and infected with S-FLUs for 24 hours. Virus infection was quantified by measuring eGFP expression with a fluorescence plate reader CLARIOstar®. Percentage infection was calculated as percentage maximum fluorescence readout from the "virus only" control. The error bars represent the standard error of the mean of titration duplicates.

7.6 Discussion and future work

7.6.1 Drugs that bind EBOV-GP

EBOV-GP is the sole player in the EBOV entry process, bearing the responsibilities of cell attachment, receptor binding and membrane fusion. Recent structural studies of EBOV-GP in complex with drugs have proposed a possible new insight into the unsolved puzzle of how multiple drugs inhibit EBOV entry. Drugs may be inhibiting EBOV via direct binding to EBOV-GP. A big hydrophobic pocket was identified at the base of the GP close to the fusion loop, and it was able to accommodate structurally varied compounds (Basu *et al.* 2011; Zhao *et al.* 2016, 2018; Ren *et al.* 2018; Shaikh *et al.* 2019). Hitherto eleven compounds have

been shown in complex with EBOV-GP in crystal structures, four of them bound with two molecules simultaneously in the same pocket.

Of particular interest was the observation that addition of a chlorine and a methyl group to compound 118 to form 118a enhanced its activity in the E-S-FLU blocking assay by 300-fold, without significantly changing its LogP and pKa^{base}. The chlorine has been shown to interact with residues in the pocket, particularly with the side chains of residues V106, A101, L515, and Y517 (note mutation to Y517V greatly reduced viral entry), as well as forming a halogen bond with the main-chain atoms of G67 and G102. These interactions were predicted to enhance binding by 118a. The group also showed that 118a was a more potent inhibitor of an EBOV-GP pseudotyped lentivirus (Shaikh *et al.* 2019). This enhancing effect of the addition of a single small chemical group to a GP binding molecule suggests that the specificity and strength of binding are important for the inhibitory effect on E-S-FLU. It provides the most convincing evidence to date that binding in the pocket is responsible for contributing to the inhibitory effects of these drugs. We plan to target future mutagenesis experiments to the contact residues for compound 118a.

The effect of improving binding of 118 by addition of a chlorine can be compared to the interaction between arbidol and H7 haemagglutinin. Both binding affinity and the IC_{50} for inhibition of Influenza virus entry were greatly enhanced by the addition of a hydroxyl group in the position that the arbidol molecule contacts a bridging water molecule in the crystal structure (Kadam and Wilson 2017). This illustrates that minimal changes to a ligand that improve contacts visible in the crystal structure can have dramatic effects on binding and functional inhibition of virus

entry. It will be interesting to compare this hydroxylated arbidol molecule in the inhibition assay for E-S-FLU and H7-S-FLU to test the specificity of the modification for Influenza.

The degree of destabilisation induced by the GP binding drugs, measured as a melting temperature shift, can be compared to the effect on stabilisation by peptide binding to class I major histocompatibility complex molecules (MHC-I). For example Springer *et al.* found that the absence of peptide resulted in a 26 ^{o}C shift in melting temperature on the H-2D^{b} molecule (Springer *et al.* 1998). In living RMA/S cells, this degree of destabilisation resulted in loss of molecules from the cell surface, which could be stabilised with externally added peptide (Townsend *et al.* 1989). We therefore looked to see if the expression of the EBOV-GP on transduced MDCK-SIAT1 cells reduced after twenty-four hours exposure to toremifene, as this would provide a very simple assay for detecting drugs that destabilised the GP. However, we did not detect any effect on surface accumulation of the GP in these conditions in preliminary experiments (data not shown).

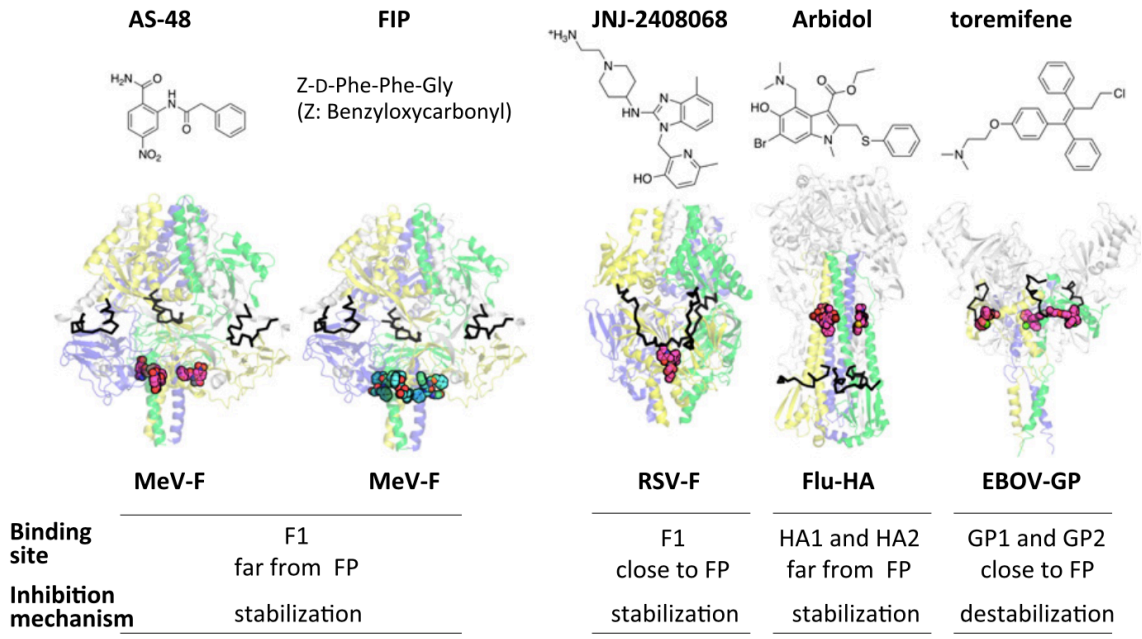


Figure 7. 18 Inhibitor-binding sites and mechanisms among class I viral fusion proteins

Figure was taken from Hashiguchi *et al.* 2018. Structures of inhibitors and inhibitor-bound class I viral fusion proteins are shown in the diagram: Measles virus fusion protein (Mev-F); Respiratory syncytial virus fusion glycoprotein (RSV-F); Influenza virus haemagglutinin (Flu-HA); Ebola virus glycoprotein (EBOV-GP). Trimeric subunits that contain the fusion loop or fusion peptide (black) are coloured in yellow, blue and green, and other subunits are in grey (e.g. in EBOV-GP, GP2 is coloured, GP1 is grey).

EBOV-GP belongs to the family of class I viral membrane fusion proteins (White and Whittaker 2016). Several other class I fusion glycoproteins also possess inhibitor binding sites (Figure 7.18) (Cianci *et al.* 2004; Plemper *et al.* 2004; Larson *et al.* 2008; Leneva *et al.* 2009; Battles *et al.* 2016; Hashiguchi *et al.* 2018). In the other viruses, drugs inhibited fusion by stabilising the pre-fusion conformation of the glycoproteins. EBOV-GP binding drugs however, destabilises the full-length protein.

One proposed mechanism is that, drug binding displaces the “DFF” loop, which may subsequently affect cathepsin cleavage of EBOV-GP, preventing the

exposure of the receptor binding site. To test this hypothesis, we pre-treated E-S-FLU with thermolysin to remove the mucin-like domain and the glycan cap. While antibodies that bind specifically to the glycan cap region no longer inhibited the cleaved E-S-FLU, toremifene still inhibited virus entry with sub-micromolar IC_{50}. This suggested that toremifene inhibited E-S-FLU at the post-cleavage stage. The drug binding site remained intact after cathepsin/thermolysin digest (Figure 7.19) (Wang *et al.* 2016). It is conceivable that drug binding to the post-cleavage GP may either destabilise the receptor binding, or inhibit fusion in the lysosome.

While the crystal structures contributes the most direct evidence for drug binding to EBOV-GP, there is still a gap in knowledge in defining the mechanistic and biological relevance of these findings to the inhibition of EBOV infection.

7.6.2 Site-directed mutagenesis of the drug binding site

We introduced site-directed mutations at the EBOV-GP drug binding pocket intending to reduce the GP-drug interaction, to test whether drug binding was required for virus inhibition. Probably because the drug binding site was right next to the fusion loop, it was very sensitive to mutations. Several single-site mutations either abolished GP folding or prevented E-S-FLU virus entry and or fusion. We successfully generated 5 mutated E-S-FLU (V66M, L184M, L184A, L186A, Y517V), which were viable, and can be tested for drug binding affinity. We will test these mutant viruses in drug inhibition titrations with GP-binding drugs and non-GP binding controls.

L184A and L186A mutations were tested by Basu *et al.*, and they showed a more than 4-fold reduction in virus inhibition potency by putative GP-binding drugs (compound 7, Basu *et al.* 2011). The interpretation of these results may not be straightforward. A mutation in the GP pocket could in principle alter the sensitivity of the GP to other mechanisms of inhibition, such as the effect of CADs integrating in the lysosome membrane to inhibit fusion.

Four mutations R64A, Y517V, D522A, and M548A were compatible with production of a folded GP at the cell surface and virus release, but virus infectivity was either abolished or greatly reduced, presumably through loss of the fusion function. Three of these four mutations are located in the fusion loop of GP2. It is tempting to speculate that this pattern of mutations mimics the effect of drugs that bind in the pocket, such as 118a and toremifene. The chlorine in 118a interacted with Y517 in the crystal structure, which was also a site where the mutation Y517V greatly reduced infective titre of E-S-FLU.

7.6.3 Toremifene-resistant EBOV-GP mutations

Next, we generated toremifene-resistant EBOV escape mutants in collaboration with Peter Halfmann (University of Wisconsin). Our group previously successfully used the escape mutant approach to map out EBOV-GP antibody binding epitopes (Rijal *et al.,* unpublished). It is also commonly used in studying virus fusion inhibitors for other lipid enveloped viruses (Larson *et al.* 2008; Leneva *et al.* 2009; Battles *et al.* 2016; Hashiguchi *et al.* 2018). Three toremifene-resistant EBOV mutants have been isolated, and their EBOV-GP contained mutations T326I, L273I, L479P respectively. Interestingly, the mutation sites were not at all close to

the drug binding pocket, and were scattered at different positions in the GP. We will verify the GP mutations by introducing them in our E-S-FLU pseudotyped virus system.

The toremifene-resistance mutations may not affect drug binding directly. Taking arbidol as the best studied virus fusion inhibitor for Influenza virus haemagglutinin (HA) as an example, arbidol inhibited HA fusion by reducing the fusion pH by 0.2 unit. Arbidol-selected mutations in contrast raised the fusion pH back to 5.0, and although arbidol still bound to the mutated HA, it no longer affected HA fusion and virus entry (Leneva *et al.* 2009). In addition, the mutations in HA selected by arbidol are distant from the actual binding site recently demonstrated in a crystal structure (Kadam and Wilson 2017).

Arbidol is a broad-spectrum antiviral compound, which has been reported to inhibit Zika virus, West Nile virus, tick-borne encephalitis virus, as well as EBOV (Teissier *et al.* 2011; Pécheur *et al.* 2016; Fink *et al.* 2018; Haviernik *et al.* 2018; Xiao *et al.* 2018). Although an arbidol-bound GP crystal structure is not yet available, our collaborator David Stuart showed that arbidol destabilised EBOV-GP in the thermal shift assay like other GP binding drugs. In addition, Peter Halfmann showed that toremifene-selected EBOV mutants were also more resistant to Arbidol inhibition. However, the escape mutants generally grew faster than WT-EBOV even in the absence of drugs, so the specificity of the toremifene mutations is still unconfirmed. We will further test the escape mutants in the presence of non-GP binding drugs to dissect the effect of these mutations on virus growth and drug resistance. Finally, arbidol has the physicochemical features of a CAD, and may

after all inhibit viral entry by its effect on the lysosome membrane rather than the very weak binding to the GP pocket.

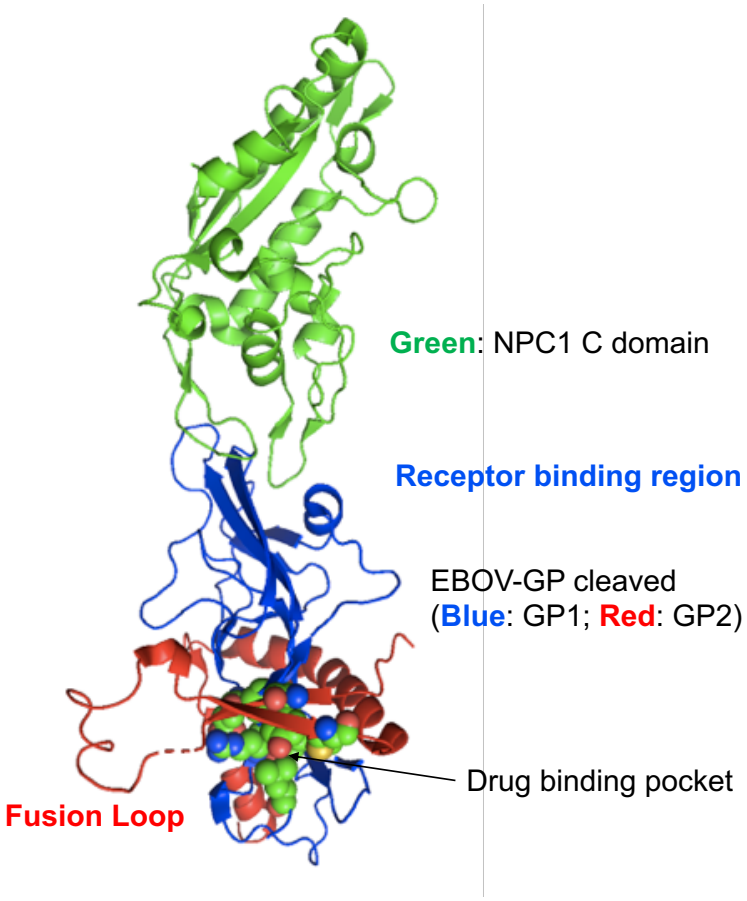


Figure 7. 19 Mutated residues mapped to the NPC1 bound EBOV-GP structure
The crystal structure of cleaved GP in complex with NPC1 domain C is displayed in cartoon representation (PDB file: 5F1B, Wang *et al*. 2016), with GP1 subunit coloured in blue, GP2 in red and NPC1 C domain coloured in green. In this chapter, we introduced mutations to 8 residues at the drug binding pocket of GP, the side-chains of altered amino acids are shown in space-filling representation.

7.6.4 Summary

At the moment, we are left with strongly suggestive evidence, that drug binding to the defined pocket on GP may contribute to the inhibitory effect of some drugs. The observation that the two strongest inhibitors toremifene and 118a both bind to EBOV-GP, and are also CADs, could be linked by suggesting that both properties are important. Achieving a high concentration of drug in the lysosome through the

CAD features may enhance any propensity to bind and destabilise GP at the defined pocket. The CAD feature may also promote intercalation in the membrane of lysosome to interfere with the fusion function of EBOV-GP, as an independent action. A full understanding of these issues is vital for optimising the design of small molecules that might be given safely to prevent or treat Ebola infections.

(BLANK PAGE)

Chapter 8 Final Summary

The first contribution of this study to the field of Ebola virus (EBOV) research is the establishment of a new EBOV pseudotype E-S-FLU (Chapter 3). S-FLU is a non-replicating pseudotyped Influenza virus, in which the haemagglutinin (HA) coding sequence has been replaced by an enhanced green fluorescent protein (eGFP) reporter. We have developed our own surrogate for EBOV because our laboratory is familiar with this technology, and have been using S-FLU both as a flu vaccine candidate and as a pseudotype system for studying infection and neutralisation of high containment level pandemic flu strains (Powell *et al.* 2012, 2019; Baz *et al.* 2015).

We successfully incorporated the EBOV glycoprotein (GP) into the S-FLU surface membrane by propagating the virus in MDCK-SIAT1 cells stably transduced with the full-length EBOV-GP. Surprisingly, MDCK-SIAT1 cells were able to tolerate high level expression of EBOV-GP without showing apparent cytotoxicity. This differs from many other cell-lines reported in the literature (Takada *et al.* 2000; Volchkov 2001; Simmons *et al.* 2002; Alazard-Dany *et al.* 2006; Mohamadzadeh, Chen and Schmaljohn 2007; Francica, Matukonis and Bates 2009). The stable MDCK-SIAT1 producer cell-line allows easy production of the E-S-FLU virus without the need for repeated transfection for each round of virus production, in comparison to retrovirus and VSV pseudotyping methods.

We demonstrated that E-S-FLU is a robust tool for high-throughput drug screens, with a single laboratory batch being sufficient to screen a library of 1,280

pharmacologically active compounds (Chapter 4, section 4.2). We identified 215 compounds that inhibited E-S-FLU infection *in vitro*, and our result showed a significant correlation with the drug screen published by Johansen *et al.* (2015), who used a recombinant GFP-expressing EBOV to screen a library of 2,635 FDA-approved drugs (Johansen *et al.* 2015).

Parallel to this study, Dr Pramila Rijal in our laboratory has used E-S-FLU to screen eighty-two monoclonal antibodies in *in vitro* neutralisation assay from vaccinees enrolled in the ChAd3-MVA vaccine trial in Oxford (Stanley *et al.* 2014; Ewer *et al.* 2016). In collaboration with Saphire *et al.*, we showed that the antibody neutralisation profile for E-S-FLU correlated well with the protection efficacy *in vivo* in mice. As a result, a new human antibody cocktail has been put together that provided complete protection of guinea pigs when given on day 3 post EBOV infection (Rijal *et al.* 2019). Moreover, Jack Tan from our lab has further developed E-S-FLU by swapping the reporter eGFP to a firefly luciferase protein, and has demonstrated the potential use of E-S-FLU as a safe model for monitoring EBOV infection *in vivo*.

We developed the results from the drug screening study, in which we showed that many compounds coming from dispersed pharmacological groups can inhibit E-S-FLU infection. Several groups have reported similar observations but none have given a clear answer as to how these drugs are acting on EBOV entry (Johansen *et al.* 2013, 2015; Gehring *et al.* 2014; Kouznetsova *et al.* 2014; Fan *et al.* 2017).

I summarise here our results with reference to five explanatory models for drug inhibition of EBOV entry. Before continuing, I would like to highlight the cationic amphiphilic (CAD) feature that is shared by most of the small molecules that inhibit EBOV infection, first described by Shoemaker *et al*. in 2013. This is a physicochemical feature with which one end of the molecule is hydrophobic and lipid soluble, and the other end possesses a weak amine base. As a result, most of these drugs are prone to concentrate in the acidic lysosomal lumen in their protonated form, a property described in 1974 as lysosomotropism (De Duve *et al.* 1974).

1) Drugs act via inactivation of acid sphingomyelinase (ASM)

This hypothesis stems from the observation that many EBOV-inhibiting-CADs are also FIASMAs (functional inhibitors of acid sphingomyelinase). After concentrating at the luminal side of lysosomes, CADs alter the electrostatic environment of the membrane. One of the consequences described by Kornhuber *et al*. is functional inactivation of acid sphingomyelinase (ASM), by dissociating the enzyme into the lysosomal lumen where it is broken down by various proteases (Kornhuber *et al.* 2008). In Chapter 5, we specifically knocked out the expression of ASM in HeLa cells by the CRISPR/Cas 9 technique and showed that E-S-FLU infection was not affected. Therefore, we concluded that the effect of CADs on ASM is not required to block EBOV-GP dependent viral entry.

2) Drugs act via direct binding to the NPC1 protein

NPC1 protein is the critical entry receptor for EBOV-GP to bind in lysosome. Binding of GP to NPC1 triggers membrane fusion of the viral membrane with the

lysosomal membrane and the release of the viral genome into the cytosol (Carette *et al.* 2011; Côté *et al.* 2011; Miller *et al.* 2012).

There are two known drug-binding sites on the NPC1 protein which may be involved in inhibition of EBOV entry. One site is at the domain C loop, where drugs can directly compete with EBOV-GP for binding to the receptor. To date these drugs have only been tested for blocking the *Zaire* species *ebolavirus* (Côté *et al.* 2011; Basu *et al.* 2015). The other site is at the sterol-sensing domain sitting in the transmembrane region, and multiple drugs have been demonstrated to bind at this site, including U18666A, astemizole, cepharanthine and itraconazole (Lu *et al.* 2015; Lyu *et al.* 2017, 2018; Trinh *et al.* 2017). Drugs binding to either of these two sites will induce an NPC disease-like phenotype, namely the accumulation of cholesterol, sphingolipids and reduced calcium concentration in the lysosome (Lloyd-Evans *et al.* 2008).

To see whether all CADs that inhibited E-S-FLU bind NPC1 protein directly, we characterised the cellular biochemistry in cells treated with a panel of 20 potent E-S-FLU inhibitors. We showed that while most CADs elevated the cholesterol level in the lysosome, many did not induce a full NPC disease-like phenotype, suggesting that NPC1 is not the only target of action producing these biochemical patterns. Itraconazole, that both binds the sterol-sensing domain and induces a complete NPC phenotype in cells, failed to block E-S-FLU and EBOV infection (Johansen *et al.* 2015; Xiao *et al.* 2018). In addition, U18666A, another confirmed NPC1 binder, required a concentration approximately 1000-fold higher than its

binding affinity for NPC1 to inhibit E-S-FLU (Lloyd-Evans *et al.* 2008; Chapter 4 section 4.3.4).

These results suggested that NPC1 binding, especially via the sterol-sensing domain, may not be the primary target for CADs that inhibit EBOV entry. Finally, we confirmed that the biochemical phenotype induced by loss of the lipid transport function of NPC1 through loss of NPC2 did not by itself inhibit EBOV-GP-dependent entry (Chapter 5, section 5.2). In contrast, specific mutations in NPC1 can prevent EBOV entry without affecting its lipid transport function (section 5.4).

Together these observations lead to the conclusion that the effects of the CADs on lipid storage and EBOV entry are independent.

3) Drugs act via endo/lysosomal calcium channels TPC1/2

Several groups showed that calcium channel inhibitors including amiodarone, bepridil, verapamil and tetrandrine blocked EBOV entry *in vitro* (Gehring *et al.* 2014; Johansen *et al.* 2015; Sakurai *et al.* 2015). Recently, Sakurai *et al.* showed more definitively that EBOV infection requires the two-pore channels 1/2 during cell entry (Sakurai *et al.* 2015). There have been no direct following up studies to confirm the importance of TPC1/2 in EBOV entry since Sakurai's claim in 2015. However, this has been slowly accepted as a dogma and several groups have begun to screen for specific drugs targeting TPC1/2 as potential EBOV treatment (Sun *et al.* 2017; Penny *et al.* 2018).

To confirm this finding, we examined two sets of independently generated TPC1/2 deficient murine embryonic fibroblasts, as well as TPC1/2 knocked out HeLa cells, which we produced in this thesis by using the CRISPR/Cas 9 technique. However, we found that neither E-S-FLU nor EBOV-GP pseudotyped lentivirus infection was affected by deletion of the TPC1/2 proteins (Chapter 6, section 6.3, 6.4). This result directly disagrees with the results from Sakurai *et al*. 2015, and will require careful comparison in collaboration with that group to identify the basis for the discrepancy.

In addition, we titrated 44 calcium flux modulators in our virus inhibition assay, and plotted the pattern of distribution of LogP and pKa^{base}. We found that the pattern was very similar to that for all of the E-S-FLU inhibitors: the active molecules clustered into the group with high LogP and pKa^{base}. We selected out a subgroup of eighteen of these drugs that were known to inhibit TPCs specifically (Chapter 6, section 6.2). Again, only nine of the TPCs blockers inhibited E-S-FLU entry and all of these were CADs.

We conclude that it is the CAD feature of these molecules that is responsible for inhibition of EBOV-GP-dependent cell entry, rather than any specific actions on calcium channels.

4) Drugs act by altering lysosomal membrane integrity

During the membrane fusion step, GP2 inserts its hydrophobic fusion loop into the lysosomal membrane, and undergoes a major conformational change (Weissenhorn *et al.* 2002; Gregory *et al.* 2011) that brings together the viral membrane and lysosomal membrane which then fuse. CADs concentrating in the

lysosomal luminal membrane may well affect this process at multiple points, such as repelling the insertion of GP2 into the membrane, interrupting conformational changes or repelling the opposing membranes through charge effect.

While we have not yet tested this hypothesis directly, we showed that a group of anti-histamines which are known to induce lysosomal membrane permeability, all effectively inhibited E-S-FLU infection potently (Chapter 4, section 4.3.5) (Aits *et al.* 2015; Ellegaard *et al.* 2016).

5) Drugs act via direct binding to EBOV-GP

Basu *et al.* and David Stuart's group have defined a hydrophobic pocket in EBOV-GP where CADs such as toremifene can bind to destabilise the viral protein (Zhao *et al.* 2016). Unlike most of the other virus fusion inhibitors that bind to stabilise the viral glycoprotein in its prefusion state, toremifene binding to EBOV-GP destabilised the protein (Zhao *et al.* 2016; Hashiguchi *et al.* 2018).

In collaboration with the Stuart group, we identified imipramine as a new EBOV-GP binder (Chapter 7, section 7.2) (Zhao *et al.* 2018). We also confirmed that with a minimal change in compound 118 to 118a, where a methyl group and chlorine group are added, the drug's inhibitory effect towards E-S-FLU was increased by 300-fold (Shaikh *et al.* 2019). This result suggested that specific drug binding to EBOV-GP is directly related to their inhibitory effect. However, we also found that not all EBOV inhibiting CADs can bind into this pocket, such as amiodarone and chloroquine. This showed that CADs may inhibit EBOV entry by other means than binding the pocket. We propose that through intercalation in the lysosome and viral

membranes the CADs can inhibit GP-dependant fusion. The most potent CADs are those that bind in the pocket, providing both actions, and can inhibit EBOV entry at nanomolar concentrations, whereas the non-binders tend to require at least a hundred-fold higher concentration.

Conclusion

The results in this thesis suggest that the most powerful of the cationic amphiphilic drugs that inhibit EBOV entry act by combining three properties: concentration in the lysosome, binding and destabilising of EBOV-GP, and an independent effect on fusion by intercalation of protonated molecules in the lysosomal membrane (summarised in Figure 8.1). The inhibition of NPC1, TPC1/2 and ASM by CADs is likely to be an independent secondary effect of the drugs concentrated in the lysosomal membrane, and is not responsible for the inhibition of EBOV infection.

This model provides a simple explanation for why many drugs inhibit EBOV infection, and provides a theoretical foundation for optimising the design of molecules that might be useful in the management of EBOV disease.

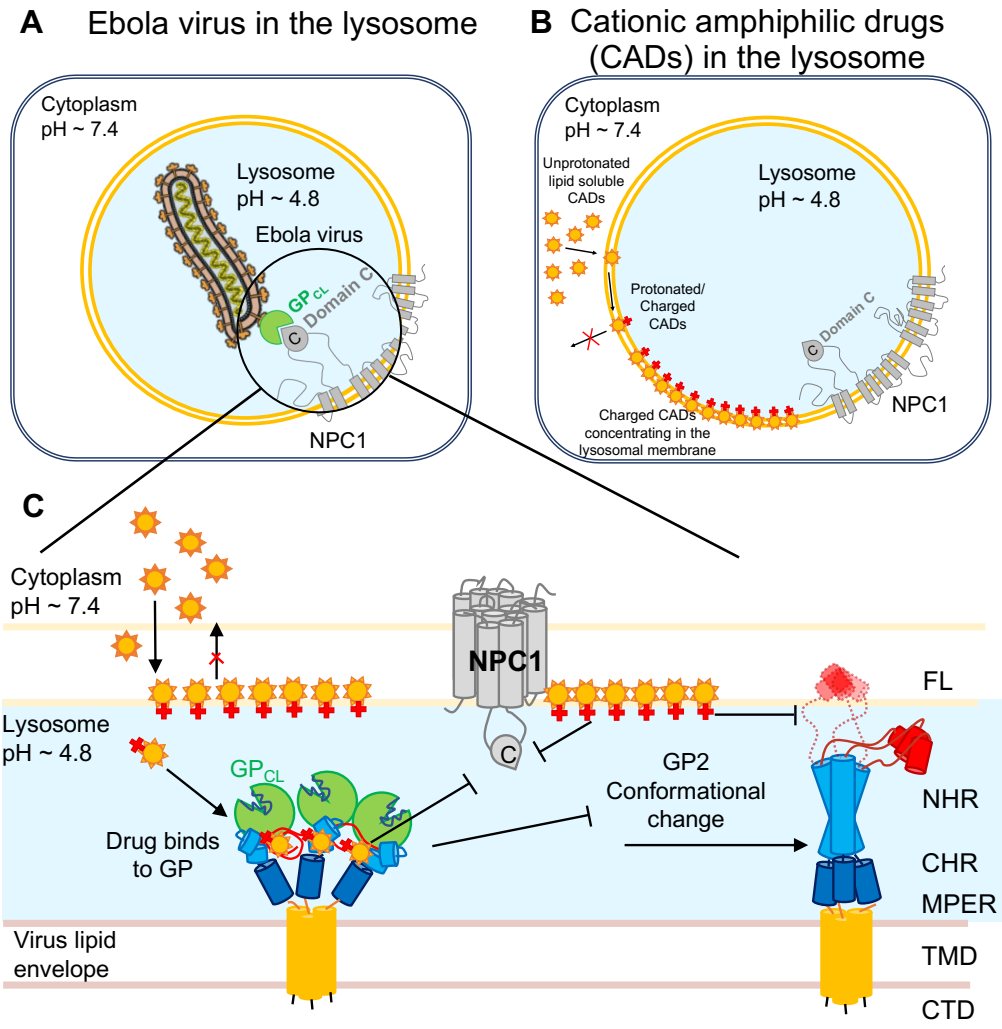


Figure 8. 1 Proposed mechanisms of CADs inhibiting EBOV entry

A: Ebola virus (EBOV) in the lysosome. The EBOV glycoprotein (GP) is processed by cathepsin B/L to a cleaved form (GP_{CL}, green), and the exposed receptor binding region binds to the NPC1 protein domain C (grey) to trigger fusion. **B**: Cationic amphiphilic drugs (CADs) in the lysosome. CADs contain a hydrophobic lipid soluble end (orange) and a weak base amine end, which remains uncharged at neutral pH and can freely diffuse through the lysosomal membrane. CADs become protonated in the acidic lysosomal environment, and the positively charged (red cross) CADs are no longer lipid-permeable and therefore become trapped at the luminal side of the lysosomal membrane. **C:** Two proposed mechanisms on how CADs inhibit EBOV. Drugs can bind directly to a hydrophobic pocket in GP near the fusion loop (FL), which destabilises the GP molecule. This may distort and prevent the receptor binding region (green) from binding NPC1 domain C (ruffled blue edges on GP_{CL}), or this may affect the conformational change of GP2 which is required for membrane fusion. In addition, the positively charged CADs intercalate in the lysosomal membrane and alter the membrane electrostatic property by disposing positive charges, and this may affect NPC1-GP_{CL} interaction or repel the hydrophobic fusion loop (GP2) from inserting into the lysosomal membrane. NHR: N-terminal heptad region; CHR: C-terminal heptad region; MPER: membrane-proximal external region; TM: transmembrane domain; CTD: cytoplasmic domain.

(BLANK PAGE)

BIBLIOGRAPHY

Abe K, Puertollano R. Role of TRP channels in the regulation of the endosomal pathway. *Physiology* 2011;**26**:14–22.

Abramowicz M, Zuccotti G, Pflomm JM. A 4-drug combination (Viekira Pak) for hepatitis C. *JAMA - J Am Med Assoc* 2015;**313**:1857–8.

Adams DJ, Dai M, Pellegrino G *et al.* Synthesis, cellular evaluation, and mechanism of action of piperlongumine analogs. *Proc Natl Acad Sci* 2012;**109**:15115–20.

Adinolfi LE, Utili R, Tonziello A *et al.* Effects of alpha interferon induction plus ribavirin with or without amantadine in the treatment of interferon non-responsive chronic hepatitis C: A randomised trial. *Gut* 2003;**52**:701–5.

Agnandji ST, Huttner A, Zinser ME *et al.* Phase 1 trials of rVSV Ebola vaccine in Africa and Europe. *N Engl J Med* 2015;**374**:1647–60.

Aits S, Kricker J, Liu B *et al.* Sensitive detection of lysosomal membrane permeabilization by lysosomal galectin puncta assay. *Autophagy* 2015;**11**:1408–24.

Alazard-Dany N, Volchkova V, Reynard O *et al.* Ebola virus glycoprotein GP is not cytotoxic when expressed constitutively at a moderate level. *J Gen Virol* 2006;**87**:1247–57.

Alvarez CP, Lasala F, Carrillo J *et al.* C-type lectins DC-SIGN and L-SIGN mediate cellular entry by Ebola Virus in cis and in trans. *J Virol* 2002;**76**:6841–4.

Aman MJ. Chasing Ebola through the endosomal labyrinth. *MBio* 2016;**7**:1–3.

Andrews KT, Fisher G, Skinner-Adams TS. Drug repurposing and human parasitic protozoan diseases. *Int J Parasitol Drugs Drug Resist* 2014;**4**:95–111.

Arndt L, Castonguay J, Arlt E *et al.* NAADP and the two-pore channel protein 1 participate in the acrosome reaction in mammalian spermatozoa. *Mol Biol Cell* 2014;**25**:948–64.

Arunachalam K, Dominic P, Lakshmanan S *et al.* Impact of drug induced Long QT syndrome: a systematic review. *J Clin Med Res* 2018;**10**:384–90.

Avota E, Gulbins E, Schneider-Schaulies S. DC-SIGN mediated sphingomyelinase-activation and ceramide generation is essential for enhancement of viral uptake in dendritic cells. *PLoS Pathog* 2011;**7**:e1001290.

Ayad RF, Assar MD, Simpson L *et al.* Causes and management of drug-induced long QT syndrome. *Proc (Bayl Univ Med Cent)* 2010;**23**:250–5.

Babalola JO, Wendeler M, Breiden B *et al.* Development of an assay for the intermembrane transfer of cholesterol by Niemann-Pick C2 protein. *Biol Chem* 2007;**388**:617–26.

Bai CQ, Mu JS, Kargbo D *et al.* Clinical and virological characteristics of Ebola virus disease patients treated with Favipiravir (T-705) - Sierra Leone, 2014. *Clin Infect Dis* 2016;**63**:1288–94.

Bampton ETW, Goemans CG, Niranjan D *et al.* The dynamics of autophagy visualized in live cells: from autophagosome formation to fusion with endo/lysosomes. *Autophagy* 2005;**1**:23–36.

Banadyga L, Hoenen T, Ambroggio X *et al.* Ebola virus VP24 interacts with NP to facilitate nucleocapsid assembly and genome packaging. *Sci Rep* 2017;**7**:7698.

Baseler L, Chertow DS, Johnson KM *et al.* The pathogenesis of Ebola virus disease. *Annu Rev Pathol Mech Dis* 2017;**12**:387.

Basler CF. Innate immune evasion by filoviruses. *Virology* 2015;**479–480**:122–130.

Basu A, Li B, Mills DM *et al.* Identification of a small-molecule entry inhibitor for filoviruses. *J Virol* 2011;**85**:3106–19.

Basu A, Mills DM, Mitchell D *et al.* Novel small molecule entry inhibitors of Ebola virus. *J Infect Dis* 2015;**212**:S425–34.

Battles MB, Langedijk JP, Furmanova-Hollenstein P *et al.* Molecular mechanism of respiratory syncytial virus fusion inhibitors. *Nat Chem Biol* 2016;**12**:87–93.

Bavari S, Bosio CM, Wiegand E *et al.* Lipid raft microdomains: a gateway for compartmentalized trafficking of Ebola and Marburg viruses. *J Exp Med* 2002;**195**:593–602.

Baz M, Boonnak K, Paskel M *et al.* Nonreplicating influenza A virus vaccines confer broad protection against lethal challenge. *MBio* 2015;**6**:1–13.

Beckmann N, Sharma D, Gulbins E *et al.* Inhibition of acid sphingomyelinase by tricyclic antidepressants and analogons. *Front Physiol* 2014;**5**:(Article 331)1–14.

Bentley EM, Mather ST, Temperton NJ *et al.* The use of pseudotypes to study viruses, virus sero-epidemiology and vaccination. *Vaccine* 2015;**33**:2955–62.

Bermejo M, Rodríguez-Teijeiro JD, Illera G *et al.* Ebola outbreak killed 5000 gorillas. *Science* 2006;**314**:1564.

Berridge MJ, Lipp P, Bootman MD. The versatility and universality of calcium signalling. *Nat Rev Mol Cell Biol* 2000;**1**:11–21.

Bhagya N, Chandrashekar KR. Tetrandrine - A molecule of wide bioactivity. *Phytochemistry* 2016;**125**:5–13.

Blom TS, Linder MD, Snow K *et al.* Defective endocytic trafficking of NPC1 and NPC2 underlying infantile Niemann-Pick type C disease. *Hum Mol Genet* 2003;**12**:257–72.

Bootman MD, Berridge MJ, Roderick HL. Calcium signalling: More messengers, more channels, more complexity. *Curr Biol* 2002;**12**:563–5.

Bornholdt ZA, Noda T, Abelson DM *et al.* Structural rearrangement of ebola virus vp40 begets multiple functions in the virus life cycle. *Cell* 2013;**154**:763–74.

Boseley, S. (December 2014). *Untested Ebola drug given to patients in Sierra Leone causes UK walkout*. Retrieved from https://www.theguardian.com/world/2014/dec/22/ebola-untested-drug-patients-sierra-leone-uk-staff-leave.

Boya P, Kroemer G. Lysosomal membrane permeabilization in cell death. *Oncogene* 2008;**27**:6434–51.

Brailoiu E, Churamani D, Cai X *et al.* Essential requirement for two-pore channel 1 in NAADP-mediated calcium signaling. *J Cell Biol* 2009;**186**:201–9.

Brailoiu E, Rahman T, Churamani D *et al.* An NAADP-gated two-pore channel targeted to the plasma membrane uncouples triggering from amplifying Ca^{2+} signals. *J Biol Chem* 2010;**285**:38511–6.

Bray M, Geisbert TW. Ebola virus: The role of macrophages and dendritic cells in the pathogenesis of Ebola hemorrhagic fever. *Int J Biochem Cell Biol* 2005;**37**:1560–6.

Brecher M, Schornberg KL, Delos SE *et al.* Cathepsin cleavage potentiates the Ebola virus glycoprotein to undergo a subsequent fusion-relevant conformational change. *J Virol* 2011;**86**:364–72.

Brindley MA, Hunt CL, Kondratowicz AS *et al.* Tyrosine kinase receptor Axl enhances entry of Zaire ebolavirus without direct interactions with the viral glycoprotein. *Virology* 2011;**415**:83–94.

De Bruin ML, Pettersson M, Meyboom RHB *et al.* Anti-HERG activity and the risk of drug-induced arrhythmias and sudden death. *Eur Heart J* 2005;**26**:590–7.

Bukreyev A, Marzi A, Feldmann F *et al.* Chimeric human parainfluenza virus bearing the Ebola virus glycoprotein as the sole surface protein is

immunogenic and highly protective against Ebola virus challenge. *Virology* 2009;**383**:348–61.

Burke DF, Smith DJ. A recommended numbering scheme for influenza A HA subtypes. *PLoS One* 2014;**9**:e112302.

Burke J, Declerq R, Ghysebrechts G. Ebola haemorrhagic fever in Zaire, 1976. Report of an international commission. *Bull World Health Organ* 1978;**56**:271–93.

Calcraft PJ, Ruas M, Pan Z *et al.* NAADP mobilizes calcium from acidic organelles through two-pore channels. *Nature* 2009;**459**:596–600.

Cancela JM, Churchill GC, Galione A. Coordination of agonist-induced Ca^{2+}-signalling patterns by NAADP in pancreatic acinar cells. *Nature* 1999;**398**:74–6.

Cang C, Bekele B, Ren D. The voltage-gated sodium channel TPC1 confers endolysosomal excitability. *Nat Chem Biol* 2014;**10**:463–9.

Carette JE, Raaben M, Wong AC *et al.* Ebola virus entry requires the cholesterol transporter Niemann-Pick C1. *Nature* 2011;**477**:340–3.

Carmeliet E, Drews L, Duker G *et al.* Voltage- and time-dependent block of the delayed K^+ current in cardiac myocytes by dofetilide. *J Pharmacol Exp Ther* 1998;**262**:809–17.

Cenedella RJ. Cholesterol synthesis inhibitor U18666A and the role of sterol metabolism and trafficking in numerous pathophysiological processes. *Lipids* 2009;**44**:477–87.

Centers for Disease Control and Prevention (CDC). Update: filovirus infections among persons with occupational exposure to nonhuman primates. *MMWR Morb Mortal Wkly Rep* 1990;**39**:266–7.

Centers for Disease Control and Prevention (CDC). Ebola-Reston virus infection among quarantined nonhuman primates—Texas, 1996. *MMWR Morb Mortal Wkly Rep* 2006;**45**:314–6.

Center for Disease Control and Prevention. (2018). Ebola (Ebola Virus Disease). *40 Years of Ebola Virus Disease around the World*. Retrieved from https://www.cdc.gov/vhf/ebola/history/chronology.html.

Chandran K, Sullivan NJ, Felbor U *et al.* Endosomal proteolysis of the Ebola virus glycoprotein is necessary for infection. *Science* 2005;**308**:1643–5.

Chen BJ, Leser GP, Morita E *et al.* Influenza virus hemagglutinin and neuraminidase, but not the matrix protein, are required for assembly and budding of plasmid-derived virus-like particles. *J Virol* 2007;**81**:7111–23.

Chen HR, Sherr DH, Hu Z *et al.* A network based approach to drug repositioning identifies plausible candidates for breast cancer and prostate cancer. *BMC Med Genomics* 2016;**9**:1–11.

Chen J, Lee KH, Steinhauer DA *et al.* Structure of the hemagglutinin precursor cleavage site, a determinant of influenza pathogenicity and the origin of the labile conformation. *Cell* 1998;**95**:409–17.

Chen Q, Tang K, Zhang X *et al.* Establishment of pseudovirus infection mouse models for *in vivo* pharmacodynamics evaluation of filovirus entry inhibitors. *Acta Pharm Sin B* 2018;**8**:200–8.

Cheng H, Lear-Rooney CM, Johansen L *et al.* Inhibition of Ebola and Marburg Virus Entry by G Protein-Coupled Receptor Antagonists. *J Virol* 2015;**89**:9932–8.

Cianci C, Yu KL, Combrink K *et al.* Orally Active Fusion Inhibitor of Respiratory Syncytial Virus. *Antimicrob Agents Chemother* 2004;**48**:413–22.

Clay JR, Ogbaghebriel A, Paquette T *et al.* A quantitative description of the E-4031-sensitive repolarization current in rabbit ventricular myocytes. *Biophys J* 1995;**69**:1830–7.

CredibleMeds (2019). *Combined List of Drugs that Prolonged QT and/or Cause Torsades de Pointes (TDP).* Retrieved from https://crediblemeds.org/pdftemp/pdf/CombinedList.pdf.

De Clercq E. Ebola virus (EBOV) infection: therapeutic strategies. *Biochem Pharmacol* 2014;**93**:1–10.

Connolly BM, Steele KE, Davis KJ *et al.* Pathogenesis of Experimental Ebola Virus Infection in Guinea Pigs. *J Infect Dis* 2008;**179**:S203–17.

Corti D, Misasi J, Mulangu S *et al.* Protective monotherapy against lethal Ebola virus infection by a potently neutralizing antibody. *Science* 2016;**351**:1339–42.

Côté M, Misasi J, Ren T *et al.* Small molecule inhibitors reveal Niemann-Pick C1 is essential for Ebola virus infection. *Nature* 2011;**477**:344–8.

Cross K, Langley W, Russell R *et al.* Composition and Functions of the Influenza Fusion Peptide. *Protein Pept Lett* 2009;**16**:766–78.

Cui J, Ren B, Tong Y *et al.* Synergistic combinations of antifungals and anti-virulence agents to fight against Candida albicans. *Virulence* 2015;**6**:362–71.

Dammermann W, Guse AH. Functional ryanodine receptor expression is required for NAADP-mediated local Ca^{2+} signaling in T-lymphocytes. *J Biol Chem* 2005;**280**:21394–9.

Davey RT, Dodd L, Proschan MA *et al.* A Randomized, Controlled Trial of ZMapp for Ebola Virus Infection. *N Engl J Med* 2016;**375**:1448–56.

Davies JP, Ioannou YA. Topological analysis of Niemann-Pick C1 protein reveals that the membrane orientation of the putative sterol-sensing domain is identical to those of 3-hydroxy-3-methylglutaryl-CoA reductase and sterol regulatory element binding protein cleavage-activating. *J Biol Chem* 2000;**275**:24367–74.

Demaison C, Parsley K, Brouns G *et al.* High-level transduction and gene expression in hematopoietic repopulating cells using a human immunodeficiency [correction of imunodeficiency] virus type 1-based lentiviral vector containing an internal spleen focus forming virus promoter. *Hum Gene Ther* 2002;**13**:803–13.

Dennis a, Wang L, Wan X *et al.* hERG channel trafficking: novel targets in drug-induced long QT syndrome. *Biochem Soc Trans* 2007;**35**:1060–3.

Deotarse PP, Jain AS, Baile MB *et al.* Drug Repositioning: A Review. *Int J Pharma Res Rev* 2015;**4**:51.

Dhama K, Karthik K, Khandia R *et al.* Advances in designing and developing vaccines, drugs, and therapies to counter Ebola virus. *Front Immunol* 2018;**9**:1803.

Dielschneider RF, Eisenstat H, Mi S *et al.* Lysosomotropic agents selectively target chronic lymphocytic leukemia cells due to altered sphingolipid metabolism. *Leukemia* 2016;**30**:1290–300.

Dong S, Yang P, Li G *et al.* Insight into the Ebola virus nucleocapsid assembly mechanism: crystal structure of Ebola virus nucleoprotein core domain at 1.8 Å resolution. *Protein Cell* 2015;**6**:351–62.

Dowall SD, Bosworth A, Watson R *et al.* Chloroquine inhibited ebola virus replication *in vitro* but failed to protect against infection and disease in the *in vivo* guinea pig model. *J Gen Virol* 2015;**96**:3484–92.

Dube D, Brecher MB, Delos SE *et al.* The Primed Ebolavirus Glycoprotein (19-Kilodalton GP1,2): Sequence and Residues Critical for Host Cell Binding. *J Virol* 2009;**83**:2883–91.

Dube D, Schornberg KL, Shoemaker CJ *et al.* Cell adhesion-dependent membrane trafficking of a binding partner for the ebolavirus glycoprotein is a determinant of viral entry. *Proc Natl Acad Sci U S A* 2010;**107**:16637–42.

Dunning J, Sahr F, Rojek A *et al.* Experimental Treatment of Ebola Virus Disease with TKM-130803: A Single-Arm Phase 2 Clinical Trial. *PLoS Med* 2016;**13**:1–19.

Duraffour S, Malvy D, Sissoko D. How to treat Ebola virus infections? A lesson from the field. *Curr Opin Virol* 2017;**24**:9–15.

De Duve C, De Barsy T, Poole B *et al.* Lysosomotropic agents. *Biochem Pharmacol* 1974;**23**;2495–2510.

Dyall J, Nelson EA, DeWald LE *et al.* Identification of Combinations of Approved Drugs With Synergistic Activity Against Ebola Virus in Cell Cultures. *J Infect Dis* 2018;**218**:S672–8.

Ekins S, Coffee M. FDA approved drugs as potential Ebola treatments. *F1000Research* 2015;**48**:1–9.

El-Saleh SC, Solaro RJ. Calmidazolium, a calmodulin antagonist, stimulates calcium-troponin C and calcium-calmodulin-dependent activation of striated muscle myofilaments. *J Biol Chem* 1987;**262**:17240–6.

Ellegaard AM, Dehlendorff C, Vind AC *et al.* Repurposing Cationic Amphiphilic Antihistamines for Cancer Treatment. *EBioMedicine* 2016;**9**:130–9.

Ellis DS, Simpson IH, Francis DP *et al.* Ultrastructure of Ebola virus particles in human liver. *J Clin Pathol* 1978;**31**:201–8.

Emergency International – Life Support for Civillian War Victims. (January 2015). *Facts, lies and tales about Ebola.* Retrieved from https://reliefweb.int/report/sierra-leone/facts-lies-and-tales-about-ebola.

Emond RT, Evans B, Bowen ET *et al.* A case of Ebola virus infection. *Br Med J* 1977;**2**:541–4.

Eriksson B, Helgstrand E, Johansson NG *et al.* Inhibition of influenza virus ribonucleic acid polymerase by ribavirin triphosphate. *Antimicrob Agents Chemother* 1977;**11**:946–51.

European Medicines Agency. (October 2014). *Speeding up development of Ebola treatments and vaccines.* Retrieved from https://www.ema.europa.eu/en/news/speeding-development-ebola-treatments-vaccines.

Ewer K, Rampling T, Venkatraman N *et al.* A Monovalent Chimpanzee Adenovirus Ebola Vaccine Boosted with MVA. *N Engl J Med* 2016;**374**:1635–46.

Falzarano D, Safronetz D, Prescott J *et al.* Lack of protection against ebola virus from chloroquine in mice and hamsters. *Emerg Infect Dis* 2015;**21**:1065–7.

Fan H, Du X, Zhang J *et al.* Selective inhibition of Ebola entry with selective estrogen receptor modulators by disrupting the endolysosomal calcium. *Sci Rep* 2017;**7**:41226.

Feldmann H, Sanchez A, Geisbert TW. 2013. Chapter 32 Filoviridae: Marburg and Eobla viruses. *Fields Virology*, 6th edition. Edited by David M. Knipe and Peter M. Howley. Philadelphia, PA, USA. Lippincott Williams & Wilkins, 2013.

Feng Z, Cerveny M, Yan Z *et al.* The VP35 Protein of Ebola Virus Inhibits the Antiviral Effect Mediated by Double-Stranded RNA-Dependent Protein Kinase PKR. *J Virol* 2006;**81**:182–92.

Fermini B, Ramirez DS, Sun S *et al.* L-type calcium channel antagonism – Translation from *in vitro* to *in vivo*. *J Pharmacol Toxicol Methods* 2017;**84**:86–92.

Fink SL, Vojtech L, Wagoner J *et al.* The Antiviral Drug Arbidol Inhibits Zika Virus. *Sci Rep* 2018;**8**:2–10.

Foo B, Williamson B, Young JC *et al.* hERG quality control and the long QT syndrome. *J Physiol* 2016;**594**:2469–81.

Formenty P, Boesch C, Wyers M *et al.* Ebola Virus Outbreak among Wild Chimpanzees Living in a Rain Forest of Cote d'Ivoire. *J Infect Dis* 1999;**179**:S120–6.

Fowler RA, Fletcher T, Fischer WA *et al.* Caring for critically ill patients with Ebola virus disease: Perspectives from West Africa. *Am J Respir Crit Care Med* 2014;**190**:733–7.

Foyouzi-Youssefi R, Arnaudeau S, Borner C *et al.* Bcl-2 decreases the free Ca^{2+} concentration within the endoplasmic reticulum. *Proc Natl Acad Sci U S A* 2000;**97**:5723–8.

Francica JR, Matukonis MK, Bates P. Requirements for cell rounding and surface protein down-regulation by Ebola virus glycoprotein. *Virology* 2009;**383**:237–47.

Friedland N, Liou H-L, Lobel P *et al.* Structure of a cholesterol-binding protein deficient in Niemann-Pick type C2 disease. *Proc Natl Acad Sci* 2003;**100**:2512–7.

Furuichi T, Cunningham KW, Muto S. A putative two pore channel AtTPC1 mediates Ca^{2+} flux in arabidopsis leaf cells. *Plant Cell Physiol* 2001;**42**:900–5.

Furuta Y, Gowen BB, Takahashi K *et al.* Favipiravir (T-705), a novel viral RNA polymerase inhibitor. *Antiviral Res* 2013;**100**:446–54.

Furuyama W, Marzi A, Nanbo A *et al.* Discovery of an antibody for pan-ebolavirus therapy. *Sci Rep* 2016;**6**:20514.

Galione A, Chuang KT, Funnell TM *et al.* Preparation and use of sea urchin egg homogenates for studying NAADP-mediated Ca^{2+} release. *Cold Spring Harb Protoc* 2014;**2014**:988–92.

Galione A, Morgan AJ, Arredouani A *et al.* NAADP as an intracellular messenger regulating lysosomal calcium-release channels. *Biochem Soc Trans* 2010;**38**:1424–31.

Gehring G, Rohrmann K, Atenchong N *et al.* The clinically approved drugs amiodarone, dronedarone and verapamil inhibit filovirus cell entry. *J Antimicrob Chemother* 2014;**69**:2123–31.

Geisbert TW, Daddario-DiCaprio KM, Geisbert JB *et al.* Vesicular stomatitis virus-based vaccines protect nonhuman primates against aerosol challenge with Ebola and Marburg viruses. *Vaccine* 2008a;**26**:6894–900.

Geisbert TW, Daddario-DiCaprio KM, Lewis MG *et al.* Vesicular stomatitis virus-based Ebola vaccine is well-tolerated and protects immunocompromised nonhuman primates. *PLoS Pathog* 2008b;**4**:e1000225.

Gerasimenko J V., Sherwood M, Tepikin A V. *et al.* NAADP, cADPR and IP3 all release Ca^{2+} from the endoplasmic reticulum and an acidic store in the secretory granule area. *J Cell Sci* 2006;**119**:226–38.

Gibb TR, Bray M, Geisbert TW *et al.* Pathogenesis of experimental Ebola Zaire virus infection in BALB/c mice. *J Comp Pathol* 2001;**125**:233–42.

Gnirß K, Kühl A, Karsten C *et al.* Cathepsins B and L activate Ebola but not Marburg virus glycoproteins for efficient entry into cell lines and macrophages independent of TMPRSS2 expression. *Virology* 2012;**424**:3–10.

Godley L, Pfeifer J, Steinhauer D *et al.* Introduction of intersubunit disulfide bonds in the membrane-distal region of the influenza hemagglutinin abolishes membrane fusion activity. *Cell* 1992;**68**:635–45.

Goldstein T, Anthony SJ, Gbakima A *et al.* The discovery of Bombali virus adds further support for bats as hosts of ebolaviruses. *Nat Microbiol* 2018;**3**:1084–9.

Gomis-Rüth FX, Dessen A, Timmins J *et al.* The matrix protein VP40 from Ebola virus octamerizes into pore-like structures with specific RNA binding properties. *Structure* 2003;**11**:423–33.

Gong X, Qian H, Zhou X *et al.* Structural insights into the Niemann-Pick C1 (NPC1)-mediated cholesterol transfer and ebola infection. *Cell* 2016;**165**:1467–78.

Goñi FM, Alonso A. Sphingomyelinases: Enzymology and membrane activity. *FEBS Lett* 2002;**531**:38–46.

Goodsell , D. (October 2014). Molecule of the Month. *Ebola Virus Proteins*. Retrieved from https://pdb101.rcsb.org/motm/178.

Gorelik A, Illes K, Heinz LX *et al.* Crystal structure of mammalian acid sphingomyelinase. *Nat Commun* 2016;**7**:1–9.

Govindaraj RG, Naderi M, Singha M *et al.* Large-scale computational drug repositioning to find treatments for rare diseases. *npj Syst Biol Appl* 2018;**4**:1–10.

Grant-Klein RJ, Van Deusen NM, Badger C V. *et al.* A multiagent filovirus DNA vaccine delivered by intramuscular electroporation completely protects mice from ebola and Marburg virus challenge. *Hum Vaccines Immunother* 2012;**8**:1703–6.

Grassmé H, Riehle A, Wilker B *et al.* Rhinoviruses infect human epithelial cells via ceramide-enriched membrane platforms. *J Biol Chem* 2005;**280**:26256–62.

Gregory SM, Harada E, Liang B *et al.* Structure and function of the complete internal fusion loop from Ebolavirus glycoprotein 2. *Proc Natl Acad Sci* 2011;**108**:11211–6.

Gregory SM, Larsson P, Nelson EA *et al.* Ebolavirus Entry Requires a Compact Hydrophobic Fist at the Tip of the Fusion Loop. *J Virol* 2014;**88**:6636–49.

van Griensven J, Edwards T, de Lamballerie X *et al.* Evaluation of Convalescent Plasma for Ebola Virus Disease in Guinea. *N Engl J Med* 2016;**374**:33–42.

Grimm C, Holdt LM, Chen C-C *et al.* High susceptibility to fatty liver disease in two-pore channel 2-deficient mice. *Nat Commun* 2014;**5**:4699.

Gruenke JA, Armstrong RT, Newcomb WW *et al.* New Insights into the Spring-Loaded Conformational Change of Influenza Virus Hemagglutinin. *J Virol* 2002;**76**:4456–66.

Gulbins E, Dreschers S, Wilker B *et al.* Ceramide, membrane rafts and infections. *J Mol Med* 2004;**82**:357–63.

Gunaratne GS, Johns ME, Hintz HM *et al.* A screening campaign in sea urchin egg homogenate as a platform for discovering modulators of NAADP-dependent Ca^{2+} signaling in human cells. *Cell Calcium* 2018a;**75**:42–52.

Gunaratne GS, Yang Y, Li F *et al.* NAADP-dependent Ca^{2+} signaling regulates Middle East respiratory syndrome-coronavirus pseudovirus translocation through the endolysosomal system. *Cell Calcium* 2018b;**75**:30–41.

Guo J, Zeng W, Chen Q *et al.* Structure of the voltage-gated two-pore channel TPC1 from Arabidopsis thaliana. *Nature* 2016;**531**:196–201.

Gupta-Wright A, Lavers J, Irvine S. Concerns about the off-licence use of amiodarone for Ebola. *BMJ* 2015;**350**:2015.

Halfmann P, Kim JH, Ebihara H *et al.* Generation of biologically contained Ebola viruses. *Proc Natl Acad Sci U S A* 2008;**105**:1129–33.

Harkin, T. (December 2014). 113th Congress (2013-2014). *S.2917-Adding Ebola to the FDA Priority Review Voucher Program Act.* Retrieved from https://www.congress.gov/bill/113th-congress/senate-bill/2917/text/173521.

Harrison JS, Higgins CD, Chandran K *et al.* Designed protein mimics of the Ebola virus glycoprotein GP2 α-helical bundle: Stability and pH effects. *Protein Sci* 2011;**20**:1587–96.

Hartlieb B, Muziol T, Weissenhorn W *et al.* Crystal structure of the C-terminal domain of Ebola virus VP30 reveals a role in transcription and nucleocapsid association. *Proc Natl Acad Sci* 2007;**104**:624–9.

Hashiguchi T, Fukuda Y, Matsuoka R *et al.* Structures of the prefusion form of measles virus fusion protein in complex with inhibitors. *Proc Natl Acad Sci* 2018;**115**:2496–2501.

Hashiguchi T, Fusco MLL, Bornholdt ZAA *et al.* Structural Basis for Marburg Virus Neutralization by a Cross-Reactive Human Antibody. *Cell* 2015;**160**:904–12.

Haviernik J, Štefánik M, Fojtíková M *et al.* Arbidol (Umifenovir): A broad-spectrum antiviral drug that inhibits medically important arthropod-borne flaviviruses. *Viruses* 2018;**10**:3–10.

He X, Dagan A, Gatt S *et al.* Simultaneous quantitative analysis of ceramide and sphingosine in mouse blood by naphthalene-2,3-dicarboxyaldehyde derivatization after hydrolysis with ceramidase. *Anal Biochem* 2005;**340**:113–22.

Head SA, Shi WQ, Yang EJ *et al.* Simultaneous targeting of NPC1 and VDAC1 by itraconazole leads to synergistic inhibition of MTOR signaling and angiogenesis. *ACS Chem Biol* 2017;**12**:174–82.

Henao-Restrepo AM, Camacho A, Longini IM *et al.* Efficacy and effectiveness of an rVSV-vectored vaccine in preventing Ebola virus disease: final results from the Guinea ring vaccination, open-label, cluster-randomised trial (Ebola Ça Suffit!). *Lancet* 2017;**389**:505–18.

Herbert AS, Davidson C, Kuehne AI *et al.* NPC1 is essential for Ebolavirus Replication and Pathogenesis *in vivo*. *MBio* 2015;**6**:1–12.

Hernandez JJ, Pryszlak M, Smith L *et al.* Giving Drugs a Second Chance: Overcoming Regulatory and Financial Hurdles in Repurposing Approved Drugs As Cancer Therapeutics. *Front Oncol* 2017;**7**:273.

Higgins ME, Davies JP, Chen FW *et al.* Niemann-pick C1 is a late endosome-resident protein that transiently associates with lysosomes and the trans-Golgi network. *Mol Genet Metab* 1999;**68**:1–13.

Hoffmann H-H, Kunz A, Simon V a *et al.* Broad-spectrum antiviral that interferes with de novo pyrimidine biosynthesis. *Proc Natl Acad Sci U S A* 2011;**108**:5777–82.

Höglinger D, Haberkant P, Aguilera-Romero A *et al.* Intracellular sphingosine releases calcium from lysosomes. *Elife* 2015;**4**:e10616.

Höglinger D, Nadler A, Haberkant P *et al.* Trifunctional lipid probes for comprehensive studies of single lipid species in living cells. *Proc Natl Acad Sci* 2017;**114**:1566–71.

Hood CL, Abraham J, Boyington JC *et al.* Biochemical and Structural Characterization of Cathepsin L-Processed Ebola Virus Glycoprotein: Implications for Viral Entry and Immunogenicity. *J Virol* 2010;**84**:2972–82.

Huang KYA, Rijal P, Jiang H *et al.* Structure–function analysis of neutralizing antibodies to H7N9 influenza from naturally infected humans. *Nat Microbiol* 2019;**4**:306–315.

Huotari J, Helenius A. Endosome maturation. *EMBO J* 2011;**30**:3481–3500.

Hurwitz R, Ferlinz K, Sandhofl K. The Tricyclic Antidepressant Desiprarnine Causes Proteolytic Degradation of Lysosomal Sphingomyelinase in Human Fibroblasts. *Biol Chem Hoppe Seyler* 1994;**375**:447–450.

Ishibashi K, Suzuki M, Imai M. Molecular cloning of a novel form (two-repeat) protein related to voltage-gated sodium and calcium channels. *Biochem Biophys Res Commun* 2000;**270**:370–6.

Ito H, Watanabe S, Sanchez A *et al.* Mutational analysis of the putative fusion domain of Ebola virus glycoprotein. *J Virol* 1999;**73**:8907–12.

Jahchan NS, Dudley JT, Mazur PK *et al.* A drug repositioning approach identifies tricyclic antidepressants as inhibitors of small cell lung cancer and other neuroendocrine tumors. *Cancer Discov* 2013;**3**:1364–77.

Jan J-T, Chatterjee S, Griffin DE. Sindbis Virus Entry into Cells Triggers Apoptosis by Activating Sphingomyelinase, Leading to the Release of Ceramide. *J Virol* 2002;**74**:6425–32.

Jeffers SA, Sanders DA, Sanchez A. Covalent Modifications of the Ebola Virus Glycoprotein. *J Virol* 2002;**76**:12463–72.

Jenkins RW, Canals D, Hannun YA. Roles and regulation of secretory and lysosomal acid sphingomyelinase. *Cell Signal* 2009;**21**:836–46.

Ji X, Olinger GG, Aris S *et al.* Mannose-binding lectin binds to Ebola and Marburg envelope glycoproteins, resulting in blocking of virus interaction with DC-SIGN and complement-mediated virus neutralization. *J Gen Virol* 2005;**86**:2535–42.

Jin H, Leser GP, Zhang J *et al.* Influenza virus hemagglutinin and neuraminidase cytoplasmic tails control particle shape. *EMBO J* 1997;**16**:1236–47.

Johansen LM, Brannan JM, Delos SE *et al.* FDA-Approved Selective Estrogen Receptor Modulators Inhibit Ebola Virus Infection. *Sci Transl Med* 2013;**5**:190ra79.

Johansen LM, Dewald LE, Shoemaker CJ *et al.* A screen of approved drugs and molecular probes identifies therapeutics with anti – Ebola virus activity. *Sci Transl Med* 2015;**7**:1–14.

Jones SM, Feldmann H, Ströher U *et al.* Live attenuated recombinant vaccine protects nonhuman primates against Ebola and Marburg viruses. *Nat Med* 2005;**11**:786–90.

Jurgeit A, McDowell R, Moese S *et al.* Niclosamide Is a Proton Carrier and Targets Acidic Endosomes with Broad Antiviral Effects. *PLoS Pathog* 2012;**8**:e1002976.

Kadam RU, Wilson IA. Structural basis of influenza virus fusion inhibition by the antiviral drug Arbidol. *Proc Natl Acad Sci* 2017;**114**:206–14.

Kaletsky RL, Simmons G, Bates P. Proteolysis of the Ebola virus glycoproteins enhances virus binding and infectivity. *J Virol* 2007;**81**:13378–84.

Kamiya K, Niwa R, Mitcheson JS *et al.* Molecular Determinants of hERG Channel Block. *Mol Pharmacol* 2006;**69**:1709–16.

Katsura H, Iwatsuki-Horimoto K, Fukuyama S *et al.* A replication-incompetent virus possessing an uncleavable hemagglutinin as an influenza vaccine. *Vaccine* 2012;**30**:6027–33.

Kaufmann AM, Krise JP. Lysosomal sequestration of amine-containing drugs: Analysis and therapeutic implications. *J Pharm Sci* 2007;**96**:729–46.

Kim JH, Johannes L, Goud B *et al.* Noninvasive measurement of the pH of the endoplasmic reticulum at rest and during calcium release. *Proc Natl Acad Sci* 1998;**95**:2997–3002.

Kim TW. Drug Repositioning Approaches for the Discovery of New Therapeutics for Alzheimer's Disease. *Neurotherapeutics* 2015;**12**:132–42.

Kindrachuk J, Wahl-Jensen V, Safronetz D *et al.* Ebola Virus Modulates Transforming Growth Factor β Signaling and Cellular Markers of Mesenchyme-Like Transition in Hepatocytes. *J Virol* 2014;**88**:9877–92.

Kintzer AF, Stroud RM. Structure, inhibition and regulation of two-pore channel TPC1 from Arabidopsis thaliana. *Nature* 2016;**531**:258–64.

Kirchhoff C, Osterhoff C, L. Y. Molecular cloning and characterization of HE1, a major secretory protein of the human epididymis. *Biol Reprod* 2005;**54**:847–56.

Klug DM, Gelb MH, Pollastri MP. Repurposing strategies for tropical disease drug discovery. *Bioorganic Med Chem Lett* 2016;**26**:2569–76.

Kneen M, Farinas J, Li Y *et al.* Green fluorescent protein as a noninvasive intracellular pH indicator. *Biophys J* 1998;**74**:1591–9.

Knott G, Doudna J. CRISPR-Cas guides the future of genetic engineering. *Science* 2018;**361**:1–4.

Ko DC, Binkley J, Sidow A *et al.* The integrity of a cholesterol-binding pocket in Niemann-Pick C2 protein is necessary to control lysosome cholesterol levels. *Proc Natl Acad Sci* 2003;**100**:2518–25.

Ko DC, Gordon MD, Jin JY *et al.* Dynamic movements of organelles containing Niemann-Pick C1 protein: NPC1 involvement in late endocytic events. *Mol Biol Cell* 2001;**12**:601–14.

Kölzer M, Werth N, Sandhoff K. Interactions of acid sphingomyelinase and lipid bilayers in the presence of the tricyclic antidepressant desipramine. *FEBS Lett* 2004;**559**:96–8.

Konde MK, Baker DP, Traore FA *et al.* Interferon β-1a for the treatment of Ebola virus disease: A historically controlled, single-arm proof-of-concept trial. *PLoS One* 2017;**12**:1–13.

Kondoh T, Letko M, Munster VJ *et al.* Single-Nucleotide Polymorphisms in Human NPC1 Influence Filovirus Entry Into Cells. *J Infect Dis* 2018;**218**:S397-S402.

Kondratowicz AS, Lennemann NJ, Sinn PL *et al.* T-cell immunoglobulin and mucin domain 1 (TIM-1) is a receptor for Zaire Ebolavirus and Lake Victoria Marburgvirus. *Proc Natl Acad Sci* 2011;**108**:8426–31.

Kornhuber J, Henkel AW, Groemer TW *et al.* Lipophilic cationic drugs increase the permeability of lysosomal membranes in a cell culture system. *J Cell Physiol* 2010a;**224**:152–64.

Kornhuber J, Muehlbacher M, Trapp S *et al.* Identification of Novel Functional Inhibitors of Acid Sphingomyelinase. *PLoS One* 2011;**6**:e23852.

Kornhuber J, Tripal P, Reichel M *et al.* Identification of new functional inhibitors of acid sphingomyelinase using a structure-property-activity relation model. *J Med Chem* 2008;**51**:219–37.

Kornhuber J, Tripal P, Reichel M *et al.* Functional inhibitors of acid sphingomyelinase (FIASMAS): A novel pharmacological group of drugs with broad clinical applications. *Cell Physiol Biochem* 2010b;**26**:9–20.

Kouznetsova J, Sun W, Martínez-Romero C *et al.* Identification of 53 compounds that block Ebola virus-like particle entry via a repurposing screen of approved drugs. *Emerg Microbes Infect* 2014;**3**:e84.

Krishnan A, Miller EH, Herbert AS *et al.* Niemann-Pick C1 (NPC1)/NPC1-like1 chimeras define sequences critical for NPC1's function as a filovirus entry receptor. *Viruses* 2012;**4**:2471–84.

Kroemer G, Jäättelä M. Lysosomes and autophagy in cell death control. *Nat Rev Cancer* 2005;**5**:886–97.

Kruth HS, Comly ME, Butler JD *et al.* Type C Niemann-Pick disease. Abnormal metabolism of low density lipoprotein in homozygous and heterozygous fibroblasts. *J Biol Chem* 1986;**261**:16769–74.

Kuhn JH, Adachi T, Adhikari NKJ *et al.* New filovirus disease classification and nomenclature. *Nat Rev Microbiol* 2019;**17**:261–3.

Kuhn JH, Bavari S. Asymptomatic Ebola virus infections—myth or reality? *Lancet Infect Dis* 2017;**17**:570–1.

Kuroda M, Fujikura D, Nanbo A *et al.* Interaction between TIM-1 and NPC1 Is Important for Cellular Entry of Ebola Virus. *J Virol* 2015;**89**:6481–93.

Kuzu OF, Toprak M, Noory MA *et al.* Effect of lysosomotropic molecules on cellular homeostasis. *Pharmacol Res* 2017;**117**:177–84.

de La Vega M-A, Wong G, Kobinger GP *et al.* The Multiple Roles of sGP in Ebola Pathogenesis. *Viral Immunol* 2014;**28**:3–9.

Lachmann RH, Te Vruchte D, Lloyd-Evans E *et al.* Treatment with miglustat reverses the lipid-trafficking defect in Niemann-Pick disease type C. *Neurobiol Dis* 2004;**16**:654–8.

Lakdawala SS, Fodor E, Subbarao K. Moving On Out: Transport and Packaging of Influenza Viral RNA into Virions. *Annu Rev Virol* 2016;**3**:411–27.

Landry JJM, Pyl PT, Rausch T *et al.* The Genomic and Transcriptomic Landscape of a HeLa Cell Line. *Genes*|*Genomes*|*Genetics* 2013;**3**:1213–24.

Langer M, Portella G, Finazzi S *et al.* Intensive care support and clinical outcomes of patients with Ebola virus disease (EVD) in West Africa. *Intensive Care Med* 2018;**44**:1266–75.

Larson RA, Dai D, Hosack VT *et al.* Identification of a Broad-Spectrum Arenavirus Entry Inhibitor. *J Virol* 2008;**82**:10768–75.

Ledgerwood JE, DeZure AD, Stanley D a *et al.* Chimpanzee Adenovirus Vector Ebola Vaccine. *N Engl J Med* 2017;**376**:928–938.

Lee J, Kim MS, Kim MA *et al.* Calmidazolium chloride inhibits growth of murine embryonal carcinoma cells, a model of cancer stem-like cells. *Toxicol Vitr* 2016;**35**:86–92.

Lee J, Nyenhuis DA, Nelson EA *et al.* Structure of the Ebola virus envelope protein MPER/TM domain and its interaction with the fusion loop explains their fusion activity. *Proc Natl Acad Sci* 2017;**114**:E7987–96.

Lee JE, Fusco ML, Hessell AJ *et al.* Structure of the Ebola virus glycoprotein bound to an antibody from a human survivor. *Nature* 2008;**454**:177–82.

Lee JE, Saphire EO. Ebolavirus glycoprotein structure and mechanism of entry. *Future Virol* 2009;**4**:621–635.

Lee PS, Zhu X, Yu W *et al.* Design and Structure of an Engineered Disulfide-Stabilized Influenza Virus Hemagglutinin Trimer. *J Virol* 2015;**89**:7417–20.

Lemieux B, Percival MD, Falgueyret JP. Quantitation of the lysosomotropic character of cationic amphiphilic drugs using the fluorescent basic amine Red DND-99. *Anal Biochem* 2004;**327**:247–51.

Leneva IA, Russell RJ, Boriskin YS *et al.* Characteristics of arbidol-resistant mutants of influenza virus: Implications for the mechanism of anti-influenza action of arbidol. *Antiviral Res* 2009;**81**:132–40.

Leroy EM, Baize S, Volchkov VE *et al.* Human asymptomatic Ebola infection and strong inflammatory response. *Lancet* 2000;**355**:2210–5.

Leroy EM, Kumulungui B, Pourrut X *et al.* Fruit bats as reservoirs of Ebola virus. *Nature* 2005;**438**:575–6.

Leung DW, Ginder ND, Fulton DB *et al.* Structure of the Ebola VP35 interferon inhibitory domain. *Proc Natl Acad Sci* 2009;**106**:411–6.

Li D, Chen T, Hu Y *et al.* An ebola virus-like particle-based reporter system enables evaluation of antiviral drugs *in vivo* under non-biosafety level 4 conditions . *J Virol* 2016;**90**:8720–8.

Lin G, Simmons G, Pöhlmann S *et al.* Differential N-linked glycosylation of human immunodeficiency virus and Ebola virus envelope glycoproteins modulates interactions with DC-SIGN and DC-SIGNR. *J Virol* 2003;**77**:1337–46.

Linden WA Van Der, Schulze CJ, Herbert AS *et al.* Cysteine Cathepsin Inhibitors as Anti-Ebola Agents. 2016;**2**:173–9.

Liscum L. Niemann-Pick type C mutations cause lipid traffic jam. *Traffic* 2000;**1**:218–25.

Liscum L, Ruggiero RM, Faust JR. The intracellular transport of low density lipoprotein-derived cholesterol is defective in Niemann-Pick type C fibroblasts. *J Cell Biol* 1989;**108**:1625–36.

Liu S, Neidhardt EA, Grossman TH *et al.* Structures of human dihydroorotate dehydrogenase in complex with antiproliferative agents. *Structure* 2000;**8**:25–33.

Lloyd-Evans E, Morgan AJ, He X *et al.* Niemann-Pick disease type C1 is a sphingosine storage disease that causes deregulation of lysosomal calcium. *Nat Med* 2008;**14**:1247–55.

Loftus SK, Morris JA, Carstea ED *et al.* in a Cholesterol Homeostasis Gene Murine Model of Niemann-Pick C Disease : Mutation in a Cholesterol Homeostasis Gene. 2008;**232**:232–6.

Logan R, Kong AC, Axcell E *et al.* Amine-containing molecules and the induction of an expanded lysosomal volume phenotype: A structure-activity relationship study. *J Pharm Sci* 2014;**103**:1572–80.

Long J, Wright E, Molesti E *et al.* Antiviral therapies against Ebola and other emerging viral diseases using existing medicines that block virus entry. *F1000Research* 2015;**4**:30.

Lonowski LA, Narimatsu Y, Riaz A *et al.* Genome editing using FACS enrichment of nuclease-expressing cells and indel detection by amplicon analysis. *Nat Protoc* 2017;**12**:581–603.

Lounkine E, Keiser MJ, Whitebread S *et al.* Large Scale Prediction and Testing of Drug Activity on Side- Effect Targets. *Nature* 2012;**486**:361–7.

Lu F, Liang Q, Abi-Mosleh L *et al.* Identification of NPC1 as the target of U18666A, an inhibitor of lysosomal cholesterol export and Ebola infection. Tontonoz P (ed.). *Elife* 2015;**4**:1–16.

Lu S, Sung T, Lin N *et al.* Lysosomal adaptation: How cells respond to lysosomotropic compounds. *PLoS One* 2017;**12**:1–22.

Lucas-Hourani M, Dauzonne D, Jorda P *et al.* Inhibition of pyrimidine biosynthesis pathway suppresses viral growth through innate immunity. *PLoS Pathog* 2013;**9**:e1003678.

Lupton HW, Lambert RD, Bumgardner DL *et al.* Inactivated vaccine for Ebola virus efficacious in guinea pig model. *Lancet* 1980;**2**:1294–5.

Luzio JP, Bright NA, Pryor PR. The role of calcium and other ions in sorting and delivery in the late endocytic pathway. *Biochem Soc Trans* 2007;**35**:1088–91.

Luzio JP, Hackmann Y, Dieckmann NMG *et al.* The biogenesis of lysosomes and lysosome-related organelles. *Cold Spring Harb Perspect Biol* 2014;**6**:a016840.

Lyu J, Yang EJ, Head SA *et al.* Pharmacological blockade of cholesterol trafficking by cepharanthine in endothelial cells suppresses angiogenesis and tumor growth. *Cancer Lett* 2017;**409**:91–103.

Lyu J, Yang EJ, Head SA *et al.* Astemizole Inhibits mTOR Signaling and Angiogenesis by Blocking Cholesterol Trafficking. *Int J Biol Sci* 2018;**14**:1175–85.

Madrid PB, Chopra S, Manger ID *et al.* A systematic screen of FDA-approved drugs for inhibitors of biological threat agents. *PLoS One* 2013;**8**:e60579.

Madrid PB, Panchal RG, Warren TK *et al.* Evaluation of Ebola Virus Inhibitors for Drug Repurposing. *ACS Infect Dis* 2015;**1**:317–26.

Malashkevich VN, Schneider BJ, McNally ML *et al.* Core structure of the envelope glycoprotein GP2 from Ebola virus at 1.9-A resolution. *Proc Natl Acad Sci U S A* 1999;**96**:2662–7.

Marceau F, Bawolak MT, Lodge R *et al.* Cation trapping by cellular acidic compartments: Beyond the concept of lysosomotropic drugs. *Toxicol Appl Pharmacol* 2012;**259**:1–12.

Markosyan RM, Miao C, Zheng YM *et al.* Induction of Cell-Cell Fusion by Ebola Virus Glycoprotein: Low pH Is Not a Trigger. *PLoS Pathog* 2016;**12**:e1005373.

Martines RB, Ng DL, Greer PW *et al.* Tissue and cellular tropism, pathology and pathogenesis of Ebola and Marburg Viruses. *J Pathol* 2014;**235**:153–74.

Martínez-Sobrido L, Cadagan R, Steel J *et al.* Hemagglutinin-Pseudotyped Green Fluorescent Protein-Expressing Influenza Viruses for the Detection of Influenza Virus Neutralizing Antibodies. *J Virol* 2010;**84**:2157–63.

Maruyama T, Rodriguez LL, Jahrling PB *et al.* Ebola Virus Can Be Effectively Neutralized by Antibody Produced in Natural Human Infection. *J Virol* 1999;**73**:6024–30.

Marzi A, Gramberg T, Simmons G *et al.* DC-SIGN and DC-SIGNR interact with the glycoprotein of Marburg virus and the S protein of severe acute respiratory syndrome coronavirus. *J Virol* 2004;**78**:12090–5.

Marzi A, Reinheckel T, Feldmann H. Cathepsin B & L Are Not Required for Ebola Virus Replication. *PLoS Negl Trop Dis* 2012;**6**:e1923.

Marzi A, Robertson SJ, Haddock E *et al.* VSV-EBOV rapidly protects macaques against infection with the 2014/15 Ebola virus outbreak strain. *Science* 2015;**349**:739–42.

Matrosovich M, Matrosovich T, Carr J *et al.* Overexpression of the alpha-2,6-Sialyltransferase in MDCK Cells Increases Influenza Virus Sensitivity to Neuraminidase Inhibitors. *J Virol* 2003;**77**:8418–25.

McLean JE, Neidhardt EA, Grossman TH *et al.* Multiple inhibitor analysis of the brequinar and leflunomide binding sites on human dihydroorotate dehydrogenase. *Biochemistry* 2001;**40**:2194–200.

Mehdi S. Cell-penetrating inhibitors of calpain. *Trends Biochem Sci* 1991;**16**:150–3.

Mehedi M, Falzarano D, Seebach J *et al.* A New Ebola Virus Nonstructural Glycoprotein Expressed through RNA Editing. *J Virol* 2011;**85**:5406–14.

Melikyan GB, Lin S, Roth MG *et al.* Amino acid sequence requirements of the transmembrane and cytoplasmic domains of influenza virus hemagglutinin for viable membrane fusion. *Mol Biol Cell* 1999;**10**:1821–36.

Melikyan GB, Markosyan RM, Roth MG *et al.* A Point Mutation in the Transmembrane Domain of the Hemagglutinin of Influenza Virus Stabilizes a Hemifusion Intermediate That Can Transit to Fusion. *Mol Biol Cell* 2000;**11**:3765–75.

Messaoudi I, Amarasinghe GK, Basler CF. Filovirus pathogenesis and immune evasion: Insights from Ebola virus and Marburg virus. *Nat Rev Microbiol* 2015;**13**:663–76.

Miller EH, Obernosterer G, Raaben M *et al.* Ebola virus entry requires the host-programmed recognition of an intracellular receptor. *EMBO J* 2012a;**31**:1947–60.

Miller ME, Adhikary S, Kolokoltsov AA *et al.* Ebolavirus Requires Acid Sphingomyelinase Activity and Plasma Membrane Sphingomyelin for Infection. *J Virol* 2012b;**86**:7473–83.

Milligan JC, Parekh D V., Fuller KM *et al.* Structural Characterization of Pan-Ebolavirus Antibody 6D6 Targeting the Fusion Peptide of the Surface Glycoprotein. *J Infect Dis* 2019;**219**:415–9.

Misasi J, Chandran K, Yang J-Y *et al.* filoviruses require endosomal cysteine proteases for entry but exhibit distinct protease preferences. *J Virol* 2012;**86**:3284–92.

Misasi J, Gilman MSAA, Kanekiyo M *et al.* Structural and molecular basis for Ebola virus neutralization by protective human antibodies. *Science* 2016;**351**:1343–6.

Modrof J, Becker S, Muhlberger E. Ebola Virus Transcription Activator VP30 Is a Zinc-Binding Protein. *J Virol* 2003;**77**:3334–8.

Mohan GS, Ye L, Li W *et al.* Less Is More: Ebola Virus Surface Glycoprotein Expression Levels Regulate Virus Production and Infectivity. *J Virol* 2015;**89**:1205–17.

Molecular Biology Institute, UCLA. Model Building/Graphics. *Structural Molecular Biology Laboratory, ChemM230D.* Retrieved from: http://people.mbi.ucla.edu/sawaya/m230d/Modelbuilding/modelbuilding.html.

Morgan AJ. Ca^{2+} dialogue between acidic vesicles and ER. *Biochem Soc Trans* 2016;**44**:546–53.

Morgan AJ, Galione A. Two-pore channels (TPCs): Current controversies. *BioEssays* 2014;**36**:173–83.

Morgan AJ, Platt FM, Lloyd-Evans E *et al.* Molecular mechanisms of endolysosomal Ca^{2+} signalling in health and disease. *Biochem J* 2011;**439**:349–78.

Mulherkar N, Raaben M, de la Torre JC *et al.* The Ebola virus glycoprotein mediates entry via a non-classical dynamin-dependent macropinocytic pathway. *Virology* 2011;**419**:72–83.

Mupapa K, Massamba M, Kibadi K *et al.* Treatment of Ebola hemorrhagic fever with blood transfusions from convalescent patients. International Scientific and Technical Committee. *J Infect Dis* 1999;**179**:S18–23.

Murin CD, Fusco ML, Bornholdt ZA *et al.* Structures of protective antibodies reveal sites of vulnerability on Ebola virus. *Proc Natl Acad Sci* 2014;**111**:17182–7.

Nadanaciva S, Lu S, Gebhard DF *et al.* A high content screening assay for identifying lysosomotropic compounds. *Toxicol Vitr* 2010;**25**:715–23.

Nagata T, Lefor AK, Hasegawa M *et al.* Favipiravir: A new medication for the Ebola Virus disease pandemic. *Disaster Med Public Health Prep* 2015;**9**:79–81.

Nanbo A, Imai M, Watanabe S *et al.* Ebolavirus is internalized into host cells via macropinocytosis in a viral glycoprotein-dependent manner. *PLoS Pathog* 2010;**6**:e1001121.

Nature Medicine. Rationalizing combination therapies. *Nat Med* 2017;**23**:1113.

Naureckiene S, Sleat DE, Lacklan H *et al.* Identification of HE1 as the second gene of Niemann-Pick C disease. *Science* 2000;**290**:2298–301.

Nayak DP, Hui EKW, Barman S. Assembly and budding of influenza virus. *Virus Res* 2004;**106**:147–65.

Naylor E, Arredouani A, Vasudevan SR *et al.* Identification of a chemical probe for NAADP by virtual screening. *Nat Chem Biol* 2009;**5**:220–6.

Ndungo E, Herbert AS, Raaben M *et al.* A single residue in Ebola virus receptor NPC1 influences cellular host range in reptiles. *mSphere* 2016;**1**:e00007–16.

Neufeld EB, Wastney M, Patel S *et al.* The Niemann-Pick C1 protein resides in a vesicular compartment linked to retrograde transport of multiple lysosomal cargo. *J Biol Chem* 1999;**274**:9627–35.

Ng CG, Griffin DE. Acid Sphingomyelinase Deficiency Increases Susceptibility to Fatal Alphavirus Encephalomyelitis. *J Virol* 2006;**80**:10989–99.

Ng M, Ndungo E, Kaczmarek ME *et al.* Filovirus receptor NPC1 contributes to species-specific patterns of ebolavirus susceptibility in bats. *Elife* 2015;**4**:1–22.

Nguyen JT, Hoopes JD, Le MH *et al.* Triple combination of amantadine, ribavirin, and oseltamivir is highly active and synergistic against drug resistant influenza virus strains *in vitro*. *PLoS One* 2010;**5**:e9332.

Oestereich L, Lüdtke A, Wurr S *et al.* Successful treatment of advanced Ebola virus infection with T-705 (favipiravir) in a small animal model. *Antiviral Res* 2014;**105**:17–21.

Ohimain EI. Recent advances in the development of vaccines for Ebola virus disease. *Virus Res* 2016;**211**:174–85.

Olival KJ, Hayman DTS. Filoviruses in bats: Current knowledge and future directions. *Viruses* 2014;**6**:1759–88.

Oprea TI, Mestres J. Drug Repurposing: Far Beyond New Targets for Old Drugs. *AAPS J* 2012;**14**:759–63.

Orlich M, Linder D, Rott R. Trypsin-resistant protease activation mutants of an influenza virus. *J Gen Virol* 1995;**76**:625–33.

Ostenfeld MS, Høyer-Hansen M, Bastholm L *et al.* Anti-cancer agent siramesine is a lysosomotropic detergent that induces cytoprotective autophagosome accumulation. *Autophagy* 2008;**4**:487–99.

Pafumi I, Festa M, Papacci F *et al.* Naringenin Impairs Two-Pore Channel 2 Activity And Inhibits VEGF-Induced Angiogenesis. *Sci Rep* 2017;**7**:1–11.

Pascal KE, Dudgeon D, Trefry JC *et al.* Development of Clinical-Stage Human Monoclonal Antibodies That Treat Advanced Ebola Virus Disease in Nonhuman Primates. *J Infect Dis* 2018;**218**:S612–26.

Patel S, Cai X. Evolution of acidic Ca^{2+} stores and their resident Ca^{2+}-permeable channels. *Cell Calcium* 2015;**57**:222–30.

Patel S, Kilpatrick BS. Two-pore channels and disease. *Biochim Biophys Acta - Mol Cell Res* 2018;**1865**:1678–86.

Pécheur E-I, Borisevich V, Halfmann P *et al.* The synthetic antiviral drug arbidol inhibits globally prevalent pathogenic viruses. *J Virol* 2016;**90**:3086–92.

Penny CJ, Vassileva K, Jha A *et al.* Mining of Ebola virus entry inhibitors identifies approved drugs as two-pore channel pore blockers. *Biochim Biophys Acta - Mol Cell Res* 2018;**1866**:1151–61.

Pentchev PG, Comly ME, Kruth HS *et al.* A defect in cholesterol esterification in Niemann-Pick disease (type C) patients. *Proc Natl Acad Sci U S A* 1985;**82**:8247–51.

Perry M. Drug Binding Interactions in the Inner Cavity of hERG Channels: Molecular Insights from Structure-Activity Relationships of Clofilium and Ibutilide Analogs. *Mol Pharmacol* 2006;**69**:509–19.

Petersen NHT, Olsen OD, Groth-Pedersen L *et al.* Transformation-Associated Changes in Sphingolipid Metabolism Sensitize Cells to Lysosomal Cell Death Induced by Inhibitors of Acid Sphingomyelinase. *Cancer Cell* 2013;**24**:379–93.

Pigott DM, Golding N, Mylne A *et al.* Mapping the zoonotic niche of Ebola virus disease in Africa. *Elife* 2014;**3**:e04395.

Platt FM, Boland B, van der Spoel AC. Lysosomal storage disorders: The cellular impact of lysosomal dysfunction. *J Cell Biol* 2012;**199**:723–34.

Platt FM, D'Azzo A, Davidson BL *et al.* Lysosomal storage diseases. *Nat Rev Dis Prim* 2018;**4**:27.

Plemper RK, Erlandson KJ, Lakdawala AS *et al.* A target site for template-based design of measles virus entry inhibitors. *Proc Natl Acad Sci* 2004;**101**:5628–33.

Powell TJ, Rijal P, McEwen-Smith RM *et al.* A single cycle influenza virus coated in H7 haemagglutinin generates neutralizing antibody responses to haemagglutinin and neuraminidase glycoproteins and protection from heterotypic challenge. *J Gen Virol* 2019;**100**:431–445.

Powell TJ, Silk JD, Sharps J *et al.* Pseudotyped Influenza A Virus as a Vaccine for the induction of Heterotypic Immunity. *J Virol* 2012;**86**:13397–406.

Prins KC, Binning JM, Shabman RS *et al.* Basic Residues within the Ebolavirus VP35 Protein Are Required for Its Viral Polymerase Cofactor Function. *J Virol* 2010;**84**:10581–91.

Pryor PR, Luzio JP. Delivery of endocytosed membrane proteins to the lysosome. *Biochim Biophys Acta - Mol Cell Res* 2009;**1793**:615–24.

Pryor PR, Mullock BM, Bright NA *et al.* The role of intraorganellar Ca^{2+} in late endosome-lysosome heterotypic fusion and in the reformation of lysosomes from hybrid organelles. *J Cell Biol* 2000;**149**:1053–62.

Qiu X, Wong G, Audet J *et al.* Reversion of advanced Ebola virus disease in nonhuman primates with ZMapp. *Nature* 2014;**514**:47–53.

Quinn K, Brindley MA, Weller ML *et al.* Rho GTPases Modulate Entry of Ebola Virus and Vesicular Stomatitis Virus Pseudotyped Vectors. *J Virol* 2009;**83**:10176–86.

Rahman T, Cai X, Brailoiu GC *et al.* Two-pore channels provide insight into the evolution of voltage-gated Ca^{2+} and Na^{+} channels. *Sci Signal* 2014;**7**:ra109.

Rajamuthiah R, Fuchs BB, Conery AL *et al.* Repurposing salicylanilide anthelmintic drugs to combat drug resistant Staphylococcus aureus. *PLoS One* 2015;**10**:1–19.

Ran FA, Hsu PD, Wright J *et al.* Genome engineering using the CRISPR-Cas9 system. *Nat Protoc* 2013;**8**:2281–308.

Reed LJ, Muench H. A simple method of estimating fifty per cent endpoints. *Am J Epidemiol* 1938;**27**:493–7.

Regula LK, Harris R, Wang F *et al.* Conformational properties of peptides corresponding to the ebolavirus GP2 membrane-proximal external region in the presence of micelle-forming surfactants and lipids. *Biochemistry* 2013;**52**:3393–3404.

Regules JA, Beigel JH, Paolino KM *et al.* A Recombinant Vesicular Stomatitis Virus Ebola Vaccine. *N Engl J Med* 2017;**376**:330–341.

Ren J, Zhao Y, Fry EE *et al.* Target Identification and Mode of Action of Four Chemically Divergent Drugs against Ebolavirus Infection. *J Med Chem* 2018;**61**:724–33.

Rietdorf K, Funnell TM, Ruas M *et al.* Two-pore Channels Form Homo- and Heterodimers. *J Biol Chem* 2011;**286**:37058–62.

Rijal P, Elias SC, Machado SR *et al.* Therapeutic Monoclonal Antibodies for Ebola Virus Infection Derived from Vaccinated Humans. *Cell Rep* 2019;**27**:172–86.

Rinkenberger N, Schoggins JW. Mucolipin-2 Cation Channel Increases Trafficking Efficiency of Endocytosed Viruses. *MBio* 2018;**9**:1–16.

Rodriguez-Lafrasse C, Rousson R, Bonnet J *et al.* Abnormal cholesterol metabolism in imipramine-treated fibroblast cultures. Similarities with Niemann-Pick type C disease. *Biochim Biophys Acta (BBA)/Lipids Lipid Metab* 1990;**1043**:123–8.

Rouquet P, Froment JM, Bermejo M *et al.* Wild animal mortality monitoring and human ebola outbreaks, Gabon and Republic of Congo, 2001-2003. *Emerg Infect Dis* 2005;**11**:283–90.

Rowe T, Abernathy RA, Hu-Primmer J *et al.* Detection of antibody to avian influenza A (H5N1) virus in human serum by using a combination of serologic assays. *J Clin Microbiol* 1999;**37**:937–43.

Ruas M, Chuang K-T, Davis LC *et al.* TPC1 has two variant isoforms, and their removal has different effects on endo-lysosomal functions compared to loss of TPC2. *Mol Cell Biol* 2014;**34**:3981–92.

Ruas M, Lianne CD, Chen C *et al.* Expression of Ca^{2+}-permeable two-pore channels rescues NAADP signalling in TPC-deficient cells. *EMBO J* 2015;**34**:1743–58.

Ruiz-Arguello MB, Goni FM, Pereira FB *et al.* Phosphatidylinositol-Dependent Membrane Fusion Induced by a Putative Fusogenic Sequence of Ebola Virus. *J Virol* 1998;**72**:1775–81.

Saeed MF, Kolokoltsov AA, Albrecht T *et al.* Cellular Entry of Ebola Virus Involves Uptake by a Macropinocytosis-Like Mechanism and Subsequent Trafficking through Early and Late Endosomes. *PLoS Pathog* 2010;**6**:e1001110.

Saeed MF, Kolokoltsov AA, Freiberg AN *et al.* Phosphoinositide-3 kinase-akt pathway controls cellular entry of ebola virus. *PLoS Pathog* 2008;**4**:e1000141.

Sahr F, Ansumana R, Massaquoi TA *et al.* Evaluation of convalescent whole blood for treating Ebola Virus Disease in Freetown, Sierra Leone. *J Infect* 2017;**74**:302–9.

Sakurai Y, Kolokoltsov A a., Chen C-CC *et al.* Two-pore channels control Ebola virus host cell entry and are drug targets for disease treatment. *Science* 2015;**347**:995–8.

Salata C, Baritussio A, Munegato D *et al.* Amiodarone and metabolite MDEA inhibit Ebola virus infection by interfering with the viral entry process. *Pathog Dis* 2015;**73**:1–9.

Salata C, Calistri A, Alvisi G *et al.* Ebolavirus Entry : From Molecular Characterization to Drug Discovery. 2019;**11**;E274.

Salata C, Calistri A, Parolin C *et al.* Antiviral activity of cationic amphiphilic drugs. *Expert Rev Anti Infect Ther* 2017;**15**:483–92.

Samuel M, Winston A, Peters B. Drug treatment for adults with HIV infection. *BMJ* 2015;**350**:h1555.

Sanchez A, Trappier SG, Mahy BW *et al.* The virion glycoproteins of Ebola viruses are encoded in two reading frames and are expressed through transcriptional editing. *Proc Natl Acad Sci* 2002;**93**:3602–7.

Sandgren KJ, Wilkinson J, Miranda-Saksena M *et al.* A differential role for macropinocytosis in mediating entry of the two forms of vaccinia virus into dendritic cells. *PLoS Pathog* 2010;**6**:e1000866.

Sandtner W, Egwolf B, Khalili-Araghi F *et al.* Ouabain binding site in a functioning Na^+/K^+ ATPase. *J Biol Chem* 2011;**286**:38177-83.

Sanguinetti MC, Tristani-Firouzi M. hERG potassium channels and cardiac arrhythmia. *Nature* 2006;**440**:463–9.

Saphire EO, Schendel SL, Fusco ML *et al.* Systematic Analysis of Monoclonal Antibodies against Ebola Virus GP Defines Features that Contribute to Protection. *Cell* 2018;**174**:938–952.e13.

Sarkar K, Kruhlak MJ, Erlandsen SL *et al.* Selective inhibition by rottlerin of macropinocytosis in monocyte-derived dendritic cells. *Immunology* 2005;**116**:513–24.

Saxena P, Hortigon-Vinagre MP, Beyl S *et al.* Correlation between human ether-a-go-go-related gene channel inhibition and action potential prolongation. *Br J Pharmacol* 2017;**174**:3081–93.

Schieder M, Rötzer K, Brüggemann A *et al.* Characterization of two-pore channel 2 (TPCN2)-mediated Ca^{2+} currents in isolated lysosomes. *J Biol Chem* 2010;**285**:21219–22.

Schnittler H, Feldmann H. Marburg and Ebola Hemorrhagic Fevers: Does the Primary Course of Infection Depend on the Accessibility of Organ-Specific Macrophages? *Clin Infect Dis* 2009;**27**:404–6.

Schornberg K, Matsuyama S, Kabsch K *et al.* Role of Endosomal Cathepsins in Entry Mediated by the Ebola Virus Glycoprotein Role of Endosomal Cathepsins in Entry Mediated by the Ebola Virus Glycoprotein. *J Virol* 2006;**80**:4174–8.

Schuchman EH. The pathogenesis and treatment of acid sphingomyelinase-deficient Niemann-Pick disease. *J Inherit Metab Dis* 2007;**30**:654–63.

Schuchman EH, Levran O, Pereira L V. *et al.* Structural organization and complete nucleotide sequence of the gene encoding human acid sphingomyelinase (SMPD1). *Genomics* 1992;**12**:197–205.

Schuchman EH, Suchi M, Takahashi T *et al.* Human acid sphingomyelinase: Isolation, nucleotide sequence, and expression of the full-length and alternatively spliced cDNAs. *J Biol Chem* 1991;**266**:8531–9.

Shah P, Wang T, Kaletsky R. A small-molecule oxocarbazate inhibitor of human cathepsin L blocks severe acute respiratory syndrome and ebola pseudotype virus infection into human embryonic. *Mol Pharmacol* 2010;**78**:319–24.

Shaikh F, Zhao Y, Alvarez L *et al.* Structure-based In Silico Screening Identifies a Potent Ebolavirus Inhibitor from a Traditional Chinese Medicine Library. *J Med Chem* 2019;**62**:2928–37.

Shchors K, Massaras A, Hanahan D. Dual Targeting of the Autophagic Regulatory Circuitry in Gliomas with Repurposed Drugs Elicits Cell-Lethal Autophagy and Therapeutic Benefit. *Cancer Cell* 2015;**28**:456–471.

She J, Guo J, Chen Q *et al.* Structural insights into the voltage and phospholipid activation of the mammalian TPC1 channel. *Nature* 2018;**556**:130–4.

Shedlock DJ, Aviles J, Talbott KT *et al.* Induction of broad cytotoxic T cells by protective DNA vaccination against Marburg and Ebola. *Mol Ther* 2013;**21**:1432–44.

Shi Y, Wu Y, Zhang W *et al.* Enabling the “host jump”: Structural determinants of receptor-binding specificity in influenza A viruses. *Nat Rev Microbiol* 2014;**12**:822–31.

Shimojima M, Ikeda Y, Kawaoka Y. The Mechanism of Axl-Mediated Ebola Virus Infection. *J Infect Dis* 2007;**196**:S259–63.

Shoemaker CJ, Schornberg KL, Delos SE *et al.* Multiple cationic amphiphiles induce a Niemann-Pick C phenotype and inhibit Ebola virus entry and infection. *PLoS One* 2013;**8**:e56265.

Siegel D, Warren TK, Palacios G *et al.* Therapeutic efficacy of the small molecule GS-5734 against Ebola virus in rhesus monkeys. *Nature* 2016;**531**:381–5.

Simmons G, Gosalia DN, Rennekamp AJ *et al.* Inhibitors of cathepsin L prevent severe acute respiratory syndrome coronavirus entry. *Proc Natl Acad Sci* 2005;**102**:11876–81.

Simmons G, Reeves JD, Grogan CC *et al.* DC-SIGN and DC-SIGNR bind Ebola glycoproteins and enhance infection of macrophages and endothelial cells. *Virology* 2003a;**305**:115–23.

Simmons G, Rennekamp AJ, Chai N *et al.* Folate receptor alpha and caveolae are not required for Ebola virus glycoprotein-mediated viral infection. *J Virol* 2003b;**77**:13433–8.

Simmons G, Wool-lewis RJ, Netter RC *et al.* Ebola Virus Glycoproteins Induce Global Surface Protein Down-Modulation and Loss of Cell Adherence Ebola Virus Glycoproteins Induce Global Surface Protein Down-Modulation and Loss of Cell Adherence. *J Virol* 2002;**76**:2518–28.

Simmons JA, D'Souza RS, Ruas M *et al.* Ebolavirus Glycoprotein Directs Fusion through NPC1^{+} Endolysosomes. *J Virol* 2016;**90**:605–10.

Sinn PL, Hickey MA, Staber PD *et al.* Lentivirus Vectors Pseudotyped with Filoviral Envelope Glycoproteins Transduce Airway Epithelia from the Apical Surface Independently of Folate Receptor Alpha. *J Virol* 2003;**77**:5902–10.

Sissoko D, Laouenan C, Folkesson E *et al.* Experimental Treatment with Favipiravir for Ebola Virus Disease (the JIKI Trial): A Historically Controlled, Single-Arm Proof-of-Concept Trial in Guinea. *PLoS Med* 2016;**13**:e1001967.

Skehel JJ, Wiley DC. Receptor Binding and Membrane Fusion in Virus Entry: The Influenza Hemagglutinin. *Annu Rev Biochem* 2000;**69**:531–69.

Skočaj M, Resnik N, Grundner M *et al.* Tracking cholesterol/sphingomyelin-rich membrane domains with the ostreolysin A-mCherry protein. *PLoS One* 2014;**9**:e92783.

Spence JS, Krause TB, Mittler E *et al.* Direct Visualization of Ebola Virus Fusion Triggering in the Endocytic Pathway. *MBio* 2016;**7**:e10857–15.

Springer S, Döring K, Skipper JCA *et al.* Fast association rates suggest a conformational change in the MHC class I molecule H-2Db upon peptide binding. *Biochemistry* 1998;**37**:3001–12.

Stanley DA, Honko AN, Asiedu C *et al.* Chimpanzee adenovirus vaccine generates acute and durable protective immunity against ebolavirus challenge. *Nat Med* 2014;**20**:1126–9.

Stech J, Garn H, Wegmann M *et al.* A new approach to an influenza live vaccine: Modification of the cleavage site of hemagglutinin. *Nat Med* 2005;**11**:683–9.

Stiborová M, Poljaková J, Martínková E *et al.* Ellipticine cytotoxicity to cancer cell lines-a comparative study. *Interdiscip Toxicol* 2011;**4**:98–105.

Suárez T, Gómara MJMJ, Goñi FM *et al.* Calcium-dependent conformational changes of membrane-bound Ebola fusion peptide drive vesicle fusion. *FEBS Letters* 2003;**535**:23–8.

Sugita Y, Matsunami H, Kawaoka Y *et al.* Cryo-EM structure of the Ebola virus nucleoprotein–RNA complex at 3.6 Å resolution. *Nature* 2018;**563**:137–140.

Sukhai MA, Prabha S, Hurren R *et al.* Lysosomal disruption preferentially targets acute myeloid leukemia cells and progenitors. *J Clin Invest* 2013;**123**:315–28.

Sun W, He S, Martínez-Romero C *et al.* Synergistic drug combination effectively blocks Ebola virus infection. *Antiviral Res* 2017;**137**:165–72.

Sunagawa M, Kosugi T, Nakamura M *et al.* Pharmacological Actions of Calmidazolium, a Calmodulin Antagonist, in Cardiovascular System. *Cardiovasc Drug Rev* 2000;**18**:211–21.

Suzuki-Inoue K, Hughes CE, Inoue O *et al.* Involvement of Src kinases and PLCγ2 in clot retraction. *Thromb Res* 2007;**120**:251–8.

Svanström H, Pasternak B, Hviid A *et al.* Use of clarithromycin and roxithromycin and risk of cardiac death: cohort study. *Bmj* 2014;**349**:g4930.

Swanson J, Watts C. Macropinocytosis. *Trends Cell Biol* 1995;**5**:424–8.

Sweiti H, Ekwunife O, Jaschinski T *et al.* Repurposed Therapeutic Agents Targeting the Ebola Virus: A Systematic Review. *Curr Ther Res - Clin Exp* 2017;**84**:10–21.

Takada A, Watanabe S, Ito H *et al.* Downregulation of beta1 integrins by Ebola virus glycoprotein: implication for virus entry. *Virology* 2000;**278**:20–6.

Takada A. Filovirus tropism: Cellular molecules for viral entry. *Front Microbiol* 2012;**3**:1–9.

Takada A, Fujioka K, Tsuiji M *et al.* Human macrophage C-type lectin specific for galactose and N-acetylgalactosamine promotes filovirus entry. *J Virol* 2004;**78**:2943–7.

Takada A, Robison C, Goto H *et al.* A system for functional analysis of Ebola virus glycoprotein. *Proc Natl Acad Sci U S A* 1997;**94**:14764–9.

Tardy C, Codogno P, Autefage H *et al.* Lysosomes and lysosomal proteins in cancer cell death (new players of an old struggle). *Biochim Biophys Acta - Rev Cancer* 2006;**1765**:101–25.

Teissier E, Zandomeneghi G, Loquet A *et al.* Mechanism of inhibition of enveloped virus membrane fusion by the antiviral drug arbidol. *PLoS One* 2011;**6**;e15874.

Tharkeshwar AK, Trekker J, Vermeire W *et al.* A novel approach to analyze lysosomal dysfunctions through subcellular proteomics and lipidomics: the case of NPC1 deficiency. *Sci Rep* 2017;**7**:41408.

Townsend A, Öhlén C, Bastin J *et al.* Association of class I major histocompatibility heavy and light chains induced by viral peptides. *Nature* 1989;**340**:443–8.

Trinh MN, Lu F, Li X *et al.* Triazoles inhibit cholesterol export from lysosomes by binding to NPC1. *Proc Natl Acad Sci* 2017;**114**:89–94.

Tscherne DM, Manicassamy B, García-Sastre A. An enzymatic virus-like particle assay for sensitive detection of virus entry. *J Virol Methods* 2010;**163**:336–43.

Tseng L-L, Huang C-J, Hsu S-S *et al.* Effect of calmidazolium on Ca^{2+} movement and proliferation in human osteosarcoma cells. *Clin Exp Pharmacol Physiol* 2004;**31**:732–7.

Turone F. Doctors trial amiodarone for Ebola in Sierra Leone. *BMJ* 2014;**349**:g7198.

Uchimoto T, Nohara H, Kamehara R *et al.* Mechanism of apoptosis induced by a lysosomotropic agent, L-Leucyl-L-Leucine methyl ester. *Apoptosis* 1999;**4**:357–62.

Vance JE, Karten B. Niemann-Pick C disease and mobilization of lysosomal cholesterol by cyclodextrin. *J Lipid Res* 2014;**55**:1609–21.

Vandenberg JI, Perry MD, Perrin MJ *et al.* hERG K^+ Channels: Structure, Function, and Clinical Significance. *Physiol Rev* 2012;**92**:1393–478.

Vanier MT. Niemann-Pick disease type C Review. *Orphanet J Rare Dis* 2010;**5**:1–18.

Vanier MT, Gissen P, Bauer P *et al.* Diagnostic tests for Niemann-Pick disease type C (NP-C): A critical review. *Mol Genet Metab* 2016;**118**:244–54.

Vanier MT, Millat G. Structure and function of the NPC2 protein. *Biochim Biophys Acta - Mol Cell Biol Lipids* 2004;**1685**:14–21.

Vanier MT, Rodriguez-Lafrasse C, Rousson R *et al.* Type C Niemann-Pick disease: spectrum of phenotypic variation in disruption of intracellular LDL-derived cholesterol processing. *Biochim Biophys Acta* 1991;**1096**:328–37.

da Veiga Pereira L, Desnick RJ, Adler DA *et al.* Regional assignment of the human acid sphingomyelinase gene (SMPD1) by PCR analysis of somatic cell hybrids and in situ hybridization to 11p15.1→p15.4. *Genomics* 1991;**9**:229–34.

Venkatachalam K, Wong CO, Zhu MX. The role of TRPMLs in endolysosomal trafficking and function. *Cell Calcium* 2015;**58**:48–56.

Volchkov VE. Recovery of Infectious Ebola Virus from Complementary DNA: RNA Editing of the GP Gene and Viral Cytotoxicity. *Science* 2001;**291**:1965–9.

Volchkov VE, Feldmann H, Volchkova VA *et al.* Processing of the Ebola virus glycoprotein by the proprotein convertase furin. *Proc Natl Acad Sci* 1998;**95**:5762–7.

te Vruchte D, Speak AO, Wallom KL *et al.* Relative acidic compartment volume as a lysosomal storage disorder-associated biomarker. *J Clin Invest* 2014;**124**:1320–8.

Wang H, Shi Y, Song J *et al.* Ebola Viral Glycoprotein Bound to Its Endosomal Receptor Niemann-Pick C1. *Cell* 2016;**164**:258–68.

Wang ML, Motamed M, Infante RE *et al.* Identification of surface residues on Niemann-Pick C2 essential for hydrophobic handoff of cholesterol to NPC1 in lysosomes. *Cell Metab* 2010;**12**:166–73.

Wang X, Zhang X, Dong X *et al.* TPC Proteins Are Phosphoinositide- Activated Sodium-Selective Ion Channels in Endosomes and Lysosomes. *Cell* 2012;**151**:372–83.

Warfield KL, Bosio CM, Welcher BC *et al.* Ebola virus-like particles protect from lethal Ebola virus infection. *Proc Natl Acad Sci* 2003;**100**:15889–94.

Warren TK, Jordan R, Lo MK *et al.* Therapeutic efficacy of the small molecule GS-5734 against Ebola virus in rhesus monkeys. *Nature* 2016;**531**:381–5.

Warren TK, Wells J, Panchal RG *et al.* Protection against filovirus diseases by a novel broad-spectrum nucleoside analogue BCX4430. *Nature* 2014;**508**:402–5.

Webb SR, Smith SE, Fried MG *et al.* Transmembrane domains of highly pathogenic viral fusion proteins exhibit trimeric association *in vitro*. *mSphere* 2018;**3**:e00047–18.

Weissenhorn W, Calder LJ, Wharton SA *et al.* The central structural feature of the membrane fusion protein subunit from the Ebola virus glycoprotein is a long triple-stranded coiled coil. *Proc Natl Acad Sci* 2002;**95**:6032–6.

Weissenhorn W, Carfí A, Lee K-H *et al.* Crystal Structure of the Ebola Virus Membrane Fusion Subunit, GP2, from the Envelope Glycoprotein Ectodomain. *Mol Cell* 1998;**2**:605–16.

Weissenhorn W, Dessen A, Calder LJ *et al.* Structural basis for membrane fusion by enveloped viruses. *Molecular Membrane Biology*. 1999;**16**:3–9.

Welsch S, Müller B, Kräusslich HG. More than one door - Budding of enveloped viruses through cellular membranes. *FEBS Lett* 2007;**581**:2089–97.

White JM, Whittaker GR. Fusion of Enveloped Viruses in Endosomes. *Traffic* 2016;**17**:593–614.

WHO. Ebola Virus Disease in West Africa — The First 9 Months of the Epidemic and Forward Projections. *N Engl J Med* 2014;**371**:1481–95.

Wilkinson DE, Page M, Mattiuzzo G *et al.* Comparison of platform technologies for assaying antibody to Ebola virus. *Vaccine* 2017;**35**:1347–52.

Williams AR, Douglas AD, Miura K *et al.* Enhancing Blockade of Plasmodium falciparum Erythrocyte Invasion: Assessing Combinations of Antibodies against PfRH5 and Other Merozoite Antigens. *PLoS Pathog* 2012;**8**:e1002991.

Wilson JA, Hevey M, Bakken R *et al.* Epitopes involved in antibody-mediated protection from Ebola virus. *Science* 2000;**287**:1664–6.

WHO. (February 2019a). *Ebola response in Democratic Republic of the Congo rrisks slowdown.* Retrieved from https://www.who.int/news-room/detail/26-02-2019-ebola-response-in-democratic-republic-of-the-congo-risks-slowdown

WHO. (March 2019b). Ebola virus disease. *Ebola situation reports: Democratic Republic of the Congo.* Retrieved from https://www.who.int/ebola/situation-reports/drc-2018/en/

WHO. (February 2018a). Ebola virus disease. *Fact sheets*. Retrieved from https://www.who.int/news-room/fact-sheets/detail/ebola-virus-disease

WHO (August 2018b). *Notes for the record: Consultation on Monitored Emergency Use of Unregistered and Investigational Interventions (MEURI) for Ebola Virus Disease (EVD).* Retrieved from https://www.who.int/ebola/drc-2018/notes-for-the-record-meuri-ebola.pdf

WHO. (October 2015). Essential medicines and health products. *Ebola research and development landscape of clinical candidates and trials.* Retrieved from https://www.who.int/medicines/ebola-treatment/rd_clinical_candidates_trials_report/en/

WHO. (2014a). Emergencies preparedness, response. *Ethical considerations for use of unregistered interventions for Ebola virus disease.* Retrieved from https://www.who.int/csr/resources/publications/ebola/ethical-considerations/en/

WHO. (September 2014b). Media centre. *Statement on the WHO Consultation on potential Ebola therapies and vaccines.* Retrieved from https://www.who.int/mediacentre/news/statements/2014/ebola-therapies-consultation/en/s

Wong AC, Sandesara RG, Mulherkar N *et al.* A Forward Genetic Strategy Reveals Destabilizing Mutations in the Ebolavirus Glycoprotein That Alter Its Protease Dependence during Cell Entry. *J Virol* 2010;**84**:163–75.

Wool-Lewis RJ, Bates P. Characterization of Ebola virus entry by using pseudotyped viruses: identification of receptor-deficient cell lines. *J Virol* 1998;**72**:3155–60.

Worthington RJ, Melander C. Combination approaches to combat multidrug-resistant bacteria. *Trends Biotechnol* 2013;**31**:177–84.

Wright CS. Structural comparison of the two distinct sugar binding sites in wheat germ agglutinin isolectin II. *J Mol Biol* 1984;**178**:91–104.

Xiao JH, Rijal P, Schimanski L *et al.* Characterization of Influenza Virus Pseudotyped with Ebolavirus Glycoprotein. *J Virol* 2018;**92**:e00941–17.

Xiong ZJ, Huang J, Poda G *et al.* Structure of Human Acid Sphingomyelinase Reveals the Role of the Saposin Domain in Activating Substrate Hydrolysis. *J Mol Biol* 2016;**428**:3026–42.

Xue H, Li J, Xie H *et al.* Review of drug repositioning approaches and resources. *Int J Biol Sci* 2018;**14**:1232–44.

Yamasaki M, Masgrau R, Morgan AJ *et al.* Organelle Selection Determines Agonist-specific Ca^{2+} Signals in Pancreatic Acinar and β Cells. *J Biol Chem* 2004;**279**:7234–40.

Yang ZY, Duckers HJ, Sullivan NJ *et al.* Identification of the Ebola virus glycoprotein as the main viral determinant of vascular cell cytotoxicity and injury. *Nat Med* 2000;**6**:886–9.

Yuan S, Cao L, Ling H *et al.* TIM-1 acts a dual-attachment receptor for Ebolavirus by interacting directly with viral GP and the PS on the viral envelope. *Protein Cell* 2015;**6**:814–24.

Zaki SR, Goldsmith CS. Pathologic Features of Filovirus Infections in Humans. *Curr Top Microbiol Immunol* 1999;**235**:97–116.

Zapatero-Belinchón F, Dietzel E, Dolnik O *et al.* Characterization of the Filovirus-Resistant Cell Line SH-SY5Y Reveals Redundant Role of Cell Surface Entry Factors. *Viruses* 2019;**11**:275.

Zhang J, Leser GP, Pekosz A *et al.* The Cytoplasmic Tails of the Influenza Virus Spike Glycoproteins Are Required for Normal Genome Packaging. *Virology* 2000;**269**:325–34.

Zhang J, Pekosz A, Lamb RA. Influenza virus assembly and lipid raft microdomains: a role for the cytoplasmic tails of the spike glycoproteins. *J Virol* 2000;**74**:4634–44.

Zhang M, Sun M, Dwyer N *et al.* Differential trafficking of the Niemann-Pick C1 and 2 proteins highlights distinct roles in late endocytic lipid trafficking. *Acta Paediatr* 2003;**92**:63–73.

Zhang Y, Li X, Carpinteiro A *et al.* Acid Sphingomyelinase Amplifies Redox Signaling in Pseudomonas aeruginosa-Induced Macrophage Apoptosis. *J Immunol* 2014;**181**:4247–54.

Zhao Y, Ren J, Fry EE *et al.* Structures of Ebola Virus Glycoprotein Complexes with Tricyclic Antidepressant and Antipsychotic Drugs. *J Med Chem* 2018;**61**:4938–45.

Zhao Y, Ren J, Harlos K *et al.* Toremifene interacts with and destabilizes the Ebola virus glycoprotein. *Nature* 2016;**535**:169–72.

Zhu MX, Evans AM, Galione A *et al.* Calcium signaling via two-pore channels: local or global, that is the question. *Am J Physiol Physiol* 2009;**298**:C430–1.

Zong X, Schieder M, Cuny H *et al.* The two-pore channel TPCN2 mediates NAADP-dependent $Ca^{(2+)}$-release from lysosomal stores. *Pflugers Arch* 2009;**458**:891–9.